

# TABLE OF CONTENTS

<u>Section</u>	<u>Page No.</u>
LIST OF ILLUSTRATIONS	iv 1/A5
SUMMARY	1 1/A7
INTRODUCTION	2 1/A8
LIST OF SYMBOLS	4 1/A10
ANALYSIS	8 1/A14
The Mathematical Model - Formulation of the Fluid Representation	8 1/A14
<u>Governing equations</u>	8 1/A14
<u>Conditions at discontinuities</u>	10 1/B2
<u>Frozen-field approximation</u>	12 1/B4
Determination of the Ionosphere Boundary	14 1/B6
Calculation of the Gasdynamic Flow Properties	20 1/B12
<u>Nose region solution - implicit unsteady Euler equation method</u>	21 1/B13
<u>Downstream region solution - shock capturing marching method</u>	25 1/C3
<u>Calculation of the streamlines</u>	27 1/C5
Calculation of the Magnetic Field	27 1/C5
Calculation of the Contour Lines	30 1/C8
Solar-Ecliptic/Solar-Wind Coordinate Transformations	31 1/C9
Properties Along a Spacecraft Trajectory	33 1/C11
RESULTS	36 1/C14
CONCLUDING REMARKS	47 1/D11
ACKNOWLEDGEMENTS	48 1/D12
APPENDIX A - COMPUTER PROGRAM USER'S MANUAL	49 1/D13
APPENDIX B - LISTING OF COMPUTER PROGRAM	131 2/D1
APPENDIX C - CATALOG OF TEST CASES	177 3/C10
REFERENCES	287 4/D10
TABLE 1	289 4/D12
FIGURES 1 THROUGH 20	291 4/E3

JUN 6 1980

NA 51.26: 3267

COMPLETED

NASA Contractor Report 3267

ORIGINAL

Application of Advanced Computational  
Procedures for Modeling Solar-Wind  
Interactions With Venus -  
Theory and Computer Code

Stephen S. Stahara, Daniel Klenke,  
Barbara C. Trudinger, and John R. Spreiter

CONTRACT NASW-3182  
MAY 1980

MICROFILMED FROM  
BEST AVAILABLE COPY

NASA

318



**NASA Contractor Report 3267**

**Application of Advanced Computational  
Procedures for Modeling Solar-Wind  
Interactions With Venus -  
Theory and Computer Code**

**Stephen S. Stahara, Daniel Klenke,  
Barbara C. Trudinger, and John R. Spreiter**  
*Nielsen Engineering & Research, Inc.  
Mountain View, California*

**Prepared for  
NASA Headquarters  
under Contract NASW-3182**



**National Aeronautics  
and Space Administration**

**Scientific and Technical  
Information Office**

**1980**

# TABLE OF CONTENTS

<u>Section</u>	<u>Page No.</u>
LIST OF ILLUSTRATIONS	iv
SUMMARY	1
INTRODUCTION	2
LIST OF SYMBOLS	4
ANALYSIS	8
The Mathematical Model - Formulation of the Fluid Representation	8
<u>Governing equations</u>	8
<u>Conditions at discontinuities</u>	10
<u>Frozen-field approximation</u>	12
Determination of the Ionosphere Boundary	14
Calculation of the Gasdynamic Flow Properties	20
<u>Nose region solution - implicit unsteady Euler equation method</u>	21
<u>Downstream region solution - shock capturing marching method</u>	25
<u>Calculation of the streamlines</u>	27
Calculation of the Magnetic Field	27
Calculation of the Contour Lines	30
Solar-Ecliptic/Solar-Wind Coordinate Transformations	31
Properties Along a Spacecraft Trajectory	33
RESULTS	36
CONCLUDING REMARKS	47
ACKNOWLEDGEMENTS	48
APPENDIX A - COMPUTER PROGRAM USER'S MANUAL	49
APPENDIX B - LISTING OF COMPUTER PROGRAM	131
APPENDIX C - CATALOG OF TEST CASES	177
REFERENCES	287
TABLE 1	289
FIGURES 1 THROUGH 20	291

# LIST OF ILLUSTRATIONS

<u>Figure</u>	<u>Page No.</u>
1. Illustration of ionopause shapes for atmospheres with various (i) constant scale heights $H/R_0$ and (ii) gravitational variation included in the scale height $\bar{H}/R_0$ .	291
2. Comparison of former and present computational procedures for determining the gasdynamic flow properties of solar wind-magneto/ionopause interactions	292
3. Transformation from physical domain to rectangular computational domain	293
4. Illustration of capability for providing an additional flow-field segment to the obstacle nose solution in the computational procedure for determining the gasdynamic flow properties of solar wind-ionopause interactions	294
5. Illustration of quantities used for streamline calculation	295
6. Illustration of quantities used for magnetic field-line calculation in the plane of magnetic symmetry	295
7. Illustration of the components of the three-dimensional magnetic field	296
8. Illustration of the sun-planet $(x_s, y_s, z_s)$ and solar wind $(x, y, z)$ coordinate systems and the azimuthal $(\Omega)$ and polar $(\phi_p)$ solar-wind angles, both shown in a positive sense	297
9. Illustration of solar-wind $(x, y, z)$ and $(X, Y, Z)$ coordinate systems and the interplanetary magnetic field and magnetic-field angles $(\alpha_p, \alpha_n)$	298
10. Bow shock locations for $M_\infty = 8.0$ , $\gamma = 5/3$ flow past constant scale-height ionopause shapes with $H/R_0 = 0.5$ and $1.0$	299
11. Bow shock shapes for flow past an ionopause shape with gravitational variation included in scale height with $H/R_0 = 0.25$ , $\gamma = 5/3$ and $M_\infty = 2.0$ and $3.0$	300
12. Overall features of Pioneer-Venus Orbiter trajectory crossings of solar-wind/Venus-ionosphere interaction region	301
13. Illustration of typical flow-field grid density for gasdynamic solution; $M_\infty = 3.0$ , $\gamma = 5/3$	302
14. P-V Orbit 6 trajectories and observational bow shock crossings as viewed in solar-wind coordinates based on inbound and outbound interplanetary solar-wind directions; also, various bow shock shapes for different interplanetary solar-wind conditions	303

# LIST OF ILLUSTRATIONS (Concluded)

<u>Figure</u>	<u>Page No.</u>
15. Comparison of observed (OPA) and theoretical time histories of ionosheath plasma properties for P-V Orbit 6 based on inbound and outbound interplanetary solar-wind conditions using a gasdynamic solution for $M_{\infty} = 13.3$ , $\gamma = 2.0$	304
16. Comparison of observed (OMAG) and theoretical time histories for the magnitude of the magnetic field for P-V Orbit 6 based on inbound and outbound interplanetary conditions using gasdynamic solution for $M_{\infty} = 13.3$ , $\gamma = 2$	305
17. P-V Orbit 3 trajectories and observational bow shock crossings as viewed in solar-wind coordinates based on inbound and outbound interplanetary solar-wind directions; also, various bow shock shapes for different interplanetary solar wind conditions	307
18. Comparison of observed and theoretical time histories of ionosheath plasma properties for P-V Orbit 3 based on inbound and outbound interplanetary solar-wind conditions	308
19. Comparison of observed (OMAG) and theoretical time histories for the magnetic field for P-V Orbit 3 based on inbound and outbound interplanetary solar-wind conditions using gasdynamic solutions $M_{\infty} = 7.38$ , $\gamma = 2.0$ for inbound and $M_{\infty} = 5.96$ , $\gamma = 2.0$ for outbound calculations	309
20. Comparison of observed (OMAG) and theoretical time histories of the magnetic field for P-V Orbit 3 based on inbound solar wind interplanetary conditions using a gasdynamic solution for $M_{\infty} = 3.0$ , $\gamma = 5/3$	311

APPLICATION OF ADVANCED COMPUTATIONAL PROCEDURES FOR  
MODELING SOLAR-WIND INTERACTIONS WITH VENUS - THEORY  
AND COMPUTER CODE

by

Stephen S. Stahara, Daniel Klenke,  
Barbara C. Trudinger, and John R. Spreiter

SUMMARY

Advanced computational procedures are developed and applied to the prediction of solar-wind interaction with nonmagnetic terrestrial-planet atmospheres, with particular emphasis to Venus. The theoretical method is based on a single-fluid, steady, dissipationless, magnetohydrodynamic continuum model, and is appropriate for the calculation of axisymmetric, supersonic, super-Alfvénic solar-wind flow past terrestrial planets. The procedures, which consist of finite-difference codes to determine the gasdynamic properties and a variety of special-purpose codes to determine the frozen magnetic field, streamlines, contours, plots, etc. of the flow, are organized into one computational program which has been extensively documented and is presented in a general user's manual included as part of this report.

Theoretical results based upon these procedures are reported for a wide variety of solar-wind conditions and ionopause obstacle shapes. Plasma and magnetic-field comparisons in the ionosheath are also provided with actual spacecraft data obtained by the Pioneer-Venus Orbiter. These results have verified the appropriateness of the basic theoretical model, and have indicated the importance of accounting for the variable oncoming direction of the interplanetary solar wind.

## INTRODUCTION

The magnetohydrodynamic models (refs. 1-9) of solar-wind interaction with planetary magneto/ionospheres and their associated calculations of the detailed flow and magnetic-field properties provide the basis of the theoretical understanding and interpretation of phenomena occurring in space around terrestrial planets from the viewpoint of a fluid rather than particle description of the flow. The general value and usefulness of results based on these models are now well established, and have advanced to the point where theoretical calculations can be used to predict important planetary and magnetic-field characteristics.

Prior to the previous work reported in reference 9, the utility of calculations based on these models was severely restricted due both to the fact that the original solution techniques employed bordered on what was barely possible at the time, as well as that considerable hand computation and intervention was required. Moreover, reported results were carried out for only a limited set of solar-wind conditions such as obstacle shape, oncoming Mach number, interplanetary magnetic field, etc., and were presented in archival publications only in the form of plots from which results for other conditions had to be determined by interpolation. The importance of the preliminary work of reference 9 was that advanced computational methods, based on current state-of-the-art algorithms, were introduced to this problem to provide the basic gasdynamic solutions. The frozen-in magnetic-field was then solved for on the high-resolution flow-field grid, and the entire computational procedure was assembled into a user-oriented program providing the detailed flow-field and magnetic-field properties in a convenient output format.

In the current work reported here, those basic procedures have been extended and generalized in several important directions. These include the capability for treating very low oncoming interplanetary gasdynamic Mach numbers ( $M_\infty = 2.0$ ), as well as quite general ionopause shapes. A new family of ionopause shapes has been developed which accounts for the effect of gravitational variation in scale height. Additionally, the capability for determining the plasma gasdynamic and magnetic-field properties along an arbitrary spacecraft trajectory, simultaneously accounting

for an arbitrary oncoming direction of the solar wind, has been developed. Moreover, a large number of sample calculations have been performed for typical solar-wind conditions and, using the output contour-plot capability, a catalog of these cases were established and are archived here for convenient quick-look use. Finally, a number of successful comparisons were made by the present computational model with actual spacecraft observations obtained from initial orbits of the Pioneer-Venus Orbiter. These comparisons have both provided a verification of the basic theoretical model as well as demonstrated its value as a convenient research tool capable of routinely providing details of the solar-wind/planetary atmosphere interaction process not previously attainable--at modest computational cost and in a format directly compatible with observational data.

# LIST OF SYMBOLS

$a$	speed of sound, $(\gamma p/\rho)^{1/2}$
$A$	Alfvén speed, $(B^2/4\pi\rho)^{1/2}$
$\bar{A}$	Jacobian matrix associated with IMP code, equal to $\partial\hat{E}/\partial\hat{U}$
$\underline{B}$	magnetic field vector
$\bar{B}$	Jacobian matrix associated with IMP code, equal to $\partial\hat{F}/\partial\hat{U}$
$C_p$	specific heat at constant pressure
$C_v$	specific heat at constant volume
$D$	distance defined by eq. (59)
$e$	internal energy, eq. (3)
$e_t$	total energy, eq. (44)
$E$	column matrix defined by eq. (42)
$\hat{E}$	column matrix associated with IMP code, equal to $(\xi_T U + \xi_X E + \xi_R F)/J$
$F$	column matrix defined by eq. (42)
$\hat{F}$	column matrix associated with IMP code, equal to $(\eta_T U + \eta_X E + \eta_R F)/J$
$g$	acceleration due to gravity
$g_k$	gravitational component, eq. (5)
$G$	column matrix defined by eq. (42)
$h$	enthalpy, eq. (47)
$h_t$	total enthalpy, eq. (47)
$H$	local scale height of atmosphere, $\bar{R}T/\bar{M}g$
$\bar{H}$	local scale height with gravitational variation, $H(R_R/R_S)^2$
$J$	Jacobian matrix, eq. (43)
$K$	constant defined by eq. (34)
$\Delta\ell$	vector length of elemental magnetic flux tube
$M$	local Mach number, $ \underline{v} /a$
$\bar{M}$	nondimensional mean molecular mass, equal to 1/2 for ionized atomic hydrogen



# LIST OF SYMBOLS (Continued)

$M_A$	local Alfven Mach number, $ \mathbf{v} /A$
$p$	pressure
$q$	shock velocity
$Q$	dummy parameter
$r$	spherical radial distance
$R$	cylindrical radial distance
$\bar{R}$	gas constant, $8.315 \times 10^7 \text{ ergs/gm}^\circ\text{K}$
$R_i$	spherical radius of ionopause, eq. (39)
$R_o$	spherical distance from center of planet to ionopause nose
$S_k$	Poynting vector component
$\Delta S$	incremental distance along streamline
$t, T$	time
$(u, v, w)$	velocity components associated with the $(X, Y, Z)$ coordinate directions, respectively
$U$	column matrix defined by eq. (42)
$\hat{U}$	column matrix associated with IMP code, equal to $U/J$
$\mathbf{v}$	velocity vector
$(x, y, z)$ or $(x_w, y_w, z_w)$	solar-wind oriented Cartesian coordinates with origin at planetary center, $x$ positive upstream and $z$ positive northward
$(x_s, y_s, z_s)$	sun-planet oriented Cartesian coordinates with origin at planetary center, $x_s$ positive toward sun, $y_s$ positive opposite to planetary orbital motion, and $z_s$ positive northward
$(x', y', z')$	solar-wind oriented Cartesian coordinates defined by an azimuthal rotation given by eq. (70)
$(X, Y, Z)$	solar-wind oriented Cartesian coordinates with origin at planetary center, $X$ positive downstream and $Z$ positive northward
$\alpha_p$	interplanetary magnetic-field angle between perpendicular and parallel components, eq. (62)
$\alpha_n$	interplanetary magnetic-field angle between normal and in-plane components, eq. (63)

# LIST OF SYMBOLS (Continued)

$\beta$	spherical polar angle, measured with origin at planet center, from subsolar point away from undisturbed solar wind direction; varies from 0 in upstream direction to $\pi$ in downstream direction; eq. (39)
$\gamma$	ratio of plasma specific heats
$\delta$	angle defined by eq. (59)
$\delta_{ik}$	Kronecker delta
$\delta_S$	local angle of bow shock wave
$(\delta_\xi, \delta_\eta)$	second-order difference operators in ( , ) direction
$\epsilon$	smoothing coefficient in IMP code
$\eta$	transformation variable, eqs. (40), (48)
$\theta$	azimuthal rotation angle in solar-wind (X,Y,Z) system, eq. (69); also shock tangency angle, eq. (59)
$\Lambda$	quantity defined by eq. (36)
$\xi$	transformation variable, eqs. (40), (48)
$\rho$	density
$\sigma$	conductivity
$\tau$	transformed time, eq. (40)
$\phi$	gravitational potential, eq. (5)
$\phi_p$	solar-wind polar angle
$\psi$	angle between outward normal to magneto/ionosphere boundary and oncoming undisturbed solar wind, eq. (32); also, angle of magnetic component $(B/B_\infty)_\perp$ , eq. (58)

## Subscripts

b	obstacle body
i	ionopause
n	normal direction
P	arbitrary point
R	reference quantity
s	planetary surface; also streamline
S	shock surface

# LIST OF SYMBOLS (Concluded)

$s_t$	stagnation conditions
$t$	tangential direction
$o$	reference quantity at subsolar point
$1$	conditions upstream of a discontinuity
$2$	conditions downstream of a discontinuity
$\infty$	interplanetary undisturbed quantity
$(\parallel, \perp, n)$	parallel, perpendicular, and normal magnetic-field components as defined in eq. (56)

## Superscripts

$\wedge$	unit vector
$*$	relative to shock

## ANALYSIS

### The Mathematical Model - Formulation of the Fluid Representation

The fundamental assumption underlying the present work and that reported in all of the references cited above is that the average bulk properties of solar-wind flow around a planetary magneto/ionosphere can be adequately described by the continuum equations of magnetohydrodynamics for a single-component perfect gas having infinite electrical conductivity and zero viscosity and thermal conductivity. Theoretical justification of this point has not yet been established, and proof remains essentially qualitative at present. The primary justification for use of the continuum fluid model is the outstanding agreement of the qualitative results predicted on this basis with those actually measured in space. It appears that the continuum model is capable of accounting both for many of the details as well as the broad features of the observations.

Governing equations.- The equations which express the conservation of the average bulk mass, momentum, energy, and magnetic field of the solar-wind plasma are given by the following expressions:

$$\frac{\partial \rho}{\partial t} + \frac{\partial}{\partial x_k} (\rho v_k) = 0 \quad (1)$$

$$\frac{\partial}{\partial t} (\rho v_i) + \frac{\partial}{\partial x_k} \left( \rho v_i v_k + P \delta_{ik} - \frac{B_i B_k}{4\pi} + \frac{B^2}{8\pi} \delta_{ik} + \frac{g_i g_k}{4\pi G} - \frac{g^2}{8\pi G} \delta_{ik} \right) = 0 \quad (2)$$

$$\frac{\partial}{\partial t} \left( \frac{\rho v^2}{2} + \rho e + \rho \phi + \frac{B^2}{8\pi} \right) + \frac{\partial}{\partial x_k} \left[ \rho v_k \left( \frac{v^2}{2} + e + \frac{P}{\rho} + \phi \right) + S_k \right] = 0 \quad (3)$$

$$\frac{\partial B_i}{\partial t} = \frac{\partial}{\partial x_k} (v_i B_k - v_k B_i), \quad \frac{\partial B_i}{\partial x_i} = 0 \quad (4)$$

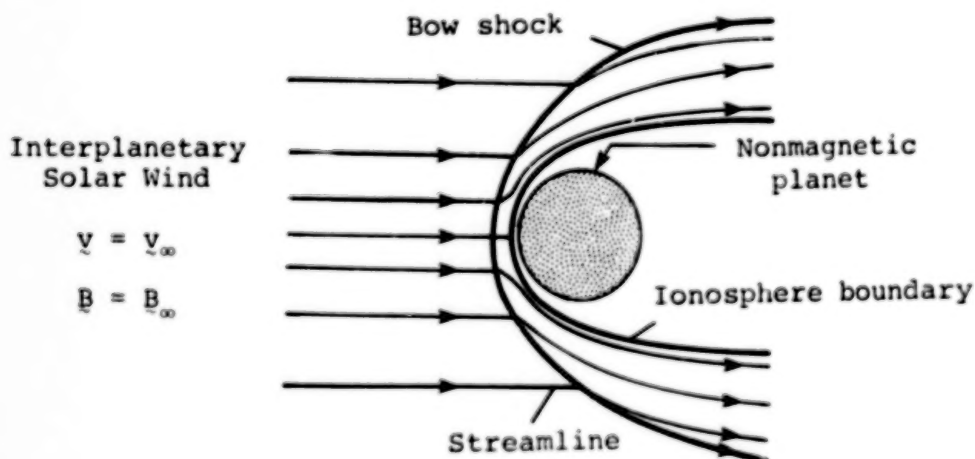
where

$$g_i = - \frac{\partial \phi}{\partial x_i} , \quad S_k = \frac{1}{4\pi} \left( v_k B^2 - B_k v_i B_i \right) \quad (5)$$

and the equation of state of a perfect gas is given by

$$p = \frac{\rho \bar{R} T}{\bar{M}} \quad (6)$$

In these equations and those to follow, the symbols  $\rho$ ,  $p$ ,  $v$ ,  $T$ ,  $e = C_v T$ , and  $h = C_p T$  refer to the density, pressure, velocity, temperature, internal energy and enthalpy, and  $C_v$  and  $C_p$  refer to the specific heats at constant volume and pressure. We define the symbol  $\bar{R} = (C_p - C_v) \bar{M} = 8.31 \times 10^7$  ergs/gm°K as the universal gas constant, and  $\bar{M}$  as the mean molecular weight nondimensionalized so that  $\bar{M} = 16$  for atomic oxygen. For fully ionized hydrogen,  $\bar{M}$  is thus 1/2. The magnetic field  $B$  and the Poynting vector  $S$  for the flux of electromagnetic energy are expressed in terms of gaussian units. The gravitational potential  $\phi$  and acceleration  $g$  are assumed to be due to massive fixed bodies so that their time derivatives are zero. These equations apply in the region exterior to the ionosphere boundary, as shown in the sketch below, and also in a degenerate sense in the ionosphere.



Conditions at discontinuities.— Because of the omission of dissipative terms in these equations, surfaces of discontinuity may develop in the solution, across which the fluid and magnetic properties change abruptly, but in such a way that mass, momentum, magnetic flux, and energy are conserved. These are approximations to comparatively thin surfaces across which similar but continuous changes in the fluid and magnetic properties occur in the corresponding theory of a dissipative gas, and correspond physically to the bow wave, ionosphere boundary, and possibly other thin regions of rapidly changing properties. Across these surfaces, continuous solutions of the dissipationless differential equations cease to exist. The flow is no longer governed solely by the differential equations (1) to (4), but must be supplemented by additional considerations. The conservation of mass, momentum, magnetic flux, and energy lead to the following conditions which relate quantities on the two sides of any such discontinuity:

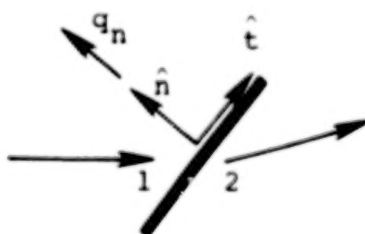
$$[\rho v_n^*] = 0 \quad (7)$$

$$[\rho \underline{v} \cdot \underline{v}_n^* + (p + B^2/8\pi) \hat{n} - B_n B_t/4\pi] = 0 \quad (8)$$

$$[B_t \cdot \underline{v}_n^* - B_n \cdot \underline{v}_t] = 0 \quad (9)$$

$$\left[ v_n^* \left( \frac{1}{2} \rho v^2 + \rho e + p + \frac{B^2}{4\pi} \right) + q_n \cdot \left( p + \frac{B^2}{8\pi} \right) - \frac{B_n (\underline{v} \cdot \underline{B})}{4\pi} \right] = 0 \quad (10)$$

Here,  $(\hat{n}, \hat{t})$  denote unit vectors normal and tangential to the discontinuity surface, as sketched below,



where  $q_n$  represents the local normal velocity of the discontinuity surface, and  $v_n^* = v_n - q_n$  is the fluid normal velocity component relative to the normal velocity  $q_n$  of the discontinuity surface. The square brackets are used to indicate the difference between the enclosed quantities on the two sides of the discontinuity, as in  $[Q] = Q_2 - Q_1$  where subscripts 1 and 2 refer to conditions on the upstream and downstream sides, respectively, of the discontinuity.

Five classes of discontinuities are described by Eqs. (7-10). Those with  $v_n^* = 0$  are called tangential discontinuities or contact discontinuities according to whether or not  $B_n$  vanishes. Discontinuities across which there is flow ( $v_n^* \neq 0$ ) are divided into three categories called rotational discontinuities, and fast and slow shock waves. Some properties which distinguish the various discontinuities are indicated by the following relationships:

Tangential:

$$v_n^* = B_n = 0, [v_t] \neq 0, [B_t] \neq 0, [\rho] \neq 0, [p + B^2/8\pi] = 0 \quad (11)$$

Contact:

$$v_n^* = 0, B_n \neq 0, [v] = [B] = [p] = 0, [\rho] \neq 0 \quad (12)$$

Rotational:

$$v_n^* = \pm B_n / \sqrt{4\pi\rho}, [v_t] = \pm [B_t] / \sqrt{4\pi\rho} \quad (13)$$

$$[\rho] = [p] = [v_n] = [v^2] = [B^2] = [B_n] = 0$$

# Fast and Slow Shock Waves:

$$v_n^* \neq 0, [\rho] > 0, [p] > 0, [B_n] = 0$$

$$\left(\rho v_n^*\right)_{\text{fast}} \geq \left(\rho v_n^*\right)_{\text{rot.}} \geq \left(\rho v_n^*\right)_{\text{slow}} \quad (14)$$

$$B_t \text{ and } B^2 \begin{pmatrix} \text{increase} \\ \text{decrease} \end{pmatrix} \text{ through } \begin{pmatrix} \text{fast} \\ \text{slow} \end{pmatrix} \text{ shock waves}$$

Of the five classes of discontinuities possible, two of these, the fast shock wave and the tangential discontinuity, are of concern in the present applications. The first relates conditions on the two sides of the bow shock wave, and any other shock waves present, while the latter has properties required to describe a boundary surface (ionopause) that separates the flowing solar wind and the planetary ionosphere. More detailed consideration of the tangential discontinuity condition leads to a determination of the ionopause shape, as described in the following sections.

With regard to conditions at the bow wave, for solar-wind flows past Venus, as well as Mars and the Earth, that discontinuity can only be represented by a fast shock wave since the mass flux through each of the other possible choices is too small. With regard to conditions at the ionopause, of the various possibilities, only the tangential discontinuity has properties compatible with those required to describe a boundary surface that separates the externally flowing solar wind and the planetary atmosphere; that is, the condition  $v_n^* = 0$  prohibits flow across the boundary, while the condition  $B_n = 0$  must hold since by assumption no magnetic field exists interior to the ionopause and the solenoidal jump condition  $[B_n] = 0$  always holds.

Frozen-field approximation.— Two important parameters characterize the solar-wind flow at any field point as described by eqs. (1-5). These are the Mach number  $M = v/a$  and the Alfvén Mach number  $M_A = v/A$ . The former is the ratio of the flow velocity to the speed of sound  $a = (\gamma p/\rho)^{1/2}$ , while the latter is the ratio of the flow velocity to the speed  $A =$



$(B^2/4\pi\rho)^{1/2}$  of a rotational or Alfvén wave propagating along the direction of the magnetic field.

For typical solar-wind conditions (refs. 5,6), both the oncoming Mach number and the Alfvén Mach number are high ( $M_\infty = M_A = O(10)$ ). In this instance, an important simplification of the magnetohydrodynamic equations occurs. This is so because the order of magnitude of the inertia term in differential equation (2) for the momentum is related to that of the magnetic terms by the square of the Alfvén Mach number. When the latter is large, therefore, the magnetic terms in eqs. (2), (3), (8), and (10) decouple from the gasdynamic portions of those equations. Furthermore, for Earth, Venus, or Mars, the strong interactive nature of the flow permits the terms involving  $\underline{g}$  and  $\underline{\phi}$  to be disregarded because of the relative smallness of their effect on the fluid motion (ref. 5). The equations for the fluid motion thereby reduce to those of gasdynamics, while the magnetic field  $\underline{B}$  can be determined subsequently by solving the remaining equations using the values for  $\underline{v}$  already determined. The magnetic field, determined in this fashion, is usually interpreted as being "frozen-in" or moving with the fluid (ref. 5).

This then results in the following differential and conservation equations; for the flow field

$$\frac{\partial \rho}{\partial t} + \frac{\partial}{\partial x_k} (\rho v_k) = 0 \quad (15)$$

$$\frac{\partial}{\partial t} (\rho v_i) + \frac{\partial}{\partial x_k} (\rho v_i v_k + p \delta_{ik}) = 0 \quad (16)$$

$$\frac{\partial}{\partial t} \left( \frac{\rho v^2}{2} + \rho e \right) + \frac{\partial}{\partial x_k} \left[ \rho v_k \left( \frac{v^2}{2} + e + p/\rho \right) \right] = 0 \quad (17)$$

$$[\rho v_n^*] = 0 \quad (18)$$

$$[\rho \underline{v} \cdot \underline{v}_n^* + p] = 0 \quad (19)$$

$$\left[ \mathbf{v}_n^* \cdot \left( \frac{1}{2} \rho v^2 + \rho e + p \right) \right] = 0 \quad (20)$$

and for the magnetic field

$$\frac{\partial B_i}{\partial t} + \frac{\partial}{\partial x_k} (v_k B_i - v_i B_k) = 0 \quad (21)$$

$$\frac{\partial B_i}{\partial x_i} = 0 \quad (22)$$

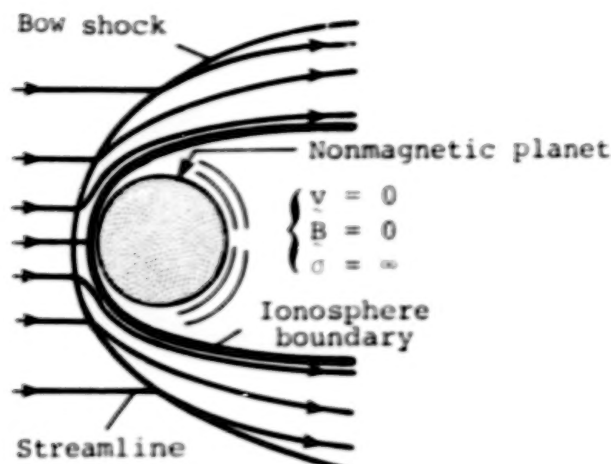
$$[B_n] = 0 \quad (23)$$

$$[B_n \cdot \mathbf{v}_t - B_t \cdot \mathbf{v}_n^*] = 0 \quad (24)$$

Equations (15) to (24) provide the governing equations which form the basis of the mathematical representation of the solar wind-magneto/ionosphere interaction problem considered here. For all of the results as well as the computer codes presented herein, we are interested exclusively in the steady-state solution to these equations which are obtained by setting  $\partial/\partial t = 0$  and  $\mathbf{v}_n^* = \mathbf{v}_n$ , i.e.  $q_n = 0$ . We have presented the unsteady equations, however, since one of the computational methods used to determine the gasdynamic solution employs an unsteady procedure, integrating in time until the steady-state solution is asymptotically obtained.

#### Determination of the Ionosphere Boundary

The determination of the ionosphere boundary initiates from the assumptions that the ionosphere, or at least the outer part of it that participates in the interaction with the solar wind, is idealized as a spherically-symmetric and hydrostatically-supported plasma having infinite electrical conductivity, effectively bound to the planet and incapable of mixing with the solar wind, as indicated in the sketch below:



This interior plasma is separated from the flowing solar plasma by a tangential discontinuity across which the relations

$$v_n = B_n = [p + B^2/8\pi] = 0 \quad (25)$$

$$[v_t] \neq 0; [B_t] \neq 0; [\rho] \neq 0$$

given previously (eq. (11)) must hold. The basis for important simplifying approximations to these conditions, which can be assumed to apply at the Venusian ionosphere boundary and possibly for that at Mars as well, is that the gas pressure  $p$  is much larger than the magnetic pressure  $B^2/8\pi$  on both sides of the ionopause. Therefore, the discontinuity pressure balance relation  $[p + B^2/8\pi] = 0$  of eq. (25) reduces to a simple equality between the ionosphere pressure and the static pressure of the flowing solar plasma adjacent to the ionopause, i.e.

$$(p)_{\text{atm.}} = (p)_{\text{flow}} \quad (26)$$

Determination of the ionospheric pressure in the vicinity of the ionopause for the ionosphere models chosen in this study proceeds from the assumption of hydrostatic support, which implies a quiescent ionosphere where the bulk motions of the gas with respect to the planet are sufficiently small ( $v = 0$ ) that equilibrium exists between the pressure gradient and gravity, viz.

$$dp/dr = -\rho g \quad (27)$$

where  $p$  and  $\rho$  are the gas pressure and density,  $r$  is the radial distance measured from the center of the planet, and  $g$  is the acceleration due to gravity. The variation of  $g$  is inversely proportional to  $r_s$ , so that  $g = g_s(r_s/r)^2$  where the subscript  $s$  denotes values at the surface of the planet. Since the density  $\rho$  is related to the pressure according to the perfect gas law eq. (6), eq. (27) can be integrated to yield

$$p = p_R \exp \left[ - \int_{R_R}^r \frac{dr}{H} \right] \quad (28)$$

where  $p_R$  is the pressure at some reference radius  $R_R$  and  $H$  is the local scale height of the atmosphere given by  $H = \bar{R}T/\bar{M}g$ .

If  $H$  is regarded as constant; that is, if variations of  $g$  and  $T$  with  $r$  are neglected, eq. (27) can be integrated directly to yield

$$p = p_R \exp \left[ - \frac{r - R_R}{H} \right] \quad (29)$$

In view of uncertainties associated with measurements of the atmospheric properties of Venus and Mars, the variation of  $p$  with  $r$  as given by eq. (29) was adopted in the initial solar wind/ionosphere applications (ref. 6) and was also used in the previous study (ref. 9) involving the initial application of advanced computational methods to this problem. With preliminary ionospheric data now available from the Pioneer-Venus spacecraft (refs. 10 and 11), some of these uncertainties for Venus have been removed. It has been found that the assumption of an isothermal ( $T = \text{constant}$ ) atmosphere at typical ionopause heights is quite reasonable. Consequently, there is no need to neglect the variation of gravity in the scale height in eq. (28). Including this effect leads to the following result for the pressure

$$p = p_R \exp \left[ - \frac{R_R \cdot (r - R_R)}{\bar{H} \cdot r} \right] \quad (30)$$

where

$$\bar{H} = H_s \cdot (R_R/R_s)^2 \quad (31)$$

and  $R_s$  is the planetary radius and  $H_s = \bar{RT}/\bar{M}g_s$ . Equations (29) and (30) provide the two models employed in this study for the ionosphere pressure variation which is required in eq. (26) for the pressure balance condition at the ionopause.

For the a priori determination of the static pressure of the flowing solar-wind plasma on the exterior boundary of the ionosphere -  $(p)_{\text{flow}}$  in eq. (26) - we use, as in all previous applications, the Newtonian approximation

$$p = p_{st} \cos^2 \psi \quad (32)$$

where  $\psi$  is the angle between the outward normal to the magnetosphere boundary and the flow direction of the oncoming undisturbed solar wind, and  $p_{st}$  is the stagnation or ram pressure exerted on the nose of the ionopause and is given by

$$p_{st} = K \rho_{\infty} v_{\infty}^2 \quad (33)$$

In this relation,  $K$  is a constant usually taken as one, but whose actual value is

$$K = \frac{1}{\gamma} \left[ \frac{\left[ (\gamma + 1)/2 \right] (\gamma + 1)}{\gamma - (\gamma - 1)/2M_{\infty}^2} \right]^{\frac{1}{\gamma - 1}} \quad (34)$$

For the high Mach number flows typical of solar-wind conditions,  $K$  approaches 0.844 for  $\gamma = 2$  and 0.881 for  $\gamma = 5/3$ . Modification of the product  $K\rho_{\infty}$  in eq. (33) to account for the presence of minor constituents such as ionized helium in the solar wind, as well as a discussion of the differences in that product between a fluid and collisionless representative, is provided in reference 8. The important implication associated with the introduction of the Newtonian approximation is that the calculation of the shape of the ionosphere boundary decouples from the calcula-

tion of the external flow. We then arrive at the following equation for the pressure balance at the ionopause locations  $R_i$ :

$$K\rho_\infty v_\infty^2 \cos^2 \psi = p_R \Lambda(R_i) \quad (35)$$

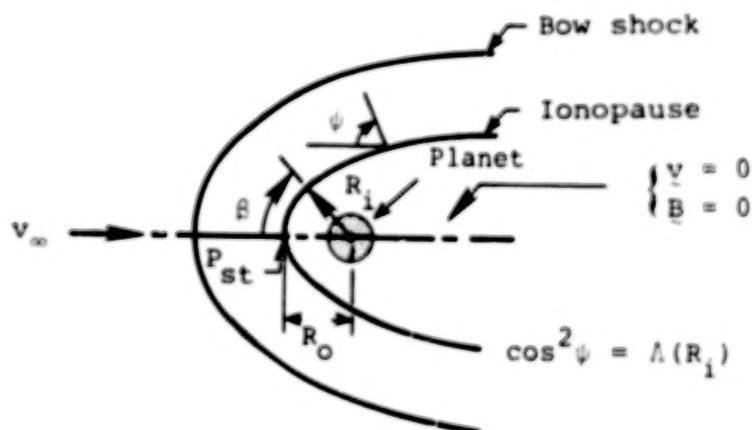
where

$$\Lambda(R_i) = \begin{cases} \exp \left[ - \left( \frac{R_i - R_R}{H} \right) \right] & g, T = \text{Const.} \\ \exp \left[ - R_R \left( \frac{R_i - R_R}{H \cdot R_i} \right) \right] & g = g_S \left( \frac{r_S}{r} \right)^2, T = \text{Const.} \end{cases} \quad (36a)$$

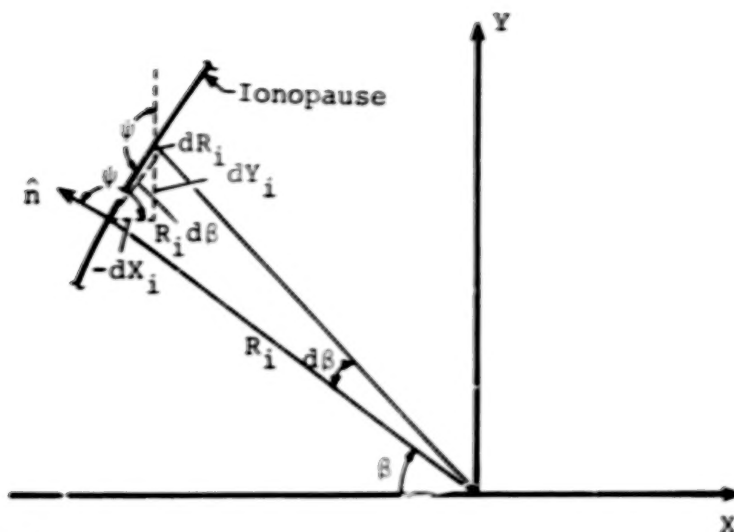
depending upon whether the gravitational variation is included in scale height or not. It is convenient to choose as the reference radius and location the stagnation point on the ionopause; that is,  $R_R = R_O$  where  $R_O$  is the distance from the center of the planet to the nose of the ionopause. This implies that  $p_R = p_O = K\rho_\infty v_\infty^2$  and that at all points along the ionosphere boundary

$$\cos^2 \psi = \Lambda(R_i) \quad (37)$$

The final mathematical statement of the free-boundary problem for determining the shape of the ionosphere boundary then is summarized in the sketch below:



In order to proceed to a final determination of the ionopause shape, it is necessary to relate the local angle  $\psi$  to the local coordinates  $(R_i, \beta)$  of the boundary. This is accomplished with the help of the following sketch



from which we find

$$\cos^2 \psi = \left( \frac{dY_i}{dS} \right)^2 = \frac{(R_i d\beta \cos \beta + dR_i \sin \beta)^2}{dR_i^2 + (R_i d\beta)^2} \quad (38)$$

This results in the following ordinary differential equation for the ordinates of the ionosphere boundary

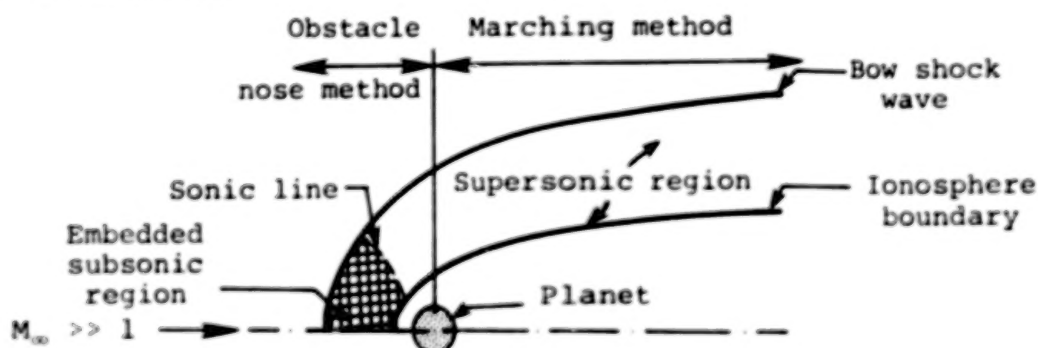
$$\frac{dR_i}{d\beta} = R_i \left[ \frac{\sin 2\beta - 2\sqrt{\Lambda - \Lambda^2}}{2(\Lambda - \sin^2 \beta)} \right] \quad 0 \leq \beta \leq \pi \quad (39)$$

where  $\Lambda$  is defined by eqs. (36a,b) and  $\beta$  is the angle measured from the subsolar point as indicated above. Results for various ionopause shapes obtained by integrating eq. (39) for different values of  $H/R_0$  using the constant scale-height model eq. (36a) were provided in ref. 9. Similar results using the isothermal model, eq. (36b) for different values of  $\bar{H}/R_0$  in the range  $0.01 \leq \bar{H}/R_0 \leq 0.5$  are provided in figure 1, where for comparison purposes the constant scale-height shapes for corresponding  $H/R_0$  values are also illustrated. We note that the range of interest for planetary applications to Venus and Mars appears to be  $0.01 \leq \bar{H}/R_0 \leq 0.10$ . Tabulated ordinates of  $Y_i/R_0$  vs.  $X/R_0$  are provided in Table 1 for  $\bar{H}/R_0 = 0.01, 0.05, 0.10, 0.20$ , and  $0.25$ , where  $Y_i = R_i \sin \beta$  is the cylindrical radial coordinate of the ionopause profile.



## Calculation of the Gasdynamic Flow Properties

Determination of the gasdynamic flow properties is, both conceptually and computationally, the most difficult and time-consuming portion of the total calculation of the solar-wind/terrestrial-planet interaction; and represents the heart of the present modeling effort insofar as the application of advanced computational procedures is concerned. The calculation consists of determining solutions to the differential equations and discontinuity conservation equations given by eqs. (15-20). Since in solar-wind/terrestrial-planet interactions, both the downstream tail region (far field) as well as the region in the vicinity of the obstacle nose (near field) are generally of interest, the computational methods selected must be capable of efficiently determining this entire flow field. In view of the need to carry the flow calculation to an arbitrary downstream distance, the most computationally-expedient procedure is to subdivide the flow field into two regions, as indicated in the sketch below:



This sketch illustrates the essential features of the high-supersonic Mach number flow typical of solar-wind flows past terrestrial planets. Of particular note is the embedded subsonic pocket located at the nose of the ionopause. The presence of this subsonic pocket necessitates use of a computational method capable of treating mixed subsonic/supersonic flows. Downstream of this region, the flow becomes supersonic and remains so for the convex shapes typical of solar-wind/ionosphere boundaries. In that region, a more computationally-economical procedure than that required near the nose can be employed. Such a subdivision of both flow field and solution procedures is common practice for calculating such flows and was employed in the previous solar-wind applications as well as in a related application to space shuttle reentry flows (ref. 12). The precise surface on which the solutions are joined is relatively



arbitrary; in our procedure it was convenient to place it along a plane through the planet center and normal to the free-stream direction of the solar wind, i.e. the dawn-dusk terminator. As illustrated in fig. 2, this position is further downstream than used in the former work in which an inverse iteration method was used for the nose region and the method of characteristics was used for the remaining supersonic region. In light of recent advances, both of the techniques used in the former procedures, particularly the inverse method, are now considered obsolete and much inferior to more current methods. In the new code, those two methods have been superceded by: (1) a new axisymmetric implicit unsteady Euler-equation solver (IMP) specifically developed for the present application, which determines the steady-state solution in the nose region by an asymptotic time-marching procedure, and (2) a shock-capturing marching solution (SCT) which spatially advances the solution downstream as far as required by solving the steady Euler equations.

Nose region solution - implicit unsteady Euler equation method. - The partial differential equations employed in the implicit (IMP) code are the unsteady gasdynamic Euler eqs. (15-20) for axisymmetric flow. These equations may be written in conservation-law form under the generalized independent variable transformation

$$\tau = T, \quad \xi = \xi(T, X, R), \quad \eta = \eta(T, X, R) \quad (40)$$

as follows

$$(U/J)_{\tau} + \left[ (\xi_T U + \xi_X E + \xi_R F) / J \right]_{\xi} + \left[ (\eta_T U + \eta_X E + \eta_R F) / J \right]_{\eta} + G = 0 \quad (41)$$

where

$$U = \begin{bmatrix} \rho \\ \rho u \\ \rho v \\ \rho e_t \end{bmatrix} \quad E = \begin{bmatrix} \rho u \\ p + \rho u^2 \\ \rho uv \\ (\rho e_t + p)u \end{bmatrix} \quad (42)$$

$$F = \begin{bmatrix} \rho v \\ \rho uv \\ p + \rho v^2 \\ (\rho e_t + p)v \end{bmatrix} \quad G = \frac{1}{RJ} \begin{bmatrix} \rho v \\ \rho uv \\ \rho v^2 \\ (\rho e_t + p)v \end{bmatrix}$$

and the Jacobian

$$J = \xi_X \eta_R - \xi_R \eta_X \quad (43)$$

In eqs. (40) through (43),  $T$  denotes time,  $X$  is the axial downstream coordinate, and  $R$  the cylindrical radial distance;  $u$  and  $v$  the velocity components in the  $X$  and  $R$  directions; and  $e_t$  is the total energy per unit mass, which for a perfect gas is related to the other quantities by

$$e_t = p/[\rho(\gamma - 1)] + (u^2 + v^2)/2 \quad (44)$$

The subscripts in eqs. (41) and (43) denote partial derivatives with respect to the indicated variable.

The analysis commences by introducing a computational mesh in polar  $(r, \beta)$  coordinates such that one family of coordinates consists of rays from the planetary center spaced at equal increments of  $\beta$  measured from the obstacle nose, and the other of curved lines intersecting each ray so as to divide the portion of it between the ionopause and the shock wave into a fixed number of equal segments. The coordinate transformation eq. (40) is then used to map the portion of the  $X, R, T$  physical space bounded by (1) the bow wave, (2) the downstream outflow boundary at  $\beta = \pi/2$ , (3) the obstacle surface, and (4) the stagnation streamline at  $\beta = 0$  into a rectangle in the  $\xi, \eta, \tau$  computational space as illustrated in fig. 3. Generally, the transformation metrics at each time step are not known beforehand, and must be determined numerically as part of the solution. Integration step size is established by using the eigenvalues of the Jacobian matrices  $\bar{A}$  and  $\bar{B}$ , where  $\bar{A} = \partial \hat{E} / \partial \hat{U}$ ,  $\bar{B} = \partial \hat{F} / \partial \hat{U}$ , and  $\hat{U} = U/J$ ,  $\hat{E} = (\xi_T U + \xi_X E + \xi_R F)/J$ , and  $\hat{F} = (\eta_T U + \eta_X E + \eta_R F)/J$ .

Boundary conditions necessary for the specification of a properly-posed mathematical problem are that the flow (a) satisfy the axisymmetric Rankine-Hugoniot shock relations derivable from eq. (41) along (1), (b) be entirely supersonic along (2), (c) be parallel to boundaries (3) and (4), and (d) be symmetric about boundary (4). Initial flow-field conditions are determined by use of an approximating formula for the coordinates of the bow shock wave which is dependent on  $\gamma$ ,  $M_\infty$  and the shape of the obstacle, and by prescribing a Newtonian pressure

distribution on the obstacle. Since the maximum entropy streamline wets the obstacle surface, that fact plus the known flow direction on the obstacle serve to determine the remainder of the flow properties on that surface. A linear variation for the flow properties between the bow shock and the obstacle is then prescribed. This provides the initial flow field which is then integrated in a time-asymptotic fashion until the steady-state solution is obtained.

The basic numerical algorithm used in the IMP code was developed by Beam and Warming (ref. 13) and is second-order accurate, noniterative, and spatially factored. In particular, the "delta form" with Euler time differencing is employed. When applied to eq. (41), the algorithm assumes the form

$$(I + \Delta\tau\delta_{\xi}\bar{A}^n)(I + \Delta\tau\delta_{\eta}\bar{B}^n)(\hat{U}^{n+1} - \hat{U}^n) = -\Delta\tau(\delta_{\xi}\hat{E}^n + \delta_{\eta}\hat{F}^n + G) \quad (45)$$

where  $\bar{A}$  and  $\bar{B}$  are the Jacobian matrices,  $I$  is the identity matrix,  $\delta_{\xi}$  and  $\delta_{\eta}$  are second-order, central-difference operators,  $\hat{U}^{n+1} = \hat{U}(n\Delta\tau)$  and  $\Delta\tau$  is the integration step size.

Equation (45) is solved at the interior points only. It requires two 4x4 block tridiagonal inversions at each time step of the integration. The solution proceeds as follows:

1. Define  $\Delta\hat{U} = \hat{U}^{n+1} - \hat{U}^n$
2. Form the right-hand side of eq. (45) and store results in the  $\hat{U}^{n+1}$  array.
3. Apply smoothing  $\hat{U}^{n+1} = \hat{U}^{n+1} - (\epsilon/8)S/J$ .
4. Define  $\bar{U} = (I + \Delta\tau\delta_{\eta}\bar{B}^n)\Delta\hat{U}$  and solve the matrix equation  $(I + \Delta\tau\delta_{\xi}\bar{A}^n)\bar{U} = \hat{U}^{n+1}$  for  $\bar{U}$  storing the result in the  $\hat{U}^{n+1}$  array.
5. Solve the matrix equation  $(I + \Delta\tau\delta_{\eta}\bar{B}^n)\Delta\hat{U} = \hat{U}^{n+1}$  for  $\Delta\hat{U}$ .
6. Obtain the values of  $\hat{U}^{n+1}$  from the relation  $\hat{U}^{n+1} = \Delta\hat{U} + \hat{U}^n$ .

7. Transfer contents of  $\hat{U}^{n+1}$  to  $\hat{U}^n$  and repeat all steps until satisfactory convergence is attained.

In step 3 a fourth-order smoothing term  $S$  is used to eliminate non-linear instabilities that may arise since the use of central differences in the spatial directions results in a neutrally stable algorithm. This smoothing term is given by

$$S_{jk} = (\hat{U}J)_{j+2,k}^{n+1} - 4[(\hat{U}J)_{j+1,k}^{n+1} + (\hat{U}J)_{j-1,k}^{n+1}] + 12(\hat{U}J)_{j,k}^{n+1} + (\hat{U}J)_{j-2,k}^{n+1} \\ + (\hat{U}J)_{j,k+2}^{n+1} - 4[(\hat{U}J)_{j,k+1}^{n+1} + (\hat{U}J)_{j,k-1}^{n+1}] + (\hat{U}J)_{j,k-2}^{n+1} \quad (46)$$

and  $\epsilon$ , the smoothing coefficient, chosen from the range  $0 \leq \epsilon \leq 0.4$  depending upon the size of the time step. The  $j$  and  $k$  indices correspond to the  $\xi$  and  $\eta$  directions, respectively. At the points adjacent to the boundaries a special form of the smoothing term is used.

At the boundaries, modification of the differencing algorithm to account for the particular conditions described above is accomplished as follows. The obstacle-surface flow-tangency condition is incorporated through the use of Kentzer's scheme (ref. 14), while at the symmetry plane, the variables are reflected according to whether they are odd or even. At the outflow boundary where the flow is entirely supersonic, the dependent variables are determined by extrapolation from the adjacent interior points. For the upstream boundary formed by the bow shock wave, the sharp discontinuity approach of reference 15 is used. The interior flow field bounded by these various boundaries is treated in shock-capturing fashion and, therefore, allows for the correct formation of secondary internal shocks.

In the initial development of the nose-region solution procedure (ref. 9), it was found that for certain ionopause obstacle shapes which have a significant amount of lateral flaring at the dawn-dusk terminator, for example, constant scale-height shapes for  $H/R_0 \geq 0.5$ , and/or cases involving low free-stream Mach numbers  $M_\infty \leq 3$ , the axial component of velocity at some points on the terminator plane  $\beta = \pi/2$  may become

subsonic. Although this has no effect whatsoever on the nose-region solver, for these cases the downstream solution cannot be obtained since the marching-region solver which determines the solution downstream of this starting plane, and which is described in detail in the following section, requires supersonic axial velocities in order to proceed. Under the work reported here, this limitation has been removed by developing the capability for adding an additional portion of the flow field, located downstream of the terminator, to the blunt-body solution as illustrated in figure 4. This effectively generalizes the capability of the present procedures to treat a wide variety of ionopause shapes - including all of the shapes of interest described by the constant scale-height and scale-height with gravitational variation atmospheric models found from eqs. (36a,b) - as well as to treat relatively low free-stream Mach numbers,  $M_\infty \approx 2.0$ . Details of this capability are provided in the Computer Program Users Manual, Section A.2.1.1 of this report.

Downstream region solution - shock capturing marching method.- Since the shock-capturing technique employed has been described previously in references 16-18, only an outline of the salient features is provided here. The analysis is based on the conservation-law form of the gasdynamic Euler equations for steady axisymmetric flow, which can be readily obtained from eqs. (40) through (44) by setting the  $\tau$  derivatives to zero. The fourth of this set of equations representing conservation of energy  $\rho e_t$  can be integrated for steady flow to yield the following relation for the total enthalpy

$$h_t = h + (u^2 + v^2)/2 = \text{constant} \quad (47)$$

where  $h = e + p/\rho = C_p T$  is the enthalpy per unit mass.

The computational mesh is defined by lines of constant  $X$  and  $(R-R_b)/(R_s-R_b)$ , where  $R_s$  and  $R_b$  are functions of  $X$  that describe the radial cylindrical coordinates of the ionopause and bow shock wave at the same  $X$  as the field point  $(X,R)$ . The three remaining partial differential equations for conservation of mass and of axial and radial momentum are then transformed to a rectangular computational space by the transformation

$$\xi = X, \quad \eta = \frac{R - R_b}{(R_s - R_b)} \quad (48)$$

to obtain

$$\partial \tilde{E} / \partial \xi + \partial \tilde{F} / \partial \eta + \tilde{G} = 0 \quad (49)$$

$$\begin{aligned} \tilde{E} &= E, \quad \tilde{F} = \left\{ F - \left[ \frac{\partial}{\partial \xi} R_b + \eta \frac{\partial}{\partial \xi} (R_s - R_b) \right] \right\} / (R_s - R_b) \\ \tilde{G} &= G + \frac{E}{R_s - R_b} \frac{\partial}{\partial \xi} (R_s - R_b) \end{aligned} \quad (50)$$

The finite-difference counterpart of eq. (49) is integrated with respect to the hyperbolic coordinate  $\xi$  to yield values of the conservative variable  $E$ . Subsequent to each integration step, the physical flow variables  $p$ ,  $\rho$ ,  $u$ , and  $v$  must be decoded from the components  $e_i$  of  $E$ . This necessitates the solution of four simultaneous, nonlinear equations consisting of eq. (47) together with the three elements  $e_i$ . This can be done readily by using the relations  $v = e_3/e_1$ ,  $p = e_2 - e_1 u$ , and  $\rho = e_1/u$  together with the expression  $h = \gamma/(\gamma-1)(p/\rho)$  for a perfect gas to determine the following quadratic equation for  $u$

$$\begin{aligned} \frac{u^2}{2} + \frac{\gamma}{\gamma-1} \left( \frac{e_2 - e_1 u}{e_1} \right) u - h_t + \left( \frac{e_3}{e_1} \right)^2 \\ = - \frac{\gamma+1}{2(\gamma-1)} u^2 + \left( \frac{\gamma}{\gamma-1} \right) \frac{e_2}{e_1} u - h_t + \left( \frac{e_3}{e_1} \right)^2 = 0 \end{aligned} \quad (51)$$

Two roots exist; one corresponds to subsonic flow and is discarded since  $u$  is always supersonic in the present application, while the other corresponds to supersonic flow and gives the desired solution.

Since only the bow shock wave is treated as a sharp discontinuity and any others that may be present are "captured" by the difference algorithm, selection of the appropriate finite difference scheme to advance the calculation in the  $\xi$  direction is of prime importance. Following the analysis of refs. 16-18, the numerical integration of eq. (49) is accomplished using the finite-difference predictor-corrector



scheme of MacCormack (ref. 19), the most efficient second-order algorithm for shock-capturing calculations. General descriptions of the method can be found in the references cited.

Calculation of the streamlines.— The streamlines are determined by integrating fluid particle trajectories through the known velocity field since this procedure was found to be more accurate than the alternative mass-flow calculation. The calculation of a particular streamline is initiated at the point where the streamline crosses the bow shock, as illustrated in figure 5. At that point, exact values of the streamline slope  $dR_S/dX$  are known in terms of the local shock angle  $\delta_S$  and free-stream quantities according to the relation

$$\frac{dR_S}{dX} = \frac{(2\cot \delta_S)(M_\infty^2 \sin^2 \delta_S - 1)}{2 + M_\infty^2(\gamma + 1 - 2\sin^2 \delta_S)} \quad (52)$$

which is contained implicitly in both the blunt-body (IMP) and marching (SCT) code solutions. At other points in the flow field, the local streamline slope is given by the ratio of radial to downstream velocity, i.e.,

$$dR_S/dX = v/u \quad (53)$$

and the streamline determination is made by stepwise integration in  $X$  using a modified third-order Euler predictor-corrector method. Bivariate linear interpolation from the flow-field grid points is employed to obtain the velocity components  $(u,v)$  required at the stepwise points along the streamline trajectory. Separate streamline calculations are made for the nose region (IMP results) and downstream region (SCT results) because of the different coordinate systems employed in those two regions.

#### Calculation of the Magnetic Field

With the flow properties known from the gasdynamic calculations, determination of the steady magnetic field  $B$  proceeds by integrating the

remaining magnetohydrodynamic equations not employed in the gasdynamic analysis, that is eqs. (21-24) with  $\partial/\partial t = 0$ :

$$\begin{aligned} \text{curl } (\underline{B} \times \underline{v}) &= 0, \quad \text{div } \underline{B} = 0 \\ [B_n \underline{v}_t - B_t \underline{v}_n] &= 0, \quad [B_n] = 0 \end{aligned} \quad (54)$$

These equations are commonly interpreted as indicating the field lines move with the fluid. The analysis associated with eqs. (54) leads to a straightforward calculation in which the vector distance from each point on an arbitrarily-selected field line to its corresponding point on an adjacent field line in the downstream direction is determined by numerically integrating  $\int \underline{v} dt$  over a fixed time interval  $\Delta t$ . Once the coordinates of the field lines are determined, the magnetic field at any point may be calculated from the relation

$$\frac{\underline{B}}{|B_\infty|} = \frac{\rho}{\rho_\infty} \frac{\Delta \underline{\ell}}{|\Delta \underline{\ell}_\infty|} \quad (55)$$

where  $\Delta \underline{\ell}$  is the vector length of a small element of a flux tube. Figure 6 clarifies these quantities for the plane of magnetic symmetry defined by the plane containing the axis of symmetry of the obstacle and the magnetic-field lines upstream of the bow wave for the special case when the latter is perpendicular to the flow. In that figure the open symbol  $\bigcirc$  denotes locations of points on the streamlines corresponding to the fixed-time interval  $\Delta t = \Delta S_\infty / v_\infty$ .

Such a procedure is valid generally, but its use in the present calculations is confined to only the component of the magnetic field  $(B)_\perp$  just described. The remainder of the magnetic-field calculation makes use of a decomposition due to Alksne and Webster (ref. 20) in which the axisymmetric properties of the gasdynamic solution and the linearity of the magnetic-field eqs. (54) are employed to derive the following relationship for the magnetic field  $B_P$  at any point P:

$$\underline{B}_P = \left( \frac{B_P}{B_\infty} \right)_n B_{\infty n} + \left( \frac{B_P}{B_\infty} \right)_\perp B_{\infty \perp} + \hat{e}_n \left( \frac{B_P}{B_\infty} \right)_n B_{\infty n} \quad (56)$$



As illustrated in figure 7, subscripts  $\infty$ ,  $\perp$ , and  $n$  refer to contributions associated with the components  $B_{\infty\infty}$  of  $B_{\infty}$  parallel to  $v_{\infty}$ ; the component  $B_{\infty\perp}$  perpendicular to  $v_{\infty}$  in the plane that contains the point P, the center of the planet, and the vector  $v_{\infty}$ ; and the component  $B_{\infty n}$  normal to the latter plane, and  $\hat{e}_n$  is a unit vector in the latter direction. The unit ratios  $(B_P/B_{\infty})_{\infty}$  and  $(B_P/B_{\infty})_n$  can be calculated directly from the gas-dynamic solution by the expressions

$$\left(\frac{B_P}{B_{\infty}}\right)_{\infty} = \frac{\rho_P v_P}{\rho_{\infty} |v_{\infty}|}, \quad \left(\frac{B_P}{B_{\infty}}\right)_n = \frac{R_P \rho_P}{R_P \rho_{\infty}} \quad (57)$$

where  $R_P$  is the radial cylindrical coordinate of the streamline through P, as indicated in figure 7.

In carrying out the determination of  $(B_P/B_{\infty})_{\perp}$  using eq. (55), values for  $|\Delta\ell|/|\Delta\ell_{\infty}|$  are determined initially at the points where the streamlines and perpendicular-component field lines intersect. A generalized quadrilateral interpolation scheme followed by a fifth-order smoothing is then employed to determine the corresponding values at the computational grid points where values for  $\rho/\rho_{\infty}$  are available for calculation of  $(B_P/B_{\infty})_{\perp}$ . At the bow shock, an exact formula is used

$$\begin{aligned} (|\Delta\ell|/|\Delta\ell_{\infty}|)^2 &= 1 + \cot^2 \theta (1+D^2) - 2D \times \csc \theta \times \cot \theta \times \cos (\theta-\delta) \\ \psi &= \theta + \sin^{-1} \left\{ [D \times \cot \theta \times \sin (\theta-\delta)] / (|\Delta\ell|/|\Delta\ell_{\infty}|) \right\} \end{aligned} \quad (58)$$

where

$$\begin{aligned} D^2 &= 1 - 4(M_{\infty}^2 \sin^2 \theta - 1)(\gamma M_{\infty}^2 \sin^2 \theta + 1) / [(\gamma + 1)^2 M_{\infty}^4 \sin^2 \theta] \\ \cot \delta &= \tan \theta \times \left\{ (\gamma + 1) M_{\infty}^2 / [2(M_{\infty}^2 \sin^2 \theta - 1)] - 1 \right\} \\ \theta &= \tan^{-1} \left[ \frac{dR_S}{dX} \right] \end{aligned} \quad (59)$$

Finally, the resultant magnetic field can then be expressed in components relative to any orthogonal (X,Y,Z) coordinate system. For convenience of illustration, we have chosen the point P to lie in the (X,Y) plane. Relative to this reference frame, the magnetic components are

$$\begin{aligned}
B_X/B_\infty &= \left[ (|B|/B_\infty)_n \cos \phi \cos \alpha_p + (|B|/B_\infty)_\perp \cos \psi \sin \alpha_p \right] \cos \alpha_n \\
B_Y/B_\infty &= \left[ (|B|/B_\infty)_n \sin \phi \cos \alpha_p + (|B|/B_\infty)_\perp \sin \psi \sin \alpha_p \right] \cos \alpha_n \\
B_Z/B_\infty &= (B/B_\infty)_n \sin \alpha_n
\end{aligned} \tag{60}$$

where  $\phi$  is the local flow angle given by

$$\phi = \tan^{-1} \left( \frac{v}{u} \right) \tag{61}$$

and the interplanetary magnetic field angles  $\alpha_p$  and  $\alpha_n$  indicated in figure 7 are defined by

$$\alpha_p = \tan^{-1} \left[ \frac{B_{\infty \perp}}{B_{\infty n}} \right] = \tan^{-1} \left[ \frac{B_{Y_\infty}}{B_{X_\infty}} \right] \tag{62}$$

$$\alpha_n = \tan^{-1} \left[ \frac{B_{\infty n}}{\sqrt{(B_{\infty n})^2 + (B_{\infty \perp})^2}} \right] = \tan^{-1} \left[ \frac{B_{Z_\infty}}{\sqrt{(B_{X_\infty})^2 + (B_{Y_\infty})^2}} \right] \tag{63}$$

The generalizations of these results when the point P is at some arbitrary (Y,Z) location, i.e. not in the (X,Y) plane, are provided below in the spacecraft trajectory section.

#### Calculation of the Contour Lines

Contours are calculated for nondimensionalized velocity  $|v|/v_\infty$ , density  $\rho/\rho_\infty$ , magnetic field components  $(|B|/B_\infty)_n$ ,  $(|B|/B_\infty)_\perp$ , and  $(B/B_\infty)_n$  by application of a modified version of a contour procedure developed at NASA/Ames Research Center. After specifying a value for the contour line, the boundary is searched for intervals which bracket the selected value. After locating one such point by interpolation, the remainder of the contour is determined by 'walking' around the contour, searching at each step for the interval and then interpolating to find the point through which the contour line next passes. This is repeated until a boundary

point is reached. Then closed contours are found in a similar manner. Linear interpolation is used throughout the process. Since the temperature is a function of  $|v|/v_\infty$  only for a specified  $M_\infty$  and  $\gamma$ ,

$$T/T_\infty = 1 + \left[ \left( \frac{\gamma - 1}{2} \right) M_\infty^2 \right] \left[ 1 - \left( \frac{|v|}{v_\infty} \right)^2 \right] \quad (64)$$

velocity contours may also be considered as temperature contours with only a relabeling required. The coordinates of the contour lines are output either or both as listings and pen plots.

#### Solar-Ecliptic/Solar-Wind Coordinate Transformations

In order to facilitate comparison of results from the current theoretical model with actual observational data obtained by a spacecraft, it is necessary to consider the appropriate transformations between the spacecraft and solar-wind coordinate systems. Part of the data required as input to the theoretical model consists of oncoming interplanetary values of solar-wind temperature, density, and velocity and magnetic-field vector components. These are naturally obtained in the spacecraft coordinate system, and are usually reported in a sun-planet or solar-ecliptic reference frame. The key coordinate system for the theoretical model is one which aligns the axial direction with the oncoming solar wind, since the gasdynamic calculation is assumed to be axisymmetric about this direction. Thus, the interplanetary input data must be transformed to the solar-wind system to initiate the theoretical determination. Once the gasdynamic and magnetic-field calculations in the solar-wind system are complete, those results must then be transformed back to the sun-planet system to allow direct comparison with spacecraft data obtained at arbitrary locations in the solar-wind/ionosphere interaction region. Consequently, direct and inverse transformations for both spatial coordinates as well as vector quantities between these reference frames are required.

For the measurements of the oncoming interplanetary solar-wind velocity we have assumed that the velocity is obtained with reference to a

sun-planet  $(x_s, y_s, z_s)$  system with origin at planetary center and in which the  $x_s$ -axis points to the sun, the  $y_s$ -axis is opposite to the planetary orbital motion, and the  $z_s$ -axis points northward. The direction of the oncoming solar wind is such that the total aberration or azimuthal angle, including planetary orbital motion, of the solar-wind velocity vector in the plane of the ecliptic is  $\Omega$  and the out-of-ecliptic plane or polar angle is  $\phi_p$ . The positive sense of the azimuthal angle is for east-to-west flow and for the polar angle for north-to-south flow, as indicated in figure 8. In that figure we have also indicated the solar-wind  $(x, y, z)$  coordinate system so defined by  $(\Omega, \phi_p)$ . For the gas-dynamic calculation, the  $(x, y, z)$  system is somewhat inconvenient since the direction of solar-wind flow is in the negative  $x$ -direction. Hence, the internal gasdynamic and magnetic-field calculations are performed in an  $(X, Y, Z)$  system as shown in figure 9.

The coordinate and vector transformations from the ecliptic sun-planet  $(x_s, y_s, z_s)$  system to the  $(X, Y, Z)$  solar-wind system are given by

$$\begin{pmatrix} Q_X \\ Q_Y \\ Q_Z \end{pmatrix} = \begin{pmatrix} -\cos \Omega \cos \phi_p & -\sin \Omega \cos \phi_p & \sin \phi_p \\ \sin \Omega & -\cos \Omega & 0 \\ -\cos \Omega \sin \phi_p & \sin \Omega \sin \phi_p & \cos \phi_p \end{pmatrix} \begin{pmatrix} Q_{x_s} \\ Q_{y_s} \\ Q_{z_s} \end{pmatrix} \quad (65)$$

where  $(Q_X, Q_Y, Q_Z)$  represents the Cartesian components of any vector referred to the solar-wind  $(X, Y, Z)$  coordinate system, and  $(Q_{x_s}, Q_{y_s}, Q_{z_s})$  represents the corresponding vector in the sun-planet ecliptic  $(x_s, y_s, z_s)$  system. Thus, for a transformation of coordinates

$$\begin{aligned} (Q_X, Q_Y, Q_Z) &= (X, Y, Z) \\ (Q_{x_s}, Q_{y_s}, Q_{z_s}) &= (x_s, y_s, z_s) \end{aligned} \quad (66)$$

while for a vector transformation of, say, the magnetic field

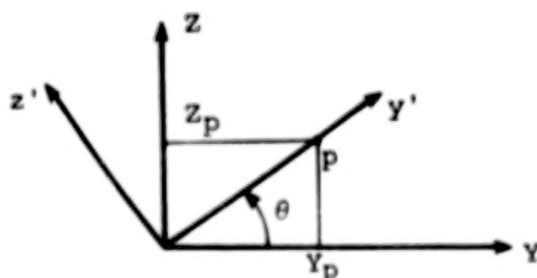
$$\begin{aligned} (Q_X, Q_Y, Q_Z) &= (B_X, B_Y, B_Z) \\ (Q_{x_s}, Q_{y_s}, Q_{z_s}) &= (B_{x_s}, B_{y_s}, B_{z_s}) \end{aligned} \quad (67)$$

The inverse transformation from the solar-wind to the sun-ecliptic system is given by

$$\begin{pmatrix} Q_{x_s} \\ Q_{y_s} \\ Q_{z_s} \end{pmatrix} = \begin{pmatrix} -\cos \Omega \cos \phi_p & \sin \Omega & -\cos \Omega \sin \phi_p \\ \sin \Omega \cos \phi_p & -\cos \Omega & \sin \Omega \sin \phi_p \\ \sin \phi_p & 0 & \cos \phi_p \end{pmatrix} \begin{pmatrix} Q_x \\ Q_y \\ Q_z \end{pmatrix} \quad (68)$$

### Properties Along a Spacecraft Trajectory

One of the primary aims of the present effort has been the development of the capability to determine plasma and magnetic-field properties, as predicted by the present theoretical model, at locations specified along an arbitrary spacecraft trajectory, and in such a form as to enable comparisons to be made directly with actual spacecraft data. To this end, the following procedure has been developed and implemented in the associated computer code. First, from the known oncoming interplanetary conditions provided in a sun-planet reference frame, the azimuthal and polar solar-wind angles  $(\Omega, \phi_p)$  are employed to establish both the location of the trajectory point in the solar-wind  $(X, Y, Z)$  frame as well as the interplanetary magnetic-field components  $(B_{X_\infty}, B_{Y_\infty}, B_{Z_\infty})$  using the transformation eq. (65). Next, the axisymmetric gasdynamic and unit magnetic-field calculations are carried out. Because the gasdynamic flow is axisymmetric in the  $(X, Y, Z)$  system, the internal coordinate system in which the trajectory calculations are actually performed may be rotated about the  $X$  axis into the most convenient orientation. If we consider a point  $P$  located at  $(X_p, Y_p, Z_p)$ , then the rotation most appropriate for the present application is indicated in the sketch below



where the angle  $\theta$  is given by

$$\theta = \tan^{-1} \left[ \frac{z_p}{y_p} \right] \quad (69)$$

This rotation defines a new coordinate system  $(x', y', z')$  where

$$\begin{pmatrix} x' \\ y' \\ z' \end{pmatrix} = \begin{pmatrix} 1 & 0 & 0 \\ 0 & \cos \theta & \sin \theta \\ 0 & -\sin \theta & \cos \theta \end{pmatrix} \begin{pmatrix} X \\ Y \\ Z \end{pmatrix} \quad (70)$$

in which

$$\begin{aligned} x' &= X_p \\ y' &= \sqrt{Y_p^2 + Z_p^2} \\ z' &= 0 \end{aligned} \quad (71)$$

Thus, the  $(x', y')$  plane which contains the  $X$  axis and the arbitrary point  $P$  corresponds directly to the plane  $(X, R) = (X_p, \sqrt{Y_p^2 + Z_p^2})$  in which the axisymmetric gasdynamic flow properties are calculated. In particular, the velocity magnitude  $v$ , density  $\rho$ , and flow angle  $\phi$  at the point  $P$  are found by bilinear interpolation through the  $(X, R)$  flow-field grid. The vector velocity in the  $(X, Y, Z)$  system is then given by the transformation

$$\begin{pmatrix} v_X \\ v_Y \\ v_Z \end{pmatrix} = \begin{pmatrix} 1 & 0 & 0 \\ 0 & \cos \theta & -\sin \theta \\ 0 & \sin \theta & \cos \theta \end{pmatrix} \begin{pmatrix} v \cos \phi \\ v \sin \phi \\ 0 \end{pmatrix} \quad (72)$$

and then in the sun-ecliptic system by the transformation given in eq. (68)

$$\begin{pmatrix} v_{x_s} \\ v_{y_s} \\ v_{z_s} \end{pmatrix} = \begin{pmatrix} -\cos \Omega \cos \phi_p & \sin \Omega & -\cos \Omega \sin \phi_p \\ \sin \Omega \cos \phi_p & -\cos \Omega & \sin \Omega \sin \phi_p \\ \sin \phi_p & 0 & \cos \phi_p \end{pmatrix} \begin{pmatrix} v_X \\ v_Y \\ v_Z \end{pmatrix} \quad (73)$$

Calculation of the magnetic field at an arbitrary point is somewhat more complicated since these components are dependent upon the orientation of the incident interplanetary magnetic field. With the known  $(B_{X_{\infty}}, B_{Y_{\infty}}, B_{Z_{\infty}})$  components, the corresponding components  $(B'_{X_{\infty}}, B'_{Y_{\infty}}, B'_{Z_{\infty}})$  in the rotated  $(x', y', z')$  system are given by

$$\begin{pmatrix} B'_{X_{\infty}} \\ B'_{Y_{\infty}} \\ B'_{Z_{\infty}} \end{pmatrix} = \begin{pmatrix} 1 & 0 & 0 \\ 0 & \cos \theta & \sin \theta \\ 0 & -\sin \theta & \cos \theta \end{pmatrix} \begin{pmatrix} B_{X_{\infty}} \\ B_{Y_{\infty}} \\ B_{Z_{\infty}} \end{pmatrix} \quad (74)$$

In this reference frame, the perpendicular, parallel, and normal interplanetary components are identified as

$$\begin{aligned} B_{\infty n} &= B'_{X_{\infty}} \\ B_{\infty \perp} &= B'_{Y_{\infty}} \\ B_{\infty \parallel} &= B'_{Z_{\infty}} \end{aligned} \quad (75)$$

Then, the magnetic field angles  $\alpha'_p$  and  $\alpha'_n$  in the rotated system are given by

$$\alpha'_p = \tan^{-1} \left[ \frac{B_{\infty \perp}}{B_{\infty n}} \right] = \tan^{-1} \left[ \frac{B'_{Y_{\infty}}}{B'_{X_{\infty}}} \right] \quad (76)$$

$$\alpha'_n = \tan^{-1} \left[ \frac{B_{\infty n}}{\sqrt{(B_{\infty \parallel})^2 + (B_{\infty \perp})^2}} \right] = \tan^{-1} \left[ \frac{B'_{Z_{\infty}}}{\sqrt{(B'_{X_{\infty}})^2 + (B'_{Y_{\infty}})^2}} \right] \quad (77)$$

The magnetic angle  $\psi$  associated with the incident perpendicular component and the unit magnetic-field ratios  $(|B|/B_{\infty})_n$ ,  $(|B|/B_{\infty})_{\perp}$ ,  $(B/B_{\infty})_n$  in the rotated system are next determined by bilinear interpolation through the flow-field grid. Then, the magnetic-field components  $(B'_x, B'_y, B'_z)$  in the rotated system are calculated from

$$B'_x = \cos \alpha'_n \left[ \cos \phi \cdot \cos \alpha'_p \cdot \left| \frac{B}{B_{\infty}} \right|_n + \cos \psi \cdot \sin \alpha'_p \cdot \left| \frac{B}{B_{\infty}} \right|_{\perp} \right] \cdot B_{\infty} \quad (78)$$

$$B'_y = \cos \alpha'_n \left( \sin \phi \cdot \cos \alpha'_p \cdot \left| \frac{B}{B_\infty} \right|_n + \sin \psi \cdot \sin \alpha'_p \cdot \left| \frac{B}{B_\infty} \right|_1 \right) \cdot B_\infty \quad (79)$$

$$B'_z = \sin \alpha'_n \cdot \left( \frac{B}{B_\infty} \right)_n \cdot B_\infty \quad (80)$$

The magnetic-field components in the solar-wind (X,Y,Z) system are then determined from the rotational transformation.

$$\begin{pmatrix} B_X \\ B_Y \\ B_Z \end{pmatrix} = \begin{pmatrix} 1 & 0 & 0 \\ 0 & \cos \theta & -\sin \theta \\ 0 & \sin \theta & \cos \theta \end{pmatrix} \begin{pmatrix} B'_x \\ B'_y \\ B'_z \end{pmatrix} \quad (81)$$

and finally in the sun-planet system from

$$\begin{pmatrix} B_{x_s} \\ B_{y_s} \\ B_{z_s} \end{pmatrix} = \begin{pmatrix} -\cos \Omega \cos \phi_p & \sin \Omega & -\cos \Omega \sin \phi_p \\ \sin \Omega \cos \phi_p & -\cos \Omega & \sin \Omega \sin \phi_p \\ \sin \phi_p & 0 & \cos \phi_p \end{pmatrix} \begin{pmatrix} B_X \\ B_Y \\ B_Z \end{pmatrix} \quad (82)$$

## RESULTS

Using the computational procedures developed under the current modeling effort, a large variety and number of different solar-wind/planetary-ionosphere interaction results were systematically obtained. These results were directed toward the following specific objectives: (1) verification of the correctness of the procedures, (2) demonstration of their flexibility and generality for a variety of cases covering ranges typical of solar-wind conditions, (3) establishment of a catalog of flow and magnetic-field results for a large number of solar-



wind flows, and (4) comparisons of theoretical predictions with data obtained from spacecraft measurements. The results obtained associated with these objectives are discussed below.

Verification of the correctness of the procedures developed under the current effort primarily involved testing the computational extensions developed regarding both the gasdynamic and magnetic-field calculation methods reported in ref. 9. For the gasdynamic solver, this consists of demonstrating the extended blunt-body capability. As discussed previously in the section describing the nose-region solution and also in section A.2.1.1 of the computer manual, that extension involves the addition to the nose-region flow field of a region downstream of the dawn-dusk terminator - which is the usual plane terminating the nose-region solution. This added capability effectively removes any restriction with regard to obstacle shape and interplanetary gasdynamic Mach number of the previous procedures (ref. 9); and permits the calculation of ionopause shapes which have significant flaring in the radial direction at the dawn-dusk terminator, as well as flows at very low ( $M_\infty \approx 2.0$ ) free-stream Mach numbers. In figure 10, we present results for the bow shock locations for  $M_\infty = 8.0$ ,  $\gamma = 5/3$  flow past constant scale-height ionopause shapes (see eq. (36a) with  $H/R_0 = 0.5$  and  $1.0$ ). The downstream solutions for neither of these shapes could be determined with the previous procedures (ref. 9), whereas with the present method they present no problem. The downstream locations to which the nose-region solutions were extended were  $X/R_0 = (0.54, 0.67)$ , respectively, for the  $H/R_0 = (0.5, 1.0)$  ionopause shapes - indicating that the addition of an extensive downstream region to the nose solution for such flows is unnecessary. This is important, as the nose-region solver requires significantly more computational time for a given flow-field region than the marching solver. Hence, minimization of the nose-region flow field is essential in minimizing the total computational time.

In figure 11, we display additional results using the extended nose-region grid capability to demonstrate the ability of the current method for calculating very low interplanetary gasdynamic Mach number flows. Bow shock locations are shown for  $M_\infty = 2.0$  and  $3.0$ ,  $\gamma = 5/3$  flows past an

ionopause obstacle shape with gravitational variation included in scale-height having  $\bar{H}/R_0 = 0.25$  (see eq. (36b)). This particular obstacle is a relatively blunt shape, as can be observed from the ionopause profiles presented previously in figure 1, and, computationally, presents a more difficult flow to determine than flows for shapes having less flaring. For applications to terrestrial planets, such as Mars and Venus, typical ionopause shapes occurring in nature appear to lie in the range  $0.01 \leq \bar{H}/R_0 \leq 0.10$ . Consequently, demonstration of the ability of the current procedures to treat successfully such flows as shown in figures 10 and 11 - which lie at the limits of interest as far as applications to nonmagnetic terrestrial planets, indicates that these procedures will not be restricted insofar as ionopause geometry and interplanetary solar-wind conditions are concerned.

Corresponding verification of the extensions to the procedures for the magnetic-field calculation has involved demonstration of the correctness of the magnetic-field prediction at any arbitrary point in the solar-wind flow field. This was accomplished by consideration of a variety of special test cases in which the location in the flow field and the incident interplanetary magnetic-field orientation were systematically changed so as to produce both symmetric and antisymmetric changes in the resultant ionosheath magnetic field, as well as to reverse the roles of the perpendicular and normal components. All of these various permutations of the magnetic-field calculation procedure were successfully verified.

One of the primary objectives of the present work was to demonstrate the flexibility and generality of the present procedures by exercising them over a wide range of ionopause geometries and solar wind oncoming conditions so as to cover, insofar as possible, the entire range of practical interest of these parameters. These calculations were to be summarized in a convenient format and then archived so as to provide at-a-glance information regarding the variation of the flow-field and unit magnetic-field quantities. The output format selected was the automatic pen-plot output option of the program involving plots of the flow-field streamlines, and contours of the velocity magnitude  $|\underline{v}|/v_\infty$ , temperature  $T/T_\infty$ , density  $\rho/\rho_\infty$ , and the field-line locations and contours of the unit magnetic-field ratios  $(|\underline{B}|/B_\infty)_u$  and  $(|\underline{B}|/B_\infty)_l$ .

The test cases selected for this catalog involved a ratio of specific heats  $\gamma = 5/3$  and the following matrix of free-stream Mach numbers  $M_\infty$  and ionopause shapes:

$$\begin{aligned}M_\infty &= \{2.0, 3.0, 5.0, 8.0, 12.0, 25.0\} \\H/R_O &= \{0.01, 0.10, 0.25\} \\\bar{H}/R_O &= \{0.10, 0.20, 0.25\}\end{aligned}$$

Thus, a total of 36 separate cases were calculated. The plot output for these cases is provided in Appendix B, which also presents a convenient page index to the individual results. These archived results provide an very convenient means of determining the overall dependence of flow-field and magnetic-field quantities with  $M_\infty$  and obstacle shape, in particular the variation of bow shock location and flow-field contour changes. We note that the range of free-stream Mach numbers selected easily spans the entire range of solar-wind conditions usually encountered, while the different obstacle shapes provide a wide variation as well, as can be observed from figure 1.

The final and ultimate check of the current procedures lies in the comparison of the results predicted by the present model with data actually measured by a spacecraft. To that end, we have made a number of preliminary comparisons with data obtained from orbits 3 and 6 of the Pioneer-Venus Orbiter spacecraft.

The overall features of the spacecraft trajectory crossings of the solar-wind/Venus-ionosphere interaction region are provided in the sketch given in figure 12. In that figure, which is referred to the sun-Venus solar-ecliptic coordinate system, we note in particular the highly elliptic spacecraft orbit (periapsis  $\approx 200$  Km, apoapsis  $\approx 66,000$  Km) and the crossings of the bow shock and ionopause surfaces. The oncoming solar-wind direction, with arbitrary azimuthal (aberration) and polar angles  $(\Omega, \phi_p)$  is as indicated, with the ionopause and bow shock surfaces symmetric about that direction. The oncoming arbitrary interplanetary magnetic field  $\mathbf{B}$  is also as indicated.

The procedural outline employed for the theoretical comparisons is as follows:

## I. Orbital data selection

Select data from an orbit when solar-wind conditions are relatively steady.

## II. Theoretical calculations

### Input:

Ionospheric  $\rho$  and  $T$  versus altitude from orbiter retarding potential analyzer (ORPA)

Solar wind  $v_{\infty}$ ,  $\rho_{\infty}$ ,  $T_{\infty}$  from orbiter plasma analyzer (OPA)

Solar wind  $B_{\infty}$  from orbiter magnetometer (OMAG)

Trajectory coordinates

Output: (Contours and/or time histories along orbital trajectory)

Ionosheath  $\rho$ ,  $T$ ,  $v$ ,  $B$  and their scalar components in solar ecliptic coordinates

## III. Comparisons with Spacecraft data

Observational ionosheath data for  $\rho$ ,  $|v|$ ,  $T$  from OPA and for  $B$  from OMAG with two sets of theoretical predictions based on {last } interplanetary solar-wind properties ( $v_{\infty}$ ,  $T_{\infty}$ ,  $\rho_{\infty}$ ,  $B_{\infty}$ )  
measured {before } bow shock {inbound } crossings.  
          {after }                {outbound }

First, the selection of the particular orbit for which theoretical calculations and data comparisons will be carried out must be made. This choice is based on spacecraft observations of the oncoming interplanetary solar wind, and for the cases reported here, the selections were made when conditions appeared relatively steady. In particular, the interplanetary conditions regarding solar-wind velocity, density, temperature and magnetic field based on the orbiter solar-wind plasma analyzer (OPA) and fluxgate magnetometer (OMAG) measurements just prior

to inbound bow shock crossing and immediately after outbound bow shock crossing were analyzed by the Pioneer-Venus investigators responsible for these instruments for a number of the initial orbits of the Pioneer-Venus spacecraft, and on this basis the selection of Orbits 3 and 6 were made.\*

To initiate the theoretical calculations, information regarding both the ionospheric obstacle shape and the oncoming interplanetary conditions are required. The determination of the obstacle shape is based on measurements of atmospheric density and temperature as a function of altitude made by the orbiter retarding potential analyzer at (ORPA) locations interior to the ionopause boundary.\*\* These measurements yield the variation of atmospheric pressure with altitude in the vicinity of ionopause altitudes. From this information, the value of the scale-height parameter from the atmospheric pressure model given by either eq. (29) or (30) can be determined. For Venus, it appears that the ionosphere/solar-wind interaction is such that the ionopause wraps tightly about the planet (ref. 10). Our calculations based on ORPA data for Orbits 3 and 6 indicate scale heights of approximately 200 Km, which yield a corresponding range of values for  $H$  and  $\bar{H}$  of  $0.02 \leq H/R_0$ ,  $\bar{H}/R_0 \leq 0.05$ . We note that for such small values of scale height, the two ionospheric pressure models eqs. (29) and (30) yield essentially the same obstacle shape, as can be seen from figure 1. For the comparisons reported here for both Orbits 3 and 6, we have selected a value of  $\bar{H}/R_0 = 0.03$ . With regard to oncoming interplanetary conditions, we require as input the solar-wind bulk velocity  $v_\infty$ , density  $\rho_\infty$ , temperature  $T_\infty$ , and magnetic field  $B_\infty$ . The first three are provided by the orbiter plasma analyzer (OPA), while the magnetic field is given by the orbiter fluxgate magnetometer (OMAG). We note that the OPA provides either ion density and temperature or electron density and temperature, but not both simultaneously. For orbits 3 and

---

\*Special thanks are due to J. H. Wolfe and J. P. Mihalov who provided information regarding the solar-wind plasma from OPA measurements (refs. 21,22) and to C. T. Russell, R. C. Elphic, and J. A. Slavin for magnetic-field information from OMAG measurements (refs. 23,24).

\*\*Special thanks are due to W. C. Knudsen and K. Spenner for providing the ionospheric plasma information from ORPA measurements (refs. 10,11).



6, ion measurements were available and have been employed. Information regarding the oncoming direction of the solar wind, as given by the angles  $(\Omega, \phi_p)$ , defines the requisite coordinate rotations required to align the gasdynamic calculation in the oncoming solar-wind direction; while information of solar-wind speed, density, and temperature serve to define the oncoming gasdynamic Mach number required to initiate the gasdynamic calculations.

With this information, the detailed gasdynamic and unit magnetic-field calculations in the ionosheath region can be carried out. In order to provide an idea of the detail obtained by the present computational procedures in these calculations, we have displayed in figure 13 the flow-field grid for one of the gasdynamic flow solutions used in the data comparisons discussed below. The result shown is for  $M_\infty = 3.0$ ,  $\gamma = 5/3$  flow past an ionopause obstacle shape with  $\bar{H}/R_0 = 0.03$ , and is shown carried to a downstream location of  $X/R_0 = 3.0$ . The flow field properties  $[v/v_\infty, \rho/\rho_\infty, T/T_\infty]$  and the unit frozen magnetic-field ratios  $[(B/B_\infty)_n, (B/B_\infty)_t, (B/B_\infty)_n]$  are determined at each intersection of the grid lines, including the bow shock, stagnation streamline, and ionopause boundaries. The final output of the calculation consists of detailed flow-field and magnetic-field properties in the ionosheath region, both in terms of tabular output and plotted contours and time histories along the orbital trajectory of the velocity magnitude and components, density, temperature, and magnetic-field magnitude and components. Complete details are provided in section A.4 of the Computer User's Manual.

For the comparisons with spacecraft data, the most convenient portion of the output format are the time-history predictions along the spacecraft orbit. The observational data used for comparisons with the theoretical predictions in the ionosheath region include plasma density, velocity, and temperature from OPA measurements and magnetic field from OMAG measurements. For the theoretical predictions, two sets of results are usually generated based on  $\left\{ \begin{matrix} \text{last} \\ \text{first} \end{matrix} \right\}$  interplanetary solar-wind properties  $(v_\infty, T_\infty, \rho_\infty, B_\infty)$  measured  $\left\{ \begin{matrix} \text{before} \\ \text{after} \end{matrix} \right\}$  bow shock  $\left\{ \begin{matrix} \text{inbound} \\ \text{outbound} \end{matrix} \right\}$  crossing.

In figure 14, we have displayed some overall flow-field results for Orbit 6. Indicated in that figure are bow shock locations for the three combinations of free-stream Mach number  $M_\infty$  and plasma specific heat ratio  $\gamma$ , i.e.  $(M_\infty, \gamma) = (13.3, 5/3), (13.3, 2), (3.0, 5/3)$  for flow about an ionopause with  $\bar{H}/R_0 = 0.03$ . Also indicated are two sets of points  $(-\bigcirc-)$ ,  $(-\square-)$  representing the spacecraft trajectory for orbit 6 as viewed in two solar-wind oriented coordinate systems. The trajectory indicated by the solid lines and circles  $(-\bigcirc-)$  is that based on the last measured direction  $(\Omega, \phi_p) = (6.5^\circ, -1.4^\circ)$  of the interplanetary solar wind just prior to crossing the bow shock on the inbound leg, while the dashed line and squares  $(-\square-)$  denotes the trajectory based on the first measured direction  $(\Omega, \phi_p) = (4.9^\circ, 7.6^\circ)$  of the solar wind immediately after crossing the bow shock on the outboard leg. We note that the spatial location of the spacecraft trajectory in solar-wind coordinates depends only on the direction  $(\Omega, \phi_p)$  of the oncoming solar wind, but not on its magnitude. With regard to the results indicated in figure 14 for the spacecraft trajectory, we observe the extremely large dependence of spatial position of a trajectory point, as viewed in solar-wind coordinates, on solar-wind direction. For the particular inbound and outbound solar-wind angles indicated, the shift in X-coordinate of a trajectory point can be as high as a quarter of the Venusian planetary radius, which obviously results in substantial differences in predicted flow and magnetic-field properties. In previous work, the influence of the angular shift in the solar wind was generally considered to be small and negligible. The current results, however, indicate that this purely geometrical effect can be surprisingly large, even for directional shifts of less than  $5^\circ$ , and must be accounted for in any realistic theoretical comparison with data. See reference 7 for another example of the importance of this effect.

Finally, with regard to the three sets of bow shock results displayed in figure 14, these calculations represent an attempt to resolve the uncertainty in the oncoming free-stream Mach number and ratio of specific heats of the plasma. Because only solar-wind ion temperatures from the OPA were available for Orbit 6, the initial calculation of the free-stream Mach number was based on the assumption that  $T_e = T_i$ , which leads to  $M_\infty = 13.3$ . A ratio of specific heats  $\gamma = 5/3$  was assumed, and these interplanetary values result in the bow shock indicated by the

dot-dash line. That shock location is in poor agreement with the observational shock crossings, indicated as occurring between the pairs of solid circles and squares. A separate uncertainty arises from the possibility that the magnetic field may act to align the plasma particle motion in its direction, thus effectively reducing the number of degrees of translational freedom from 3 to 2 and thereby increasing the ratio of specific heats from  $5/3$  to 2. To investigate this possibility, we have repeated the  $M_\infty = 13.3$  calculation using  $\gamma = 2$ . That result is indicated by the dashed line, and is in better but still not completely satisfactory agreement with the observed shock locations. Finally, if it is assumed that the oncoming interplanetary electron temperature is not equal to the ion temperature, but is substantially higher, we are lead to low Mach numbers of the order of  $M_\infty = 3-5$ . We have displayed bow shock results of a  $M_\infty = 3.0$ ,  $\gamma = 5/3$  calculation in figure 14 as the solid line, and observe that based on this Mach number and the inbound solar-wind direction, the observational shock crossings display very good agreement with the theoretical results.

Figure 15 displays the time-history comparisons of the theoretically-predicted bulk plasma density, speed and temperature in the ionosheath region with OPA measurements of these quantities. These theoretical results were based on a gasdynamic flow solution with  $M_\infty = 13.3$ ,  $\gamma = 2.0$ . In these results, the solid lines with circles correspond to results based on inbound interplanetary conditions, while the dashed lines with squares correspond to outbound conditions. We note that while the few data points available are in general agreement with the theoretical calculations, the lack of more detailed plasma measurements in the ionosheath prevents a definitive conclusion. The OPA instrument requires approximately 9 minutes to acquire sufficient data to enable predictions of the bulk plasma quantities. While this time lag presents no problem when the spacecraft is in the interplanetary solar wind, the large resolution time effectively averages the plasma quantities in the ionosheath over such a large spatial range that only overall comparisons of the bulk plasma properties are possible.

The situation is quite different for the magnetic field, as the OMAG instrument provides essentially instantaneous magnetic-field measurements. Comparisons of the frozen magnetic-field predictions with data



are displayed in figures 16(a,b). These comparisons employ the gas-dynamic solution  $M_\infty = 13.3$ ,  $\gamma = 2$  for which plasma properties were given in figure 15. In figure 16a, we display two sets of theoretical calculations for the magnitude of the magnetic field, based on the inbound and outbound interplanetary magnetic field conditions as indicated on the figure. In these comparisons, we observe very good agreement with both sets of predictions. In particular, on the inbound leg, the theoretical predictions based on the inbound interplanetary conditions are in very good agreement with the data, while the outbound-condition predictions are clearly not as favorable. On the other hand, as we proceed in time along the outbound leg, the opposite is true. Here, the outbound-condition predictions are in very good agreement with the data, while the inbound-condition predictions are notably inferior, particularly with regard to shock crossing. Corresponding results for the magnetic-field components are provided in figure 16b, and display a similar behavior. The agreement of the theoretical results with data for the individual components is remarkable, confirming the accuracy of the frozen-field model, as well as the shift of the ionosheath magnetic field from a solution related to inbound interplanetary conditions to one related to outbound conditions.

For Orbit 3, similar comparisons as those shown in figures 14-16 for Orbit 6 are given in figures 17 to 19. In figure 17, we have provided the bow shock locations for five different combinations of  $M_\infty$  and  $\gamma$  as indicated. The Mach numbers  $M_\infty = 7.38, 5.96$  correspond, respectively, to the inbound and outbound interplanetary conditions for  $|\underline{v}_\infty|, \rho_\infty, T_\infty$  as measured by the OPA, while the two values of  $\gamma = 5/3, 2$  used in the calculations represent our uncertainty of the ratio of plasma specific heats. We have also indicated for reference the bow shock location for  $M_\infty = 3.0, \gamma = 5/3$  as given previously in figure 14 for Orbit 6. Note that the observational shock crossings are again closest to the  $M_\infty = 3.0, \gamma = 5/3$  shock. Also provided in figure 17 are the orbital trajectories as viewed in solar-wind coordinates for the inbound  $(\Omega, \phi_p) = (3.3^\circ, 0.15^\circ)$  and outbound  $(\Omega, \phi_p) = (3.7^\circ, 4.9^\circ)$  solar-wind directions.

The comparisons for the bulk plasma properties for Orbit 3 are provided in figure 18. Again we note an overall agreement for bulk plasma speed and density, but note an observable discrepancy in the temperature.

This is thought to be indicative of the manner in which the bulk properties from the theoretical model are being interpreted in relation to the observational measurements; i.e. the theoretical values correspond to those for a single-component plasma, while the measurements are in terms of a multi-component plasma. Whether the theoretical plasma properties require rescaling or reformulation, or whether their present formulation is appropriate for comparison with the multi-component data, appears to be a necessary and important subject for future study.

Results for the magnetic-field comparisons are displayed in figures 19(a,b), which provide time-histories of both the magnitude and the individual magnetic-field components based on both inbound and outbound interplanetary conditions. We note again, although the shock crossing comparisons are somewhat in disagreement since the gasdynamic flow fields used in these results were for  $M_\infty = 7.56$ ,  $5.96$  and  $\gamma = 2$ , the reasonable comparisons are obtained for the ionosheath magnetic field. In particular, we observe the drift with time along the trajectory of the trajectory of the agreement of theory with data from the predictions based on inbound interplanetary conditions on the inbound leg, to those based on outbound conditions on the outbound leg.

In order to demonstrate the improvement obtained in magnetic-field results when a gasdynamic flow-field solution is employed which more closely agrees with the observational bow shock location, we have displayed in figure 20(a,b) the analogous time-history magnetic-field comparisons when using a  $M_\infty = 3.0$ ,  $\gamma = 5/3$  gasdynamic result. In this case, results were computed for only the inbound direction  $(\Omega, \phi_p) = (3.3^\circ, 0.15^\circ)$  of the solar wind. As can be seen, there is a marked improvement in the agreement near the bow shock, and quite good agreement throughout the ionosheath as well as, for both the magnitude and the individual magnetic-field components. We note that the general agreement of theory and observation of the individual components demonstrates both the accuracy of the calculation and, in particular, the need for accounting in the theoretical results of the variable direction of the interplanetary solar wind.

## CONCLUDING REMARKS

The application of advanced computational procedures was undertaken for the purpose of modeling the interaction of the solar wind with non-magnetic planets, with particular emphasis on Venus. Based on the successful theoretical model employed previously (ref. 9), i.e., the steady, dissipationless, magnetohydrodynamic model for axisymmetric, supersonic, super-Alfvénic solar-wind flow, a number of important theoretical extensions have been developed and included in the computational procedures. These include the capability for treating very low oncoming interplanetary gasdynamic Mach numbers ( $M_\infty \approx 2.0$ ), as well as quite general ionopause shapes. A new family of ionopause shapes has been developed which includes the effect of gravitational variation in scale height, and has been incorporated in the computational program. Additionally, the capability for determining the plasma gasdynamic and magnetic-field properties along any arbitrary spacecraft trajectory, accounting for an arbitrary oncoming direction of the solar wind, has been developed. All of these developments have been incorporated into an assemblage of computer codes to enable detailed calculations of the solar-wind interaction with planetary atmospheres. The computer codes have been extensively documented and are described in a computer user's manual included as part of this report.

Comparisons are reported which verify the correctness of these new procedures, and which demonstrate their capability for computing a wide range of flows encompassing those typical of solar-wind conditions about terrestrial planetary atmospheres. A catalog of sample solar-wind flows covering a large number of flow conditions and ionopause geometries was established, and reported in summary format in the forms of contour plots of important flow-field and magnetic-field properties. Finally, successful comparisons of results from the theoretical model were made with actual spacecraft data obtained from initial orbits of the Pioneer-Venus Orbiter. These results have indicated the importance, heretofore largely neglected, of the directional variability of the oncoming solar wind. All of these results, taken in toto, serve to verify the basic theoretical model which underlies the present procedures. Furthermore, it demonstrates the value of the present computational procedures as a research tool capable of routinely providing - at small computation cost

and in a format directly compatible with experimental observations - details of the solar-wind/planetary atmosphere interaction process not previously attainable.

With regard to future uses as well as improvements of the present model, the obvious need for a detailed study involving comparisons between theory and observations for a large number of orbits of the Pioneer-Venus Orbiter is clear. Based on the preliminary comparisons for orbits 3 and 6, the frozen magnetic-field model appears to be remarkably accurate for relatively quiet-time conditions. Similar comparisons of the plasma properties indicate a need for an improved interpretation of the results from the single-fluid theory in terms of multi-component measurements. Questions regarding the possible suppression by the interplanetary magnetic field of the number of degrees of freedom of the plasma require further study and could be clarified through systematic comparisons with data. Additionally, observations from the Pioneer-Venus Orbiter of the nightside ionosphere of Venus have indicated a more complex and dynamic structure than suspected. These observations point, in particular, toward the need for improvement of the simple model used in the present method for the determination of the ionosphere boundary. This improved determination would involve an iterative procedure in which a balance of the sum of the solar-wind gasdynamic plus magnetic pressure along the ionopause surface would be maintained against the ionospheric pressure. The present method, which balances the Newtonian pressure distribution against the ionospheric pressure, represents the first step in this iteration.

#### ACKNOWLEDGEMENTS

Support for the research reported in this investigation was provided by National Aeronautics and Space Administration, Headquarters under Contract NASW-3182 with Robert Murphy as Technical Monitor. Special thanks are given to J. H. Wolfe and J. D. Mihalov for generously providing solar-wind plasma information from Pioneer-Venus Orbiter plasma analyzer measurements, to C. T. Russell and J. A. Slavin for magnetic field information from Pioneer-Venus Orbiter fluxgate magnetometer measurements, and W. C. Knudsen for ionosphere plasma information from Pioneer-Venus Orbiter retarding potential analyzer measurements.

## APPENDIX A

### COMPUTER PROGRAM USER'S MANUAL

**BLANK PAGE**

APPENDIX A  
COMPUTER PROGRAM USER'S MANUAL

TABLE OF CONTENTS

<u>Section</u>	<u>Page No.</u>
A.1 INTRODUCTION	53
A.2 PROGRAM DESCRIPTION	54
A.2.1 Calculation Procedure	56
A.2.1.1 Blunt-body calculation	56
A.2.1.2 Marching calculation	58
A.2.1.3 Streamline calculation	59
A.2.1.4 Magnetic-field calculation	61
A.2.1.5 Contour calculation and plot generation	64
A.2.1.6 Trajectory calculation	65
A.2.2 Rerun Option	70
A.2.3 Program Limitations and Precautions	70
A.2.4 Convergence Criteria for Blunt-Body Calculation	71
A.3 DESCRIPTION OF INPUT	72
A.3.1 Dictionary of Input Variables	72
A.3.2 Preparation of Input Data	77
A.3.3 Format of Input Data	81
A.4 DESCRIPTION OF OUTPUT	85
A.5 PROGRAM ERROR MESSAGES	87
A.6 SAMPLE CASE	90
FIGURES A.1 THROUGH A.6	92

**BLANK PAGE**



## APPENDIX A

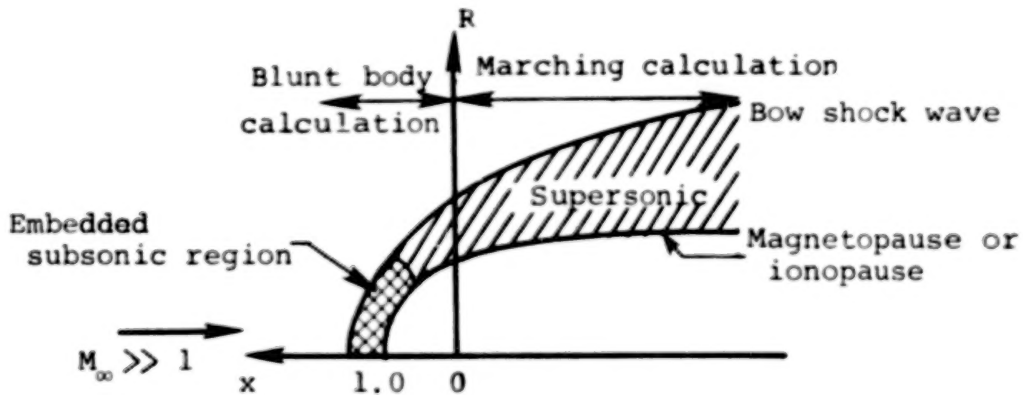
### A.1 INTRODUCTION

The purpose of this appendix is to describe the operation of the assemblage of computer codes which were developed in conjunction with the theoretical work presented in this report and organized into one program, and to provide sufficient detail to permit understanding and use of the program. The program computes the flow field of the solar wind about a terrestrial planet, using a procedure for the calculation of supersonic/hypersonic flow about an axisymmetric blunt body. The corresponding frozen-in magnetic field is calculated from the previously-determined velocity and density fields. Streamlines and contour lines of various flow-field properties and magnetic-field components are also determined. Next, these flow-field and magnetic-field values are calculated for points along a user-specified trajectory.

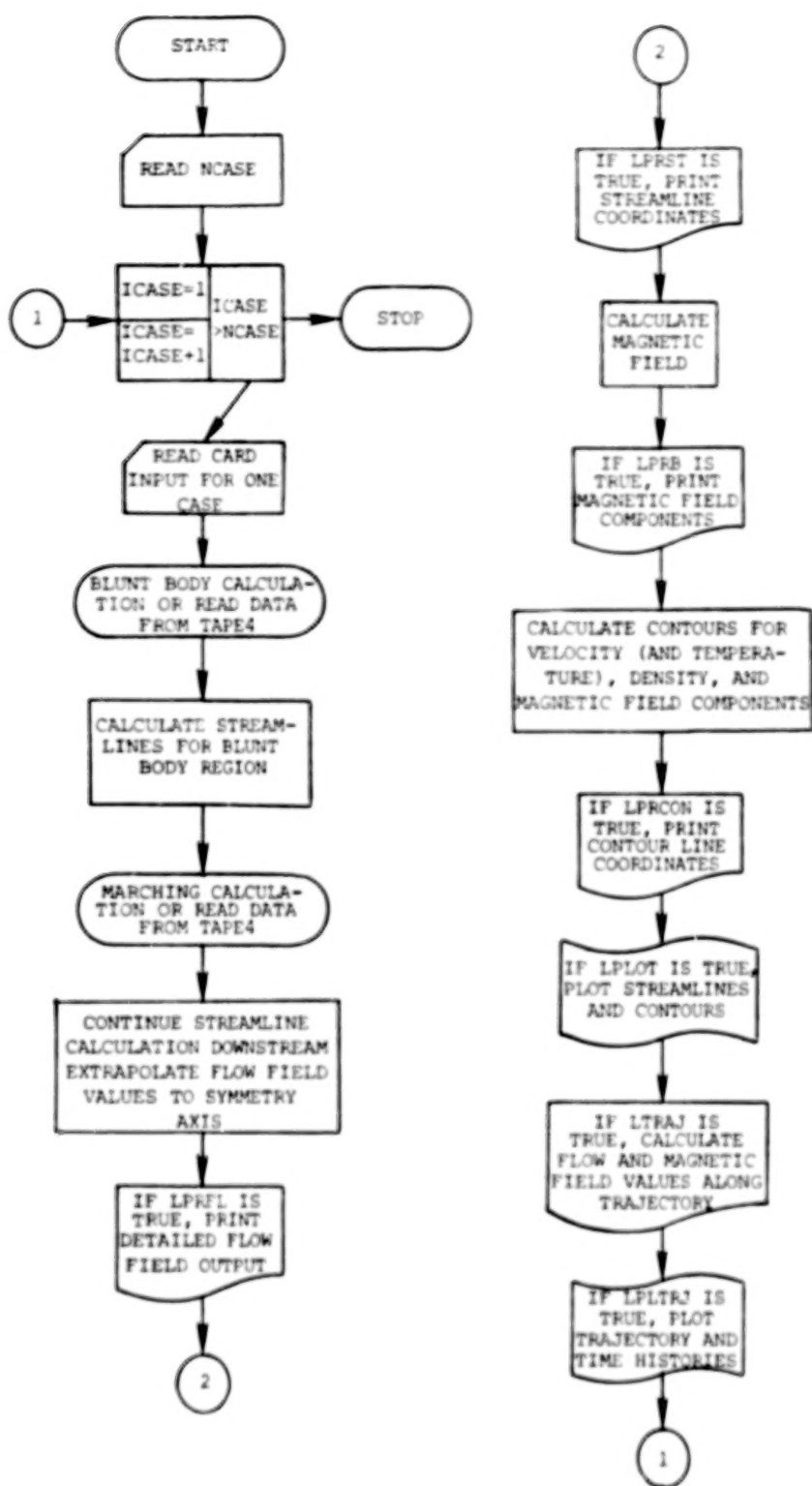
A description of the general operating procedure of the program is given, with descriptions of input and output. The program is written in FORTRAN IV and has been developed on a CDC 7600 computer. University Computing Company (UCC) Standard Plotting Software and Functional Software packages are used to produce automated plots. Files used, besides TAPE5 for INPUT and TAPE6 for OUTPUT, are TAPE1 for the plot file (system default), TAPE4 for input file for rerun option, and TAPE9 for storing data for rerun. Typical run times for cases using the default parameters are 110 to 120 seconds, using the OPT=2 compiler. For a case using the rerun option, which employs a previously-calculated flow field, the run time is approximately 15 seconds. The storage requirements are 146K<sub>8</sub> for small core memory and 273K<sub>8</sub> for large core memory.

## A.2 PROGRAM DESCRIPTION

For computational purposes, the flow is subdivided into two regions, as indicated in the sketch below, with the center of the planet as origin.



The region near the nose of the magnetopause/ionopause includes all of the imbedded subsonic flow and part of the supersonic flow. An axisymmetric implicit unsteady Euler equation solver is used to calculate this part of the flow field. Using the solution plane at  $x = 0.0$  to provide starting conditions, the flow field in the purely supersonic downstream region is determined by integrating the steady Euler equations using a spatial-marching procedure. Streamlines, the magnetic field, and contours are calculated using the entire flow field, distinguishing between the two regions as required by the different forms of the computational grids. A rerun capability is provided, where flow-field data is read from a file written on a previous run, rather than repeating the blunt-body and marching calculations. The computations proceed as shown in the sketch below, which provides an overall flow chart of the complete program. The program provides for several cases to be run consecutively.



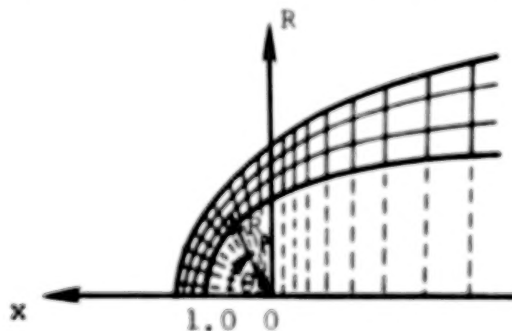
Program Flow Chart

### A.2.1 Calculation Procedure

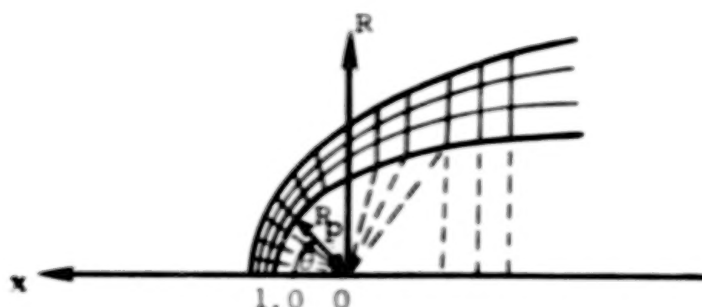
After reading in the number of cases in the run, each case is calculated independently. Subroutine INPUT reads in all card input required for one case, viz. a title, flow conditions, obstacle geometry, calculation and print control parameters, and desired contour values. The user may supply the obstacle geometry in the form of a shape table for an axisymmetric body, or use one of the default shapes which are calculated internally by the program. These default shapes are the magnetopause equatorial trace, constant scale-height ionopauses, and ionopauses having gravitational variation in scale-height. The input is printed as the first item of output.

#### A.2.1.1 Blunt-body calculation

A computational mesh in polar ( $R_p, \theta$ ) coordinates is established for the blunt-body calculation; then, for the marching calculation, this is extended into a cylindrical ( $x, R$ ) system, as indicated below:



This method has proven effective except for certain obstacle shapes which have a significant amount of flaring at the terminator and/or cases involving low free-stream Mach numbers  $M_\infty \leq 3$ . Under such conditions, the axial component of velocity may become subsonic at the starting plane of a marching calculation (terminator) and the calculation cannot proceed. In this case the blunt-body grid must be extended past  $\theta = 90^\circ$  as shown below:



The number of rays added to the blunt-body mesh is controlled by the input variable NXADD, and are limited by the requirement,  $NBLUNT + NXADD \leq 39$ .

All lengths,  $x$ ,  $R$ ,  $R_p$ , are normalized so that the nose of the obstacle is at  $x = 1.0$ . For the default shapes, rays at equal angular increments of  $\Delta\theta$  are used, starting at  $-\Delta\theta/2$ , up to  $90^\circ + \Delta\theta$ , where  $\Delta\theta = 90^\circ/(NBLUNT-1.5)$ , and NBLUNT is an input parameter describing the number of angular mesh points to be used in the blunt-body calculation. Program default value is  $NBLUNT = 24$ , so that for the default mesh,  $\Delta\theta = 4^\circ$ . The obstacle shape is determined by integrating the appropriate differential equation by a trapezoidal predictor-corrector method. For a user-supplied shape, the  $\theta$  grid is determined by rays from the origin through the first NBLUNT points, and the reflection of the first ray about the  $x$ -axis. Values for  $R_p$  are determined by dividing the line segments between the body and bow shock wave into  $NR-1$  equal intervals. Thus, including the obstacle and bow shock wave, the grid forms  $NR$  arcs around the obstacle. A starting solution for the blunt-body calculation is obtained by guessing a bow shock shape and by prescribing a Newtonian pressure distribution on the body. Noting that the maximum entropy streamline wets the body, other flow properties on the body surface can then be calculated. An initial flow field is then established by linear interpolation between the obstacle and the guessed bow shock, where the Rankine-Hugoniot relations hold. The integration proceeds in time for ITER steps. The initial bow shock shape used for the magnetopause equatorial trace and for an

ionopause with  $H/R_O \geq 0.1$  is a correlation shape depending on  $(M_\infty, \gamma, H/R_O)$  and given by the parabola  $R_p = \delta_1 \sqrt{\delta_O - x/\delta_O}$  where

$$\delta_O = 1.0 + 1.1 \{[(\gamma-1)M_\infty^2 + 2]/(\gamma+1)M_\infty^2\} \times (0.9 + 0.5 H/R_O)$$

$$\delta_1 = \Delta_O \{ (1.273 + 0.009 M_\infty^2) (0.904 + 0.655 H/R_O) \\ \times [3.95 - 5.3 H/R_O + 3.85 (H/R_O)^2] \} + (R_{body})_{x=0.0}$$

$$\Delta_O = \{[(\gamma-1)M_\infty^2 + 2]/[(\gamma+1)M_\infty^2]\} \times 0.78$$

For a user-supplied obstacle shape and for an ionopause with  $H/R_O < 0.1$ , the initial shock shape used is the curve  $R_p = \sqrt{[1 + \Delta_O (1 + 0.68 \theta^2 + 0.16 \theta^4)]}$ . Information on convergence, the final sonic line locations, and the body and final bow shock shape are printed from this calculation.

The flow chart for the blunt-body code is shown in Figure A.1(a).

#### A.2.1.2 Marching calculation

The results at the  $\theta = 90^\circ$  plane of the blunt-body calculation are used as starting conditions for the marching calculation, after proper variable normalization for the internal marching calculation. For default geometries, the obstacle shape is determined by integration of the appropriate differential equation proceeding from the nose downstream at equal  $\theta$  increments to form a body-shape table. The stepsize along the x-axis is recalculated at every ICONST(49) with ICONST(49) being set to 10. At each x-location,  $R_{body}$  is determined by linear interpolation. The computational mesh is extended by adding the line perpendicular to the x-axis at each step, divided in the same manner as for the blunt nose. The calculation marches downstream with a maximum stepsize of 1.0 until the terminal location specified

by the user has been passed. However, the number of steps is limited to 75, after which the calculation will end regardless of the x-location. The coordinates of the obstacle and bow shock are printed at each step.

The grid coordinates and flow-field values are written to a file, TAPE9, which may be saved to use as input for a later run. This rerun option, which replaces construction of the computational mesh and performance of the blunt-body and marching calculations with the reading of the rerun input file TAPE4, is described in section A.2.2. The flow chart for the marching calculation is provided in figure A.1(b).

#### A.2.1.3 Streamline calculation

The streamlines are calculated in two sections, following each of the flow-field calculations. Using the results of the blunt-body calculation, i.e. the  $(x,R)$  grid coordinates,  $(R_p,\theta)$  grid coordinates, density  $\rho/\rho_\infty$ , and velocity components  $v_X/v_\infty$  and  $v_R/v_\infty$ , the velocity magnitude  $|v|/v_\infty$  and flow angle  $\phi$  are calculated. Density  $\rho/\rho_\infty$  and velocity magnitude  $|v|/v_\infty$  are first smoothed along the rays of constant- $\theta$ , using a third-degree least-squares fit with respect to  $R_p$ . Streamlines are then calculated downstream to  $x = 0.0$ , using the trajectory method and integrating through the velocity field by means of a third-order modified Euler integration procedure with the grid locations on the bow shock used as starting positions. The flow angle  $\phi = \tan^{-1}(v_R/v_X)$  at each point is determined using bivariate linear interpolation first in  $\theta$ , then  $R_p$ . Points for which  $\theta < 0^\circ$  or  $\theta > 90^\circ$  are discarded in the interpolation.

The marching calculation provides  $(x,R)$  grid coordinates, and values of density  $\rho/\rho_t$ , and velocity components  $v_X/v_t$  and  $v_R/v_t$ , where  $t$  denotes free-stream stagnation conditions. For compatibility with the blunt-body solution, the flow-field values are converted to  $\rho/\rho_\infty$ ,  $v_X/v_\infty$ ,  $v_R/v_\infty$  before calculating the resultant velocity magnitude



$|y|/v_\infty$  and flow angle  $\phi$ . The streamline calculation is continued downstream, employing the same method as in the nose region. Starting positions on the shock wave for the streamline calculation in the marching zone are set at equal R-increments, with a maximum of 50 streamlines calculated. The flow angle is determined using bivariate linear interpolation first in  $x$ , then in  $R$ .

Along the symmetry axis, values of  $x$ ,  $\rho/\rho_\infty$ , and  $|y|/v_\infty$  are determined by extrapolation, using a third-order Lagrangian polynomial in  $\theta$  on each arc of the computational grid. Exact values for the stagnation streamline are used where possible, viz. at the bow shock

$$\rho/\rho_\infty = (\gamma+1)M_\infty^2 / [(\gamma-1)M_\infty^2 + 2]$$

$$|y|/v_\infty = 1/(\rho/\rho_\infty)$$

at the body surface

$$\begin{aligned} \rho/\rho_\infty &= (\rho/\rho_\infty)_{\text{shock}} \cdot \left\{ \left[ \frac{[(\gamma+1)M_\infty]^2}{4\gamma M_\infty^2 - 2(\gamma-1)} \right]^{1/(\gamma-1)} \right\} \\ |y|/v_\infty &= 0.0 \\ x &= 1.0 \end{aligned}$$

Detailed flow-field output may now be printed by subroutine FLOUT, with LPRFL as print control variable. In addition to grid coordinates, density, velocities and flow angle, values of temperature  $T/T_\infty$  and pressure  $P/P_\infty$  are output, where

$$T/T_\infty = 1 + [(\gamma-1)/2] \cdot M_\infty^2 \cdot [1 - (|y|/v_\infty)^2]$$

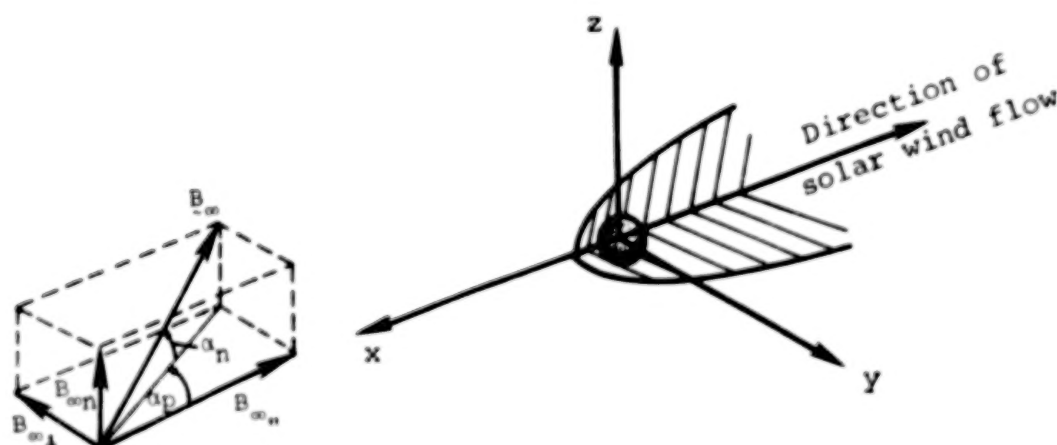
$$P/P_\infty = (\rho/\rho_\infty) (T/T_\infty)$$



Streamline coordinates may also be printed by subroutine STOUT, with LPRST as print control variable. A plot of the streamlines is generated if the variable LPLOT is true. A flow chart of the streamline calculation is shown in figure A.1(c).

#### A.2.1.4 Magnetic-field calculation

The magnetic field is determined by separately calculating the unit components whose directions are parallel, perpendicular, and normal to the flow, in the undisturbed solar wind. These components are then added vectorially, the resultant being expressed in orthogonal  $(x,y,z)$  components. The angles in the free stream  $\alpha_p$  and  $\alpha_n$  between the magnetic field and the flow, as shown in the sketch below, are either input or, in the case of a trajectory calculation, are calculated internally from the input interplanetary magnetic field.



The magnetic-field components are calculated using the following formulae in which  $\underline{e}$  signifies a vector of magnitude  $e$  in the direction of the component field line, and  $\hat{n}$  the unit normal vector.

$$\left(\frac{\underline{B}}{B_{\infty}}\right)_{\infty} = \left(\frac{v}{v_{\infty}}\right)\left(\frac{\rho}{\rho_{\infty}}\right); \quad \left(\frac{\underline{B}}{B_{\infty}}\right)_{\perp} = \left(\frac{\Delta \underline{\ell}}{\Delta \ell_{\infty}}\right)\left(\frac{\rho}{\rho_{\infty}}\right); \quad \left(\frac{\underline{B}}{B_{\infty}}\right)_n = \left(\frac{R}{R_{\infty}}\right)\left(\frac{\rho}{\rho_{\infty}}\right)$$

$$\left(\frac{\underline{B}}{B_{\infty}}\right) = \left(\frac{\underline{B}}{B_{\infty}}\right)_{\infty} \left(\frac{B_{\infty}}{B_{\infty}}\right) + \left(\frac{\underline{B}}{B_{\infty}}\right)_{\perp} \left(\frac{B_{\infty}}{B_{\infty}}\right) + \hat{n} \left(\frac{\underline{B}}{B_{\infty}}\right)_n \left(\frac{B_{\infty}}{B_{\infty}}\right)$$

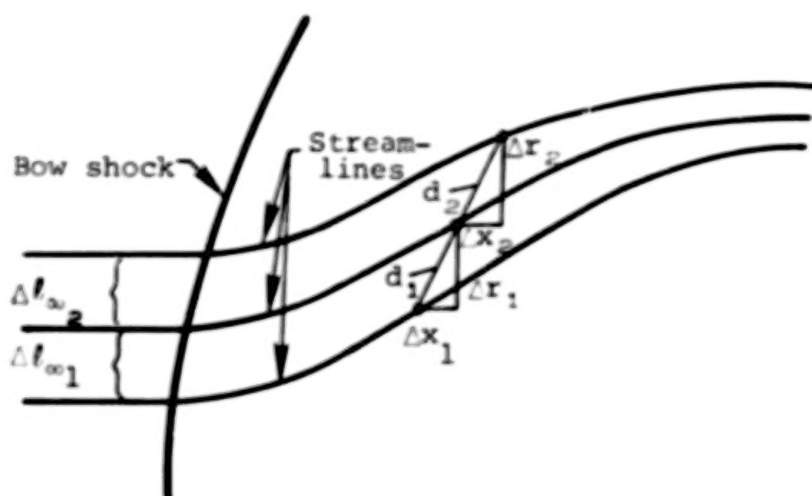
The magnetic-field line vector component  $\underline{B}_{\infty}$  which results from the interplanetary component  $B_{\infty}$  that is parallel to the undisturbed solar flow has local magnitude given by  $(|v|/v_{\infty})(\rho/\rho_{\infty})$ , and the same local direction  $\phi$  as the fluid flow. Determination of the normal magnetic-field component  $B_n$  requires calculation of  $R/R_{\infty}$ , where  $R_{\infty}$  is the free-stream cylindrical R-ordinate of the streamline through the point under consideration. This is calculated by linearly interpolating in the local radial cylindrical coordinate  $R$  between the streamlines, with  $R/R_{\infty} = 1.0$  along the x-axis. The magnetic-field vector component  $\underline{B}_{\perp}$  resulting from the interplanetary component  $B_{\infty\perp}$  which is perpendicular to the undisturbed solar-wind flow requires the distance vector  $\Delta \underline{\ell}/\Delta \ell_{\infty}$ , whose magnitude is  $|\Delta \underline{\ell}|/\Delta \ell_{\infty}$  and direction is  $\psi$ , where  $|\Delta \underline{\ell}|/\Delta \ell_{\infty}$  is the stretching factor of the perpendicular field at the point, and  $\psi$  is the direction of the field line through the point. The magnitude and direction of  $\Delta \underline{\ell}/\Delta \ell_{\infty}$  are calculated according to

$$\frac{|\Delta \underline{\ell}|}{\Delta \ell_{\infty}} = \frac{d_1 \cdot d_2}{d_1 + d_2} \cdot \frac{1}{\Delta \ell_{\infty 1} + \Delta \ell_{\infty 2}}$$

and

$$\psi = \frac{\tan^{-1} \left( \frac{\Delta r_1}{\Delta x_1} \right) \cdot d_2 + \tan^{-1} \left( \frac{\Delta r_2}{\Delta x_2} \right) \cdot d_1}{(d_1 + d_2)}$$

where the quantities  $d_1$ ,  $d_2$ ,  $\Delta x_1$ ,  $\Delta x_2$ ,  $\Delta r_1$ ,  $\Delta r_2$ ,  $\Delta \ell_{\infty 1}$ , and  $\Delta \ell_{\infty 2}$  are described by the sketch below. The points marked (•) on the streamlines represent equal-time intervals in the flow.



The perpendicular field lines are determined by integrating  $\int y dt$  along each streamline, using trapezoidal integration to locate points along the streamline at regular increments in time,  $\Delta t$ , starting at a perpendicular field line ahead of the bow shock. Values for  $|\Delta \xi|/\Delta \ell_{\infty}$  and  $\psi$  are calculated at the points where the perpendicular field lines and streamlines intersect, interpolating only along the field lines. A generalized quadrilateral interpolation scheme is then employed to determine  $|\Delta \xi|/\Delta \ell_{\infty}$  and  $\psi$  at the computational grid points, using the quadrilateral containing the point formed by the intersection of pairs of adjacent streamlines and perpendicular field lines. At the bow shock, an exact formula is used, viz.

$$(|\Delta \xi|/\Delta \ell_{\infty})^2 = 1 + \cot^2 \theta (1 + D^2) - 2D \times \csc \theta \times \cot \theta \times \cos(\theta - \delta)$$

$$\psi = \theta + \sin^{-1} [D \times \cot \theta \times \sin(\theta - \delta) / (|\Delta \xi|/\Delta \ell_{\infty})]$$

where

$$D^2 = 1 - 4(M_\infty^2 \sin^2 \theta - 1)(\gamma M_\infty^2 \sin^2 \theta + 1) / [(\gamma + 1)^2 M_\infty^4 \sin^2 \theta]$$

$$\cot \delta = \tan \theta \times \{(\gamma + 1)M_\infty^2 / [2(M_\infty^2 \sin^2 \theta - 1)] - 1\}$$

$$\theta = \tan^{-1} \left( \frac{dR_{\text{shock}}}{dx} \right)$$

The values of  $|\Delta \underline{\ell}|/\Delta \ell_\infty$  at the grid points are smoothed using fifth-order least-squares fit with respect to arc length along the arcs of the grid. The resultant magnetic field can then be expressed in orthogonal (x,y,z) components. The code determines these components for the case when the field point is located in the (x,y) plane, i.e.,  $z = 0$ . These components are given by

$$B_x/B_\infty = \cos \alpha_n \times [\cos \phi \times \cos \alpha_p \times (|\underline{B}|/B_\infty)_n \\ + \cos \psi \times \sin \alpha_p \times (|\underline{B}|/B_\infty)_\perp]$$

$$B_y/B_\infty = \cos \alpha_n \times [\sin \phi \times \cos \alpha_p \times (|\underline{B}|/B_\infty)_n \\ + \sin \psi \times \sin \alpha_p \times (|\underline{B}|/B_\infty)_\perp]$$

$$B_z/B_\infty = \sin \alpha_n \times (B/B_\infty)_n$$

Magnetic-field components may now be printed by subroutine BOUT, with LPRB as print control parameter. The magnetic field is not calculated when LPRB = .FALSE. and KBCON=0. A flow chart of the magnetic-field calculation is shown in figure A.1(d).

#### A.2.1.5 Contour calculation and plot generation

Contours are calculated for velocity  $|\underline{v}|/v_\infty$ , density  $\rho/\rho_\infty$ , and magnetic components  $(|\underline{B}|/B_\infty)_n$ ,  $(|\underline{B}|/B_\infty)_\perp$ , and  $(|\underline{B}|/B_\infty)_n$ . The method used is a modified version of a procedure developed by R. Sorenson

of NASA/Ames Research Center. The boundary is searched for intervals which bracket a contour point. Having found one point, the remainder of the contour is determined by 'walking' around the contour, searching at each step for the interval through which the contour line next passes, until a boundary point is reached. Then closed contours are found in a similar manner. Linear interpolation is used throughout the process. Note that since  $T/T_\infty$  is a function of  $|v|/v_\infty$  only, velocity contours may also be considered as temperature contours. Temperature and velocity are related by the following function.

$$T/T_\infty = 1 + \frac{\gamma-1}{2} M_\infty^2 \left[ 1 - \left( \frac{|v|}{v_\infty} \right)^2 \right]$$

The coordinates of the contour lines can be printed by subroutine CONOUT, with LPRCON as print control parameter.

The program segment which controls the generation of contour plots is accessed only when  $L\text{PLOT} = .\text{TRUE}$ . The UCC Plot Routines used to produce these plots are AXIS, CHAR, DASH, DOTLN, ENPLT, GREEK, MATH, NUMPLT, PLOT, PLTLN, POLAR, RESET, SCALF, and VECTOR. A flow chart of the contour calculation and plot generation in figure A.1(e).

#### A.2.1.6 Trajectory calculation

This segment of the program provides theoretical plasma and magnetic-field properties in an output form that is useful for direct comparison with actual spacecraft data. Given a sequence of coordinates describing the spacecraft trajectory, the program calculates the density, temperature, and velocity and magnetic-field components at each point. Generation of trajectory plots is controlled by the logical variable LPLTRJ. The trajectory calculation proceeds as follows.

Input to this calculation includes interplanetary values of temperature, density, velocity, and magnetic field together with

the trajectory coordinates. The trajectory input is required as a function of time and normalized by planetary radius. If the logical variable LSUN is TRUE, then it is assumed that the trajectory coordinates and vector quantities are expressed in terms of a sun-planet (ecliptic) coordinate system. In this case, these quantities are converted by the program into a solar-wind coordinate system by the transformation

$$\begin{pmatrix} x_w \\ y_w \\ z_w \end{pmatrix} = \begin{pmatrix} \cos \Omega \cos \phi_p & -\sin \Omega \cos \phi_p & \sin \phi_p \\ \sin \Omega & \cos \Omega & 0 \\ -\cos \Omega \sin \phi_p & \sin \Omega \sin \phi_p & \cos \phi_p \end{pmatrix} \begin{pmatrix} x_s \\ y_s \\ z_s \end{pmatrix}$$

where  $(x_w, y_w, z_w)$  are coordinates in the solar-wind system and  $(x_s, y_s, z_s)$  are coordinates in the sun-planet system. The angles  $\Omega$  and  $\phi_p$  are the azimuthal (total aberration) and polar angles, respectively. The azimuthal angle,  $\Omega$ , is the angle in the plane of the ecliptic between the sun-planet line and the oncoming solar-wind, i.e., the  $x_s$ -axis and the  $x_w$ -axis as shown in figure A.2. The angle  $\phi_p$ , positive for southward solar-wind flow, measures the deviation of the solar-wind from the plane of the ecliptic. Figure A.2 illustrates the transformation from sun-planet ecliptic coordinates to solar-wind coordinates. In this case the azimuthal and polar angles indicated are both positive.

If LSUN is FALSE, it is assumed that all input data are referenced to the solar-wind coordinate system and this transformation is not performed.

In order to conform with the internal flow-field and magnetic-field calculations, the signs of the x and y components of the trajectory and vector quantities are reversed. This is, in effect, another coordinate transformation which is defined by

$$\begin{pmatrix} x_c \\ y_c \\ z_c \end{pmatrix} = \begin{pmatrix} -1 & 0 & 0 \\ 0 & -1 & 0 \\ 1 & 0 & 1 \end{pmatrix} \begin{pmatrix} x_w \\ y_w \\ z_w \end{pmatrix} = \begin{pmatrix} -\cos \Omega \cos \phi_p & -\sin \Omega \cos \phi_p & \sin \phi_p \\ \sin \Omega & -\cos \Omega & 0 \\ -\cos \Omega \sin \phi_p & \sin \Omega \sin \phi_p & \cos \phi_p \end{pmatrix} \begin{pmatrix} x_s \\ y_s \\ z_s \end{pmatrix}$$

where  $(x_c, y_c, z_c)$  are coordinates referenced to the internal calculation system. This transformation is illustrated in figure A.3. Also shown in figure A.3 is the relationship of the interplanetary parallel, perpendicular, and normal magnetic field components to the internal calculation system. Specifically,

$$B_{\infty p} = B_{x_c}, \quad B_{\infty \perp} = B_{y_c}, \quad \text{and} \quad B_{\infty n} = B_{z_c}$$

The angles  $\alpha_p$  and  $\alpha_n$  are now calculated from the relationships

$$\alpha_p = \tan^{-1} \left( \frac{B_{y_c}}{B_{x_c}} \right)$$

and

$$\alpha_n = \tan^{-1} \left( \frac{B_{y_c}}{\sqrt{(B_{x_c})^2 + (B_{y_c})^2}} \right)$$

At this point, all data is in a form compatible with the internal calculations and the program can interpolate for flow and magnetic-field values along the trajectory. The following procedure is repeated at each trajectory point. Noting that the flow is axisymmetric, the coordinate system may be rotated to the most convenient orientation for the calculation. The present  $(x_c, y_c, z_c)$  coordinates are converted to  $(x_c, R)$  coordinates by a rotation in the  $(y_c, z_c)$  plane about the  $x_c$ -axis through the angle  $\theta = \tan^{-1}[z_c/y_c]$ . This rotation defines a new coordinate system  $(x', y', z')$  in which  $z' = 0$ . Subroutine IJRAJ now locates the point with reference to the computational flow-field grid. The point is either within the ionopause, in the grid



region, or beyond the bow shock. If the point is within the ionopause, all values are set to zero. If the point lies beyond the bow shock, all quantities assume their free-stream values. For points within the grid, the velocity magnitude, density, and flow angle  $\phi$  are found by interpolation using function FTRAJ. From the flow angle  $\phi$  and the rotation angle  $\theta$ , velocity components in the  $(x_c, y_c, z_c)$  system can be calculated according to

$$\begin{aligned}v_{x_c} &= v \cos \phi \\v_{y_c} &= v \sin \phi \cos \theta \\v_{z_c} &= v \sin \phi \sin \theta\end{aligned}$$

Calculation of the magnetic field is complicated somewhat because the components are dependent on the incident magnetic field. Using  $\alpha_p$  and  $\alpha_n$ ,  $B'_{x_\infty}$ ,  $B'_{y_\infty}$ , and  $B'_{z_\infty}$  are calculated in the rotated  $(x', y', z')$  system by

$$\begin{aligned}B'_{x_\infty} &= B_{x_{c_\infty}} \\B'_{y_\infty} &= B_{y_{c_\infty}} \cos \theta + B_{z_{c_\infty}} \sin \theta \\B'_{z_\infty} &= -B_{y_{c_\infty}} \sin \theta + B_{z_{c_\infty}} \cos \theta\end{aligned}$$

Then  $\alpha'_p$  and  $\alpha'_n$  are defined by

$$\alpha'_p = \tan^{-1} \left( \frac{B'_{y_\infty}}{B'_{x_\infty}} \right) \text{ and } \alpha'_n = \tan^{-1} \left[ \frac{B'_{z_\infty}}{\sqrt{(B'_{x_\infty})^2 + (B'_{y_\infty})^2}} \right]$$

Interpolation is then carried out to determine the magnetic angle  $\psi$  and the ratios  $\left| \frac{B}{B_\infty} \right|_n$ ,  $\left| \frac{B}{B_\infty} \right|_1$ , and  $\left( \frac{B}{B_\infty} \right)_n$  in the rotated system again using the function FTRAJ. Next, the magnetic-field components  $B'_x$ ,  $B'_y$ ,  $B'_z$  in the rotated system are calculated from

$$B'_x = \cos \alpha'_n \left[ \cos \phi \cdot \cos \alpha'_p \cdot \left| \frac{B}{B_\infty} \right|_n + \cos \psi \cdot \sin \alpha'_p \cdot \left| \frac{B}{B_\infty} \right|_1 \right] \cdot B_\infty$$

$$B'_y = \cos \alpha'_n \left[ \sin \phi \cdot \cos \alpha'_p \cdot \left| \frac{B}{B_\infty} \right|_n + \sin \psi \cdot \sin \alpha'_p \cdot \left| \frac{B}{B_\infty} \right|_1 \right] \cdot B_\infty$$

$$B'_z = \sin \alpha'_n \cdot \left( \frac{B}{B_\infty} \right)_n \cdot B_\infty$$

Finally, these magnetic-field components are rotated back through the angle  $\theta$  to yield magnetic-field components referenced to the internal calculation system  $(x_c, y_c, z_c)$  by

$$\begin{pmatrix} B_{x_c} \\ B_{y_c} \\ B_{z_c} \end{pmatrix} = \begin{pmatrix} 1 & 0 & 0 \\ 0 & \cos \theta & -\sin \theta \\ 0 & \sin \theta & \cos \theta \end{pmatrix} \begin{pmatrix} B'_x \\ B'_y \\ B'_z \end{pmatrix}$$

Subroutine TROUT now prints the trajectory output in both the solar-wind  $(x_c, y_c, z_c)$  and the sun-planet  $(x_s, y_s, z_s)$  coordinate systems using the transformation below to obtain sun-planet magnetic-field vector components from solar-wind magnetic-field vector components.

$$\begin{pmatrix} B_{x_s} \\ B_{y_s} \\ B_{z_s} \end{pmatrix} = \begin{pmatrix} -\cos \Omega \cos \phi_p & \sin \Omega & -\cos \Omega \sin \phi_p \\ \sin \Omega \cos \phi_p & -\cos \Omega & \sin \Omega \sin \phi_p \\ \sin \phi_p & 0 & \cos \phi_p \end{pmatrix} \begin{pmatrix} B_{x_c} \\ B_{y_c} \\ B_{z_c} \end{pmatrix}$$

The transformation of the solar-wind velocity components ( $v_{x_C}$ ,  $v_{y_C}$ ,  $v_{z_C}$ ) into sun-planet components ( $v_{x_S}$ ,  $v_{y_S}$ ,  $v_{z_S}$ ) is also done using the same transformation.

Finally, if LPLTRJ is true, a file of trajectory plots is created. A flow chart for this program segment is shown in figure A.1(f).

#### A.2.2 Rerun Option

The rerun option is used when LRERUN = .TRUE. The blunt-body and marching calculations are replaced with the reading of grid coordinates and flow-field values from the rerun file, TAPE4, which contains data written to TAPE9, then saved, on a previous run. Different values for any parameter not used in the flow-field calculations may be specified, viz. contour values, plot length, magnetic-field angles, and output options. Values of AMACH, GAMMA, and HRO are required input, to ensure that the input rerun file does contain the case desired for rerun. If the geometry is user-supplied, the body-shape table will be read from TAPE4, and should not be input from cards.

After reading the card input, MACH, GAMMA, and HRO are tested against values from TAPE4. The grid coordinates and flow-field values from the blunt-body calculation are read in, then smoothed, and streamlines calculated for this region, as previously described. The results of the marching calculation are then read, and the streamline calculation continued downstream. The calculations then proceed as described in section A.2.1.

A run must not contain more than one case which uses the rerun option.

#### A.2.3 Program Limitations and Precautions

The program makes some assumptions about the geometry of the obstacle shape around which flow is to be calculated, and about the

flow field. The obstacle shape is assumed to be monotonically increasing in cylindrical radius  $R$ , going downstream. The nose of the obstacle is at  $x = 1.0$ . The origin of the  $(x,R)$  coordinate system is the center of the planet. Obstacle shapes with sharp corners should be avoided. In the magnetic-field calculation, the first streamline is assumed to be inside the arc described by the grid points immediately off the body, downstream of  $x = 0.0$ . To reduce computational costs, a grid using  $NR = 10$  may be used, in which case a lower value of  $CN$  may be required. This would reduce the running time by approximately 40 percent. A free-stream Mach number less than 2.0 is not advised.

#### A.2.4 Convergence Criteria for Blunt-Body Calculation

The output provides two measures of the convergence of the blunt-body calculation. The RMS of shock speed and maximum shock speed are printed at each iteration. These quantities should both tend to zero as the iterations proceed. A value for  $q_{RMS}$ , RMS of shock speed, of

$$q_{RMS} < \sqrt{\gamma} \times M_{\infty} \times 10^{-3}$$

where  $\gamma$  is the specific heat ratio, and  $M_{\infty}$  is the free-stream Mach number, usually indicates a converged solution. The RMS of error in enthalpy,  $HT$ , should be less than 1 percent, with the maximum enthalpy error also of that order.

The Courant number,  $CN$ , determines the time step size used by the calculation. A value not greater than the default of 3.0 should be used. For low Mach numbers or a coarser mesh than the default grid, a lower value may be preferable. If the default value does not generate a converged solution, or if the error message from subroutine SHOCK is printed, try lowering  $CN$  in increments of 0.5 to find a better value of  $CN$ . User-supplied bodies may also require a lower Courant number.

### A.3 DESCRIPTION OF INPUT

This section describes the card input for the program. An alphabetized dictionary of input variables is provided, defining the variables, listing default values and limitations. A discussion of the preparation of the card input is then presented, followed by a description of the input card format.

#### A.3.1 Dictionary of Input Variables

- AMACH free-stream Mach number;  $3.0 \leq \text{AMACH} \leq 25.0$  is recommended
- ANGN the angle, in degrees, measuring the deviation of the free-stream magnetic field from the plane in which  $B_{\infty n}$  and  $B_{\infty 1}$  lie; equal to  $\tan^{-1} \left[ B_{\infty n} / \sqrt{|B_{\infty n}^2| + |B_{\infty 1}^2|} \right]$ ; see figure A.3, measured in the  $(x_C, y_C, z_C)$  coordinate system; only specified when interplanetary magnetic-field components not specified.
- ANGP the angle, in degrees, measuring the deviation of the in-plane magnetic component  $(B_{\infty n} + B_{\infty 1})$  from the direction of flow; equal to  $\tan^{-1} (B_{\infty n} / B_{\infty 1})$ ; see figure A.3, measured in the  $(x_C, y_C, z_C)$  coordinate system; only specified when interplanetary magnetic-field components not specified.
- AZANG angle in the ecliptic plane between the sun-planet line and the direction of solar-wind flow. See figure A.2 for positive direction.
- BCON(I) KBCON-dimensional array specifying values to be used for magnetic field strength contours
- BINF magnetic field strength free-stream value; set to 1.0 if plots desired in nondimensionalized units.

BX1  $x_s$ -component of interplanetary magnetic field; referred to sun-planet coordinates  
 BY1  $y_s$ -component of interplanetary magnetic field; referred to sun-planet coordinates  
 BZ1  $z_s$ -component of interplanetary magnetic field; referred to sun-planet coordinates  
 CN Courant number used for blunt-body calculation; program default value is 3.0  
 GAMMA ratio of plasma specific heats  
 HRO obstacle geometry indicator:  
     HRO > 0. - ionopause with  $H/R_0 = HRO$   
     HRO = 0. - magnetopause equatorial trace  
     HRO < 0. - geometry is user-supplied  
 ITER integer, number of iterations for blunt-body calculation; program default value is 300  
 KBCON integer, number of values specified for magnetic-field contours;  $0 \leq KBCON \leq 20$   
 KRCON integer, number of values specified for density contours;  $0 \leq KRCON \leq 20$   
 KVCON integer, number of values specified for velocity magnitude contours;  $0 \leq KVCON \leq 20$   
 LGRAV logical variable indicating whether default ionopause is calculated with gravitational variation in scale height  
     FALSE - no  
     TRUE - yes

LPLOT	<p>logical variable indicating whether to create plots or plot file</p> <p>FALSE - no</p> <p>TRUE - yes</p>
LPLTRJ	<p>logical variable indicating whether to create trajectory and time history plots</p> <p>FALSE - no</p> <p>TRUE - yes</p>
LPRB	<p>logical variable indicating whether to print magnetic field output</p> <p>FALSE - no</p> <p>TRUE - yes</p>
LPRCON	<p>logical variable indicating whether to print coordinates of contours lines</p> <p>FALSE - no</p> <p>TRUE - yes</p>
LPRFL	<p>logical variable indicating whether to print detailed flow-field output</p> <p>FALSE - no</p> <p>TRUE - yes</p>
LPRST	<p>logical variable indicating whether to print coordinates of streamlines</p> <p>FALSE - no</p> <p>TRUE - yes</p>
LRERUN	<p>logical variable indicating whether this case uses rerun option</p> <p>FALSE - perform blunt-body and marching calculations</p> <p>TRUE - read results of a previous calculation from TAPE4</p>



LRSTRT      logical variable indicating whether to use previous shock shape as initial guess for blunt body  
              TRUE    - use shock shape from previous solution.  
                       (Must have a full solution as an earlier run in same job.)  
              FALSE - use default initial guess for shock shape

LSUN        logical variable indicating whether trajectory input is referenced to sun-planet coordinate system  
              FALSE - trajectory input in solar-wind coordinates  
              TRUE  - trajectory input in sun-planet coordinates

LTRAJ       logical variable indicating whether to perform a trajectory calculation  
              TRUE  - trajectory calculation, data provided  
              FALSE - no trajectory calculation

MARKT(I)   NMARKT - dimensional array specifying points to be marked for cross reference. If  $K = \text{NMARKT}(I)$ , the Kth point of the trajectory is to be marked.

NBLUNT      integer, number of angular mesh points for blunt-body calculation; for user-supplied geometry,  $\text{XX}(\text{NBLUNT}-1)=0.0$ ; program default value, and maximum, is 24

NBOD        integer, number of points in body-shape table when geometry is user-supplied;  $1 \leq \text{NBOD} \leq 100$

NCASE       integer, number of cases to be run consecutively;  $\text{NCASE} > 1$

NMARKT      integer, numbered values specified for cross reference points;  $0 \leq \text{NMARKT} \leq 12$ .

NR          integer, number of radial mesh points; program default value, and maximum, is 19

NTRAJ	integer, number of points specified in trajectory table
NXADD	integer, number of points to be added to blunt-body grid past $\theta = 90^\circ$ , default value is 0.
POLANG	angle, measured in degrees, between the plane of the ecliptic and direction of solar-wind flow; positive for southward flow; see figure A.2
RCON(I)	KRCON - dimensional array specifying values to be used for density contours
RHOINF	density-free stream value; set to 1.0 if plots desired in nondimensional units
RPLNT	radius of planet in units of nose radius, $R_{PLNT}/R_0$
RR(I)	NBOD - dimensional array representing the R-locations, in cylindrical (x,R) coordinates, of the user-supplied body shape; in units of nose radius
TITLE	descriptive heading of the case, to be printed on the first page of output; may contain up to 80 characters, including blanks
TMPINF	free-stream temperature; set to 1.0 if plots desired in nondimensional units
TTRAJ(I)	NTRAJ - dimensioned array specifying time locations of trajectory points
VCON(I)	KVCON - dimensional array specifying values to be used for velocity contours

VINF	free-stream velocity; set to 1.0 if plots desired in non-dimensional units
XCALC	terminal downstream x-location for marching calculation of flow field; XCALC < 0.0; program default value is -1.0
XPLOT	terminal downstream x-location for calculation of streamlines, magnetic field, and contours; XCALC $\leq$ XPLOT $\leq$ 0.0; program default value is -1.0
XTRAJ(I)	NTRAJ - dimensioned array specifying $x_g$ -locations of trajectory points; in units of planetary radius; when (ANGP,ANGN) are specified, XTRAJ(I) is referred to solar-wind $x_c$ -locations; see figures A.2 and A.3
XX(I)	NBOD - dimensional array representing the x-locations, in cylindrical (x,R) coordinates, of the user-supplied body shape; in units of nose radius. See figures A.2 and A.3
YTRAJ(I)	NTRAJ - dimensioned array specifying $y_g$ -locations of trajectory points; in units of planetary radius; when (ANGP,ANGN) are specified, YTRAJ(I) is referred to solar-wind $y_c$ -locations; see figures A.2 and A.3
ZTRAJ(I)	NTRAJ - dimensioned array specifying $z_g$ -locations of trajectory points; in units of planetary radius; when (ANGP,ANGN) are specified, ZTRAJ(I) is referred to solar-wind $z_c$ -locations; see figures A.2 and A.3

### A.3.2 Preparation of Input Data

The card input for a run consists of one card containing the number of cases to be run consecutively, Item 0, followed by a set of input for each case, Item 1 through Item 7, and Item 8 if required. Where a default value is to be used, the input field should be left blank.

For each case, all required variables which do not assume their default values should be specified. The input format for all cards is described in section A.3.3.

Item 0 - This item consists of one card, containing the number of cases in this run, NCASE.

Item 1 - This card provides identification of the case, TITLE, which is printed on the first page of the output for this case.

Item 2 - This card contains information on the flow conditions and body geometry, and parameters required for the blunt-body and marching calculations. AMACH, GAMMA, and HRO must be specified for each case. For the rerun option, the values are tested against the values from the rerun file. The parameters XCALC, NR, NBLUNT, CN, ITER are used only when the flow field is to be calculated. These variables each assume a default value if the input field is blank.

Item 3 - This item consists of one card containing the rerun indicator, LRERUN, the output control variables LPRFL, LPRST, LPRCON, LPRB, and LPLOT, the trajectory indicator LTRAJ, and the restart indicator LRSTRT.

Item 4 - This card contains the variables XPLOT, ANGP, ANGN, NXADD, and LGRAV. The value for XPLOT is changed by the program to be the x-location of the marching calculation immediately upstream of the input value for XPLOT. The angles describing the deviation of the magnetic field from the flow, ANGP and ANGN, are not required when LPRB = .FALSE; KBCON = 0, and LTRAJ = .FALSE. since the magnetic field is not calculated under these conditions. ANGP is the angle between the vectors  $(\underline{B}_{\infty n} + \underline{B}_{\infty 1})$  and  $\underline{v}_{\infty}$ , while ANGN is the angle between  $\underline{B}_{\infty}$  and  $(\underline{B}_{\infty n} + \underline{B}_{\infty 1})$ , where  $\underline{B}_{\infty n}$ ,  $\underline{B}_{\infty 1}$ ,  $\underline{B}_{\infty n}$  are the components of the free-stream magnetic field,  $\underline{B}_{\infty}$ , which are parallel, perpendicular, and normal to  $\underline{v}_{\infty}$ , and are as indicated in figure A.3. The two angles ANGP and ANGN fully determine the half plane for which the magnetic field

is to be calculated. The magnetic field for the other half of the plane may be calculated by rerunning with the sign of ANGP reversed. When  $(B_{\infty n} + B_{\infty 1}) = 0$ ,  $ANGN = +90^\circ$ ,  $ANGP = 0^\circ$ ; and, when  $B_{\infty n} = 0$ ,  $ANGN = 0^\circ$ . Note that ANGP and ANGN are referenced to the  $(x_c, y_c, z_c)$  system and are specified only when the interplanetary magnetic-field components are not specified.

If both LTRAJ = .TRUE. and LSUN = .TRUE., then ANGP and ANGN are calculated internally from the interplanetary magnetic-field components BX1, BY1, and BZ1.

Item 5 - This item contains the values for the velocity contours. The first card contains KVCON, the number of values specified for VCON. If KVCON > 0, the contour values are then read. Up to three cards may be required to accommodate the values, eight per card, maximum of 20. The contour values should be monotonically increasing, with at least one value within the range of the magnitude of the velocity in the region for which contours are to be calculated.

Item 6 - This item contains the values for the density contours. The description is similar to that for Item 5, with KRCON being the number of values specified, and RCON the array of values.

Item 7 - This item contains the values for the magnetic-field contours. The description is similar to that for Item 5, with KBCON being the number of values specified, and BCON the array of values. Note that the same contour values are used for the parallel and perpendicular components.

Item 8 - This optional item is required when HRO < 0.0 and LRERUN = .FALSE., and contains the body-shape table for the user-supplied geometry. The first card contains NBOD, the number of points in the shape table. The next NBOD cards contain the cylindrical (x,R) coordinates of these points, [XX(I), RR(I)], one point per card. The points supplied by the user determine the  $\theta$ -spacing of the mesh used for the

blunt-body calculation. The first point should be near, but not on, the x-axis. A suggested location is such that the  $\theta$ -spacing between the first point and the x-axis is half the  $\theta$ -spacing between the first two points. The blunt-body calculation adds a point which is the reflection about the x-axis of the first point in the body-shape table. The  $(NBLUNT-1)^{th}$  point should be at  $x = 0.0$ . The  $BLUNT^{th}$  point is also used to create the grid for the blunt-body calculation. The coordinates must be normalized so that the planet center is at  $(0.,0.)$  and the nose of the body at  $(1.,0.)$ .

Item 9 - This optional item is read only when LTRAJ is TRUE. The first card contains NTRAJ, the number of points in the trajectory. Then follows NTRAJ cards, each containing the time T, and location  $(x_s, y_s, z_s)$  of one point. The time values should be monotonically increasing. At present,  $NTRAJ \leq 100$  is required. Note that when ANGP and ANGN are specified, the trajectory is specified in  $(x_c, y_c, z_c)$  coordinates.

Item 10 - This item is read only when LTRAJ is TRUE. The variable LPLTRJ indicates whether plots are to be produced of the trajectory and time histories. The relative size of the planet to the ionopause is given by RPLNT, which may be 0.0, in which case, a value of 1.0 is assumed in the calculations, but the planet is not drawn on the plots. Next are the four free-stream values  $v_\infty, T_\infty, \rho_\infty, B_\infty$ . If the plots are desired to be in nondimensional units, any or all of these values may be input as 1.0. Each quantity must have a value, zero is not permissible.

Item 11 - This item is read only when LTRAJ is TRUE. The first card contains NMARKT, the number of values specified for MARKT, (presently maximum of 12). If NMARKT = 0, only this card is required. If NMARKT > 0, the values of MARKT are read, 8 per card.

Item 12 - This item, which includes the variables LSUN, AZANG, POLANG, BX1, BY1, and BZ1, is read only when LTRAJ is true.

### A.3.3 Format of Input Data

Four format types are used for the input data. For real numbers (F-format), a decimal point is required. Integers (I-format) should be right-adjusted in the field. For logical variables (L-format), the first non-blank character in the field, which should be 'T' or 'F', determines the value. Note that a blank input field is interpreted as 'FALSE'. The title, which is in A-format, may contain any valid character.

A description of the card format of the input data follows, with item numbers corresponding to those in section A.3.2:



Item No. 0: 1 card

Variable	NCASE
Card Column	10
Format type	I

Item No. 1: 1 card

Variable	Title
Card Column	80
Format type	A

Item No. 2: 1 card

Variable	AMACH	GAMMA	HRO	XCALC	NR	NBLUNT	CN	ITER
Card column	10	20	30	40	50	60	70	80
Format type	F	F	F	F	F	F	F	F

Item No. 3: 1 card

Variable	LRERUN	LPRFL	LPRST	LPRCON	LPRB	LPLOT	LTRAJ	LRSTRT
Card column	10	20	30	40	50	60	70	80
Format type	L	L	L	L	L	L	L	L

Item No. 4: 1 card

Variable	"PLOT	ANGP	ANGN	NXADD	LGRAV
Card column	10	20	30	40	50
Format type	F	F	F	N	L

Item No. 5: a) 1 card

Variable	KVCON
Card column	10
Format type	I

b) 0 to 3 cards as needed for up to 20 values, 8 per card

Variable	VCON(1)	VCON(2)			VCON(KVCON)			
Card column	10	20	30	40	50	60	70	80
Format type	F	F	F	F	F	F	F	F

Item No. 6: a) 1 card

Variable	KRCON
Card column	10
Format type	I

b) 0 to 3 cards

Variable	RCON(1)	RCON(2)			RCON(KRCON)			
Card column	10	20	30	40	50	60	70	80
Format type	F	F	F	F	F	F	F	F

Item No. 7 a) 1 card

Variable	KBCON
Card column	10
Format type	I

b) 0 to 3 cards

Variable	BCON(1)	BCON(2)			BCON(KBCON)			
Card column	10	20	30	40	50	60	70	80
Format type	F	F	F	F	F	F	F	F

Item No. 8 a) 1 card (this item required only when HRO < 0.0 and LRERUN = .FLASE.)

Variable	NBOD
Card column	10
Format type	I

b) NBOD cards

XX(I)	RR(I)
10	20

Item No. 9: a) 1 card (this item read only when LTRAJ is TRUE)

Variable	NTRAJ
Card column	10
Format type	I

b) NTRAJ cards

Variable	TTRAJ(I)	XTRAJ(I)	YTRAJ(I)	ZTRAJ(I)
Card column	10	20	30	40
Format type	F	F	F	F

Item No. 10: 1 card (this item read only when LTRAJ is TRUE)

Variable	LPLTRJ	RPLNT	VINF	RHOINF	TMPINF	BINF
Card column	10	20	30	40	50	60
Format type	L	F	F	F	F	F

Item No. 11: a) 1 card (this item read only when LTRAJ is TRUE)

Variable	NMARKT
Card column	10
Format type	I

b) 0-2 cards

Variable	MARKT(1)	MARKT(2)			MARKT(NMARKT)		
Card column	10	20	30	40	50	60	70
Format type	I	I	I	I	I	I	I

Item No. 12: 1 card (this item read only when LTRAJ is TRUE)

Variable	LSUN	AZANG	POLANG	BX1	BY1	BZ1
Card column	10	20	30	40	50	60
Format type	L	F	F	F	F	F

#### A.4 DESCRIPTION OF OUTPUT

This section describes the output of the computer program. The contents of each output item are specified and discussed. The printed output consists of seven items, five of which are optional and are controlled with input parameters. Plotted output is also optional.

The first output item consists of a banner page and the input data. The input is presented in two forms: first, as images of the input cards, and then with identification of each variable. Default values are printed as if they were input. Parameters CN, NR, NBLUNT, ITER for the blunt-body calculation and XCALC, the terminal location for the marching calculation, are printed only when the flow field is to be calculated. When the obstacle geometry is user-supplied, the input body-shape table is printed. For a default geometry, the body shape is indicated by the description "default ionopause shape for constant scale height with  $H/R_0 = \text{ "}$ , or "default ionopause shape with gravitational variation in scale height,  $H/R_0 = \text{ "}$ . Trajectory input is printed only when LTRAJ is true.

The second output item is not printed when LRERUN = .TRUE. From the blunt-body calculation, the shock speed at each iteration, the final enthalpy error, final sonic-line location, and body and final bow-shock shape are printed. For the marching calculation, the downstream x-location and body and shock ordinates are output. There is no control variable allowing the user to suppress this item of output when the flow field is calculated.

Detailed flow-field output is the third item, and is printed only when LPRFL = .TRUE. Coordinates are labeled as X/D, R/D, RP/D, or X/R<sub>0</sub>, R/R<sub>0</sub>, RP/R<sub>0</sub>, to emphasize that distances are normalized by the distance from the center of the planet to the nose of the body, D for the magnetopause, R<sub>0</sub> for an ionopause. Along the symmetry axis, the values printed are velocity magnitude V/V<sub>INF</sub>, density RHO/RHO<sub>INF</sub>,

temperature  $T/TINF$ , and pressure  $P/PINF$ . Over the rest of the flow field, values are also given for velocity components  $VX/VINF$ ,  $VR/VINF$ , and flow angle  $\phi$ . Note that the flow angle is the deviation of the flow about the obstacle, and so  $0^\circ \leq \phi \leq 90^\circ$ .

The next output item is the  $(x,R)$  coordinates of the streamlines. For blunt-body region, the  $(R_p, \theta)$  coordinates of the starting position on the bow shock wave are also given. This item is printed only when  $LPRST = .TRUE$ .

The magnetic-field components are then printed, if  $LPPRB = .TRUE$ . The location of each point is defined in  $(R_p, \theta)$  coordinates for the blunt-body region, and  $(x,R)$  coordinates for the downstream marching region. The components along field lines parallel, perpendicular, and normal to the flow in the free stream are printed as  $B/BINF(PARALLEL)$ ,  $B/BINF(PERP)$ ,  $B/BINF(NORMAL)$ . The orthogonal  $(x_c, y_c, z_c)$  components of the resultant are printed as  $BX/BINF(RESULTANT)$ ,  $BY/BINF(RESULTANT)$ ,  $BZ/BINF(RESULTANT)$ . The magnetic field in the symmetry  $(x_c, y_c)$  plane, defined by the vector sum  $[(B/B_\infty)_u + (B/B_\infty)_d]$ , is also printed, and is given by the magnitude  $B/BINF(IN-PLANE)$  and direction  $B-ANGLE(IN-PLANE)$  of the vector. We note, as pointed out in the text, that the orthogonal magnetic-field components printed here correspond to those in the  $(x_c, y_c)$  plane, i.e.,  $z_c = 0$ .

The next item printed is the  $(x_c, R)$  coordinates of the contours, for which  $LPRCON$  is the logical control variable. Noting that temperature and velocity contours coincide, the corresponding value of  $T/TINF$  is printed along with  $V/VINF$  for the velocity contours. There are three nonfatal error messages which may occur - see section A.5.

Trajectory output is the last item to be printed. This output is presented first in terms of the solar-wind coordinate system  $(x_c, y_c, z_c)$ , and then in terms of sun-planet coordinates  $(x_s, y_s, z_s)$ .

The trajectory coordinates are printed as a function of time and are shown normalized by both  $R_0$  and the planetary radius. Next, flow and magnetic-field components are printed for each trajectory point. This output is presented in both nondimensional and dimensionalized forms and includes  $|\underline{v}|$ ,  $v_x$ ,  $v_y$ ,  $v_z$ , density, temperature,  $|\underline{B}|$ ,  $B_x$ ,  $B_y$ , and  $B_z$ .

The program also has the capability to produce two sets of plotted output using UCC plot routines AXIS, CHAR, DASH, DOTLN, ENPLT, GREEK, MATH, NUMPLT, PLOT, PLTLN, POLAR, SCALF, and VECTOR. The first set of plots is generated when  $LPLT = .TRUE.$  and provides a pictorial representation of the streamlines and contours with a maximum of seven frames produced. The first frame is a plot of the streamlines followed by contour plots of velocity magnitude, temperature, and density. The next three frames are contour plots of the unit parallel, perpendicular, and normal magnetic-field components. These plots are referred to the solar-wind  $(x,R)$  coordinate system.

The second set of plots is produced according to the value of the logical variable  $LPLTRJ$ . This set consists of twelve plots. The first frame is a projection of the trajectory rotated onto the  $x$ - $R$  plane. The second frame is a plot of the trajectory projected onto the  $y_c$ - $z_c$  plane. The remaining frames are time-history plots of density, temperature, velocity, and magnetic field. The velocity plots include magnitude and three components as do the magnetic field plots. The vector components are referred to the sun-planet ecliptic  $(x_s, y_s, z_s)$  coordinates.

#### A.5 PROGRAM ERROR MESSAGES

This section lists the messages printed by the program, and indicates what action should be taken by the user.

(1)               \*\*\*\*\* EXECUTION TERMINATED \*\*\*\*\*  
RERUN DATA ON TAPE4 DOES NOT AGREE  
WITH CASE SPECIFIED ON CARD INPUT:  
MACH NO.           GAMMA               H/RO

FROM CARDS  
FROM TAPE4

The first three parameters of item 2 of the input for a case using the rerun option should agree with those used when creating the file. The tolerance used in comparing the values is  $10^{-5}$ . For a user-supplied geometry, it is sufficient for both values of  $H/R_0$  to be negative.

(2)               \*\*\*\*\* EXECUTION TERMINATED \*\*\*\*\*  
ARRAY OF CONTOUR VALUES IMPROPERLY SPECIFIED

When specified, the contour values should be monotonically increasing with at least one value in the range of the velocity, density, or magnetic-field strength for the region under consideration. This error does not inhibit generation of the rerun file.

(3)           CONTOUR SEARCH ABORTED - TABLE OVERFLOW IN NAD

The program allows for 29 contour lines to be found, storing the starting address of each contour line in array NAD. This message indicates that at least one more contour line could be found. If the user requires all the contours of the levels specified, the case should be rerun in two parts. Otherwise, reduce the number of contour levels specified.

(4)           CONTOUR SEARCH ABORTED - TABLE OVERFLOW IN (X,Y)

The contour lines may be described by up to 1000 points, stored in arrays X and Y. This message indicates that more points would be



required for the contour lines requested. The last contour line found will be incomplete. As with (3), either reduce the number of contour levels or run as two cases.

(5)       NEGATIVE PRESSURE DETECTED BY SHOCK AT J=  
          PN=                    PO=                    PTAU=

This message is printed by the blunt-body code when a negative pressure has been calculated at the shock on this iteration, at radial locations J. The quantities printed are: PN, the pressure calculated on this step; PO, the pressure from the previous step; and PTAU, the partial derivative of pressure with respect to time. This condition indicates that the shock wave motion is too extreme. Lowering the value of CN, and thus reducing the time step, may remove the problem.

The following messages (6)-(10) usually result from using an obstacle geometry which is in some way too severe for the program to handle in its present form. The obstacle slope may be sufficiently high at  $x = 0.0$  that the axial Mach number becomes subsonic in the starting solution for the marching calculation, or there may be a sharp corner in the profile. Check input, particularly free-stream Mach number and body geometry.

(6)       NEGATIVE PRESSURE ON BODY DETECTED BY BNDRY, PB=       AT J=

This message indicates that a negative pressure on the body, PB, has been calculated at radial location J.

(7)       NEGATIVE PRESSURE OR DENSITY ON BODY DETECTED BY BNDRYM AT X=  
          PB=                    RHOB=                    VXB=                    VRB=

The program makes internal corrections when this condition occurs, resulting pressure PB, density RHOB, and velocity components VXB and VRB.

# TABLE OF CONTENTS

<u>Section</u>	<u>Page No.</u>
LIST OF ILLUSTRATIONS	iv 1/A5
SUMMARY	1 1/A7
INTRODUCTION	2 1/A8
LIST OF SYMBOLS	4 1/A10
ANALYSIS	8 1/A14
The Mathematical Model - Formulation of the Fluid Representation	8 1/A14
<u>Governing equations</u>	8 1/A14
<u>Conditions at discontinuities</u>	10 1/B2
<u>Frozen-field approximation</u>	12 1/B4
Determination of the Ionosphere Boundary	14 1/B6
Calculation of the Gasdynamic Flow Properties	20 1/B12
<u>Nose region solution - implicit unsteady Euler equation method</u>	21 1/B13
<u>Downstream region solution - shock capturing marching method</u>	25 1/C3
<u>Calculation of the streamlines</u>	27 1/C5
Calculation of the Magnetic Field	27 1/C5
Calculation of the Contour Lines	30 1/C8
Solar-Ecliptic/Solar-Wind Coordinate Transformations	31 1/C9
Properties Along a Spacecraft Trajectory	33 1/C11
RESULTS	36 1/C14
CONCLUDING REMARKS	47 1/D11
ACKNOWLEDGEMENTS	48 1/D12
APPENDIX A - COMPUTER PROGRAM USER'S MANUAL	49 1/D13
APPENDIX B - LISTING OF COMPUTER PROGRAM	131 2/D1
APPENDIX C - CATALOG OF TEST CASES	177 3/C10
REFERENCES	287 4/D10
TABLE 1	289 4/D12
FIGURES 1 THROUGH 20	291 4/E3

(8) NEGATIVE SIGMA-BAR-1 IN EIGENM INDICATES SUBSONIC FLOW AT I=

(9) NEGATIVE SIGMA-BAR-2 IN EIGENM INDICATES SUBSONIC FLOW AT I=

These messages are printed when subsonic flow is detected by the marching calculation. The computed stepsize for this region will be quite small.

(10) -----BODY TURN STOPPED AT M2=100-----

This message indicates that the body has a sharp corner, which has been limited to  $100^\circ$  when being transformed.

#### A.6 SAMPLE CASE

The sample case presented in this section is based on actual interplanetary conditions as measured by the solar-wind plasma analyzer, the fluxgate magnetometer, and retarding potential plasma analyzer on the Pioneer-Venus Orbiter for orbit 3.

The sample case is run alone and is set up to produce all possible output. The gasdynamic solution is to be calculated about a default ionopause shape with  $H/R_0 = 0.03$ ,  $M_\infty = 3.0$ , and  $\gamma = 5/3$ . The value of  $H/R_0$  is based on measurements of ionospheric density and temperature by the retarding potential plasma analyzer. Streamlines, magnetic-field components, and contours are desired to a downstream location of  $-5.5 x/R_0$ . Contour values are specified for all quantities. Interplanetary values for velocity magnitude and direction, density, and temperature were provided by the solar-wind plasma analyzer and for the magnetic field by the fluxgate magnetometer.

The input data is tabulated in figure A.4, with item numbers corresponding to those in sections A.3.2 and A.3.3. The first card, item 0, indicates that there is one case to run. The remaining

fifty-five cards provide the data for this case. Item 1 contains the identifying title. On the next card, item 2, values are specified for AMACH, GAMMA, HRO, and XCALC. The other data fields are left blank to indicate that the default values will be used. The values of the logical variables of item 3 specify that the flow field is to be calculated and that full printed and plotted output is to be produced. Item 4 defines the plot length to be  $-5.5 x/R_0$ . The fields for ANGP and ANGN are left blank as they are to be calculated internally by the program. Items 5, 6, and 7 specify the contour levels to be used - 14 for velocity and temperature, 11 for density, and 13 for magnetic-field strength. Item 8 is omitted because the obstacle geometry is one of the default shapes for which the coordinates are calculated internally. The next 37 cards, item 9, are the trajectory coordinates, indicating time (in minutes from periapsis and the three spacial coordinates normalized by planetary radius). Item 10 indicates that trajectory plots are to be generated. This item also specifies free-stream values of velocity, density, temperature, and magnetic-field strength. The next two cards, item 11, indicates that the fourth, ninth, eleventh, and nineteenth trajectory points are to be marked on the plots for cross-reference. The last input card, item 12 indicates that the given trajectory coordinates are expressed in sun-planet coordinates. The azimuthal and polar angles,  $\Omega$  and  $\phi_p$ , are also specified by this item as are the free-stream magnetic-field components.

Figure A.5 presents portions of the printed output from this sample case. The full printed output is approximately 6,000 lines. Figure A.6 shows the 19 plots which are produced by the program for this case.

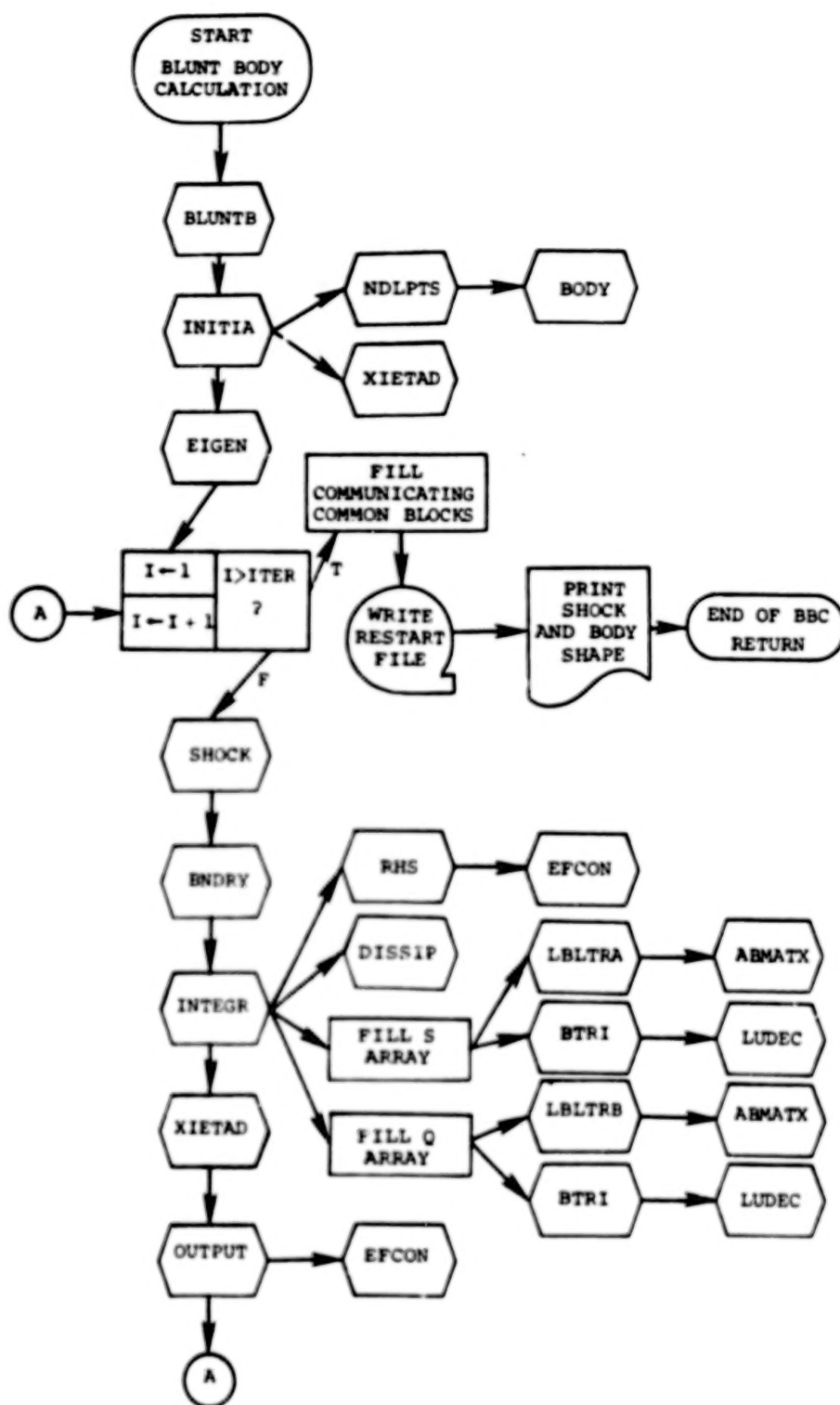


Figure A.1(a).- Flow chart for blunt-body calculation.

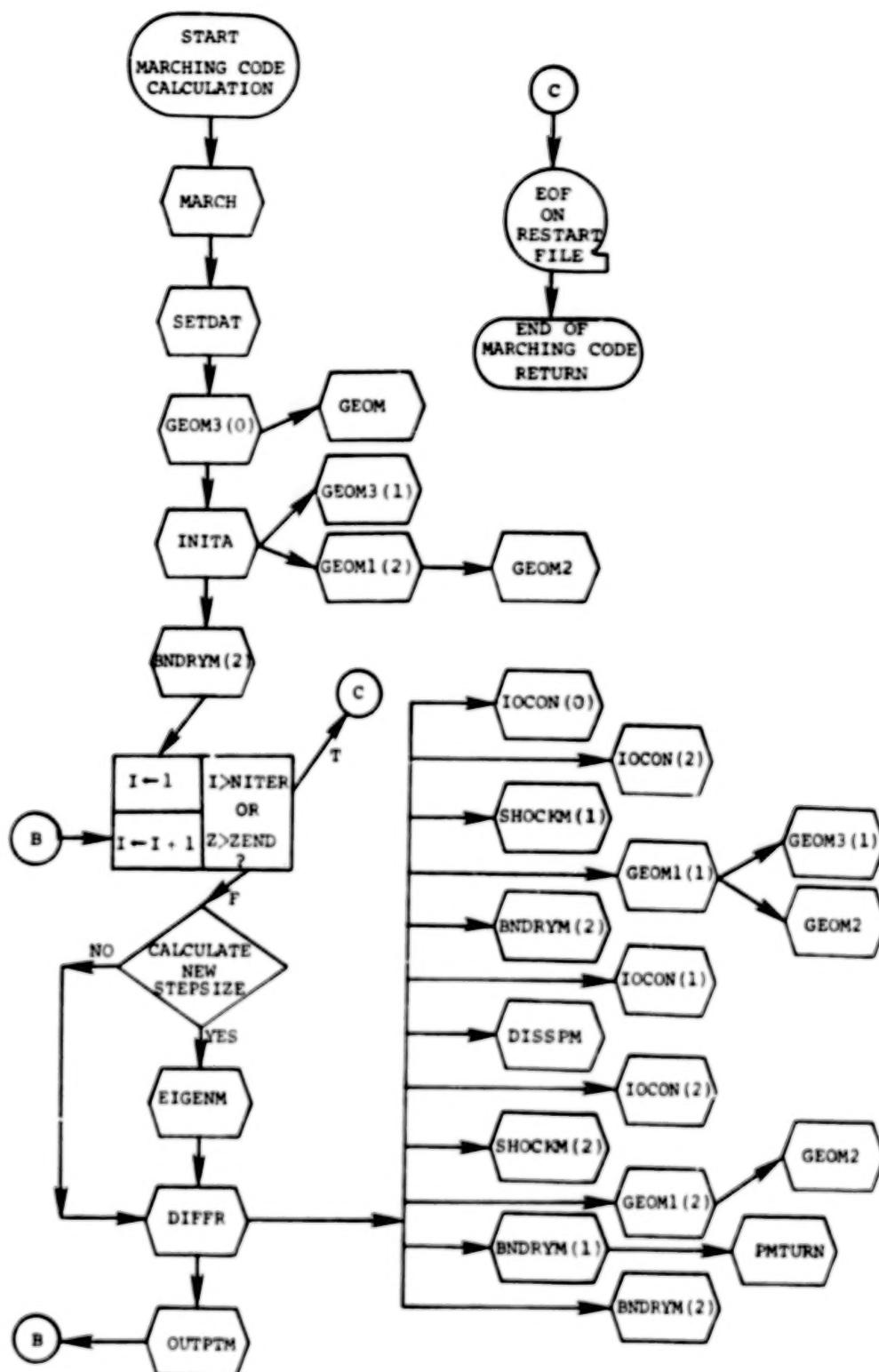


Figure A.1(b).- Flow chart for marching calculation.

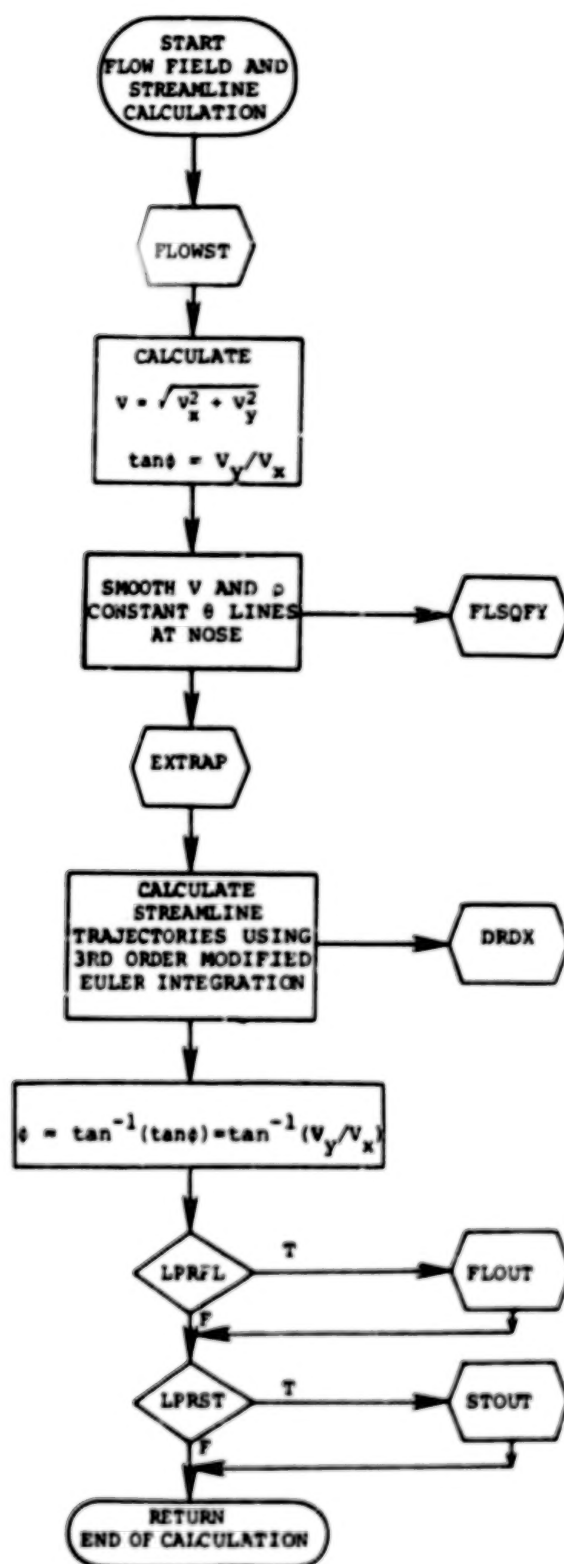


Figure A.1(c).- Flow chart of streamline calculation.



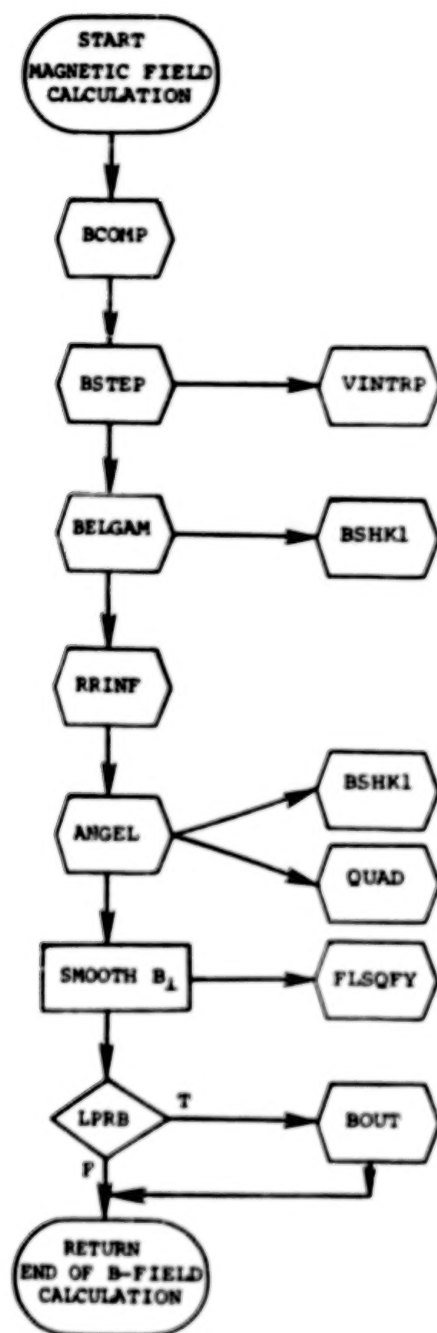


Figure A.1(d).- Flow chart of magnetic-field calculation.



Figure A.1(e).- Flow chart of contour and plot generation calculation.

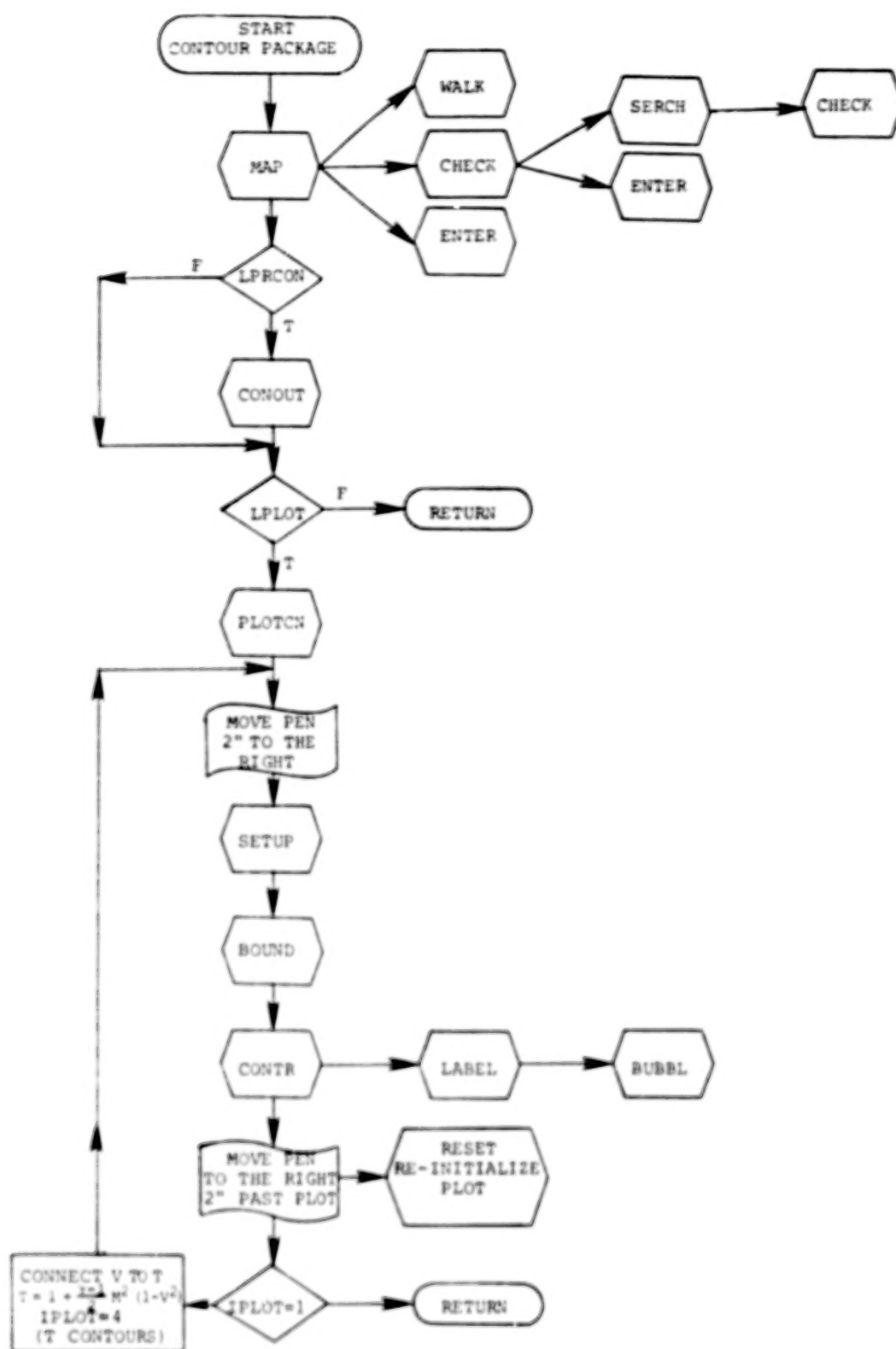


Figure A.1(e).- Concluded

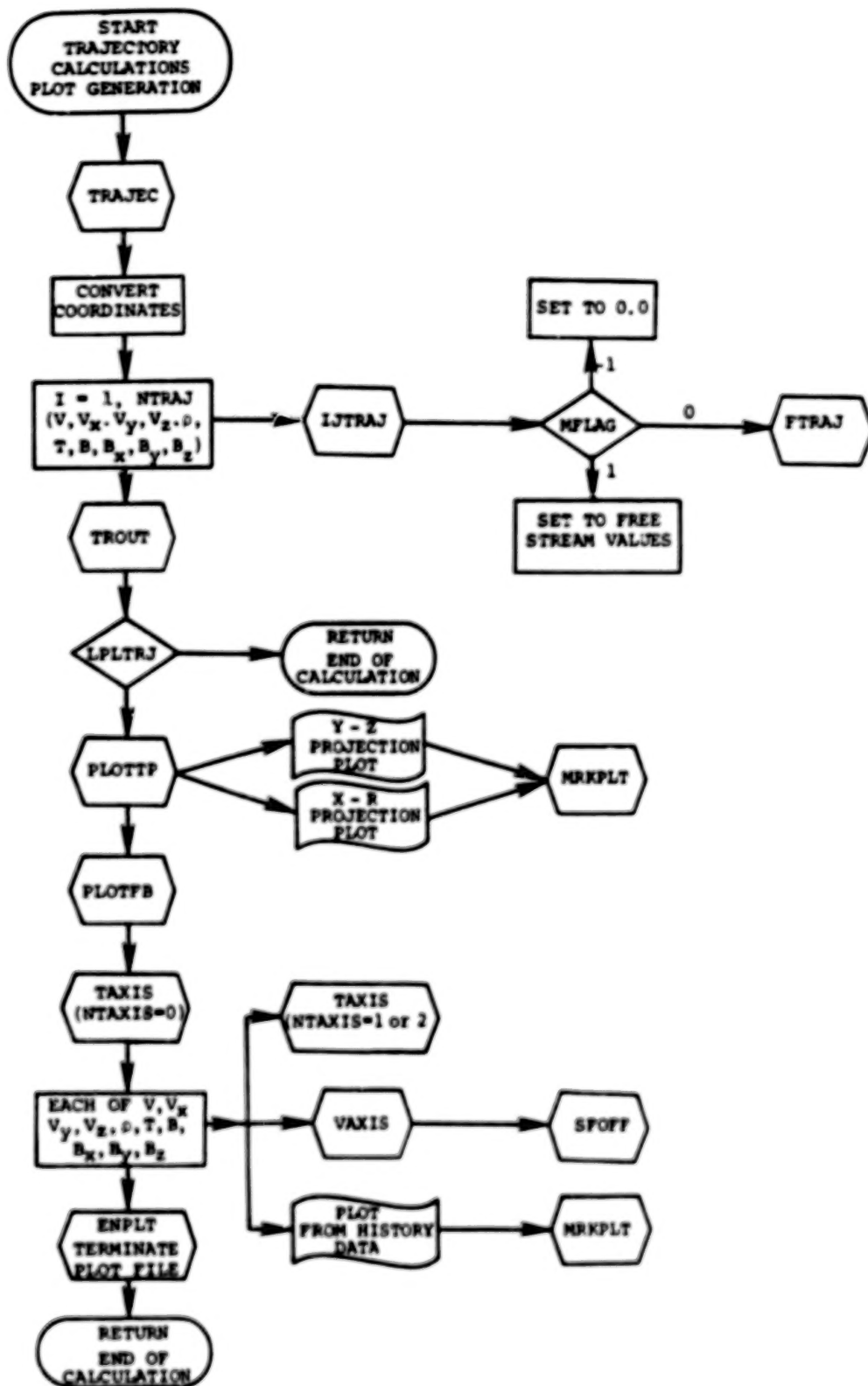


Figure A.1(f).- Flow chart of trajectory calculation.

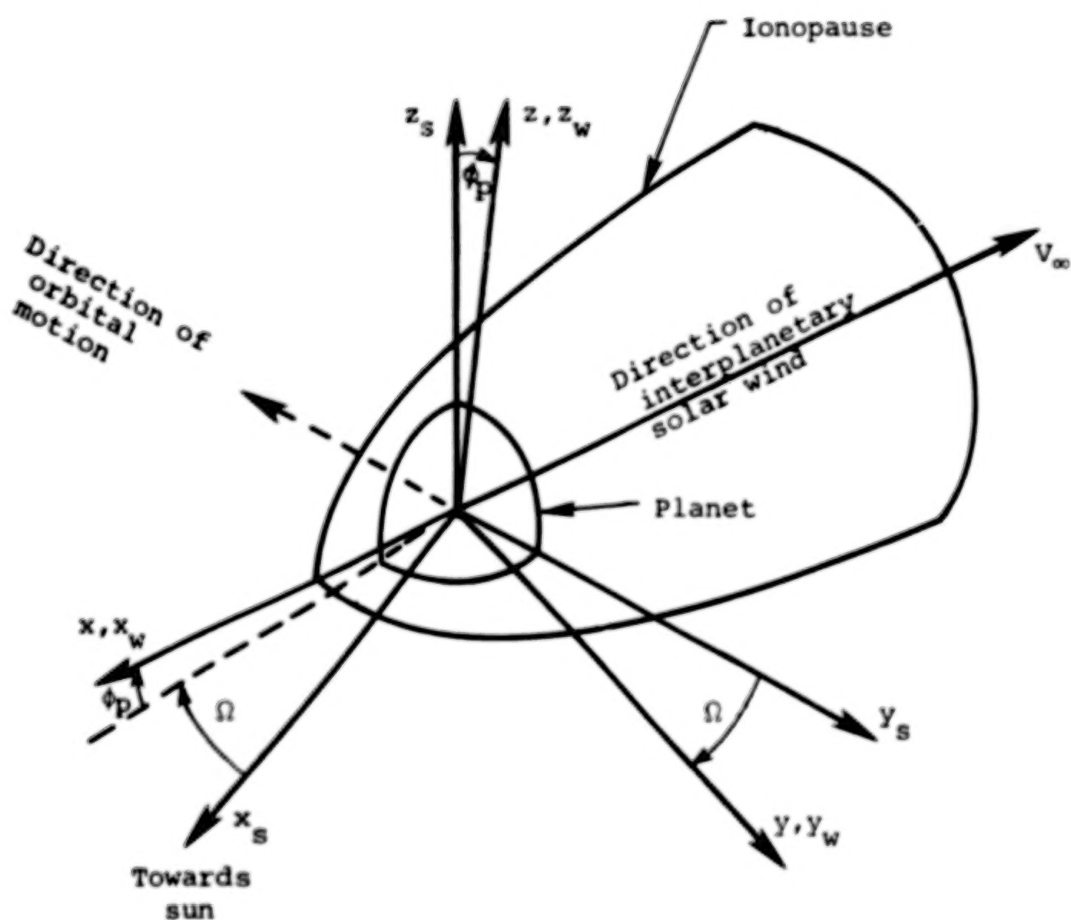


Figure A.2.- Illustration of the azimuthal ( $\Omega$ ) and polar ( $\phi_p$ ) solar-wind angles, both shown in a positive sense.

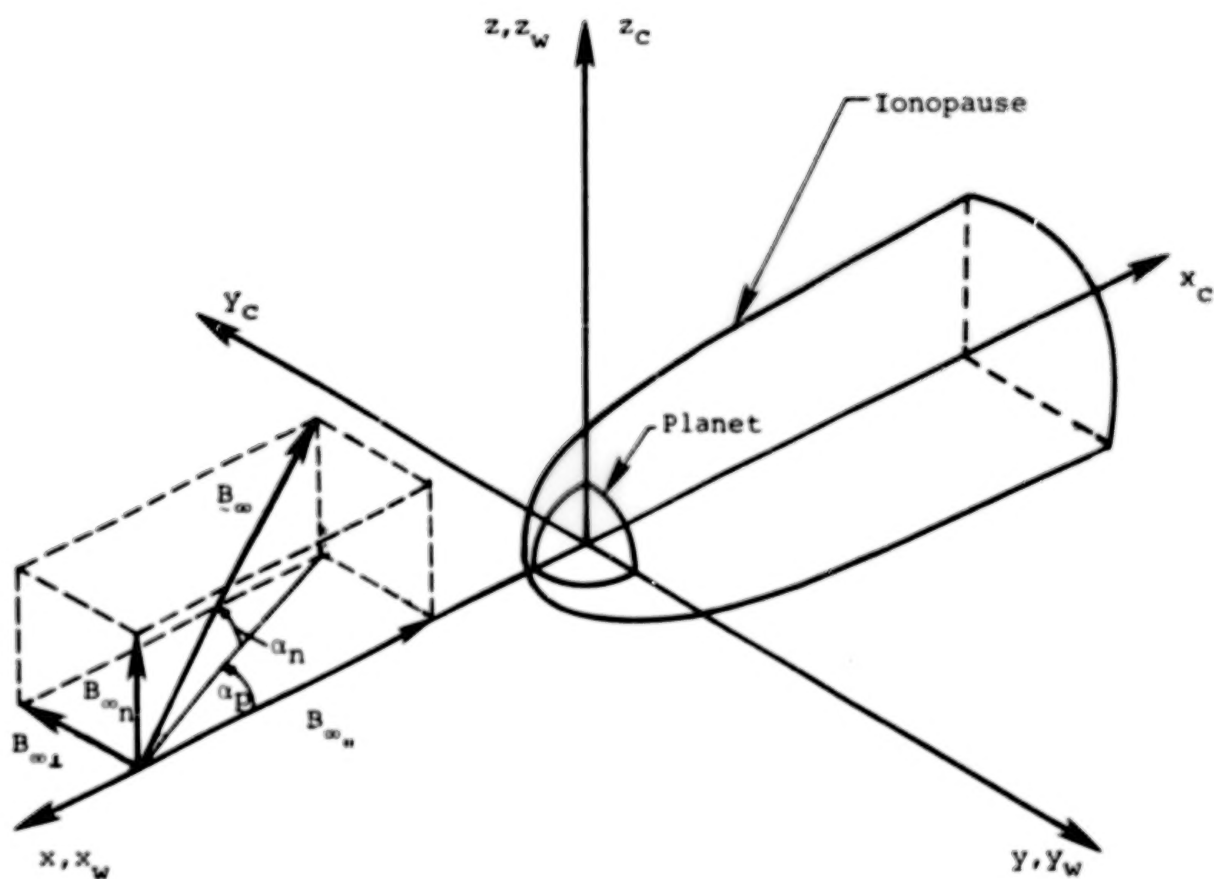


Figure A.3.- Illustration of the interplanetary magnetic field and magnetic-field angles  $(\alpha_p, \alpha_n)$  in the solar-wind aligned coordinate systems  $(x, y, z)$ ,  $(x_w, y_w, z_w)$ , and  $(x_c, y_c, z_c)$ .

Item No.	Column No.	10	20	30	40	50	60	70	80
0	1								
1		SAMPLE CASE (DEFAULT IONOPAUSE SHAPE WITH H/RO = 0.03)							
2		3.0	1.6666667	0.03	-10.0				
3		F	T	T	T	T	T	F	
4		-5.5							
5	14								
		0.1	0.2	0.3	0.4	0.5	0.6	0.7	0.75
		0.8	0.93	0.85	0.9	0.92	0.94		
6	11								
		0.5	0.8	1.2	1.6	2.0	2.5	3.0	3.5
		3.8	4.0	4.2					
7	13								
		0.45	0.6	0.8	1.0	1.25	1.5	2.0	2.5
		3.0	3.5	4.0	5.0	6.0			
9	35								
		-90.870	-0.843	3.787	2.027				
		-85.537	-0.765	3.600	2.045				
		-80.203	-0.684	3.393	2.062				
		-74.870	-0.600	3.177	2.073				
		-70.603	-0.533	2.999	2.078				
		-64.203	-0.430	2.721	2.079				
		-57.802	-0.324	2.427	2.067				
		-51.402	-0.217	2.118	2.043				
		-40.735	-0.034	1.562	1.961				
		-38.668	-0.017	1.509	1.951				
		-38.602	-0.010	1.422	1.932				
		-35.935	0.049	1.281	1.902				
		-34.867	0.67	1.232	1.886				
		-32.735	0.158	1.108	1.852				
		-24.202	0.2456	0.5826	1.6658				
		-21.002	0.2954	0.3749	1.5693				
		-16.735	0.356	0.090	1.409				
		-14.602	0.382	-0.052	1.315				
		-11.402	0.415	-0.205	1.150				
		-8.102	0.437	-0.478	0.945				
		-4.900	0.442	-0.703	0.660				
		6.298	0.309	-1.042	-0.266				
		9.498	0.237	-1.055	-0.546				
		12.593	0.160	-1.038	-0.801				
		17.393	0.034	-0.966	-1.162				
		29.127	-0.275	-0.673	-1.887				
		34.460	-0.407	-0.512	-2.155				
		43.860	-0.561	-0.312	-2.444				
		47.260	-0.705	-0.108	-2.670				
		53.660	-0.844	0.0982	-2.925				
		56.862	-0.91	0.201	-3.031				
		58.993	-0.954	0.269	-3.097				
		60.060	-0.975	0.303	-3.131				
		62.193	-1.018	0.371	-3.195				
		67.528	-1.122	0.541	-3.347				
		73.928	-1.241	0.739	-3.514				
		80.328	-1.357	0.839	-3.671				
10		T	0.968	392.0	20.2	102000.	8.8225		
11	4								
	4		9	11	19				
12	T	3.3	0.15	-1.74	-8.64	0.4			

Figure A.4.- Card input for sample case.



[illegible]

102

SAMPLE CASE: 17, FAULT TOWERHOUSE SHAPE WITH HRRF = 1.000

INPUT VARIABLES  
 \*\*\*\*\*

INTERPLANETARY PATH WPL = 3.000

SPECIFIC HEAT RATIO = 1.000

OPTIMIZE GEOMETRY: NO, RATE, T, INITIAL SHAPE  
 FOR CONSTANT SMALL FLIGHT WITH HRRF = 1.0

PARAMETER AND POINT BODY CALCULATION

WPL, NO POINTS WITH POINTS = 14  
 WPL, NO ANGULAR POINTS = 24  
 WPL, NO ADDITIONAL POINTS IN  
 POINT BODY PATH = 1  
 PARAMETER WPL = 3.000  
 WPL, NO ITERATIONS = 300

TERMINAL POINT/IN LOCATION FOR MATCHING CALCULATION, WPL=3.000

TERMINAL POINT/IN LOCATION FOR PLOTTING, WPL=3.000

LODGN = 0  
 LOFFL = 0  
 LOFFT = 0  
 LOFFTH = 0  
 LOFFR = 0  
 LOFFM = 0  
 LOFFX = 0  
 LOFFY = 0  
 LOFFZ = 0  
 LOFFW = 0

Figure A.5.- Continued.



# MICROFILMED FROM BEST AVAILABLE COPY

## PLANT ANDY CALCULATION \*\*\*\*\*

ITERATION 1	PLANT ANDY CALCULATION	MAXIMUM SWICH SPINCH 1.400000-2 AT 3000
ITERATION 2	PLANT ANDY CALCULATION	MAXIMUM SWICH SPINCH 1.400000-2 AT 3000
ITERATION 3	PLANT ANDY CALCULATION	MAXIMUM SWICH SPINCH 1.400000-2 AT 3000
ITERATION 4	PLANT ANDY CALCULATION	MAXIMUM SWICH SPINCH 1.400000-2 AT 3000
ITERATION 5	PLANT ANDY CALCULATION	MAXIMUM SWICH SPINCH 1.400000-2 AT 3000

ITERATION 100	PLANT ANDY CALCULATION	MAXIMUM SWICH SPINCH 1.400000-2 AT 3000
ITERATION 100	PLANT ANDY CALCULATION	MAXIMUM SWICH SPINCH 1.400000-2 AT 3000
ITERATION 100	PLANT ANDY CALCULATION	MAXIMUM SWICH SPINCH 1.400000-2 AT 3000
ITERATION 100	PLANT ANDY CALCULATION	MAXIMUM SWICH SPINCH 1.400000-2 AT 3000

### FINAL OUTPUT LINE LOCATION

PL1	1.4000	PL1	1.4000
PL2	1.4000	PL2	1.4000
PL3	1.4000	PL3	1.4000
PL4	1.4000	PL4	1.4000
PL5	1.4000	PL5	1.4000
PL6	1.4000	PL6	1.4000
PL7	1.4000	PL7	1.4000
PL8	1.4000	PL8	1.4000
PL9	1.4000	PL9	1.4000
PL10	1.4000	PL10	1.4000
PL11	1.4000	PL11	1.4000
PL12	1.4000	PL12	1.4000
PL13	1.4000	PL13	1.4000
PL14	1.4000	PL14	1.4000
PL15	1.4000	PL15	1.4000
PL16	1.4000	PL16	1.4000
PL17	1.4000	PL17	1.4000
PL18	1.4000	PL18	1.4000
PL19	1.4000	PL19	1.4000
PL20	1.4000	PL20	1.4000

PLANT ANDY CALCULATION PLANT ANDY CALCULATION PLANT ANDY CALCULATION

### PLANT ANDY CALCULATION

J	PLANT ANDY	PLANT ANDY	PLANT ANDY	PLANT ANDY
1	1.4000	1.4000	1.4000	1.4000
2	1.4000	1.4000	1.4000	1.4000
3	1.4000	1.4000	1.4000	1.4000
4	1.4000	1.4000	1.4000	1.4000
5	1.4000	1.4000	1.4000	1.4000
6	1.4000	1.4000	1.4000	1.4000
7	1.4000	1.4000	1.4000	1.4000
8	1.4000	1.4000	1.4000	1.4000
9	1.4000	1.4000	1.4000	1.4000
10	1.4000	1.4000	1.4000	1.4000
11	1.4000	1.4000	1.4000	1.4000
12	1.4000	1.4000	1.4000	1.4000
13	1.4000	1.4000	1.4000	1.4000
14	1.4000	1.4000	1.4000	1.4000
15	1.4000	1.4000	1.4000	1.4000
16	1.4000	1.4000	1.4000	1.4000
17	1.4000	1.4000	1.4000	1.4000
18	1.4000	1.4000	1.4000	1.4000
19	1.4000	1.4000	1.4000	1.4000
20	1.4000	1.4000	1.4000	1.4000
21	1.4000	1.4000	1.4000	1.4000
22	1.4000	1.4000	1.4000	1.4000
23	1.4000	1.4000	1.4000	1.4000
24	1.4000	1.4000	1.4000	1.4000

Figure A.5.- Continued.

NUMERICAL EVALUATION  
\*\*\*\*\*

STEP NO.	NUMERICAL EVALUATION	STEP CONTRAST	TIME DERIVATIVE
1	-0.000	1.0150	2.0000
2	-0.000	1.0150	2.0000
3	-0.000	1.0150	2.0000
4	-0.000	1.0150	2.0000
5	-0.000	1.0150	2.0000
6	-0.000	1.0150	2.0000
7	-0.000	1.0150	2.0000
8	-0.000	1.0150	2.0000
9	-0.000	1.0150	2.0000
10	-0.000	1.0150	2.0000
11	-0.000	1.0150	2.0000
12	-0.000	1.0150	2.0000
13	-0.000	1.0150	2.0000
14	-0.000	1.0150	2.0000
15	-0.000	1.0150	2.0000
16	-0.000	1.0150	2.0000
17	-0.000	1.0150	2.0000
18	-0.000	1.0150	2.0000
19	-0.000	1.0150	2.0000
20	-0.000	1.0150	2.0000
21	-0.000	1.0150	2.0000
22	-0.000	1.0150	2.0000
23	-0.000	1.0150	2.0000
24	-0.000	1.0150	2.0000
25	-0.000	1.0150	2.0000
26	-0.000	1.0150	2.0000
27	-0.000	1.0150	2.0000
28	-0.000	1.0150	2.0000
29	-0.000	1.0150	2.0000
30	-0.000	1.0150	2.0000
31	-0.000	1.0150	2.0000
32	-0.000	1.0150	2.0000
33	-0.000	1.0150	2.0000
34	-0.000	1.0150	2.0000
35	-0.000	1.0150	2.0000
36	-0.000	1.0150	2.0000
37	-0.000	1.0150	2.0000
38	-0.000	1.0150	2.0000
39	-0.000	1.0150	2.0000
40	-0.000	1.0150	2.0000
41	-0.000	1.0150	2.0000
42	-0.000	1.0150	2.0000
43	-0.000	1.0150	2.0000
44	-0.000	1.0150	2.0000
45	-0.000	1.0150	2.0000
46	-0.000	1.0150	2.0000
47	-0.000	1.0150	2.0000
48	-0.000	1.0150	2.0000
49	-0.000	1.0150	2.0000
50	-0.000	1.0150	2.0000
51	-0.000	1.0150	2.0000
52	-0.000	1.0150	2.0000
53	-0.000	1.0150	2.0000
54	-0.000	1.0150	2.0000
55	-0.000	1.0150	2.0000
56	-0.000	1.0150	2.0000
57	-0.000	1.0150	2.0000
58	-0.000	1.0150	2.0000
59	-0.000	1.0150	2.0000
60	-0.000	1.0150	2.0000

NUMERICAL EVALUATION  
\*\*\*\*\*

NUMERICAL EVALUATION (CONTINUED) IN COMPARISON WITH THEORETICAL VALUES

STEP	TIME	VALUE	THEORETICAL	PERCENT
1	1.0000	0.0000	0.0000	0.0000
2	1.0150	0.0000	0.0000	0.0000
3	1.0300	0.0000	0.0000	0.0000
4	1.0450	0.0000	0.0000	0.0000
5	1.0600	0.0000	0.0000	0.0000
6	1.0750	0.0000	0.0000	0.0000
7	1.0900	0.0000	0.0000	0.0000
8	1.1050	0.0000	0.0000	0.0000
9	1.1200	0.0000	0.0000	0.0000
10	1.1350	0.0000	0.0000	0.0000
11	1.1500	0.0000	0.0000	0.0000
12	1.1650	0.0000	0.0000	0.0000
13	1.1800	0.0000	0.0000	0.0000
14	1.1950	0.0000	0.0000	0.0000
15	1.2100	0.0000	0.0000	0.0000
16	1.2250	0.0000	0.0000	0.0000
17	1.2400	0.0000	0.0000	0.0000
18	1.2550	0.0000	0.0000	0.0000
19	1.2700	0.0000	0.0000	0.0000
20	1.2850	0.0000	0.0000	0.0000

Figure A.5.- Continued.

[illegible][illegible][illegible][illegible]

07

[illegible]

89097978241 88101 (1987) 90 92, 93, 94, 95, 96, 97, 98, 99, 100, 101, 102, 103, 104, 105, 106, 107, 108, 109, 110, 111, 112, 113, 114, 115, 116, 117, 118, 119, 120, 121, 122, 123, 124, 125, 126, 127, 128, 129, 130, 131, 132, 133, 134, 135, 136, 137, 138, 139, 140, 141, 142, 143, 144, 145, 146, 147, 148, 149, 150, 151, 152, 153, 154, 155, 156, 157, 158, 159, 160, 161, 162, 163, 164, 165, 166, 167, 168, 169, 170, 171, 172, 173, 174, 175, 176, 177, 178, 179, 180, 181, 182, 183, 184, 185, 186, 187, 188, 189, 190, 191, 192, 193, 194, 195, 196, 197, 198, 199, 200, 201, 202, 203, 204, 205, 206, 207, 208, 209, 210, 211, 212, 213, 214, 215, 216, 217, 218, 219, 220, 221, 222, 223, 224, 225, 226, 227, 228, 229, 230, 231, 232, 233, 234, 235, 236, 237, 238, 239, 240, 241, 242, 243, 244, 245, 246, 247, 248, 249, 250, 251, 252, 253, 254, 255, 256, 257, 258, 259, 260, 261, 262, 263, 264, 265, 266, 267, 268, 269, 270, 271, 272, 273, 274, 275, 276, 277, 278, 279, 280, 281, 282, 283, 284, 285, 286, 287, 288, 289, 290, 291, 292, 293, 294, 295, 296, 297, 298, 299, 300, 301, 302, 303, 304, 305, 306, 307, 308, 309, 310, 311, 312, 313, 314, 315, 316, 317, 318, 319, 320, 321, 322, 323, 324, 325, 326, 327, 328, 329, 330, 331, 332, 333, 334, 335, 336, 337, 338, 339, 340, 341, 342, 343, 344, 345, 346, 347, 348, 349, 350, 351, 352, 353, 354, 355, 356, 357, 358, 359, 360, 361, 362, 363, 364, 365, 366, 367, 368, 369, 370, 371, 372, 373, 374, 375, 376, 377, 378, 379, 380, 381, 382, 383, 384, 385, 386, 387, 388, 389, 390, 391, 392, 393, 394, 395, 396, 397, 398, 399, 400, 401, 402, 403, 404, 405, 406, 407, 408, 409, 410, 411, 412, 413, 414, 415, 416, 417, 418, 419, 420, 421, 422, 423, 424, 425, 426, 427, 428, 429, 430, 431, 432, 433, 434, 435, 436, 437, 438, 439, 440, 441, 442, 443, 444, 445, 446, 447, 448, 449, 450, 451, 452, 453, 454, 455, 456, 457, 458, 459, 460, 461, 462, 463, 464, 465, 466, 467, 468, 469, 470, 471, 472, 473, 474, 475, 476, 477, 478, 479, 480, 481, 482, 483, 484, 485, 486, 487, 488, 489, 490, 491, 492, 493, 494, 495, 496, 497, 498, 499, 500, 501, 502, 503, 504, 505, 506, 507, 508, 509, 510, 511, 512, 513, 514, 515, 516, 517, 518, 519, 520, 521, 522, 523, 524, 525, 526, 527, 528, 529, 530, 531, 532, 533, 534, 535, 536, 537, 538, 539, 540, 541, 542, 543, 544, 545, 546, 547, 548, 549, 550, 551, 552, 553, 554, 555, 556, 557, 558, 559, 560, 561, 562, 563, 564, 565, 566, 567, 568, 569, 570, 571, 572, 573, 574, 575, 576, 577, 578, 579, 580, 581, 582, 583, 584, 585, 586, 587, 588, 589, 590, 591, 592, 593, 594, 595, 596, 597, 598, 599, 600, 601, 602, 603, 604, 605, 606, 607, 608, 609, 610, 611, 612, 613, 614, 615, 616, 617, 618, 619, 620, 621, 622, 623, 624, 625, 626, 627, 628, 629, 630, 631, 632, 633, 634, 635, 636, 637, 638, 639, 640, 641, 642, 643, 644, 645, 646, 647, 648, 649, 650, 651, 652, 653, 654, 655, 656, 657, 658, 659, 660, 661, 662, 663, 664, 665, 666, 667, 668, 669, 670, 671, 672, 673, 674, 675, 676, 677, 678, 679, 680, 681, 682, 683, 684, 685, 686, 687, 688, 689, 690, 691, 692, 693, 694, 695, 696, 697, 698, 699, 700, 701, 702, 703, 704, 705, 706, 707, 708, 709, 710, 711, 712, 713, 714, 715, 716, 717, 718, 719, 720, 721, 722, 723, 724, 725, 726, 727, 728, 729, 730, 731, 732, 733, 734, 735, 736, 737, 738, 739, 740, 741, 742, 743, 744, 745, 746, 747, 748, 749, 750, 751, 752, 753, 754, 755, 756, 757, 758, 759, 760, 761, 762, 763, 764, 765, 766, 767, 768, 769, 770, 771, 772, 773, 774, 775, 776, 777, 778, 779, 780, 781, 782, 783, 784, 785, 786, 787, 788, 789, 790, 791, 792, 793, 794, 795, 796, 797, 798, 799, 800, 801, 802, 803, 804, 805, 806, 807, 808, 809, 810, 811, 812, 813, 814, 815, 816, 817, 818, 819, 820, 821, 822, 823, 824, 825, 826, 827, 828, 829, 830, 831, 832, 833, 834, 835, 836, 837, 838, 839, 840, 841, 842, 843, 844, 845, 846, 847, 848, 849, 850, 851, 852, 853, 854, 855, 856, 857, 858, 859, 860, 861, 862, 863, 864, 865, 866, 867, 868, 869, 870, 871, 872, 873, 874, 875, 876, 877, 878, 879, 880, 881, 882, 883, 884, 885, 886, 887, 888, 889, 890, 891, 892, 893, 894, 895, 896, 897, 898, 899, 900, 901, 902, 903, 904, 905, 906,

[illegible]

0000000001 000001 1 00000000 0000 00 0000 0 0000000

行	姓名	性别	年龄	民族	籍贯	文化程度	职业	工作单位	住址	联系电话	电子邮箱
1	张三	男	25	汉族	山东	高中	教师	某某中学	某某路	12345678	zhangsan@163.com
2	李四	女	22	汉族	河南	初中	学生	某某中学	某某路	23456789	lisi@163.com
3	王五	男	28	汉族	河北	高中	教师	某某中学	某某路	34567890	wangwu@163.com
4	赵六	女	20	汉族	湖南	初中	学生	某某中学	某某路	45678901	zhaoliu@163.com
5	孙七	男	23	汉族	广东	高中	教师	某某中学	某某路	56789012	sunqi@163.com
6	周八	女	21	汉族	四川	初中	学生	某某中学	某某路	67890123	zhouba@163.com
7	吴九	男	26	汉族	浙江	高中	教师	某某中学	某某路	78901234	wujiu@163.com
8	郑十	女	19	汉族	湖北	初中	学生	某某中学	某某路	89012345	zhengshi@163.com
9	冯十一	男	24	汉族	广西	高中	教师	某某中学	某某路	90123456	fengshi1@163.com
10	陈十二	女	27	汉族	福建	初中	学生	某某中学	某某路	01234567	chen12@163.com
11	林十三	男	20	汉族	江西	高中	教师	某某中学	某某路	12345678	lin13@163.com
12	黄十四	女	23	汉族	安徽	初中	学生	某某中学	某某路	23456789	huang14@163.com
13	周十五	男	25	汉族	山西	高中	教师	某某中学	某某路	34567890	zhou15@163.com
14	吴十六	女	22	汉族	云南	初中	学生	某某中学	某某路	45678901	wu16@163.com
15	郑十七	男	26	汉族	贵州	高中	教师	某某中学	某某路	56789012	zheng17@163.com
16	冯十八	女	19	汉族	海南	初中	学生	某某中学	某某路	67890123	feng18@163.com
17	陈十九	男	24	汉族	重庆	高中	教师	某某中学	某某路	78901234	chen19@163.com
18	林二十	女	27	汉族	陕西	初中	学生	某某中学	某某路	89012345	lin20@163.com
19	黄二十一	男	20	汉族	甘肃	高中	教师	某某中学	某某路	90123456	huang21@163.com
20	周二十二	女	23	汉族	宁夏	初中	学生	某某中学	某某路	01234567	zhou22@163.com

[illegible]

	1	2	3	4	5	6	7	8	9	10	11	12	13	14	15	16	17	18	19	20	21	22	23	24	25	26	27	28	29	30	31	32	33	34	35	36	37	38	39	40	41	42	43	44	45	46	47	48	49	50	51	52	53	54	55	56	57	58	59	60	61	62	63	64	65	66	67	68	69	70	71	72	73	74	75	76	77	78	79	80	81	82	83	84	85	86	87	88	89	90	91	92	93	94	95	96	97	98	99	100
1	1	2	3	4	5	6	7	8	9	10	11	12	13	14	15	16	17	18	19	20	21	22	23	24	25	26	27	28	29	30	31	32	33	34	35	36	37	38	39	40	41	42	43	44	45	46	47	48	49	50	51	52	53	54	55	56	57	58	59	60	61	62	63	64	65	66	67	68	69	70	71	72	73	74	75	76	77	78	79	80	81	82	83	84	85	86	87	88	89	90	91	92	93	94	95	96	97	98	99	100
2	1	2	3	4	5	6	7	8	9	10	11	12	13	14	15	16	17	18	19	20	21	22	23	24	25	26	27	28	29	30	31	32	33	34	35	36	37	38	39	40	41	42	43	44	45	46	47	48	49	50	51	52	53	54	55	56	57	58	59	60	61	62	63	64	65	66	67	68	69	70	71	72	73	74	75	76	77	78	79	80	81	82	83	84	85	86	87	88	89	90	91	92	93	94	95	96	97	98	99	100
3	1	2	3	4	5	6	7	8	9	10	11	12	13	14	15	16	17	18	19	20	21	22	23	24	25	26	27	28	29	30	31	32	33	34	35	36	37	38	39	40	41	42	43	44	45	46	47	48	49	50	51	52	53	54	55	56	57	58	59	60	61	62	63	64	65	66	67	68	69	70	71	72	73	74	75	76	77	78	79	80	81	82	83	84	85	86	87	88	89	90	91	92	93	94	95	96	97	98	99	100
4	1	2	3	4	5	6	7	8	9	10	11	12	13	14	15	16	17	18	19	20	21	22	23	24	25	26	27	28	29	30	31	32	33	34	35	36	37	38	39	40	41	42	43	44	45	46	47	48	49	50	51	52	53	54	55	56	57	58	59	60	61	62	63	64	65	66	67	68	69	70	71	72	73	74	75	76	77	78	79	80	81	82	83	84	85	86	87	88	89	90	91	92	93	94	95	96	97	98	99	100
5	1	2	3	4	5	6	7	8	9	10	11	12	13	14	15	16	17	18	19	20	21	22	23	24	25	26	27	28	29	30	31	32	33	34	35	36	37	38	39	40	41	42	43	44	45	46	47	48	49	50	51	52	53	54	55	56	57	58	59	60	61	62	63	64	65	66	67	68	69	70	71	72	73	74	75	76	77	78	79	80	81																			

**Figure A.5.- Continued.**





W <sub>1</sub> 1.00	1.0000
W <sub>2</sub> 1.00	1.0000
W <sub>3</sub> 1.00	1.0000
W <sub>4</sub> 1.00	1.0000
W <sub>5</sub> 1.00	1.0000
W <sub>6</sub> 1.00	1.0000
W <sub>7</sub> 1.00	1.0000
W <sub>8</sub> 1.00	1.0000
W <sub>9</sub> 1.00	1.0000
W <sub>10</sub> 1.00	1.0000
W <sub>11</sub> 1.00	1.0000
W <sub>12</sub> 1.00	1.0000
W <sub>13</sub> 1.00	1.0000
W <sub>14</sub> 1.00	1.0000
W <sub>15</sub> 1.00	1.0000
W <sub>16</sub> 1.00	1.0000
W <sub>17</sub> 1.00	1.0000
W <sub>18</sub> 1.00	1.0000
W <sub>19</sub> 1.00	1.0000
W <sub>20</sub> 1.00	1.0000
W <sub>21</sub> 1.00	1.0000
W <sub>22</sub> 1.00	1.0000
W <sub>23</sub> 1.00	1.0000
W <sub>24</sub> 1.00	1.0000
W <sub>25</sub> 1.00	1.0000
W <sub>26</sub> 1.00	1.0000
W <sub>27</sub> 1.00	1.0000
W <sub>28</sub> 1.00	1.0000
W <sub>29</sub> 1.00	1.0000
W <sub>30</sub> 1.00	1.0000
W <sub>31</sub> 1.00	1.0000
W <sub>32</sub> 1.00	1.0000
W <sub>33</sub> 1.00	1.0000
W <sub>34</sub> 1.00	1.0000
W <sub>35</sub> 1.00	1.0000
W <sub>36</sub> 1.00	1.0000
W <sub>37</sub> 1.00	1.0000
W <sub>38</sub> 1.00	1.0000
W <sub>39</sub> 1.00	1.0000
W <sub>40</sub> 1.00	1.0000
W <sub>41</sub> 1.00	1.0000
W <sub>42</sub> 1.00	1.0000
W <sub>43</sub> 1.00	1.0000
W <sub>44</sub> 1.00	1.0000
W <sub>45</sub> 1.00	1.0000
W <sub>46</sub> 1.00	1.0000
W <sub>47</sub> 1.00	1.0000
W <sub>48</sub> 1.00	1.0000
W <sub>49</sub> 1.00	1.0000
W <sub>50</sub> 1.00	1.0000

PROGRAM FOR W<sub>1</sub> TO W<sub>50</sub> (W<sub>1</sub> TO W<sub>50</sub> AT 1.00) W<sub>1</sub> TO W<sub>50</sub> AT 1.00 W<sub>1</sub> TO W<sub>50</sub> AT 1.00

W <sub>1</sub> 1.00	1.0000
W <sub>2</sub> 1.00	1.0000
W <sub>3</sub> 1.00	1.0000
W <sub>4</sub> 1.00	1.0000
W <sub>5</sub> 1.00	1.0000
W <sub>6</sub> 1.00	1.0000
W <sub>7</sub> 1.00	1.0000
W <sub>8</sub> 1.00	1.0000
W <sub>9</sub> 1.00	1.0000
W <sub>10</sub> 1.00	1.0000

PROGRAM FOR W<sub>1</sub> TO W<sub>50</sub> (W<sub>1</sub> TO W<sub>50</sub> AT 1.00) W<sub>1</sub> TO W<sub>50</sub> AT 1.00 W<sub>1</sub> TO W<sub>50</sub> AT 1.00

W <sub>1</sub> 1.00	1.0000
W <sub>2</sub> 1.00	1.0000
W <sub>3</sub> 1.00	1.0000
W <sub>4</sub> 1.00	1.0000
W <sub>5</sub> 1.00	1.0000

Figure A.5.- Continued.

本報地址：新加坡 禧街 112 號 11 樓 1101 室  
 電話：(65) 6733 1111 傳真：(65) 6733 4466  
 廣告部：(65) 6733 1111 郵政信箱：新加坡 1111 號

[illegible]

111



7	7.0774	7.0774	7.0774	7.0774	7.0774	7.0774	7.0774	7.0774	7.0774
8	7.0774	7.0774	7.0774	7.0774	7.0774	7.0774	7.0774	7.0774	7.0774
9	7.0774	7.0774	7.0774	7.0774	7.0774	7.0774	7.0774	7.0774	7.0774
10	7.0774	7.0774	7.0774	7.0774	7.0774	7.0774	7.0774	7.0774	7.0774
11	7.0774	7.0774	7.0774	7.0774	7.0774	7.0774	7.0774	7.0774	7.0774
12	7.0774	7.0774	7.0774	7.0774	7.0774	7.0774	7.0774	7.0774	7.0774
13	7.0774	7.0774	7.0774	7.0774	7.0774	7.0774	7.0774	7.0774	7.0774
14	7.0774	7.0774	7.0774	7.0774	7.0774	7.0774	7.0774	7.0774	7.0774
15	7.0774	7.0774	7.0774	7.0774	7.0774	7.0774	7.0774	7.0774	7.0774
16	7.0774	7.0774	7.0774	7.0774	7.0774	7.0774	7.0774	7.0774	7.0774
17	7.0774	7.0774	7.0774	7.0774	7.0774	7.0774	7.0774	7.0774	7.0774
18	7.0774	7.0774	7.0774	7.0774	7.0774	7.0774	7.0774	7.0774	7.0774
19	7.0774	7.0774	7.0774	7.0774	7.0774	7.0774	7.0774	7.0774	7.0774

\*\*\*\*\*

\*\*\*\*\*

\*\*\*\*\*

\*\*\*\*\*

\*\*\*\*\*

\*\*\*\*\*

MICROFILMED FROM  
BEST AVAILABLE COPY

Figure A.5.- Continued.

본 연구는 2014년 12월 1일부터 2015년 11월 30일까지 1년간 실시된 것으로, 연구기간 동안 연구대상자를 대상으로 설문조사, 인터뷰, 관찰, 문헌연구 등을 실시하였다. 연구결과를 바탕으로 연구의 결론을 도출하고, 연구의 한계점과 향후 연구의 방향을 제시하였다.

DATE	DESCRIPTION	AMOUNT
1941	...	...
1942	...	...
1943	...	...
1944	...	...
1945	...	...
1946	...	...
1947	...	...
1948	...	...
1949	...	...
1950	...	...
1951	...	...
1952	...	...
1953	...	...
1954	...	...
1955	...	...
1956	...	...
1957	...	...
1958	...	...
1959	...	...
1960	...	...
1961	...	...
1962	...	...
1963	...	...
1964	...	...
1965	...	...
1966	...	...
1967	...	...
1968	...	...
1969	...	...
1970	...	...
1971	...	...
1972	...	...
1973	...	...
1974	...	...
1975	...	...
1976	...	...
1977	...	...
1978	...	...
1979	...	...
1980	...	...
1981	...	...
1982	...	...
1983	...	...
1984	...	...
1985	...	...
1986	...	...
1987	...	...
1988	...	...
1989	...	...
1990	...	...
1991	...	...
1992	...	...
1993	...	...
1994	...	...
1995	...	...
1996	...	...
1997	...	...
1998	...	...
1999	...	...
2000	...	...
2001	...	...
2002	...	...
2003	...	...
2004	...	...
2005	...	...
2006	...	...
2007	...	...
2008	...	...
2009	...	...
2010	...	...
2011	...	...
2012	...	...
2013	...	...
2014	...	...
2015	...	...
2016	...	...
2017	...	...
2018	...	...
2019	...	...
2020	...	...
2021	...	...
2022	...	...
2023	...	...
2024	...	...
2025	...	...
2026	...	...
2027	...	...
2028	...	...
2029	...	...
2030	...	...
2031	...	...
2032	...	...
2033	...	...
2034	...	...
2035	...	...
2036	...	...
2037	...	...
2038	...	...
2039	...	...
2040	...	...
2041	...	...
2042	...	...
2043	...	...
2044	...	...
2045	...	...
2046	...	...
2047	...	...
2048	...	...
2049	...	...
2050	...	...
2051	...	...
2052	...	...
2053	...	...
2054	...	...
2055	...	...
2056	...	...
2057	...	...
2058	...	...
2059	...	...
2060	...	...
2061	...	...
2062	...	...
2063	...	...
2064	...	...
2065	...	...
2066	...	...
2067	...	...
2068	...	...
2069	...	...
2070	...	...
2071	...	...
2072	...	...
2073	...	...
2074	...	...
2075	...	...
2076	...	...
2077	...	...
2078	...	...
2079	...	...
2080	...	

DATE	TIME
0000	0000
0001	0001
0002	0002
0003	0003
0004	0004
0005	0005
0006	0006
0007	0007
0008	0008
0009	0009
0010	0010
0011	0011
0012	0012
0013	0013
0014	0014
0015	0015
0016	0016
0017	0017
0018	0018
0019	0019
0020	0020
0021	0021
0022	0022
0023	0023
0024	0024
0025	0025
0026	0026
0027	0027
0028	0028
0029	0029
0030	0030
0031	0031
0032	0032
0033	0033
0034	0034
0035	0035
0036	0036
0037	0037
0038	0038
0039	0039
0040	0040
0041	0041
0042	0042
0043	0043
0044	0044
0045	0045
0046	0046
0047	0047
0048	0048
0049	0049
0050	0050
0051	0051
0052	0052
0053	0053
0054	0054
0055	0055
0056	0056
0057	0057
0058	0058
0059	0059
0060	0060
0061	0061
0062	0062
0063	0063
0064	0064
0065	0065
0066	0066
0067	0067
0068	0068
0069	0069
0070	0070
0071	0071
0072	0072
0073	0073
0074	0074
0075	0075
0076	0076
0077	0077
0078	0078
0079	0079
0080	0080
0081	0081
0082	0082
0083	0083
0084	0084
0085	0085
0086	0086
0087	0087
0088	0088
0089	0089
0090	0090
0091	0091
0092	0092
0093	0093
0094	0094
0095	0095
0096	0096
0097	0097
0098	0098
0099	0099

[illegible]

● 221	● 222
● 223	● 224
● 225	● 226
● 227	● 228
● 229	● 230
● 231	● 232
● 233	● 234
● 235	● 236
● 237	● 238
● 239	● 240
● 241	● 242
● 243	● 244
● 245	● 246
● 247	● 248
● 249	● 250
● 251	● 252
● 253	● 254
● 255	● 256
● 257	● 258
● 259	● 260
● 261	● 262
● 263	● 264
● 265	● 266
● 267	● 268
● 269	● 270
● 271	● 272
● 273	● 274
● 275	● 276
● 277	● 278
● 279	● 280
● 281	● 282
● 283	● 284
● 285	● 286
● 287	● 288
● 289	● 290
● 291	● 292
● 293	● 294
● 295	● 296
● 297	● 298
● 299	● 300
● 301	● 302
● 303	● 304
● 305	● 306
● 307	● 308
● 309	● 310
● 311	● 312
● 313	● 314
● 315	● 316
● 317	● 318
● 319	● 320
● 321	● 322
● 323	● 324
● 325	● 326
● 327	● 328
● 329	● 330
● 331	● 332
● 333	● 334
● 335	● 336
● 337	● 338
● 339	● 340
● 341	● 342
● 343	● 344
● 345	● 346
● 347	● 348
● 349	● 350
● 351	● 352
● 353	● 354
● 355	● 356
● 357	● 358
● 359	● 360
● 361	● 362
● 363	● 364
● 365	● 366
● 367	● 368
● 369	● 370
● 371	● 372
● 373	● 374
● 375	● 376
● 377	● 378
● 379	● 380
● 381	● 382
● 383	● 384
● 385	● 386
● 387	● 388
● 389	● 390
● 391	● 392
● 393	● 394
● 395	● 396
● 397	● 398
● 399	● 400
● 401	● 402
● 403	● 404
● 405	● 406
● 407	● 408
● 409	● 410
● 411	● 412
● 413	● 414
● 415	● 416
● 417	● 418
● 419	● 420
● 421	● 422
● 423	● 424
● 425	● 426
● 427	● 428
● 429	● 430
● 431	● 432
● 433	● 434
● 435	● 436
● 437	● 438
● 439	● 440
● 441	● 442
● 443	● 444
● 445	● 446
● 447	● 448
● 449	● 450
● 451	● 452
● 453	● 454
● 455	● 456
● 457	● 458
● 459	● 460
● 461	● 462
● 463	● 464
● 465	● 466
● 467	● 468
● 469	● 470
● 471	● 472
● 473	● 474
● 475	● 476
● 477	● 478
● 479	● 480
● 481	● 482
● 483	● 484
● 485	● 486
● 487	● 488
● 489	● 490
● 491	● 492
● 493	● 494
● 495	● 496
● 497	● 498
● 499	● 500

[illegible]

114

인문·사회과학영역 2월 10일(수) 1차 시험 · 100분 · 100점

日期	姓名	性别	年龄	职业	住址	备注
1949.10.1	王德胜	男	45	工人	上海南京路	
1949.10.2	李德胜	男	45	工人	上海南京路	
1949.10.3	张德胜	男	45	工人	上海南京路	
1949.10.4	赵德胜	男	45	工人	上海南京路	
1949.10.5	刘德胜	男	45	工人	上海南京路	
1949.10.6	陈德胜	男	45	工人	上海南京路	
1949.10.7	周德胜	男	45	工人	上海南京路	
1949.10.8	吴德胜	男	45	工人	上海南京路	
1949.10.9	孙德胜	男	45	工人	上海南京路	
1949.10.10	郑德胜	男	45	工人	上海南京路	
1949.10.11	冯德胜	男	45	工人	上海南京路	
1949.10.12	朱德胜	男	45	工人	上海南京路	
1949.10.13	马德胜	男	45	工人	上海南京路	
1949.10.14	林德胜	男	45	工人	上海南京路	
1949.10.15	黄德胜	男	45	工人	上海南京路	
1949.10.16	周德胜	男	45	工人	上海南京路	
1949.10.17	吴德胜	男	45	工人	上海南京路	
1949.10.18	孙德胜	男	45	工人	上海南京路	
1949.10.19	郑德胜	男	45	工人	上海南京路	
1949.10.20	冯德胜	男	45	工人	上海南京路	
1949.10.21	朱德胜	男	45	工人	上海南京路	
1949.10.22	马德胜	男	45	工人	上海南京路	
1949.10.23	林德胜	男	45	工人	上海南京路	
1949.10.24	黄德胜	男	45	工人	上海南京路	
1949.10.25	周德胜	男	45	工人	上海南京路	
1949.10.26	吴德胜	男	45	工人	上海南京路	
1949.10.27	孙德胜	男	45	工人	上海南京路	
1949.10.28	郑德胜	男	45	工人	上海南京路	
1949.10.29	冯德胜	男	45	工人	上海南京路	
1949.10.30	朱德胜	男	45	工人	上海南京路	

[illegible]

700	700
701	701
702	702
703	703
704	704
705	705
706	706
707	707
708	708
709	709
710	710
711	711
712	712
713	713
714	714
715	715
716	716
717	717
718	718
719	719
720	720
721	721
722	722
723	723
724	724
725	725
726	726
727	727
728	728
729	729
730	730
731	731
732	732
733	733
734	734
735	735
736	736
737	737
738	738
739	739
740	740
741	741
742	742
743	743
744	744
745	745
746	746
747	747
748	748
749	749
750	750
751	751
752	752
753	753
754	754
755	755
756	756
757	757
758	758
759	759
760	760
761	761
762	762
763	763
764	764
765	765
766	766
767	767
768	768
769	769
770	770
771	771
772	772
773	773
774	774
775	775
776	776
777	777
778	778
779	779
780	780
781	781
782	782
783	783
784	784
785	785
786	786
787	787
788	788
789	789
790	790
791	791
792	792
793	793
794	794
795	795
796	796
797	797
798	798
799	799
800	800

MICROFILMED FROM  
BEST AVAILABLE COPY





© 2000 Blackwell Science Ltd *Journal of Internal Medicine* 247: 361–367

● 2009年10月1日

[illegible]

## SINUSoidal AND NON-SINUSoidal COMPONENTS ALONG TRAJECTORY

.....

© 1998 by The McGraw-Hill Companies, Inc.

[illegible]

Figure A.5.- Continued.

FLOW FIELD AND MAGNETIC FIELD COMPONENTS ALONG TRAJECTORY  
(SOLAR WIND COORDINATE SYSTEM)

(DIMENSIONAL, USING INPUT INTERPLANETARY VALUES)

INTERPLANETARY MACH NUMBER = 3.30 INTERPLANETARY MAGNETIC FIELD  
RATIO OF SPECIFIC HEATS = 1.0667 MAGNITUDE = 0.022+01  
INTERPLANETARY VELOCITY = 3.021E+02 X-COMPONENT = 1.730E+00  
INTERPLANETARY DENSITY = 2.021E+01 Y-COMPONENT = 4.726E+00  
INTERPLANETARY TEMPERATURE = 1.023E+03 Z-COMPONENT = 4.032E+01

N	TIME	UW	VW	WW	UW	TEMP	FW	UW	FW	UW
1	-00.0700	3.021E+02	3.021E+02	0.	0.	2.020E+01	1.020E+01	0.020E+00	1.230E+00	4.726E+00
2	-01.1372	3.021E+02	3.021E+02	0.	0.	2.020E+01	1.020E+01	0.020E+00	1.230E+00	4.726E+00
3	-02.2044	3.021E+02	3.021E+02	0.	0.	2.020E+01	1.020E+01	0.020E+00	1.230E+00	4.726E+00
4	-03.2716	3.021E+02	3.021E+02	0.	0.	2.020E+01	1.020E+01	0.020E+00	1.230E+00	4.726E+00
5	-04.3388	3.021E+02	3.021E+02	0.	0.	2.020E+01	1.020E+01	0.020E+00	1.230E+00	4.726E+00
6	-05.4060	3.021E+02	3.021E+02	0.	0.	2.020E+01	1.020E+01	0.020E+00	1.230E+00	4.726E+00
7	-06.4732	3.021E+02	3.021E+02	0.	0.	2.020E+01	1.020E+01	0.020E+00	1.230E+00	4.726E+00
8	-07.5404	3.021E+02	3.021E+02	0.	0.	2.020E+01	1.020E+01	0.020E+00	1.230E+00	4.726E+00
9	-08.6076	3.021E+02	3.021E+02	0.	0.	2.020E+01	1.020E+01	0.020E+00	1.230E+00	4.726E+00
10	-09.6748	3.021E+02	3.021E+02	0.	0.	2.020E+01	1.020E+01	0.020E+00	1.230E+00	4.726E+00
11	-10.7420	3.021E+02	3.021E+02	0.	0.	2.020E+01	1.020E+01	0.020E+00	1.230E+00	4.726E+00
12	-11.8092	3.021E+02	3.021E+02	0.	0.	2.020E+01	1.020E+01	0.020E+00	1.230E+00	4.726E+00
13	-12.8764	3.021E+02	3.021E+02	0.	0.	2.020E+01	1.020E+01	0.020E+00	1.230E+00	4.726E+00
14	-13.9436	3.021E+02	3.021E+02	0.	0.	2.020E+01	1.020E+01	0.020E+00	1.230E+00	4.726E+00
15	-15.0108	3.021E+02	3.021E+02	0.	0.	2.020E+01	1.020E+01	0.020E+00	1.230E+00	4.726E+00
16	-16.0780	3.021E+02	3.021E+02	0.	0.	2.020E+01	1.020E+01	0.020E+00	1.230E+00	4.726E+00
17	-17.1452	3.021E+02	3.021E+02	0.	0.	2.020E+01	1.020E+01	0.020E+00	1.230E+00	4.726E+00
18	-18.2124	3.021E+02	3.021E+02	0.	0.	2.020E+01	1.020E+01	0.020E+00	1.230E+00	4.726E+00
19	-19.2796	3.021E+02	3.021E+02	0.	0.	2.020E+01	1.020E+01	0.020E+00	1.230E+00	4.726E+00
20	-20.3468	3.021E+02	3.021E+02	0.	0.	2.020E+01	1.020E+01	0.020E+00	1.230E+00	4.726E+00
21	-21.4140	3.021E+02	3.021E+02	0.	0.	2.020E+01	1.020E+01	0.020E+00	1.230E+00	4.726E+00
22	-22.4812	3.021E+02	3.021E+02	0.	0.	2.020E+01	1.020E+01	0.020E+00	1.230E+00	4.726E+00
23	-23.5484	3.021E+02	3.021E+02	0.	0.	2.020E+01	1.020E+01	0.020E+00	1.230E+00	4.726E+00
24	-24.6156	3.021E+02	3.021E+02	0.	0.	2.020E+01	1.020E+01	0.020E+00	1.230E+00	4.726E+00
25	-25.6828	3.021E+02	3.021E+02	0.	0.	2.020E+01	1.020E+01	0.020E+00	1.230E+00	4.726E+00
26	-26.7500	3.021E+02	3.021E+02	0.	0.	2.020E+01	1.020E+01	0.020E+00	1.230E+00	4.726E+00
27	-27.8172	3.021E+02	3.021E+02	0.	0.	2.020E+01	1.020E+01	0.020E+00	1.230E+00	4.726E+00
28	-28.8844	3.021E+02	3.021E+02	0.	0.	2.020E+01	1.020E+01	0.020E+00	1.230E+00	4.726E+00
29	-29.9516	3.021E+02	3.021E+02	0.	0.	2.020E+01	1.020E+01	0.020E+00	1.230E+00	4.726E+00
30	-31.0188	3.021E+02	3.021E+02	0.	0.	2.020E+01	1.020E+01	0.020E+00	1.230E+00	4.726E+00
31	-32.0860	3.021E+02	3.021E+02	0.	0.	2.020E+01	1.020E+01	0.020E+00	1.230E+00	4.726E+00
32	-33.1532	3.021E+02	3.021E+02	0.	0.	2.020E+01	1.020E+01	0.020E+00	1.230E+00	4.726E+00
33	-34.2204	3.021E+02	3.021E+02	0.	0.	2.020E+01	1.020E+01	0.020E+00	1.230E+00	4.726E+00
34	-35.2876	3.021E+02	3.021E+02	0.	0.	2.020E+01	1.020E+01	0.020E+00	1.230E+00	4.726E+00
35	-36.3548	3.021E+02	3.021E+02	0.	0.	2.020E+01	1.020E+01	0.020E+00	1.230E+00	4.726E+00
36	-37.4220	3.021E+02	3.021E+02	0.	0.	2.020E+01	1.020E+01	0.020E+00	1.230E+00	4.726E+00
37	-38.4892	3.021E+02	3.021E+02	0.	0.	2.020E+01	1.020E+01	0.020E+00	1.230E+00	4.726E+00

TRAJECTORY CALCULATION  
\*\*\*\*\*  
(X-Y-Z PLANET COORDINATE SYSTEM)

TRAJECTORY COORDINATES

PL/PLANET = 1.0331

N	TIME	XPL	YPL	ZPL	UPL	VPL	WPL	XPL	YPL	ZPL
1	-00.0700	-0.0100	1.0000	1.0000	1.0000	0.0000	0.0000	1.0000	1.0000	1.0000
2	-01.1372	-0.0100	1.0000	1.0000	1.0000	0.0000	0.0000	1.0000	1.0000	1.0000
3	-02.2044	-0.0100	1.0000	1.0000	1.0000	0.0000	0.0000	1.0000	1.0000	1.0000
4	-03.2716	-0.0100	1.0000	1.0000	1.0000	0.0000	0.0000	1.0000	1.0000	1.0000
5	-04.3388	-0.0100	1.0000	1.0000	1.0000	0.0000	0.0000	1.0000	1.0000	1.0000
6	-05.4060	-0.0100	1.0000	1.0000	1.0000	0.0000	0.0000	1.0000	1.0000	1.0000
7	-06.4732	-0.0100	1.0000	1.0000	1.0000	0.0000	0.0000	1.0000	1.0000	1.0000
8	-07.5404	-0.0100	1.0000	1.0000	1.0000	0.0000	0.0000	1.0000	1.0000	1.0000
9	-08.6076	-0.0100	1.0000	1.0000	1.0000	0.0000	0.0000	1.0000	1.0000	1.0000
10	-09.6748	-0.0100	1.0000	1.0000	1.0000	0.0000	0.0000	1.0000	1.0000	1.0000
11	-10.7420	-0.0100	1.0000	1.0000	1.0000	0.0000	0.0000	1.0000	1.0000	1.0000
12	-11.8092	-0.0100	1.0000	1.0000	1.0000	0.0000	0.0000	1.0000	1.0000	1.0000
13	-12.8764	-0.0100	1.0000	1.0000	1.0000	0.0000	0.0000	1.0000	1.0000	1.0000
14	-13.9436	-0.0100	1.0000	1.0000	1.0000	0.0000	0.0000	1.0000	1.0000	1.0000
15	-15.0108	-0.0100	1.0000	1.0000	1.0000	0.0000	0.0000	1.0000	1.0000	1.0000
16	-16.0780	-0.0100	1.0000	1.0000	1.0000	0.0000	0.0000	1.0000	1.0000	1.0000
17	-17.1452	-0.0100	1.0000	1.0000	1.0000	0.0000	0.0000	1.0000	1.0000	1.0000
18	-18.2124	-0.0100	1.0000	1.0000	1.0000	0.0000	0.0000	1.0000	1.0000	1.0000
19	-19.2796	-0.0100	1.0000	1.0000	1.0000	0.0000	0.0000	1.0000	1.0000	1.0000
20	-20.3468	-0.0100	1.0000	1.0000	1.0000	0.0000	0.0000	1.0000	1.0000	1.0000
21	-21.4140	-0.0100	1.0000	1.0000	1.0000	0.0000	0.0000	1.0000	1.0000	1.0000
22	-22.4812	-0.0100	1.0000	1.0000	1.0000	0.0000	0.0000	1.0000	1.0000	1.0000
23	-23.5484	-0.0100	1.0000	1.0000	1.0000	0.0000	0.0000	1.0000	1.0000	1.0000
24	-24.6156	-0.0100	1.0000	1.0000	1.0000	0.0000	0.0000	1.0000	1.0000	1.0000
25	-25.6828	-0.0100	1.0000	1.0000	1.0000	0.0000	0.0000	1.0000	1.0000	1.0000
26	-26.7500	-0.0100	1.0000	1.0000	1.0000	0.0000	0.0000	1.0000	1.0000	1.0000
27	-27.8172	-0.0100	1.0000	1.0000	1.0000	0.0000	0.0000	1.0000	1.0000	1.0000
28	-28.8844	-0.0100	1.0000	1.0000	1.0000	0.0000	0.0000	1.0000	1.0000	1.0000
29	-29.9516	-0.0100	1.0000	1.0000	1.0000	0.0000	0.0000	1.0000	1.0000	1.0000
30	-31.0188	-0.0100	1.0000	1.0000	1.0000	0.0000	0.0000	1.0000	1.0000	1.0000
31	-32.0860	-0.0100	1.0000	1.0000	1.0000	0.0000	0.0000	1.0000	1.0000	1.0000
32	-33.1532	-0.0100	1.0000	1.0000	1.0000	0.0000	0.0000	1.0000	1.0000	1.0000
33	-34.2204	-0.0100	1.0000	1.0000	1.0000	0.0000	0.0000	1.0000	1.0000	1.0000
34	-35.2876	-0.0100	1.0000	1.0000	1.0000	0.0000	0.0000	1.0000	1.0000	1.0000
35	-36.3548	-0.0100	1.0000	1.0000	1.0000	0.0000	0.0000	1.0000	1.0000	1.0000
36	-37.4220	-0.0100	1.0000	1.0000	1.0000	0.0000	0.0000	1.0000	1.0000	1.0000
37	-38.4892	-0.0100	1.0000	1.0000	1.0000	0.0000	0.0000	1.0000	1.0000	1.0000

Figure A.5.- Continued.



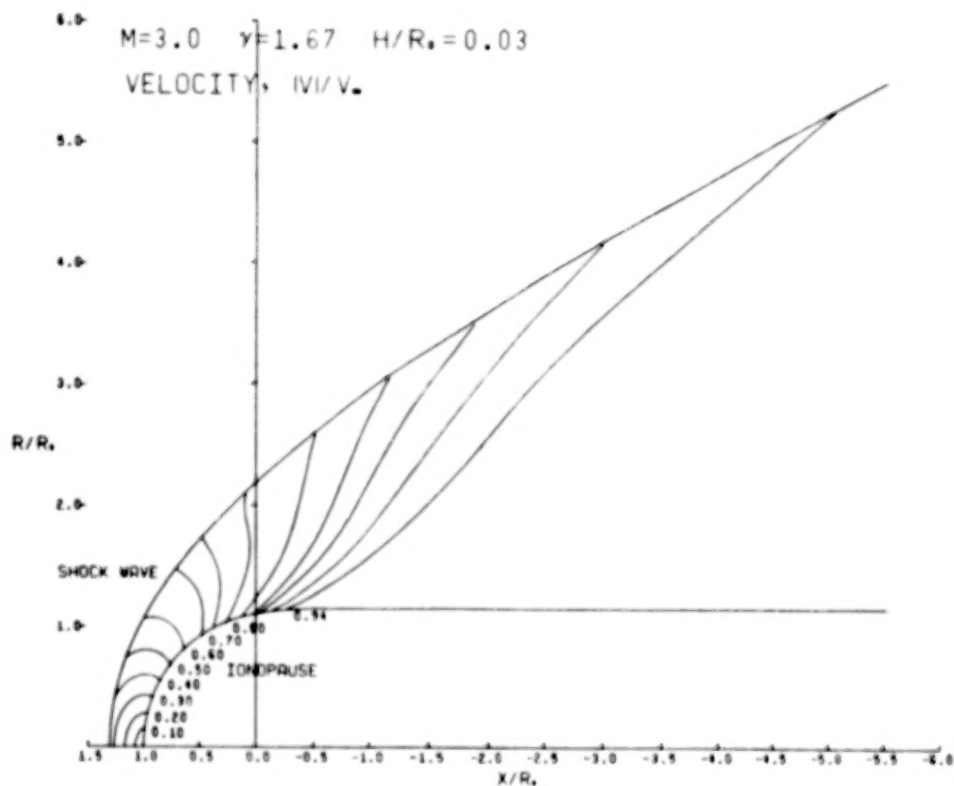
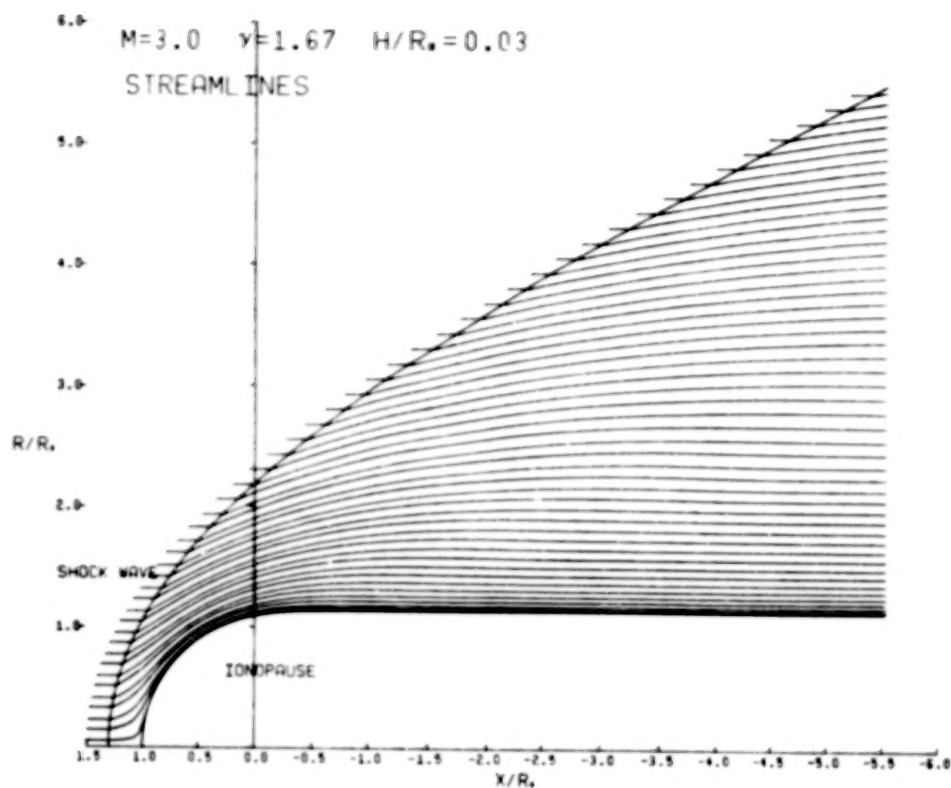


Figure A.6.- Plot output for sample case.

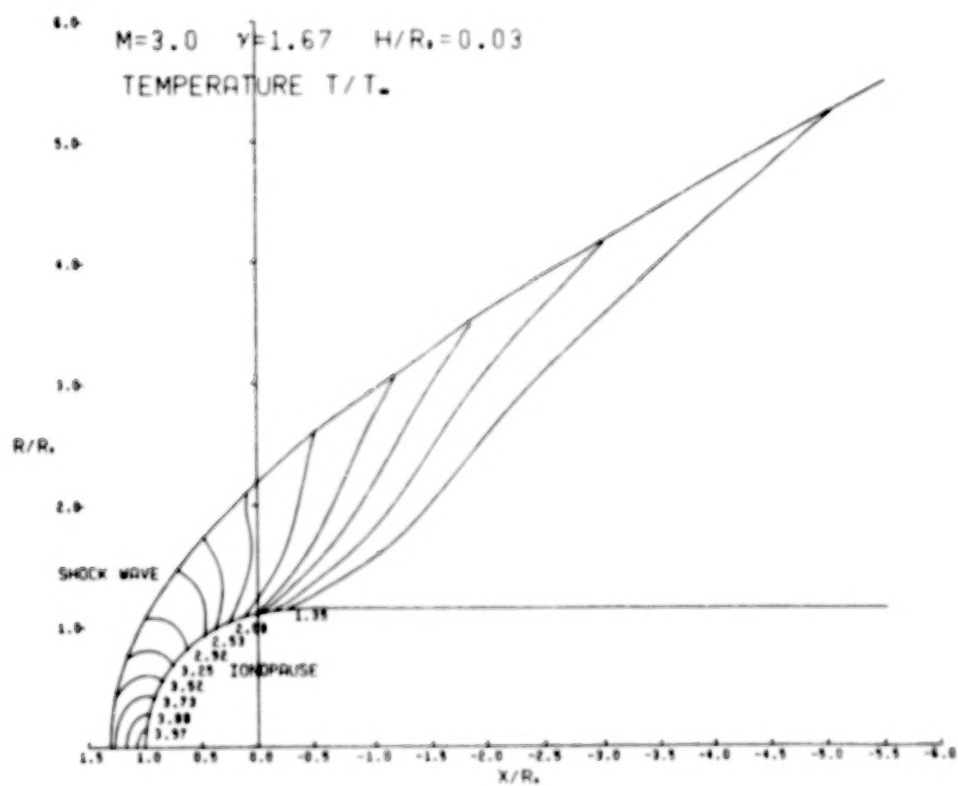
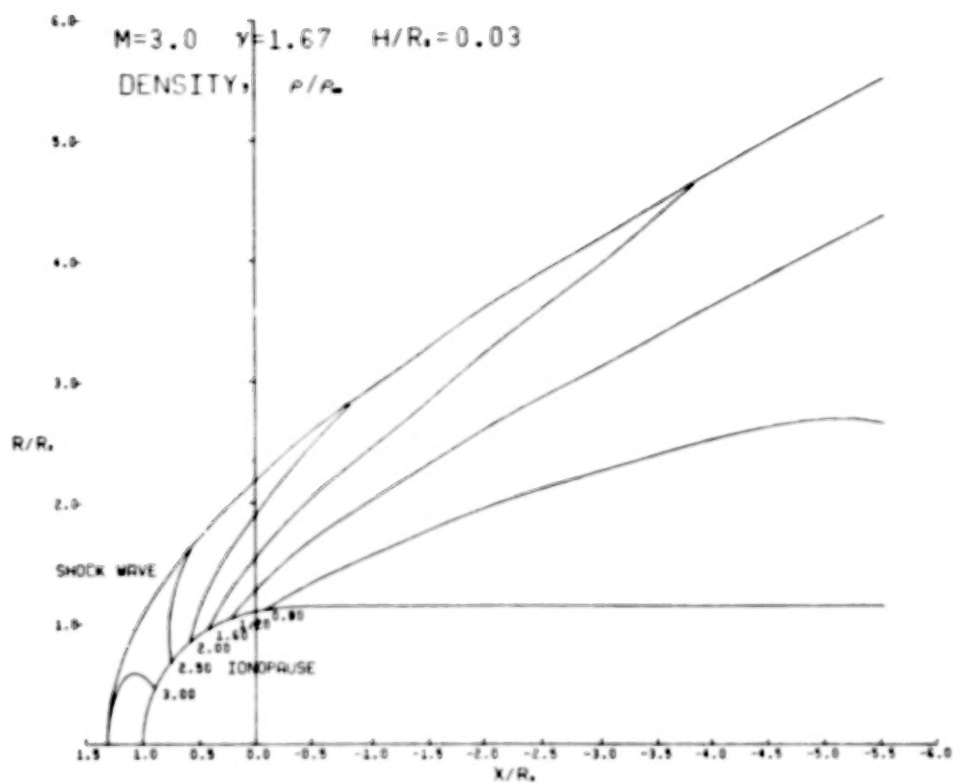


Figure A.6.- Continued

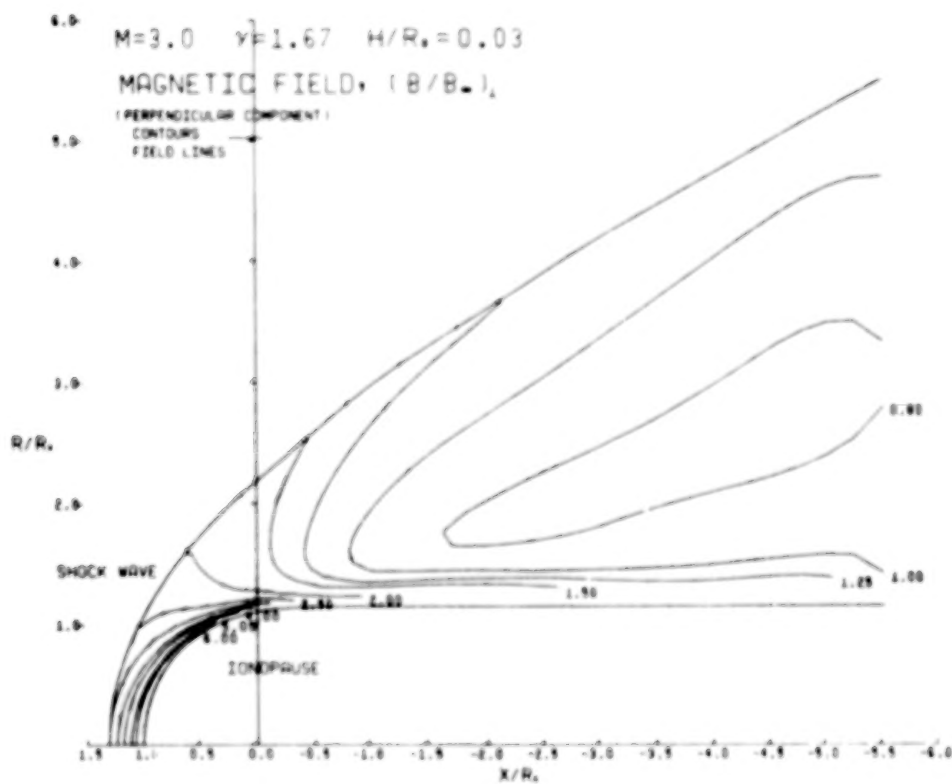
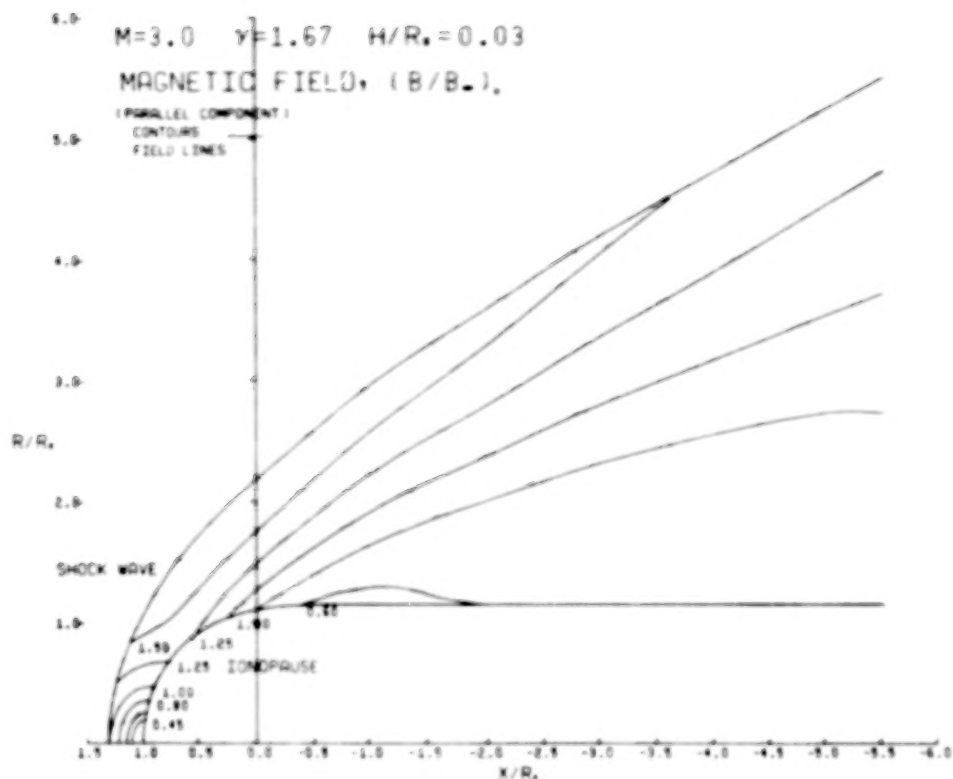


Figure A.6.- Continued

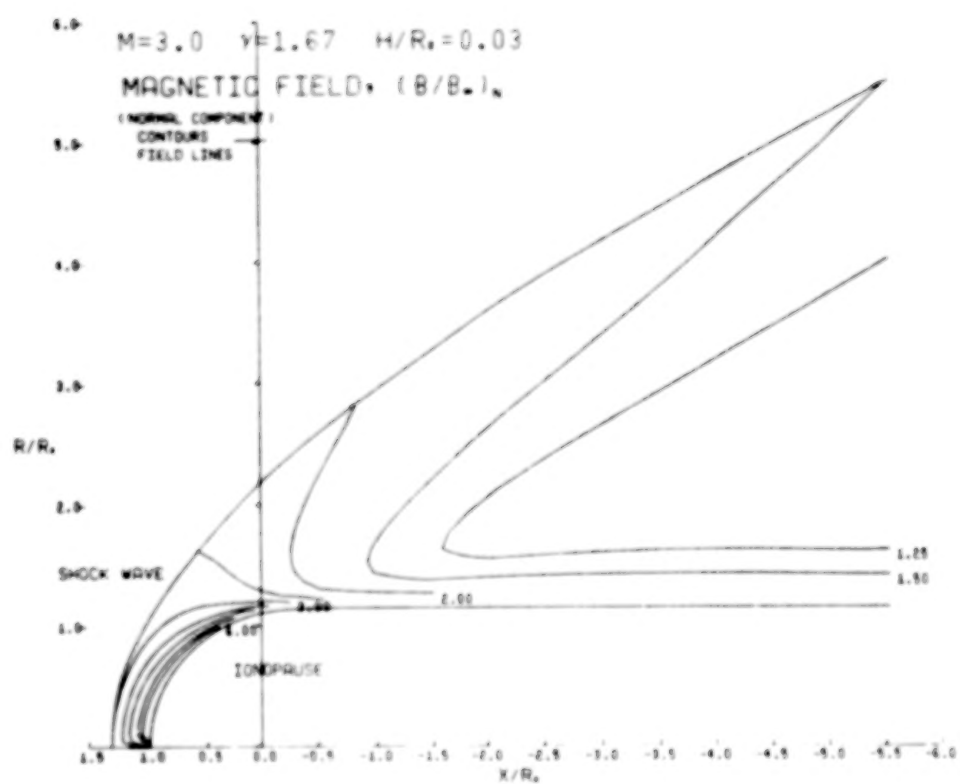


Figure A.6.- Continued



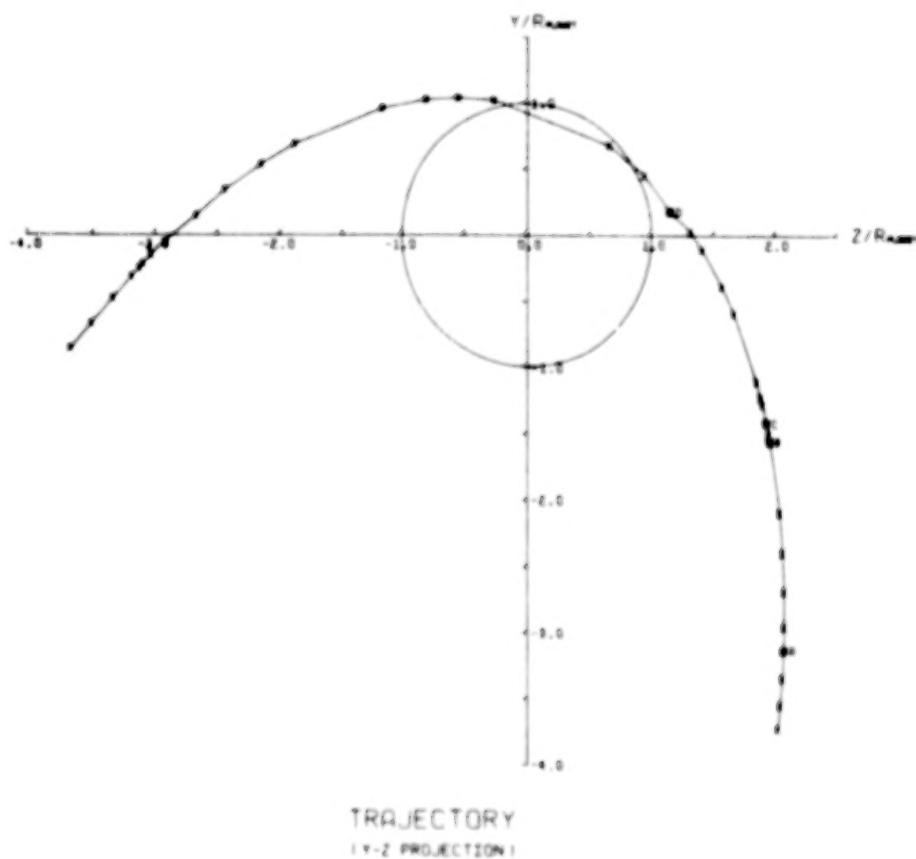
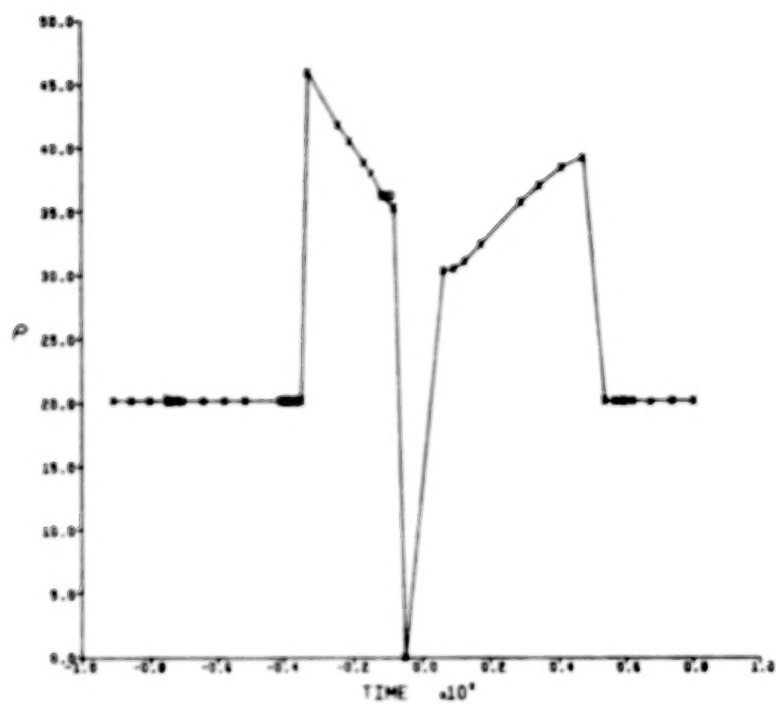


Figure A.6.- Continued

# DENSITY vs TIME



# TEMPERATURE vs TIME

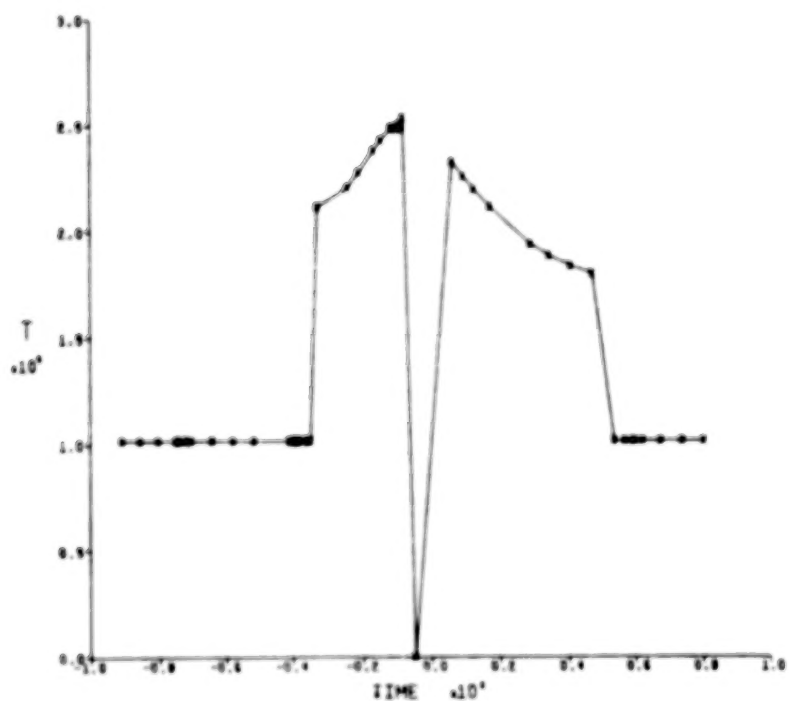


Figure A.6.- Continued.

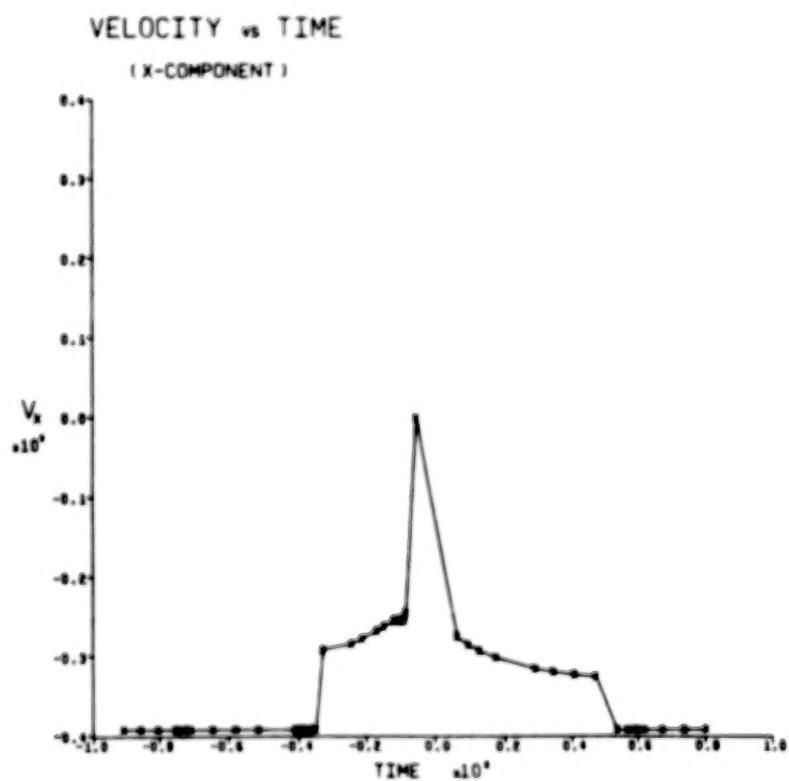
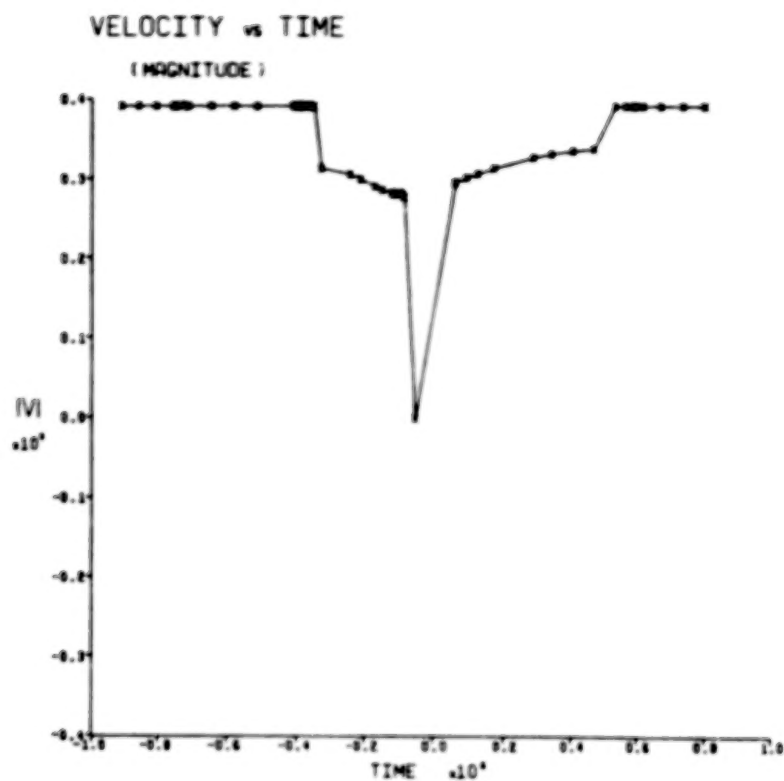


Figure A.6.- Continued

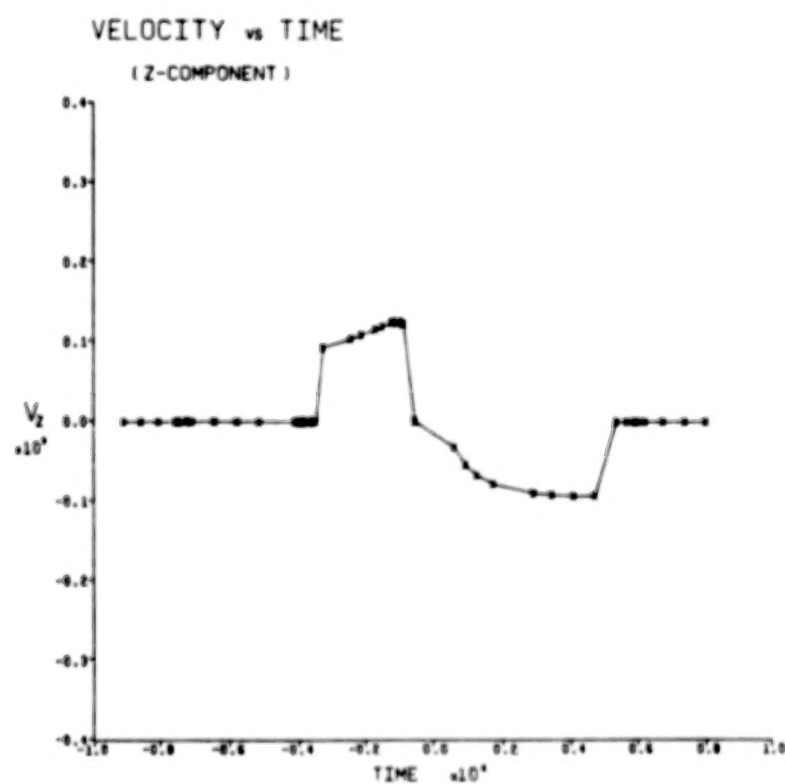
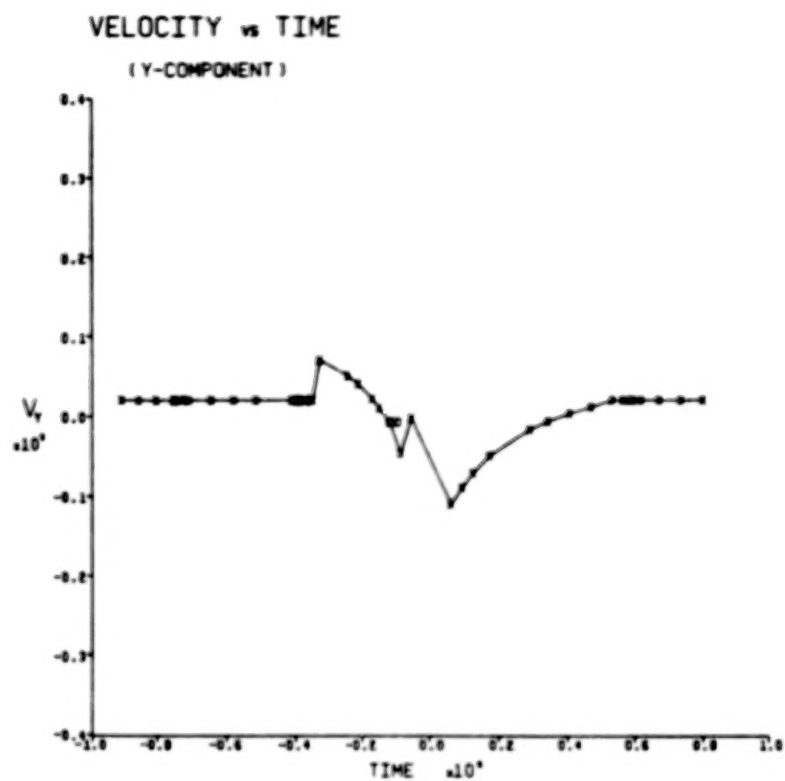


Figure A.6.- Continued.

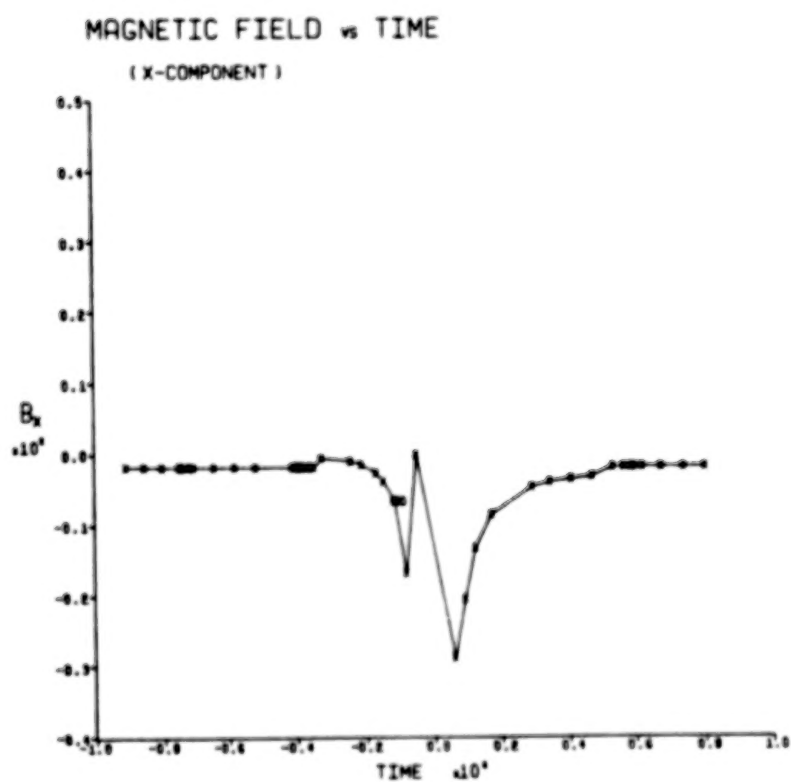
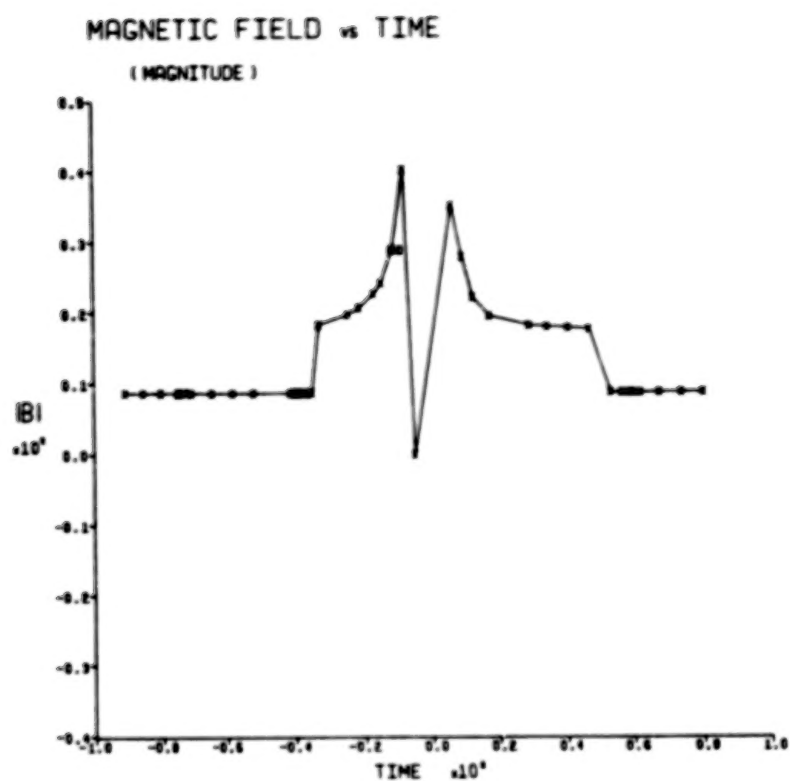


Figure A.6.- Continued.

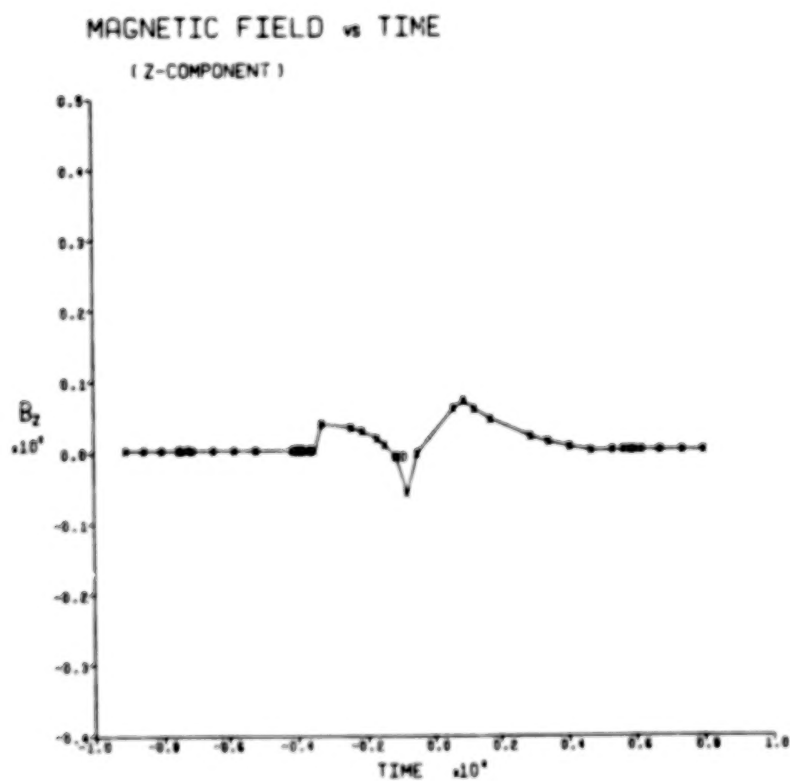
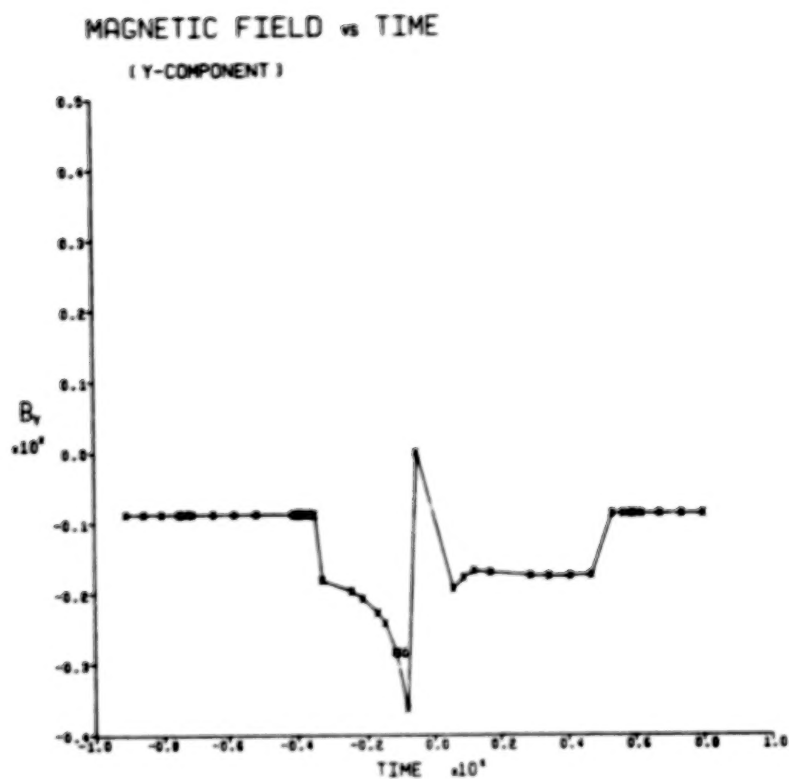


Figure A.6.- Concluded.

**BLANK PAGE**

## **APPENDIX B**

### **LISTING OF COMPUTER PROGRAM**





19

ANSWER

3

974









**BLANK PAGE**

**BLANK PAGE**



```

WFL=WHFLI
DO 50 N=1,NCL
IF=MAX(1,N)
NPTS=IF-1
CALL VECTORCONTRIN,CONTRIN(N),NPTS,1,1,1

```

```

C
F LABEL CONTOURS.
F
F DETERMINE WHICH END OF CONTOUR LINE IS CLOSER
F TO BOUNDARY.
F LABEL CONTOUR AT THAT END.
F

```

```

F FIND MINIMUM DISTANCE FROM CONTOUR END POINTS
F TO BOUNDARY.
F

```

```

F
F N=1
F VC=CONTRIN(N)
F VC=CONTRIN(N)
F NPTS=0
F DO 10 I=1,NPTS
F N=CONTRIN(I)-VC+2*CONTRIN(I)-VC+2
F IF N=0 GO TO 10
F

```

```

F 10 CONTINUE
F I=I+1 GO TO 10
F N=CONTRIN(I)-VC+2*CONTRIN(I)-VC+2
F IF N=0 GO TO 10
F

```

```

F 10 CONTINUE
F N=CONTRIN(I)-VC+2*CONTRIN(I)-VC+2
F

```

```

F DETERMINE WHICH END OF CONTOUR LINE IS
F CLOSER TO BOUNDARY.
F

```

```

F V1=CONTRIN(I),V2=CONTRIN(I+1)
F V1=CONTRIN(I),V2=CONTRIN(I+1)
F V1=CONTRIN(I),V2=CONTRIN(I+1)
F

```

```

F 20 V1=CONTRIN(I),V2=CONTRIN(I+1)
F V1=CONTRIN(I),V2=CONTRIN(I+1)
F

```

```

F 30 CONTINUE
F V1=CONTRIN(I),V2=CONTRIN(I+1)
F

```

```

F 5 CONTINUE
F
F MINIMUM LABEL CHECKS THE ARRAY OF LABELS
F DETERMINED BY OVERLAP. IF A LABEL OVERLAPS,
F IT IS NOT SAVED UNLESS IT DIFFERS A MINIMUM
F OR MAXIMUM CONTOUR VALUE.
F ARRAY I4 CONTAINS INDICES OF LABELS TO BE
F SAVED.
F

```

```

F CALL LABEL
F

```

```

F LABEL CONTOUR LINES
F

```

```

F DO 10 I=1,NPTS
F N=CONTRIN(I)
F CALL VECTORCONTRIN,CONTRIN(N),NPTS,1,1,1
F

```

```

F DRAW STREAMLINES
F

```

```

F 70 CONTINUE
F DO 70 N=1,NPTS
F N=CONTRIN(N)
F V1=CONTRIN(N),V2=CONTRIN(N+1)
F V1=CONTRIN(N),V2=CONTRIN(N+1)
F V1=CONTRIN(N),V2=CONTRIN(N+1)
F

```

```

F 80 CONTINUE
F CALL VECTORCONTRIN,CONTRIN(N),NPTS,1,1,1
F

```

```

F 90 CONTINUE
F RETURN
F

```

```

F DRAW STREAMLINES FOR MAGNETIC FIELD PLOT
F

```

```

CONTO 23
CONTO 24
CONTO 25
CONTO 26
CONTO 27
CONTO 28
CONTO 29
CONTO 30
CONTO 31
CONTO 32
CONTO 33
CONTO 34
CONTO 35
CONTO 36
CONTO 37
CONTO 38
CONTO 39
CONTO 40
CONTO 41
CONTO 42
CONTO 43
CONTO 44
CONTO 45
CONTO 46
CONTO 47
CONTO 48
CONTO 49
CONTO 50
CONTO 51
CONTO 52
CONTO 53
CONTO 54
CONTO 55
CONTO 56
CONTO 57
CONTO 58
CONTO 59
CONTO 60
CONTO 61
CONTO 62
CONTO 63
CONTO 64
CONTO 65
CONTO 66
CONTO 67
CONTO 68
CONTO 69
CONTO 70
CONTO 71
CONTO 72
CONTO 73
CONTO 74
CONTO 75
CONTO 76
CONTO 77
CONTO 78
CONTO 79
CONTO 80
CONTO 81
CONTO 82
CONTO 83
CONTO 84
CONTO 85
CONTO 86
CONTO 87
CONTO 88
CONTO 89
CONTO 90
CONTO 91
CONTO 92
CONTO 93
CONTO 94
CONTO 95
CONTO 96
CONTO 97
CONTO 98
CONTO 99
CONTO 100

```

```

100 DO 110 N=1,NPTS
F N=CONTRIN(N)
F V1=CONTRIN(N),V2=CONTRIN(N+1)
F V1=CONTRIN(N),V2=CONTRIN(N+1)
F V1=CONTRIN(N),V2=CONTRIN(N+1)
F

```

```

120 CONTINUE
F DO 120 N=1,NPTS
F CALL VECTORCONTRIN,CONTRIN(N),NPTS,1,1,1
F

```

```

130 CONTINUE
F 110 CONTINUE
F RETURN
F

```

```

F DRAW PERPENDICULAR FIELD LINES FOR MAGNETIC FIELD PLOT
F

```

```

150 CONTINUE
F V1=CONTRIN(N),V2=CONTRIN(N+1)
F V1=CONTRIN(N),V2=CONTRIN(N+1)
F V1=CONTRIN(N),V2=CONTRIN(N+1)
F V1=CONTRIN(N),V2=CONTRIN(N+1)
F

```

```

170 CONTINUE
F J=J+1
F 160 CONTINUE
F

```

```

180 CONTINUE
F V1=CONTRIN(N),V2=CONTRIN(N+1)
F V1=CONTRIN(N),V2=CONTRIN(N+1)
F V1=CONTRIN(N),V2=CONTRIN(N+1)
F

```

```

200 CONTINUE
F V1=CONTRIN(N),V2=CONTRIN(N+1)
F V1=CONTRIN(N),V2=CONTRIN(N+1)
F V1=CONTRIN(N),V2=CONTRIN(N+1)
F

```

```

220 CONTINUE
F V1=CONTRIN(N),V2=CONTRIN(N+1)
F V1=CONTRIN(N),V2=CONTRIN(N+1)
F V1=CONTRIN(N),V2=CONTRIN(N+1)
F

```

```

240 CONTINUE
F V1=CONTRIN(N),V2=CONTRIN(N+1)
F V1=CONTRIN(N),V2=CONTRIN(N+1)
F V1=CONTRIN(N),V2=CONTRIN(N+1)
F

```

```

260 CONTINUE
F V1=CONTRIN(N),V2=CONTRIN(N+1)
F V1=CONTRIN(N),V2=CONTRIN(N+1)
F V1=CONTRIN(N),V2=CONTRIN(N+1)
F

```

```

280 CONTINUE
F V1=CONTRIN(N),V2=CONTRIN(N+1)
F V1=CONTRIN(N),V2=CONTRIN(N+1)
F V1=CONTRIN(N),V2=CONTRIN(N+1)
F

```

```

300 CONTINUE
F V1=CONTRIN(N),V2=CONTRIN(N+1)
F V1=CONTRIN(N),V2=CONTRIN(N+1)
F V1=CONTRIN(N),V2=CONTRIN(N+1)
F

```

```

320 CONTINUE
F V1=CONTRIN(N),V2=CONTRIN(N+1)
F V1=CONTRIN(N),V2=CONTRIN(N+1)
F V1=CONTRIN(N),V2=CONTRIN(N+1)
F

```

```

340 CONTINUE
F V1=CONTRIN(N),V2=CONTRIN(N+1)
F V1=CONTRIN(N),V2=CONTRIN(N+1)
F V1=CONTRIN(N),V2=CONTRIN(N+1)
F

```

```

360 CONTINUE
F V1=CONTRIN(N),V2=CONTRIN(N+1)
F V1=CONTRIN(N),V2=CONTRIN(N+1)
F V1=CONTRIN(N),V2=CONTRIN(N+1)
F

```

```

380 CONTINUE
F V1=CONTRIN(N),V2=CONTRIN(N+1)
F V1=CONTRIN(N),V2=CONTRIN(N+1)
F V1=CONTRIN(N),V2=CONTRIN(N+1)
F

```

```

400 CONTINUE
F V1=CONTRIN(N),V2=CONTRIN(N+1)
F V1=CONTRIN(N),V2=CONTRIN(N+1)
F V1=CONTRIN(N),V2=CONTRIN(N+1)
F

```

```

420 CONTINUE
F V1=CONTRIN(N),V2=CONTRIN(N+1)
F V1=CONTRIN(N),V2=CONTRIN(N+1)
F V1=CONTRIN(N),V2=CONTRIN(N+1)
F

```

```

440 CONTINUE
F V1=CONTRIN(N),V2=CONTRIN(N+1)
F V1=CONTRIN(N),V2=CONTRIN(N+1)
F V1=CONTRIN(N),V2=CONTRIN(N+1)
F

```

```

460 CONTINUE
F V1=CONTRIN(N),V2=CONTRIN(N+1)
F V1=CONTRIN(N),V2=CONTRIN(N+1)
F V1=CONTRIN(N),V2=CONTRIN(N+1)
F

```

```

480 CONTINUE
F V1=CONTRIN(N),V2=CONTRIN(N+1)
F V1=CONTRIN(N),V2=CONTRIN(N+1)
F V1=CONTRIN(N),V2=CONTRIN(N+1)
F

```

```

500 CONTINUE
F V1=CONTRIN(N),V2=CONTRIN(N+1)
F V1=CONTRIN(N),V2=CONTRIN(N+1)
F V1=CONTRIN(N),V2=CONTRIN(N+1)
F

```

```

520 CONTINUE
F V1=CONTRIN(N),V2=CONTRIN(N+1)
F V1=CONTRIN(N),V2=CONTRIN(N+1)
F V1=CONTRIN(N),V2=CONTRIN(N+1)
F

```

```

CONTO 101
CONTO 102
CONTO 103
CONTO 104
CONTO 105
CONTO 106
CONTO 107
CONTO 108
CONTO 109
CONTO 110
CONTO 111
CONTO 112
CONTO 113
CONTO 114
CONTO 115
CONTO 116
CONTO 117
CONTO 118
CONTO 119
CONTO 120
CONTO 121
CONTO 122
CONTO 123
CONTO 124
CONTO 125
CONTO 126
CONTO 127
CONTO 128
CONTO 129
CONTO 130
CONTO 131
CONTO 132
CONTO 133
CONTO 134
CONTO 135
CONTO 136
CONTO 137
CONTO 138
CONTO 139
CONTO 140
CONTO 141
CONTO 142
CONTO 143
CONTO 144
CONTO 145
CONTO 146
CONTO 147
CONTO 148
CONTO 149
CONTO 150
CONTO 151
CONTO 152
CONTO 153
CONTO 154
CONTO 155
CONTO 156
CONTO 157
CONTO 158
CONTO 159
CONTO 160
CONTO 161
CONTO 162
CONTO 163
CONTO 164
CONTO 165
CONTO 166
CONTO 167
CONTO 168
CONTO 169
CONTO 170
CONTO 171
CONTO 172
CONTO 173
CONTO 174
CONTO 175
CONTO 176
CONTO 177
CONTO 178
CONTO 179
CONTO 180
CONTO 181
CONTO 182
CONTO 183
CONTO 184
CONTO 185
CONTO 186
CONTO 187
CONTO 188
CONTO 189
CONTO 190

```



```

104 YS(ND)=YS(ND-1)+YS(ND-YS(ND-1))+XND(ND-1)/YS(ND-YS(ND-1)) CONTN 101
IF YS(ND) LT. YND(ND) N1=N CONTN 102
205 CONTINUE CONTN 103
N1=250*WMAX/BN CONTN 104
CALL MTE(YS(ND),YS(N1),YS(N1+1),YS(N1+1),2D,3) CONTN 105
250 CONTINUE CONTN 106
22 CONTINUE CONTN 107
RETURN CONTN 108
END CONTN 109

```

```

SUBROUTINE CCONTN CONTN 2
CONTN 3
SUBROUTINE CCONTN CONTN 4
CONTN 5
CONTN 6
CONTN 7
CONTN 8
CONTN 9
CONTN 10
CONTN 11
CONTN 12
CONTN 13
CONTN 14
CONTN 15
CONTN 16
CONTN 17
CONTN 18
CONTN 19
CONTN 20
CONTN 21
CONTN 22
CONTN 23
CONTN 24
CONTN 25
CONTN 26
CONTN 27
CONTN 28
CONTN 29
CONTN 30
CONTN 31
CONTN 32
CONTN 33
CONTN 34
CONTN 35
CONTN 36
CONTN 37
CONTN 38
CONTN 39
CONTN 40
CONTN 41
CONTN 42
CONTN 43
CONTN 44
CONTN 45
CONTN 46
CONTN 47
CONTN 48
CONTN 49
CONTN 50
CONTN 51
CONTN 52
CONTN 53
CONTN 54
CONTN 55
CONTN 56
CONTN 57
CONTN 58
CONTN 59
CONTN 60
CONTN 61
CONTN 62
CONTN 63
CONTN 64
CONTN 65
CONTN 66
CONTN 67
CONTN 68
CONTN 69
CONTN 70
CONTN 71
CONTN 72
CONTN 73
CONTN 74
CONTN 75
CONTN 76
CONTN 77
CONTN 78
CONTN 79
CONTN 80
CONTN 81
CONTN 82
CONTN 83
CONTN 84
CONTN 85
CONTN 86
CONTN 87
CONTN 88
CONTN 89
CONTN 90
CONTN 91
CONTN 92
CONTN 93
CONTN 94
CONTN 95
CONTN 96
CONTN 97
CONTN 98
CONTN 99
CONTN 100
CONTN 101
CONTN 102
CONTN 103
CONTN 104
CONTN 105
CONTN 106
CONTN 107
CONTN 108
CONTN 109
CONTN 110
CONTN 111
CONTN 112
CONTN 113
CONTN 114
CONTN 115
CONTN 116
CONTN 117
CONTN 118
CONTN 119
CONTN 120
CONTN 121
CONTN 122
CONTN 123
CONTN 124
CONTN 125
CONTN 126
CONTN 127
CONTN 128
CONTN 129
CONTN 130
CONTN 131
CONTN 132
CONTN 133
CONTN 134
CONTN 135
CONTN 136
CONTN 137
CONTN 138
CONTN 139
CONTN 140
CONTN 141
CONTN 142
CONTN 143
CONTN 144
CONTN 145
CONTN 146
CONTN 147
CONTN 148
CONTN 149
CONTN 150
CONTN 151
CONTN 152
CONTN 153
CONTN 154
CONTN 155
CONTN 156
CONTN 157
CONTN 158
CONTN 159
CONTN 160
CONTN 161
CONTN 162
CONTN 163
CONTN 164
CONTN 165
CONTN 166
CONTN 167
CONTN 168
CONTN 169
CONTN 170
CONTN 171
CONTN 172
CONTN 173
CONTN 174
CONTN 175
CONTN 176
CONTN 177
CONTN 178
CONTN 179
CONTN 180
CONTN 181
CONTN 182
CONTN 183
CONTN 184
CONTN 185
CONTN 186
CONTN 187
CONTN 188
CONTN 189
CONTN 190
CONTN 191
CONTN 192
CONTN 193
CONTN 194
CONTN 195
CONTN 196
CONTN 197
CONTN 198
CONTN 199
CONTN 200

```

```

101 NO 110 I=2, NMAX
ASCH(I,1)=NPEP(I,1)
110 CONTINUE
CALL NAPSCH(2,CONTN,CONTY,KBCON,2,KCON,NAB,1000,30,TCW,
* 2,1,NMAX,NMAX)
TPLOT=7
IF (LPCON) CALL CONDOTCON,FACT,NHINDY
IF (LPLT) CALL PLOTEN
NO 120 J=1,NMAX
NO 123 I=2,NMAX
ASCH(I,1)=NPEP(I,1)
123 CONTINUE
CALL NAPSCH(2,CONTN,CONTY,KBCON,2,KCON,NAB,1000,30,TCW,
* 2,1,NMAX,NMAX)
TPLOT=7
IF (LPCON) CALL CONDOTCON,FACT,NHINDY
IF (LPLT) CALL PLOTEN
210 CONTINUE
IF (LPLT) CALL ENPLT(3,3,0,0)
RETURN
END

```

```

FUNCTION NPEP(X)
CONTN 2
CONTN 3
CONTN 4
CONTN 5
CONTN 6
CONTN 7
CONTN 8
CONTN 9
CONTN 10
CONTN 11
CONTN 12
CONTN 13
CONTN 14
CONTN 15
CONTN 16
CONTN 17
CONTN 18
CONTN 19
CONTN 20
CONTN 21
CONTN 22
CONTN 23
CONTN 24
CONTN 25
CONTN 26
CONTN 27
CONTN 28
CONTN 29
CONTN 30
CONTN 31
CONTN 32
CONTN 33
CONTN 34
CONTN 35
CONTN 36
CONTN 37
CONTN 38
CONTN 39
CONTN 40
CONTN 41
CONTN 42
CONTN 43
CONTN 44
CONTN 45
CONTN 46
CONTN 47
CONTN 48
CONTN 49
CONTN 50
CONTN 51
CONTN 52
CONTN 53
CONTN 54
CONTN 55
CONTN 56
CONTN 57
CONTN 58
CONTN 59
CONTN 60
CONTN 61
CONTN 62
CONTN 63
CONTN 64
CONTN 65
CONTN 66
CONTN 67
CONTN 68
CONTN 69
CONTN 70
CONTN 71
CONTN 72
CONTN 73
CONTN 74
CONTN 75
CONTN 76
CONTN 77
CONTN 78
CONTN 79
CONTN 80
CONTN 81
CONTN 82
CONTN 83
CONTN 84
CONTN 85
CONTN 86
CONTN 87
CONTN 88
CONTN 89
CONTN 90
CONTN 91
CONTN 92
CONTN 93
CONTN 94
CONTN 95
CONTN 96
CONTN 97
CONTN 98
CONTN 99
CONTN 100
CONTN 101
CONTN 102
CONTN 103
CONTN 104
CONTN 105
CONTN 106
CONTN 107
CONTN 108
CONTN 109
CONTN 110
CONTN 111
CONTN 112
CONTN 113
CONTN 114
CONTN 115
CONTN 116
CONTN 117
CONTN 118
CONTN 119
CONTN 120
CONTN 121
CONTN 122
CONTN 123
CONTN 124
CONTN 125
CONTN 126
CONTN 127
CONTN 128
CONTN 129
CONTN 130
CONTN 131
CONTN 132
CONTN 133
CONTN 134
CONTN 135
CONTN 136
CONTN 137
CONTN 138
CONTN 139
CONTN 140
CONTN 141
CONTN 142
CONTN 143
CONTN 144
CONTN 145
CONTN 146
CONTN 147
CONTN 148
CONTN 149
CONTN 150
CONTN 151
CONTN 152
CONTN 153
CONTN 154
CONTN 155
CONTN 156
CONTN 157
CONTN 158
CONTN 159
CONTN 160
CONTN 161
CONTN 162
CONTN 163
CONTN 164
CONTN 165
CONTN 166
CONTN 167
CONTN 168
CONTN 169
CONTN 170
CONTN 171
CONTN 172
CONTN 173
CONTN 174
CONTN 175
CONTN 176
CONTN 177
CONTN 178
CONTN 179
CONTN 180
CONTN 181
CONTN 182
CONTN 183
CONTN 184
CONTN 185
CONTN 186
CONTN 187
CONTN 188
CONTN 189
CONTN 190
CONTN 191
CONTN 192
CONTN 193
CONTN 194
CONTN 195
CONTN 196
CONTN 197
CONTN 198
CONTN 199
CONTN 200

```

[illegible]

```

SUBROUTINE EXTRAP
      THIS ROUTINE CALCULATES EXTRAPOLATED VALUES OF
      UHS AND DVS AT POINTS ALONG THE BOUNDARY THETA=0 USING
      A LOGARITHMIC INTERPOLATING POLYNOMIAL WITH
      THREE UNEQUALLY SPACED POINTS ON EACH RADIAL CURVE.
      COMMON PLOUNT/ THETA(25),DP(25,25),UPLUNT
      COMMON PORDRHS/ VORD(100),VORD(100),VSW(120),VSW(100),
      * UORD(100),DORD(100),GORD(100),DORD(100)
      COMMON PFLDUF/ VC(20,100),VC(2,100),VF(2,100),HOF(20,100)
      COMMON /SWRCH/ DORD(100),DT(100)
      CALCULATE LOGARITHMIC COEFFICIENTS
      THZ0=THETA(21)-THETA(10)
      THZ1=THETA(21)-THETA(4)
      THZ2=THETA(21)-THETA(10)
      THZ3=THETA(21)-THETA(4)
      THZ4=THETA(21)-THETA(10)
      THZ5=THETA(21)-THETA(4)
      THZ6=THETA(21)-THETA(10)
      THZ7=THETA(21)-THETA(4)
      THZ8=THETA(21)-THETA(10)
      THZ9=THETA(21)-THETA(4)
      THZ10=THETA(21)-THETA(10)
      THZ11=THETA(21)-THETA(4)
      THZ12=THETA(21)-THETA(10)
      THZ13=THETA(21)-THETA(4)
      THZ14=THETA(21)-THETA(10)
      THZ15=THETA(21)-THETA(4)
      THZ16=THETA(21)-THETA(10)
      THZ17=THETA(21)-THETA(4)
      THZ18=THETA(21)-THETA(10)
      THZ19=THETA(21)-THETA(4)
      THZ20=THETA(21)-THETA(10)
      THZ21=THETA(21)-THETA(4)
      THZ22=THETA(21)-THETA(10)
      THZ23=THETA(21)-THETA(4)
      THZ24=THETA(21)-THETA(10)
      THZ25=THETA(21)-THETA(4)
      THZ26=THETA(21)-THETA(10)
      THZ27=THETA(21)-THETA(4)
      THZ28=THETA(21)-THETA(10)
      THZ29=THETA(21)-THETA(4)
      THZ30=THETA(21)-THETA(10)
      THZ31=THETA(21)-THETA(4)
      THZ32=THETA(21)-THETA(10)
      THZ33=THETA(21)-THETA(4)
      THZ34=THETA(21)-THETA(10)
      THZ35=THETA(21)-THETA(4)
      THZ36=THETA(21)-THETA(10)
      THZ37=THETA(21)-THETA(4)
      THZ38=THETA(21)-THETA(10)
      THZ39=THETA(21)-THETA(4)
      THZ40=THETA(21)-THETA(10)
      THZ41=THETA(21)-THETA(4)
      THZ42=THETA(21)-THETA(10)
      THZ43=THETA(21)-THETA(4)
      THZ44=THETA(21)-THETA(10)
      THZ45=THETA(21)-THETA(4)
      THZ46=THETA(21)-THETA(10)
      THZ47=THETA(21)-THETA(4)
      THZ48=THETA(21)-THETA(10)
      THZ49=THETA(21)-THETA(4)
      THZ50=THETA(21)-THETA(10)
      THZ51=THETA(21)-THETA(4)
      THZ52=THETA(21)-THETA(10)
      THZ53=THETA(21)-THETA(4)
      THZ54=THETA(21)-THETA(10)
      THZ55=THETA(21)-THETA(4)
      THZ56=THETA(21)-THETA(10)
      THZ57=THETA(21)-THETA(4)
      THZ58=THETA(21)-THETA(10)
      THZ59=THETA(21)-THETA(4)
      THZ60=THETA(21)-THETA(10)
      THZ61=THETA(21)-THETA(4)
      THZ62=THETA(21)-THETA(10)
      THZ63=THETA(21)-THETA(4)
      THZ64=THETA(21)-THETA(10)
      THZ65=THETA(21)-THETA(4)
      THZ66=THETA(21)-THETA(10)
      THZ67=THETA(21)-THETA(4)
      THZ68=THETA(21)-THETA(10)
      THZ69=THETA(21)-THETA(4)
      THZ70=THETA(21)-THETA(10)
      THZ71=THETA(21)-THETA(4)
      THZ72=THETA(21)-THETA(10)
      THZ73=THETA(21)-THETA(4)
      THZ74=THETA(21)-THETA(10)
      THZ75=THETA(21)-THETA(4)
      THZ76=THETA(21)-THETA(10)
      THZ77=THETA(21)-THETA(4)
      THZ78=THETA(21)-THETA(10)
      THZ79=THETA(21)-THETA(4)
      THZ80=THETA(21)-THETA(10)
      THZ81=THETA(21)-THETA(4)
      THZ82=THETA(21)-THETA(10)
      THZ83=THETA(21)-THETA(4)
      THZ84=THETA(21)-THETA(10)
      THZ85=THETA(21)-THETA(4)
      THZ86=THETA(21)-THETA(10)
      THZ87=THETA(21)-THETA(4)
      THZ88=THETA(21)-THETA(10)
      THZ89=THETA(21)-THETA(4)
      THZ90=THETA(21)-THETA(10)
      THZ91=THETA(21)-THETA(4)
      THZ92=THETA(21)-THETA(10)
      THZ93=THETA(21)-THETA(4)
      THZ94=THETA(21)-THETA(10)
      THZ95=THETA(21)-THETA(4)
      THZ96=THETA(21)-THETA(10)
      THZ97=THETA(21)-THETA(4)
      THZ98=THETA(21)-THETA(10)
      THZ99=THETA(21)-THETA(4)
      THZ100=THETA(21)-THETA(10)
      THZ101=THETA(21)-THETA(4)
      THZ102=THETA(21)-THETA(10)
      THZ103=THETA(21)-THETA(4)
      THZ104=THETA(21)-THETA(10)
      THZ105=THETA(21)-THETA(4)
      THZ106=THETA(21)-THETA(10)
      THZ107=THETA(21)-THETA(4)
      THZ108=THETA(21)-THETA(10)
      THZ109=THETA(21)-THETA(4)
      THZ110=THETA(21)-THETA(10)
      THZ111=THETA(21)-THETA(4)
      THZ112=THETA(21)-THETA(10)
      THZ113=THETA(21)-THETA(4)
      THZ114=THETA(21)-THETA(10)
      THZ115=THETA(21)-THETA(4)
      THZ116=THETA(21)-THETA(10)
      THZ117=THETA(21)-THETA(4)
      THZ118=THETA(21)-THETA(10)
      THZ119=THETA(21)-THETA(4)
      THZ120=THETA(21)-THETA(10)
      THZ121=THETA(21)-THETA(4)
      THZ122=THETA(21)-THETA(10)
      THZ123=THETA(21)-THETA(4)
      THZ124=THETA(21)-THETA(10)
      THZ125=THETA(21)-THETA(4)
      THZ126=THETA(21)-THETA(10)
      THZ127=THETA(21)-THETA(4)
      THZ128=THETA(21)-THETA(10)
      THZ129=THETA(21)-THETA(4)
      THZ130=THETA(21)-THETA(10)
      THZ131=THETA(21)-THETA(4)
      THZ132=THETA(21)-THETA(10)
      THZ133=THETA(21)-THETA(4)
      THZ134=THETA(21)-THETA(10)
      THZ135=THETA(21)-THETA(4)
      THZ136=THETA(21)-THETA(10)
      THZ137=THETA(21)-THETA(4)
      THZ138=THETA(21)-THETA(10)
      THZ139=THETA(21)-THETA(4)
      THZ140=THETA(21)-THETA(10)
      THZ141=THETA(21)-THETA(4)
      THZ142=THETA(21)-THETA(10)
      THZ143=THETA(21)-THETA(4)
      THZ144=THETA(21)-THETA(10)
      THZ145=THETA(21)-THETA(4)
      THZ146=THETA(21)-THETA(10)
      THZ147=THETA(21)-THETA(4)
      THZ148=THETA(21)-THETA(10)
      THZ149=THETA(21)-THETA(4)
      THZ150=THETA(21)-THETA(10)
      THZ151=THETA(21)-THETA(4)
      THZ152=THETA(21)-THETA(10)
      THZ153=THETA(21)-THETA(4)
      THZ154=THETA(21)-THETA(10)
      THZ155=THETA(21)-THETA(4)
      THZ156=THETA(21)-THETA(10)
      THZ157=THETA(21)-THETA(4)
      THZ158=THETA(21)-THETA(10)
      THZ159=THETA(21)-THETA(4)
      THZ160=THETA(21)-THETA(10)
      THZ161=THETA(21)-THETA(4)
      THZ162=THETA(21)-THETA(10)
      THZ163=THETA(21)-THETA(4)
      THZ164=THETA(21)-THETA(10)
      THZ165=THETA(21)-THETA(4)
      THZ166=THETA(21)-THETA(10)
      THZ167=THETA(21)-THETA(4)
      THZ168=THETA(21)-THETA(10)
      THZ169=THETA(21)-THETA(4)
      THZ170=THETA(21)-THETA(10)
      THZ171=THETA(21)-THETA(4)
      THZ172=THETA(21)-THETA(10)
      THZ173=THETA(21)-THETA(4)
      THZ174=THETA(21)-THETA(10)
      THZ175=THETA(21)-THETA(4)
      THZ176=THETA(21)-THETA(10)
      THZ177=THETA(21)-THETA(4)
      THZ178=THETA(21)-THETA(10)
      THZ179=THETA(21)-THETA(4)
      THZ180=THETA(21)-THETA(10)
      THZ181=THETA(21)-THETA(4)
      THZ182=THETA(21)-THETA(10)
      THZ183=THETA(21)-THETA(4)
      THZ184=THETA(21)-THETA(10)
      THZ185=THETA(21)-THETA(4)
      THZ186=THETA(21)-THETA(10)
      THZ187=THETA(21)-THETA(4)
      THZ188=THETA(21)-THETA(10)
      THZ189=THETA(21)-THETA(4)
      THZ190=THETA(21)-THETA(10)
      THZ191=THETA(21)-THETA(4)
      THZ192=THETA(21)-THETA(10)
      THZ193=THETA(21)-THETA(4)
      THZ194=THETA(21)-THETA(10)
      THZ195=THETA(21)-THETA(4)
      THZ196=THETA(21)-THETA(10)
      THZ197=THETA(21)-THETA(4)
      THZ198=THETA(21)-THETA(10)
      THZ199=THETA(21)-THETA(4)
      THZ200=THETA(21)-THETA(10)
      THZ201=THETA(21)-THETA(4)
      THZ202=THETA(21)-THETA(10)
      THZ
```





[illegible]

1. J. 1994.2	2
2. J. 1994.2	3
3. J. 1994.2	4
4. J. 1994.2	5
5. J. 1994.2	6
6. J. 1994.2	7
7. J. 1994.2	8
8. J. 1994.2	9
9. J. 1994.2	10
10. J. 1994.2	11
11. J. 1994.2	12
12. J. 1994.2	13
13. J. 1994.2	14
14. J. 1994.2	15
15. J. 1994.2	16
16. J. 1994.2	17
17. J. 1994.2	18
18. J. 1994.2	19
19. J. 1994.2	20
20. J. 1994.2	21
21. J. 1994.2	22
22. J. 1994.2	23
23. J. 1994.2	24
24. J. 1994.2	25
25. J. 1994.2	26
26. J. 1994.2	27
27. J. 1994.2	28
28. J. 1994.2	29
29. J. 1994.2	30
30. J. 1994.2	31
31. J. 1994.2	32

[illegible]

1990/91	2
1991/92	2
1992/93	2
1993/94	2
1994/95	2
1995/96	2
1996/97	2
1997/98	2
1998/99	2
1999/00	2
2000/01	2
2001/02	2
2002/03	2
2003/04	2
2004/05	2
2005/06	2
2006/07	2
2007/08	2
2008/09	2
2009/10	2
2010/11	2
2011/12	2
2012/13	2
2013/14	2
2014/15	2
2015/16	2
2016/17	2
2017/18	2
2018/19	2
2019/20	2
2020/21	2
2021/22	2
2022/23	2
2023/24	2
2024/25	2
2025/26	2
2026/27	2
2027/28	2
2028/29	2
2029/30	2
2030/31	2
2031/32	2
2032/33	2
2033/34	2
2034/35	2
2035/36	2
2036/37	2
2037/38	2
2038/39	2
2039/40	2
2040/41	2
2041/42	2
2042/43	2
2043/44	2
2044/45	2
2045/46	2
2046/47	2
2047/48	2
2048/49	2
2049/50	2
2050/51	2
2051/52	2
2052/53	2
2053/54	2
2054/55	2
2055/56	2
2056/57	2
2057/58	2
2058/59	2
2059/60	2
2060/61	2
2061/62	2
2062/63	2
2063/64	2
2064/65	2
2065/66	2
2066/67	2
2067/68	2
2068/69	2
2069/70	2
2070/71	2
2071/72	2
2072/73	2
2073/74	2
2074/75	2
2075/76	2
2076/77	2
2077/78	2
2078/79	2
2079/80	2
2080/81	2
2081/82	2
2082/83	2
2083/84	2
2084/85	2
2085/86	2
2086/87	2
2087/88	2
2088/89	2
2089/90	2
2090/91	2
2091/92	2
2092/93	2
2093/94	2
2094/95	2
2095/96	2
2096/97	2
2097/98	2
2098/99	2
2099/00	2
2100/01	2
2101/02	2
2102/03	2
2103/04	2
2104/05	2
2105/06	2
2106/07	2
2107/08	2
2108/09	2
2109/10	2
2110/11	2
2111/12	2
2112/13	2
2113/14	2
2114/15	2
2115/16	2
2116/17	2
2117/18	2
2118/19	2
2119/20	2
2120/21	2
2121/22	2
2122/23	2
2123/24	2
2124/25	2
2125/26	2
2126/27	2
2127/28	2
2128/29	2
2129/30	2
2130/31	2
2131/32	2
2132/33	2
2133/34	2
2134/35	2
2135/36	2
2136/37	2
2137/38	2
2138/39	2
2139/40	2
2140/41	2
2141/42	2
2142/43	2
2143/44	2
2144/45	2
2145/46	2
2146/47	2
2147/48	2
2148/49	2
2149/50	2
2150/51	2
2151/52	2
2152/53	2
2153/54	2
2154/55	2
2155/56	2
2156/57	2
2157/58	2
2158/59	2
2159/60	2
2160/61	2
2161/62	2
2162/63	2
2163/64	2
2164/65	2
2165/66	2
2166/67	2
2167/68	

























153

SPECIAL	1
SPECIAL	2
SPECIAL	3
SPECIAL	4
SPECIAL	5
SPECIAL	6
SPECIAL	7
SPECIAL	8
SPECIAL	9
SPECIAL	10
SPECIAL	11
SPECIAL	12
SPECIAL	13
SPECIAL	14

1000

[illegible]

STP0000	87
STP0001	88
STP0002	89
STP0003	90
STP0004	91
STP0005	92
STP0006	93
STP0007	94
STP0008	95
STP0009	96
STP0010	97
STP0011	98
STP0012	99
STP0013	100
STP0014	101
STP0015	102
STP0016	103
STP0017	104
STP0018	105
STP0019	106
STP0020	107
STP0021	108
STP0022	109
STP0023	110
STP0024	111
STP0025	112
STP0026	113
STP0027	114
STP0028	115
STP0029	116
STP0030	117
STP0031	118
STP0032	119
STP0033	120
STP0034	121
STP0035	122
STP0036	123
STP0037	124
STP0038	125
STP0039	126
STP0040	127
STP0041	128
STP0042	129
STP0043	130
STP0044	131
STP0045	132
STP0046	133
STP0047	134
STP0048	135
STP0049	136
STP0050	137
STP0051	138
STP0052	139
STP0053	140
STP0054	141
STP0055	142
STP0056	143
STP0057	144
STP0058	145
STP0059	146
STP0060	147
STP0061	148
STP0062	149
STP0063	150
STP0064	151
STP0065	152
STP0066	153
STP0067	154
STP0068	155
STP0069	156
STP0070	157
STP0071	158
STP0072	159
STP0073	160
STP0074	161
STP0075	162
STP0076	163
STP0077	164
STP0078	165
STP0079	166
STP0080	167
STP0081	168
STP0082	169
STP0083	170
STP0084	171
STP0085	172
STP0086	173
STP0087	174
STP0088	175
STP0089	176
STP0090	177
STP0091	178
STP0092	179
STP0093	180
STP0094	181
STP0095	182
STP0096	183
STP0097	184
STP0098	185
STP0099	186
STP0100	187
STP0101	188
STP0102	189
STP0103	190
STP0104	191
STP0105	192
STP0106	193
STP0107	194
STP0108	195
STP0109	196
STP0110	197
STP0111	198
STP0112	199
STP0113	200
STP0114	201
STP0115	202
STP0116	203
STP0117	204
STP0118	205
STP0119	206
STP0120	207
STP0121	208
STP0122	209
STP0123	210
STP0124	211
STP0125	212
STP0126	213
STP0127	214
STP0128	215
STP0129	216
STP0130	217
STP0131	218
STP0132	219
STP0133	220
STP0134	221
STP0135	222
STP0136	223
STP0137	224
STP0138	225
STP0139	226
STP0140	227
STP0141	228
STP0142	229
STP0143	230
STP0144	231
STP0145	232
STP0146	233
STP0147	234
STP0148	235
STP0149	236
STP0150	237
STP0151	238
STP0152	239
STP0153	240
STP0154	241
STP0155	242
STP0156	243
STP0157	244
STP0158	245
STP0159	246
STP0160	247
STP0161	248
STP0162	249
STP0163	250
STP0164	251
STP0165	252
STP0166	253
STP0167	254
STP0168	255
STP0169	256
STP0170	257

[illegible]

STMT1	20
STMT2	20
STMT3	30
STMT4	31
STMT5	32
STMT6	33
STMT7	34
STMT8	35
STMT9	36
STMT10	37
STMT11	38
STMT12	39
STMT13	40
STMT14	41
STMT15	42
STMT16	43
STMT17	44
STMT18	45
STMT19	46
STMT20	47
STMT21	48
STMT22	49
STMT23	50
STMT24	51
STMT25	52
STMT26	53
STMT27	54
STMT28	55
STMT29	56
STMT30	57
STMT31	58
STMT32	59
STMT33	60
STMT34	61
STMT35	62
STMT36	63
STMT37	64
STMT38	65
STMT39	66
STMT40	67
STMT41	68
STMT42	69
STMT43	70
STMT44	71
STMT45	72
STMT46	73
STMT47	74
STMT48	75
STMT49	76
STMT50	77
STMT51	78
STMT52	79
STMT53	80
STMT54	81
STMT55	82
STMT56	83
STMT57	84
STMT58	85
STMT59	86
STMT60	87
STMT61	88
STMT62	89
STMT63	90
STMT64	91
STMT65	92
STMT66	93
STMT67	94
STMT68	95
STMT69	96
STMT70	97
STMT71	98
STMT72	99
STMT73	100
STMT74	101
STMT75	102
STMT76	103
STMT77	104
STMT78	105
STMT79	106
STMT80	107
STMT81	108
STMT82	109
STMT83	110
STMT84	111
STMT85	112
STMT86	113
STMT87	114
STMT88	115
STMT89	116
STMT90	117
STMT91	118
STMT92	119
STMT93	120
STMT94	121
STMT95	122
STMT96	123
STMT97	124
STMT98	125
STMT99	126
STMT100	127
STMT101	128
STMT102	129
STMT103	130
STMT104	131
STMT105	132
STMT106	133
STMT107	134
STMT108	135
STMT109	136
STMT110	137
STMT111	138
STMT112	139
STMT113	140
STMT114	141
STMT115	142
STMT116	143
STMT117	144
STMT118	145
STMT119	146
STMT120	147
STMT121	148
STMT122	149
STMT123	150
STMT124	151
STMT125	152
STMT126	153
STMT127	154
STMT128	155
STMT129	156
STMT130	157
STMT131	158
STMT132	159
STMT133	160
STMT134	161
STMT135	162
STMT136	163
STMT137	164
STMT138	165
STMT139	166
STMT140	167
STMT141	168
STMT142	169
STMT143	170
STMT144	171
STMT145	172
STMT146	173
STMT147	174
STMT148	175
STMT149	176
STMT150	177
STMT151	178
STMT152	179
STMT153	180
STMT154	181
STMT155	182
STMT156	183
STMT157	184
STMT158	185
STMT159	186
STMT160	187
STMT161	188
STMT162	189
STMT163	190
STMT164	191
STMT165	192
STMT166	193
STMT167	194
STMT168	195
STMT169	196
STMT170	197
STMT171	198
STMT172	199
STMT173	200
STMT174	201
STMT175	202
STMT176	203
STMT177	204
STMT178	205
STMT179	206
STMT180	207
STMT181	208
STMT182	209
STMT183	210
STMT184	211
STMT185	212
STMT186	





```

      RTTRAJ=10000
100 CONTINUE
      C
      C      OUTPUT TOJECTORY INFORMATION, AND CREATE PLOTS IF REQUESTED
      C
      CALL INPUT
      IF (LWTRAJPLT) GO TO 200
      CALL PLOTTP
      CALL PLOTTP
200 CONTINUE
      RETURN
      END

```

THIS SIMULATING POINTS THE TRAJECTORY COORDINATES AND THE  
FLUX FIELD AND MAGNETIC FIELD COMPONENTS ALONG THE TRAJECTORY  
AS TRAILS WITH TIME AS THE REFERENCE QUANTITY.

[illegible]

WITH COORDINATES (X,Y,Z,0) AT A PORTION OF TIME,  
IN UNITS OF BOTH D, AND PLANET

[illegible]

WITH THE FLOW FIELD AND MAGNETIC FIELD COMPONENTS  
NON-DIMENSIONAL WITH RESPECT TO FREE STREAM

[illegible]

WRITE OUT FILM FIELD AND MAGNETIC FIELD COMPONENTS  
OF/UNIONALIZED BY INPUT FOR STREAM VALUES

1 2 3 4 5 6 7 8 9 10 11 12 13 14 15 16 17 18 19 20  
 21 22 23 24 25 26 27 28 29 30 31 32 33 34 35 36 37 38 39 40  
 41 42 43 44 45 46 47 48 49 50 51 52 53 54 55 56 57 58 59 60  
 61 62 63 64 65 66 67 68 69 70 71 72 73 74 75 76 77 78 79 80  
 81 82 83 84 85 86 87 88 89 90 91 92 93 94 95 96 97 98 99 100  
 101 102 103 104 105 106 107 108 109 110 111 112 113 114 115 116 117 118 119 120  
 121 122 123 124 125 126 127 128 129 130 131 132 133 134 135 136 137 138 139 140  
 141 142 143 144 145 146 147 148 149 150 151 152 153 154 155 156 157 158 159 160  
 161 162 163 164 165 166 167 168 169 170 171 172 173 174 175 176 177 178 179 180  
 181 182 183 184 185 186 187 188 189 190 191 192 193 194 195 196 197 198 199 200  
 201 202 203 204 205 206 207 208 209 210 211 212 213 214 215 216 217 218 219 220  
 221 222 223 224 225 226 227 228 229 230 231 232 233 234 235 236 237 238 239 240  
 241 242 243 244 245 246 247 248 249 250 251 252 253 254 255 256 257 258 259 260  
 261 262 263 264 265 266 267 268 269 270 271 272 273 274 275 276 277 278 279 280  
 281 282 283 284 285 286 287 288 289 290 291 292 293 294 295 296 297 298 299 300  
 301 302 303 304 305 306 307 308 309 310 311 312 313 314 315 316 317 318 319 320  
 321 322 323 324 325 326 327 328 329 330 331 332 333 334 335 336 337 338 339 340  
 341 342 343 344 345 346 347 348 349 350 351 352 353 354 355 356 357 358 359 360  
 361 362 363 364 365 366 367 368 369 370 371 372 373 374 375 376 377 378 379 380  
 381 382 383 384 385 386 387 388 389 390 391 392 393 394 395 396 397 398 399 400  
 401 402 403 404 405 406 407 408 409 410 411 412 413 414 415 416 417 418 419 420  
 421 422 423 424 425 426 427 428 429 430 431 432 433 434 435 436 437 438 439 440  
 441 442 443 444 445 446 447 448 449 450 451 452 453 454 455 456 457 458 459 460  
 461 462 463 464 465 466 467 468 469 470 471 472 473 474 475 476 477 478 479 480  
 481 482 483 484 485 486 487 488 489 490 491 492 493 494 495 496 497 498 499 500  
 501 502 503 504 505 506 507 508 509 510 511 512 513 514 515 516 517 518 519 520  
 521 522 523 524 525 526 527 528 529 530 531 532 533 534 535 536 537 538 539 540  
 541 542 543 544 545 546 547 548 549 550 551 552 553 554 555 556 557 558 559 560  
 561 562 563 564 565 566 567 568 569 570 571 572 573 574 575 576 577 578 579 580  
 581 582 583 584 585 586 587 588 589 590 591 592 593 594 595 596 597 598 599 600  
 601 602 603 604 605 606 607 608 609 610 611 612 613 614 615 616 617 618 619 620  
 621 622 623 624 625 626 627 628 629 630 631 632 633 634 635 636 637 638 639 640  
 641 642 643 644 645 646 647 648 649 650 651 652 653 654 655 656 657 658 659 660  
 661 662 663 664 665 666 667 668 669 670 671 672 673 674 675 676 677 678 679 680  
 681 682 683 684 685 686 687 688 689 690 691 692 693 694 695 696 697 698 699 700  
 701 702 703 704 705 706 707 708 709 710 711 712 713 714 715 716 717 718 719 720  
 721 722 723 724 725 726 727 728 729 730 731 732 733 734 735 736 737 738 739 740  
 741 742 743 744 745 746 747 748 749 750 751 752 753 754 755 756 757 758 759 760  
 761 762 763 764 765 766 767 768 769 770 771 772 773 774 775 776 777 778 779 780  
 781 782 783 784 785 786 787 788 789 790 791 792 793 794 795 796 797 798 799 800  
 801 802 803 804 805 806 807 808 809 810 811 812 813 814 815 816 817 818 819 820  
 821 822 823 824 825 826 827 828 829 830 831 832 833 834 835 836 837 838 839 840  
 841 842 843 844 845 846 847 848 849 850 851 852 853 854 855 856 857 858 859 860  
 861 862 863 864 865 866 867 868 869 870 871 872 873 874 875 876 877 878 879 880  
 881 882 883 884 885 886 887 888 889 890 891 892 893 894 895 896 897 898 899 900  
 901 902 903 904 905 906 907 908 909 910 911 912 913 914 915 916 917 918 919 920  
 921 922 923 924 925 926 927 928 929 930 931 932 933 934 935 936 937 938 939 940  
 941 942 943 944 945 946 947 948 949 950 951 952 953 954 955 956 957 958 959 960  
 961 962 963 964 965 966 967 968 969 970 971 972 973 974 975 976 977 978 979 980  
 981 982 983 984 985 986 987 988 989 990 991 992 993 994 995 996 997 998 999 1000
 </

9904010000	11.0
9904020000	11.0
9904030000	11.0
9904040000	11.0
9904050000	11.0
9904060000	11.0
9904070000	11.0
9904080000	11.0
9904090000	11.0
9904100000	11.0
9904110000	11.0
9904120000	11.0
9904130000	11.0
9904140000	11.0
9904150000	11.0
9904160000	11.0
9904170000	11.0
9904180000	11.0
9904190000	11.0
9904200000	11.0
9904210000	11.0
9904220000	11.0
9904230000	11.0
9904240000	11.0
9904250000	11.0
9904260000	11.0
9904270000	11.0
9904280000	11.0
9904290000	11.0
9904300000	11.0
9904310000	11.0
9904320000	11.0
9904330000	11.0
9904340000	11.0
9904350000	11.0
9904360000	11.0
9904370000	11.0
9904380000	11.0
9904390000	11.0
9904400000	11.0
9904410000	11.0
9904420000	11.0
9904430000	11.0
9904440000	11.0
9904450000	11.0
9904460000	11.0
9904470000	11.0
9904480000	11.0
9904490000	11.0
9904500000	11.0
9904510000	11.0
9904520000	11.0
9904530000	11.0
9904540000	11.0
9904550000	11.0
9904560000	11.0
9904570000	11.0
9904580000	11.0
9904590000	11.0
9904600000	11.0
9904610000	11.0
9904620000	11.0
9904630000	11.0
9904640000	11.0
9904650000	11.0
9904660000	11.0
9904670000	11.0
9904680000	11.0
9904690000	11.0
9904700000	11.0
9904710000	11.0
9904720000	11.0
9904730000	11.0
9904740000	11.0
9904750000	11.0
9904760000	11.0
9904770000	11.0
9904780000	11.0
9904790000	11.0
9904800000	11.0
9904810000	11.0
9904820000	11.0
9904830000	11.0
9904840000	11.0
9904850000	11.0
9904860000	11.0
9904870000	11.0
9904880000	11.0
9904890000	11.0
9904900000	11.0
9904910000	11.0
9904920000	11.0
9904930000	11.0
9904940000	11.0
9904950000	11.0
9904960000	11.0
9904970000	11.0
9904980000	11.0
9904990000	11.0
9905000000	11.0

70000	2
70000	3
70000	4
70000	5
70000	6

THAT	7
W	2
ABOUT	2
ABOUT	2
ABOUT	2
ABOUT	2
TO THAT	2
TO THAT	2
TO THAT	4
TO THAT	9
WHAT	2
TO THAT	2
TO THAT	2
SUMAT	4
TO THAT	14
WHAT	2

1000000	1000000
1000000	1000000
1000000	1000000

70001	21
70002	23
70003	22
70004	23
70005	24
70006	24
70007	26
70008	27
70009	28
70010	28
70011	30
70012	31
70013	32
70014	33
70015	34

70-1017	85
70-1017	86
70-1017	87

7000000	50
7000000	50
7000000	40
7000000	41
7000000	42
7000000	43
7000000	44
7000000	45
7000000	46

TO: JET	47
TO: JET	48
TO: JET	49

70000	90
70001	91
70002	92
70003	93
70004	94
70005	95
70006	96
70007	97
70008	98
70009	99
70010	00

[illegible]

TRANSFER OUTPUT QUANTITIES TO SUB-PLANT COORDINATE SYSTEM

[illegible][illegible]

9.2 分析: 由题知, 当  $x=0$  时,  $y=0$ , 故  $0$  是方程的一个根. 又由题知, 当  $x=1$  时,  $y=1$ , 故  $1$  也是方程的一个根. 所以, 方程的根为  $0$  和  $1$ .

WITH COORDINATES (X,Y,Z) AS A FUNCTION OF TIME  
IN UNITS OF BOTH CM AND DEGREES

[illegible]

04 CONTINUE

```

0017F 10,10001
0017F 10,10021
0017F 10,10041
0017F 10,10061
      OR     W0, W0A0
0017F 10,21001  R0, W0A0A0A0, W0A0A0A0, W0A0A0A0, W0A0A0A0,
      W0A0A0A0, W0A0A0A0, W0A0A0A0, W0A0A0A0, W0A0A0A0,
      W0A0A0A0, W0A0A0A0, W0A0A0A0, W0A0A0A0

```

```

C
C      WRITE PLOW FIELD AND MAGNETIC FIELD COMPONENTS
C      DIMENSIONALIZED BY INPUT "CONSTANT" VALUE"

```

WP17 16.1800  
 WP17 16.1802  
 WP17 16.1804  
 WP17 16.1700 : BRAC M, GAHR, RINF, VINF, FDI, R-WINF, FDI, TAPINF, ...  
 WP17 16.1701 : AYANA, POLANE





# TABLE OF CONTENTS

<u>Section</u>	<u>Page No.</u>
LIST OF ILLUSTRATIONS	iv 1/A5
SUMMARY	1 1/A7
INTRODUCTION	2 1/A8
LIST OF SYMBOLS	4 1/A10
ANALYSIS	8 1/A14
The Mathematical Model - Formulation of the Fluid Representation	8 1/A14
<u>Governing equations</u>	8 1/A14
<u>Conditions at discontinuities</u>	10 1/B2
<u>Frozen-field approximation</u>	12 1/B4
Determination of the Ionosphere Boundary	14 1/B6
Calculation of the Gasdynamic Flow Properties	20 1/B12
<u>Nose region solution - implicit unsteady Euler equation method</u>	21 1/B13
<u>Downstream region solution - shock capturing marching method</u>	25 1/C3
<u>Calculation of the streamlines</u>	27 1/C5
Calculation of the Magnetic Field	27 1/C5
Calculation of the Contour Lines	30 1/C8
Solar-Ecliptic/Solar-Wind Coordinate Transformations	31 1/C9
Properties Along a Spacecraft Trajectory	33 1/C11
RESULTS	36 1/C14
CONCLUDING REMARKS	47 1/D11
ACKNOWLEDGEMENTS	48 1/D12
APPENDIX A - COMPUTER PROGRAM USER'S MANUAL	49 1/D13
APPENDIX B - LISTING OF COMPUTER PROGRAM	131 2/D1
APPENDIX C - CATALOG OF TEST CASES	177 3/C10
REFERENCES	287 4/D10
TABLE 1	289 4/D12
FIGURES 1 THROUGH 20	291 4/E3

[illegible]

Q1/INTA	2
Q2/INTA	2
Q3/INTA	4
Q4/INTA	2
Q1/INTB	4
Q2/INTB	4
Q3/INTB	2
Q4/INTB	2
Q1/INTC	2
Q2/INTC	2
Q3/INTC	2
Q4/INTC	2
Q1/INTD	2
Q2/INTD	2
Q3/INTD	2
Q4/INTD	2
Q1/INTE	2
Q2/INTE	2
Q3/INTE	2
Q4/INTE	2
Q1/INTF	2
Q2/INTF	2
Q3/INTF	2
Q4/INTF	2
Q1/INTG	2
Q2/INTG	2
Q3/INTG	2
Q4/INTG	2
Q1/INTH	2
Q2/INTH	2
Q3/INTH	2
Q4/INTH	2
Q1/INTI	2
Q2/INTI	2
Q3/INTI	2
Q4/INTI	2
Q1/INTJ	2
Q2/INTJ	2
Q3/INTJ	2
Q4/INTJ	2
Q1/INTK	2
Q2/INTK	2
Q3/INTK	2
Q4/INTK	2
Q1/INTL	2
Q2/INTL	2
Q3/INTL	2
Q4/INTL	2
Q1/INTM	2
Q2/INTM	2
Q3/INTM	2
Q4/INTM	2
Q1/INTN	2
Q2/INTN	2
Q3/INTN	2
Q4/INTN	2
Q1/INTO	2
Q2/INTO	2
Q3/INTO	2
Q4/INTO	2
Q1/INTP	2
Q2/INTP	2
Q3/INTP	2
Q4/INTP	2
Q1/INTQ	2
Q2/INTQ	2
Q3/INTQ	2
Q4/INTQ	2
Q1/INTR	2
Q2/INTR	2
Q3/INTR	2
Q4/INTR	2
Q1/INTS	2
Q2/INTS	2
Q3/INTS	2
Q4/INTS	2
Q1/INTT	2
Q2/INTT	2
Q3/INTT	2
Q4/INTT	2
Q1/INTU	2
Q2/INTU	2
Q3/INTU	2
Q4/INTU	2
Q1/INTV	2
Q2/INTV	2
Q3/INTV	2
Q4/INTV	2
Q1/INTW	2
Q2/INTW	2
Q3/INTW	2
Q4/INTW	2
Q1/INTX	2
Q2/INTX	2
Q3/INTX	2
Q4/INTX	2
Q1/INTY	2
Q2/INTY	2
Q3/INTY	2
Q4/INTY	2
Q1/INTZ	2
Q2/INTZ	2
Q3/INTZ	2
Q4/INTZ	2

[illegible]

01/1997	78
02/1997	77
03/1997	87
04/1997	91
05/1997	89
06/1997	83
07/1997	86
08/1997	94
09/1997	87
10/1997	87
11/1997	81
12/1997	77
01/1998	83
02/1998	87
03/1998	90
04/1998	94
05/1998	90
06/1998	94
07/1998	94
08/1998	98
09/1998	98
10/1998	98
11/1998	98
12/1998	98
01/1999	98
02/1999	98
03/1999	98
04/1999	98
05/1999	98
06/1999	98
07/1999	98
08/1999	98
09/1999	98
10/1999	98
11/1999	98
12/1999	98
01/2000	98
02/2000	98
03/2000	98
04/2000	98
05/2000	98
06/2000	98
07/2000	98
08/2000	98
09/2000	98
10/2000	98
11/2000	98
12/2000	98
01/2001	98
02/2001	98
03/2001	98
04/2001	98
05/2001	98
06/2001	98
07/2001	98
08/2001	98
09/2001	98
10/2001	98
11/2001	98
12/2001	98
01/2002	98
02/2002	98
03/2002	98
04/2002	98
05/2002	98
06/2002	98
07/2002	98
08/2002	98
09/2002	98
10/2002	98
11/2002	98
12/2002	98
01/2003	98
02/2003	98
03/2003	98
04/2003	98
05/2003	98
06/2003	98
07/2003	98
08/2003	98
09/2003	98
10/2003	98
11/2003	98
12/2003	98
01/2004	98
02/2004	98
03/2004	98
04/2004	98
05/2004	98
06/2004	98
07/2004	98
08/2004	98
09/2004	98
10/2004	98
11/2004	98
12/2004	98
01/2005	98
02/2005	98
03/2005	98
04/2005	98
05/2005	98
06/2005	98
07/2005	98
08/2005	98
09/2005	98
10/2005	98
11/2005	98
12/2005	98
01/2006	98
02/2006	98
03/2006	98
04/2006	98
05/2006	98
06/2006	98
07/2006	98
08/2006	98
09/2006	98
10/2006	98
11/2006	98
12/2006	98
01/2007	98
02/2007	98
03/2007	98
04/2007	98
05/2007	98
06/2007	98
07/2007	98
08/2007	98
09/2007	98
10/2007	98
11/2007	98
12/2007	98
01/2008	98
02/2008	98
03/2008	98
04/2008	98
05/2008	98
06/2008	98
07/2008	98
08/2008	98
09/2008	98
10/2008	98
11/2008	98
12/2008	98
01/2009	98
02/2009	98
03/2009	98
04/2009	98
05/2009	98
06/2009	98
07/2009	98
08/2009	98
09/2009	98
10/2009	98
11/2009	98
12/2009	98
01/2010	98
02/2010	98
03/2010	98
04/2010	98
05/2010	98
06/2010	98
07/2010	98
08/2010	98
09/2010	98
10/2010	98
11/2010	98
12/2010	98
01/2011	98
02/2011	98
03/	



[illegible]

[illegible]

WTOT	7
COM3	7
COM2	3
COM4	7
COM5	9
LTOT	7
LTOT	3
LTOT	4
WTOT	6
WTOT	7
WTOT	6
WTOT	6
WTOT	10

[illegible]

0701	11
0702	12
0703	13
0704	14
0705	15
0706	16
0707	17
0708	18
0709	19
0710	20
0711	21
0712	22
0713	23
0714	24
0715	25
0716	26
0717	27
0718	28
0719	29
0720	30
0721	31
0722	32
0723	33
0724	34
0725	35
0726	36
0727	37
0728	38
0729	39
0730	40
0731	41
0732	42
0733	43
0734	44
0735	45
0736	46
0737	47
0738	48
0739	49
0740	50
0741	51
0742	52
0743	53
0744	54
0745	55
0746	56
0747	57
0748	58
0749	59
0750	60
0751	61
0752	62
0753	63
0754	64
0755	65
0756	66
0757	67
0758	68
0759	69
0760	70
0761	71
0762	72
0763	73
0764	74
0765	75
0766	76
0767	77









**BLANK PAGE**

**BLANK PAGE**

OUTPUT	67
OUTPUT	68
OUTPUT	69
OUTPUT	70
OUTPUT	71
OUTPUT	72
OUTPUT	73
OUTPUT	74
OUTPUT	75
OUTPUT	76
OUTPUT	77
OUTPUT	78
OUTPUT	79

0404	2
0405	7
0406	3
0407	4
0408	3
0409	5
0410	7
0411	8
0412	8
0413	10
0414	11
0415	17
0416	13
0417	14
0418	15
0419	16
0420	17
0421	18
0422	10
0423	20
0424	21
0425	20
0426	24
0427	24
0428	26
0429	27
0430	28
0431	28
0432	29
0433	30
0434	30
0435	31
0436	31
0437	31
0438	31
0439	31
0440	31
0441	31
0442	31
0443	31
0444	31
0445	31
0446	31
0447	31
0448	31
0449	31
0450	31
0451	31
0452	31
0453	31
0454	31
0455	31
0456	31
0457	31
0458	31
0459	31
0460	31
0461	31
0462	31
0463	31
0464	31
0465	31
0466	31
0467	31
0468	31
0469	31
0470	31
0471	31
0472	31
0473	31
0474	31
0475	31
0476	31
0477	31
0478	31
0479	31
0480	31
0481	31
0482	31
0483	31
0484	31
0485	31
0486	31
0487	31
0488	31
0489	31
0490	31
0491	31
0492	31
0493	31
0494	31
0495	31
0496	31
0497	31
0498	31
0499	31
0500	31

940704	2
940705	2
940706	3
940707	4
940708	4
940709	4
940710	4
940711	5
940712	5
940713	5
940714	5
940715	5
940716	5
940717	5
940718	5
940719	5
940720	5
940721	5
940722	5
940723	5
940724	5
940725	5
940726	5
940727	5
940728	5
940729	5
940730	5
940731	5
940732	5
940733	5
940734	5
940735	5
940736	5
940737	5
940738	5
940739	5
940740	5
940741	5
940742	5
940743	5
940744	5
940745	5
940746	5
940747	5
940748	5
940749	5
940750	5
940751	5
940752	5
940753	5
940754	5
940755	5
940756	5
940757	5
940758	5
940759	5
940760	5
940761	5
940762	5
940763	5
940764	5
940765	5
940766	5
940767	5
940768	5
940769	5
940770	5
940771	5
940772	5
940773	5
940774	5
940775	5
940776	5
940777	5
940778	5
940779	5
940780	5
940781	5
940782	5
940783	5
940784	5
940785	5
940786	5
940787	5
940788	5
940789	5
940790	5
940791	5
940792	5
940793	5
940794	5
940795	5
940796	5
940797	5
940798	5
940799	5
940800	5

540DC	29
540DE	26
540DF	27
540DG	24
540DH	30
540DI	31
540DJ	32
540DK	33
540DL	34
540DM	35
540DN	36
540DO	37
540DP	38
540DQ	39
540DR	40
540DS	41
540DT	42
540DU	43
540DV	44
540DW	45
540DX	46
540DY	47
540DZ	48
540EA	49
540EB	50
540EC	51
540ED	52
540EE	53
540EF	54
540EG	55
540EH	56
540EI	57
540EJ	58
540EK	59
540EL	60
540EM	61
540EN	62
540EO	63
540EP	64
540EQ	65
540ER	66
540ES	67
540ET	68
540EU	69
540EV	70
540EW	71
540EX	72
540EY	73
540EZ	74
540FA	75
540FB	76
540FC	77
540FD	78
540FE	79
540FF	80
540FG	81
540FH	82
540FI	83
540FJ	84
540FK	85
540FL	86
540FM	87
540FN	88
540FO	89
540FP	90
540FQ	91
540FR	92
540FS	93
540FT	94
540FU	95
540FV	96
540FW	97
540FX	98
540FY	99
540FZ	100
540GA	101
540GB	102
540GC	103
540GD	104
540GE	105
540GF	106
540GG	107
540GH	108
540GI	109
540GJ	110
540GK	111
540GL	112
540GM	113
540GN	114
540GO	115
540GP	116
540GQ	117
540GR	118
540GS	119
540GT	120
540GU	121
540GV	122
540GW	123
540GX	124
540GY	125
540GZ	126
540HA	127
540HB	128
540HC	129
540HD	130
540HE	131
540HF	132
540HG	133
540HH	134
540HI	135
540HJ	136
540HK	137
540HL	138
540HM	139
540HN	140
540HO	141
540HP	142
540HQ	143
540HR	144
540HS	145
540HT	146
540HU	147
540HV	148
540HW	149
540HX	150
540HY	151
540HZ	152
540IA	153
540IB	154
540IC	155
540ID	156
540IE	157
540IF	158
540IG	159
540IH	160
540II	161
540IJ	162
540IK	163
540IL	164
540IM	165
540IN	166
540IO	167
540IP	168
540IQ	169
540IR	170
540IS	171
540IT	172
540IU	173
540IV	174
540IW	175
540IX	176
540IY	177
540IZ	178
540JA	179
540JB	180
540JC	181
540JD	182
540JE	183
540JF	184
540JG	185
540JH	186
540JI	187
540JJ	188
540JK	189
540JL	190
540JM	191
540JN	192
540JO	193
540JP	194
540JQ	195
540JR	196
540JS	197
540JT	198
540JU	199
540JV	200
540JW	201
540JX	202
540JY	203
540JZ	204
540KA	205
540KB	206
540KC	207
540KD	208
540KE	209
540KF	210
540KG	211
540KH	212
540KI	213

**REPORTING NAME**

040000 2

[illegible]





```

C==CALCULATE GEOMETRIC FACTORS BASED ON NEW BODY AND UNDER GEOMETRY
CALL GEOM(1)
C==APPLY THE PLANT ON SYMMETRY BOUNDARY CONDITIONS
CALL ANSYS(1)
C==FORM THERMODYNAMIC CONSERVATION VARIABLES AT ALL POINTS
CALL TFORM(1)
DO 3 J=1,NPTS
DO 3 J=1,NPTZ
DO 3 J=1,N
CONTINUE
C==THERMODYNAMIC FUNCTION
F1TS=0.0
IF (TFORM(1),N1,C,0) .OR. (TFORM(1),N1,C,0) *ALL DESSP(1),J,K,NPTS)
T1TS,J,K,0) GO TO 0
T1TS(1),N1TS) GO TO 5
C==COMPRESSION IN FIELD
F1TSP(J,K)=5.0E10*(F1TS(J,K)-T1TS(J,K)-T1TS(J,K)-F1TS(J,K)
+T1TS(J,K)+1.0E10*(F1TS(J,K)-T1TS(J,K)-1.0E10*(F1TS(J,K)+T1TS(J,K)
GO TO 5
0
C==COMPRESSION AT SANDH
F1TSP(J,K)=5.0E10*(F1TS(J,K)-T1TS(J,K)-T1TS(J,K)-F1TS(J,K)
+T1TS(J,K)+1.0E10*(F1TS(J,K)-T1TS(J,K)-1.0E10*(F1TS(J,K)+T1TS(J,K)
GO TO 5
0
C==COMPRESSION AT BODY
F1TSP(J,K)=5.0E10*(F1TS(J,K)-T1TS(J,K)-T1TS(J,K)-F1TS(J,K)-F1TS(J,K)
+T1TS(J,K)+1.0E10*(F1TS(J,K)-T1TS(J,K)-1.0E10*(F1TS(J,K)+T1TS(J,K)
GO TO 5
0
C==FORM THERMODYNAMIC VARIABLES
CALL TFORM(1)
C==CALCULATE CORRECTED THERM VALUES
CALL TFORM(1)
C==CALCULATE GEOMETRIC FACTORS BASED ON NEW BODY AND NEW SANDH GEOMETRY
CALL GEOM(1)
C==APPLY THE NEW VARIABLES
CALL ANSYS(1)
C==APPLY THE PLANT ON SYMMETRY BOUNDARY CONDITIONS
CALL ANSYS(1)
END

```

[illegible]

```

E
C===== CHNPTGAS10  =  LAY SAMPLING
C===== CHNPTGAS15  =  WB SAMPLING
C===== CHNPTGAS19  =  ATW SPORED SAMPLING

```

```

      PRINTNTHIN(2,1,2)
C...*****THESE THING IN THE RAPID STRECTION
DO      NTH=0, 9 ,END, 2 ,LE, NTH+1 DO 9
      NTH=17,91 GO TO 9
      JUNT
      ON TO &
      ? DOWS
      CO EN A

```

[illegible][illegible]

```

9  JPN=
10  C11550=C105710+0+J120000000, J0+2, K1=J12700, J00+7, K1=0, P=0, M1=0, J0+1, K1
11  0=J12700, J00+1, K1=0, P=0, M1=0, J0+1, K1
12  END
21  C105710=
13  JPN=J0, K=0, M1=0, J=J1, K=J12700 TO 00
14  JPN=J1, K=J12700 TO 00
15  JPN=0
16  C11550=J0, K=0
17  JPN=0
18  JPN=0
27  JPN=J
37  C11550=C105710+0+J120000000, J0+1, K1=J12700, J00+7, K1=0, P=0, M1=0, J0+1, K1
38  C11550=J0, K=0
39  C11550=J0, K=0
C
C
C===== C105710+0+J120000000
C===== C105710+0+J120000000
C===== C105710+0+J120000000
C
C
J  C11550=J0, K=0
C===== C11550=J0, K=0, P=0, M1=0, J0+1, K1=J12700
11  C105710=
12  JPN=J0, K=0, M1=0, J=J1, K=J12700 TO 00
13  JPN=J1, K=J12700 TO 00
14  JPN=0
15  C11550=J0, K=0
16  C11550=J0, K=0
17  C11550=J0, K=0
18  C11550=J0, K=0
19  C11550=J0, K=0
20  C11550=J0, K=0
21  C11550=J0, K=0
22  C11550=J0, K=0
23  C11550=J0, K=0
24  C11550=J0, K=0
25  C11550=J0, K=0
26  C11550=J0, K=0
27  C11550=J0, K=0
28  C11550=J0, K=0
29  C11550=J0, K=0
30  C11550=J0, K=0
31  C11550=J0, K=0
32  C11550=J0, K=0
33  C11550=J0, K=0
34  C11550=J0, K=0
35  C11550=J0, K=0
36  C11550=J0, K=0
37  C11550=J0, K=0
38  C11550=J0, K=0
39  C11550=J0, K=0
40  C11550=J0, K=0
41  C11550=J0, K=0
42  C11550=J0, K=0
43  C11550=J0, K=0
44  C11550=J0, K=0
45  C11550=J0, K=0
46  C11550=J0, K=0
47  C11550=J0, K=0
48  C11550=J0, K=0
49  C11550=J0, K=0
50  C11550=J0, K=0
51  C11550=J0, K=0
52  C11550=J0, K=0
53  C11550=J0, K=0
54  C11550=J0, K=0
55  C11550=J0, K=0
56  C11550=J0, K=0
57  C11550=J0, K=0
58  C11550=J0, K=0
59  C11550=J0, K=0
60  C11550=J0, K=0
61  C11550=J0, K=0
62  C11550=J0, K=0
63  C11550=J0, K=0
64  C11550=J0, K=0
65  C11550=J0, K=0
66  C11550=J0, K=0
67  C11550=J0, K=0
68  C11550=J0, K=0
69  C11550=J0, K=0
70  C11550=J0, K=0
71  C11550=J0, K=0
72  C11550=J0, K=0
73  C11550=J0, K=0
74  C11550=J0, K=0
75  C11550=J0, K=0
76  C11550=J0, K=0
77  C11550=J0, K=0
78  C11550=J0, K=0
79  C11550=J0, K=0
80  C11550=J0, K=0
81  C11550=J0, K=0
82  C11550=J0, K=0
83  C11550=J0, K=0
84  C11550=J0, K=0
85  C11550=J0, K=0
86  C11550=J0, K=0
87  C11550=J0, K=0
88  C11550=J0, K=0
89  C11550=J0, K=0
90  C11550=J0, K=0
91  C11550=J0, K=0
92  C11550=J0, K=0
93  C11550=J0, K=0
94  C11550=J0, K=0
95  C11550=J0, K=0
96  C11550=J0, K=0
97  C11550=J0, K=0
98  C11550=J0, K=0
99  C11550=J0, K=0
100  C11550=J0, K=0

```

[illegible]

017555000	22
017555000	23
017555000	24
017555000	25
017555000	26
017555000	27
017555000	28
017555000	29
017555000	31
017555000	32
017555000	33
017555000	34
017555000	35
017555000	36
017555000	37
017555000	38
017555000	39
017555000	40
017555000	42
017555000	43
017555000	44
017555000	45
017555000	46
017555000	47
017555000	48
017555000	49
017555000	50
017555000	51
017555000	52
017555000	53
017555000	54
017555000	55
017555000	56
017555000	57
017555000	58
017555000	59
017555000	60
017555000	61
017555000	62
017555000	63
017555000	64
017555000	65
017555000	66
017555000	67
017555000	68
017555000	69
017555000	70
017555000	71
017555000	72
017555000	73
017555000	74
017555000	75
017555000	76
017555000	77
017555000	78
017555000	79
017555000	80
017555000	81
017555000	82
017555000	83
017555000	84
017555000	85
017555000	86
017555000	87
017555000	88
017555000	89
017555000	90
017555000	91
017555000	92
017555000	93
017555000	94
017555000	95
017555000	96
017555000	97
017555000	98
017555000	99
017555000	100

000000	0
010000	1
020000	2
030000	3
040000	4
050000	5
060000	6
070000	7
080000	8
090000	9
100000	10
110000	11
120000	12
130000	13
140000	14
150000	15
160000	16
170000	17
180000	18
190000	19
200000	20
210000	21
220000	22
230000	23
240000	24
250000	25
260000	26
270000	27
280000	28
290000	29
300000	30
310000	31
320000	32
330000	33
340000	34
350000	35
360000	36
370000	37
380000	38
390000	39
400000	40
410000	41
420000	42
430000	43
440000	44
450000	45
460000	46
470000	47
480000	48
490000	49
500000	50
510000	51
520000	52
530000	53
540000	54
550000	55
560000	56
570000	57
580000	58
590000	59
600000	60
610000	61
620000	62
630000	63
640000	64
650000	65
660000	66
670000	67
680000	68
690000	69
700000	70
710000	71
720000	72
730000	73
740000	74
750000	75
760000	76
770000	77
780000	78
790000	79
800000	80
810000	81
820000	82
830000	83
840000	84
850000	85
860000	86
870000	87
880000	88
890000	89
900000	90
910000	91
920000	92
930000	93
940000	94
950000	95
960000	96
970000	97
980000	98
990000	99









[illegible]

INITA	94
INITA	99
INITA	96
INITA	98
INITA	99
INITA	99
INITA	01
INITA	92
INITA	93
INITA	94
INITA	95
INITA	96
INITA	97
INITA	98
INITA	100
INITA	101
INITA	102
INITA	103
INITA	104
INITA	105
INITA	106
INITA	107
INITA	108
INITA	109
INITA	110
INITA	111
INITA	112
INITA	113
INITA	114
INITA	115
INITA	116
INITA	117
INITA	118
INITA	119
INITA	120
INITA	121
INITA	122
INITA	123
INITA	124
INITA	125
INITA	126
INITA	127
INITA	128
INITA	129
INITA	130
INITA	131
INITA	132
INITA	133
INITA	134
INITA	135
INITA	136
INITA	137
INITA	138
INITA	139
INITA	140
INITA	141
INITA	142
INITA	143
INITA	144
INITA	145
INITA	146
INITA	147
INITA	148
INITA	149
INITA	150
INITA	151
INITA	152
INITA	153
INITA	154
INITA	155
INITA	156
INITA	157
INITA	158
INITA	159
INITA	160

[illegible]

10V404	2
10V405	2
10V406	2
10V407	2
10V408	4
10V409	4
10V410	4
10V411	4
10V412	4
10V413	4
10V414	4
10V415	4
10V416	4
10V417	4
10V418	4
10V419	4
10V420	4
10V421	4
10V422	4
10V423	4
10V424	4
10V425	4
10V426	4
10V427	4
10V428	4
10V429	4
10V430	4
10V431	4
10V432	4
10V433	4
10V434	4
10V435	4
10V436	4
10V437	4
10V438	4
10V439	4
10V440	4
10V441	4
10V442	4
10V443	4
10V444	4
10V445	4
10V446	4
10V447	4
10V448	4
10V449	4
10V450	4
10V451	4
10V452	4
10V453	4
10V454	4
10V455	4
10V456	4
10V457	4
10V458	4
10V459	4
10V460	4
10V461	4
10V462	4
10V463	4
10V464	4
10V465	4
10V466	4
10V467	4
10V468	4
10V469	4
10V470	4
10V471	4
10V472	4
10V473	4
10V474	4
10V475	4
10V476	4
10V477	4
10V478	4
10V479	4
10V480	4
10V481	4
10V482	4
10V483	4
10V484	4
10V485	4
10V486	4
10V487	4
10V488	4
10V489	4
10V490	4
10V491	4
10V492	4
10V493	4
10V494	4
10V495	4
10V496	4
10V497	4
10V498	4
10V499	4
10V500	4





#### 24. PRIMARY DETERMINATION

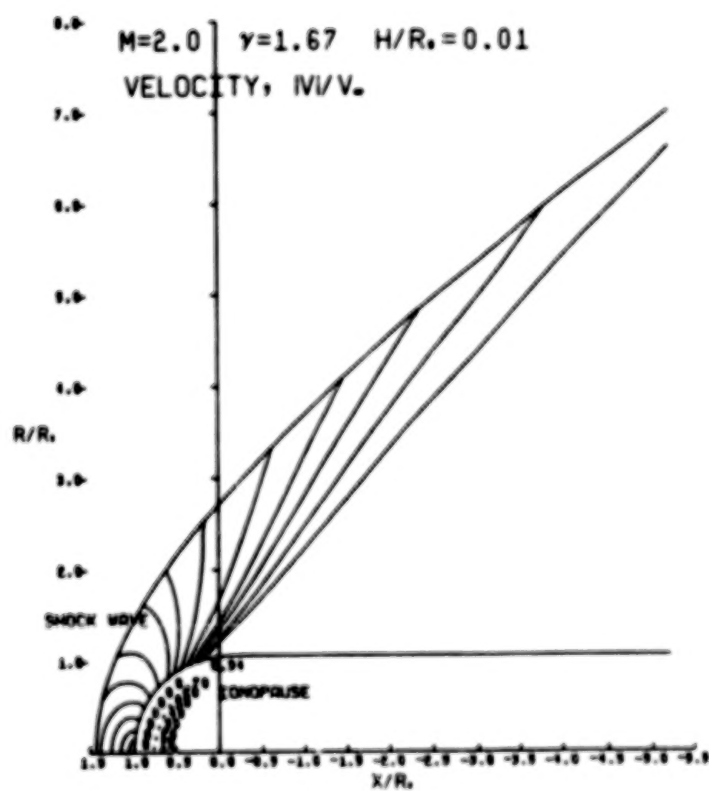
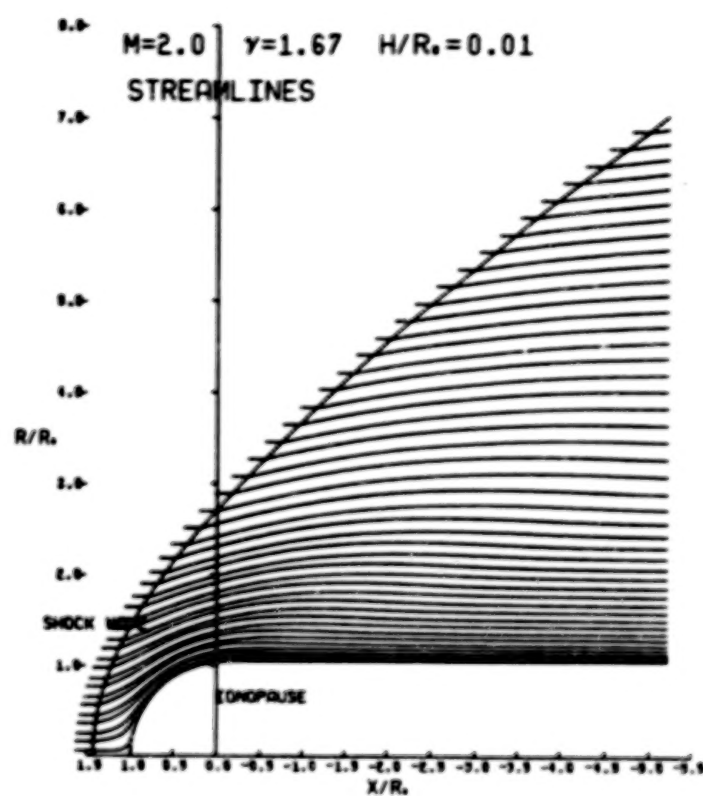
SETHAT	45
SETHAT	44
SETHAT	45
SETHAT	46
SETHAT	47
SETHAT	48
SETHAT	49
SETHAT	50
SETHAT	51
SETHAT	52
SETHAT	53
SETHAT	54
SETHAT	55
SETHAT	56
SETHAT	57
SETHAT	58
SETHAT	59
SETHAT	60
SETHAT	61
SETHAT	62
SETHAT	63
SETHAT	64
SETHAT	65
SETHAT	66
SETHAT	67
SETHAT	68
SETHAT	69
SETHAT	70
SETHAT	71
SETHAT	72
SETHAT	73
SETHAT	74
SETHAT	75
SETHAT	76
SETHAT	77
SETHAT	78
SETHAT	79
SETHAT	80
SETHAT	81
SETHAT	82
SETHAT	83
SETHAT	84
SETHAT	85
SETHAT	86
SETHAT	87
SETHAT	88
SETHAT	89
SETHAT	90
SETHAT	91
SETHAT	92
SETHAT	93
SETHAT	94
SETHAT	95
SETHAT	96
SETHAT	97
SETHAT	98
SETHAT	99
SETHAT	100

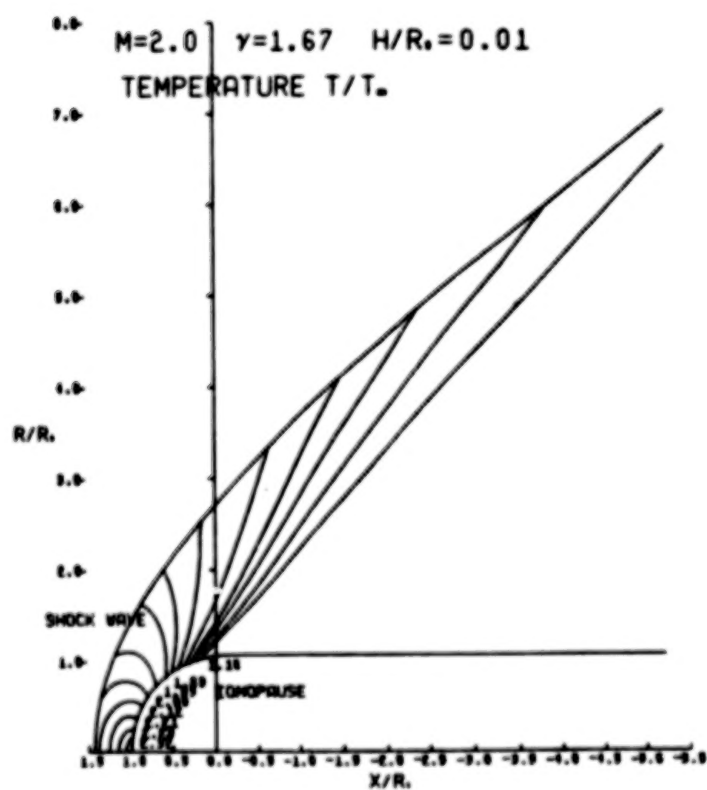
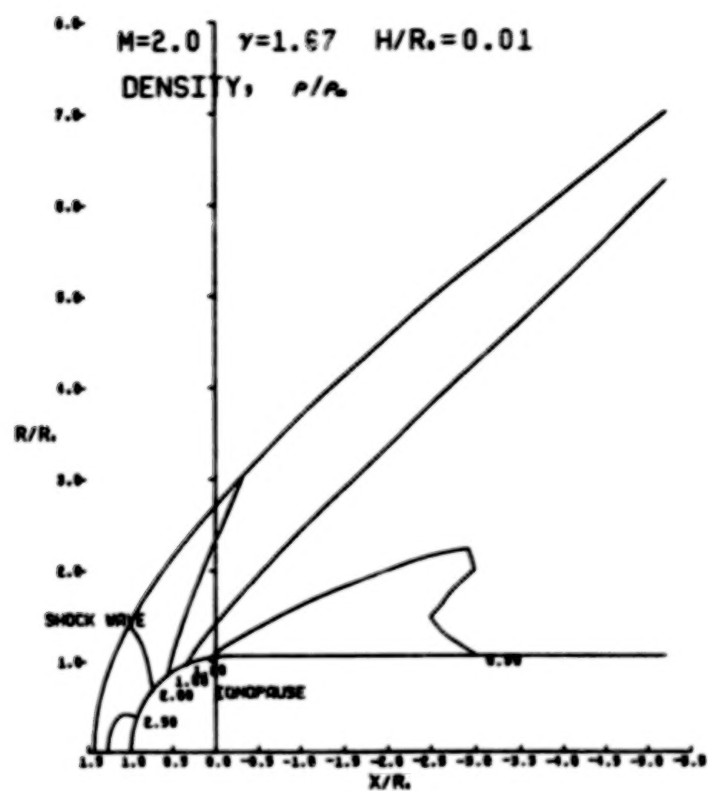
**BLANK PAGE**

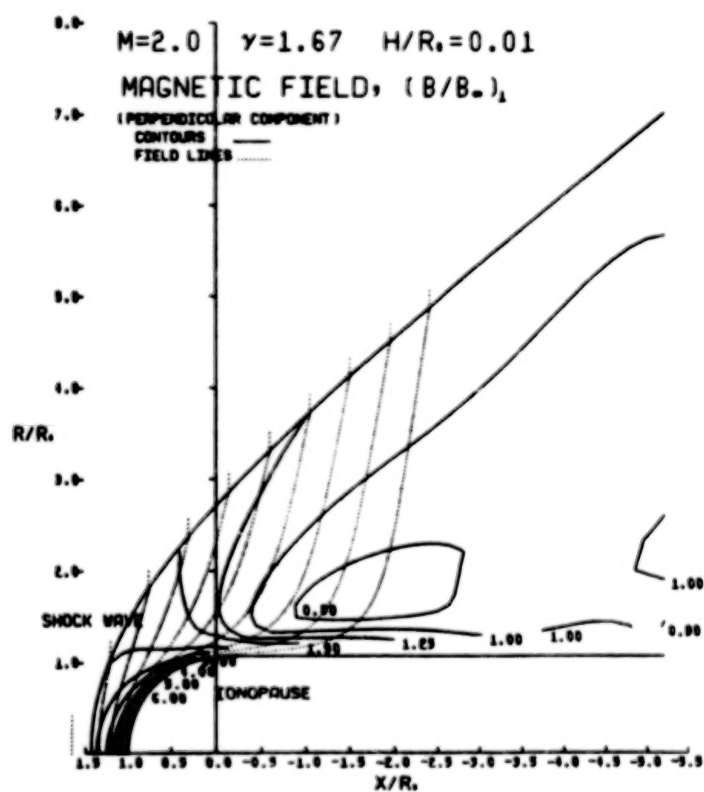
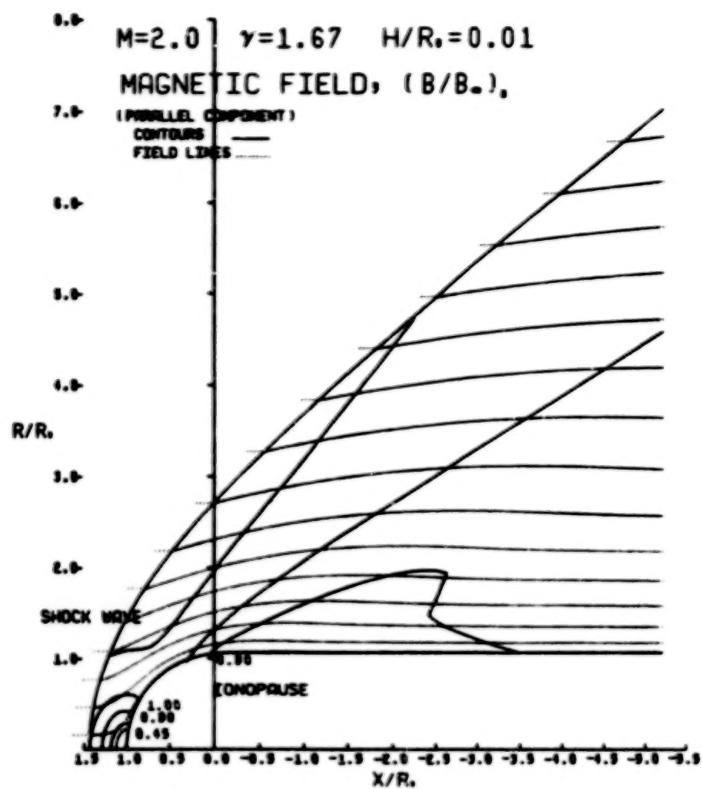


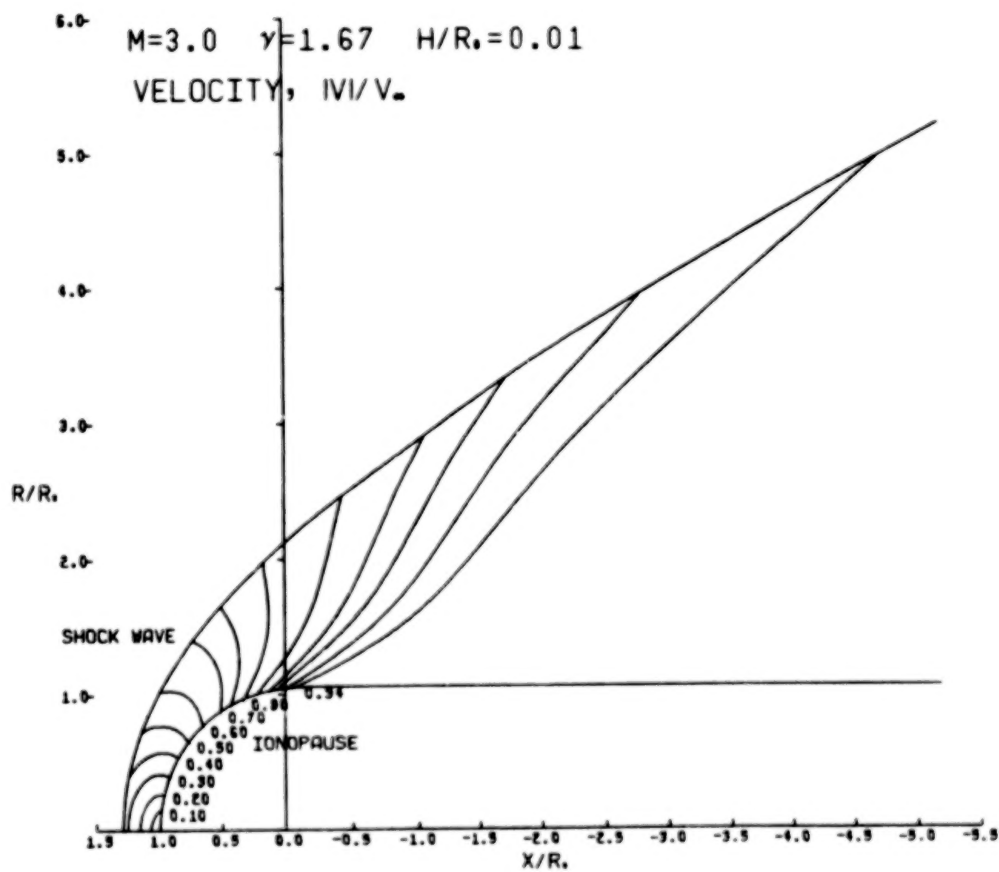
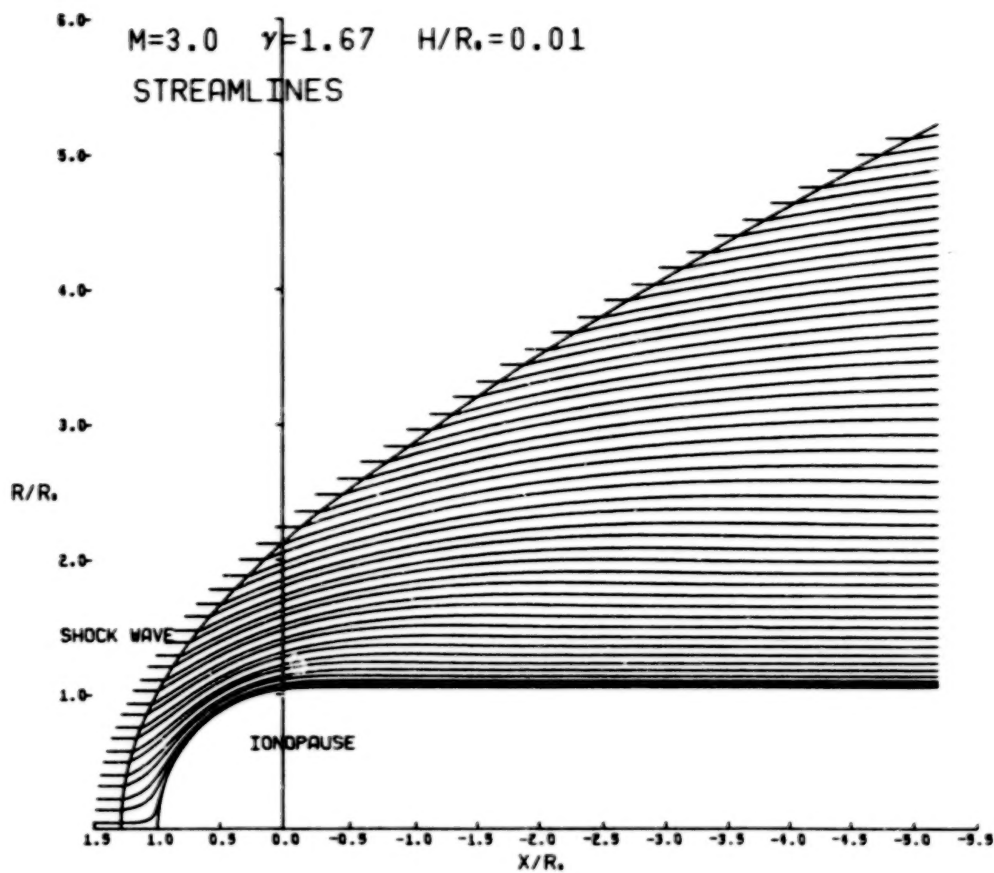
**APPENDIX C**  
**CATALOG OF TEST CASES**

$H/R_0$	$M_\infty$	$\gamma$	(Page No.) Streamlines	(Page No.) Velocity magnitude $ v /v_\infty$	(Page No.) Density $\rho/\rho_\infty$	(Page No.) Temperature $T/T_\infty$	(Page No.) Parallel magnetic field $( B /B_\infty)_\parallel$	(Page No.) Perpendicular magnetic field $( B /B_\infty)_\perp$
.01	2.0	5/3	179	179	180	180	181	181
↓	3.0	↓	182	182	183	183	184	184
	5.0		185	185	186	186	187	187
	8.0		188	188	189	189	190	190
	12.0		191	191	192	192	193	193
	25.0		194	194	195	195	196	196
.10	2.0		197	197	198	198	199	199
↓	3.0		200	200	201	201	202	202
	5.0		203	203	204	204	205	205
	8.0		206	206	207	207	208	208
	12.0		209	209	210	210	211	211
	25.0		212	212	213	213	214	214
.25	2.0		215	215	216	216	217	217
↓	3.0		218	218	219	219	220	220
	5.0		221	221	222	222	223	223
	8.0		224	224	225	225	226	226
	12.0		227	227	228	228	229	229
↓	25.0	↓	230	230	231	231	232	232
$H/R_0$	$M_\infty$	$\gamma$	Streamlines	$ v /v_\infty$	$\rho/\rho_\infty$	$T/T_\infty$	$( B /B_\infty)_\parallel$	$( B /B_\infty)_\perp$
.10	2.0	5/3	233	233	234	234	235	235
↓	3.0	↓	236	236	237	237	238	238
	5.0		239	239	240	240	241	241
	8.0		242	242	243	243	244	244
	12.0		245	245	246	246	247	247
	25.0		248	248	249	249	250	250
.20	2.0		251	251	252	252	253	253
↓	3.0		254	254	255	255	256	256
	5.0		257	257	258	258	259	259
	8.0		260	260	261	261	262	262
	12.0		263	263	264	264	265	265
	25.0		266	266	267	267	268	268
.25	2.0		269	269	270	270	271	271
↓	3.0		272	272	273	273	274	274
	5.0		275	275	276	276	277	277
	8.0		278	278	279	279	280	280
	12.0		281	281	282	282	283	283
↓	25.0	↓	284	284	285	285	286	286

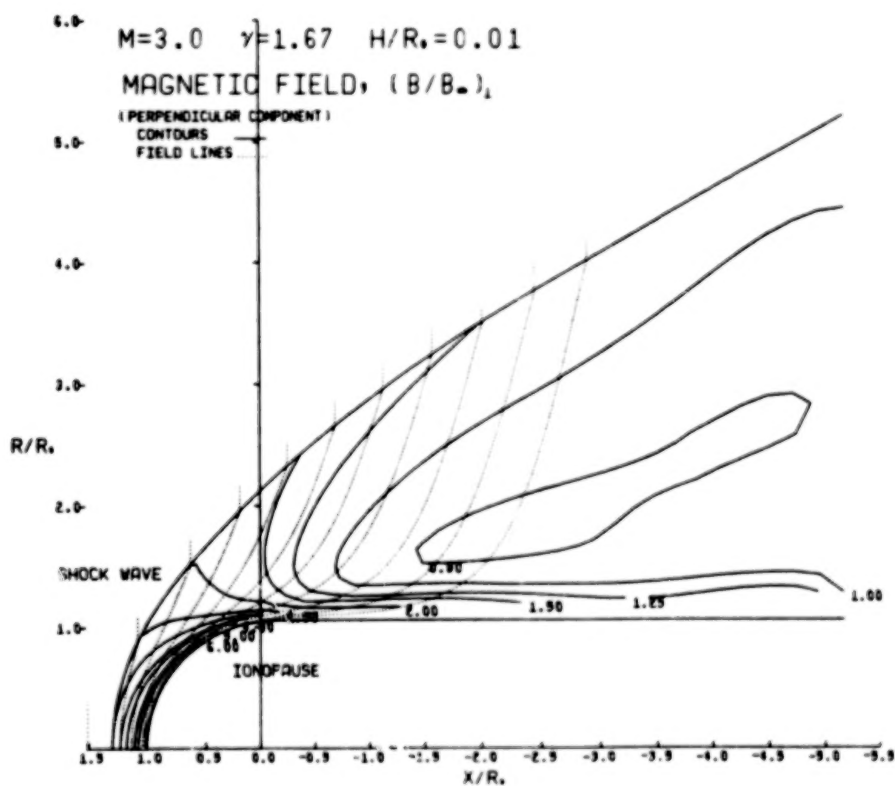
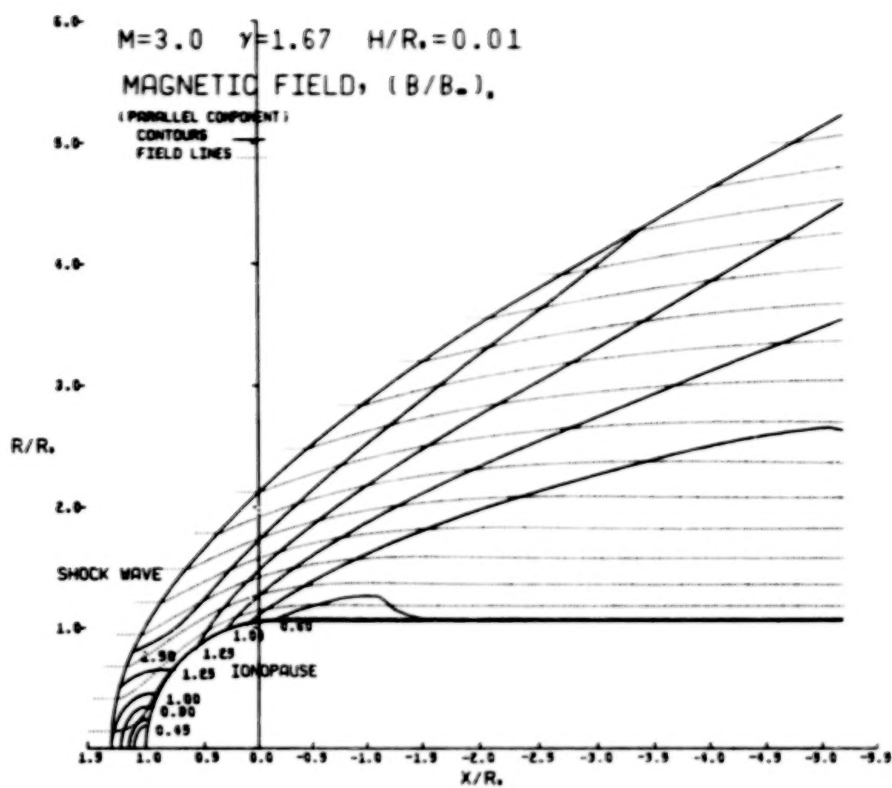




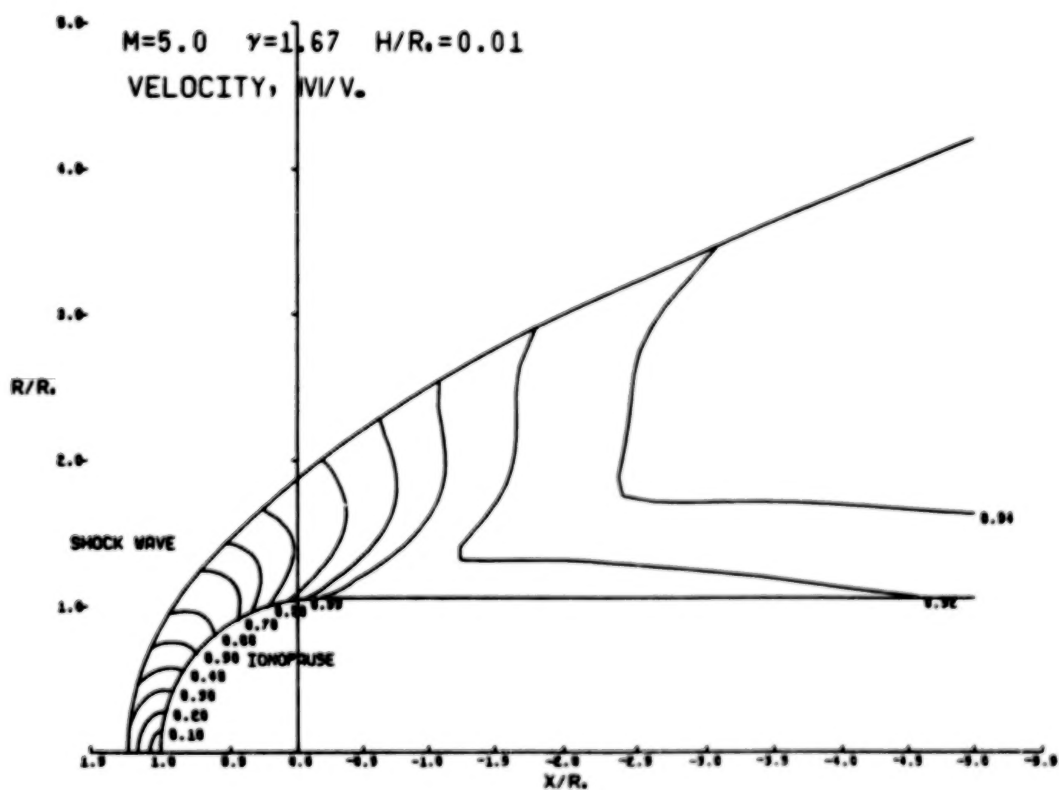
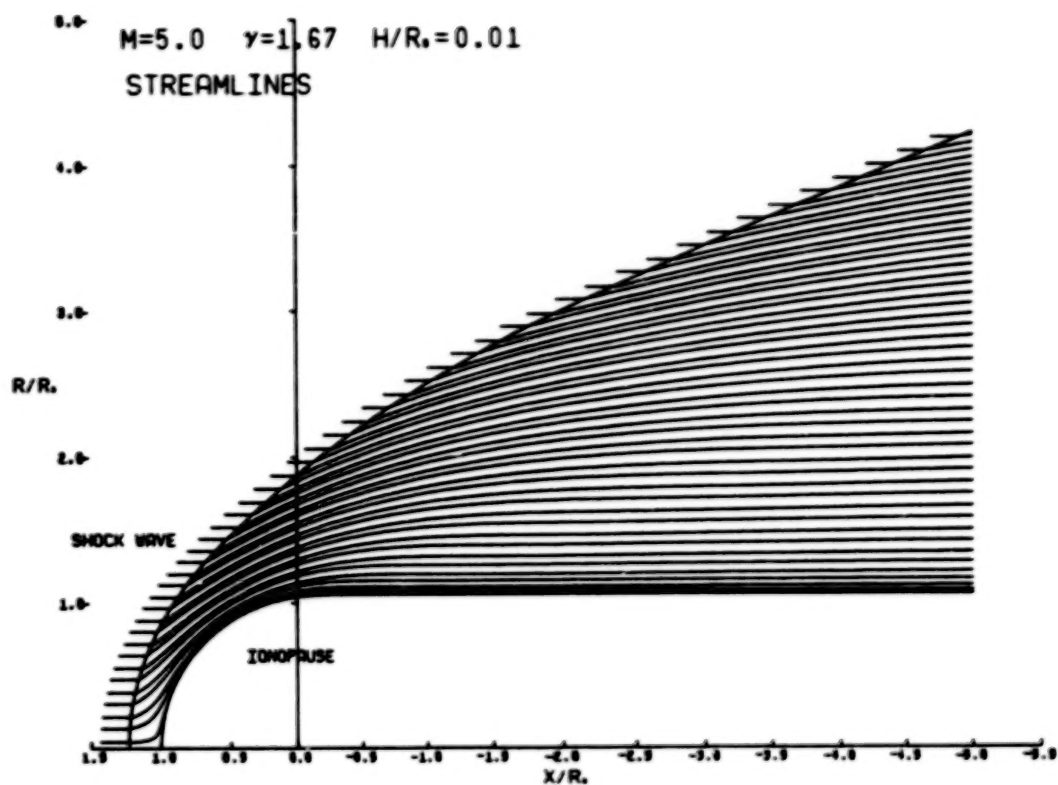


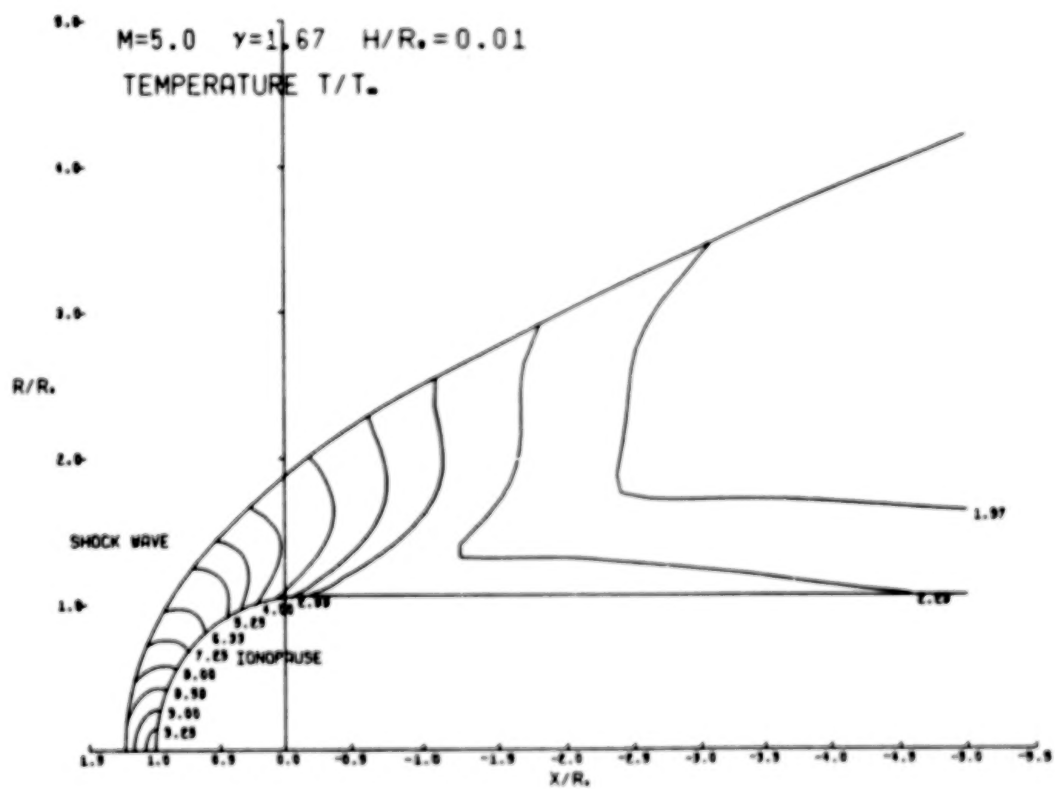
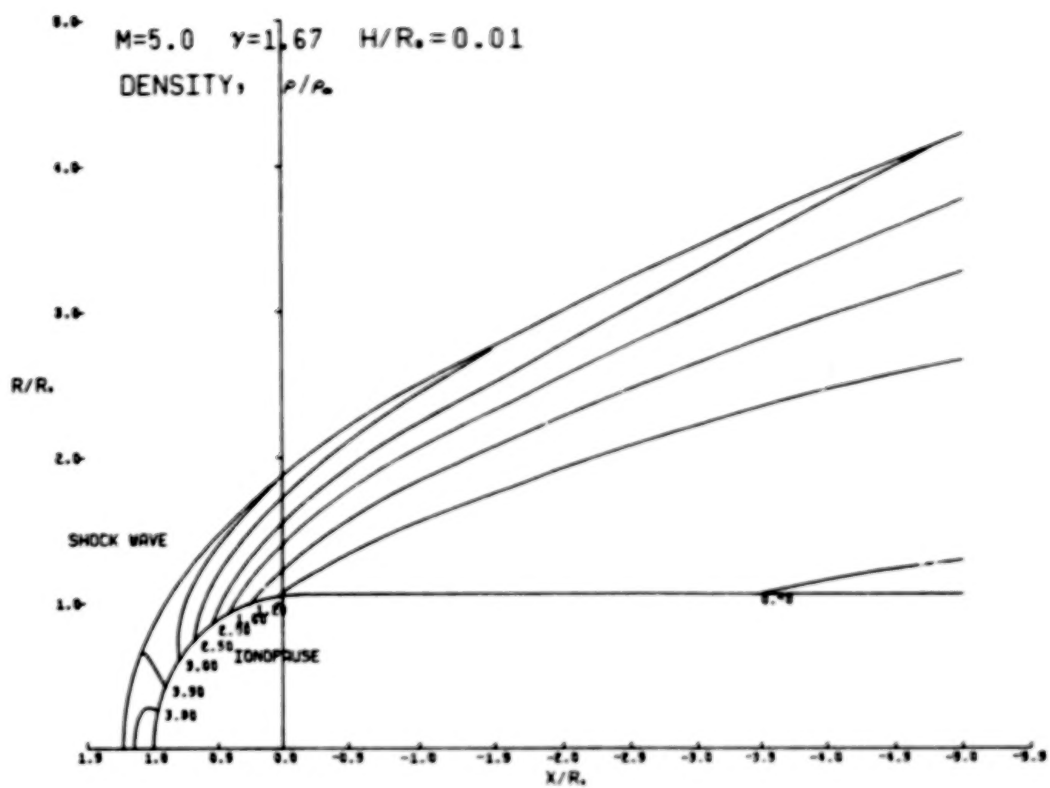


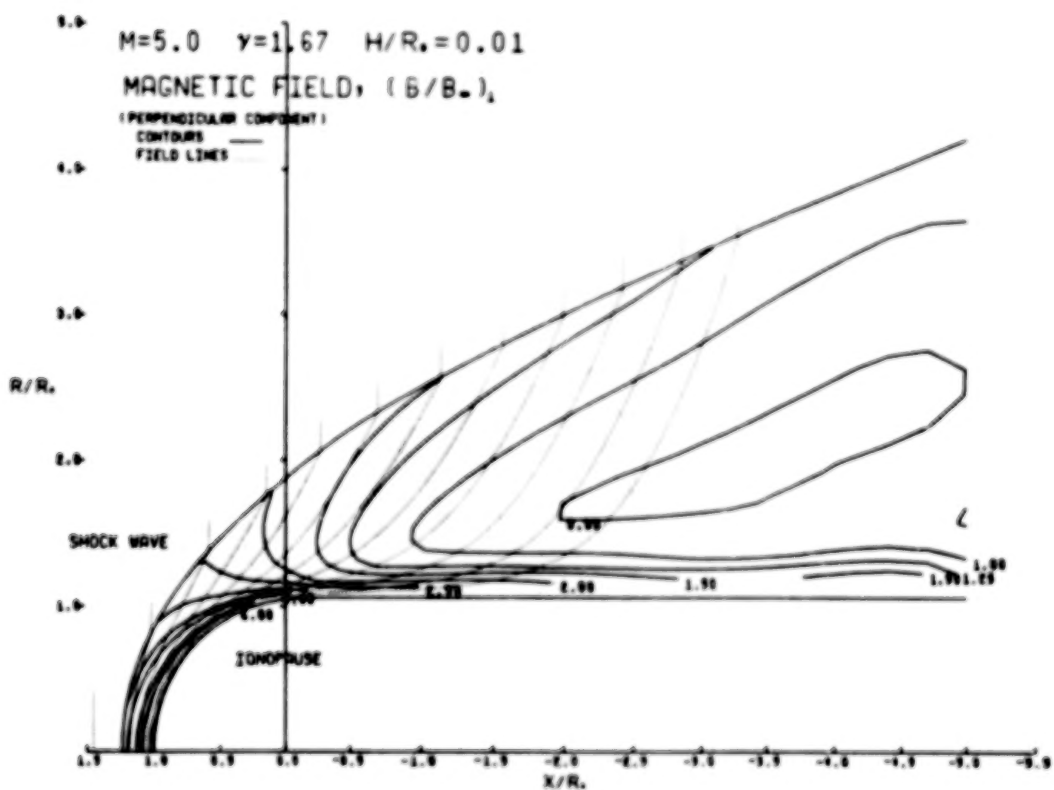
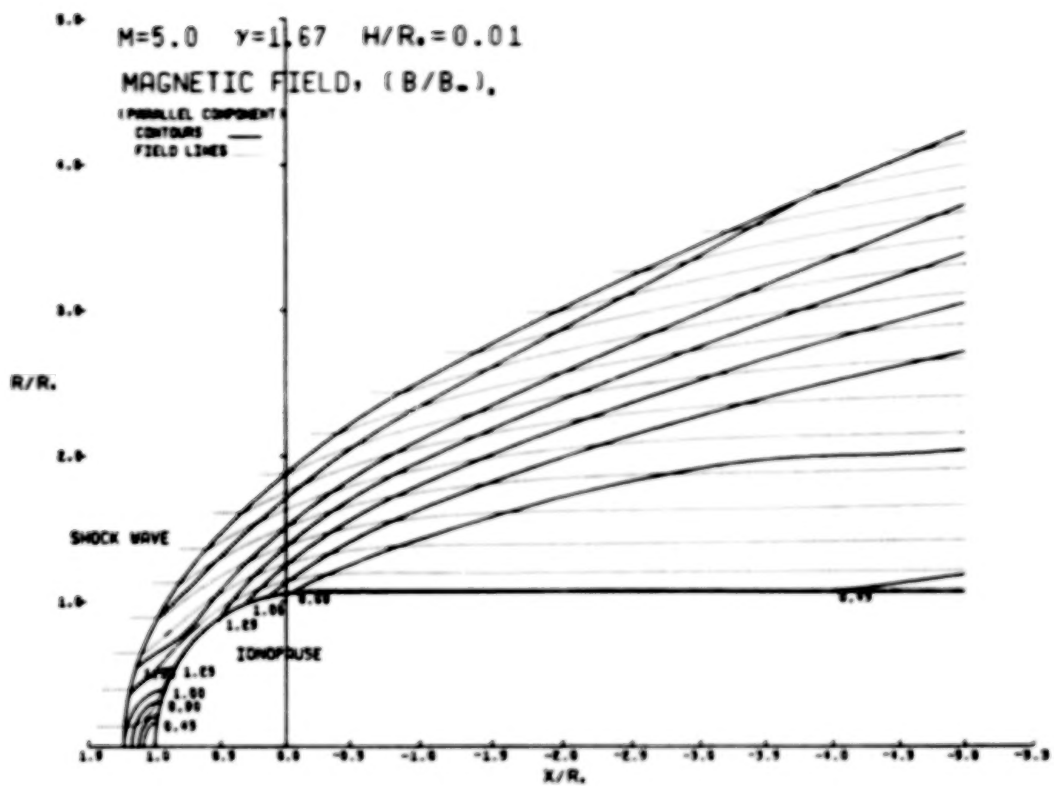


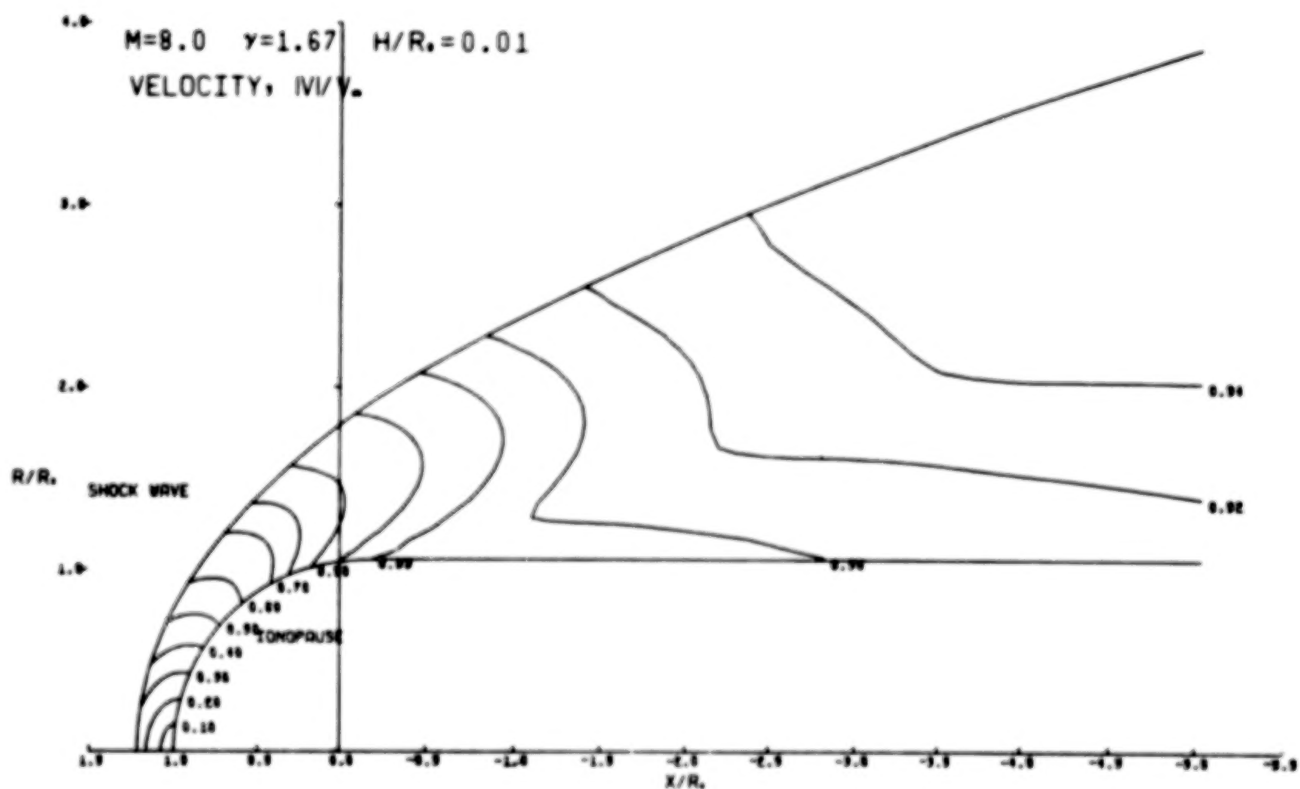
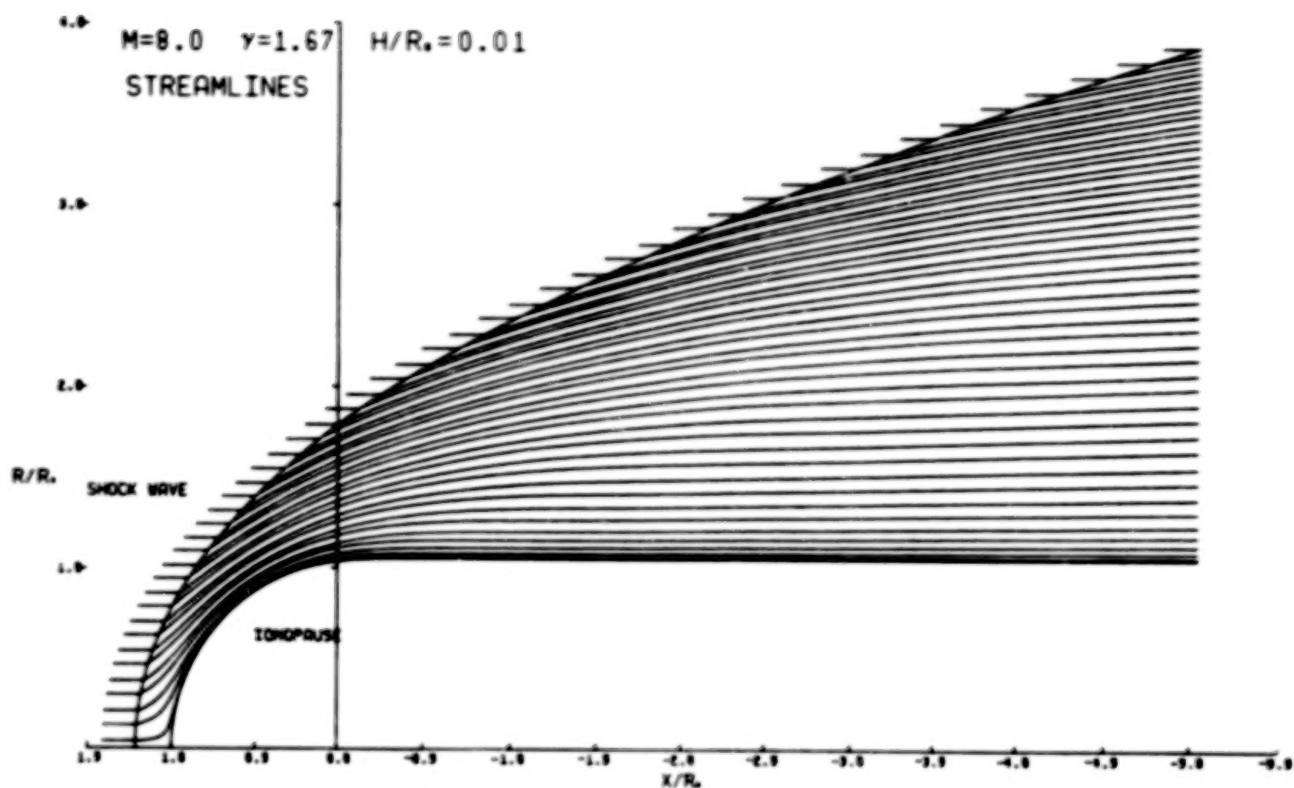


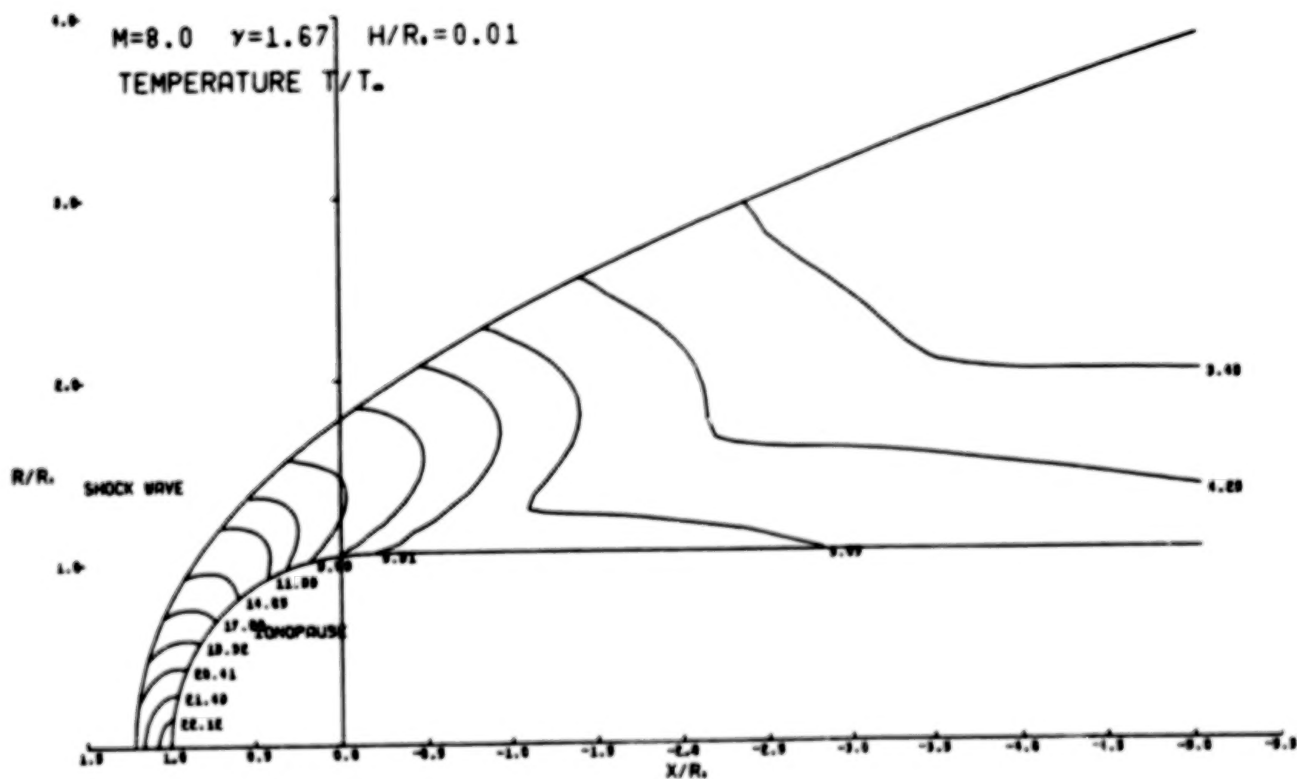
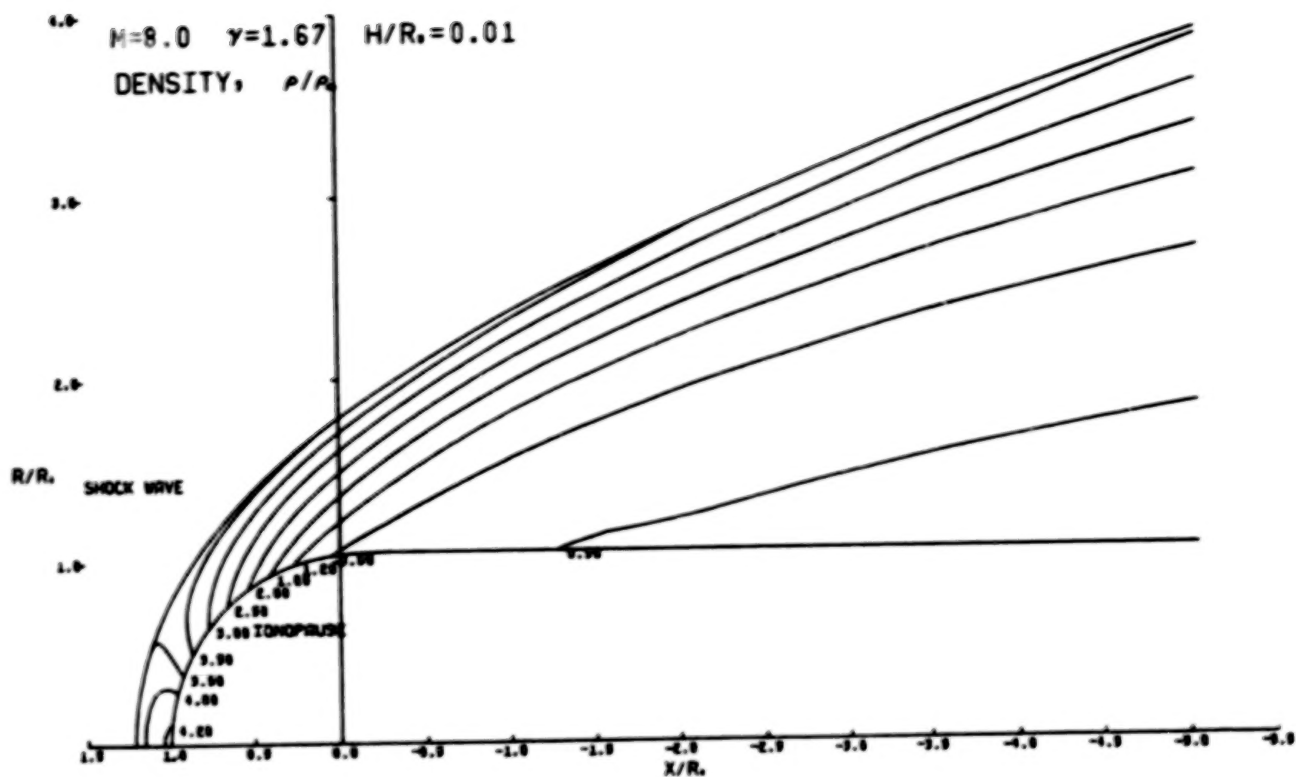


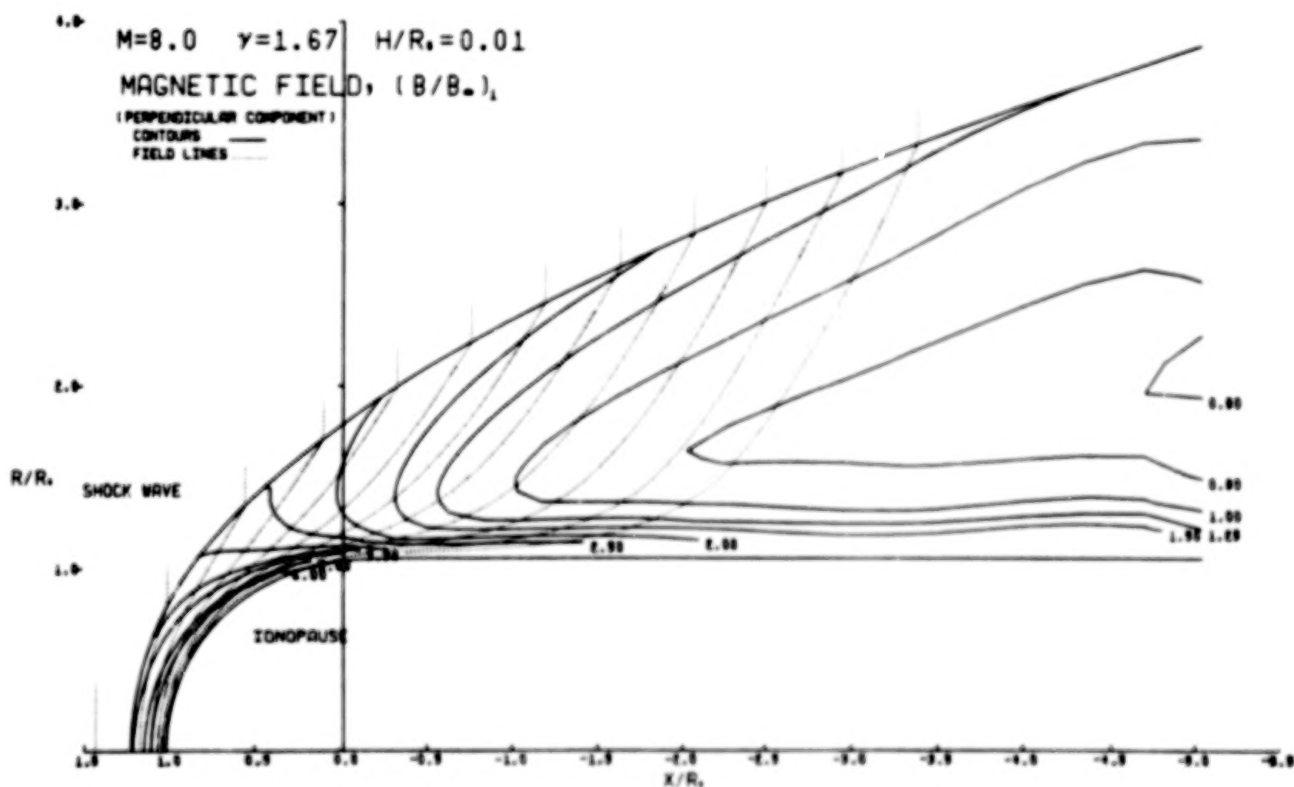
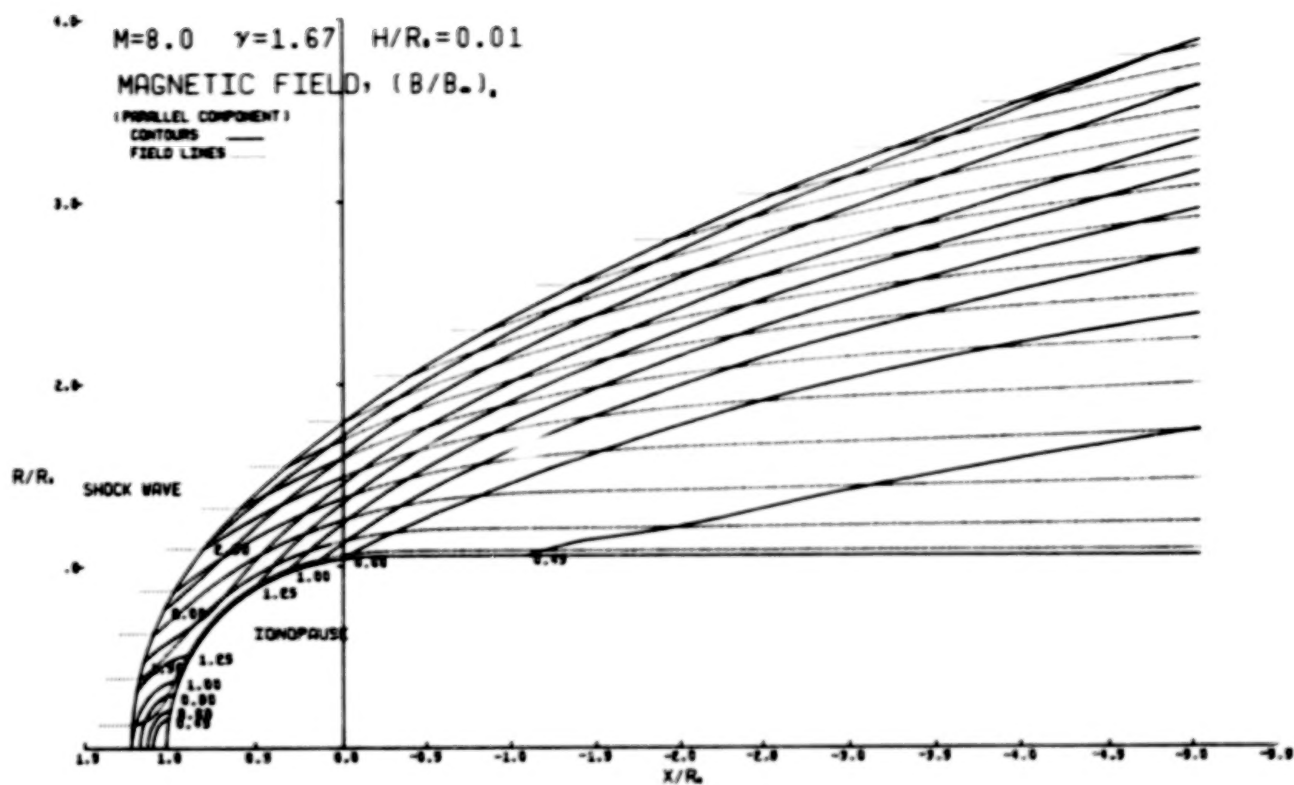


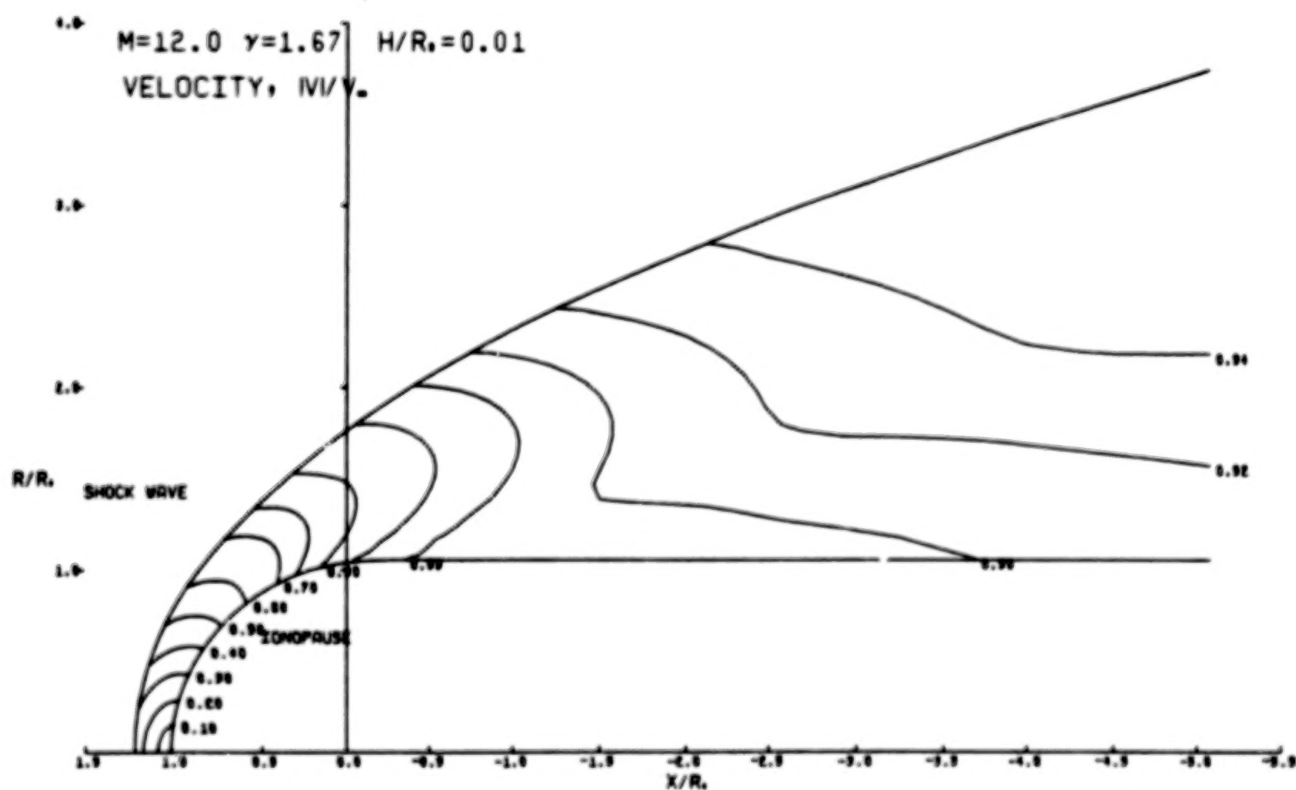
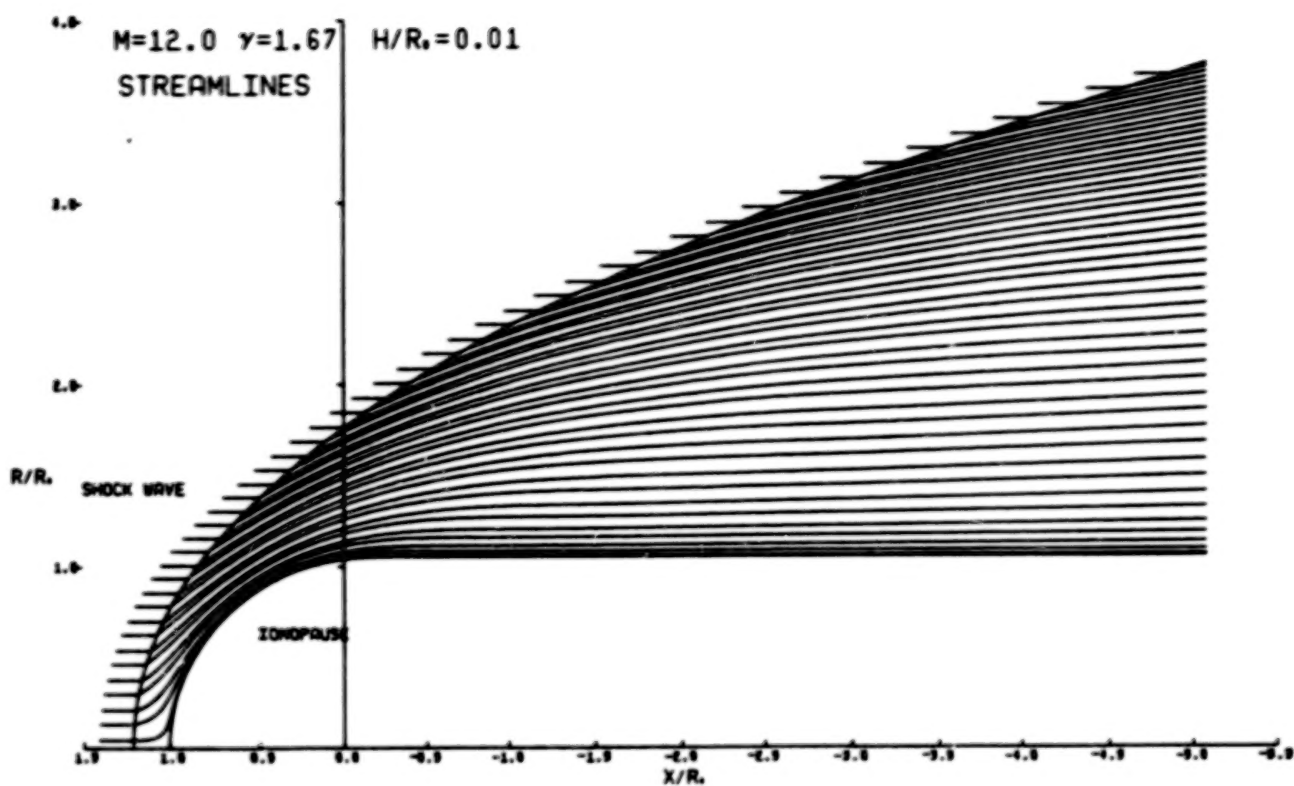






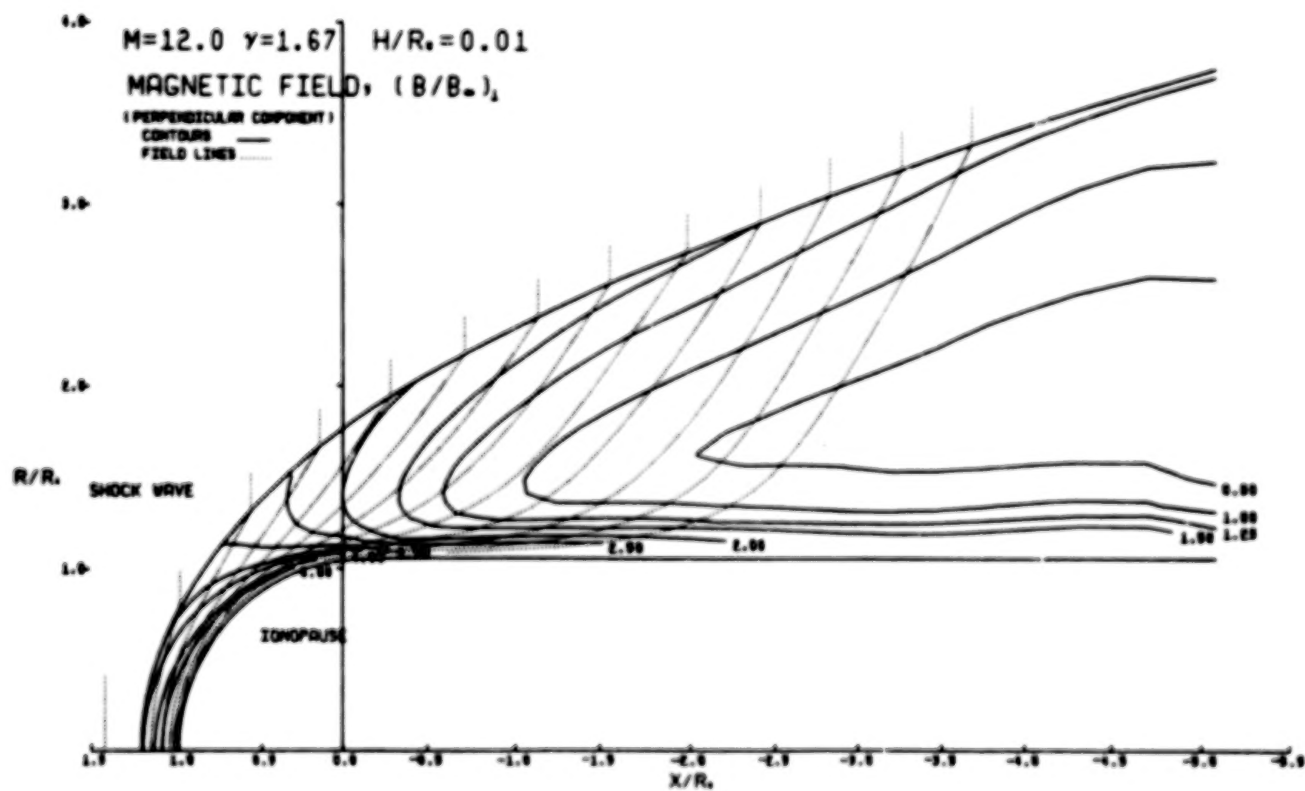
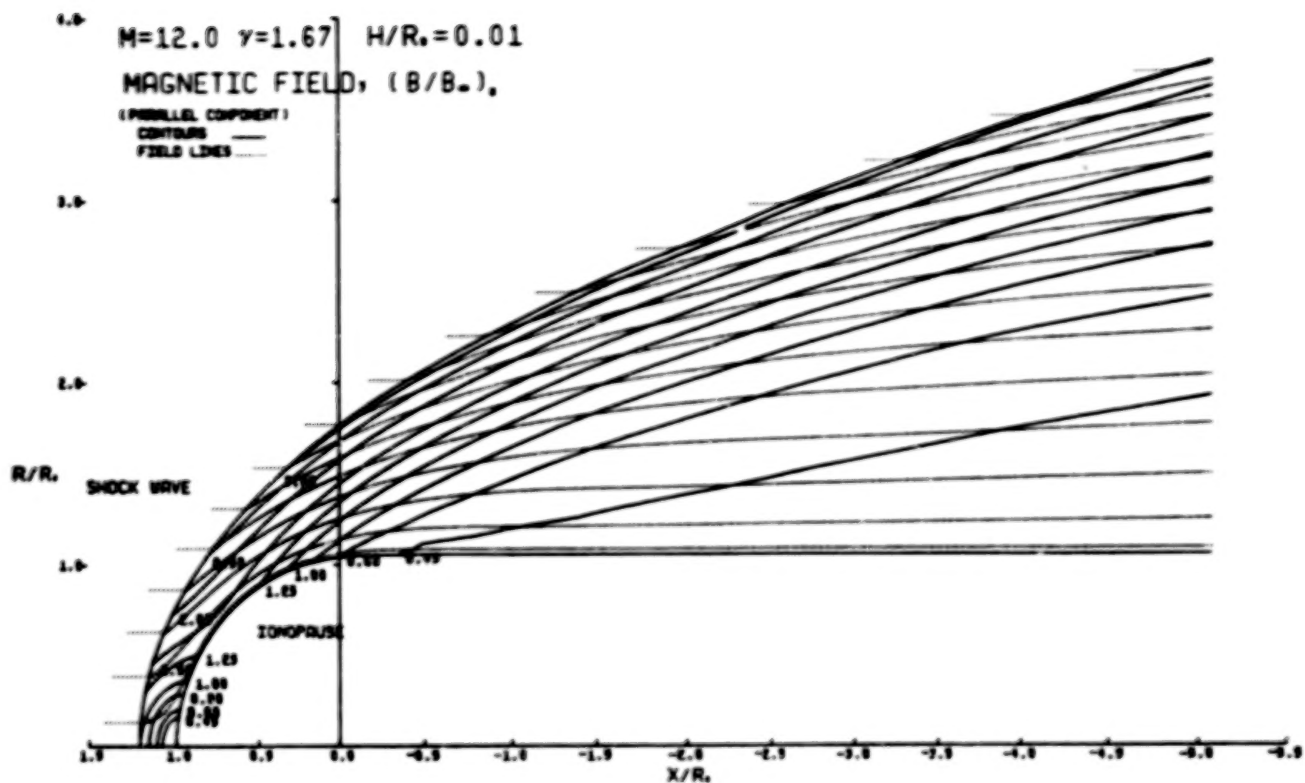


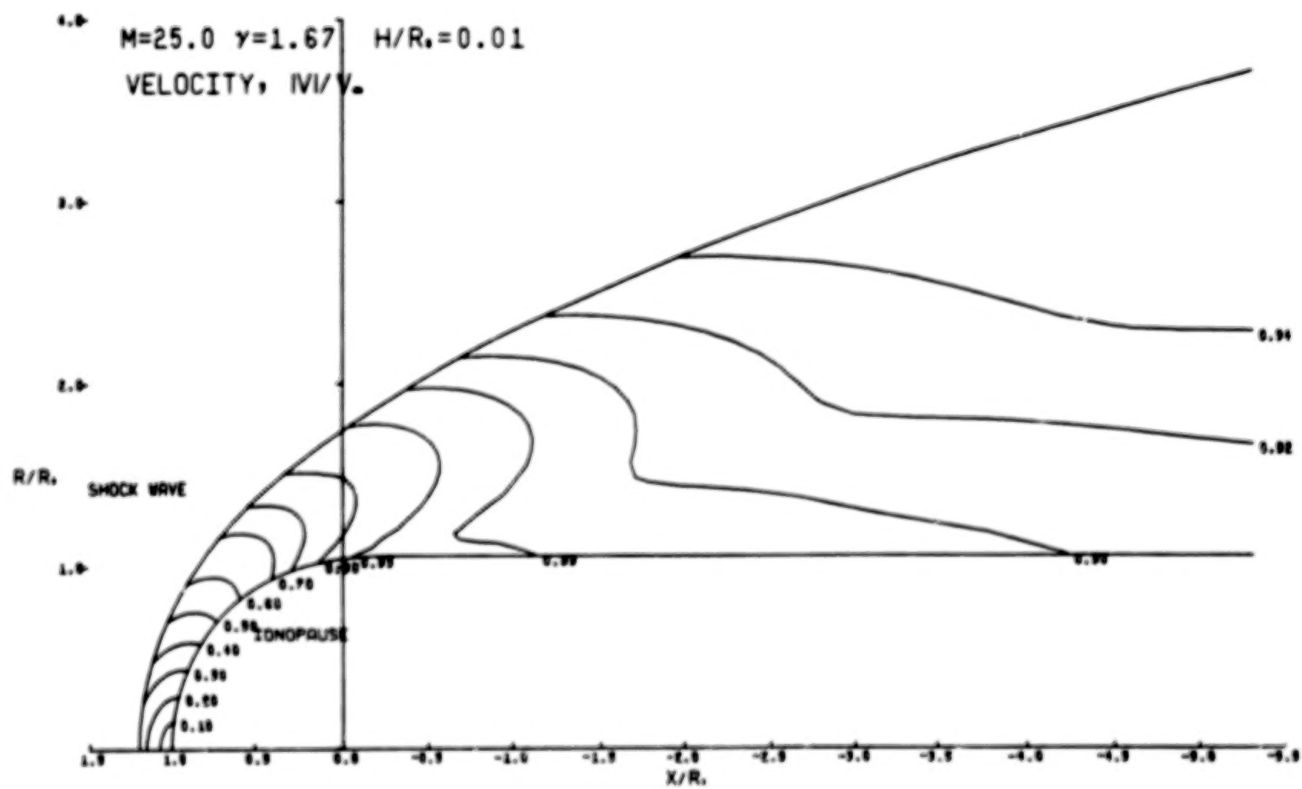
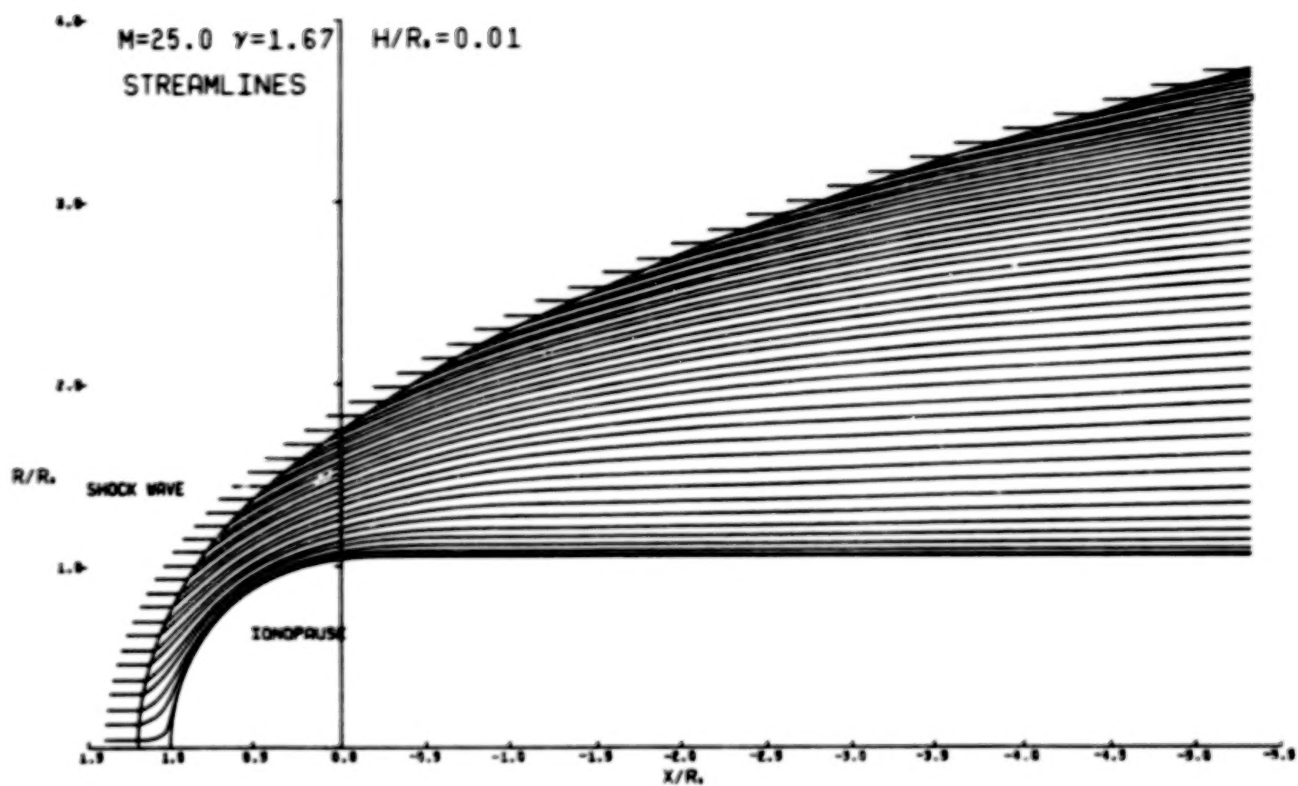




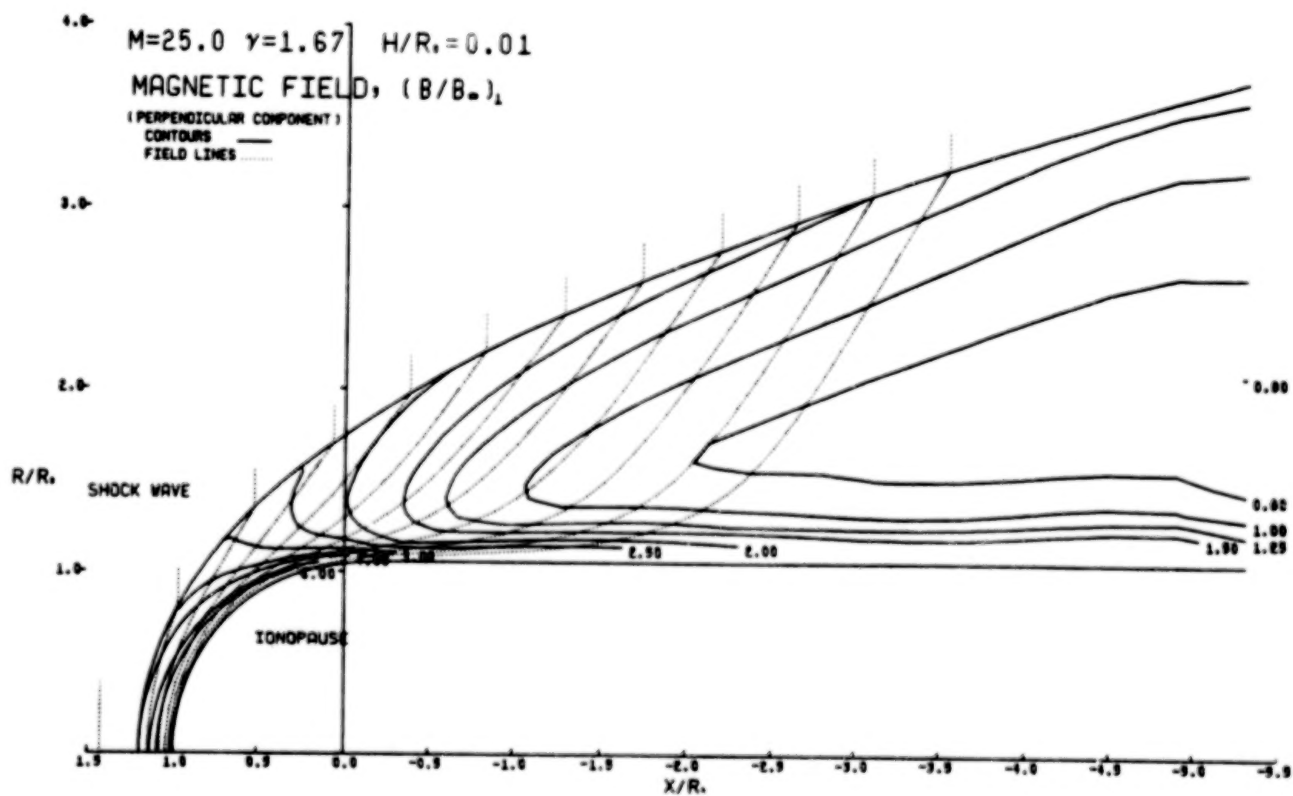
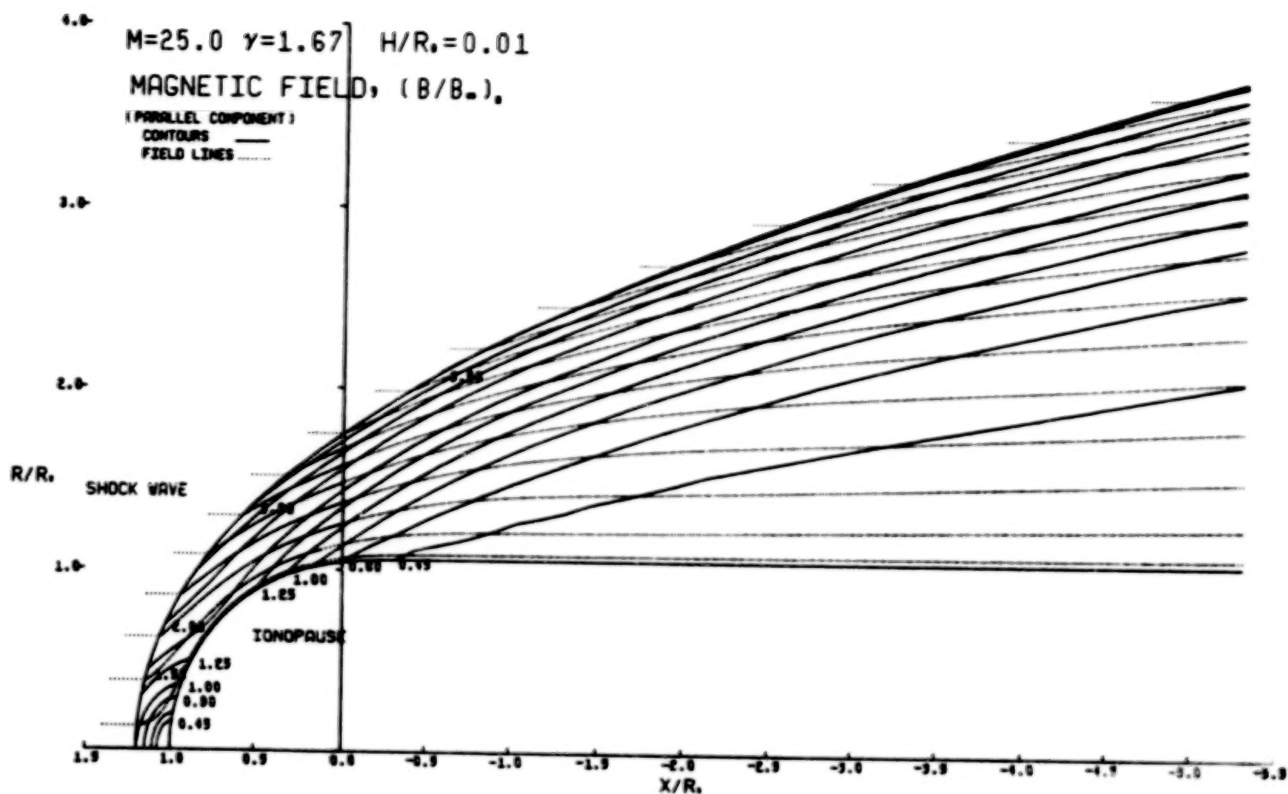


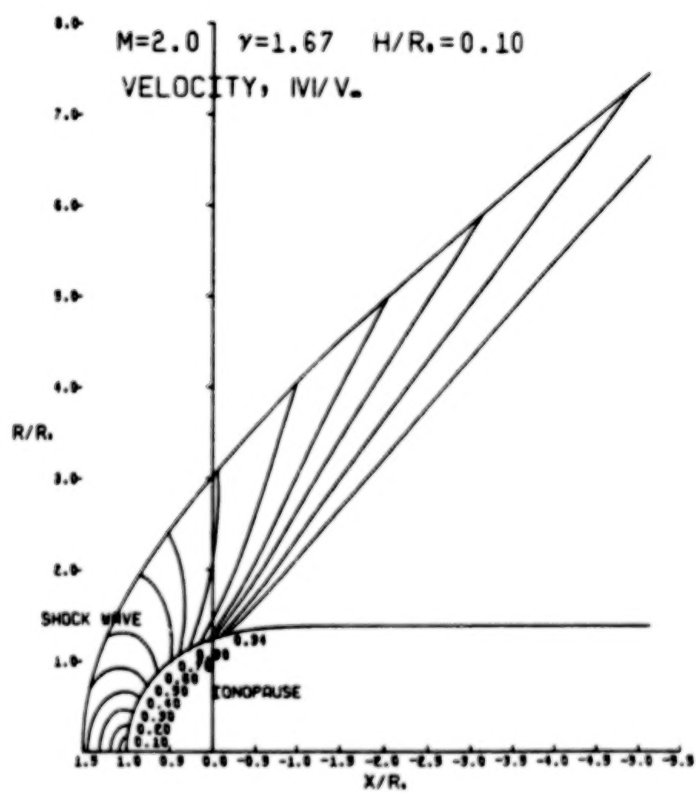
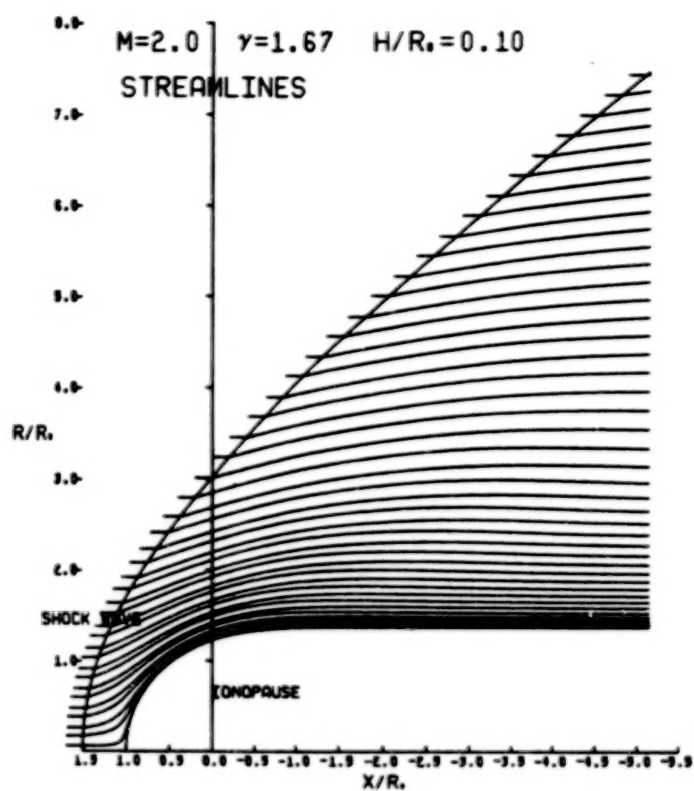


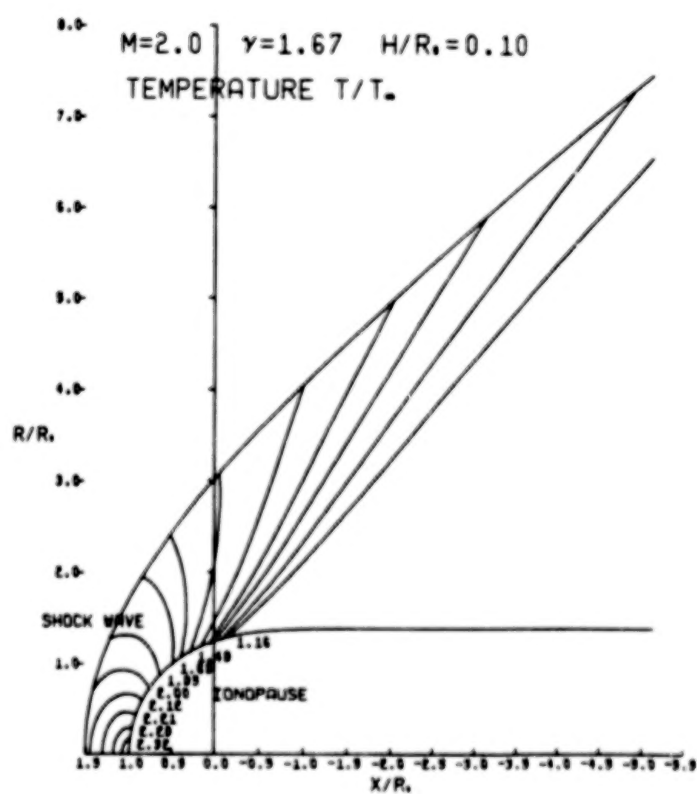
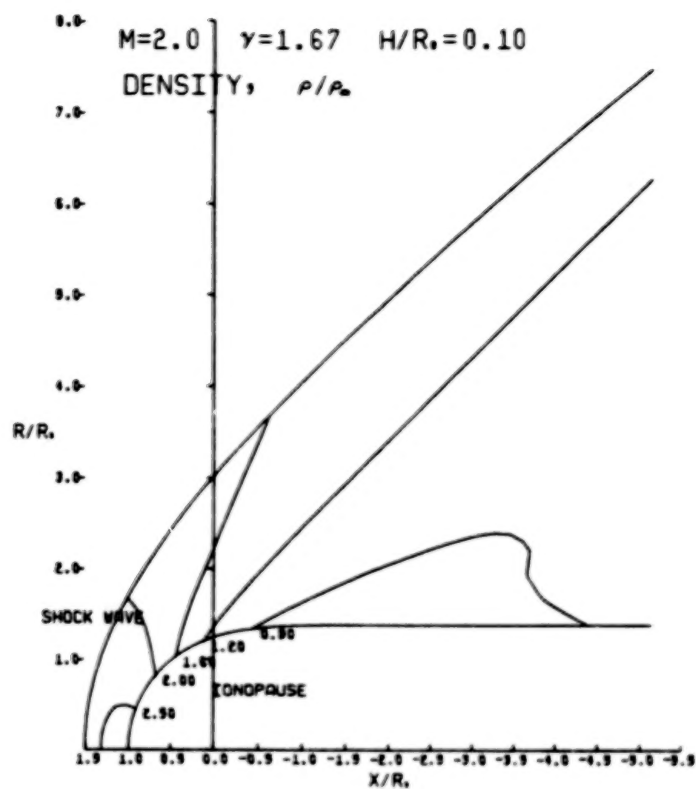


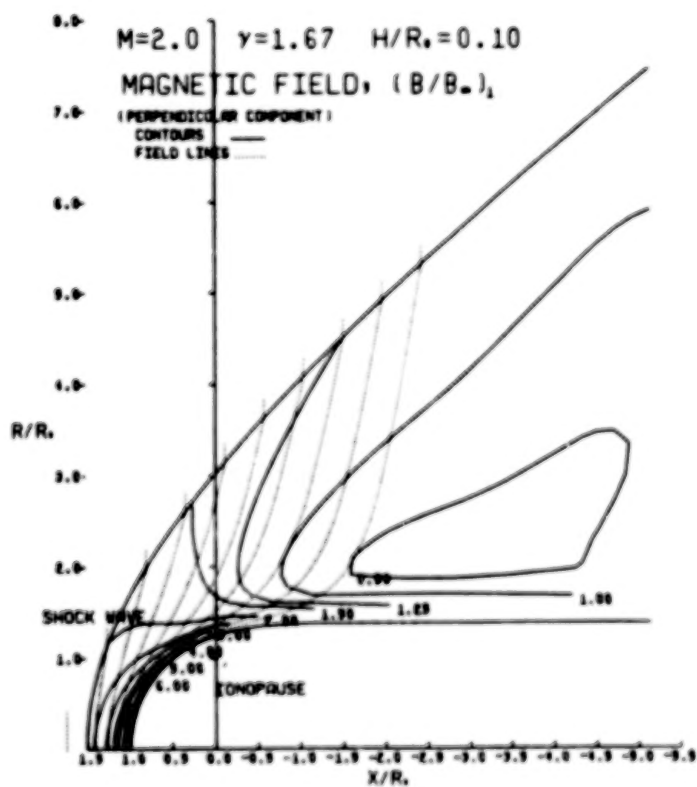
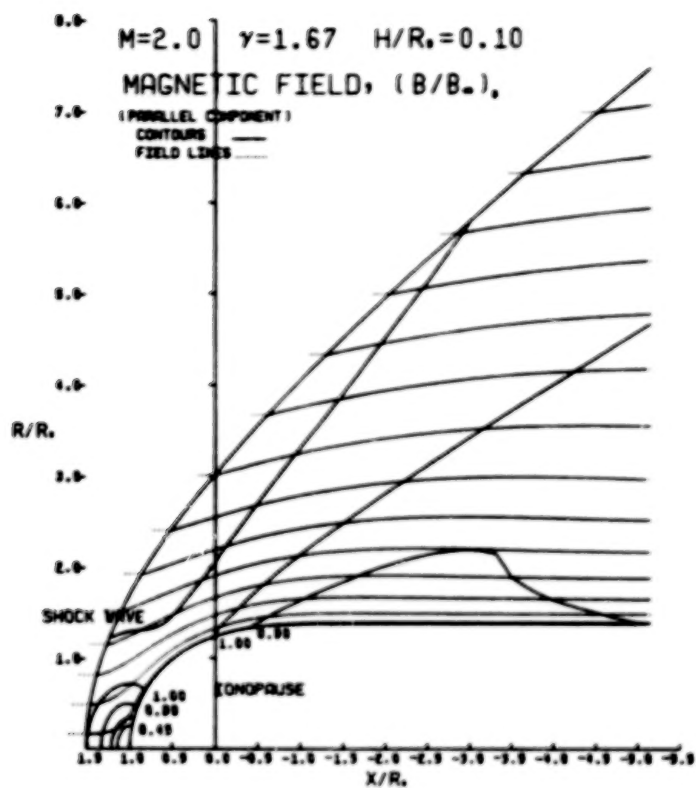


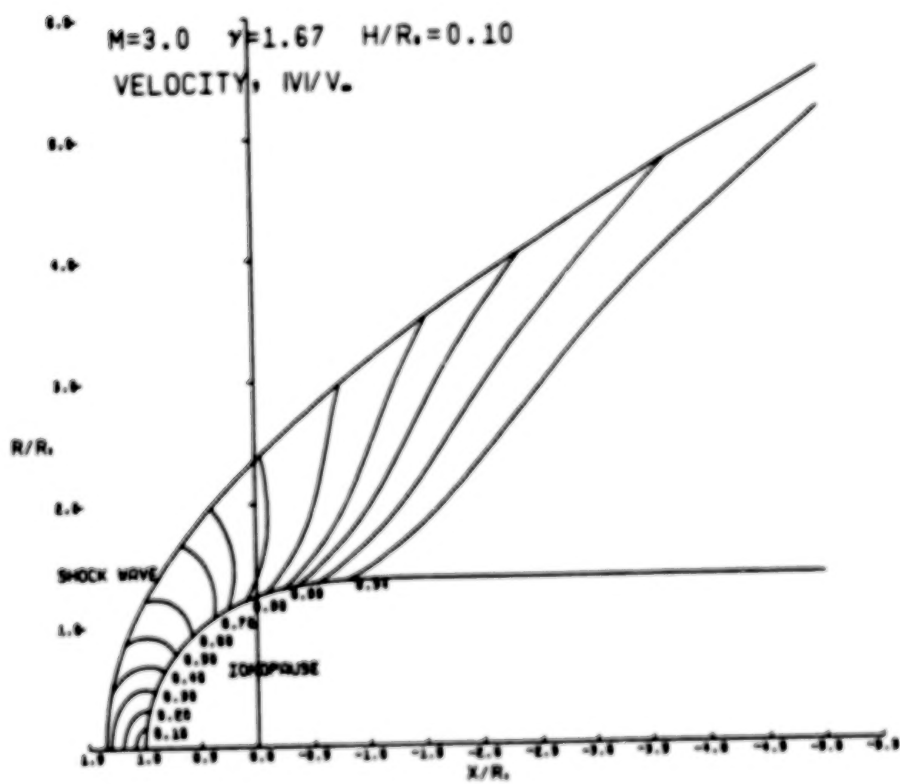
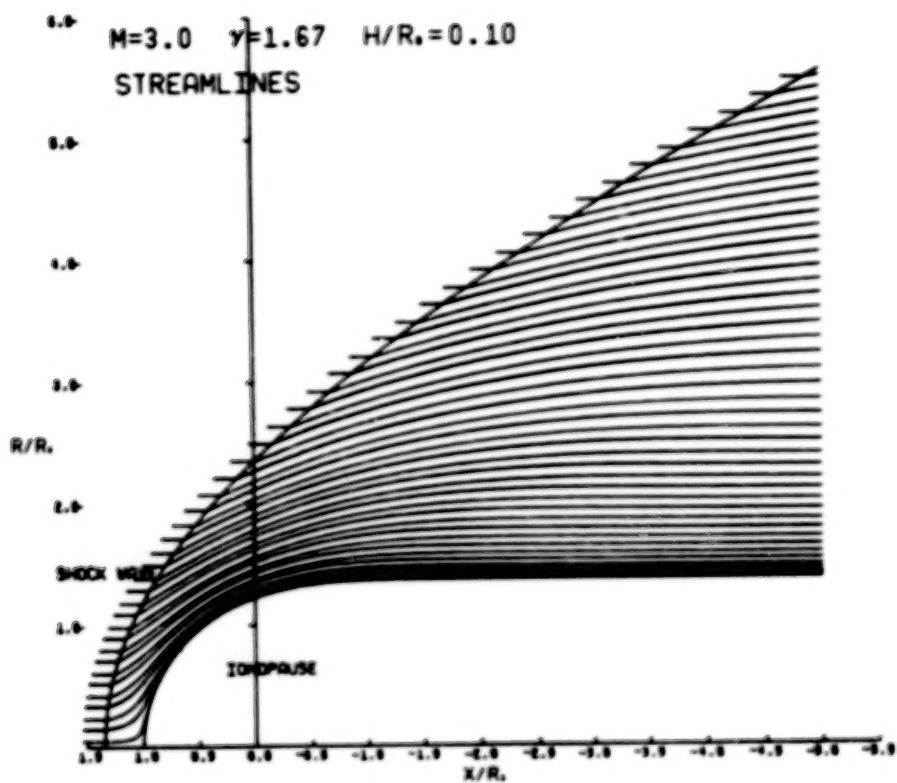






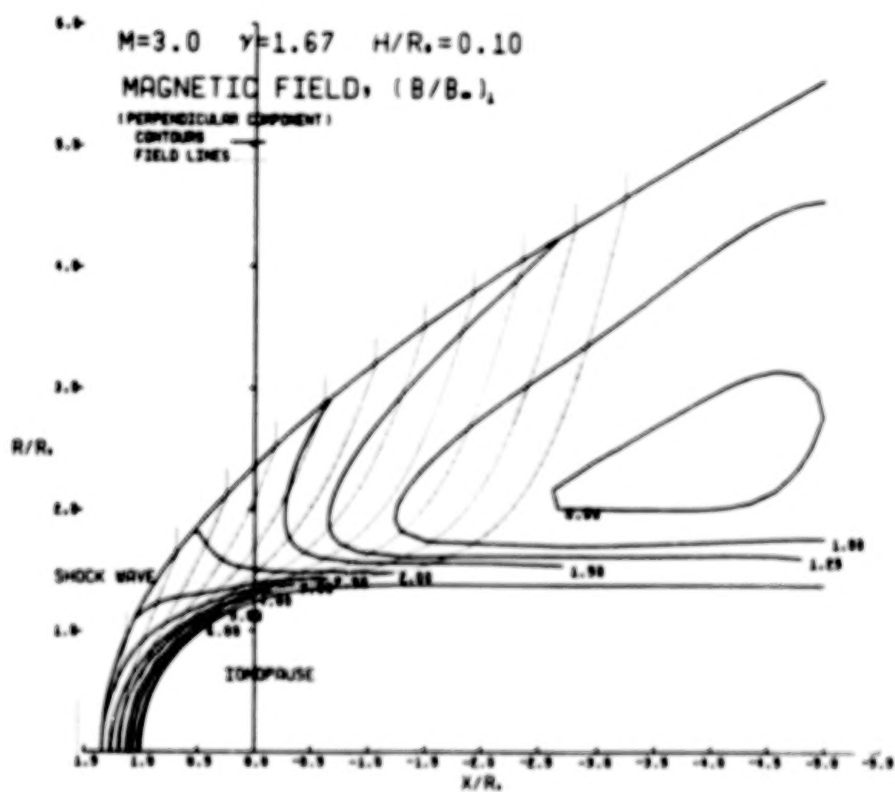
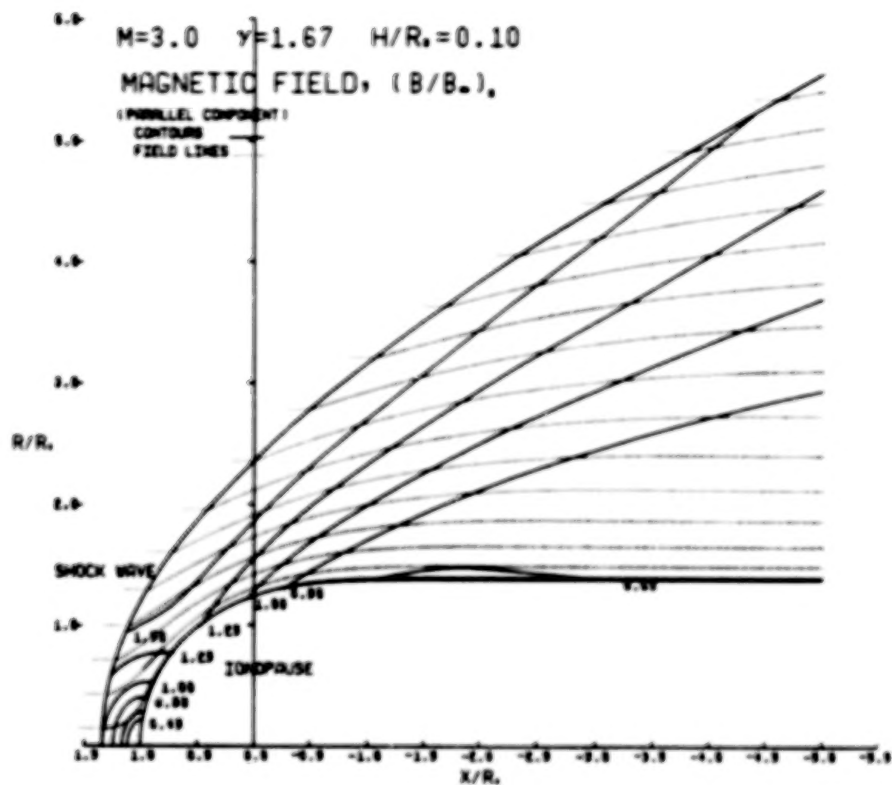


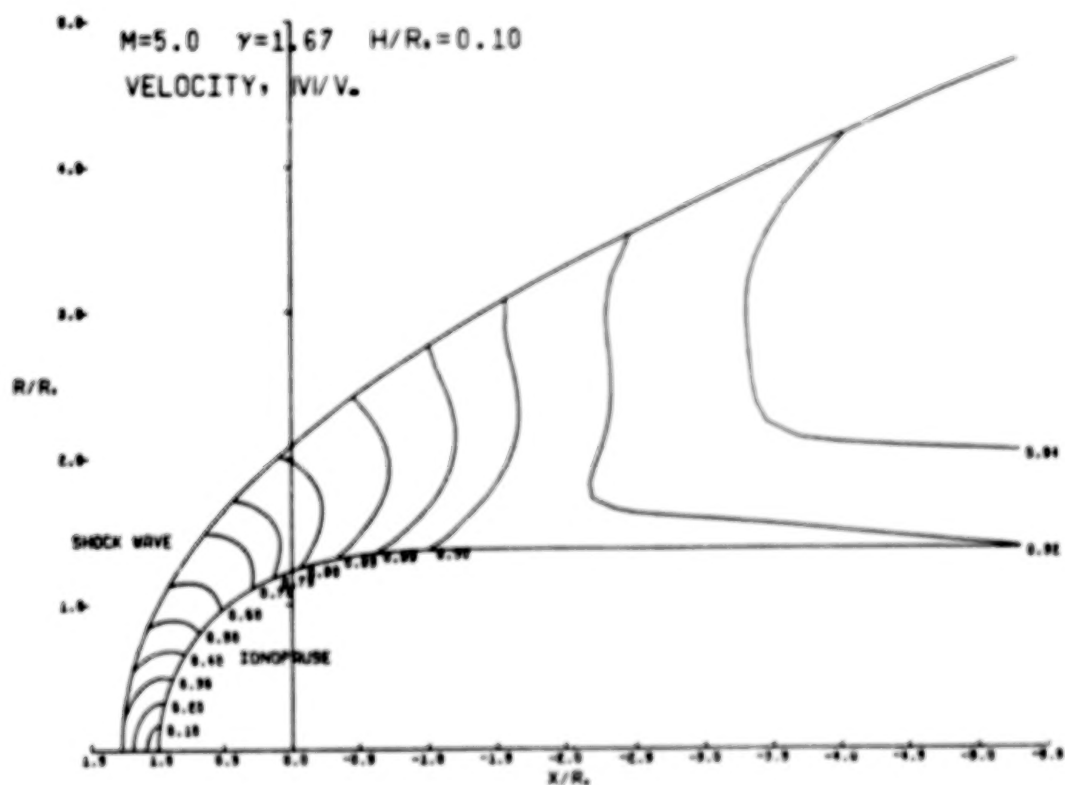
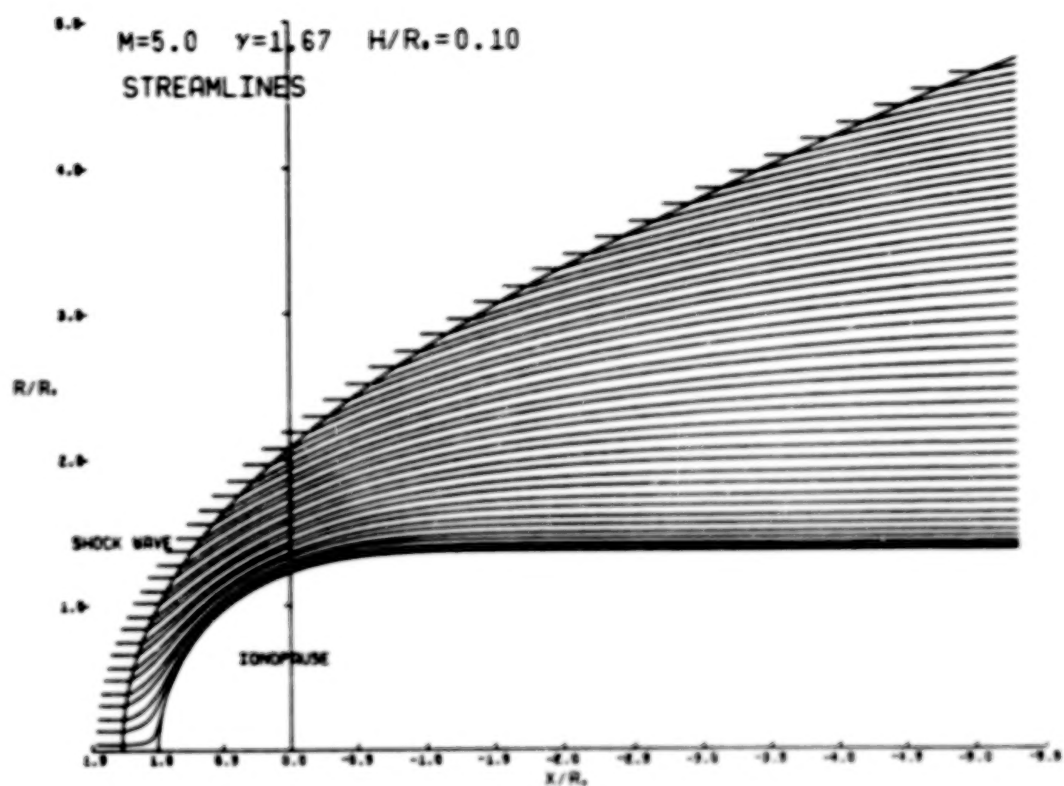




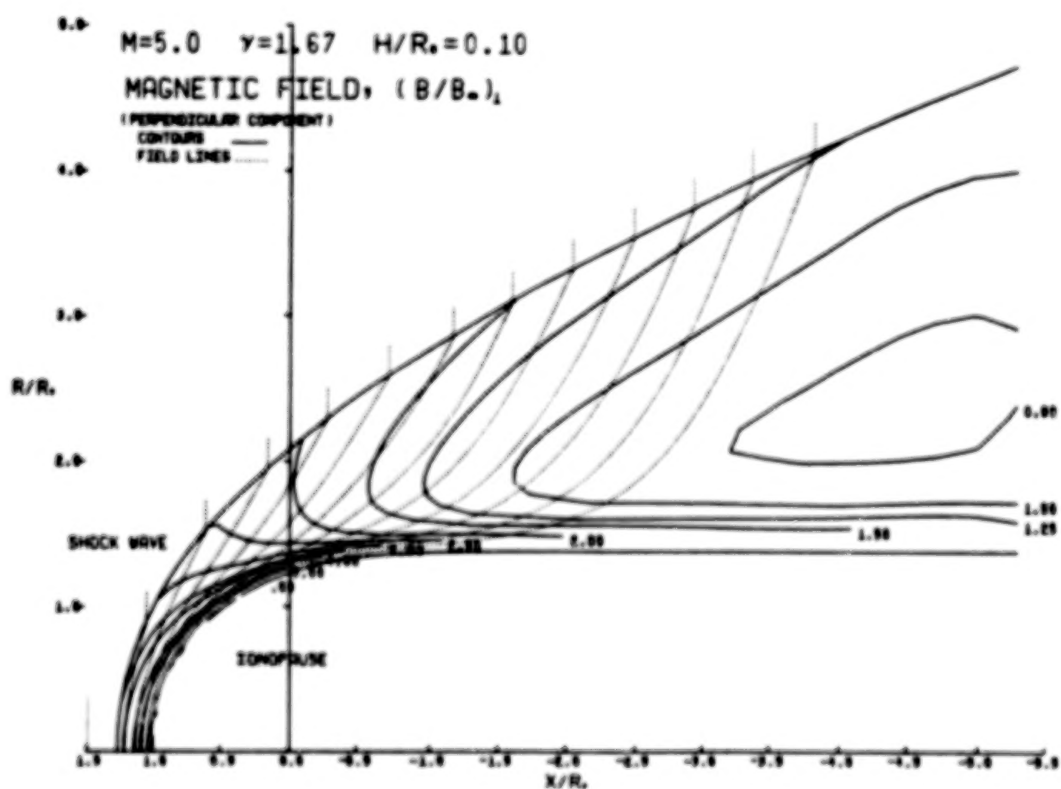
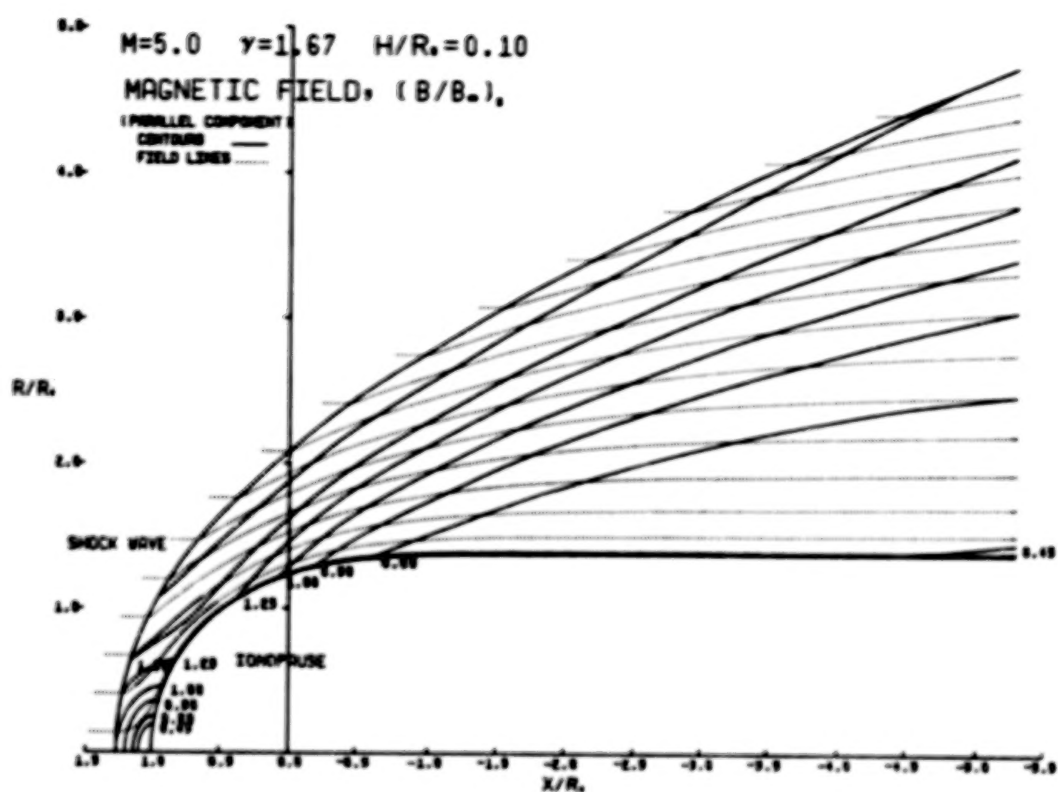


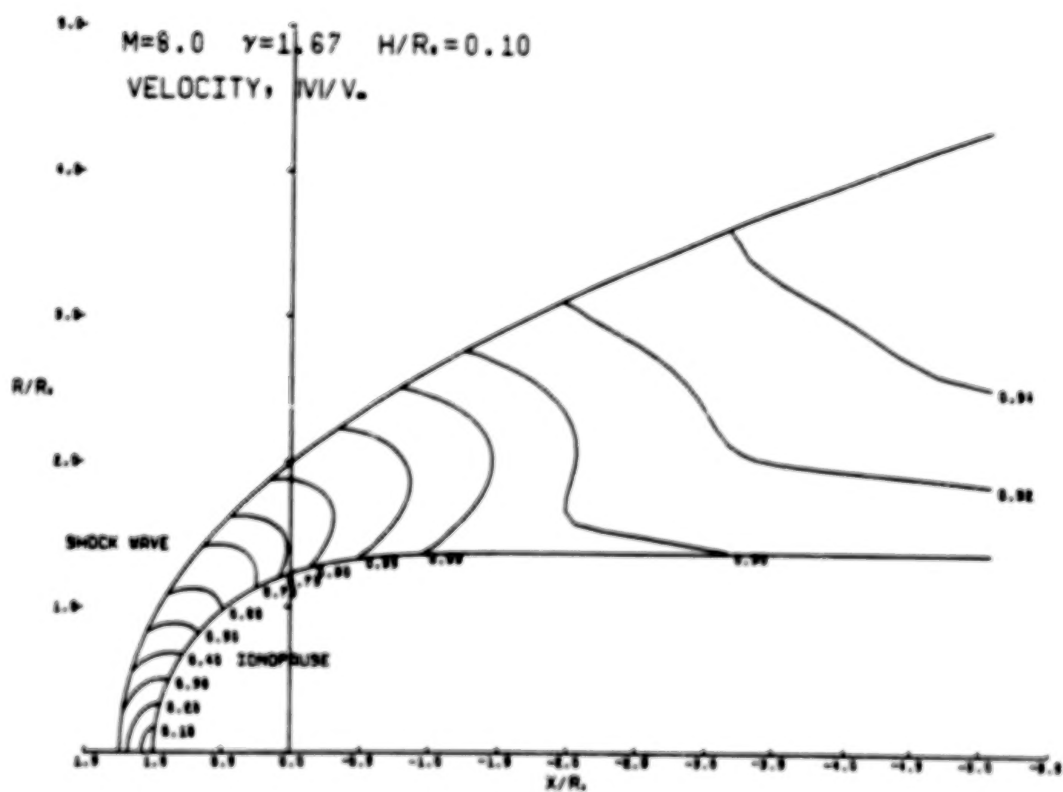
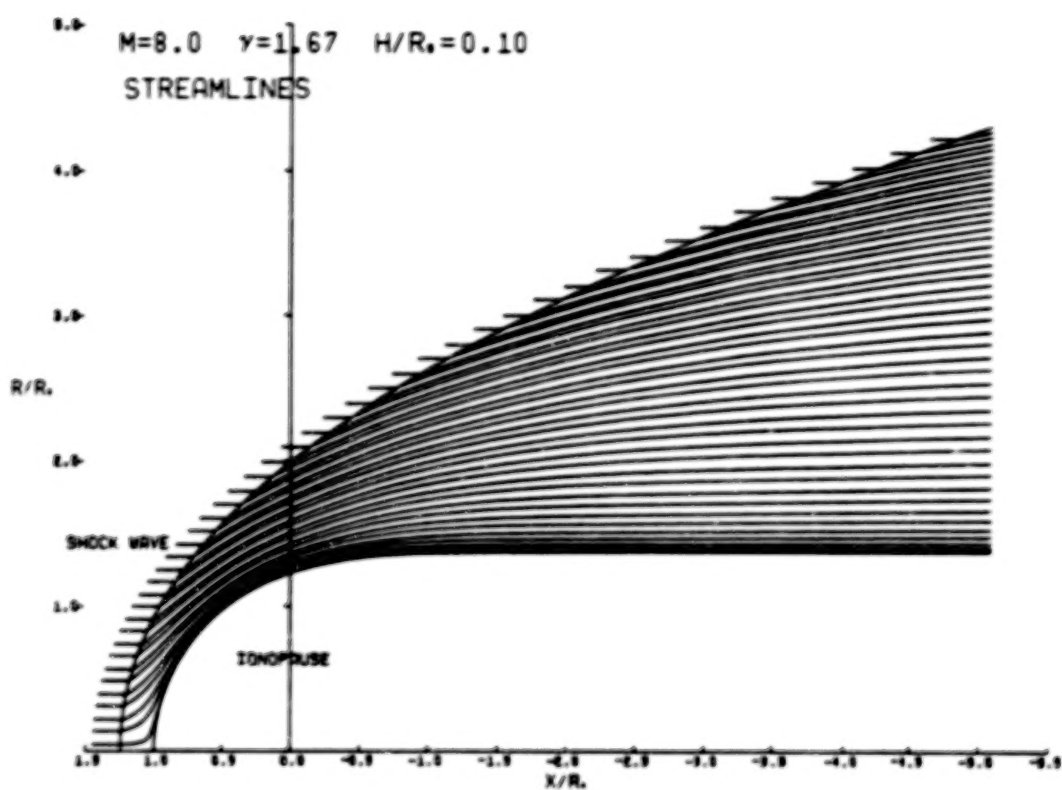




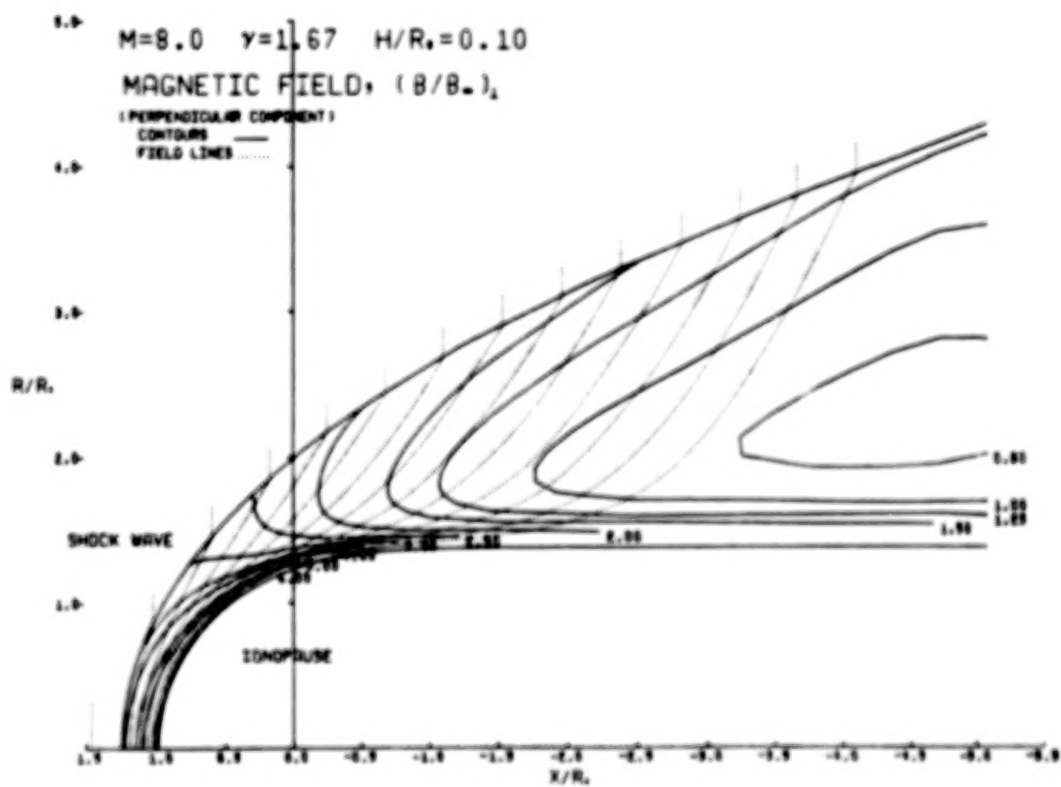
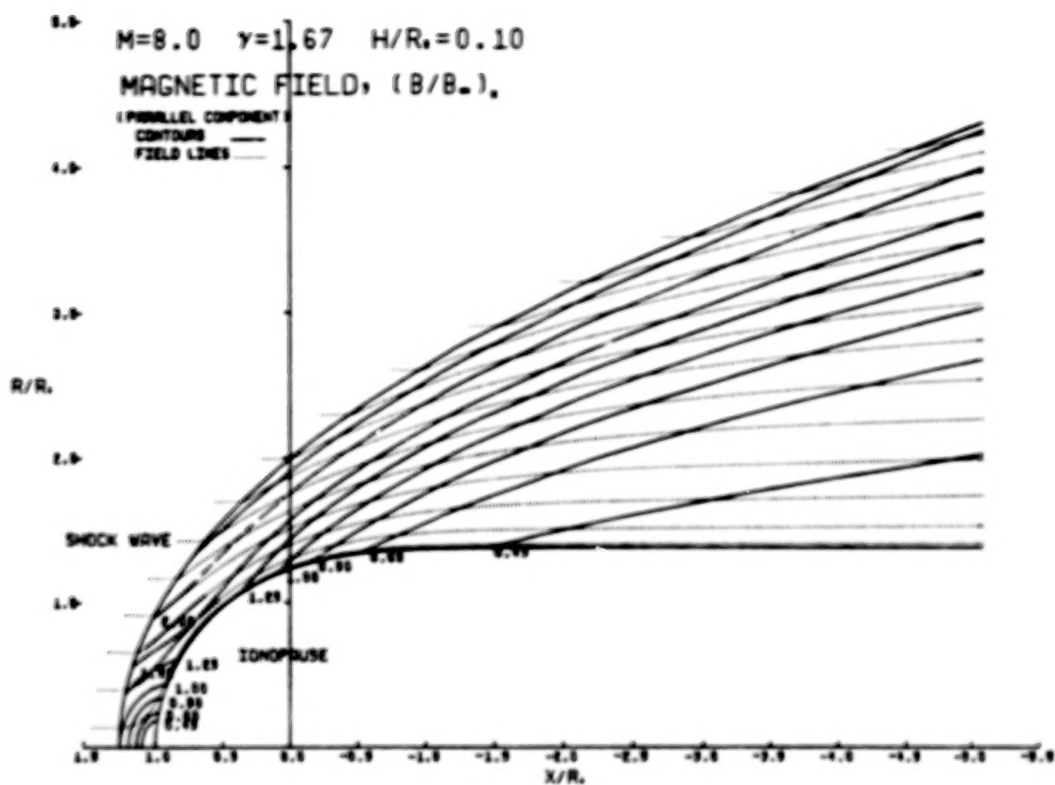




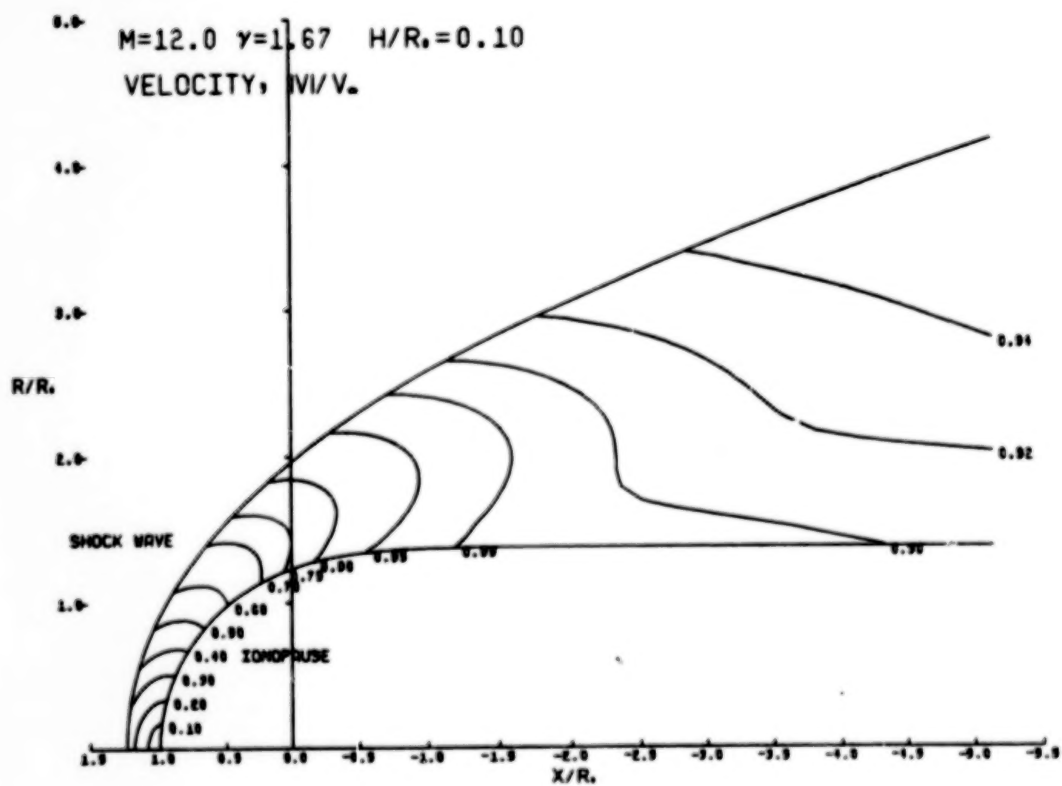
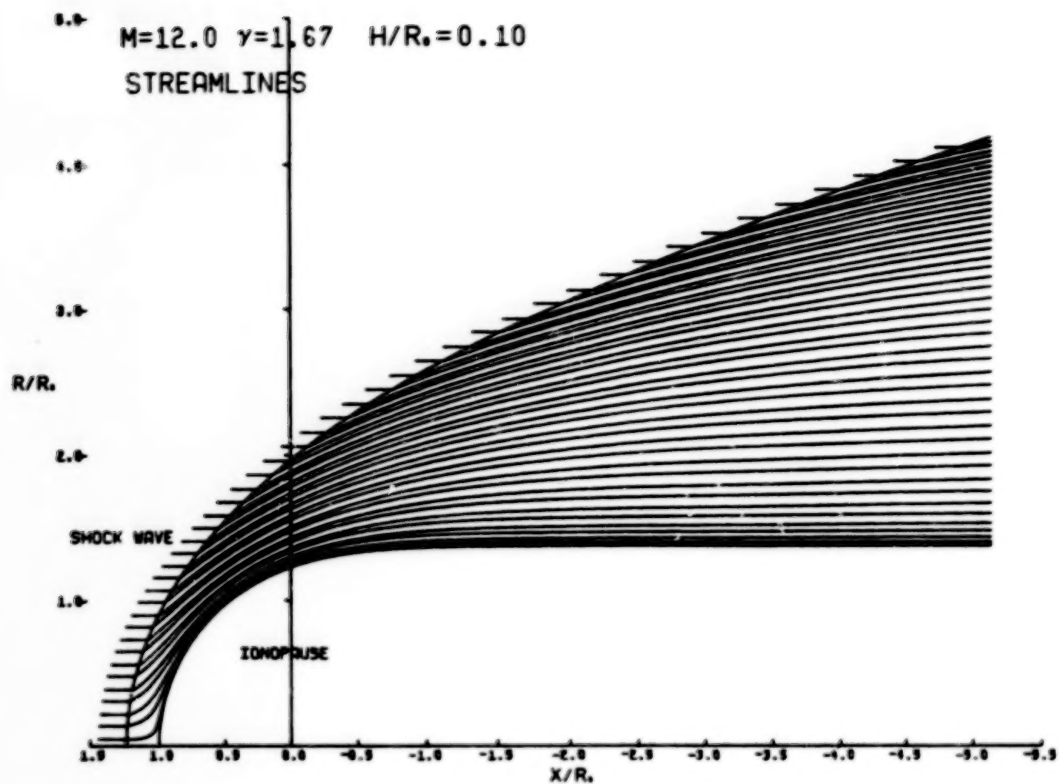






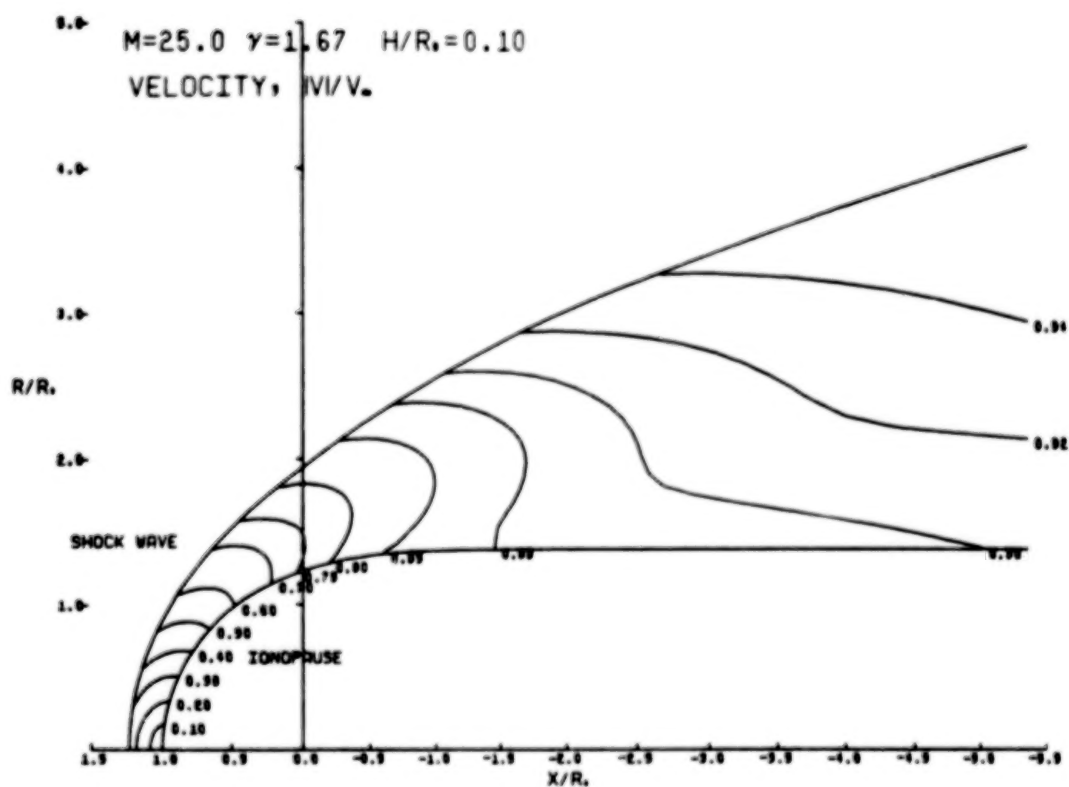
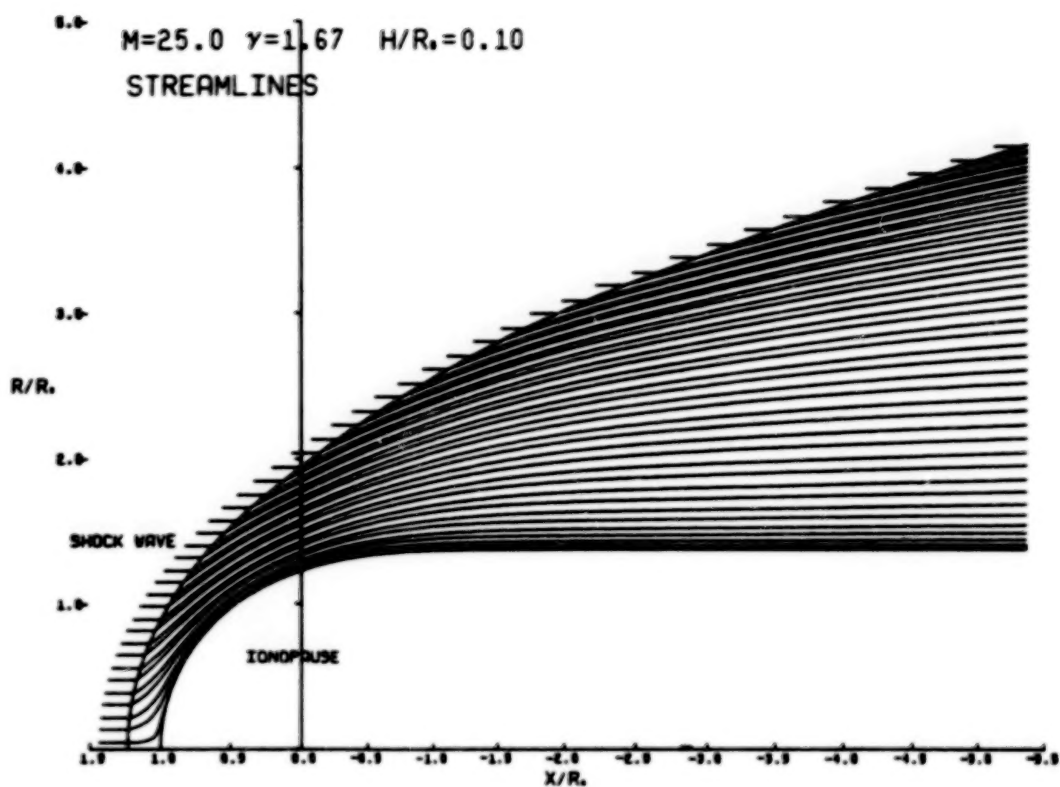


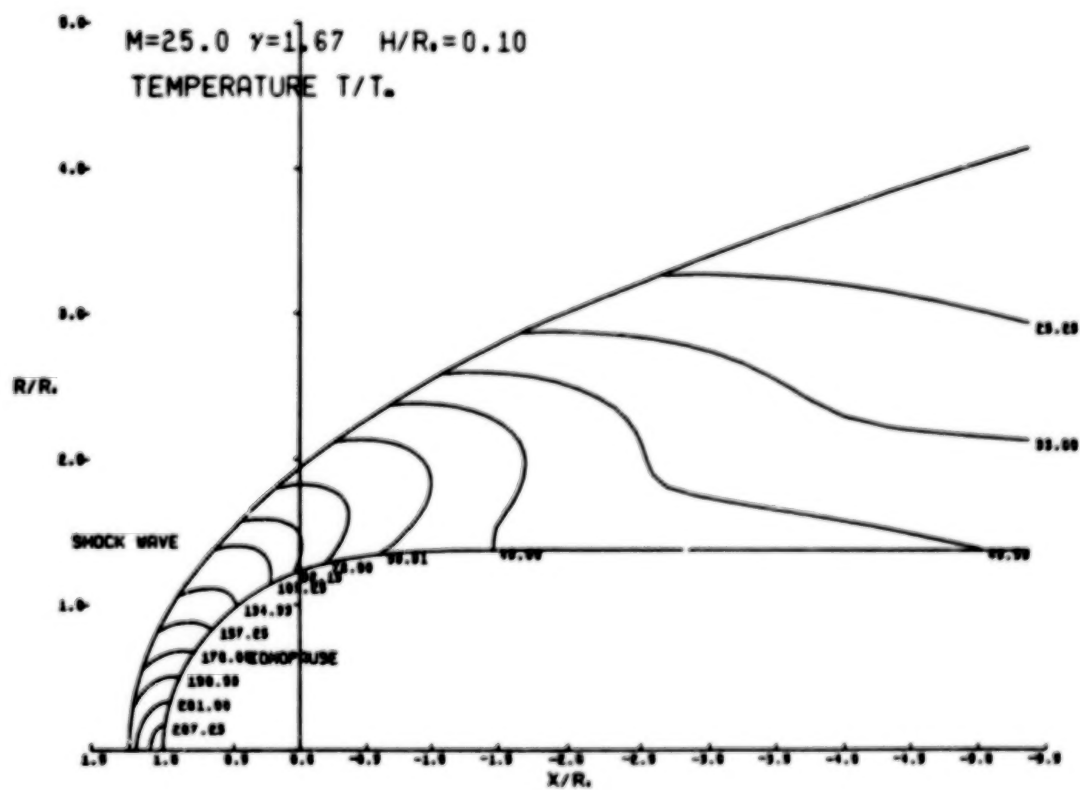
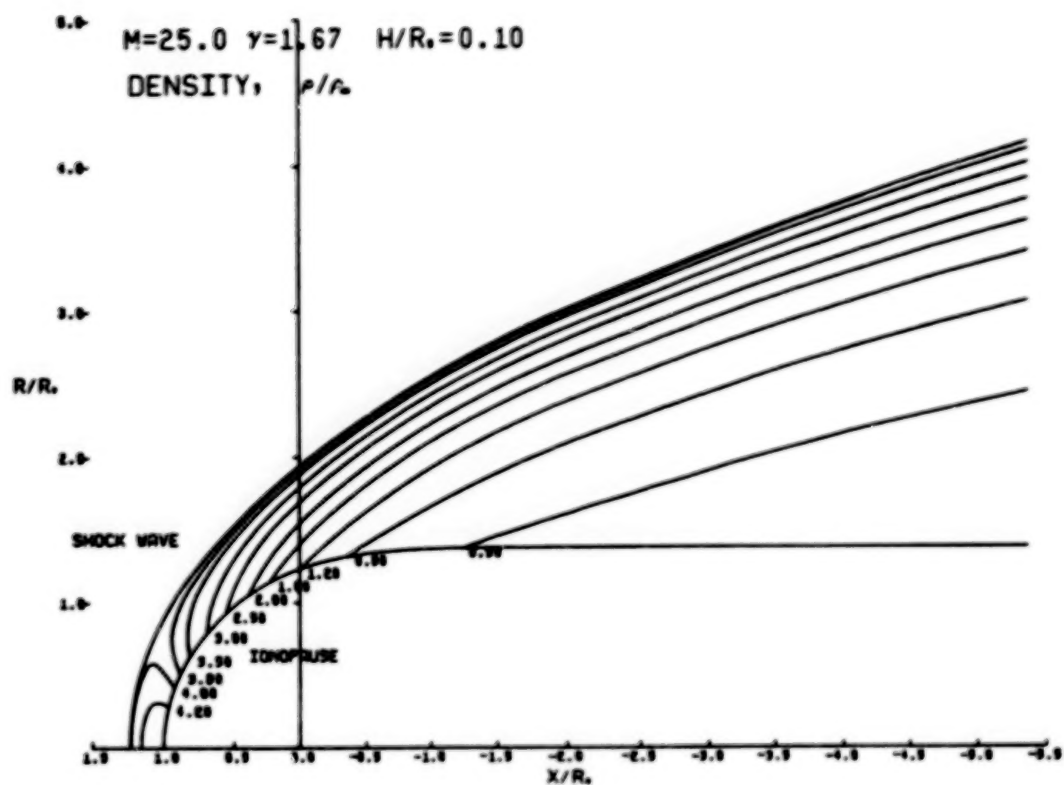




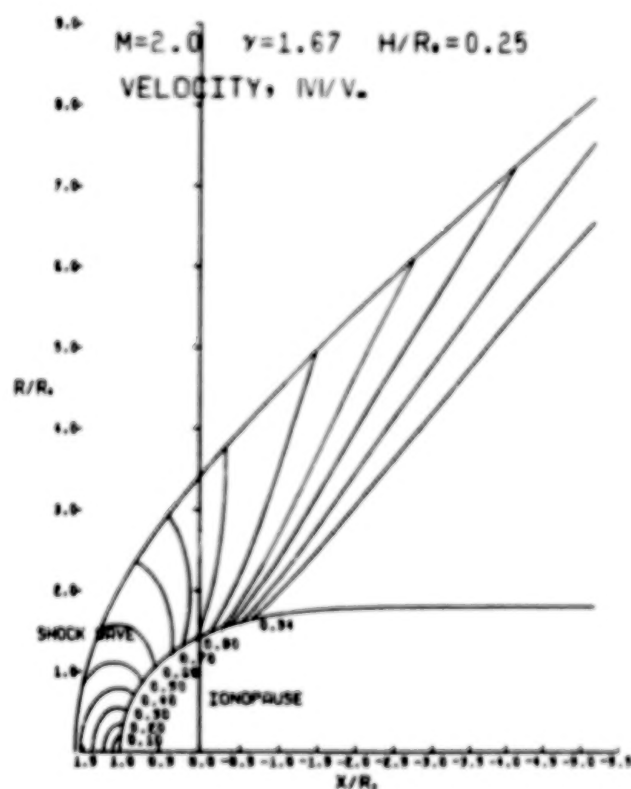
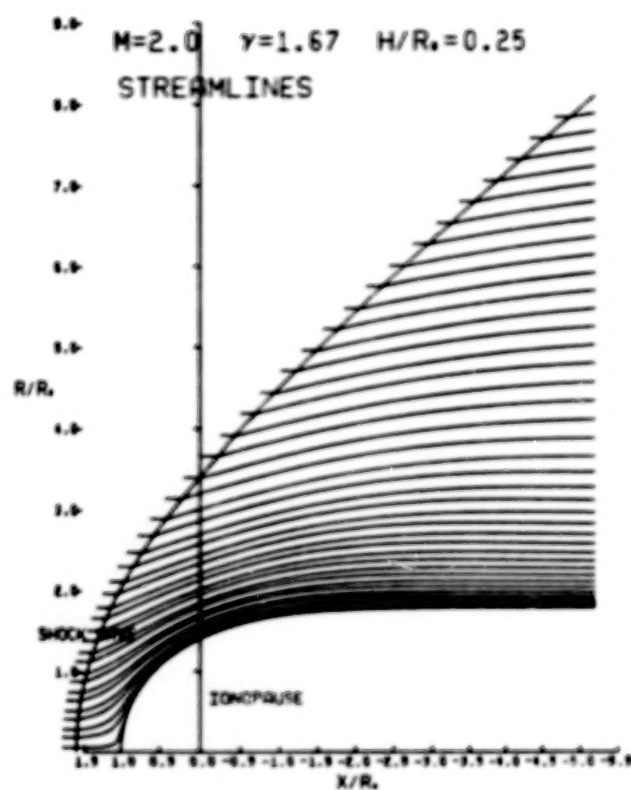






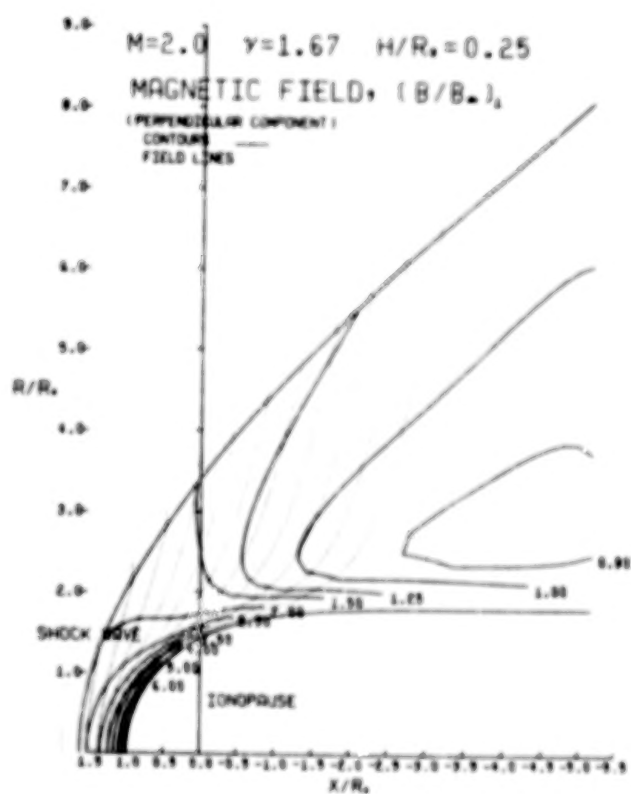
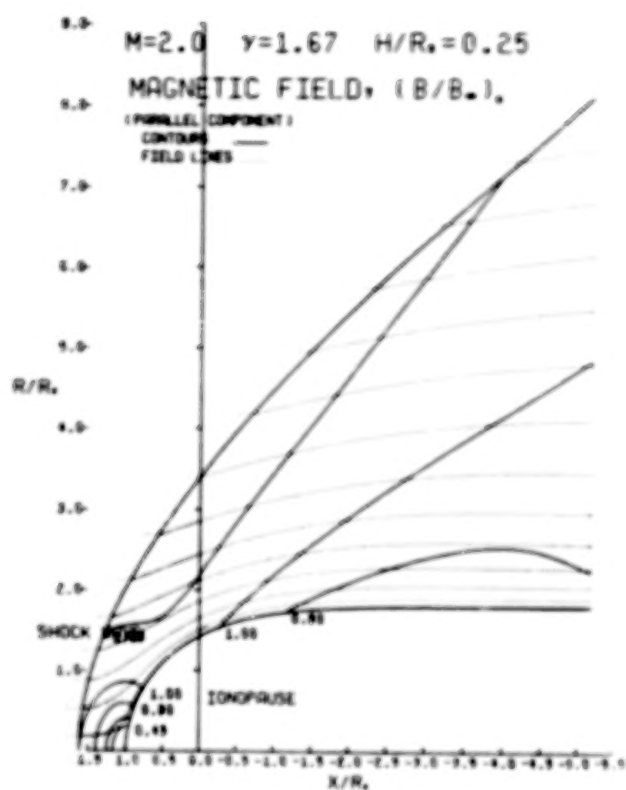


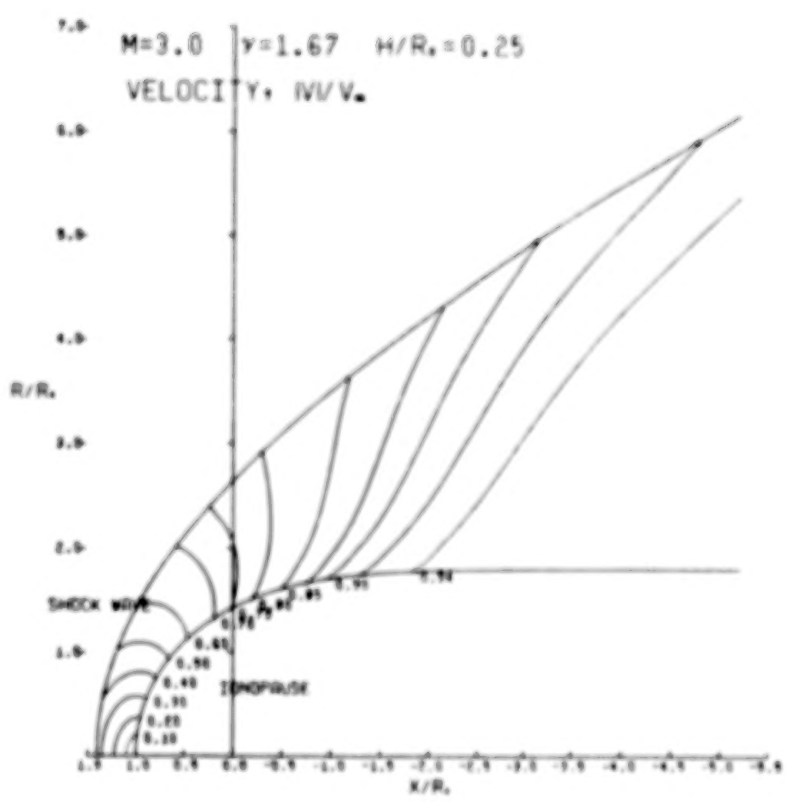
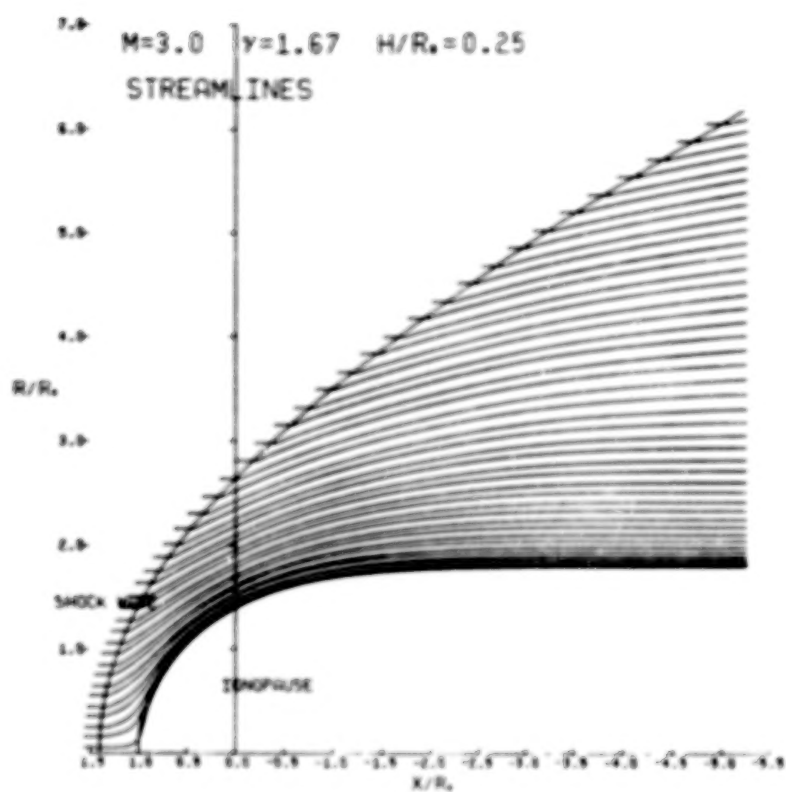


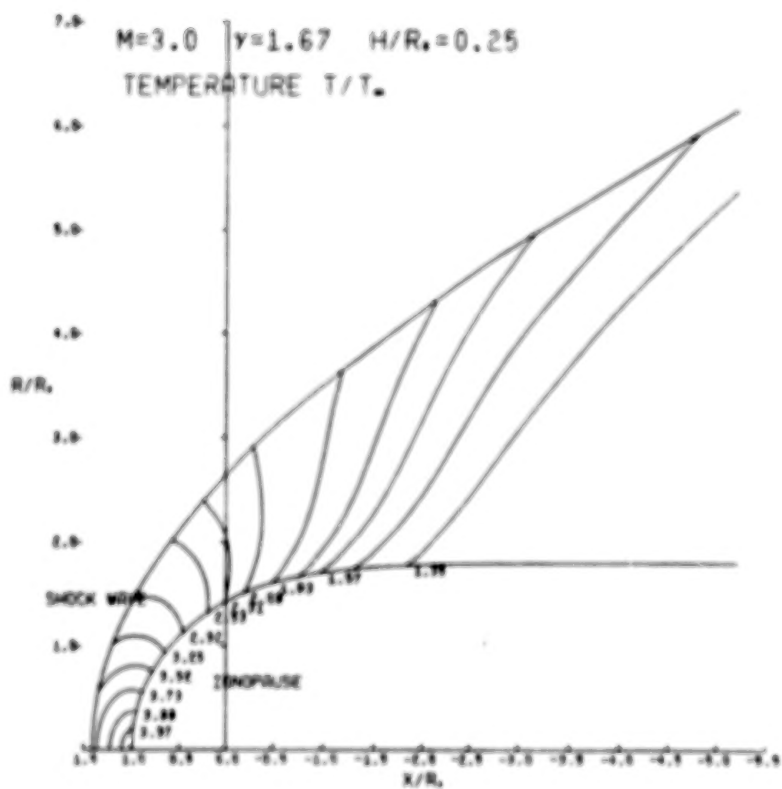
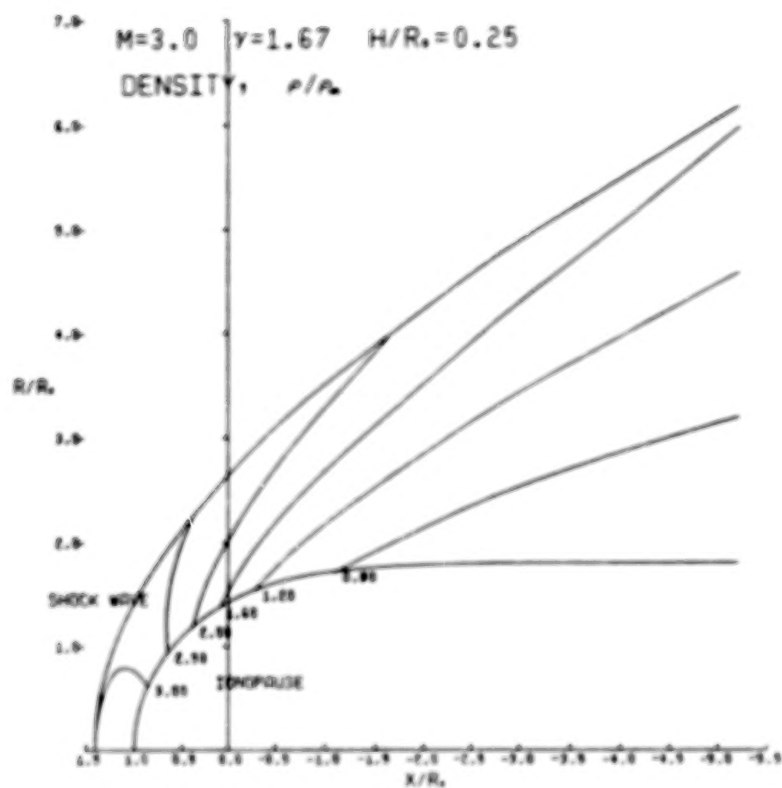


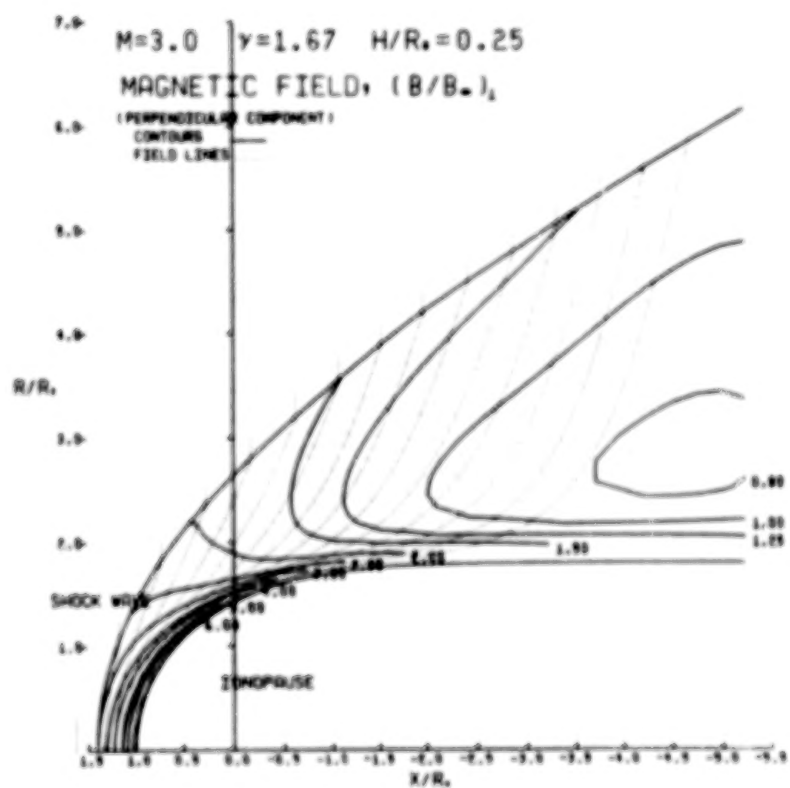
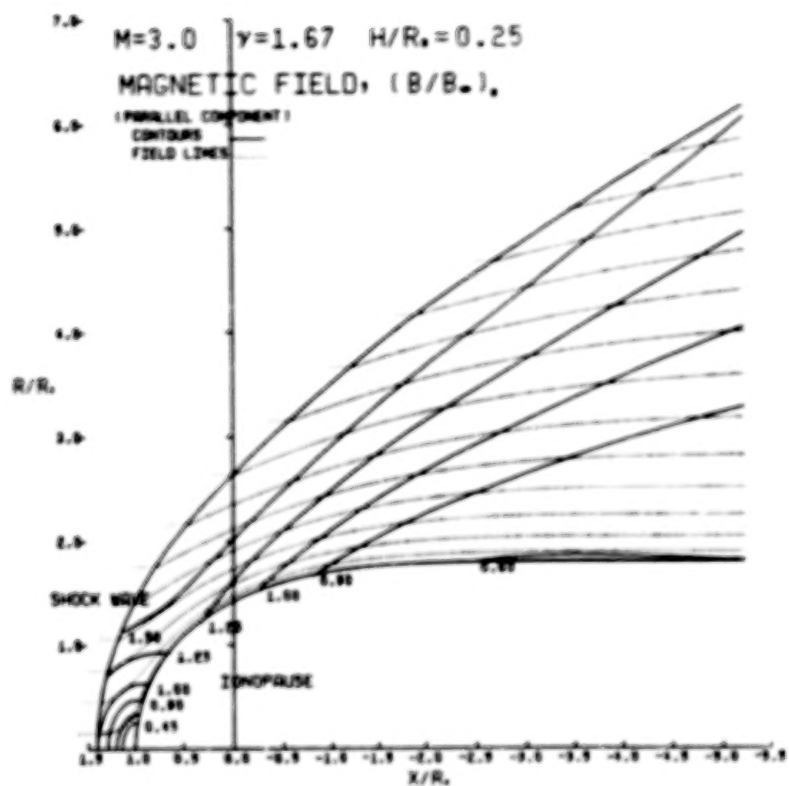


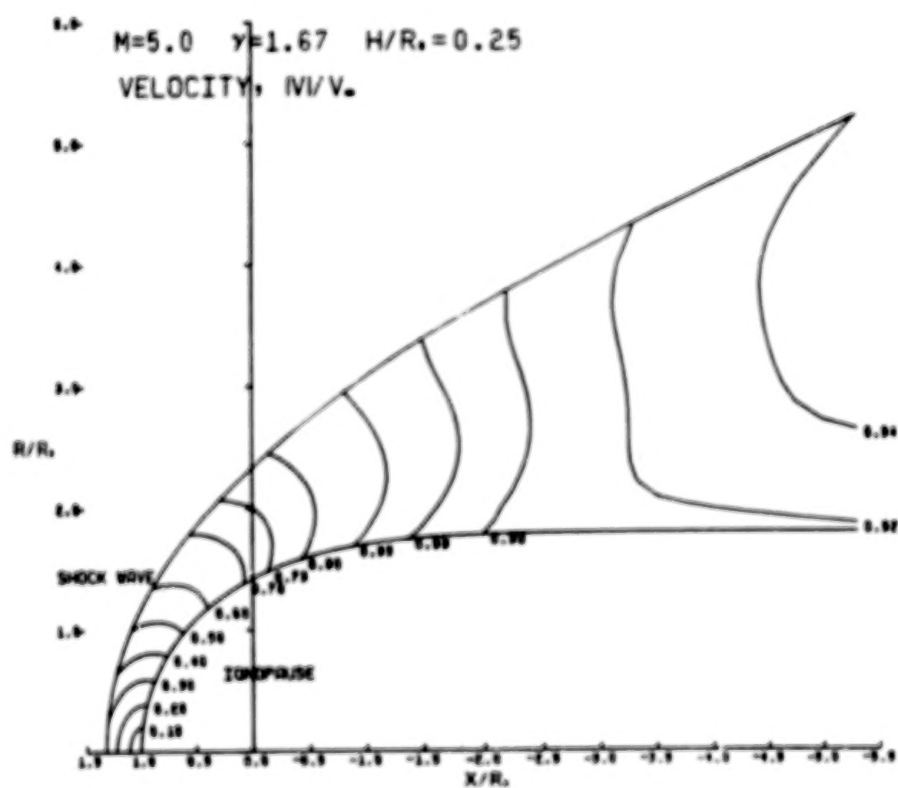
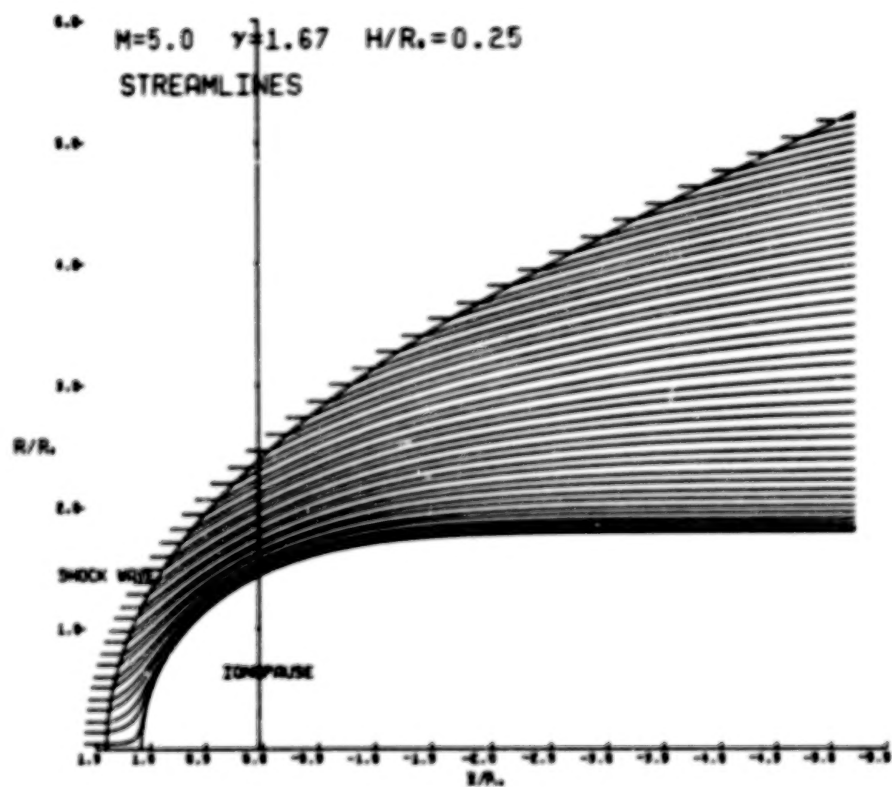


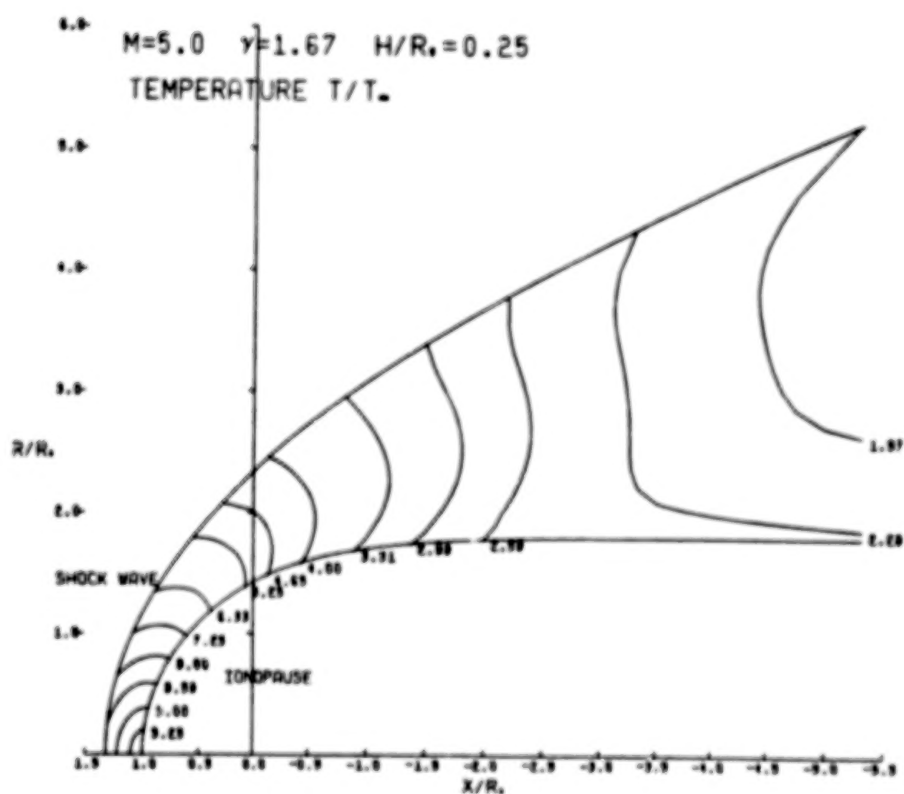
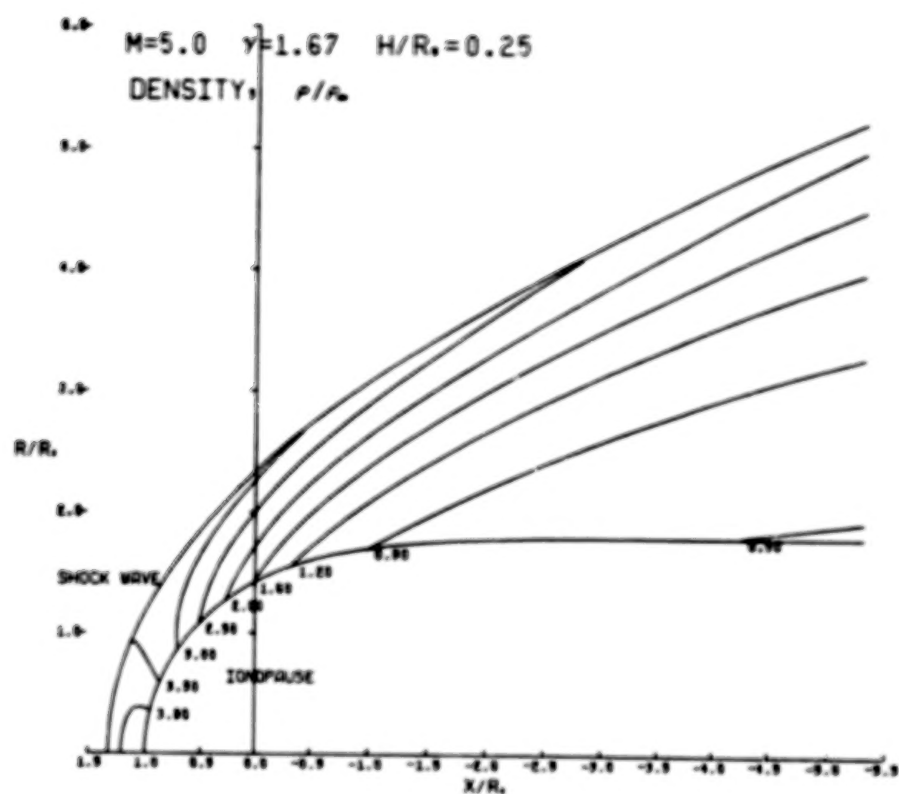


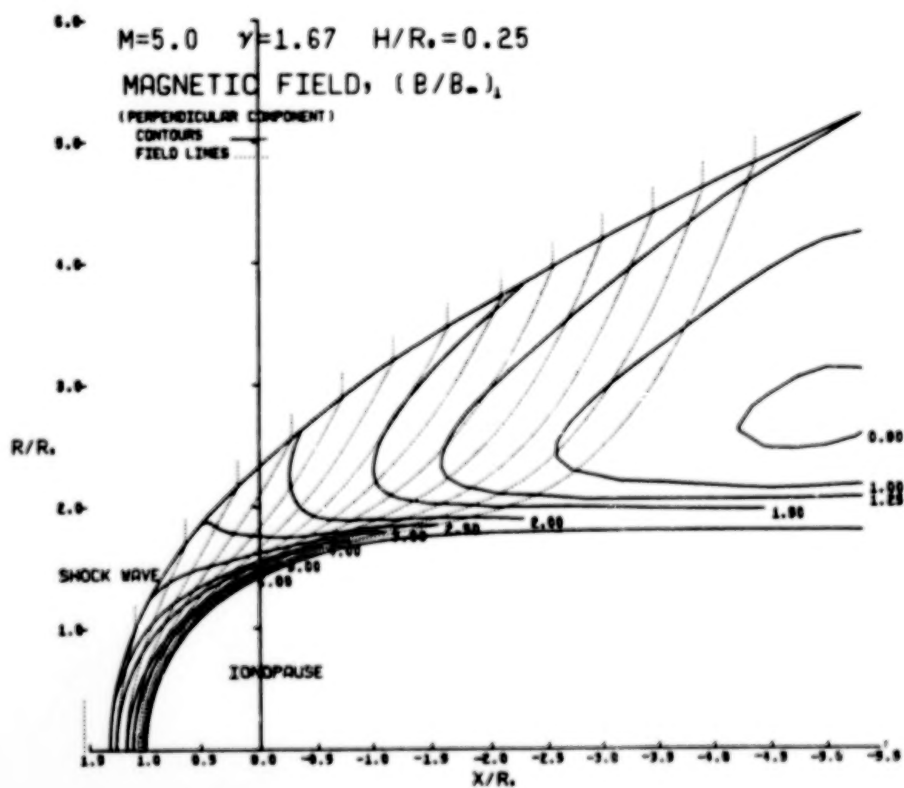
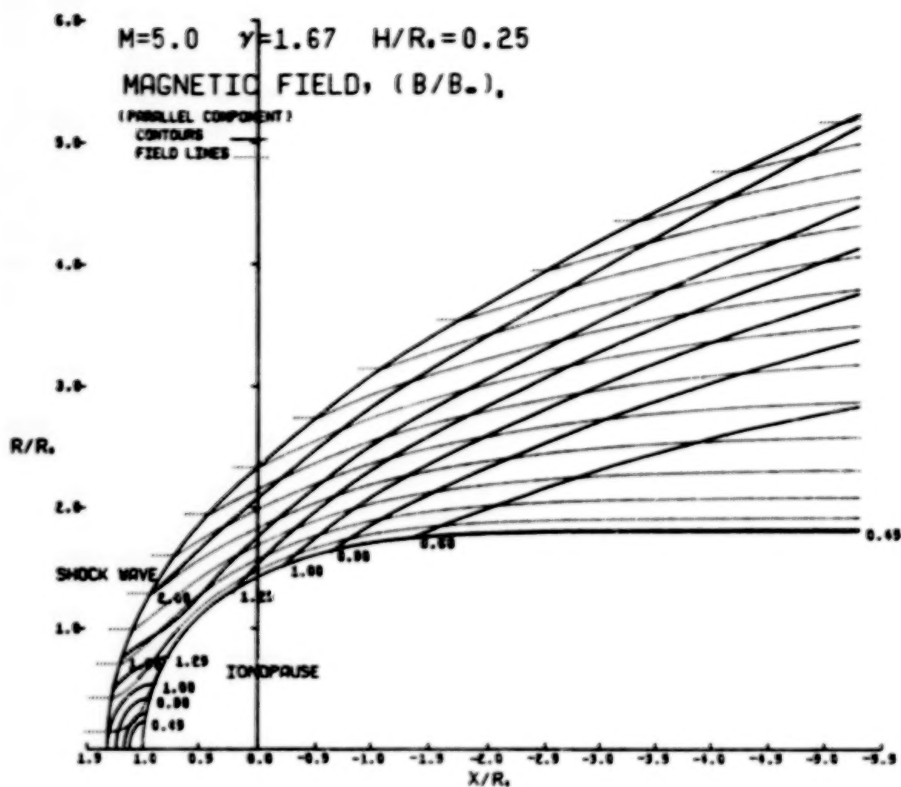


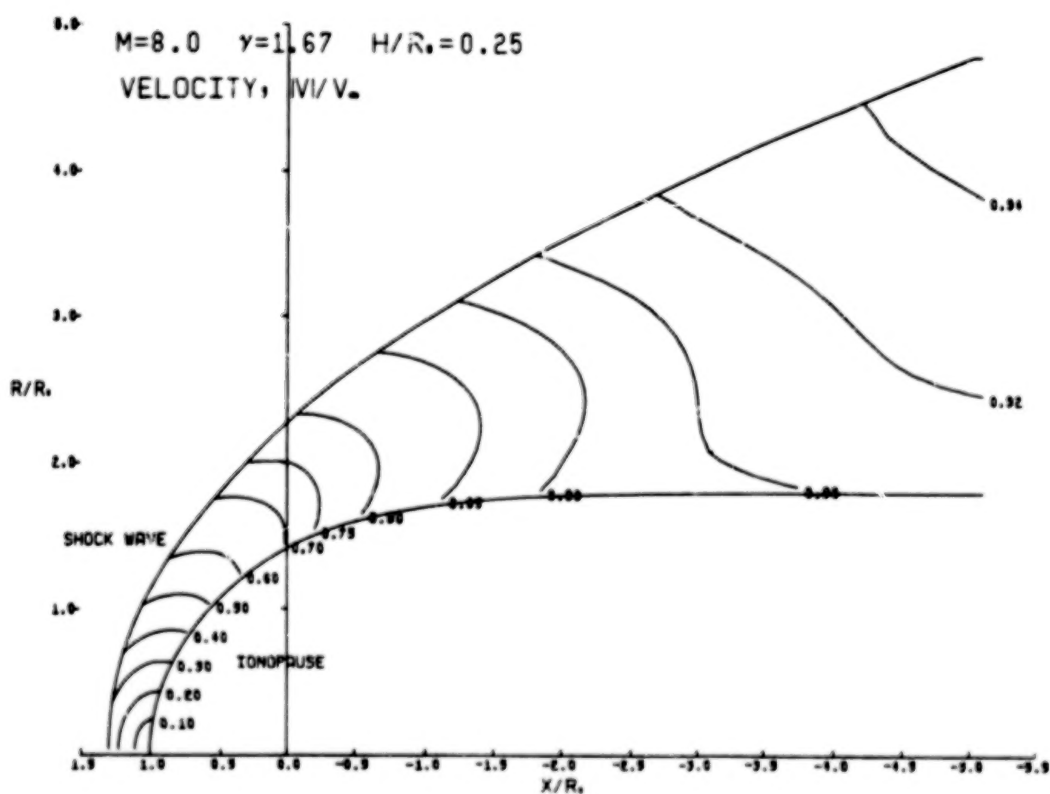
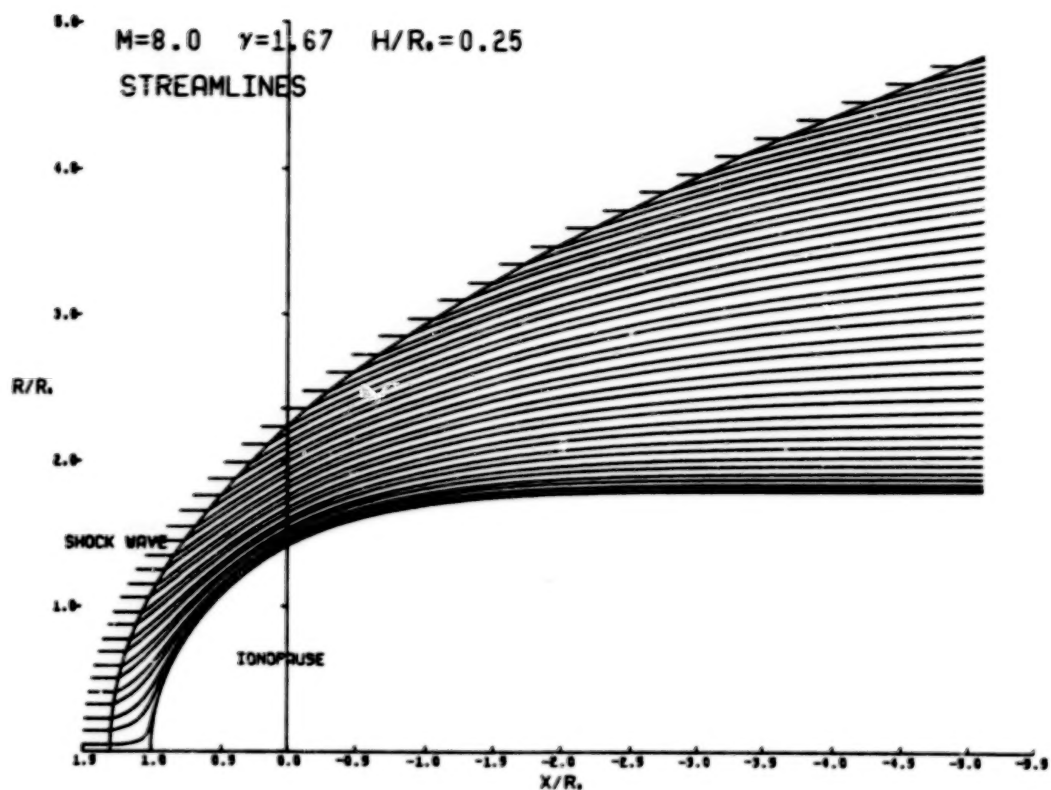




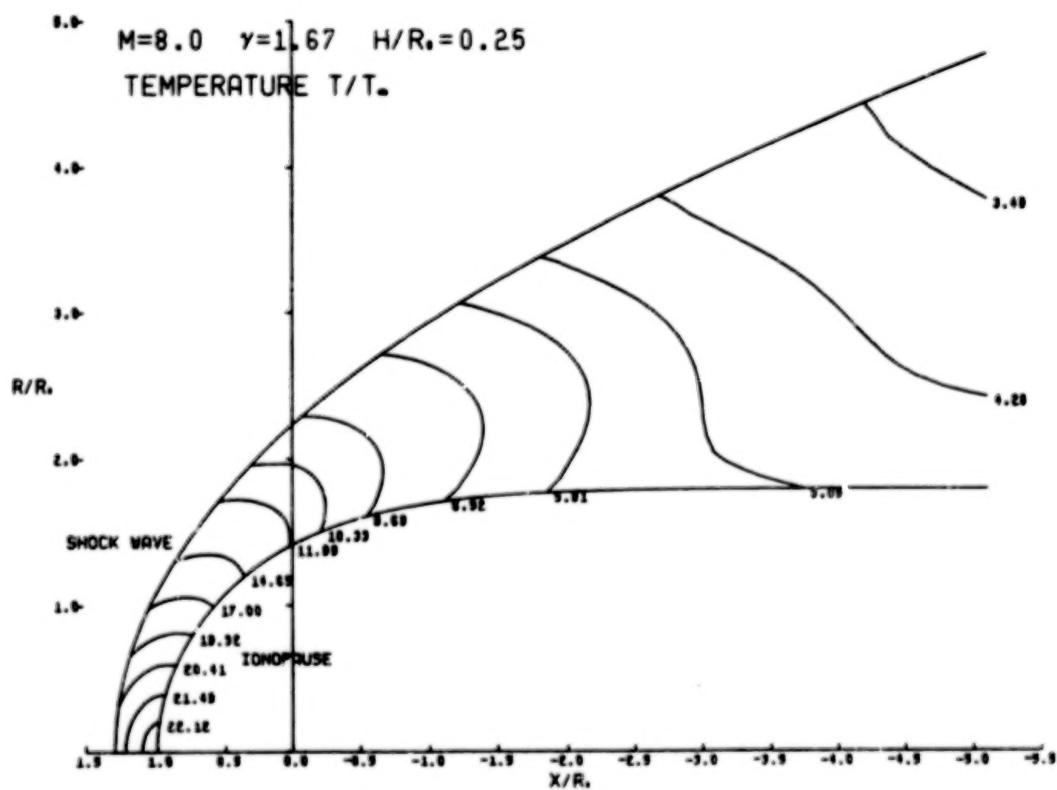
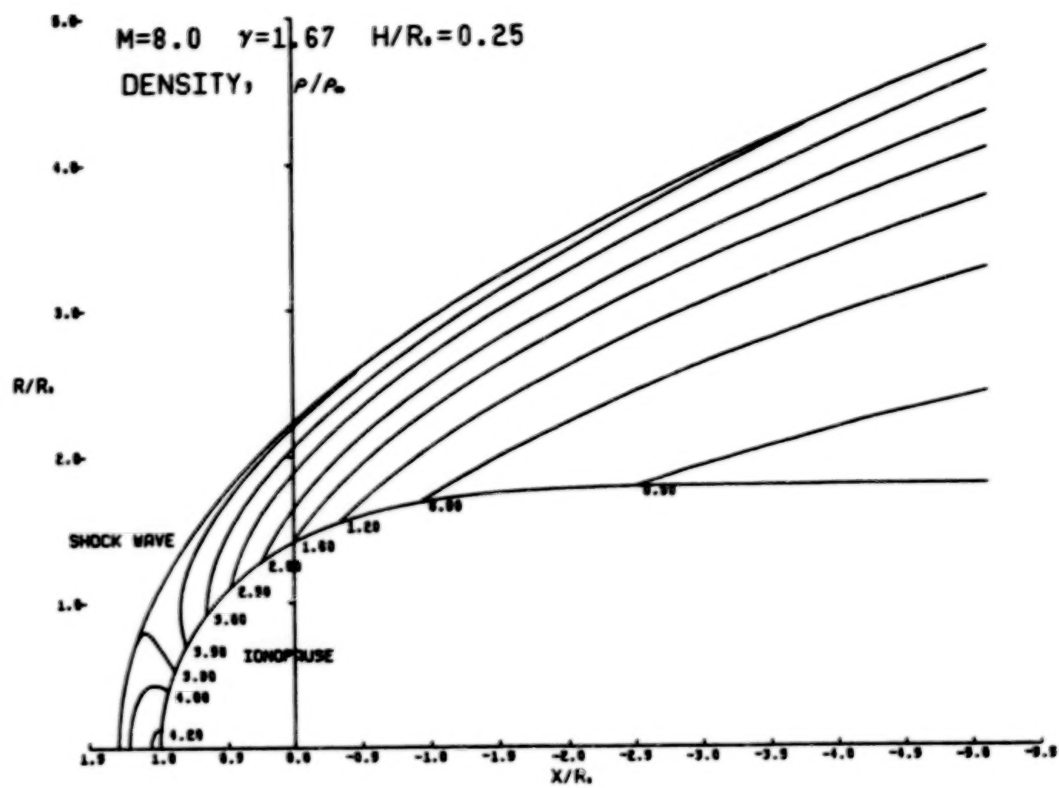


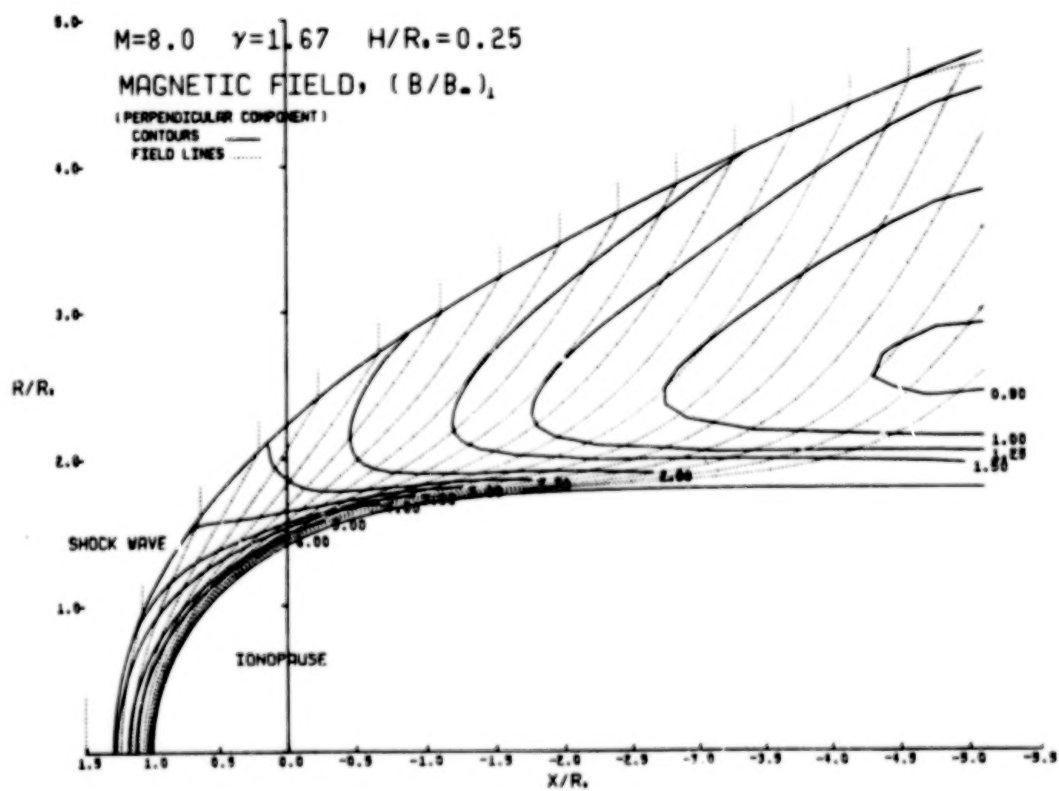
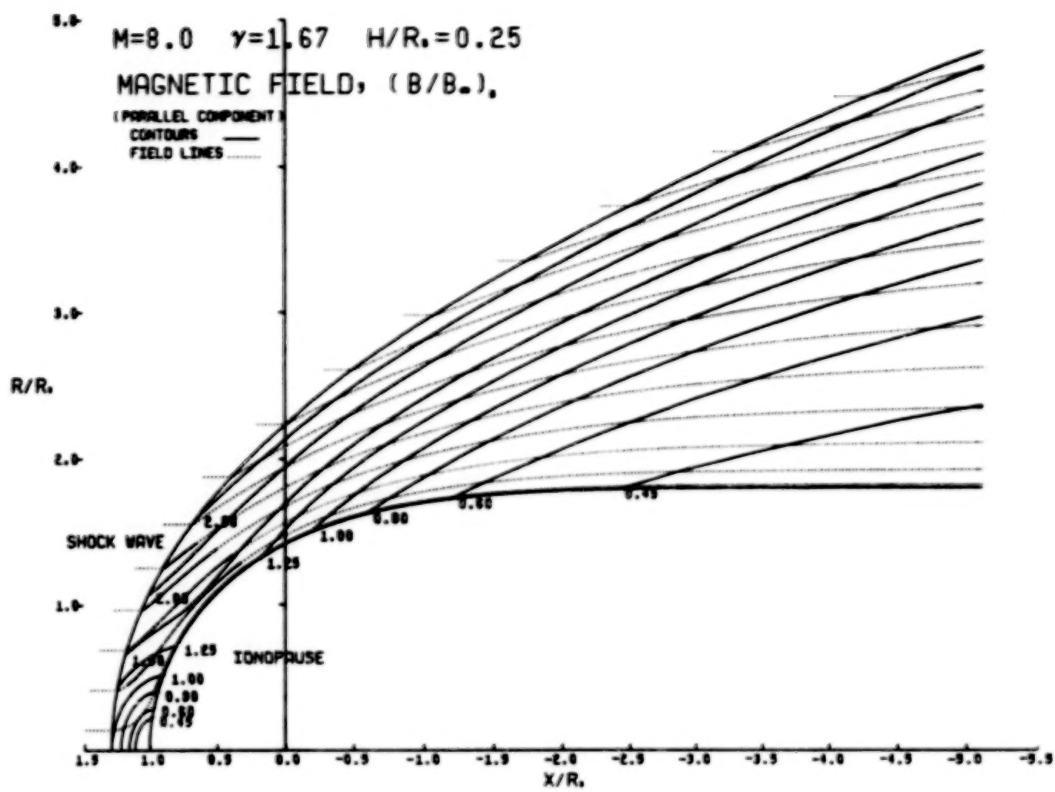


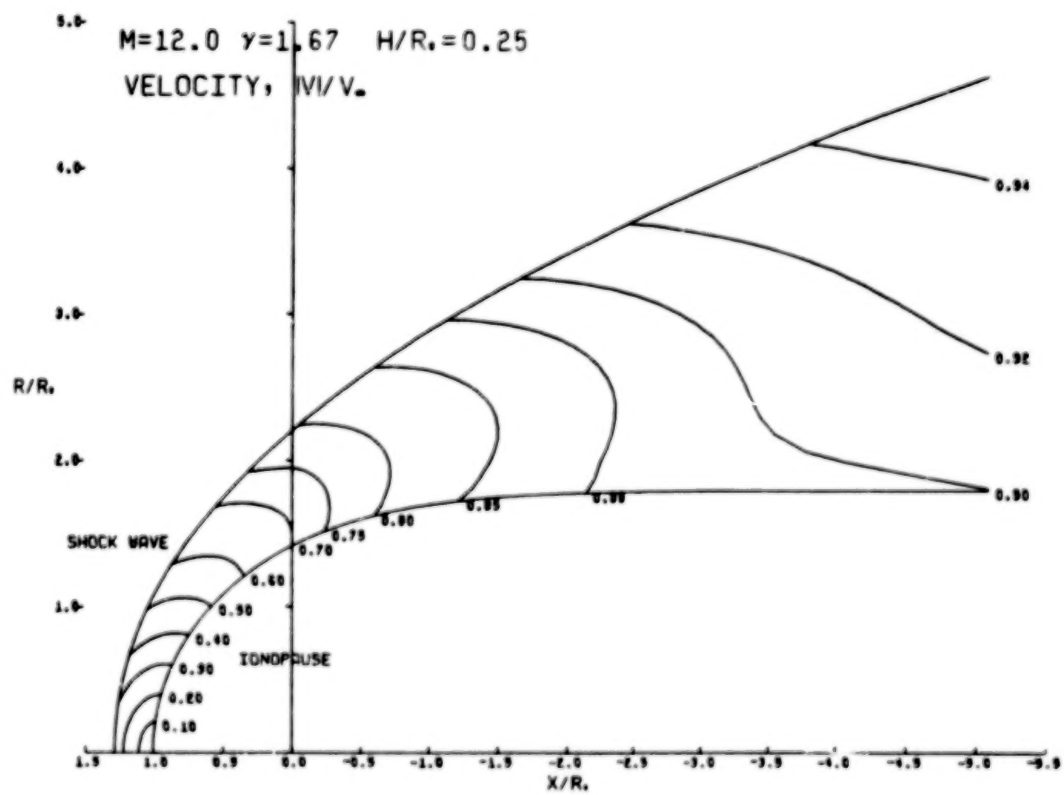
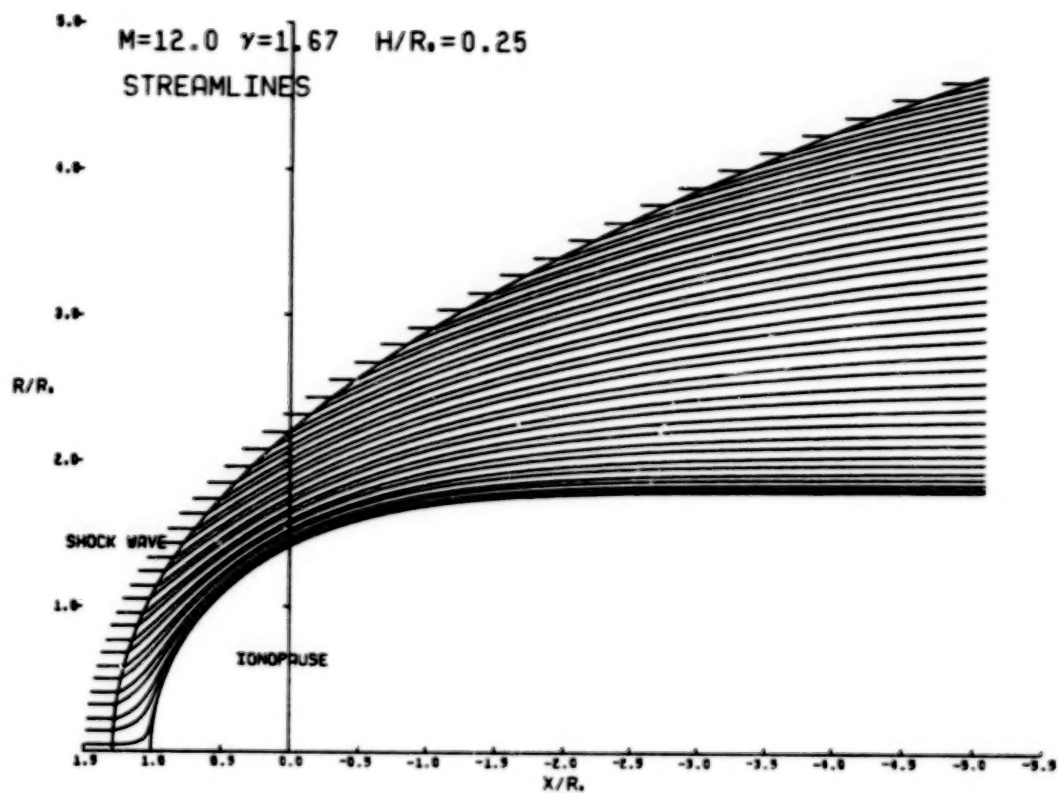


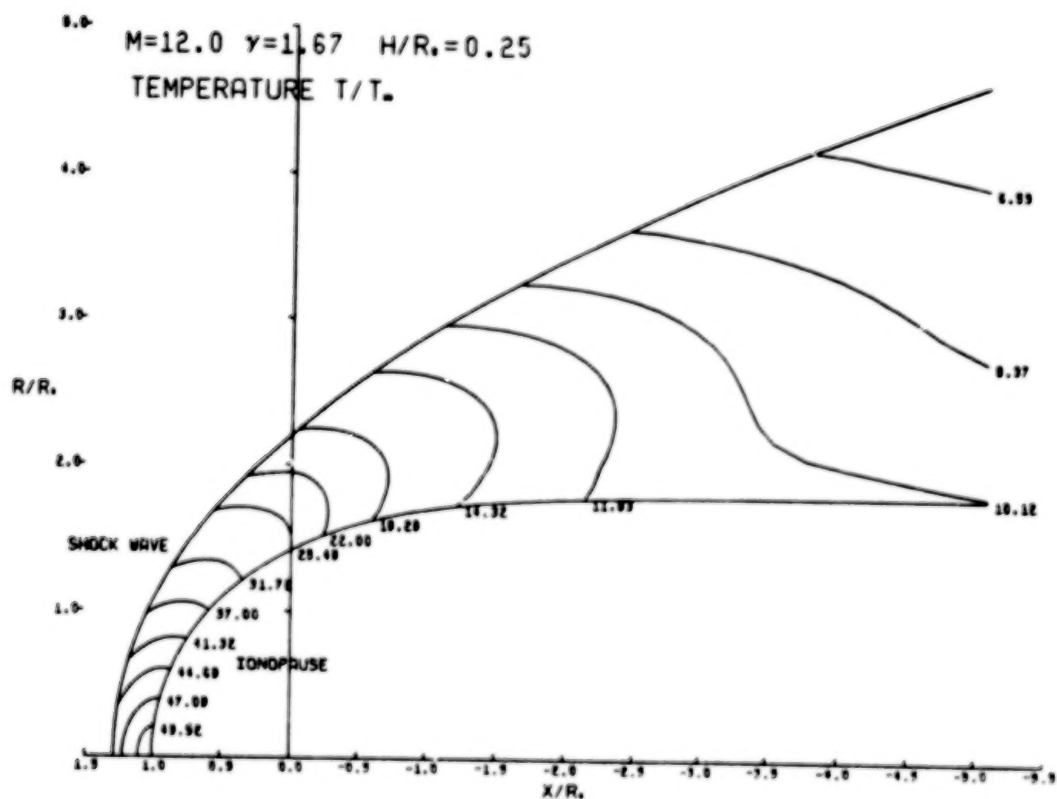
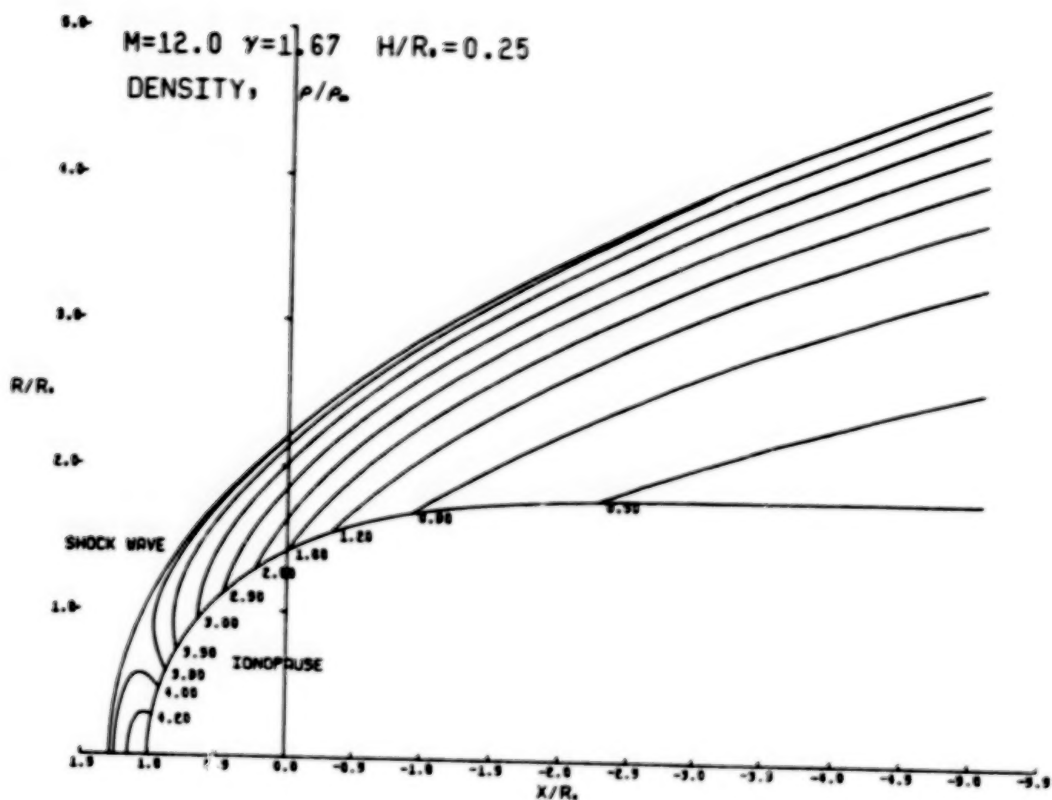




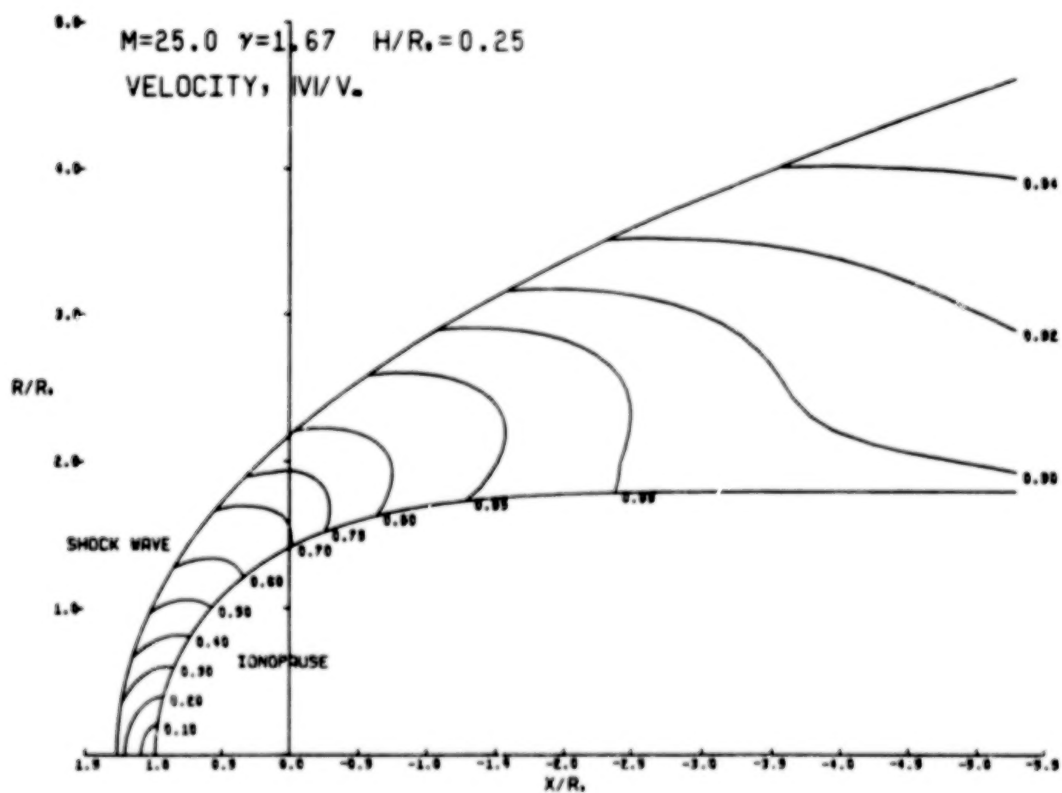
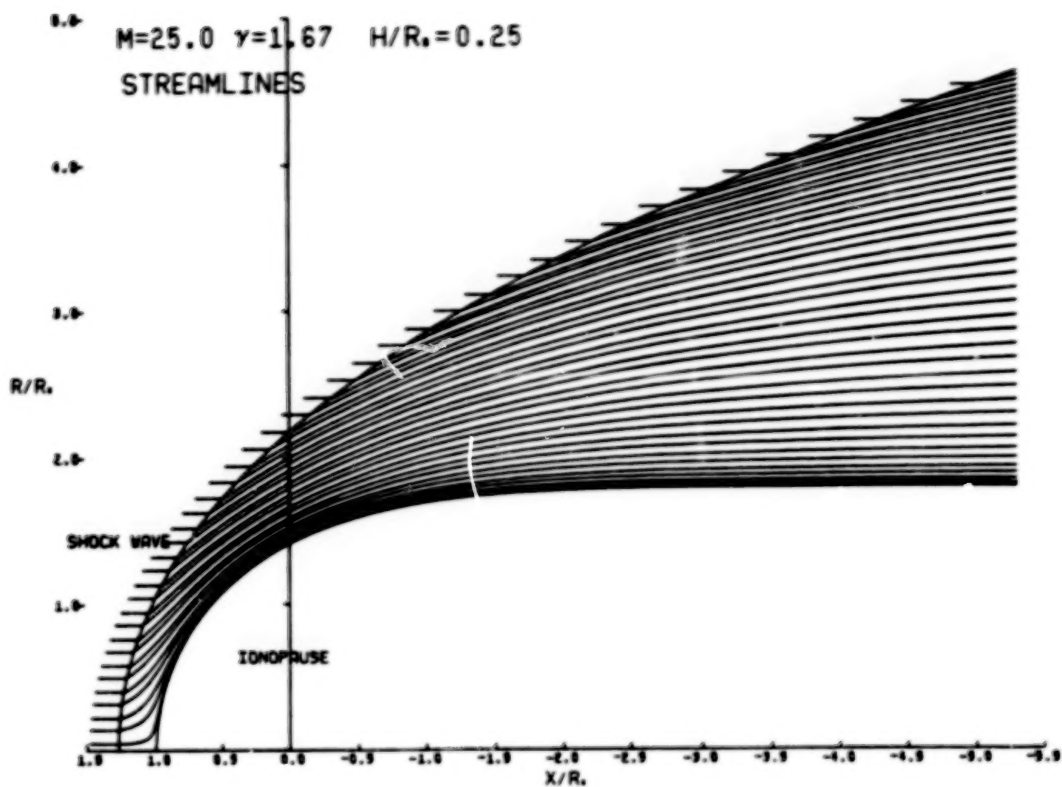


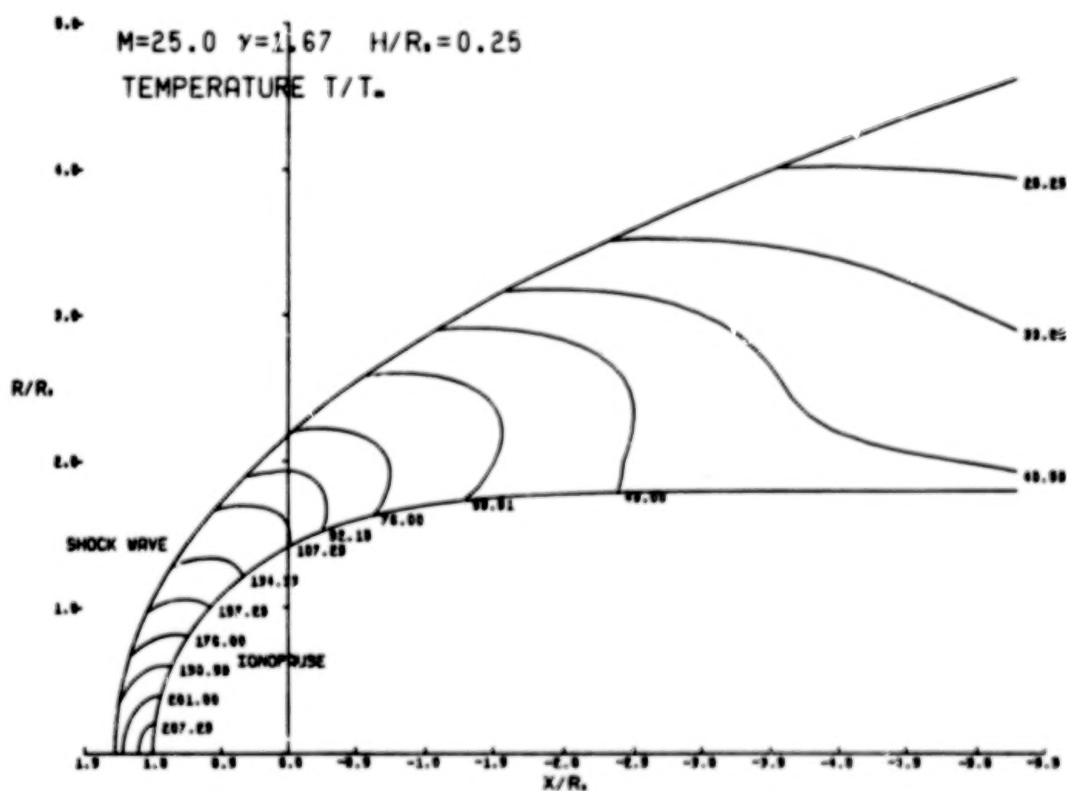
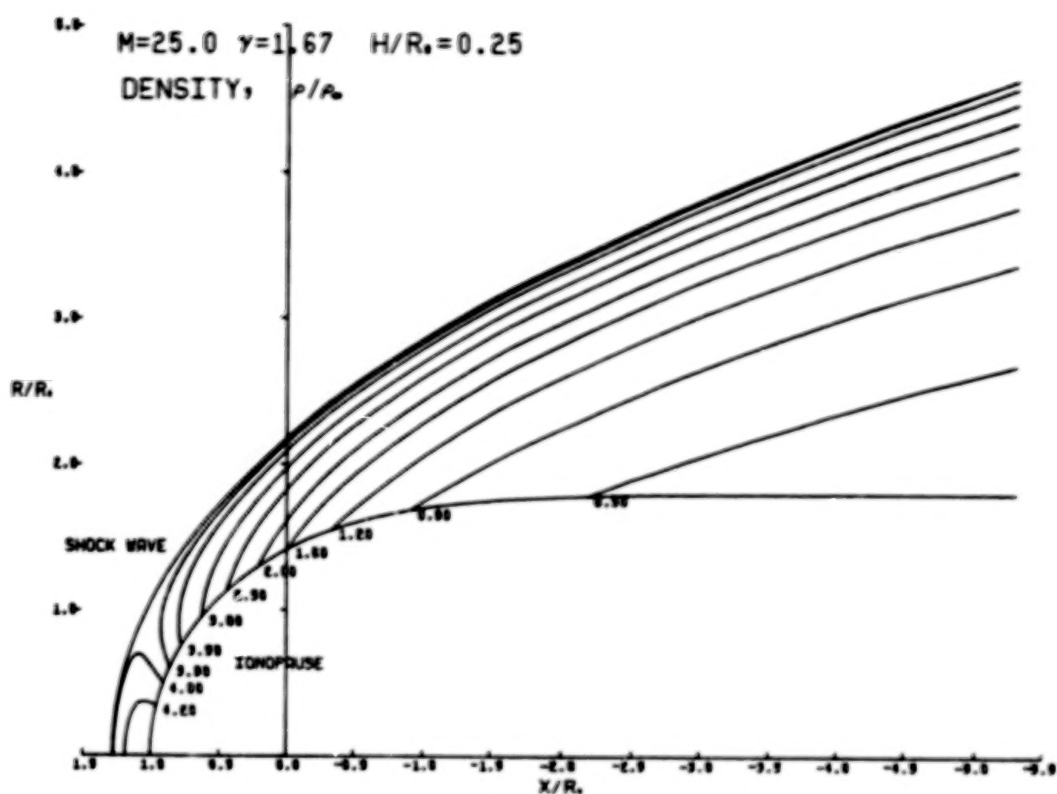


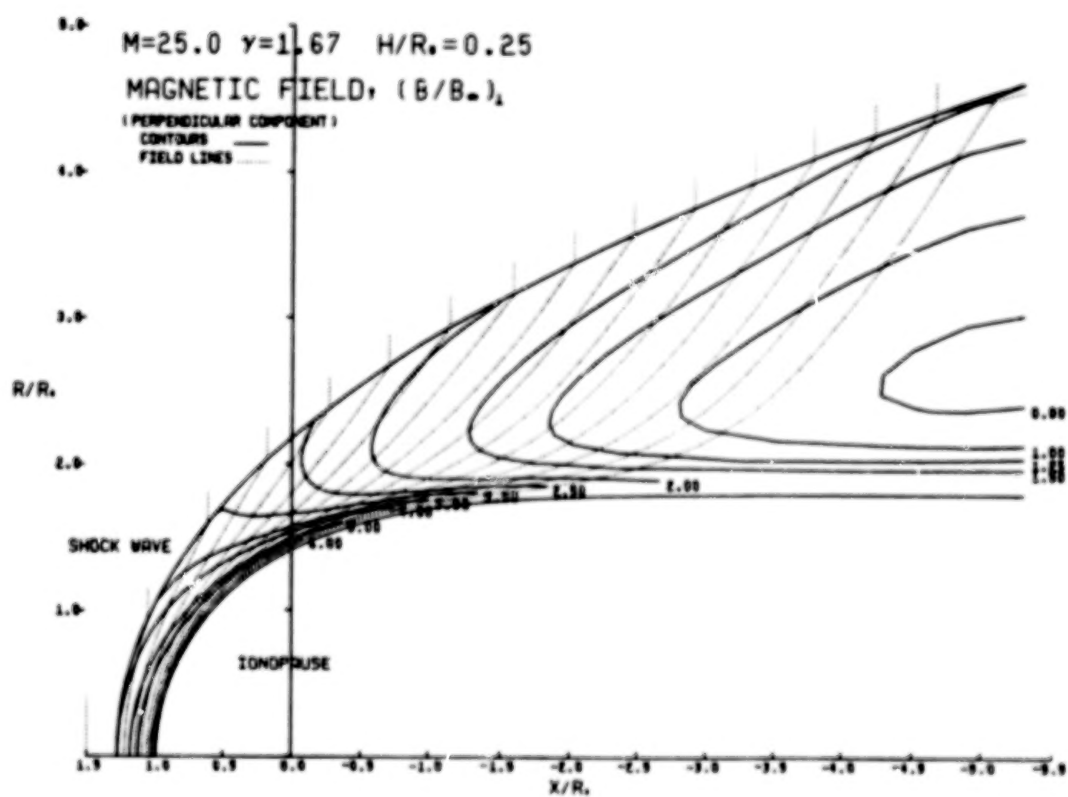
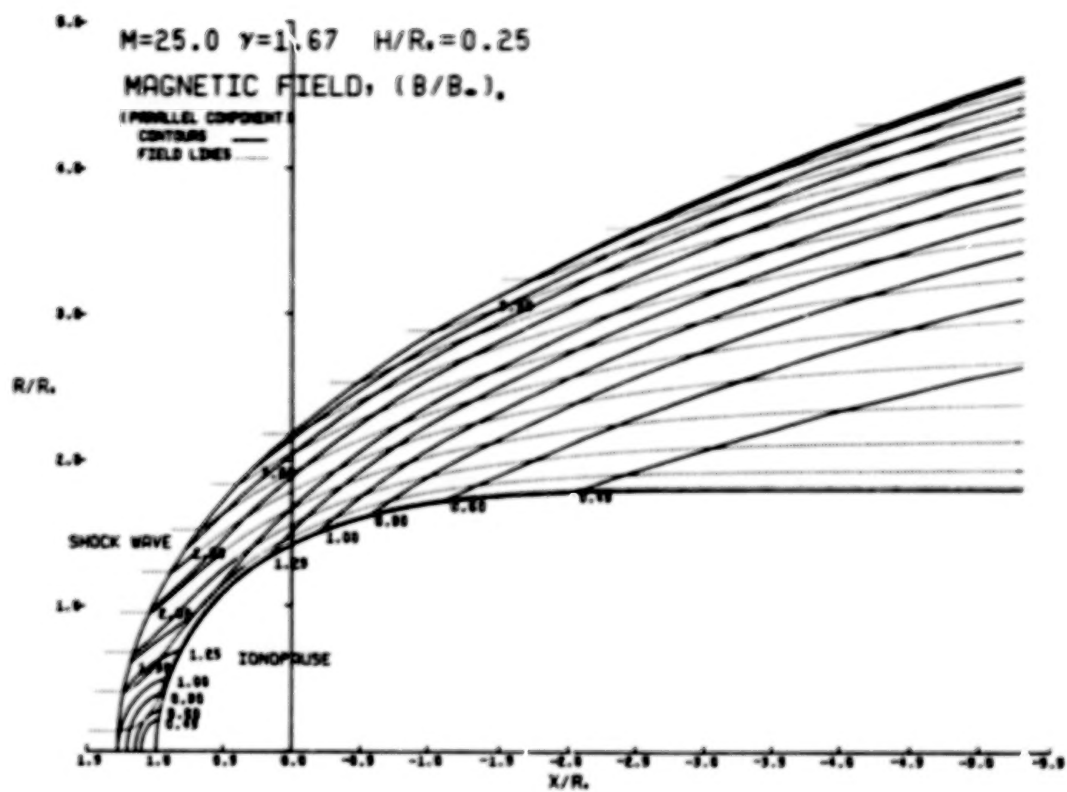




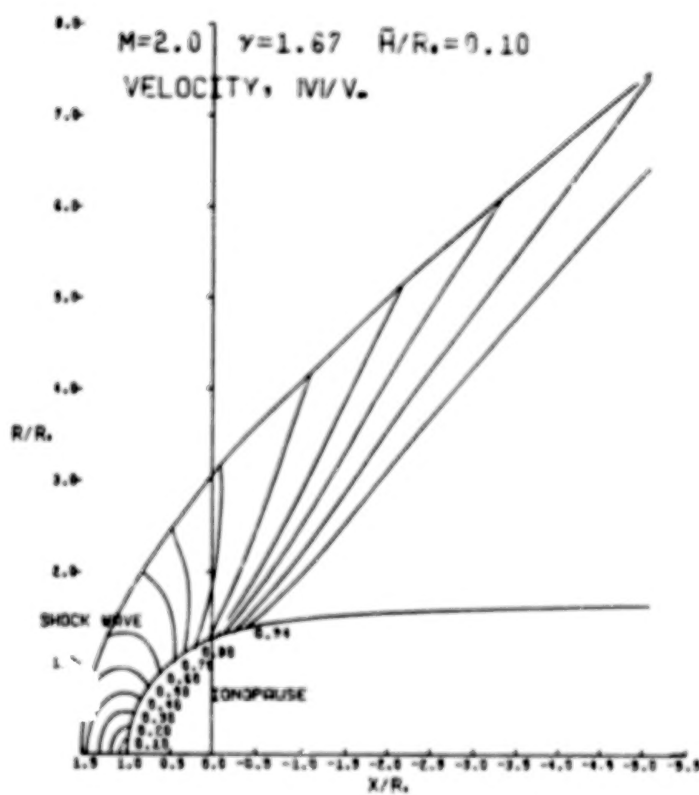
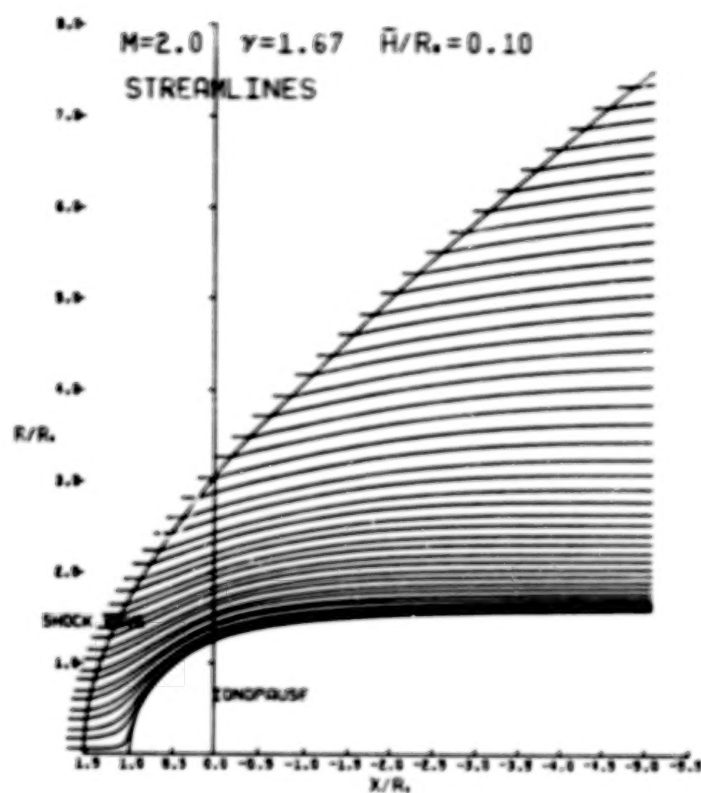


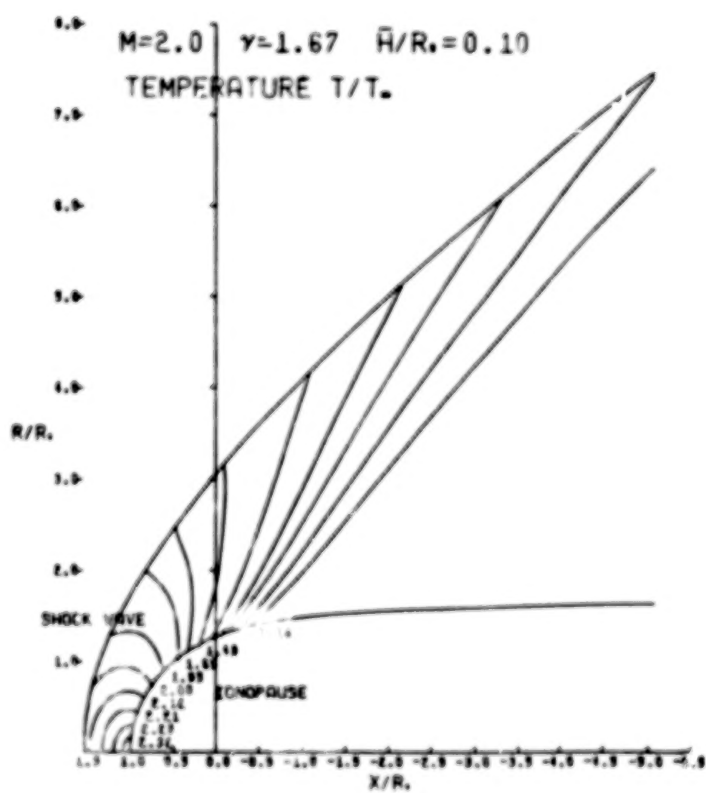
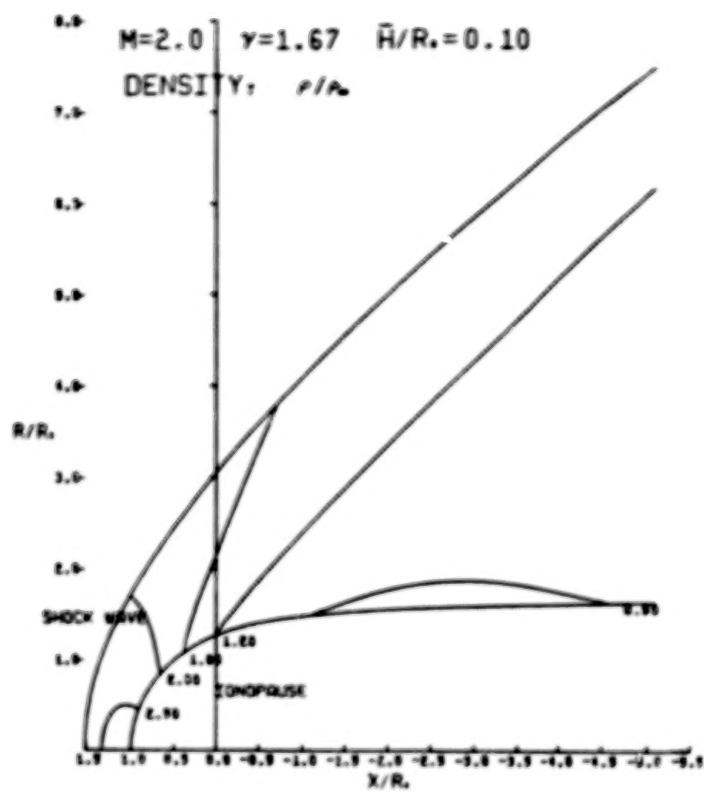


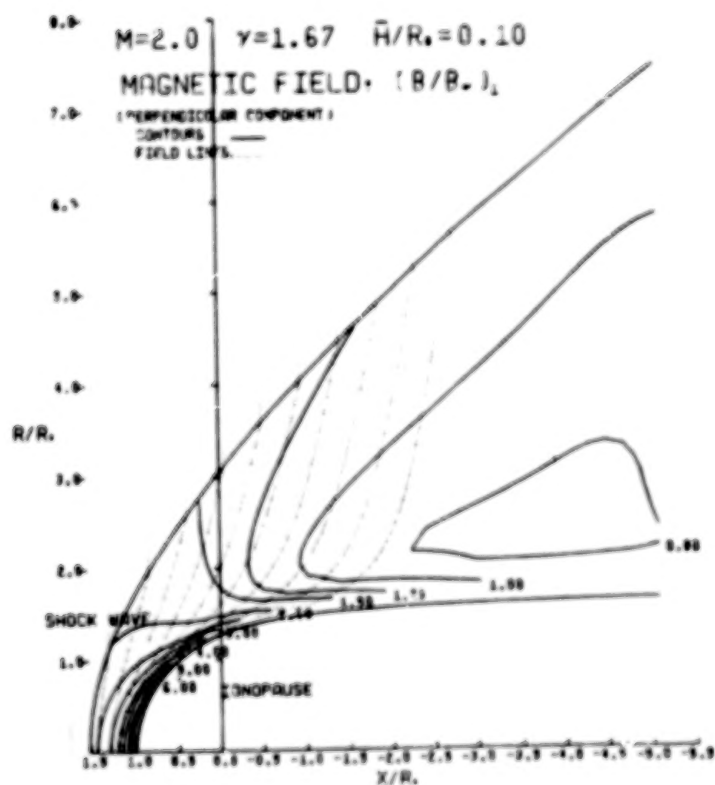
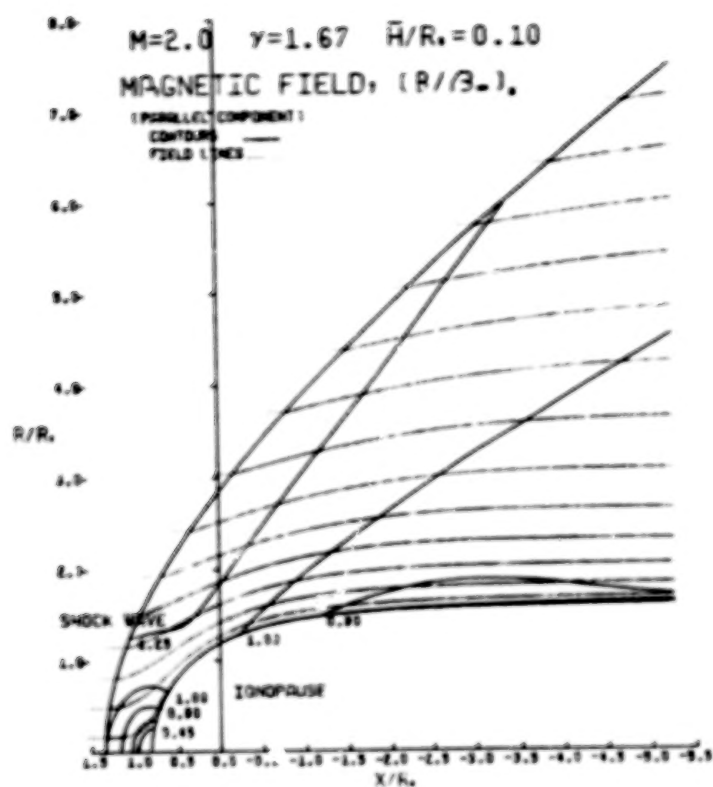


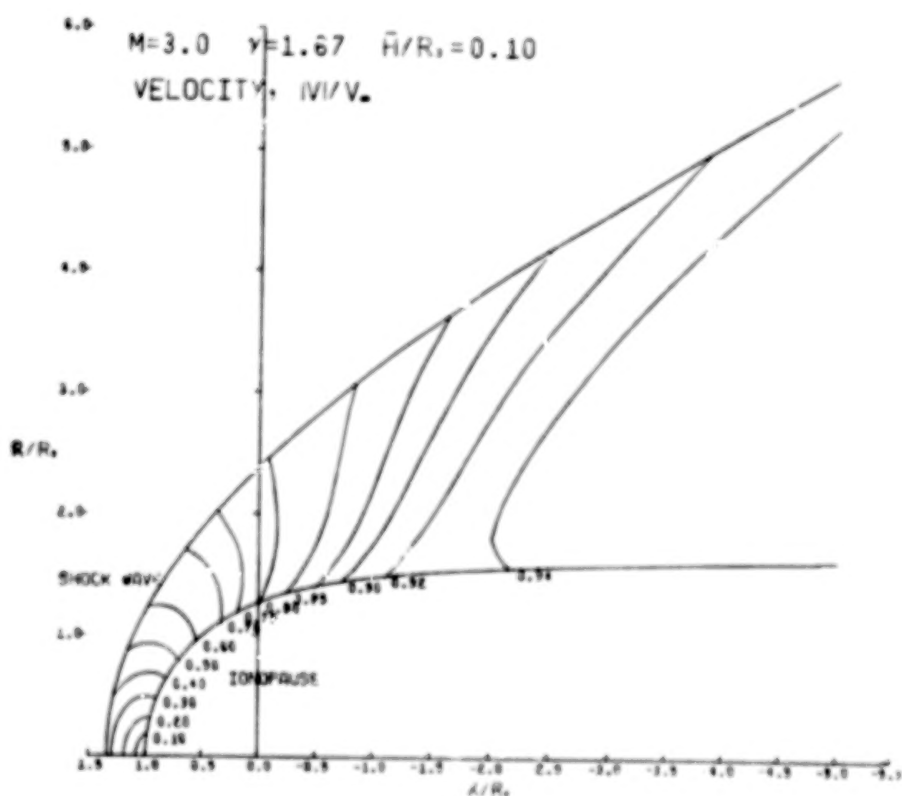
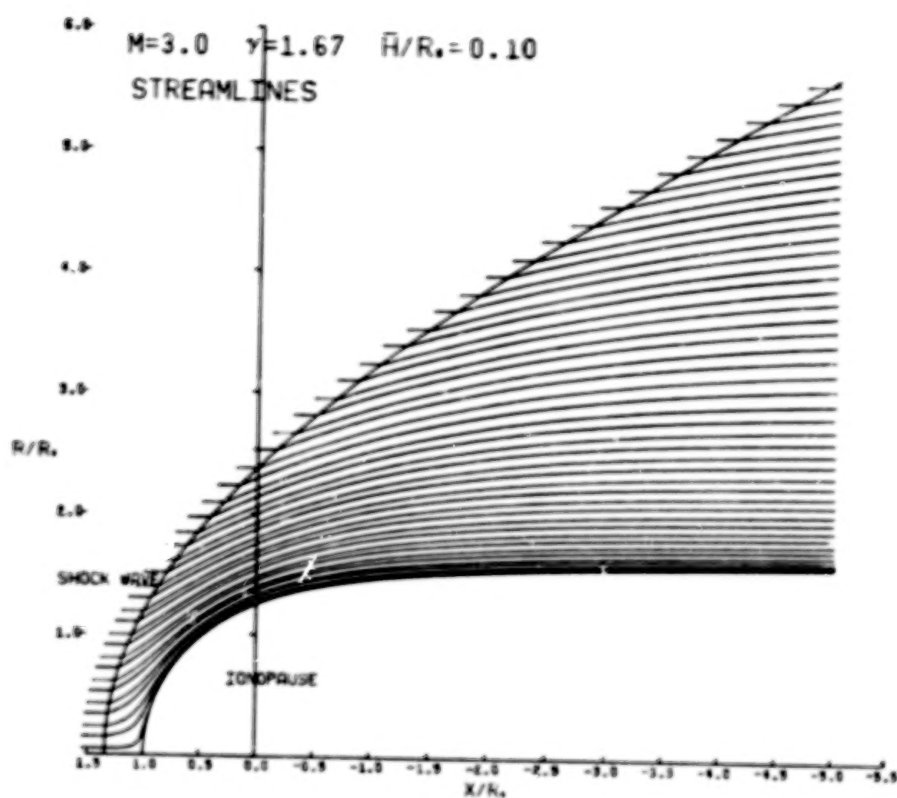






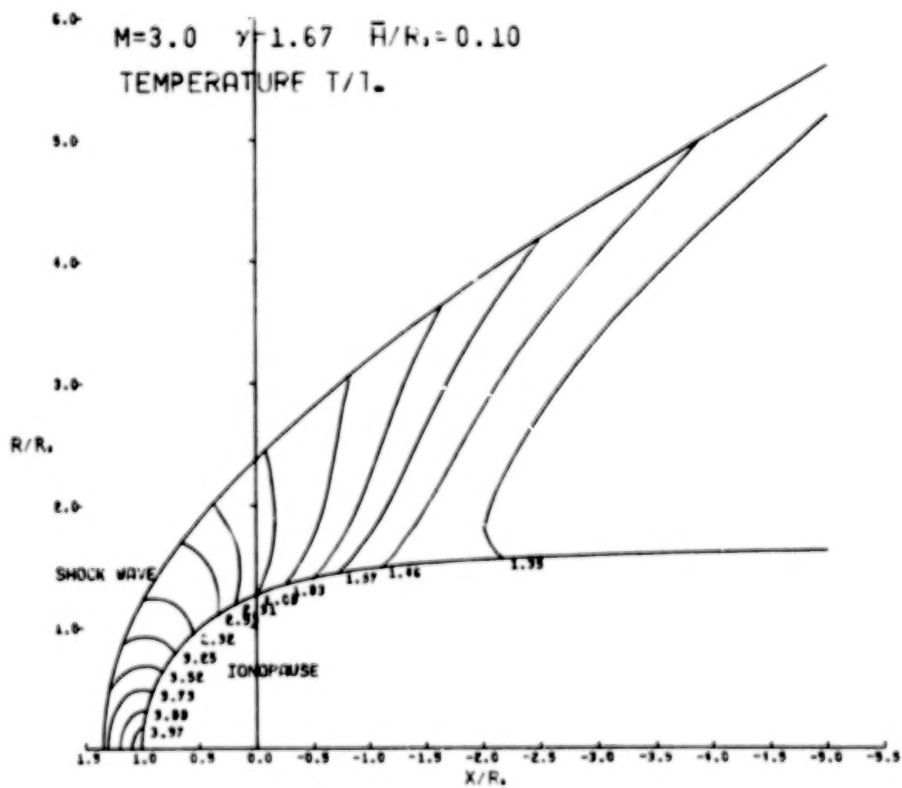
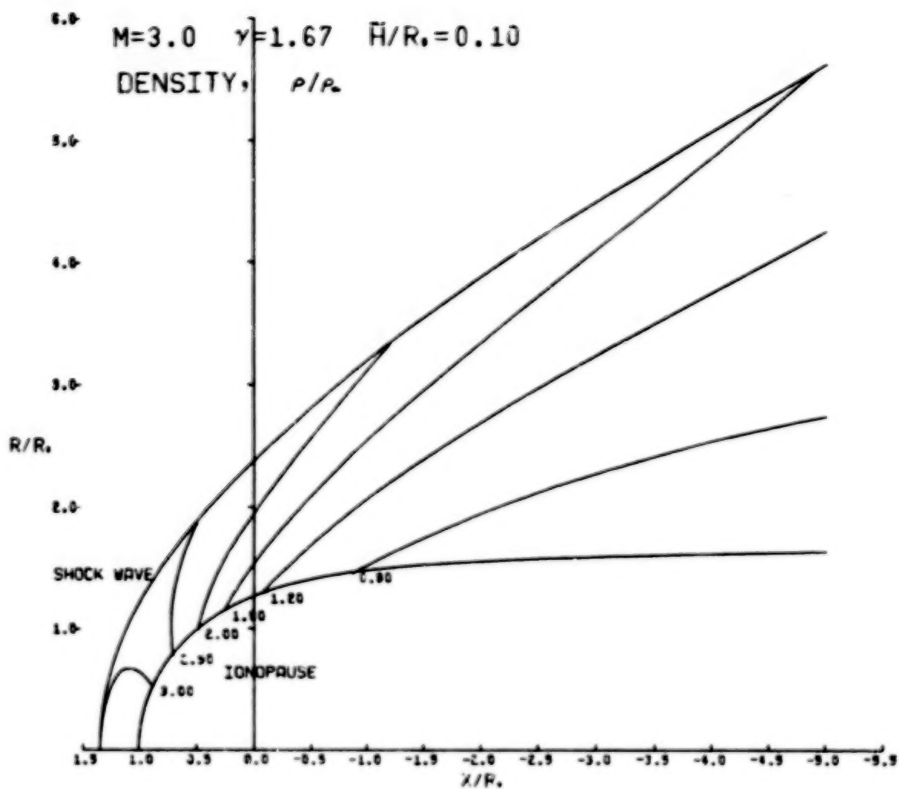


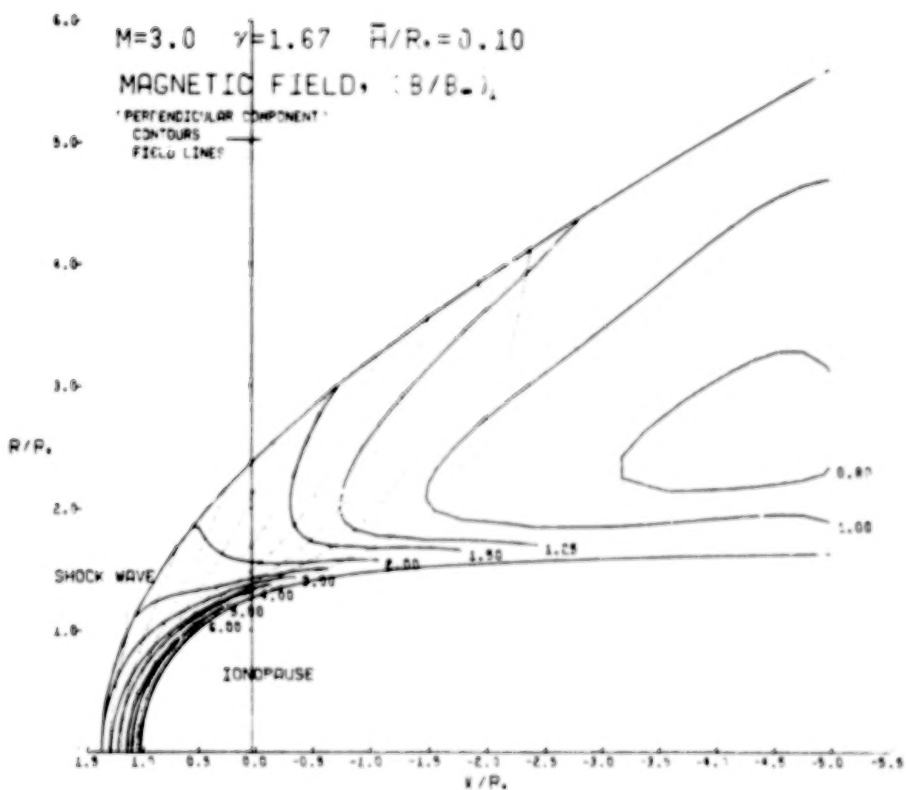
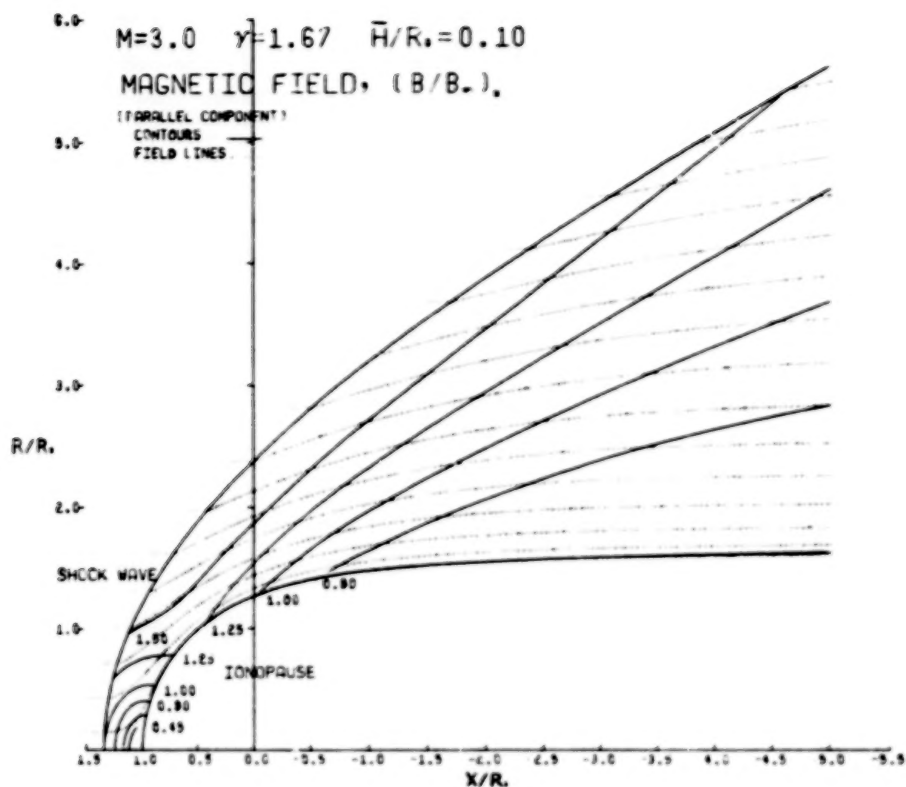


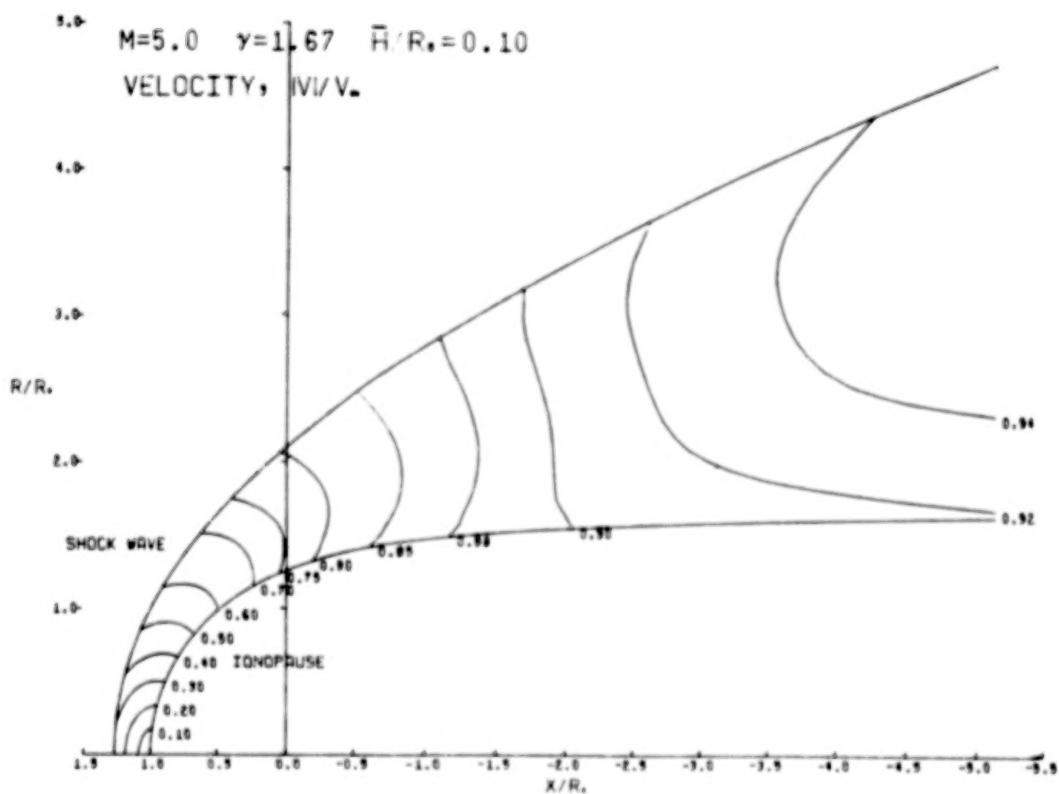
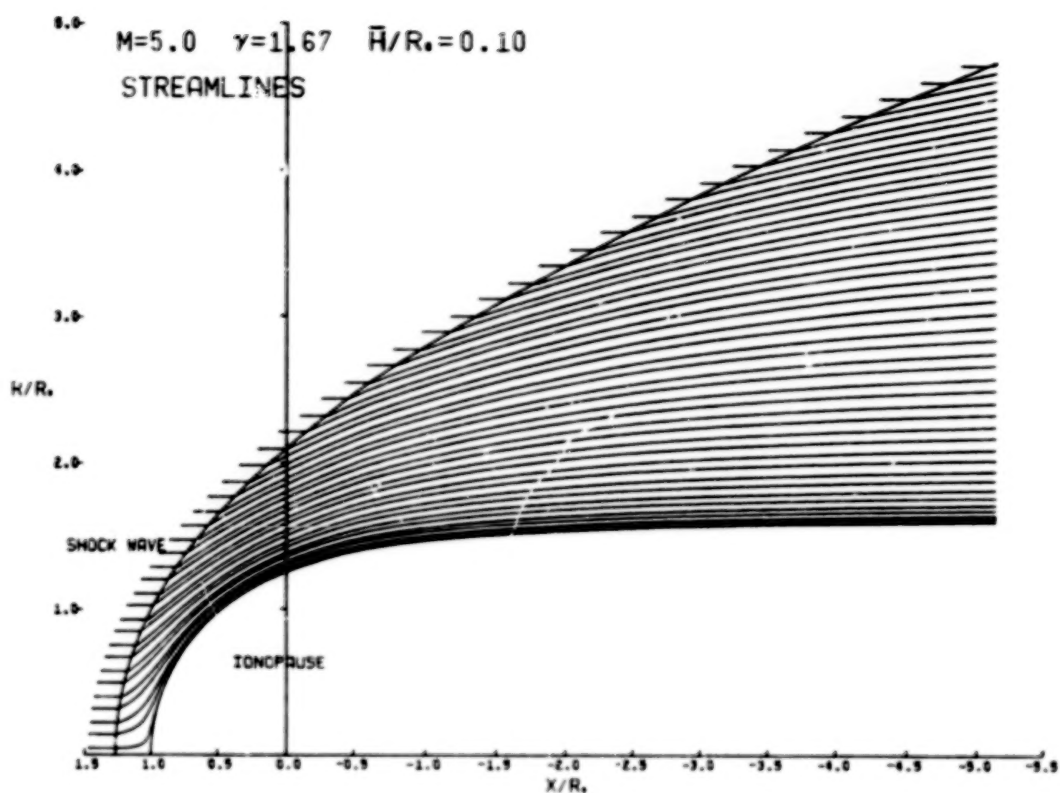


# TABLE OF CONTENTS

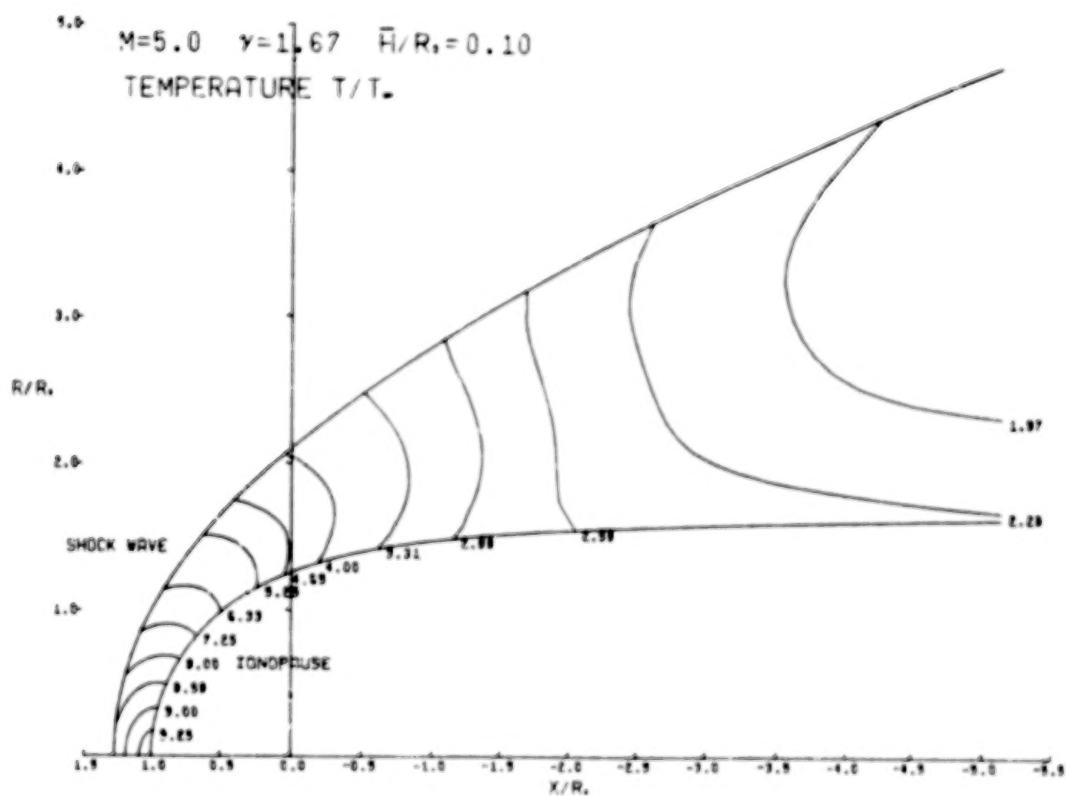
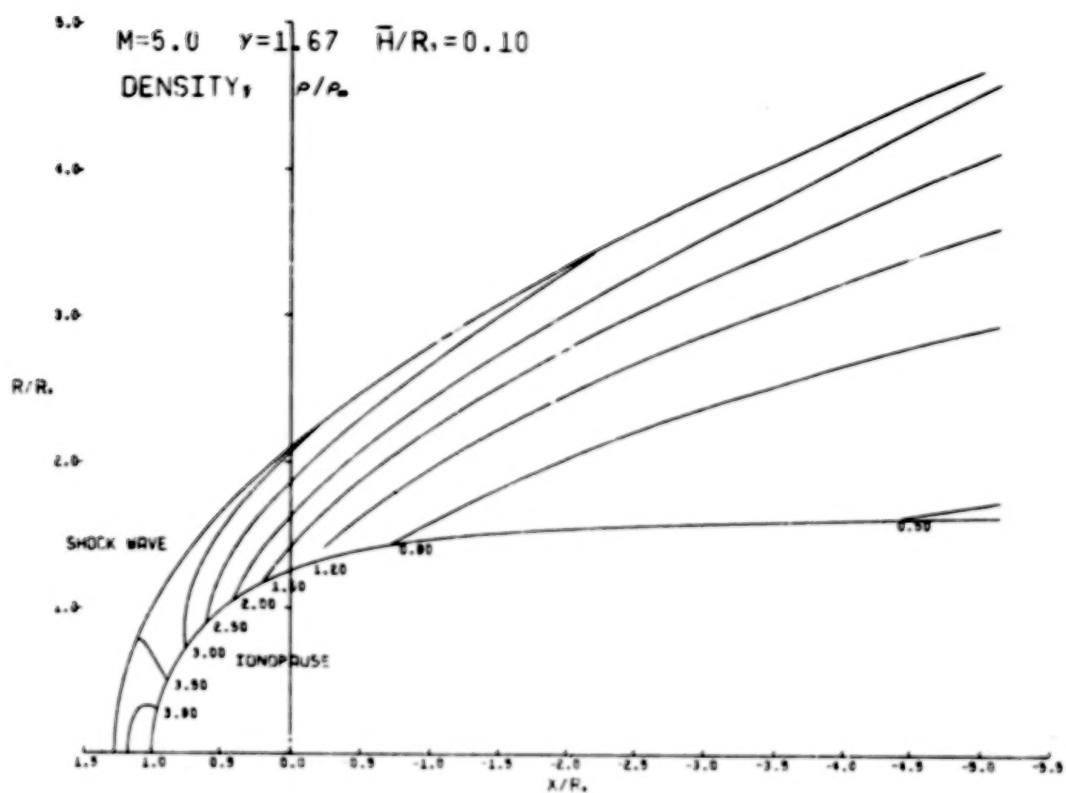
<u>Section</u>	<u>Page No.</u>
LIST OF ILLUSTRATIONS	iv 1/A5
SUMMARY	1 1/A7
INTRODUCTION	2 1/A8
LIST OF SYMBOLS	4 1/A10
ANALYSIS	8 1/A14
The Mathematical Model - Formulation of the Fluid Representation	8 1/A14
<u>Governing equations</u>	8 1/A14
<u>Conditions at discontinuities</u>	10 1/B2
<u>Frozen-field approximation</u>	12 1/B4
Determination of the Ionosphere Boundary	14 1/B6
Calculation of the Gasdynamic Flow Properties	20 1/B12
<u>Nose region solution - implicit unsteady Euler equation method</u>	21 1/B13
<u>Downstream region solution - shock capturing marching method</u>	25 1/C3
<u>Calculation of the streamlines</u>	27 1/C5
Calculation of the Magnetic Field	27 1/C5
Calculation of the Contour Lines	30 1/C8
Solar-Ecliptic/Solar-Wind Coordinate Transformations	31 1/C9
Properties Along a Spacecraft Trajectory	33 1/C11
RESULTS	36 1/C14
CONCLUDING REMARKS	47 1/D11
ACKNOWLEDGEMENTS	48 1/D12
APPENDIX A - COMPUTER PROGRAM USER'S MANUAL	49 1/D13
APPENDIX B - LISTING OF COMPUTER PROGRAM	131 2/D1
APPENDIX C - CATALOG OF TEST CASES	177 3/C10
REFERENCES	287 4/D10
TABLE 1	289 4/D12
FIGURES 1 THROUGH 20	291 4/E3

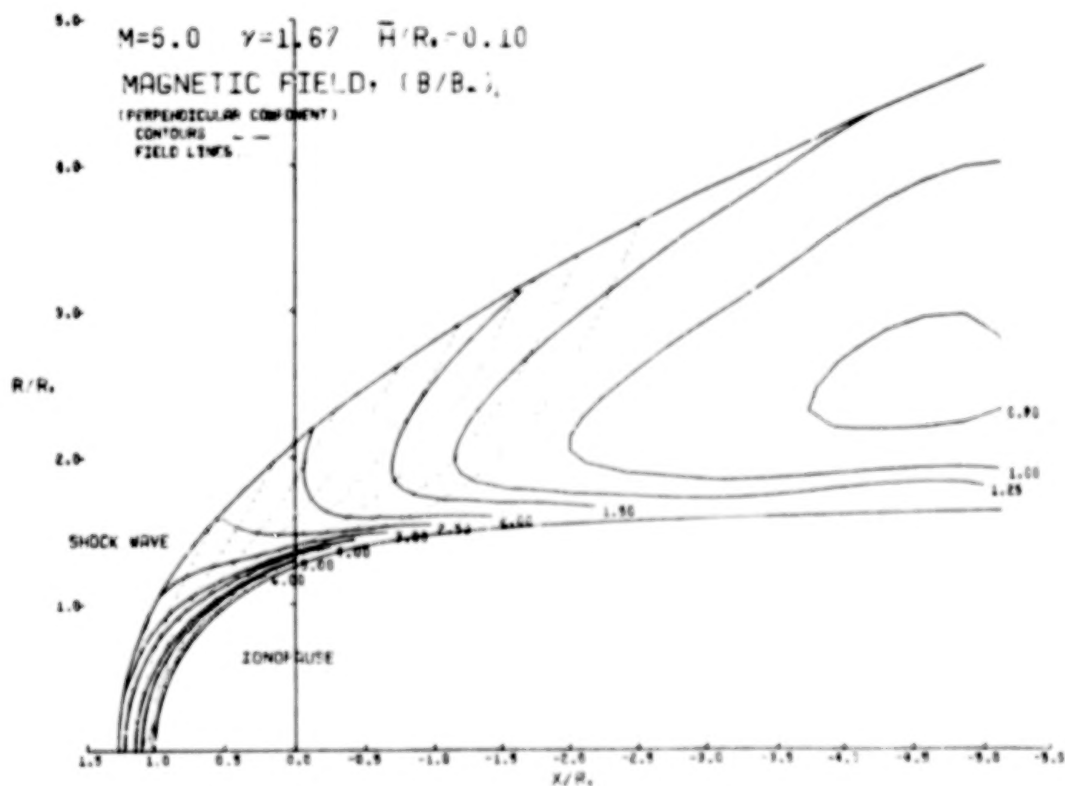
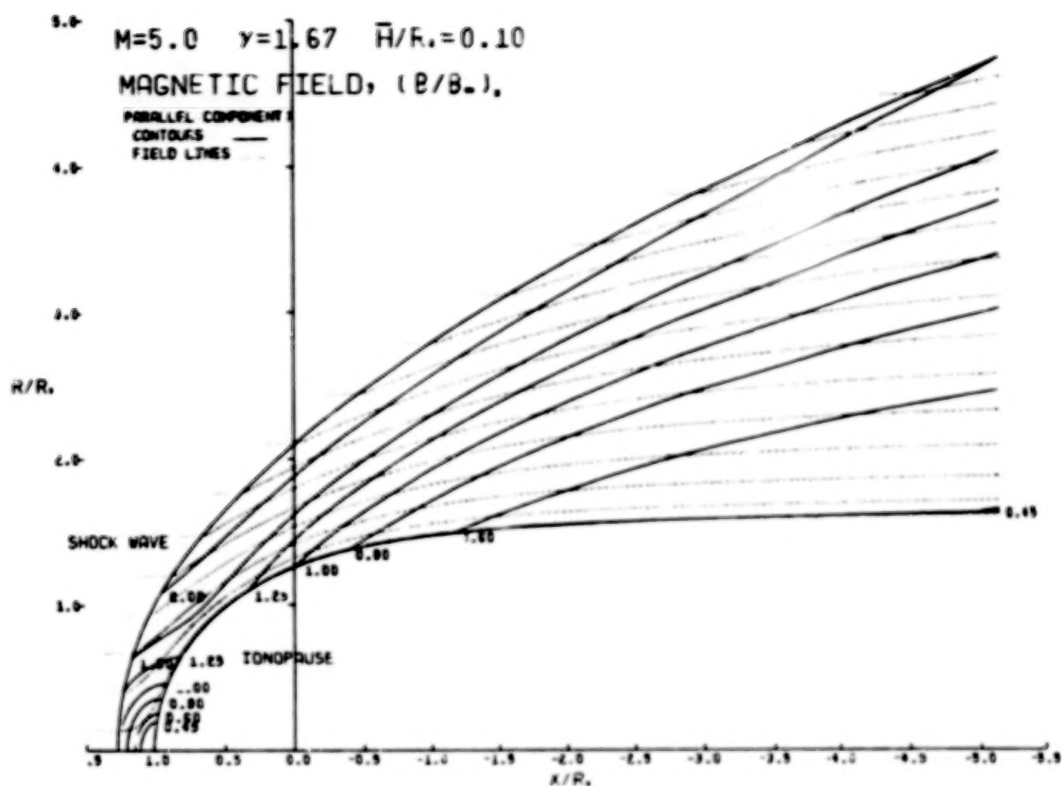


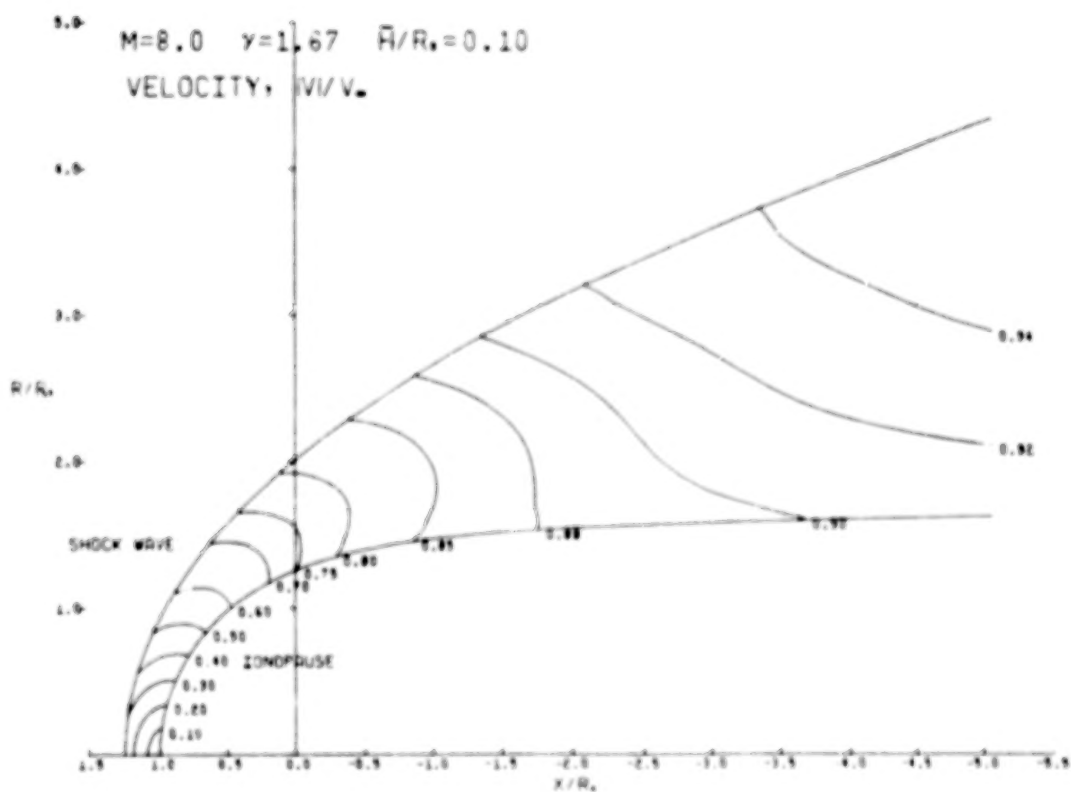
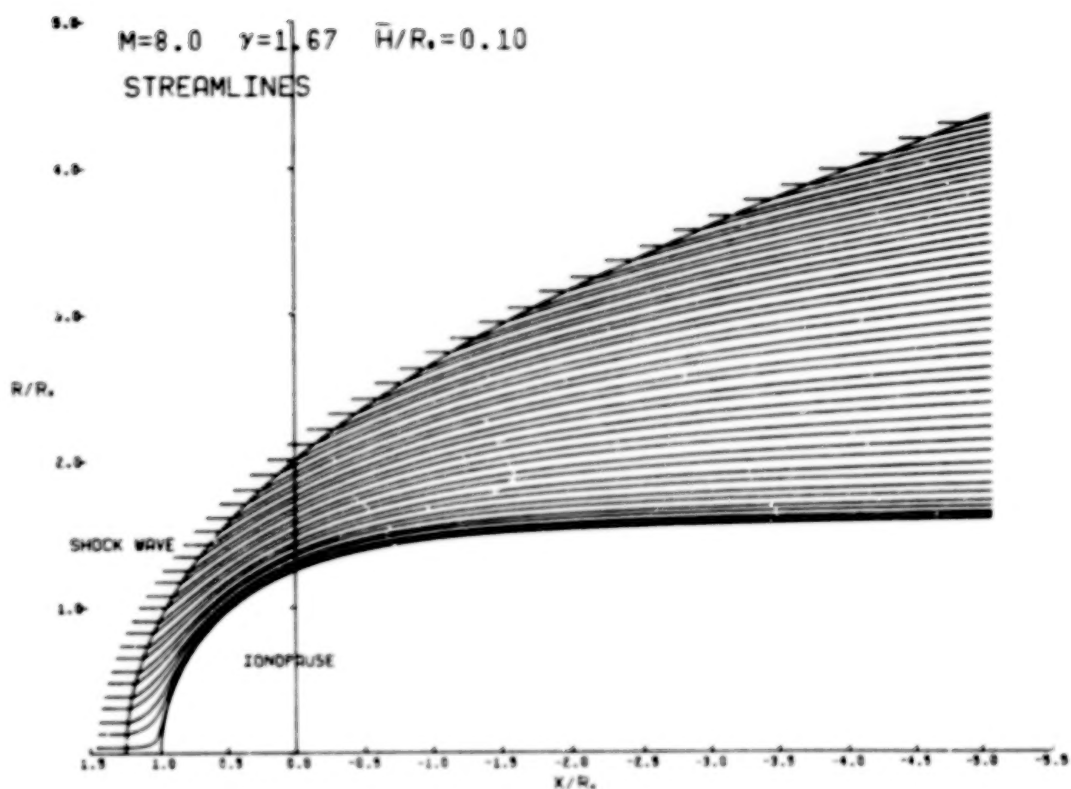


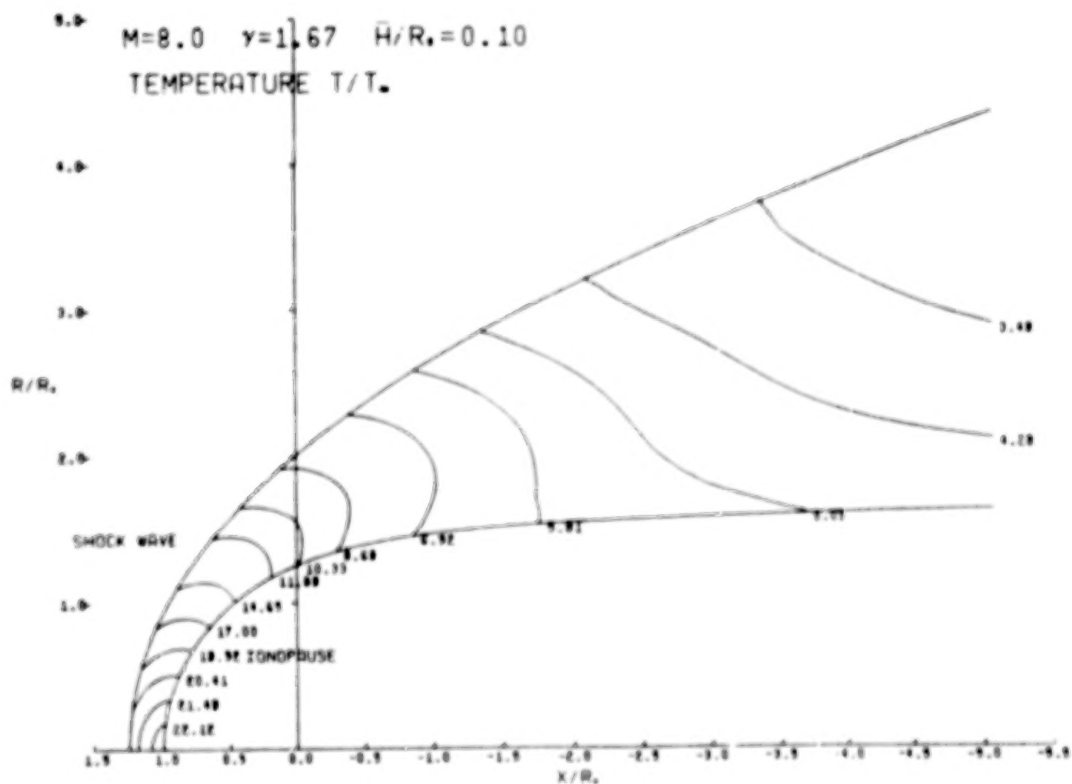
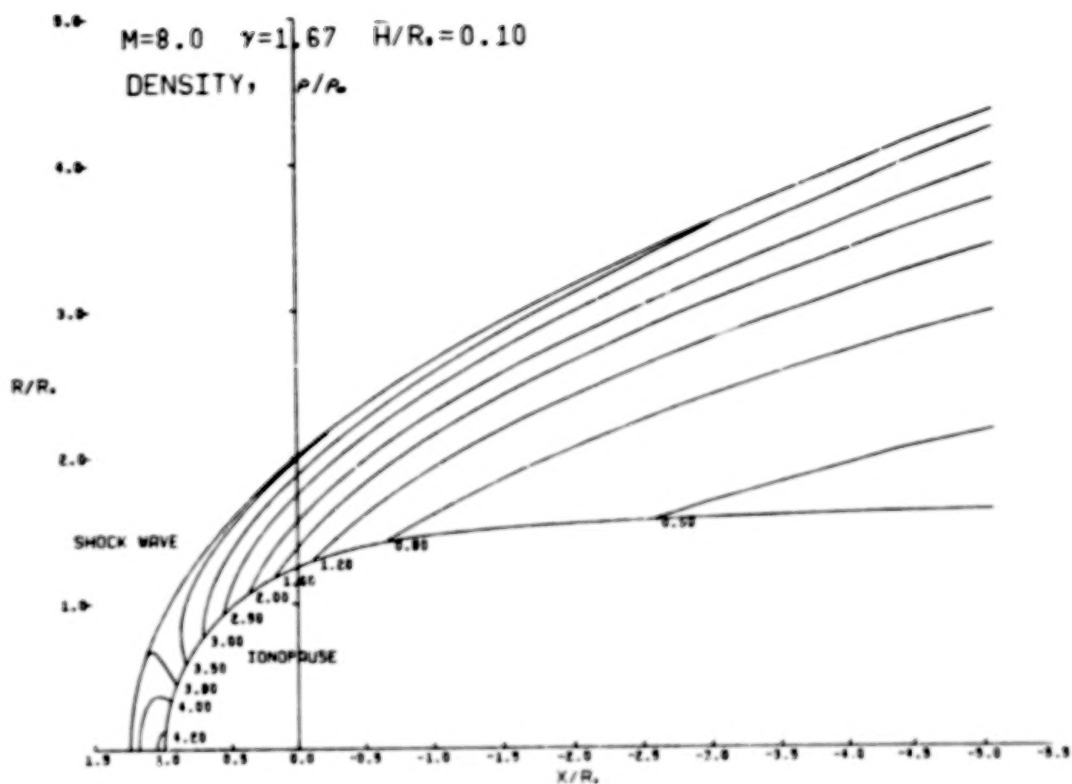


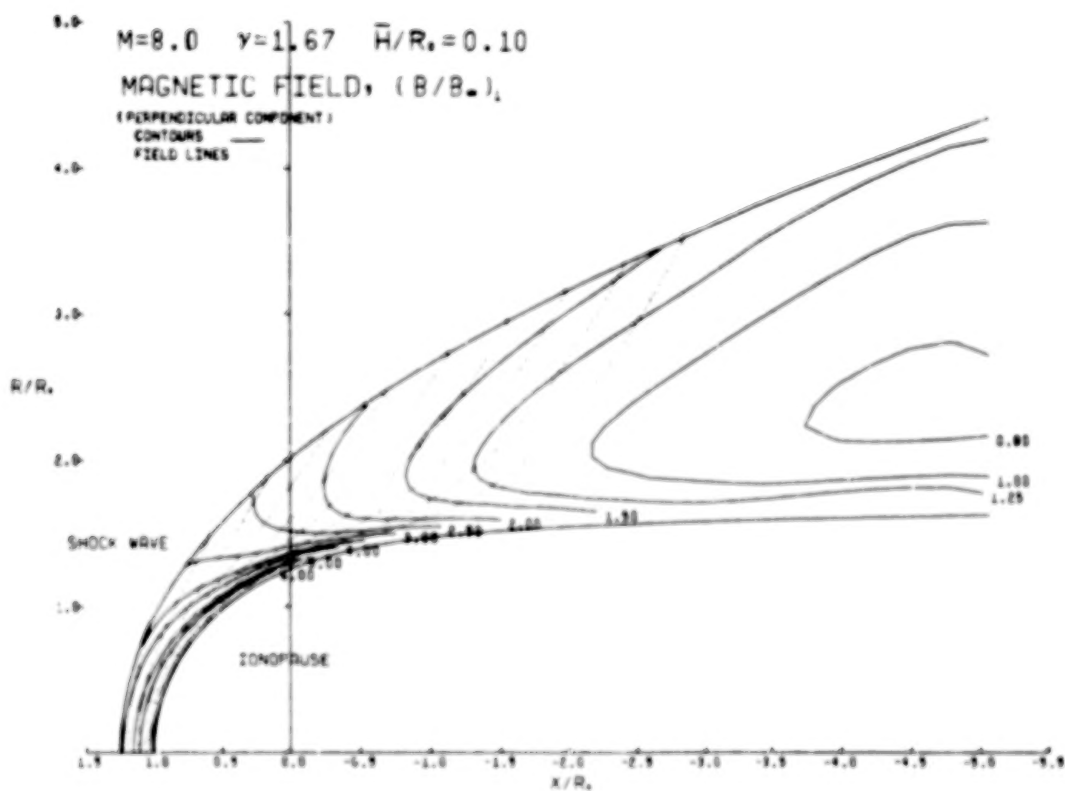
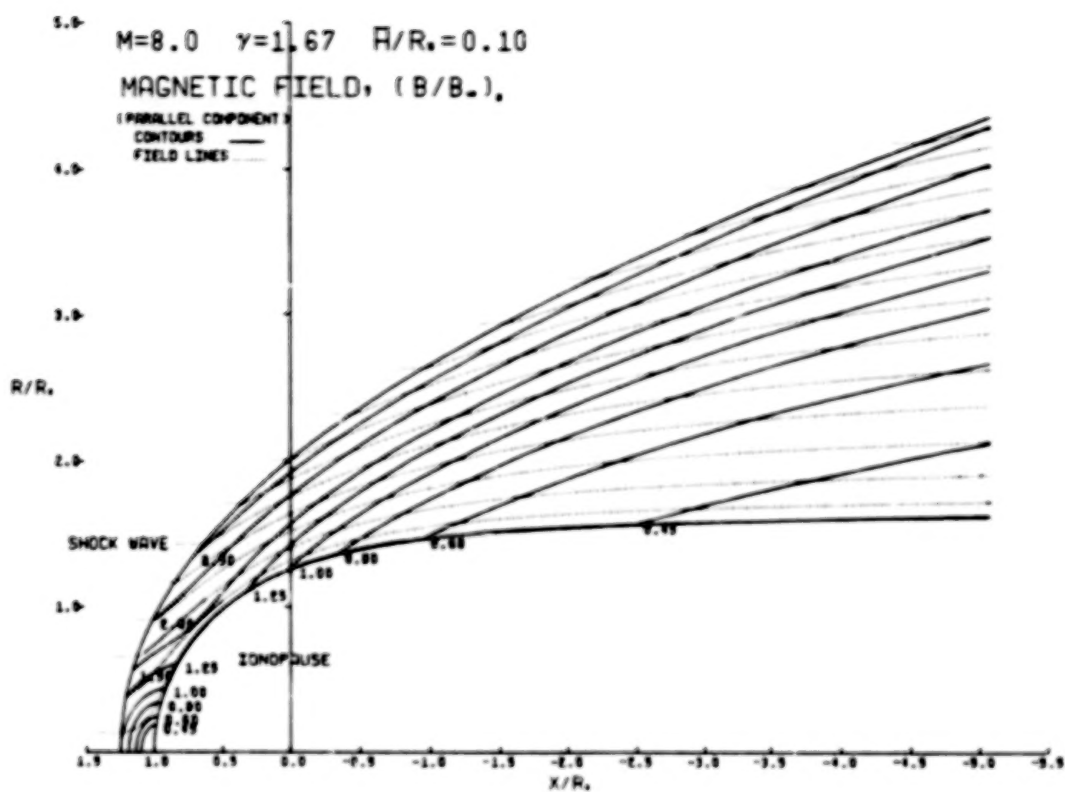


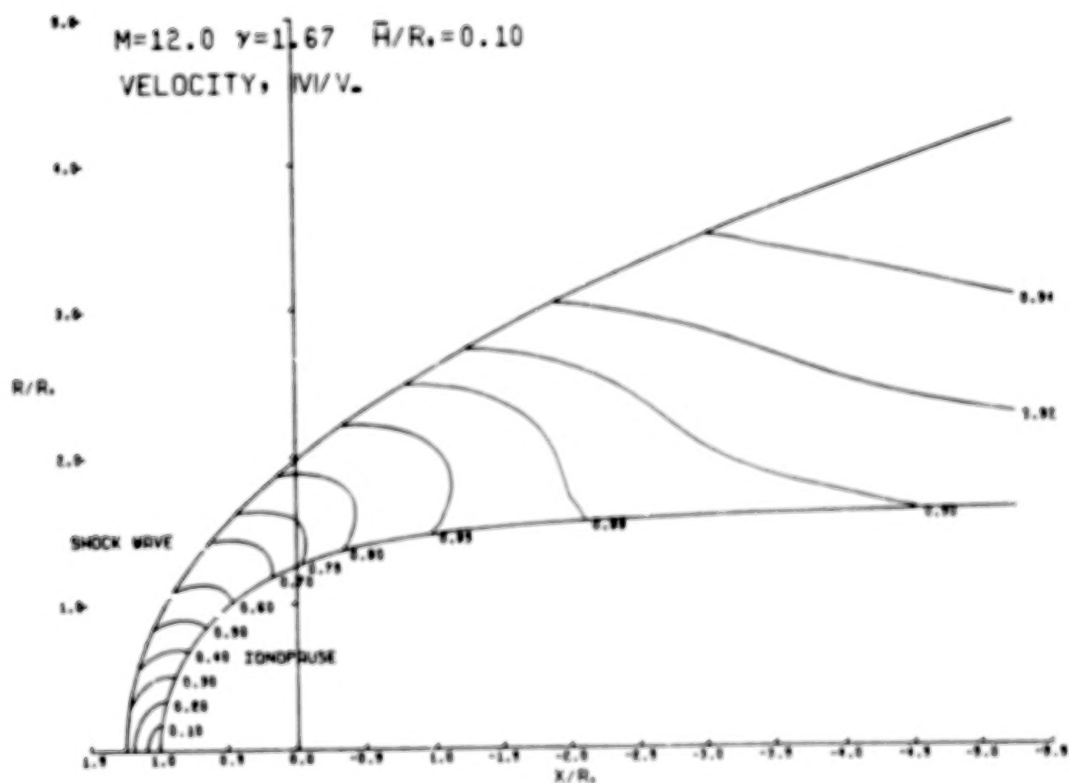
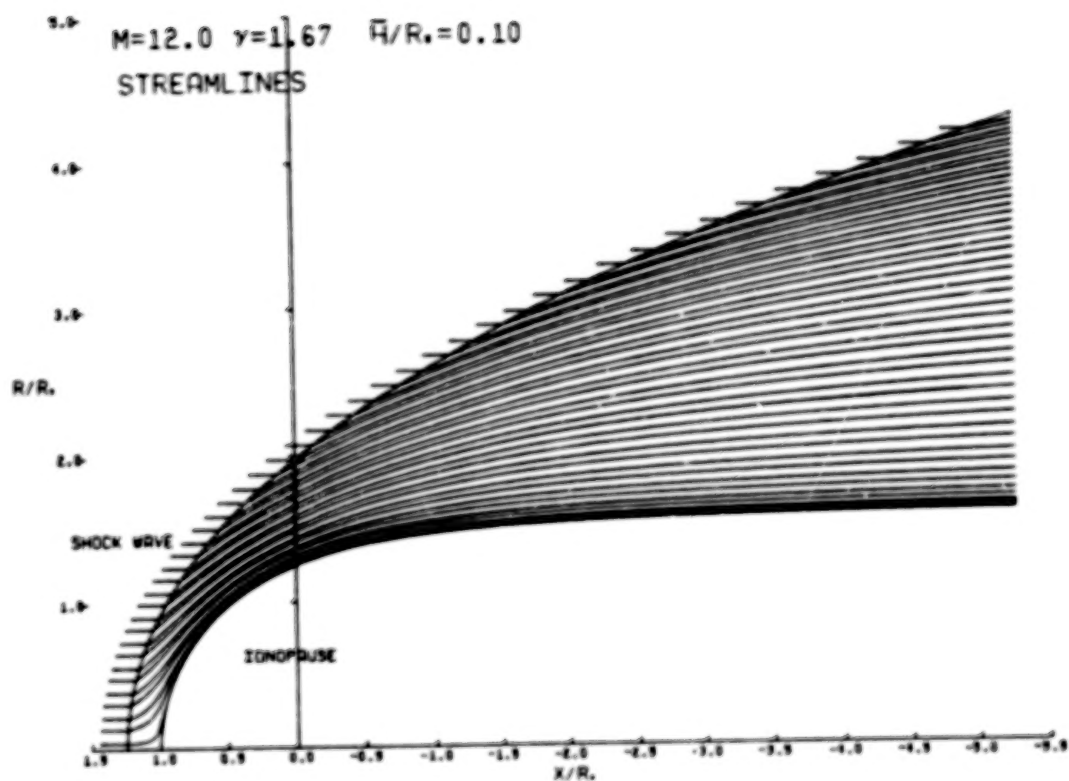




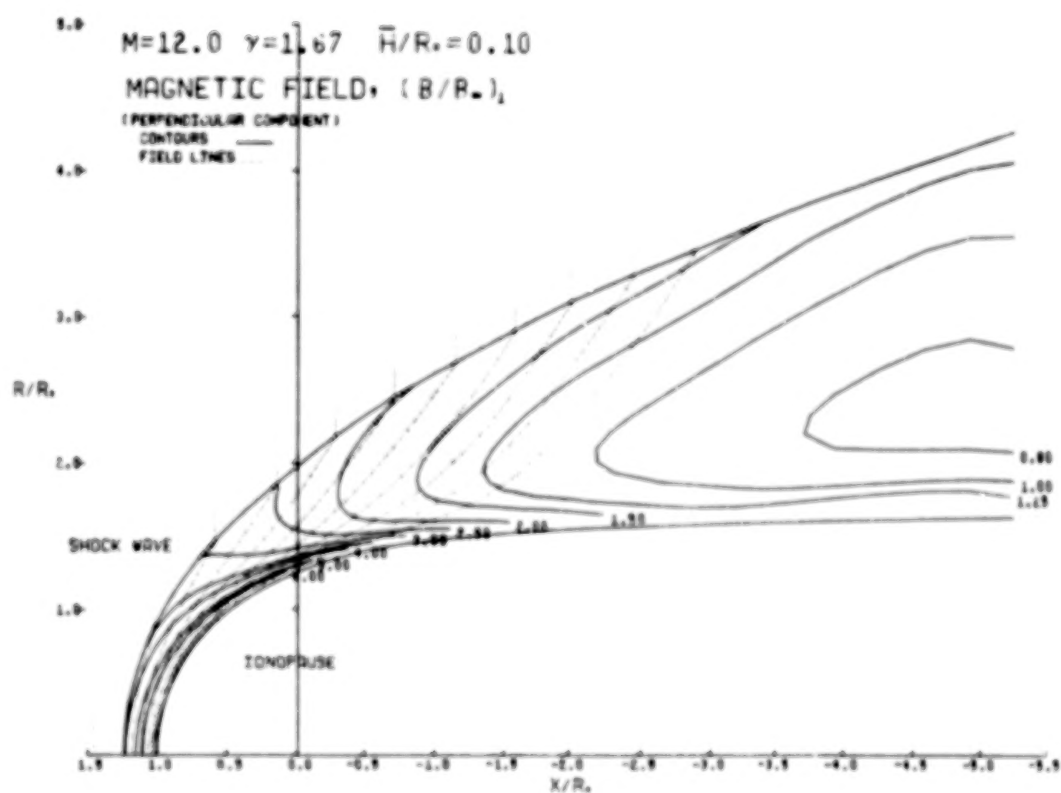
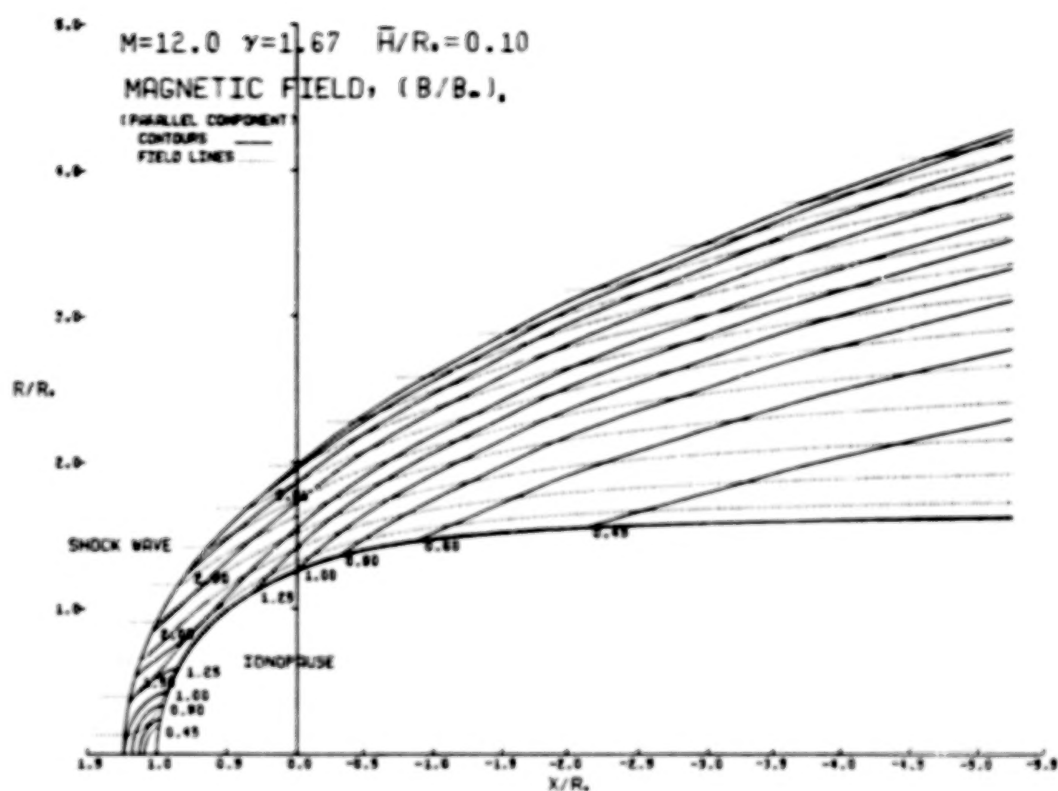




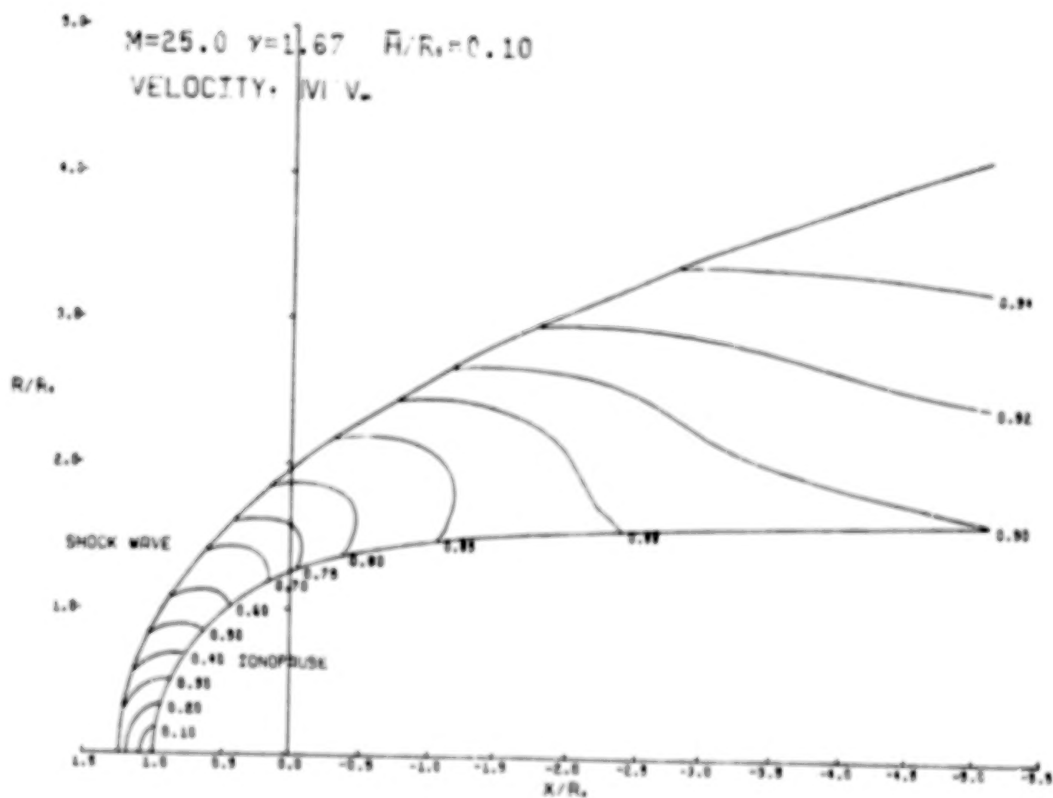
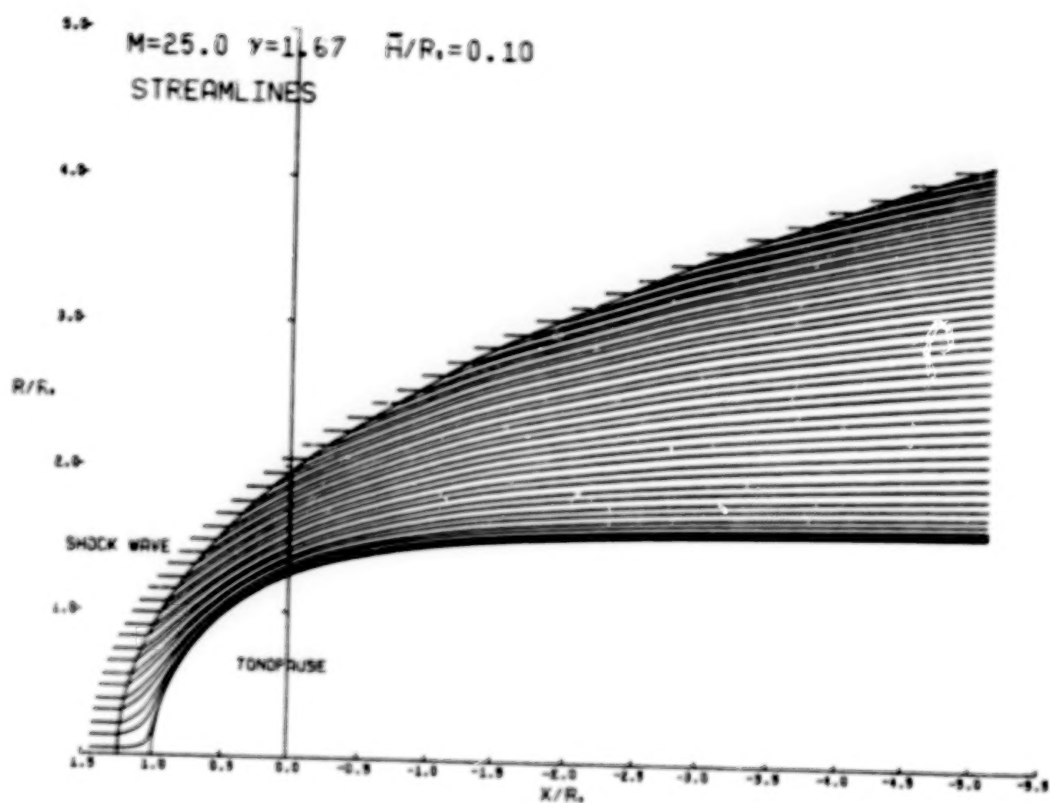


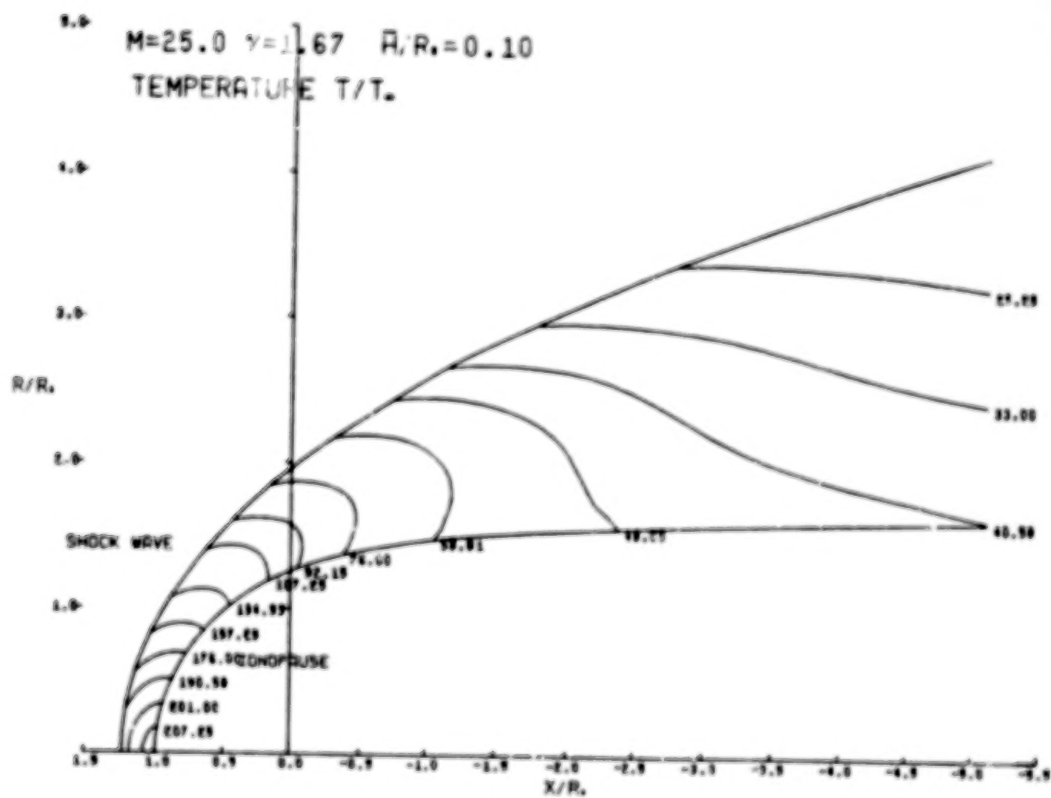
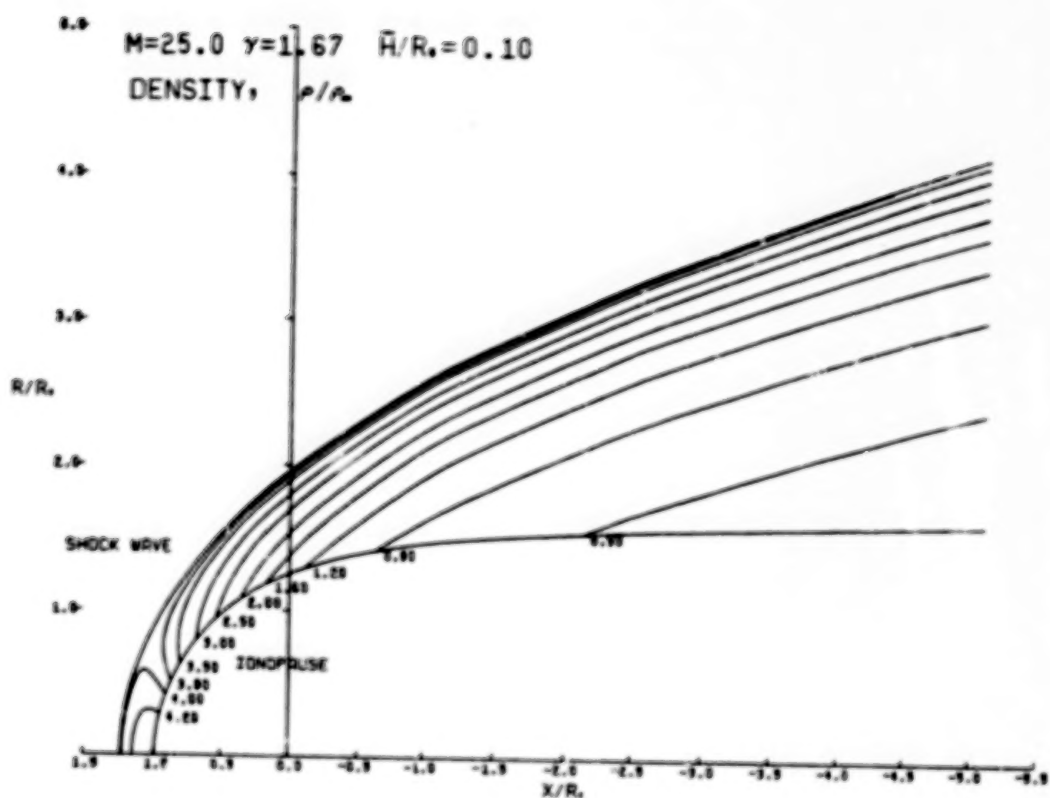


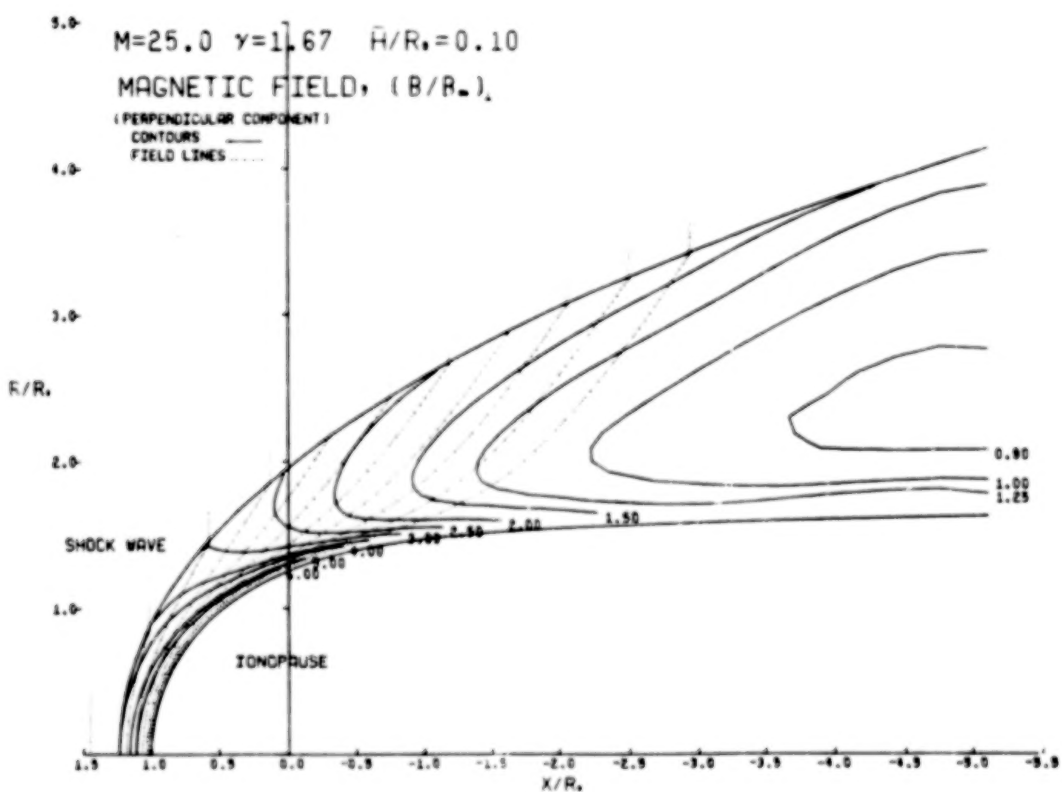
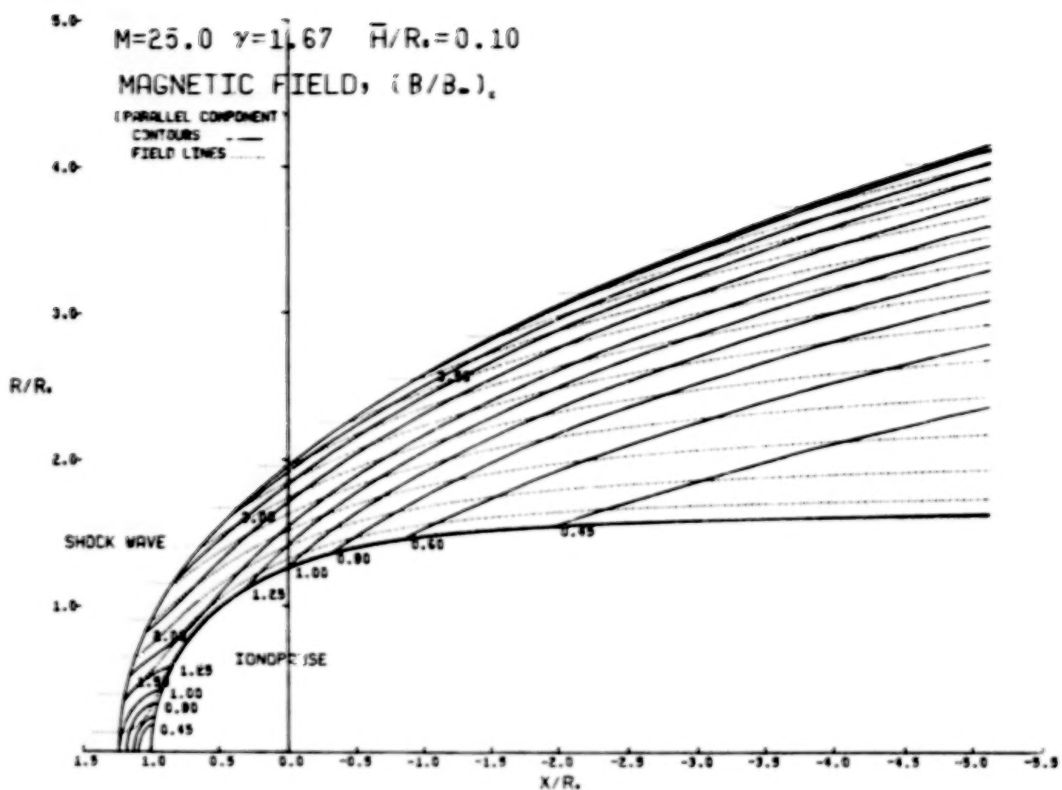


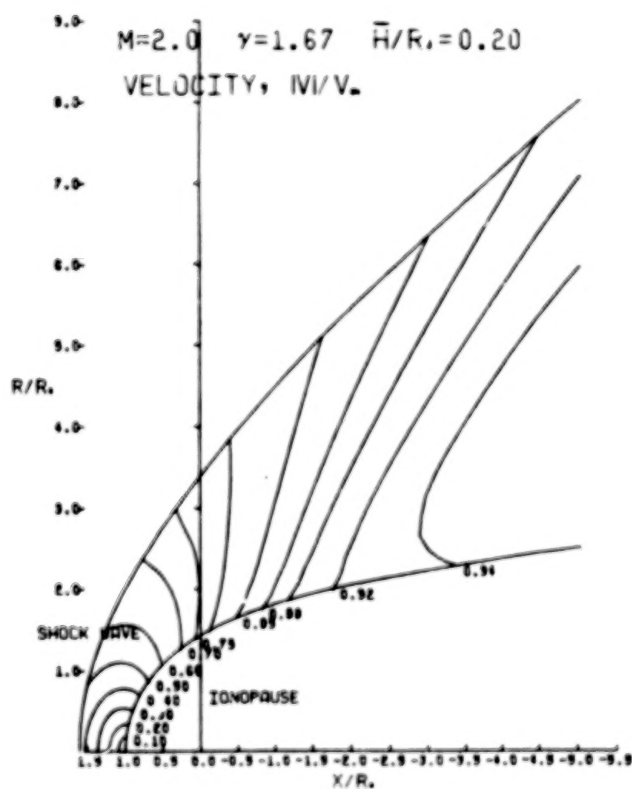
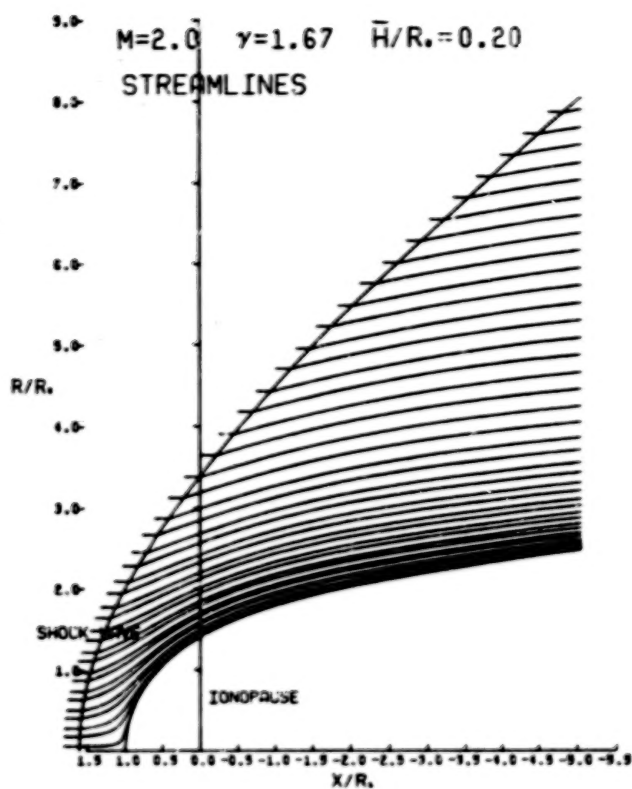


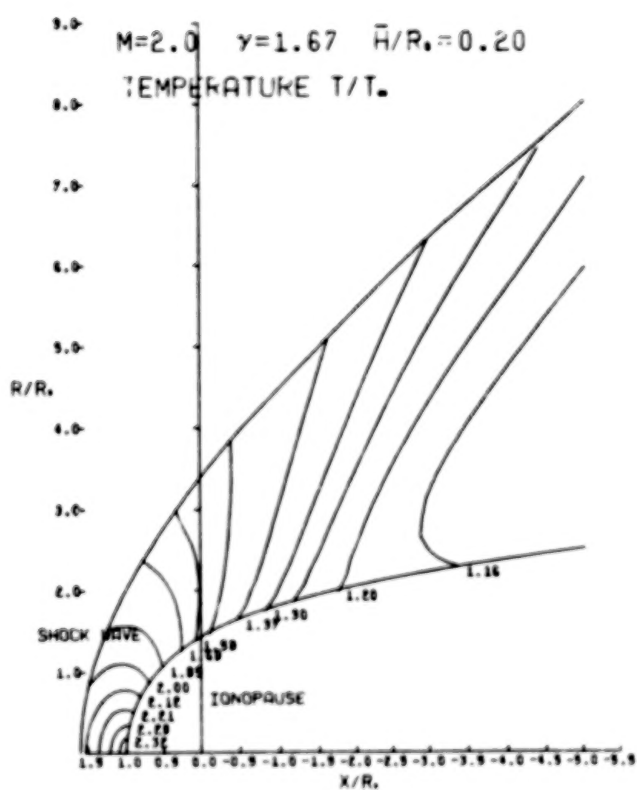
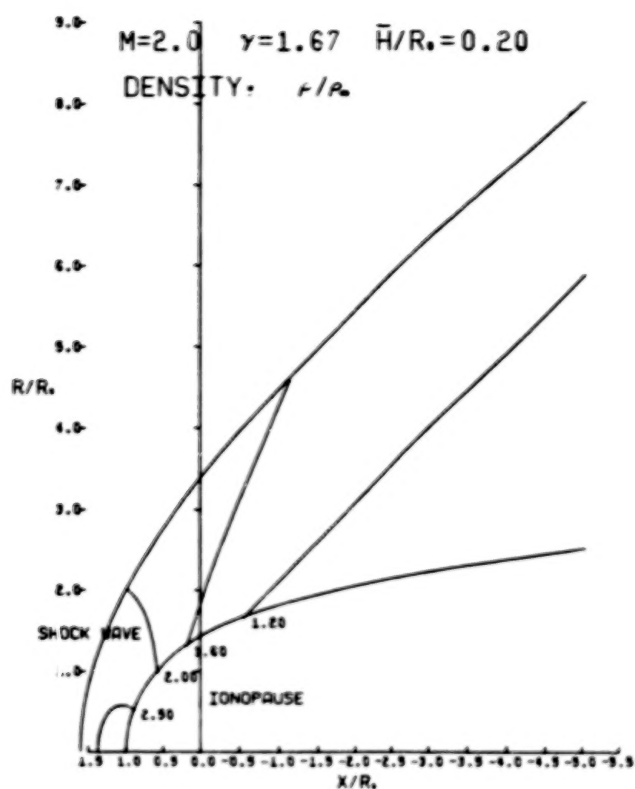


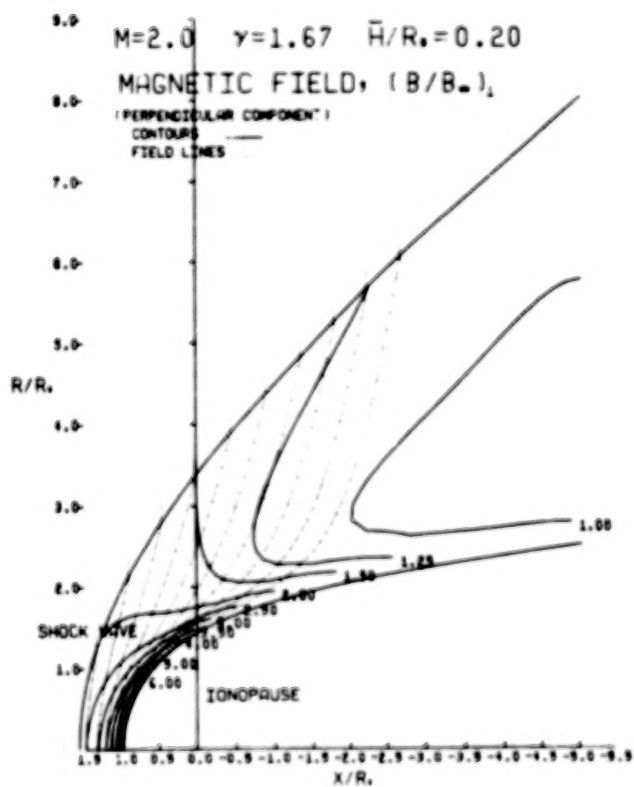
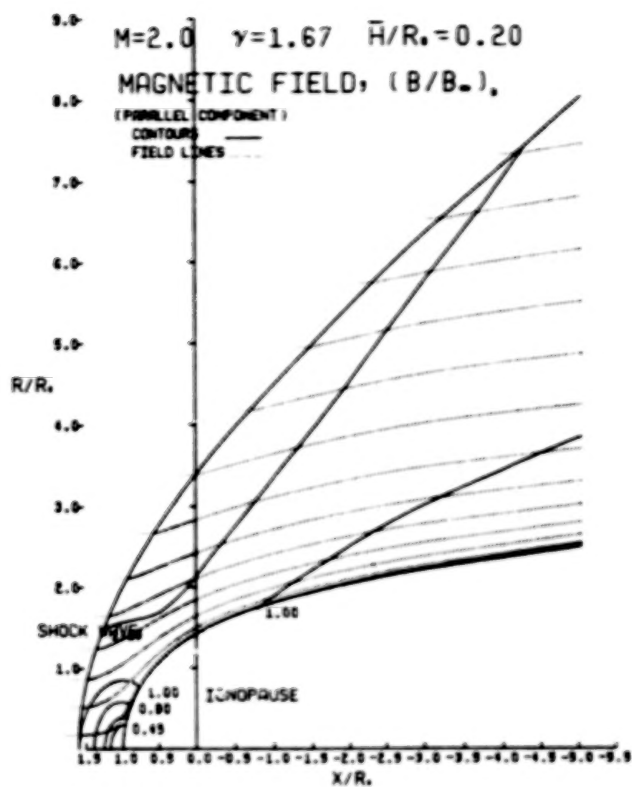


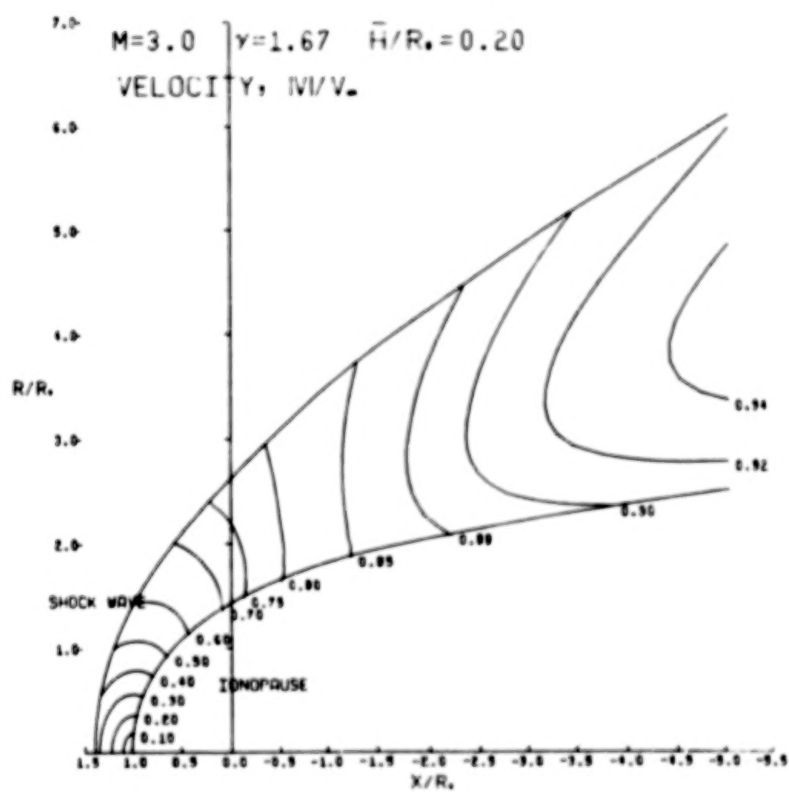
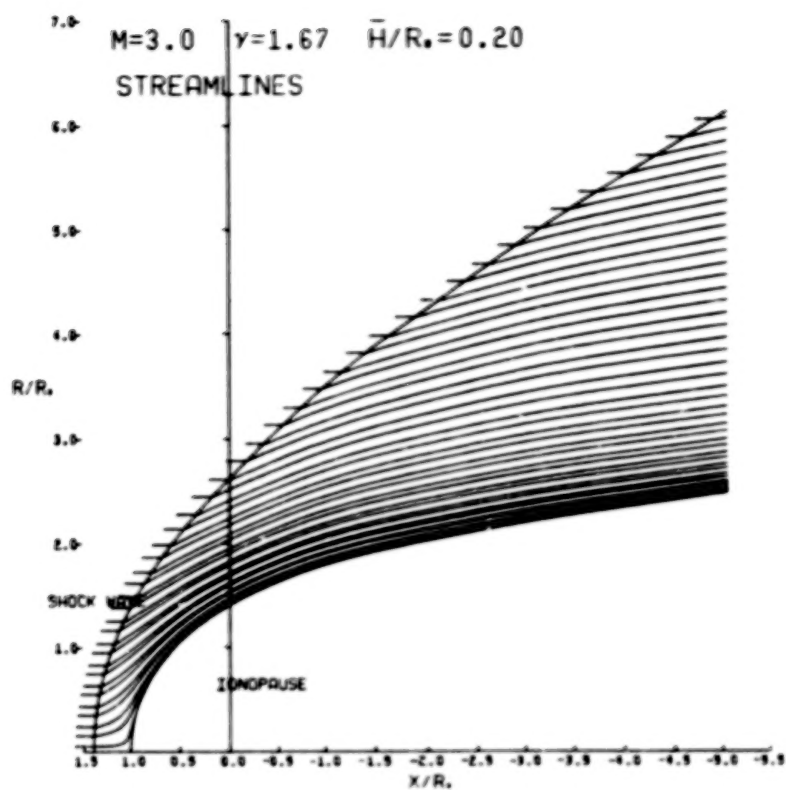








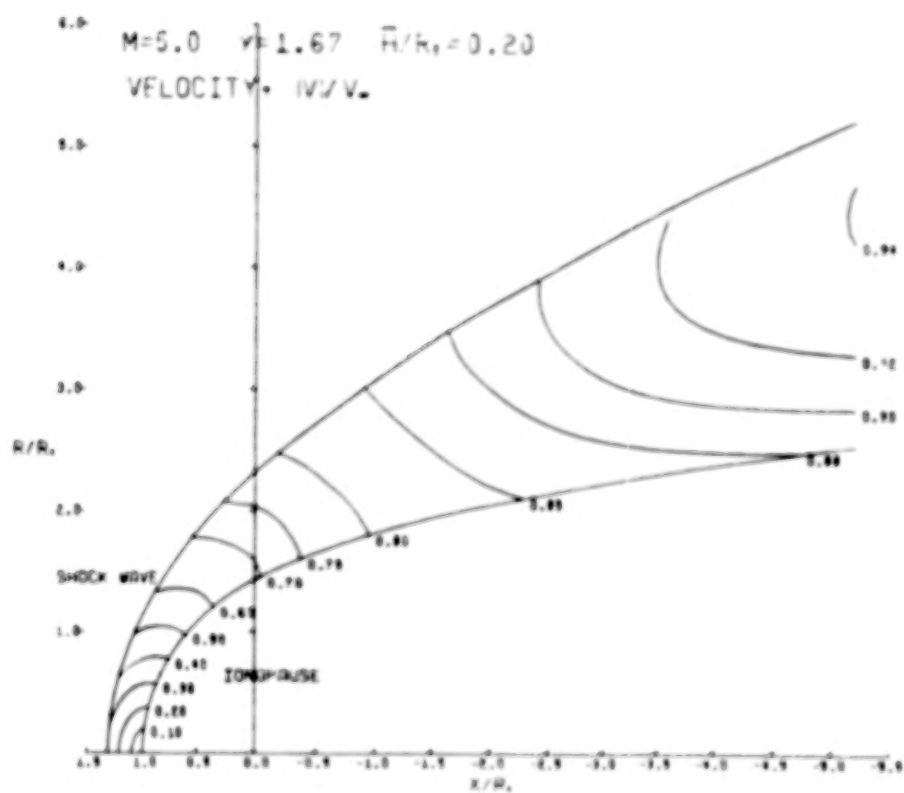
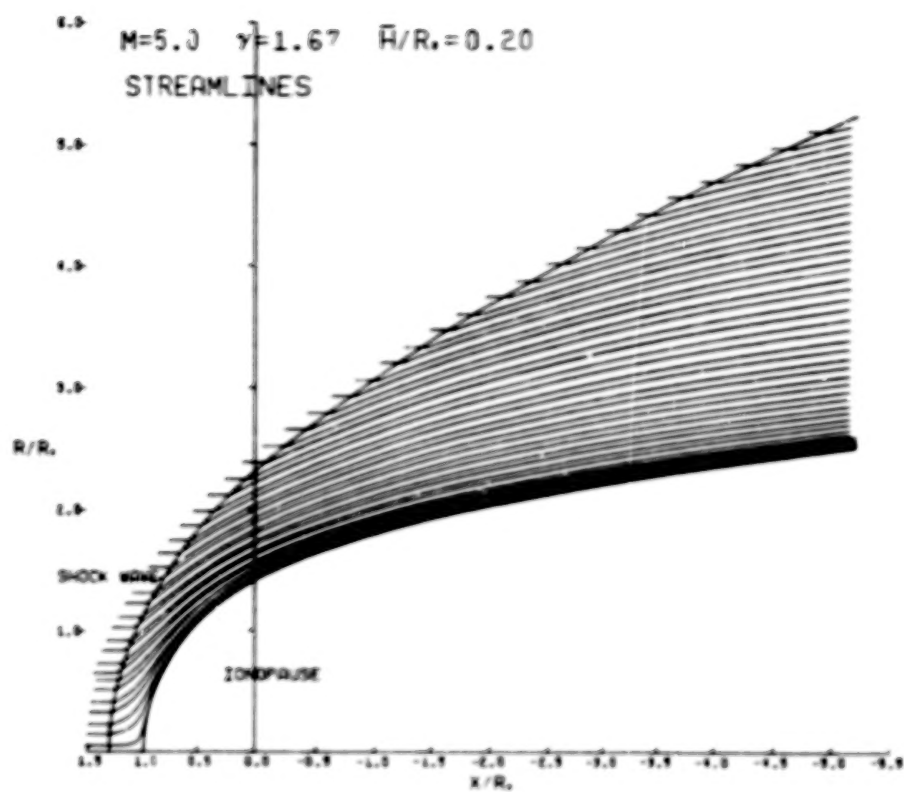


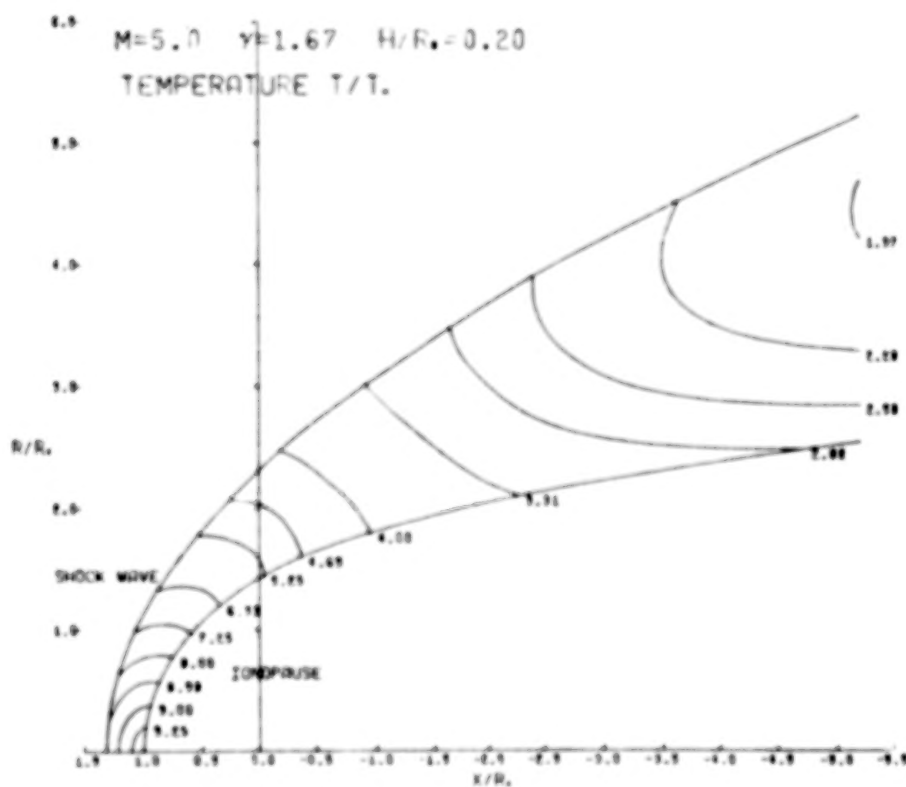
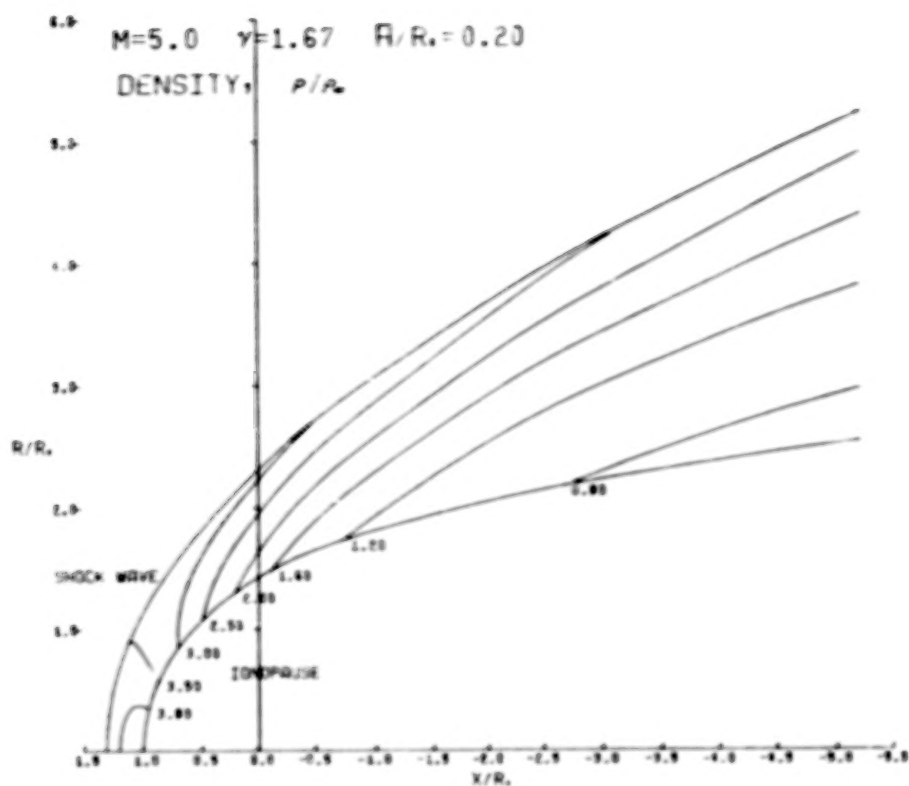


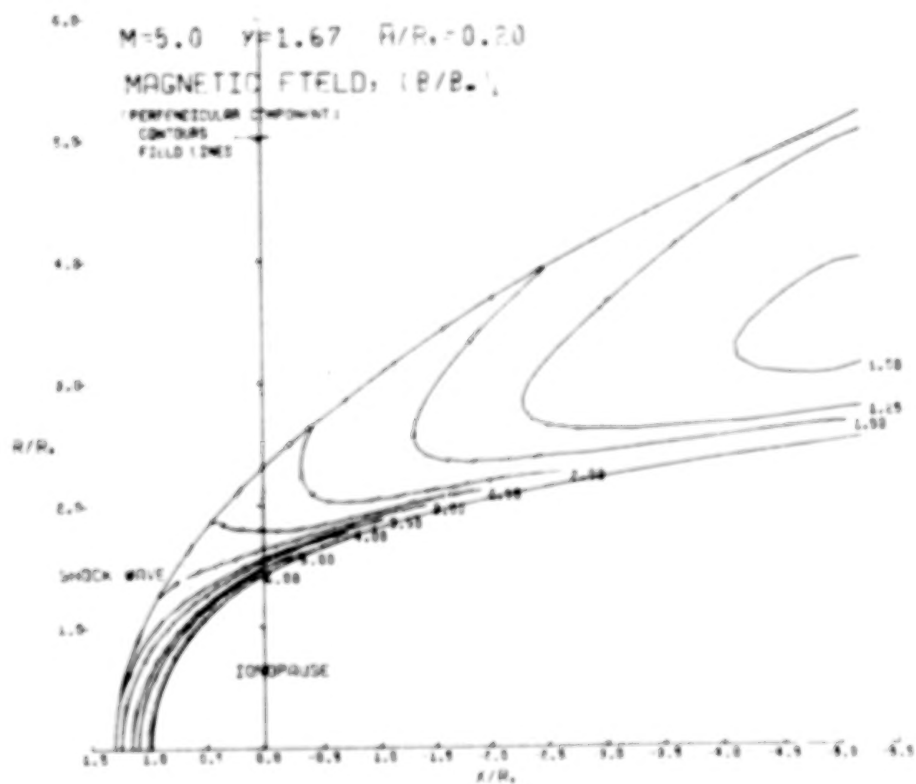
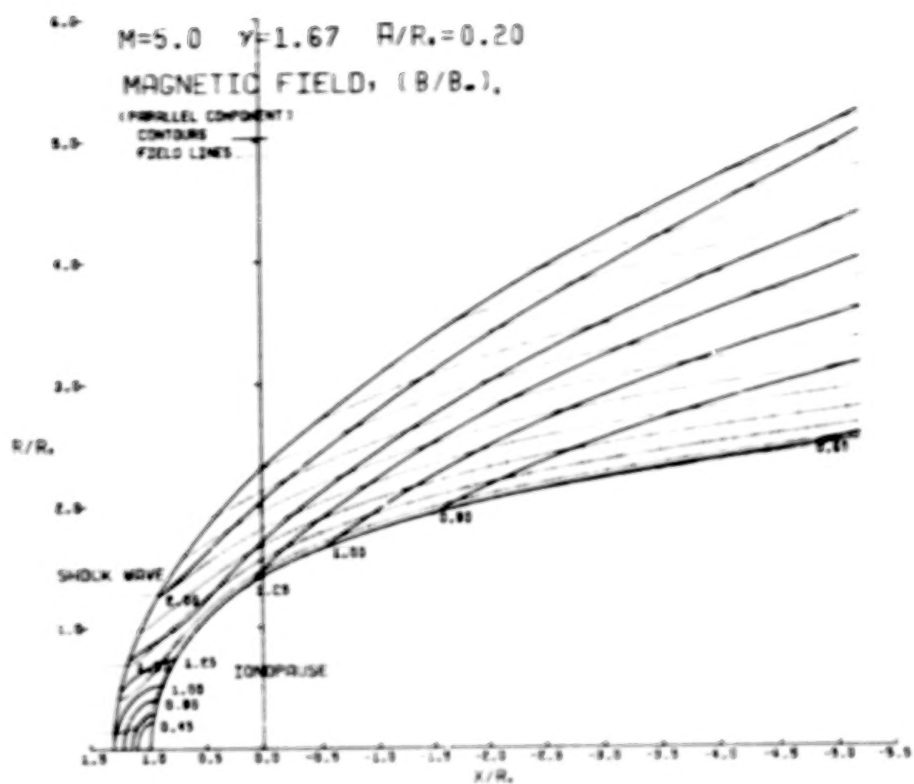


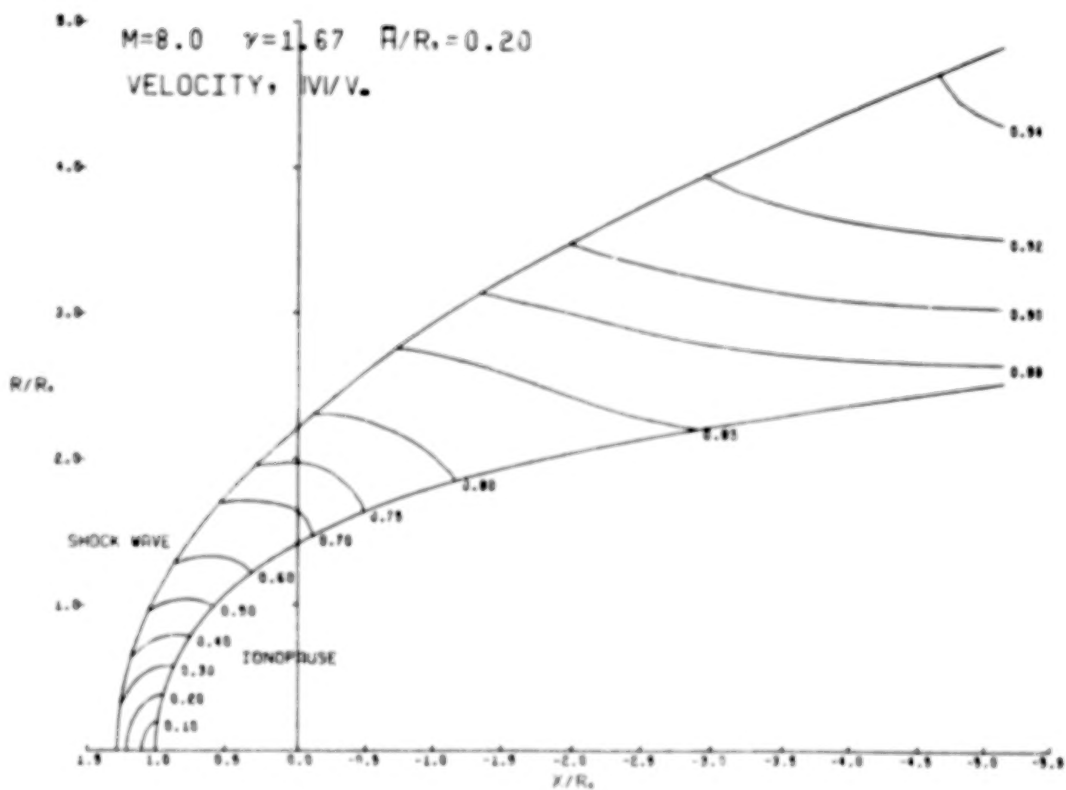
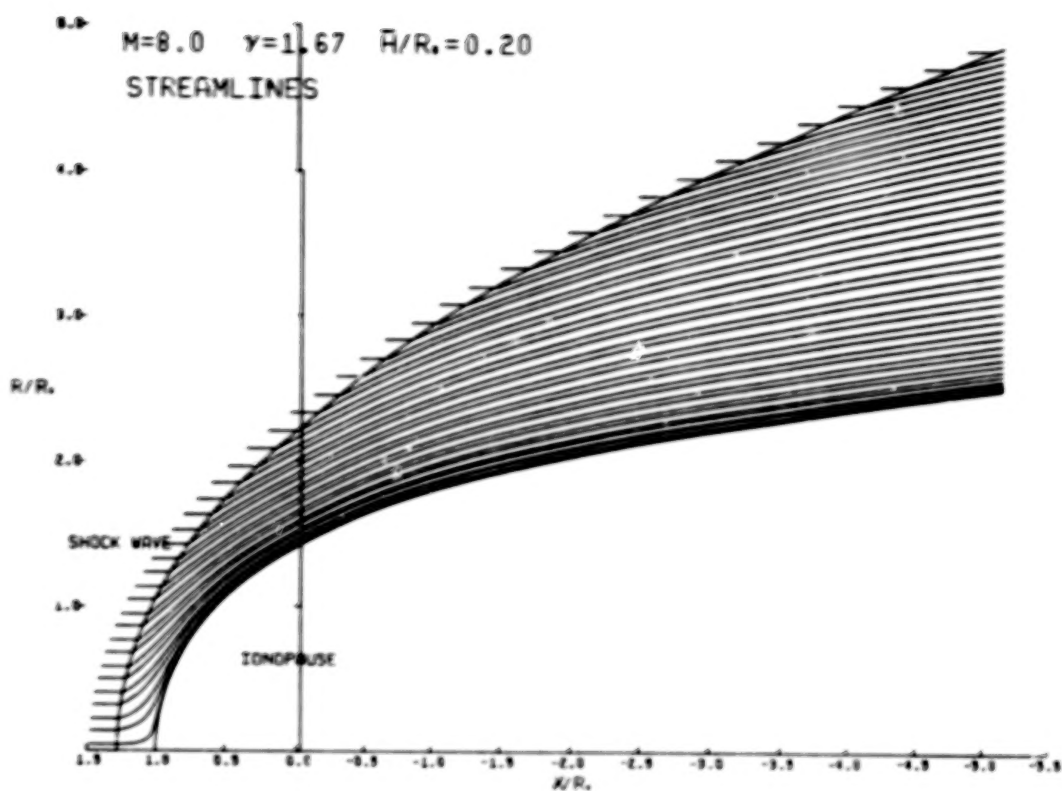


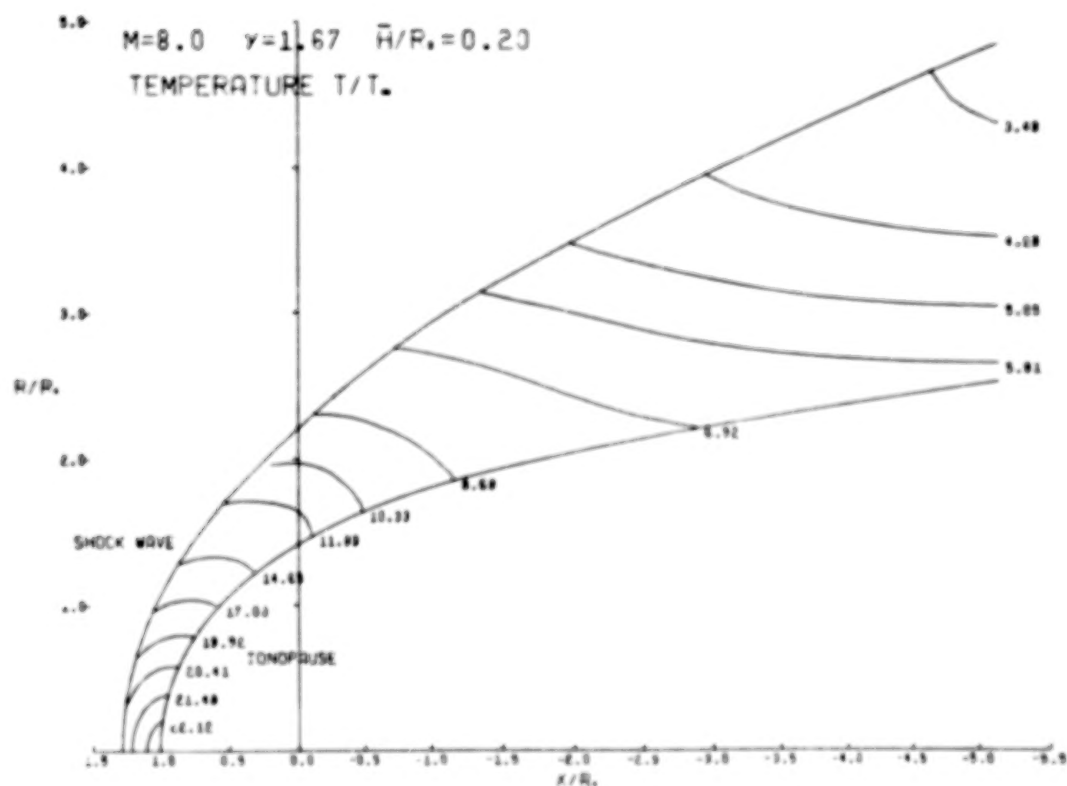
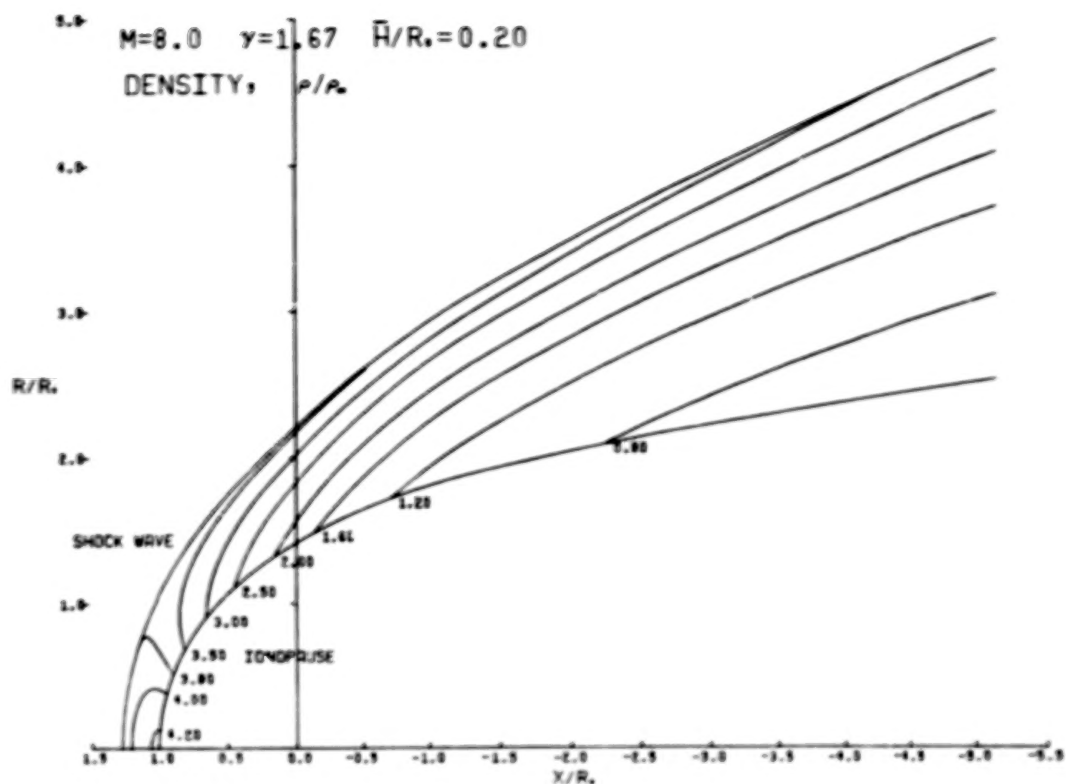


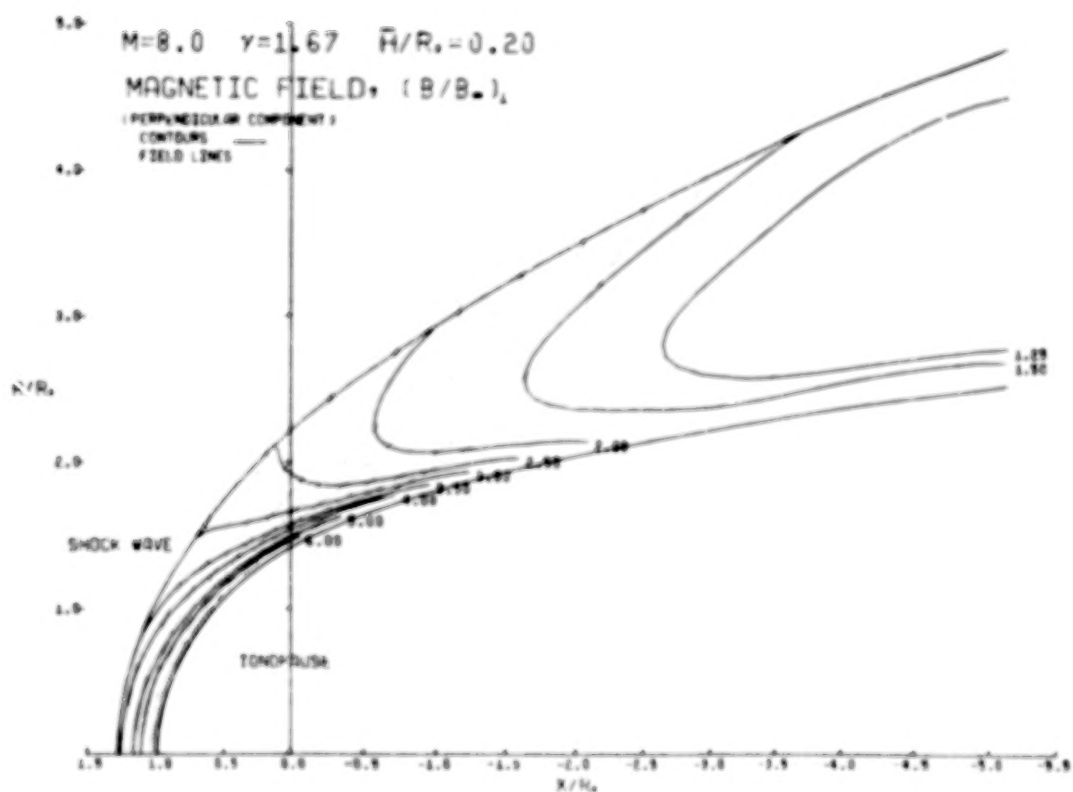
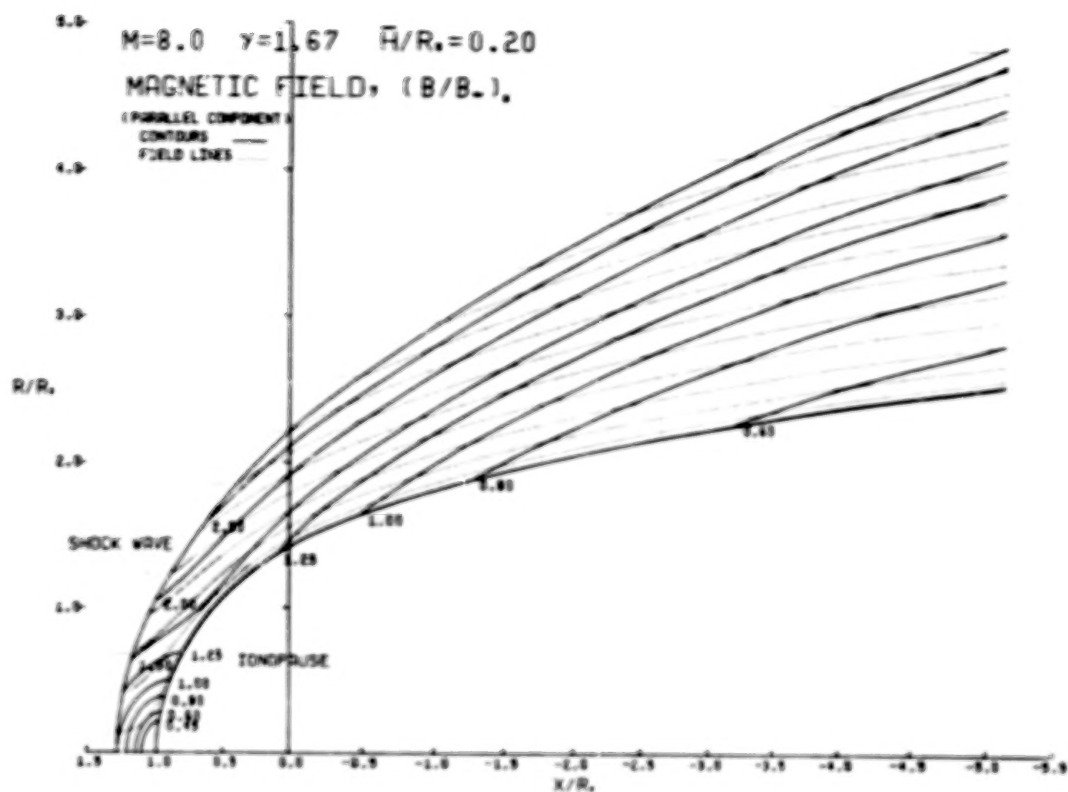


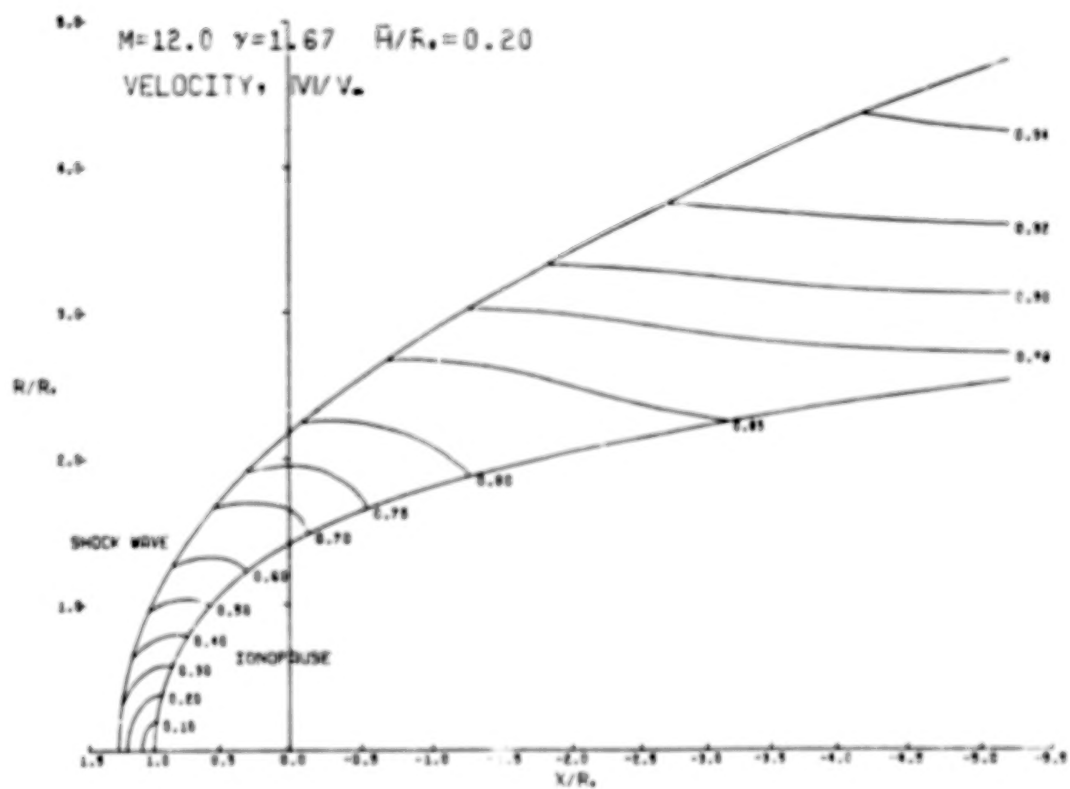
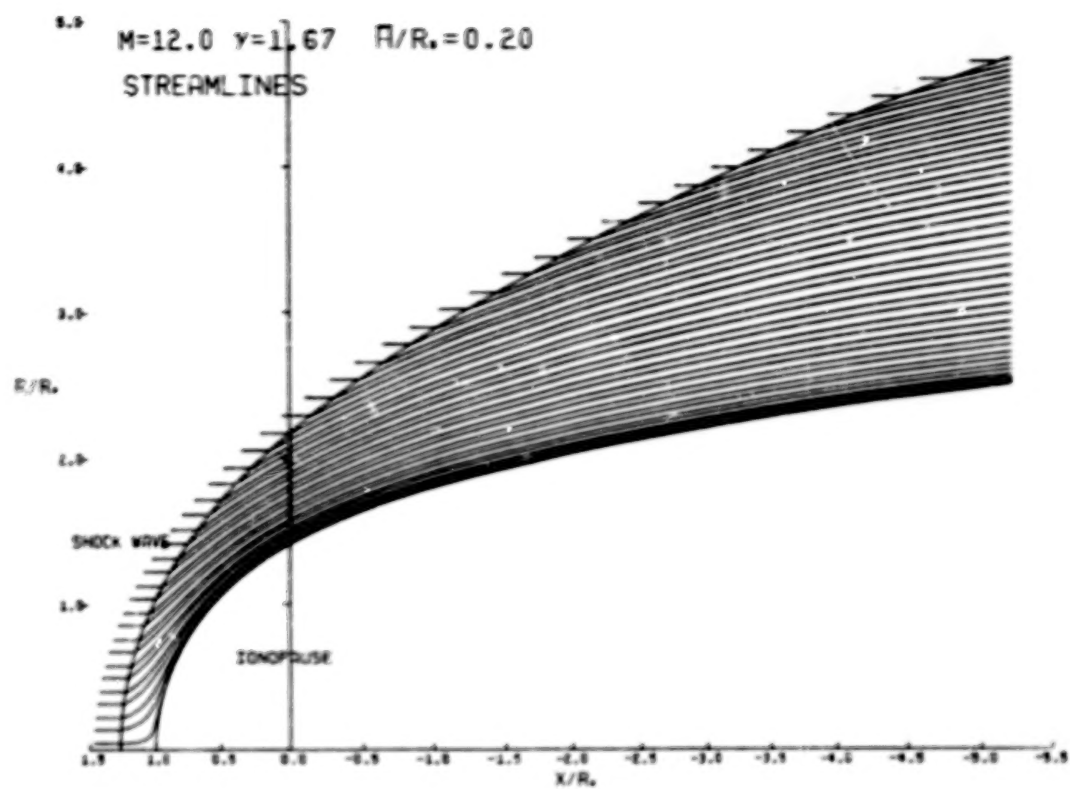




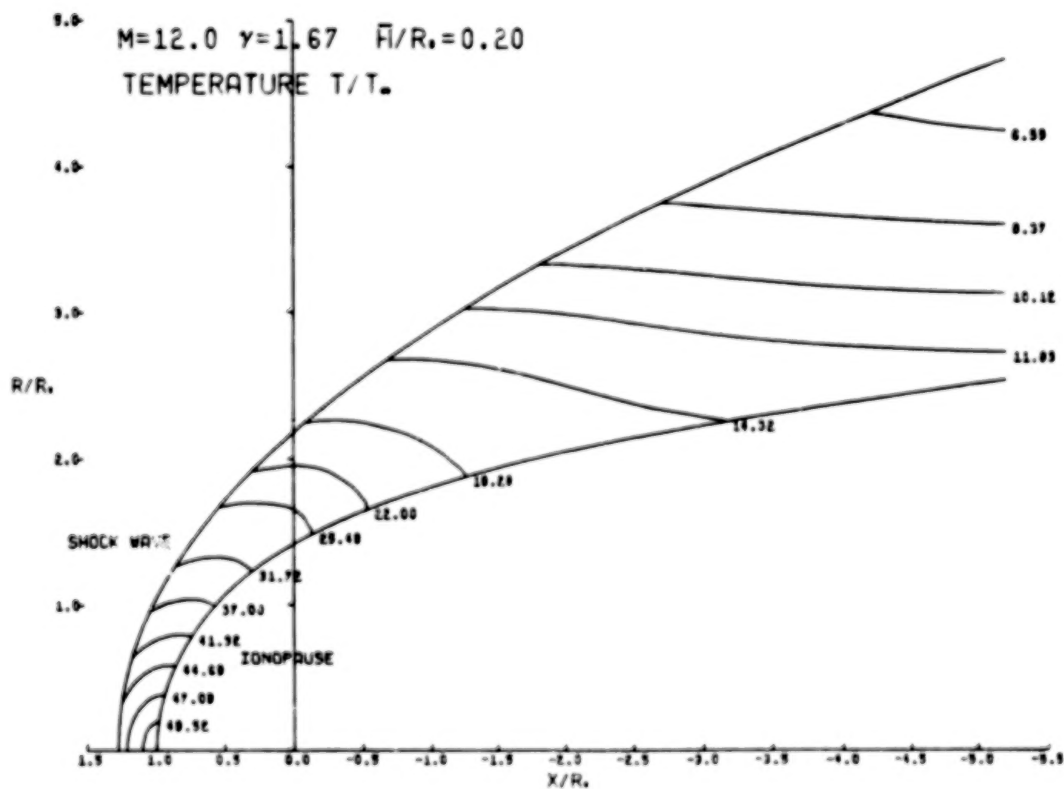
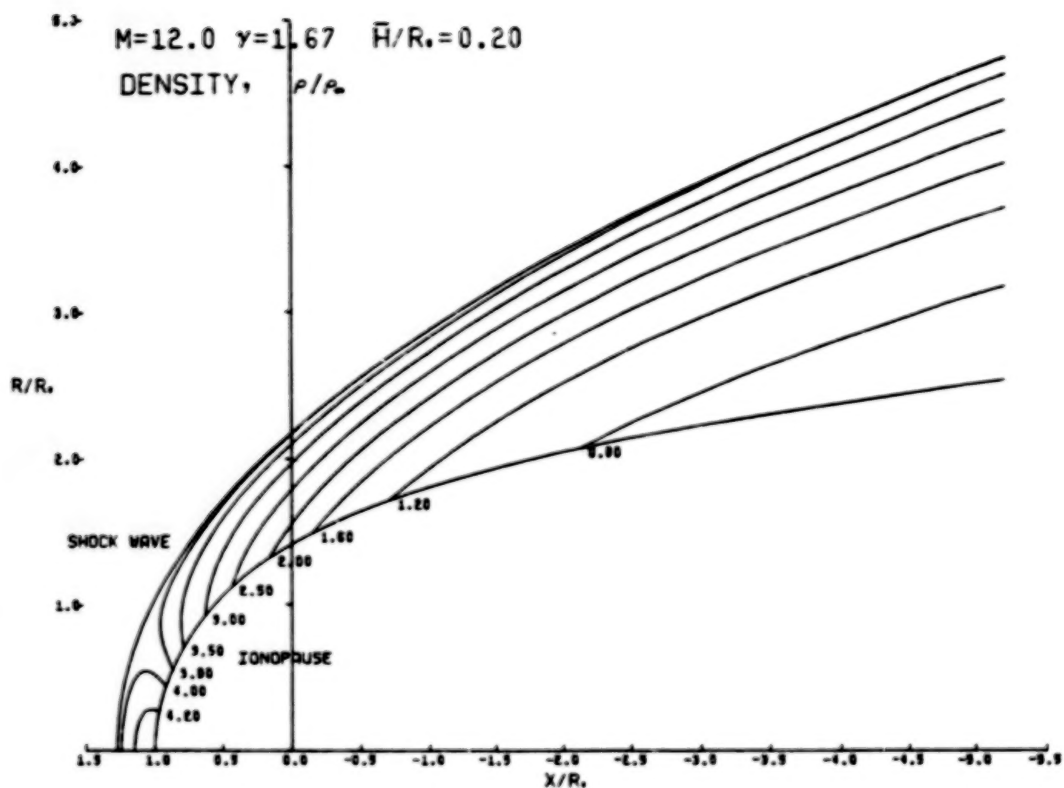


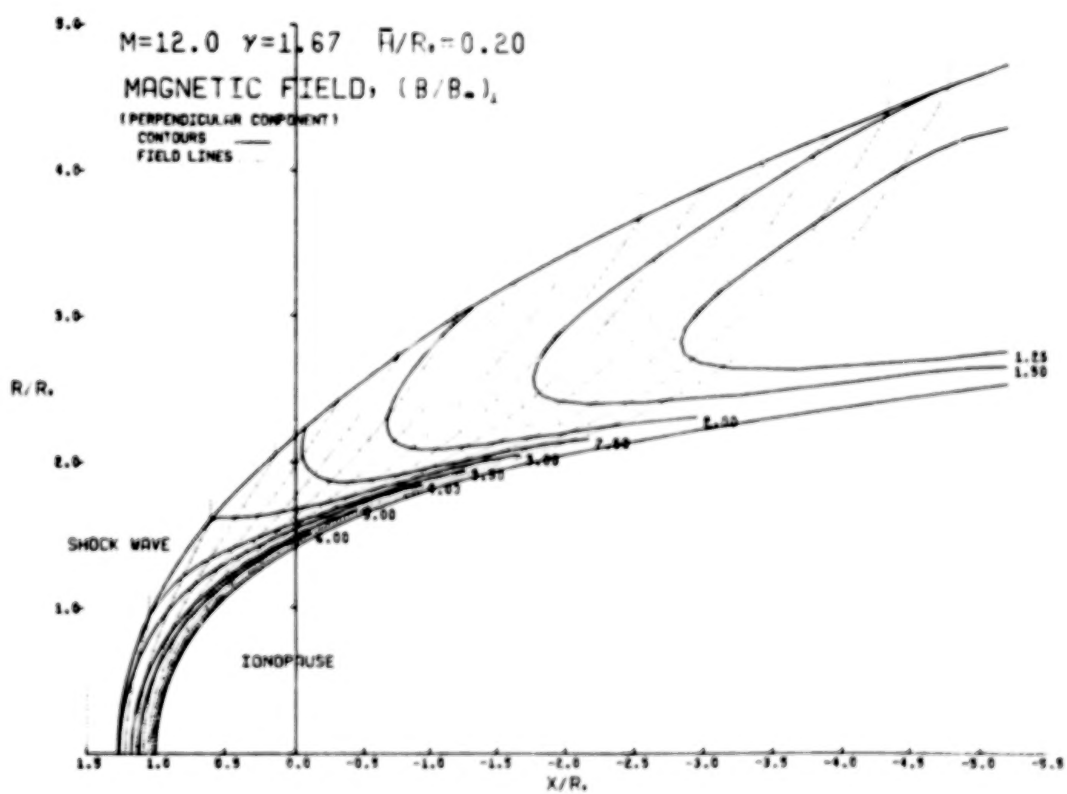
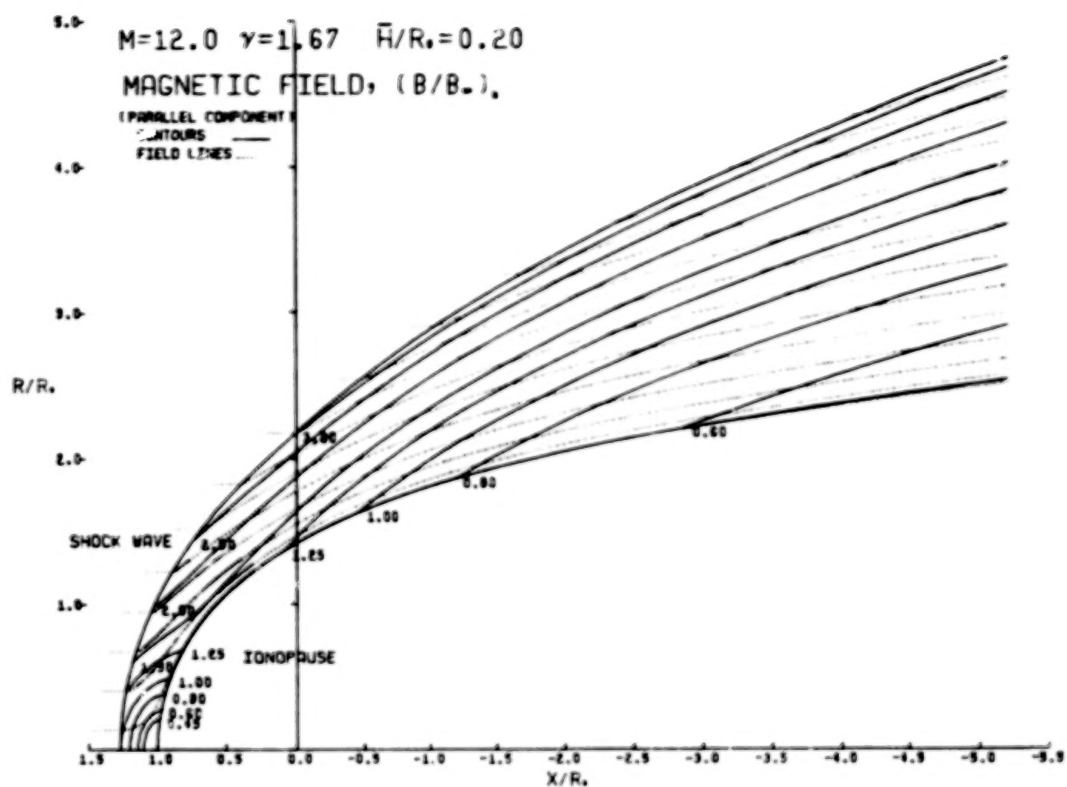


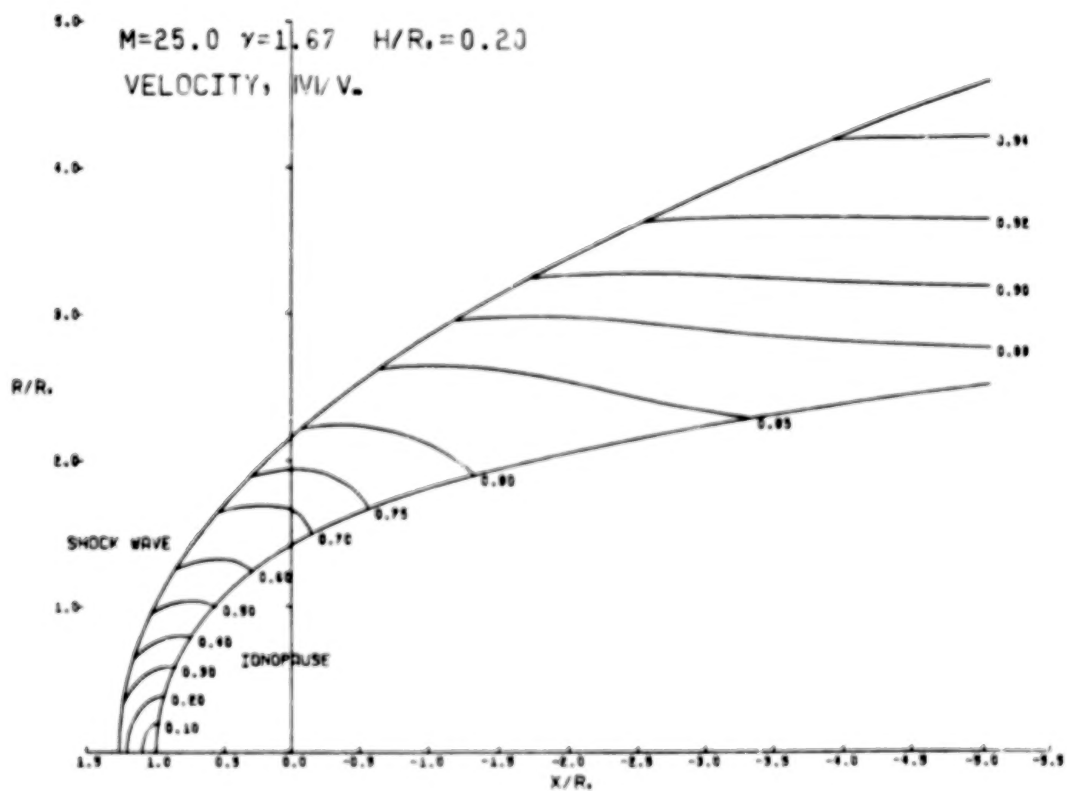
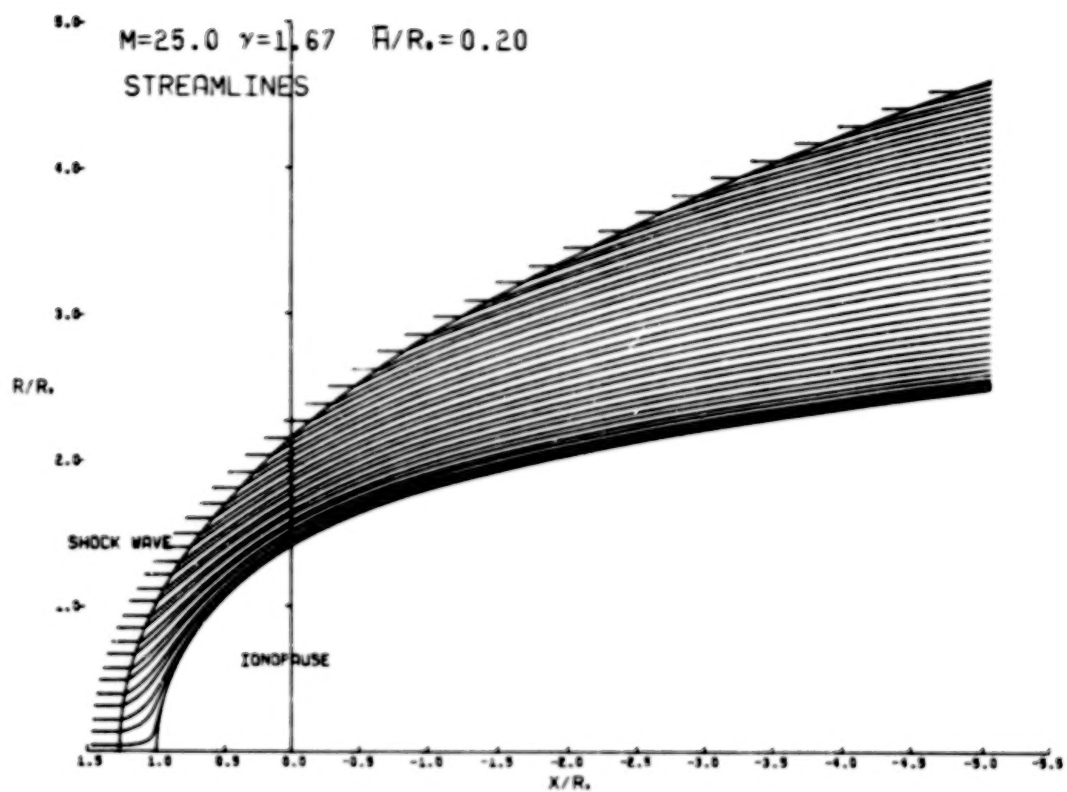


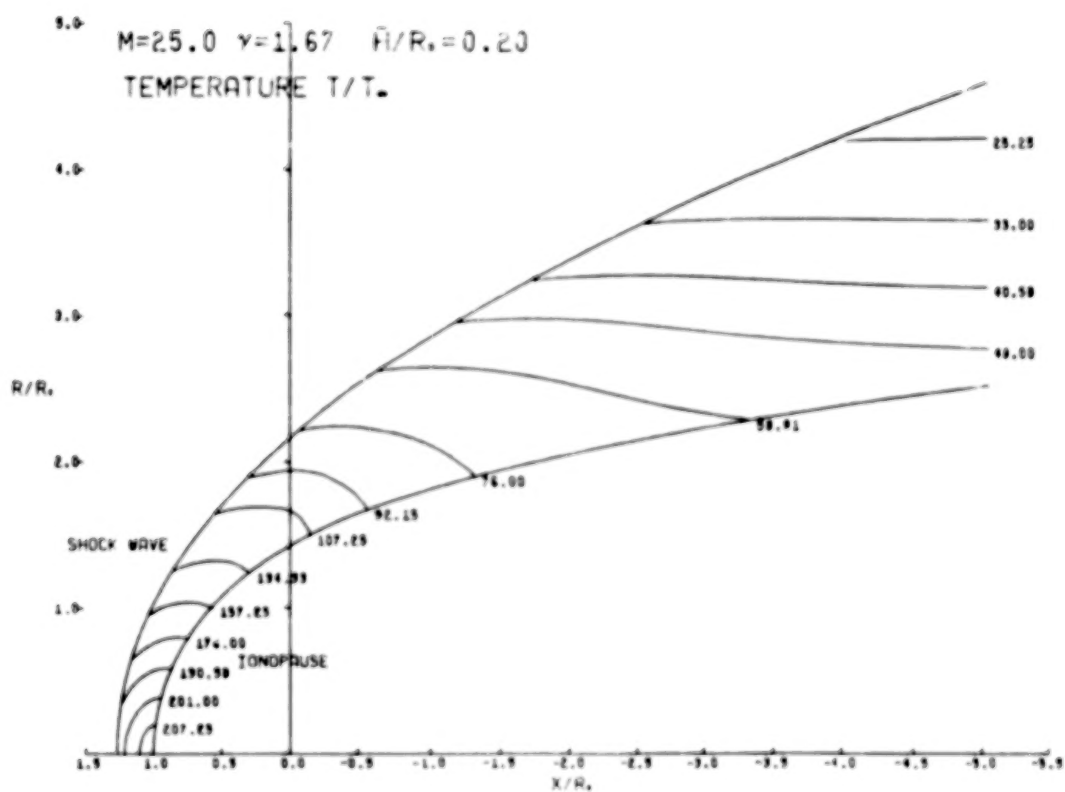
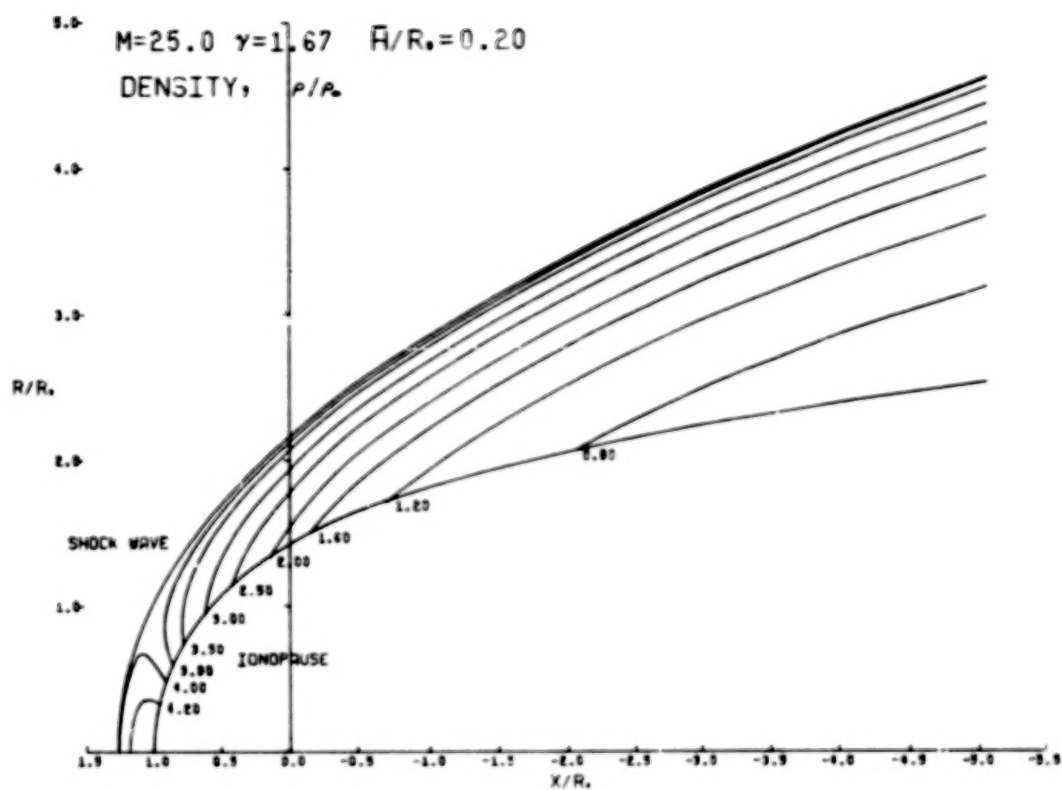


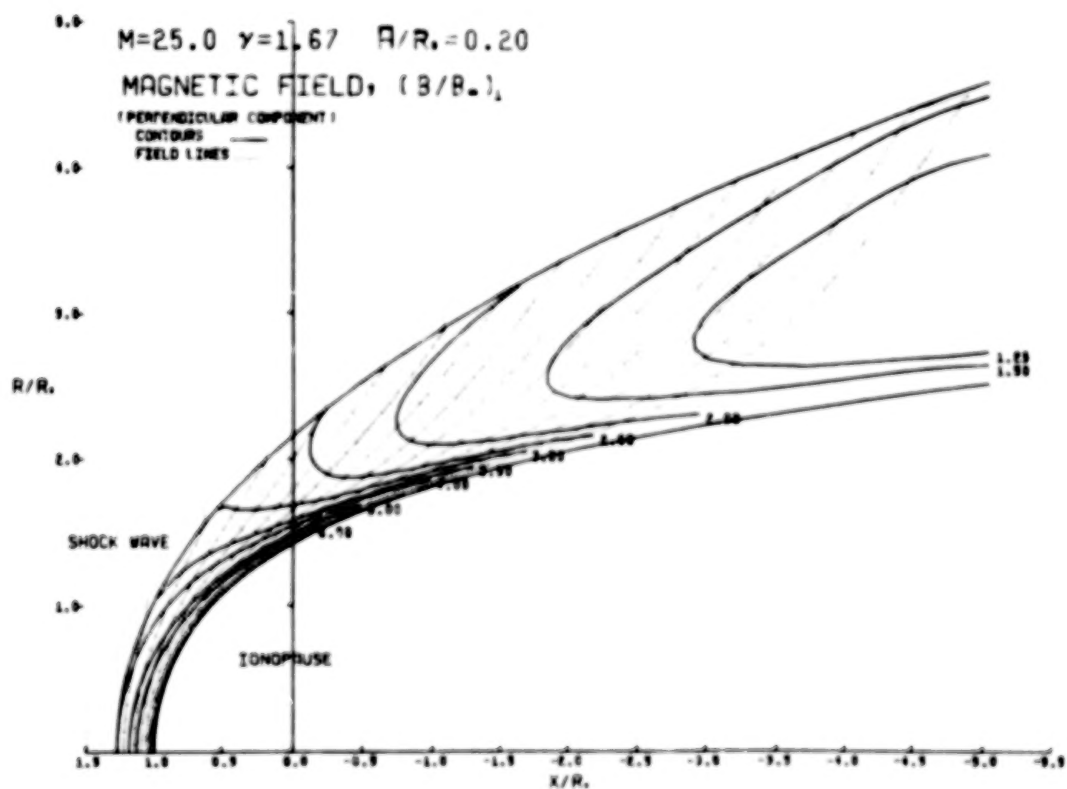
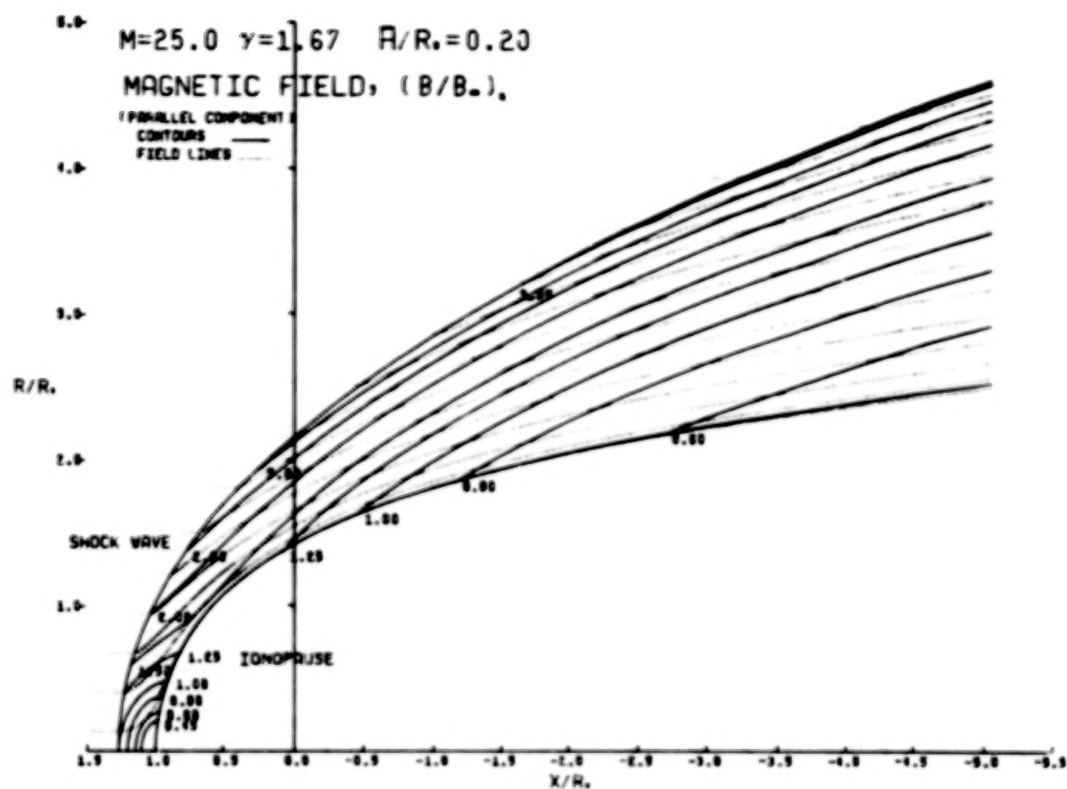


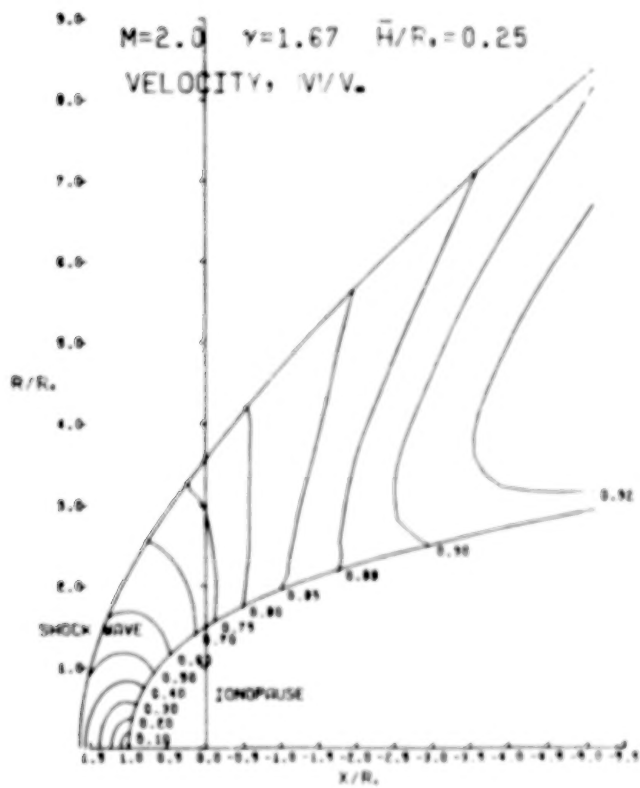
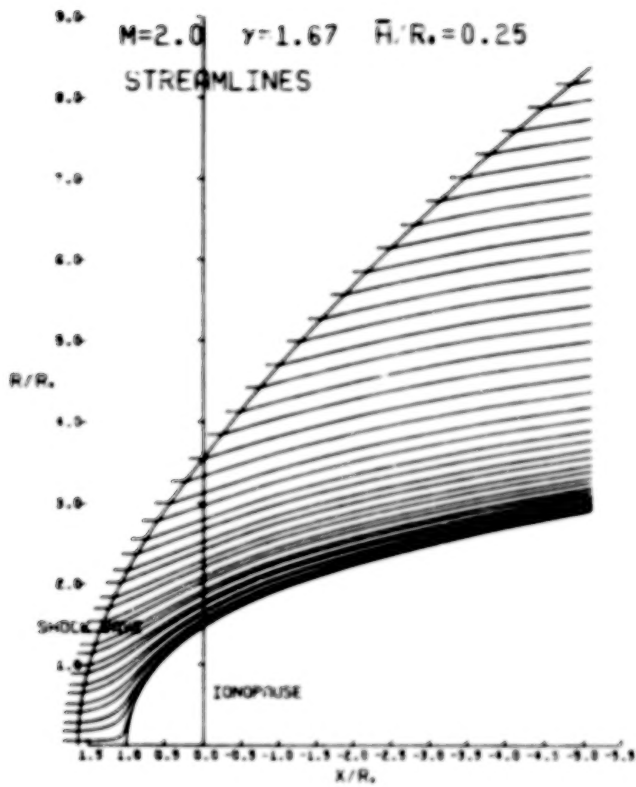


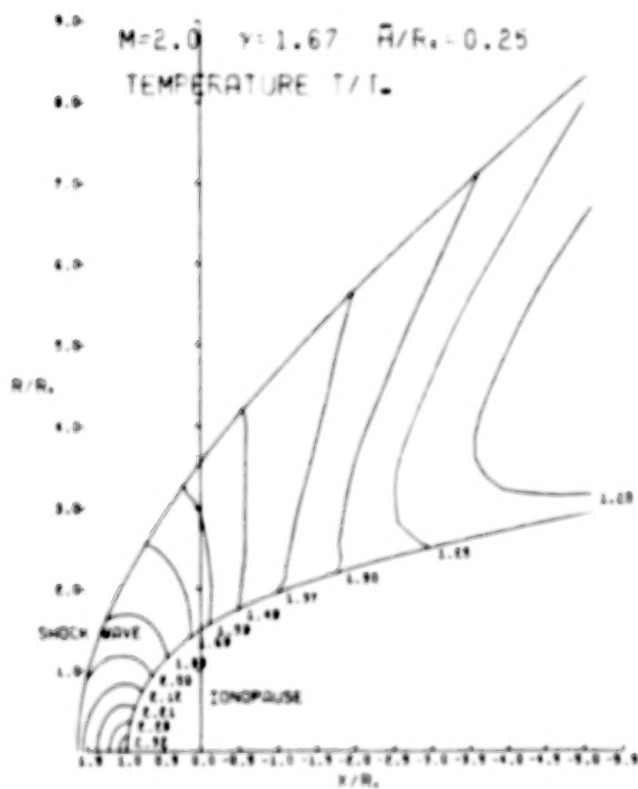
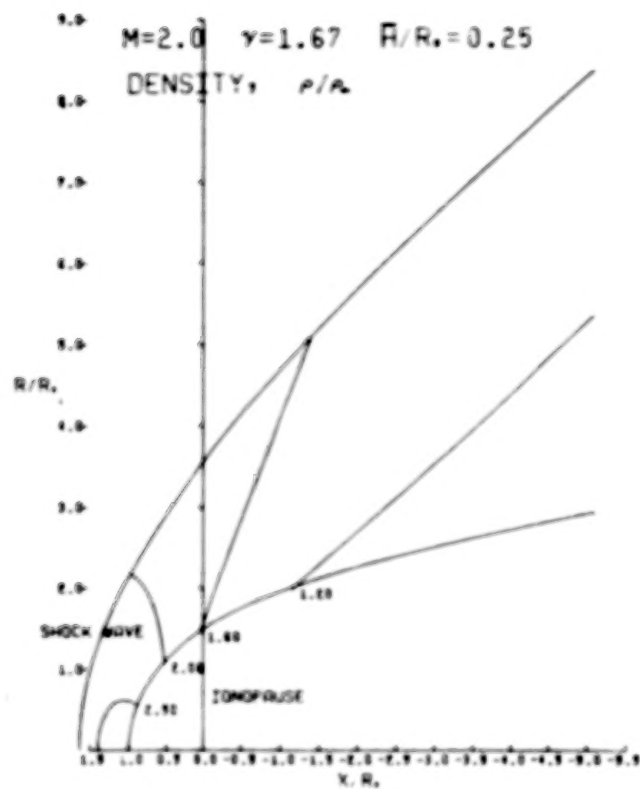


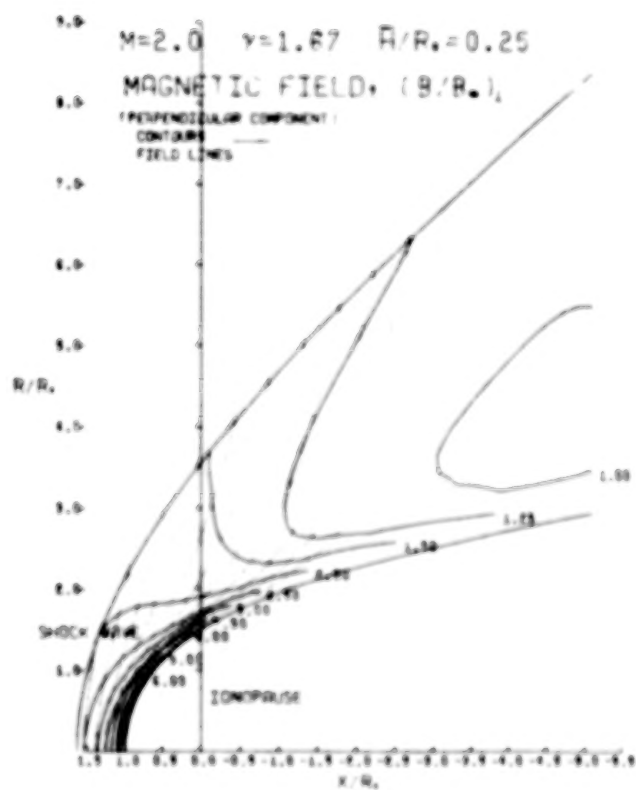
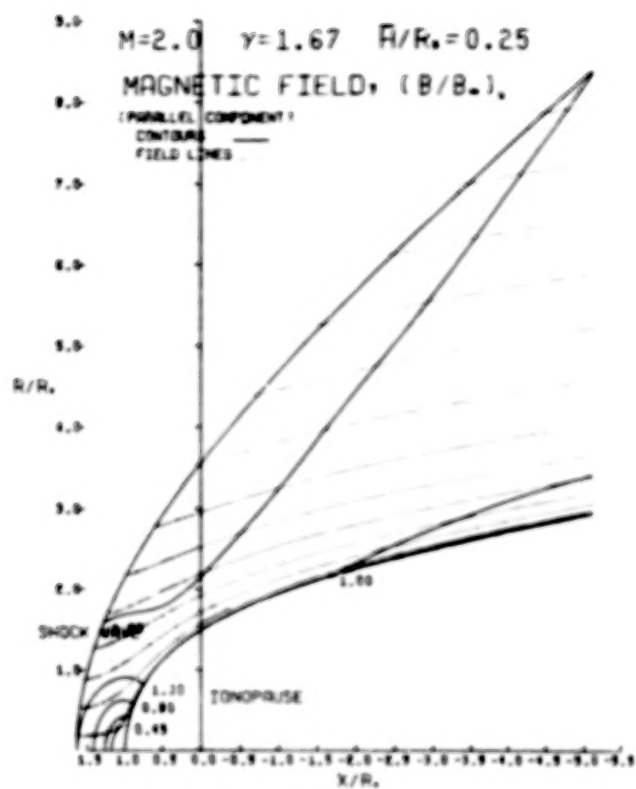




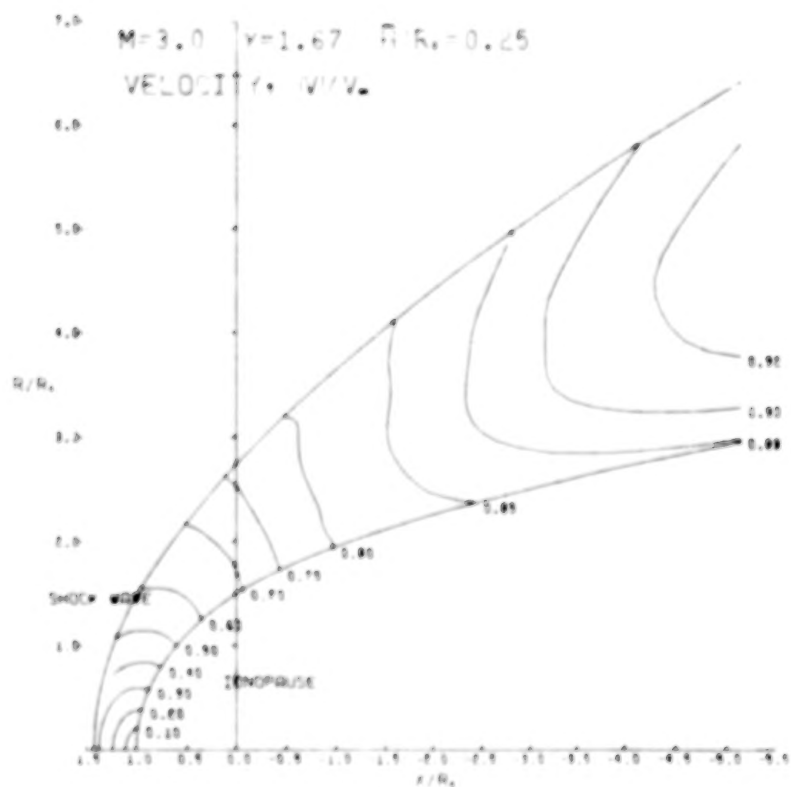
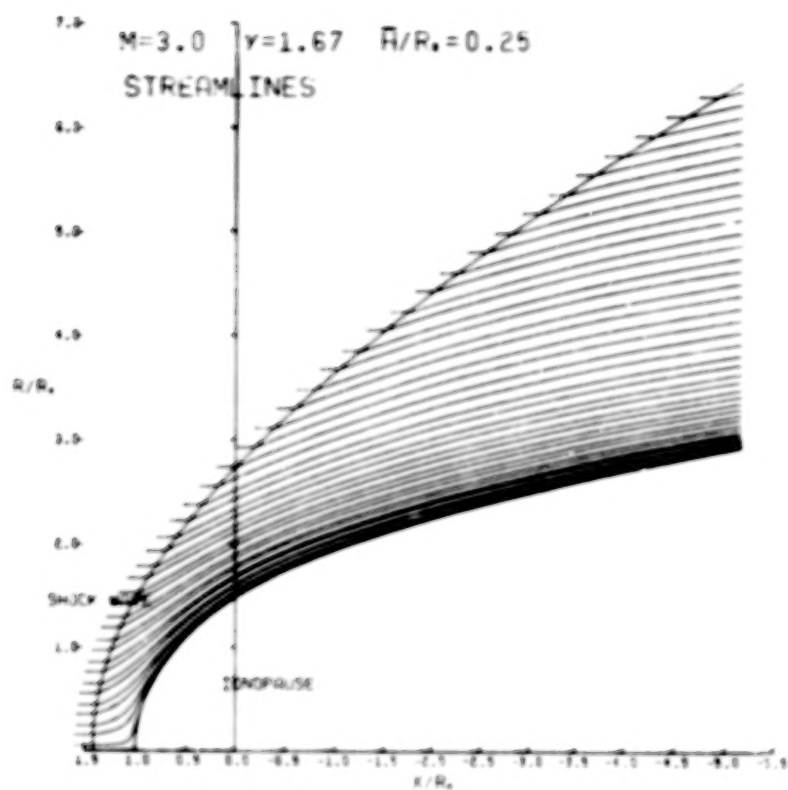


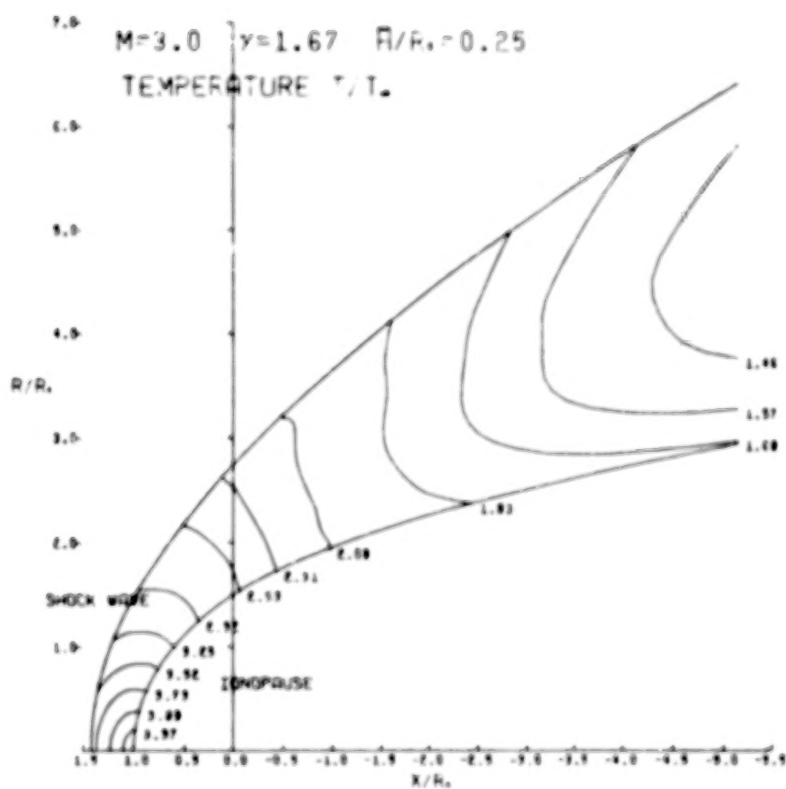
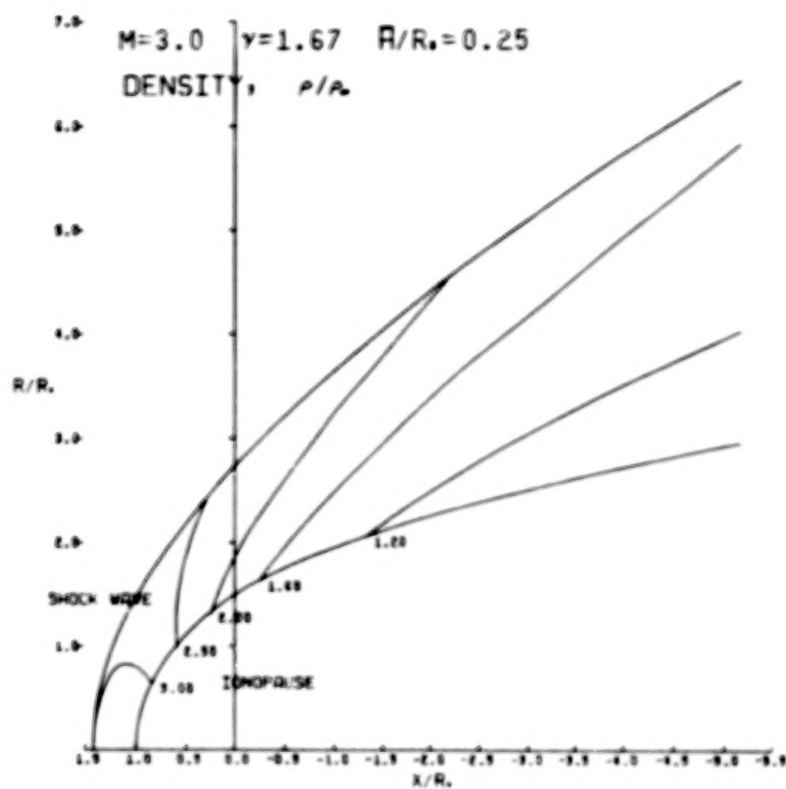


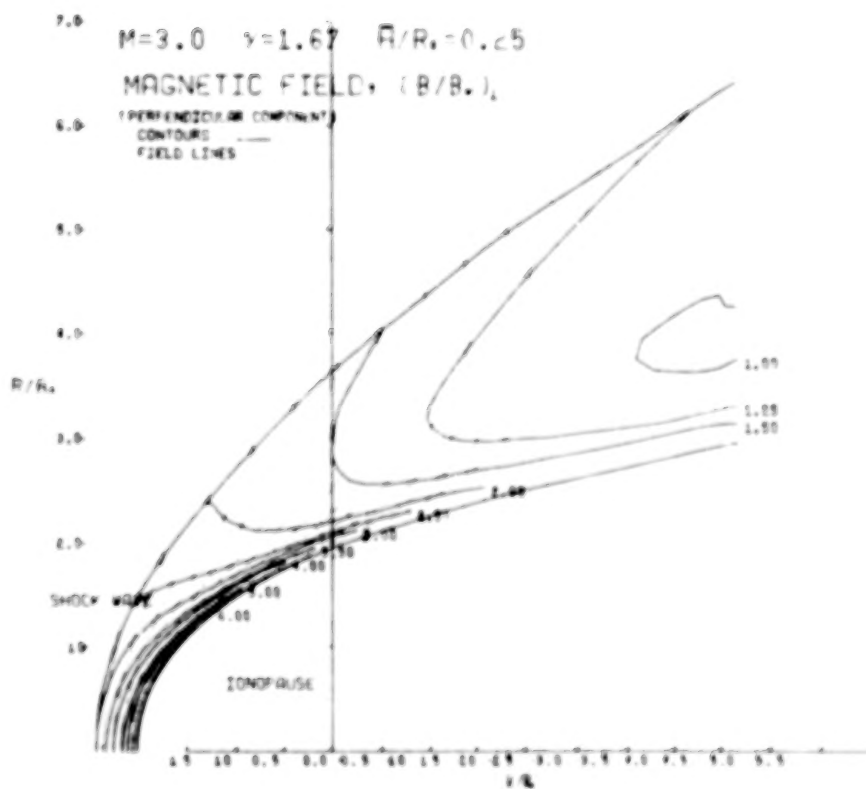
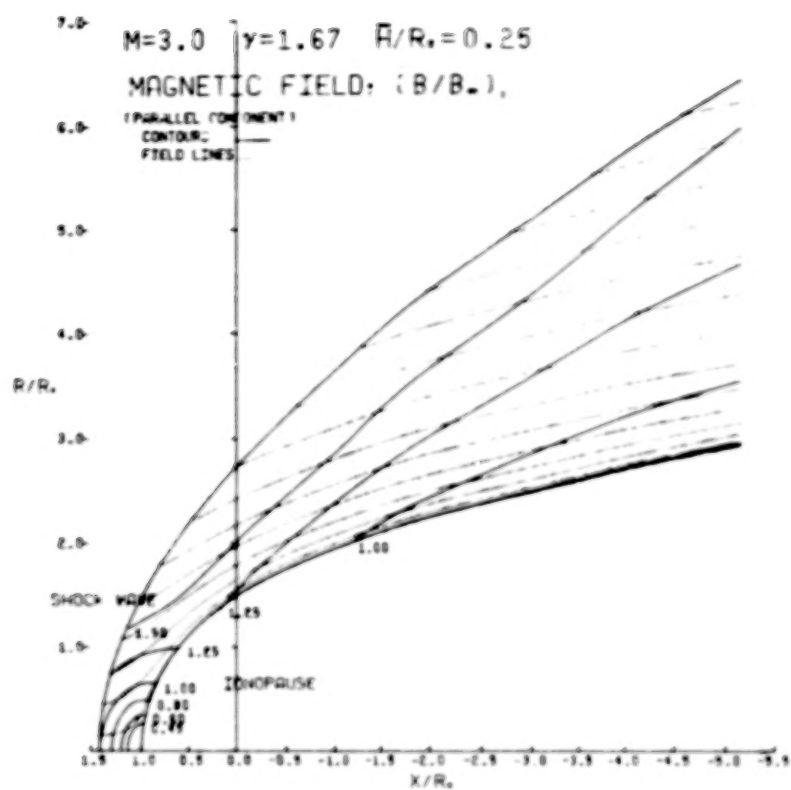


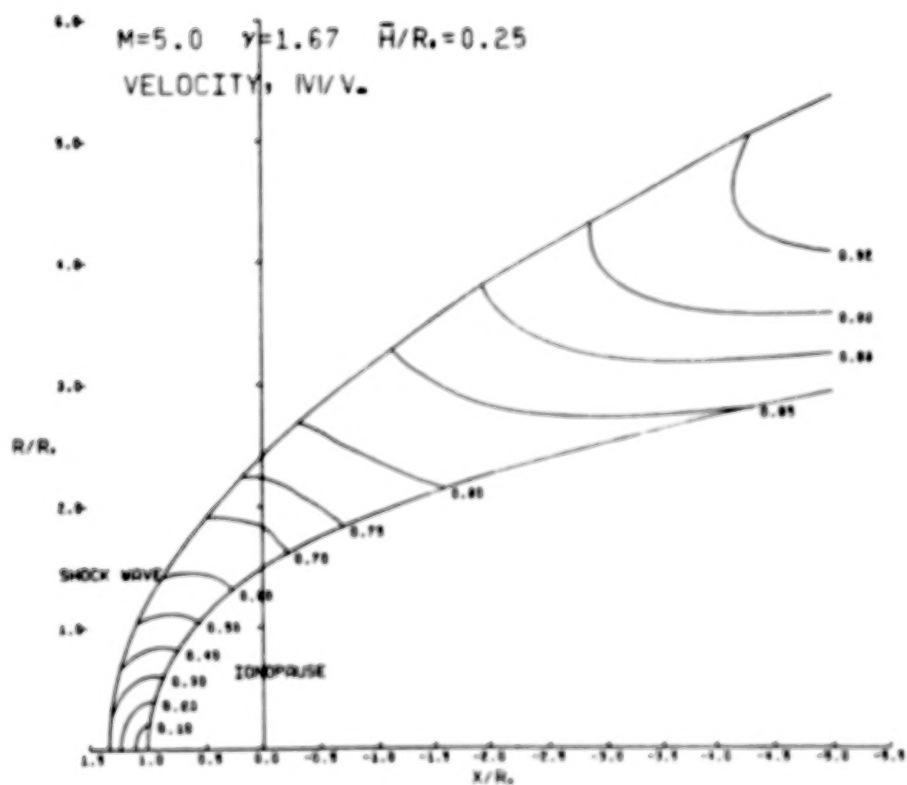
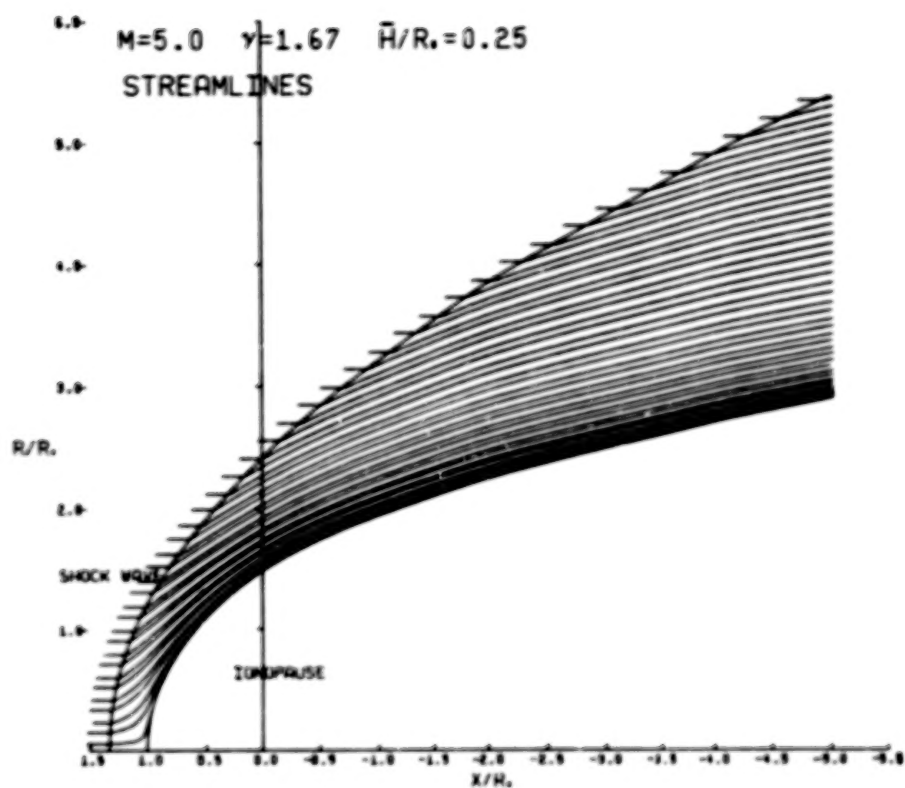




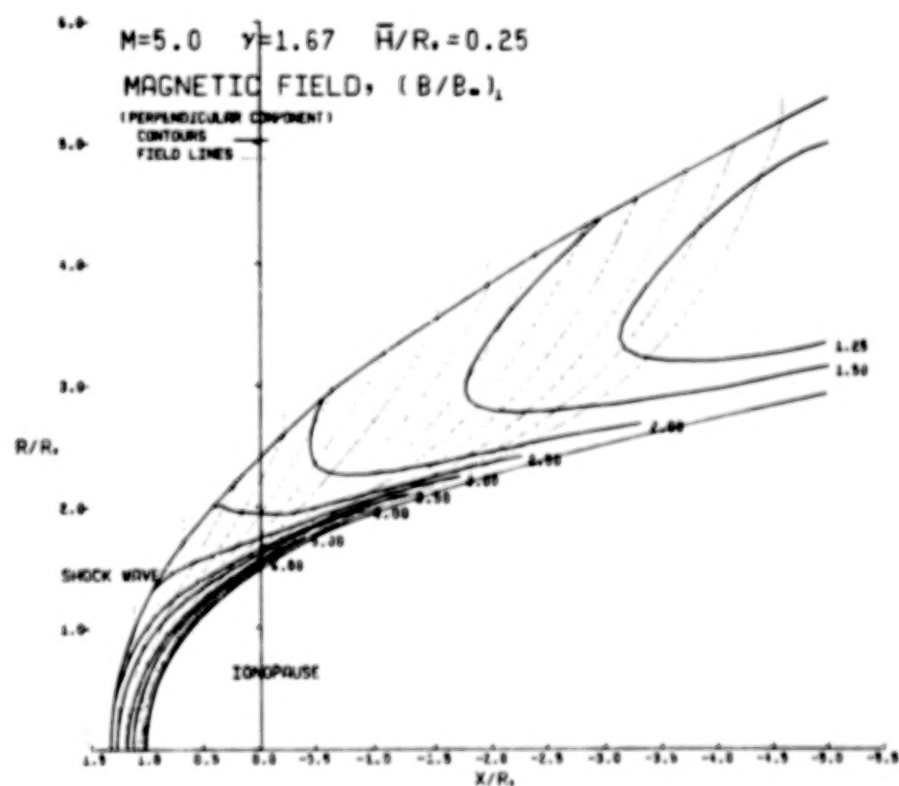
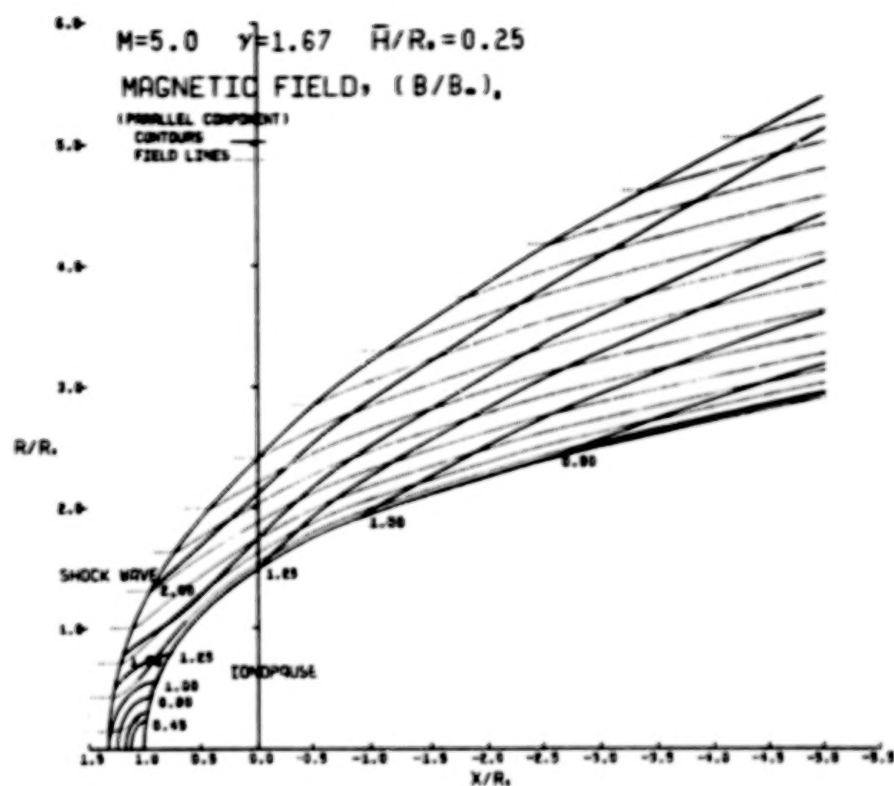


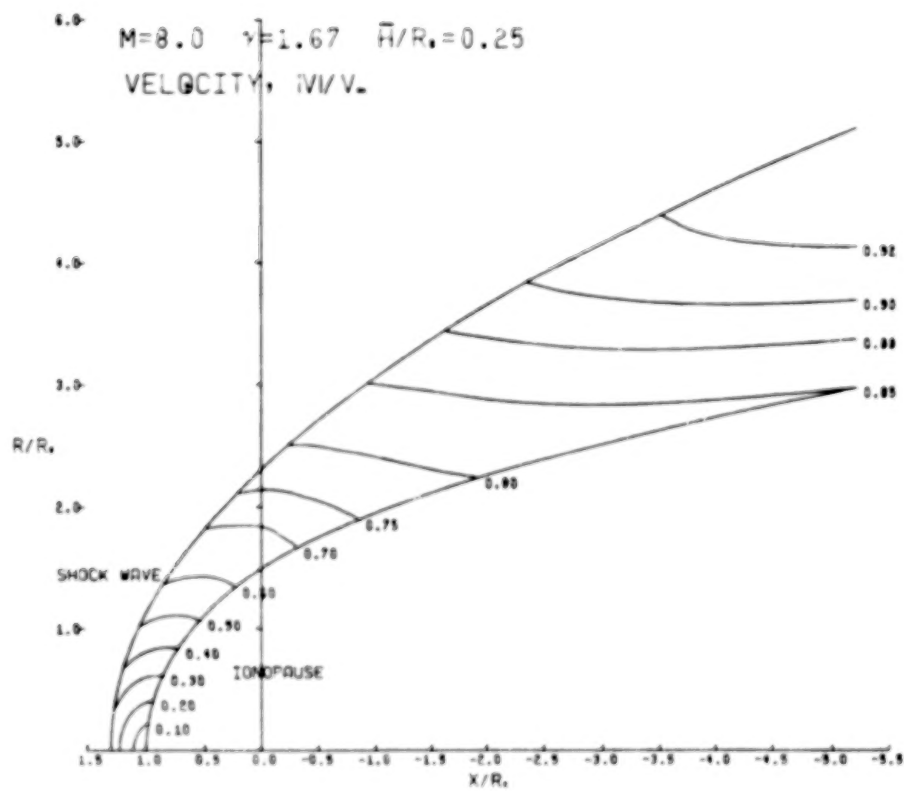
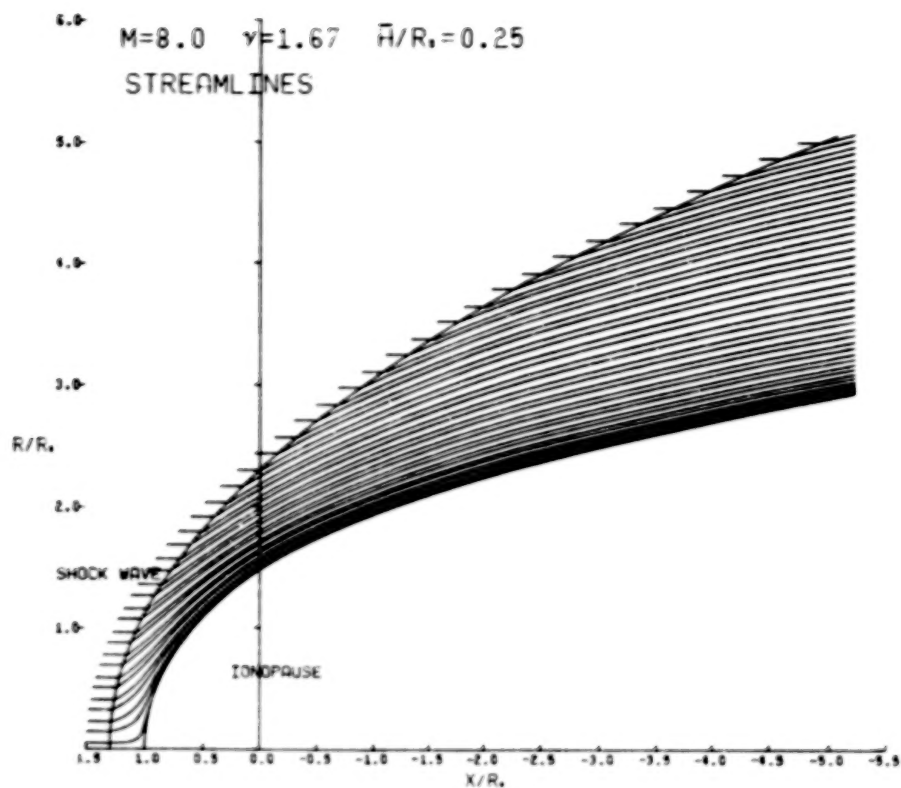


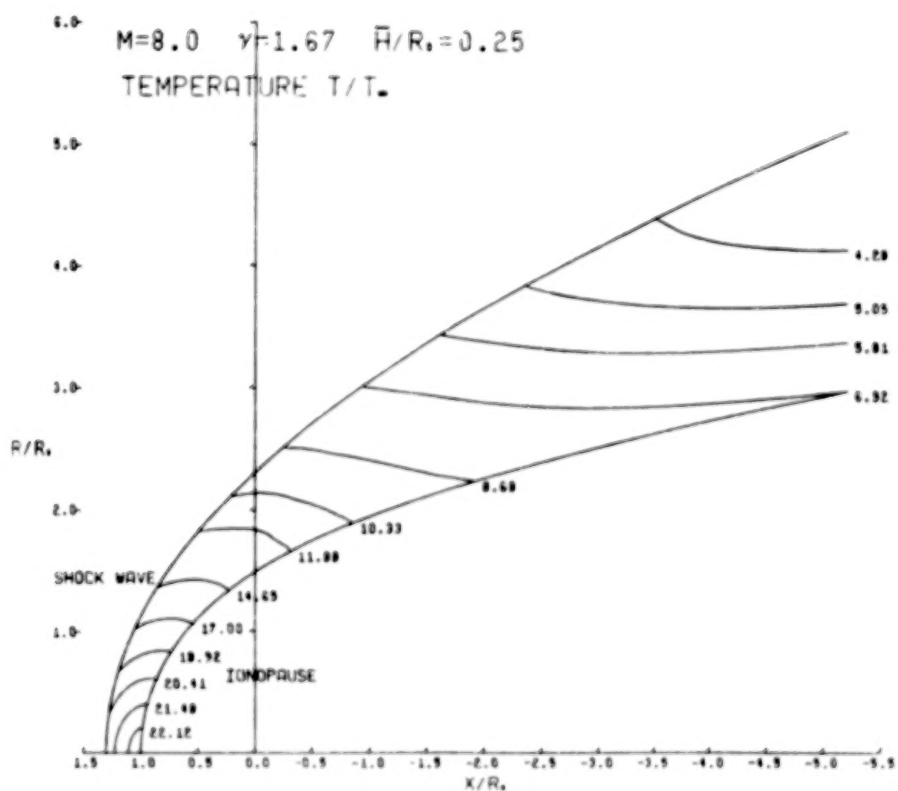
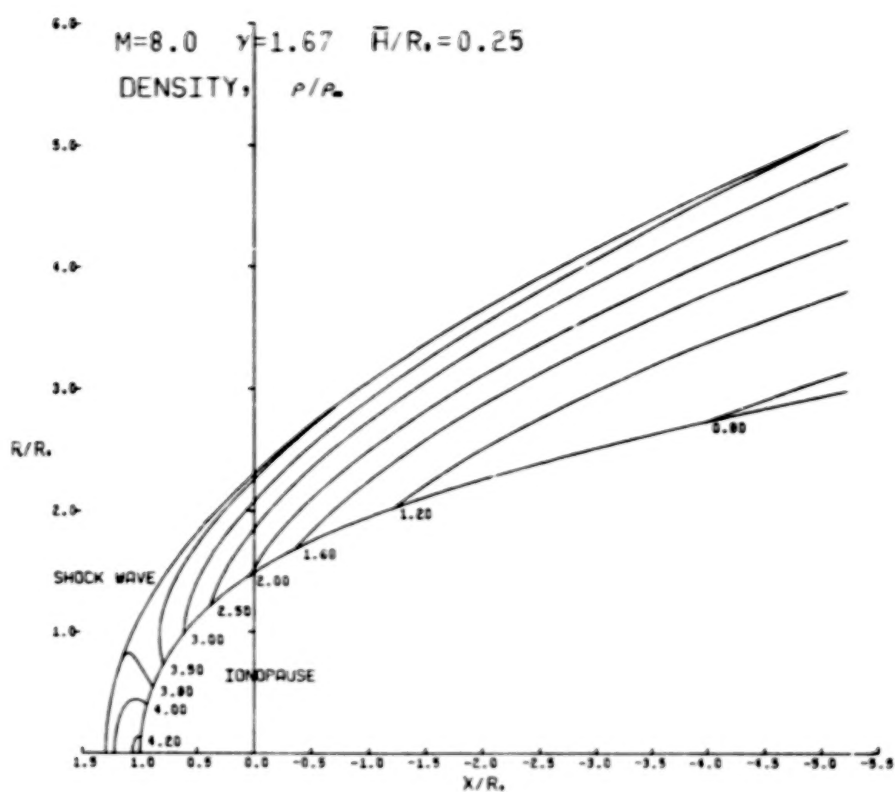




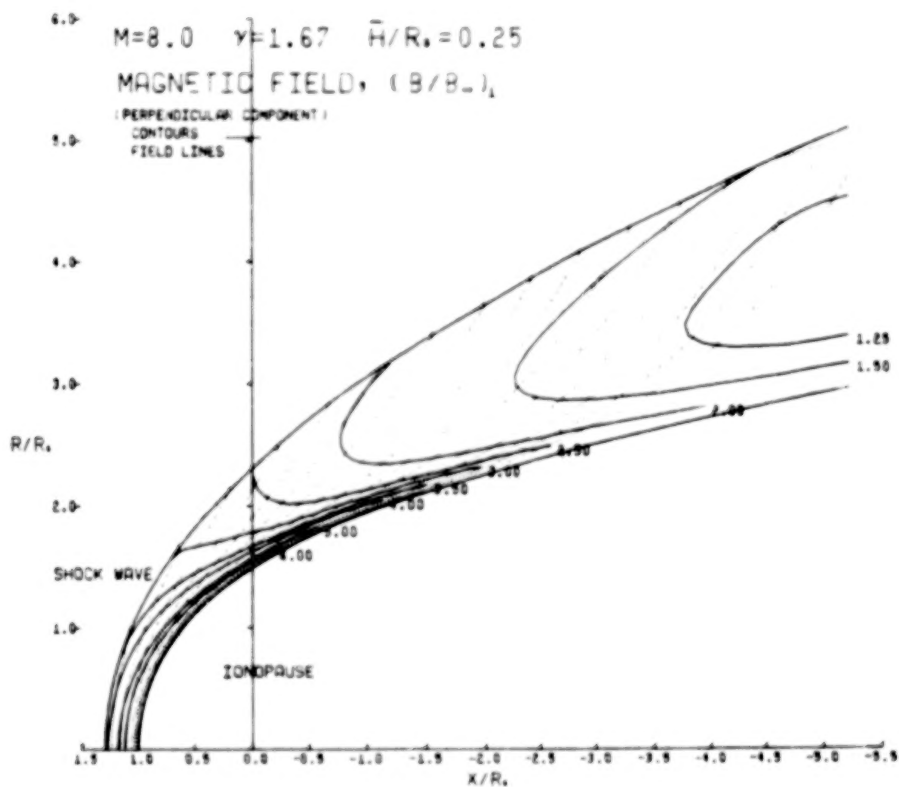
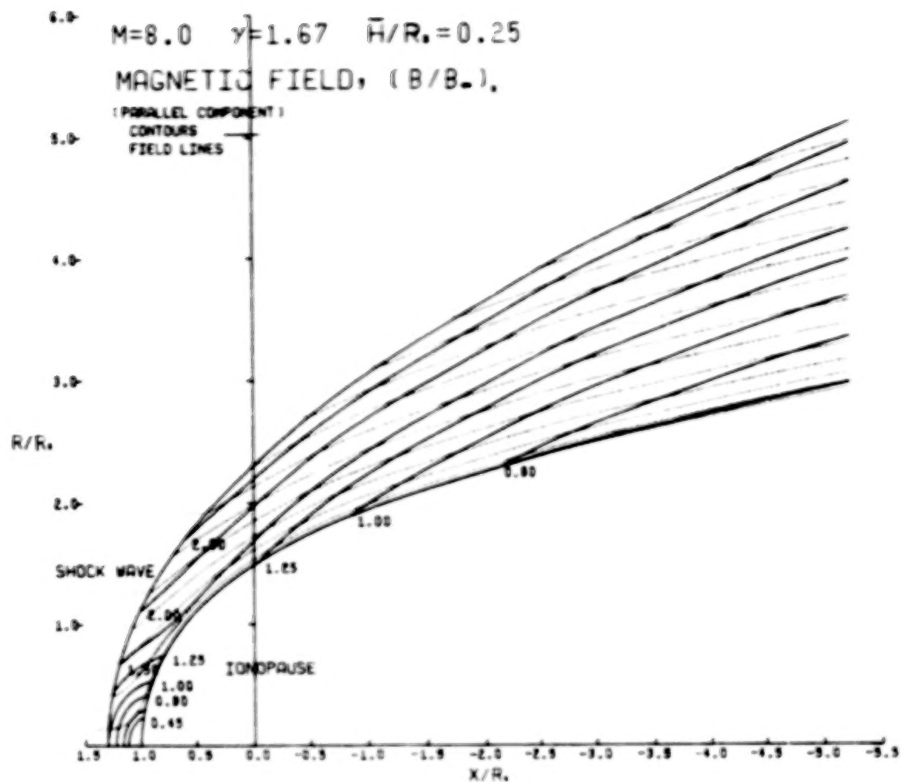


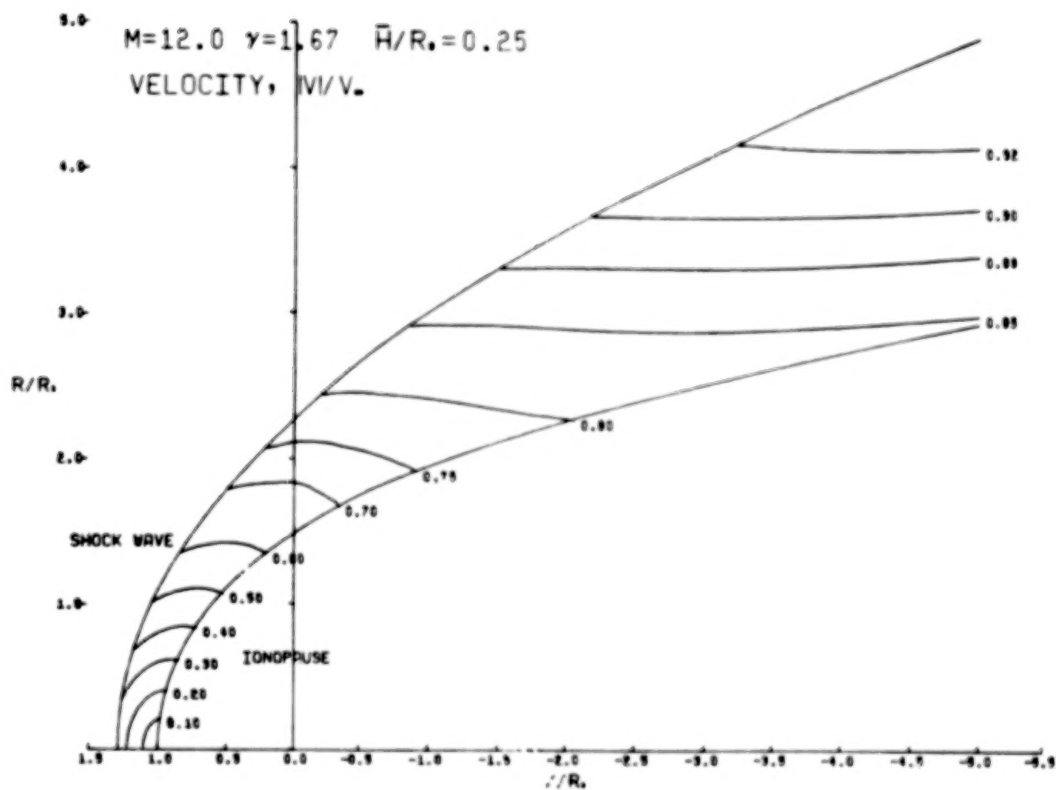
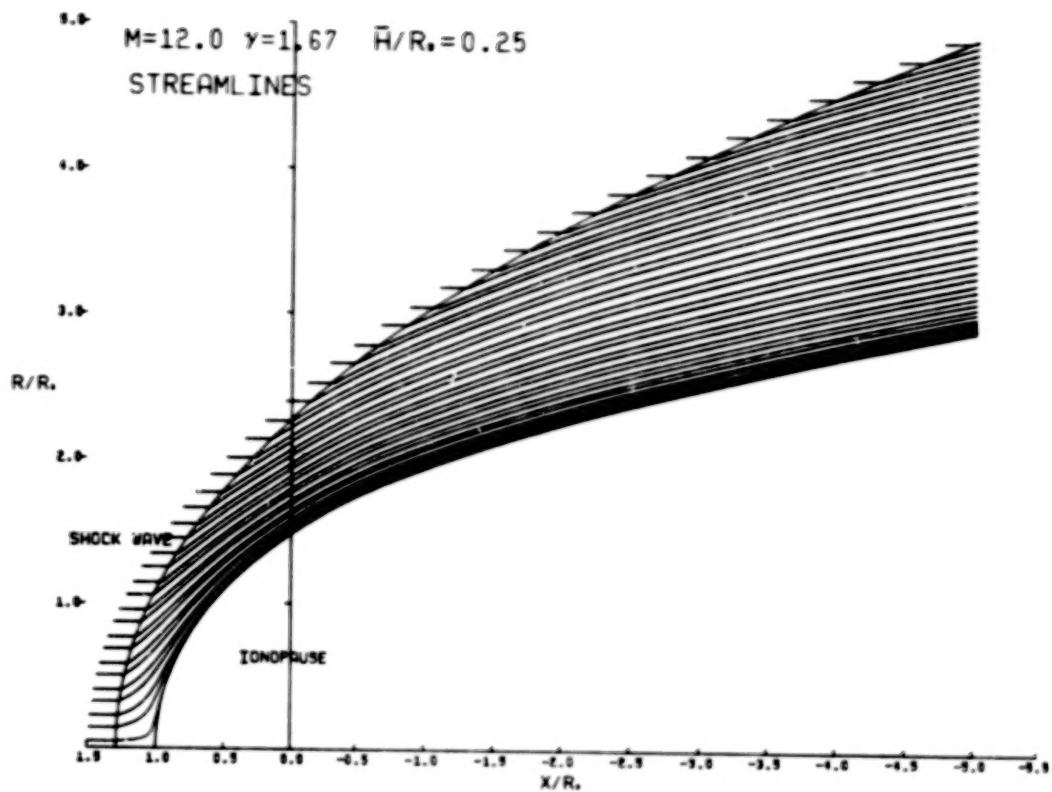


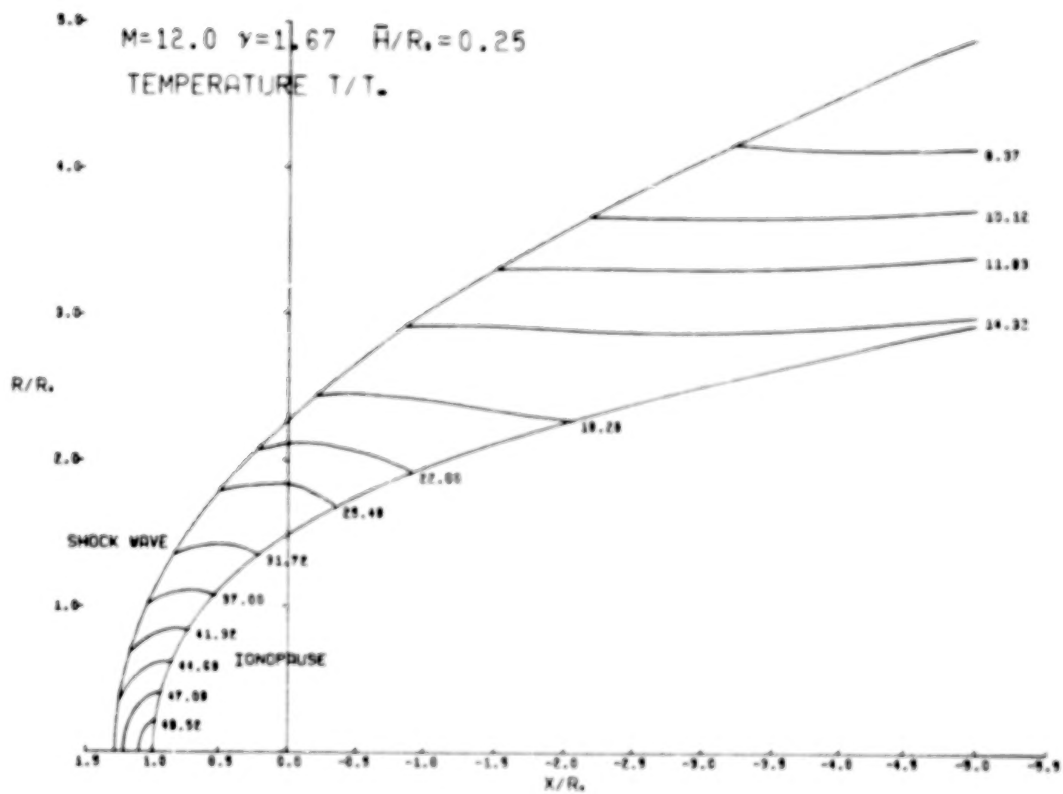
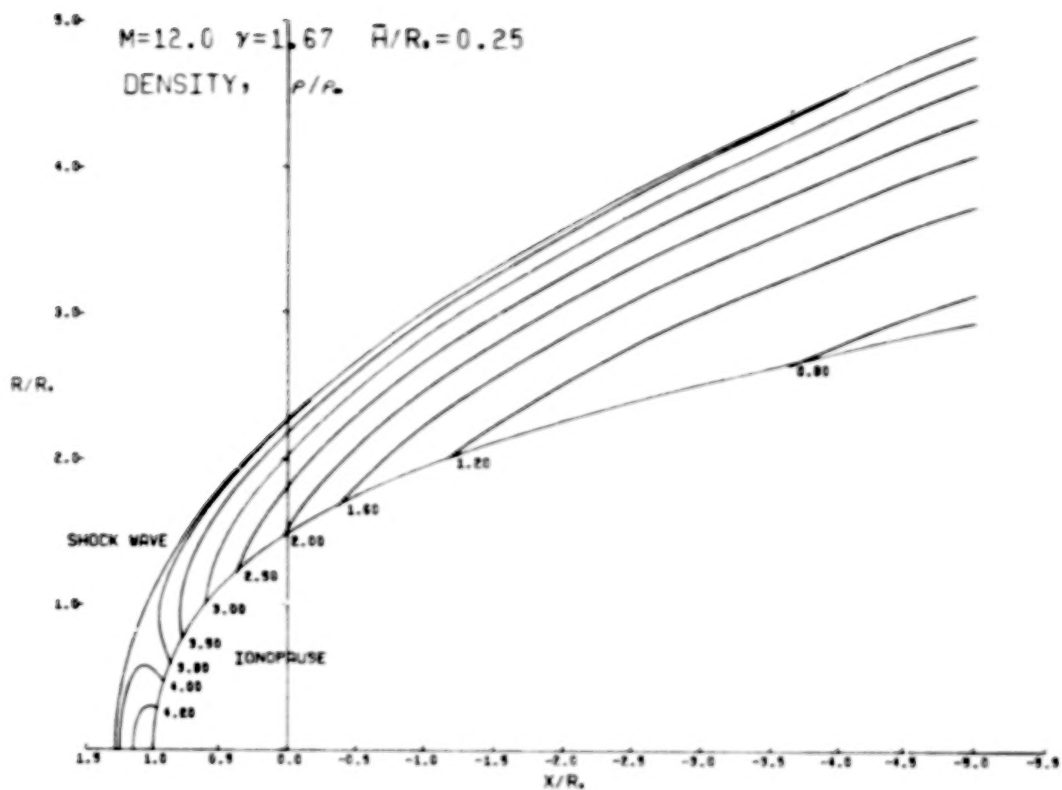


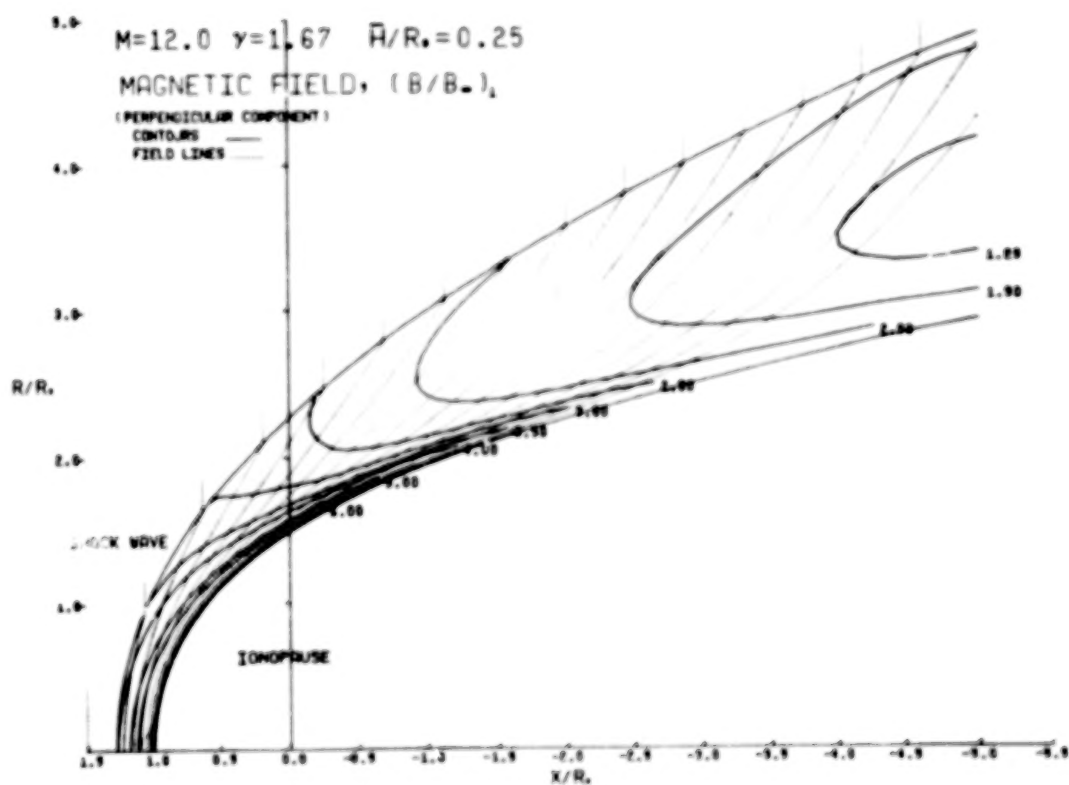
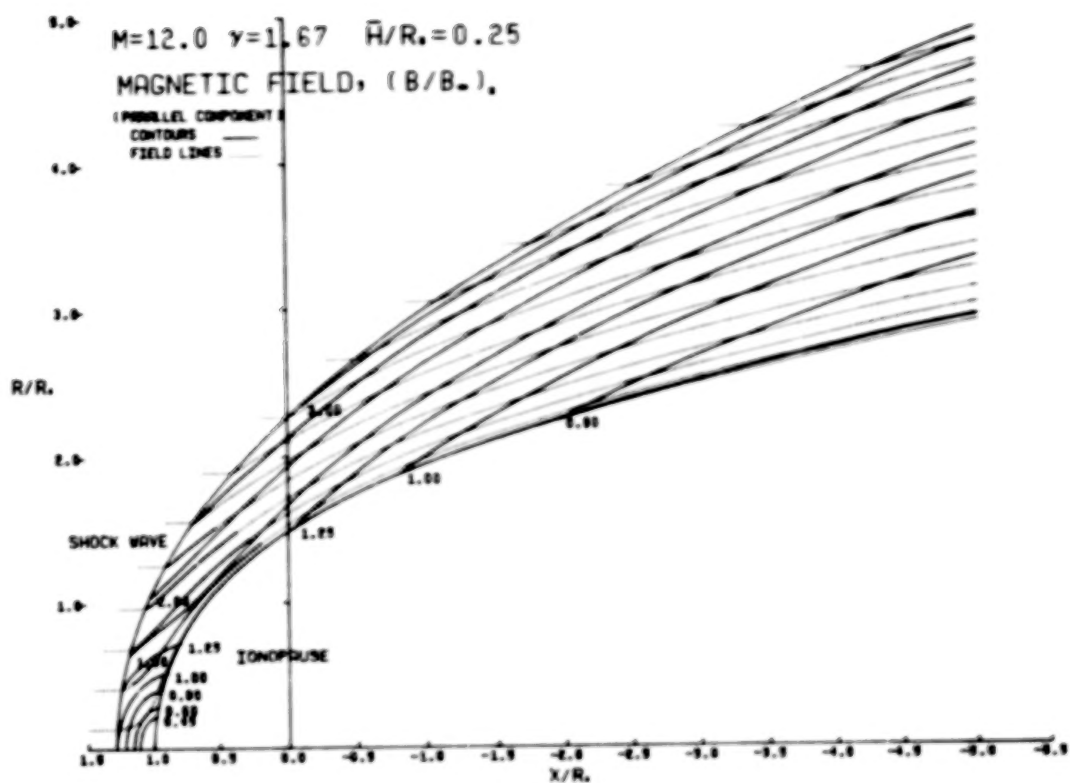


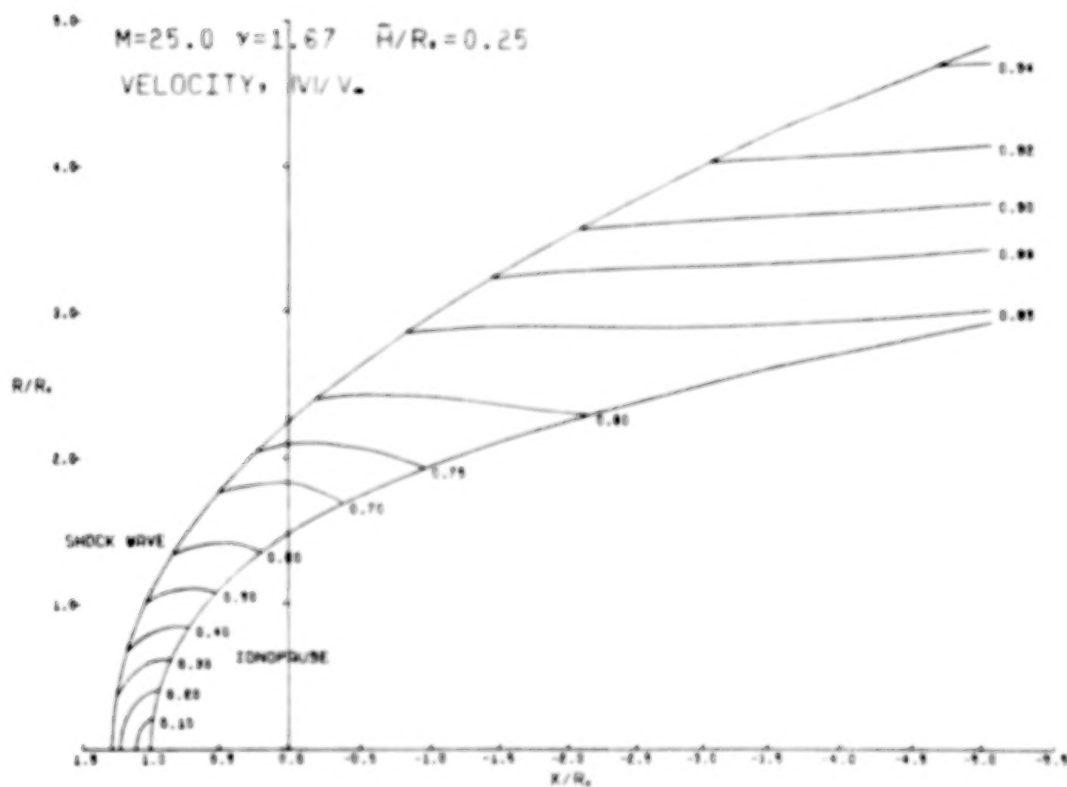
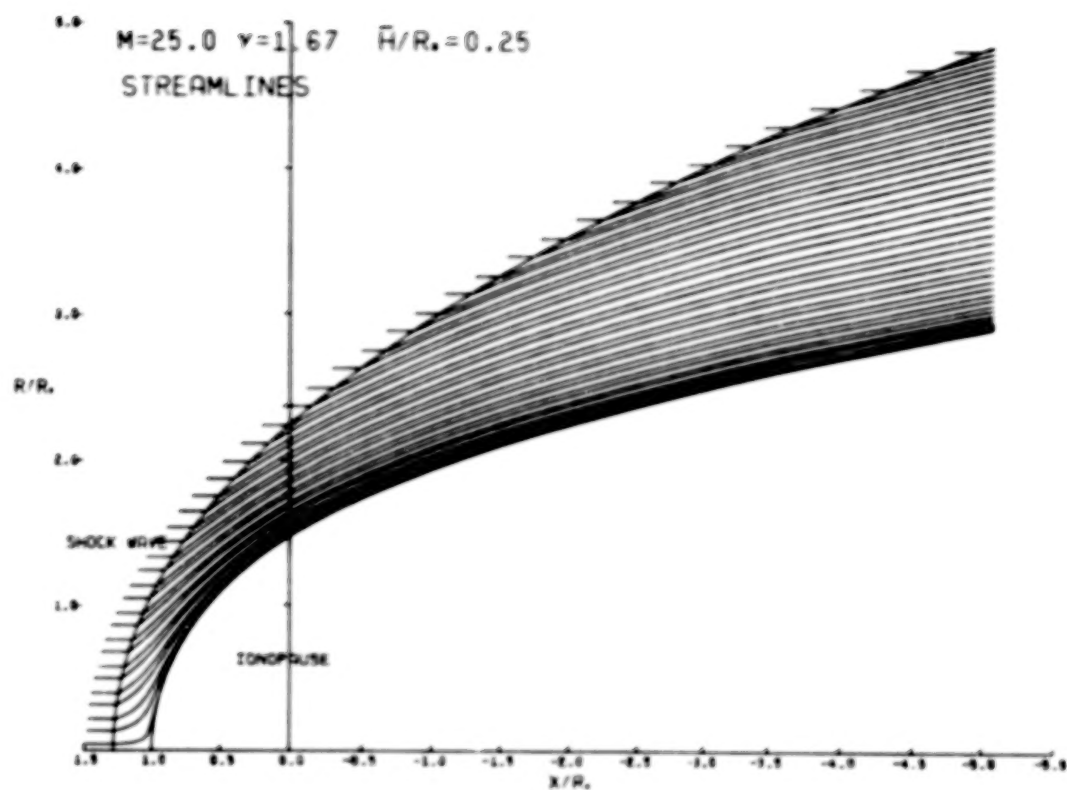


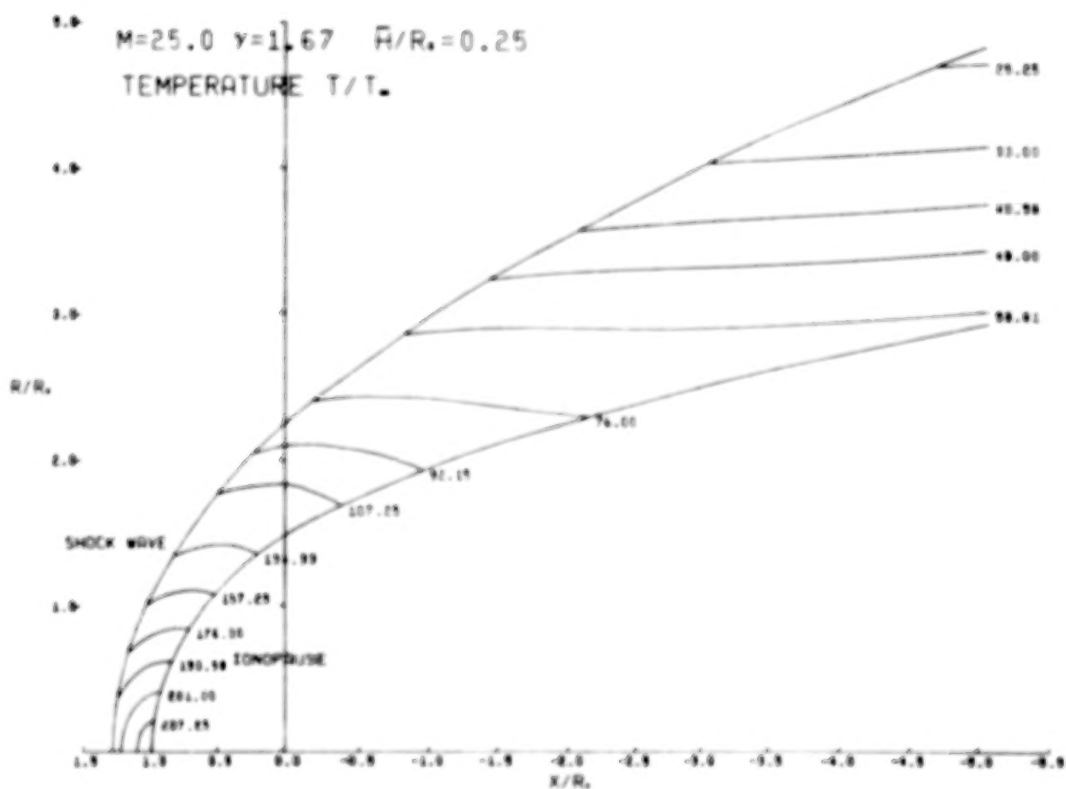
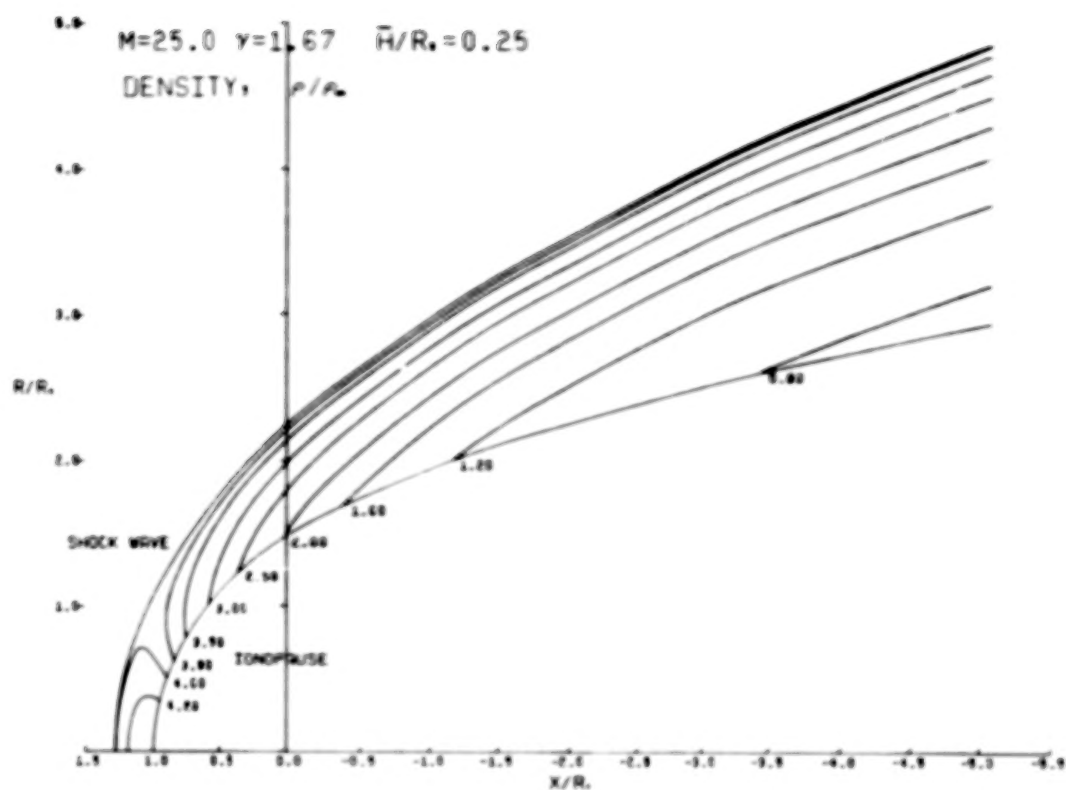


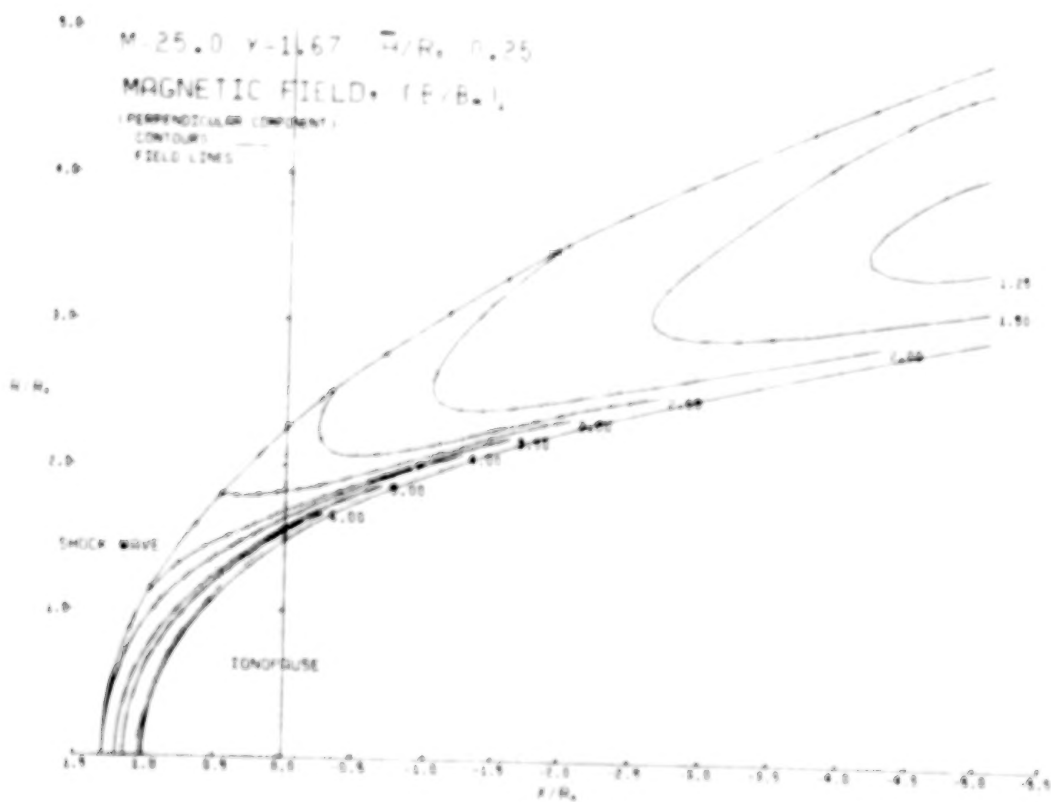
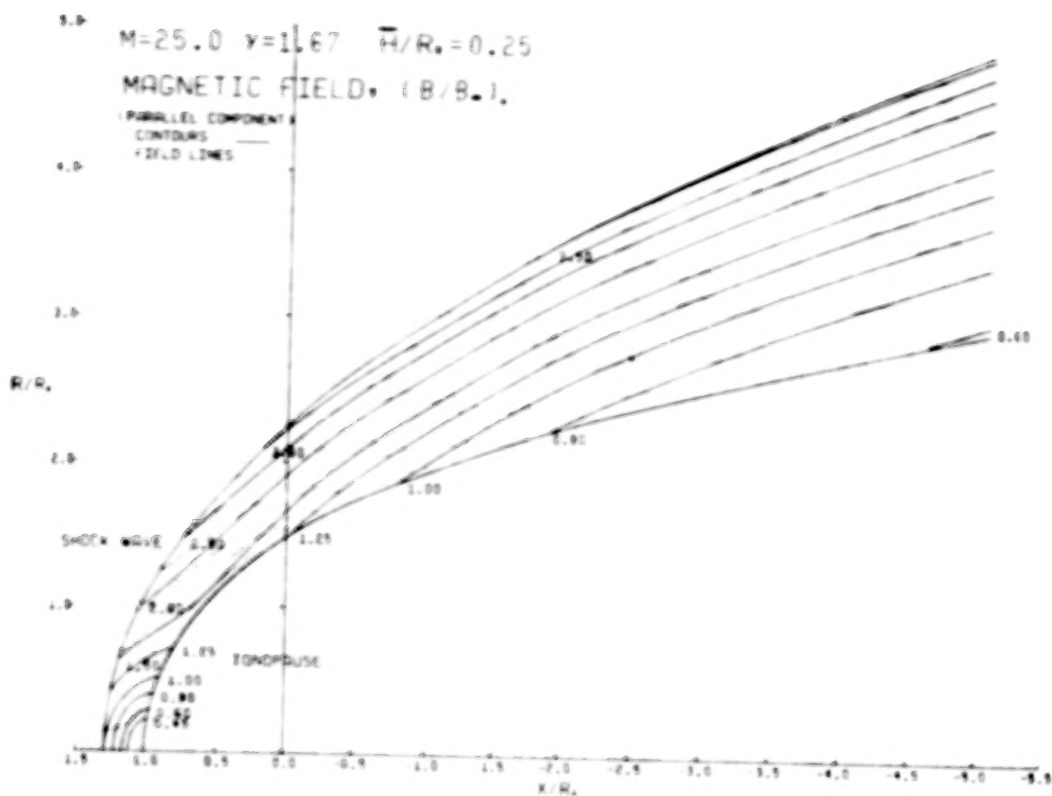












## REFERENCES

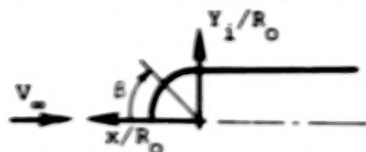
1. Spreiter, J. R. and Jones, W. P.: On the Effect of a Weak Interplanetary Magnetic Field on the Interaction Between the Solar Wind and the Geomagnetic Field. *J. Geophys. Res.*, Vol. 68, 1963, pp. 3555-3564.
2. Spreiter, J. R., Alksne, A. Y., and Summers, A. L.: Hydromagnetic Flow Around the Magnetopause. *Plan. & Space Sci.*, Vol. 14, 1966, pp. 223-253.
3. Dryer, M. and Faye-Petersen, R.: Magnetogasdynamic Boundary Condition for a Self-Consistent Solution to the Closed Magnetopause. *AIAA Journal*, Vol. 4, 1966, pp. 246-254.
4. Dryer, M. and Heckman, G. R.: Application of the Hypersonic Analogy to the Standing Shock of Mars. *Solar Phys.*, Vol. 2, 1967, pp. 112-120.
5. Spreiter, J. R., Alksne, A. Y., and Summers, A. L.: External Aerodynamics of the Magnetosphere. *Physics of the Magnetosphere* (Ed. R. L. Carovillano, J. F. McClay, and H. R. Radoski), D. Reidel Pub. Co., 1968, pp. 304-378 (also NASA TN 4482, 1968).
6. Spreiter, J. R., Summers, A. L., and Rizzi, A. W.: Solar Wind Flow Past Nonmagnetic Planets - Venus and Mars. *Plan. & Space Sci.*, Vol. 18, 1970, pp. 1281-1289.
7. Spreiter, J. R. and Rizzi, A. W.: Aligned Magnetohydrodynamics Solution for Solar Wind Flow Past the Earth's Magnetosphere. *Acta Astronautica*, Vol. 1, 1974, pp. 15-35.
8. Spreiter, J. R.: Magnetohydrodynamic and Gasdynamic Aspects of Solar-Wind Flow Around Terrestrial Planets: A Critical Review. *NASA SP-397*, 1975, pp. 135-150.
9. Stahara, S. S., Chaussee, D. S., Trudinger, B. C., and Spreiter, J. R.: Computational Techniques for Solar Wind Flows Past Terrestrial Planets - Theory and Computer Programs. *NASA CR-2924*, Nov. 1977.
10. Knudsen, W. C., Spenser, K., Spreiter, J. R., Miller, K. L., and Novak, V.: Thermal Structure and Major Ion Composition of the Venusian Ionosphere: First RPA Results from Venus Orbiter. *Science*, Vol. 203, No. 4382, Feb. 1979, pp. 757-763.
11. Knudsen, W. C., Spenser, K., Whitter, R. C., Spreiter, J. R., Miller, K. L., and Novak, V.: Thermal Structure and Energy Influx to the Day- and Nightside Venus Ionosphere. *Science*, Vol. 205, No. 4401, July 1979, pp. 105-107.
12. Kuhn, G. D., Goodwin, F. K., and Perkins, S. C., Jr.: User's Manual for Space-Shuttle Computer Programs. *NEAR TR 110*, Apr. 1976.



# REFERENCES (Concluded)

13. Beam, R. M. and Warming, R. F.: An Implicit Finite-Difference Algorithm for Hyperbolic Systems in Conservation-Law Form. *J. Comp. Phys.*, Vol. 22, No. 1, Sept. 1976.
14. Kentzer, C. P.: Discretization of Boundary Conditions on Moving Discontinuities. *Proceedings of the Second International Conference on Numerical Methods in Fluid Dynamics, Lecture Notes in Physics*, Vol. 8, M. Holt, ed., Berkeley, CA, 1970, pp. 108-113.
15. Thomas, P. D., Vinokur, M., Bastionon, R., and Conti, R. J.: Numerical Solution for the Three-Dimensional Hypersonic Flow Field of a Blunt Delta Body. *AIAA J.*, Vol. 10, July 1972, pp. 887-894.
16. Kutler, P., Reinhardt, W. A., and Warming, R. F.: Numerical Computations of Multi-Shocked Three-Dimensional Supersonic Flow Fields with Real Gas Effects. *AIAA Paper No. 72-702*, June 1972.
17. Kutler, P., Reinhardt, W. A., and Warming, R. F.: Multi-Shocked, Three-Dimensional Supersonic Flow Fields with Real Gas Effects. *AIAA J.*, Vol. 11, May 1973, pp. 657-664.
18. Chaussee, D. S., Holtz, T., and Kutler, P.: Inviscid Supersonic/Hypersonic Body Flow Fields and Aerodynamics from Shock-Capturing Technique Calculations. *AIAA Paper No. 75-837*, June 1975.
19. MacCormack, R. W.: The Effect of Viscosity in Hypervelocity Impact Cratering. *AIAA Paper No. 69-354*, 1969.
20. Alksne, A. Y. and Webster, D. L.: Magnetic and Electric Fields in the Magnetosheath. *Plan. & Space Sci.*, Vol. 18, 1970, pp. 1203-1212.
21. Wolfe, J., Intriligator, D. S., Mihalov, J., Collard, H., McKibbin, D., Whitten, R., and Barnes, A.: Initial Observations of the Pioneer Venus Orbiter Solar Wind Plasma Experiment. *Science*, Vol. 203, No. 4382, Feb. 1979, pp. 750-752.
22. Intriligator, D. S., Collard, H. R., Mihalov, J. P., Whitten, R. C., and Wolfe, J. H.: Electron Observation and Ion Flows from the Pioneer Venus Orbiter Plasma Analyzer Experiment. *Science*, Vol. 205, No. 4401, July 1979, pp. 116-119.
23. Russell, C. T., Elphic, R. C., and Slavin, J. A.: Initial Pioneer Venus Magnetic Field Results: Dayside Observations. *Science*, Vol. 203, No. 4382, Feb. 1979, pp. 745-748.
24. Russell, C. T., Elphic, R. C., and Slavin, J. A.: Initial Pioneer Venus Magnetic Field Results: Nightside Observations. *Science*, Vol. 205, No. 4401, July 1979, pp. 114-116.

Table 1.- Ordinates of Various Ionopause Shapes



$\theta$	IONOPAUSE		IONOPAUSE		IONOPAUSE		IONOPAUSE		IONOPAUSE	
	$\bar{H}/R_0 = 0.01$		$\bar{H}/R_0 = 0.05$		$\bar{H}/R_0 = 0.10$		$\bar{H}/R_0 = 0.20$		$\bar{H}/R_0 = 0.25$	
	$x/R_0$	$Y_i/R_0$	$x/R_0$	$Y_i/R_0$	$x/R_0$	$Y_i/R_0$	$x/R_0$	$Y_i/R_0$	$x/R_0$	$Y_i/R_0$
0°	1.0000	0.0000	1.0000	0.0000	1.0000	0.0000	1.0000	0.0000	1.0000	0.0000
2°	0.9994	0.0349	0.9995	0.0349	0.9995	0.0349	0.9995	0.0349	0.9996	0.0349
6°	0.9946	0.1045	0.9950	0.1046	0.9953	0.1046	0.9958	0.1047	0.9960	0.1047
10°	0.9851	0.1737	0.9861	0.1739	0.9870	0.1740	0.9883	0.1743	0.9888	0.1744
14°	0.9709	0.2421	0.9727	0.2425	0.9746	0.2430	0.9771	0.2436	0.9781	0.2439
18°	0.9520	0.3093	0.9550	0.3103	0.9580	0.3113	0.9622	0.3126	0.9638	0.3132
22°	0.9285	0.3751	0.9330	0.3770	0.9374	0.3787	0.9435	0.3812	0.9459	0.3822
26°	0.9006	0.4393	0.9068	0.4423	0.9127	0.4451	0.9211	0.4492	0.9243	0.4508
30°	0.8684	0.5014	0.8764	0.5060	0.8840	0.5104	0.8949	0.5167	0.8991	0.5191
34°	0.8320	0.5612	0.8419	0.5679	0.8514	0.5743	0.8649	0.5834	0.8701	0.5869
38°	0.7916	0.6185	0.8035	0.6278	0.8148	0.6366	0.8312	0.6494	0.8374	0.6543
42°	0.7474	0.6729	0.7613	0.6854	0.7745	0.6973	0.7935	0.7145	0.8009	0.7211
46°	0.6995	0.7243	0.7153	0.7407	0.7303	0.7563	0.7520	0.7787	0.7604	0.7874
50°	0.6482	0.7725	0.6658	0.7934	0.6824	0.8133	0.7066	0.8421	0.7159	0.8532
54°	0.5937	0.8172	0.6128	0.8435	0.6309	0.8683	0.6571	0.9044	0.6673	0.9184
58°	0.5363	0.8582	0.5565	0.8906	0.5756	0.9212	0.6035	0.9657	0.6143	0.9831
62°	0.4761	0.8954	0.4971	0.9349	0.5168	0.9719	0.5456	1.0261	0.5569	1.0473
66°	0.4135	0.9287	0.4346	0.9761	0.4543	1.0203	0.4504	1.1147	0.4947	1.1744
70°	0.3487	0.9581	0.3691	1.0142	0.3882	1.0665	0.4163	1.1437	0.4274	1.1744
74°	0.2820	0.9833	0.3009	1.0492	0.3184	1.1103	0.3444	1.2010	0.3548	1.2374
78°	0.2135	1.0046	0.2298	1.0811	0.2448	1.1517	0.2673	1.2574	0.2764	1.3001
82°	0.1436	1.0219	0.1560	1.1098	0.1674	1.1908	0.1845	1.3130	0.1915	1.3628
86°	0.0724	1.0354	0.0794	1.1355	0.0858	1.2276	0.0956	1.3677	0.0997	1.4254
90°	0.0000	1.0454	0.0000	1.1583	0.0000	1.2620	0.0000	1.4218	0.0000	1.4883
94°	-0.0736	1.0523	-0.0824	1.1782	-0.0905	1.2943	-0.1032	1.4753	-0.1085	1.5516
98°	-0.1485	1.0566	-0.1680	1.1955	-0.1861	1.3244	-0.2148	1.5284	-0.2271	1.6156
102°	-0.2251	1.0591	-0.2572	1.2102	-0.2875	1.3524	-0.3361	1.5813	-0.3572	1.6807
106°	-0.3040	1.0603	-0.3506	1.2226	-0.3953	1.3785	-0.4686	1.6343	-0.5010	1.7472
110°	-0.3861	1.0607	-0.4488	1.2330	-0.5106	1.4027	-0.6142	1.6875	-0.6608	1.8156
114°	-0.4723	1.0609	-0.5527	1.2415	-0.6346	1.4253	-0.7753	1.7414	-0.8400	1.8866

**BLANK PAGE**

**BLANK PAGE**

Table 1.- Concluded.

$\beta$	IONO PAUSE		IONO PAUSE		IONO PAUSE		IONO PAUSE		IONO PAUSE	
	$\bar{H}/R_0 = 0.01$		$\bar{H}/R_0 = 0.05$		$\bar{H}/R_0 = 0.10$		$\bar{H}/R_0 = 0.20$		$\bar{H}/R_0 = 0.25$	
	$x/R_0$	$Y_i/R_0$	$x/R_0$	$Y_i/R_0$	$x/R_0$	$Y_i/R_0$	$x/R_0$	$Y_i/R_0$	$x/R_0$	$Y_i/R_0$
118°	-0.5641	1.0610	-0.6638	1.2484	-0.7690	1.4462	-0.9551	1.7963	-1.0427	1.9610
122°	-0.6630	1.0610	-0.7835	1.2539	-0.9159	1.4657	-1.1578	1.8529	-1.2746	2.0397
126°	-0.7708	1.0610	-0.9142	1.2583	-1.0782	1.4840	-1.3890	1.9118	-1.5434	2.1243
130°	-0.8903	1.0610	-1.0587	1.2617	-1.2597	1.5012	-1.6562	1.9738	-1.8598	2.2165
134°	-1.0246	1.0610	-1.2209	1.2643	-1.4654	1.5175	-1.9703	2.0403	-2.2393	2.3189
138°	-1.1783	1.0610	-1.4064	1.2664	-1.7027	1.5331	-2.3465	2.1128	-2.7047	2.4353
142°	-1.3580	1.0610	-1.6229	1.2679	-1.9817	1.5482	-2.8081	2.1939	-3.2913	2.5715
146°	-1.5730	1.0610	-1.8816	1.2692	-2.3176	1.5632	-3.3909	2.2872	-4.0570	2.7365
150°	-1.8377	1.0610	-2.1999	1.2701	-2.7338	1.5784	-4.1545	2.3986	-5.1025	2.9460
154°	-2.1754	1.0610	-2.6057	1.2709	-3.2686	1.5942	-5.2045	2.5384	-6.6208	3.2292
158°	-2.6262	1.0610	-3.1471	1.2715	-3.9884	1.6114	-6.7470	2.7260	-9.0300	3.6484
162°	-3.3654	1.0610	-3.9152	1.2721	-5.0210	1.6314	-9.2448	3.0038	-13.4322	4.3644
166°	-4.2564	1.0610	-5.1047	1.2727	-6.6450	1.6568	-13.9882	3.4877	-23.9161	5.9630
170°	-6.0204	1.0610	-7.2230	1.2736	-10.1609	1.7004	-26.3596	4.6480		
174°	-10.1111	1.0610	-12.1370	1.2758	-16.8192	1.7678				

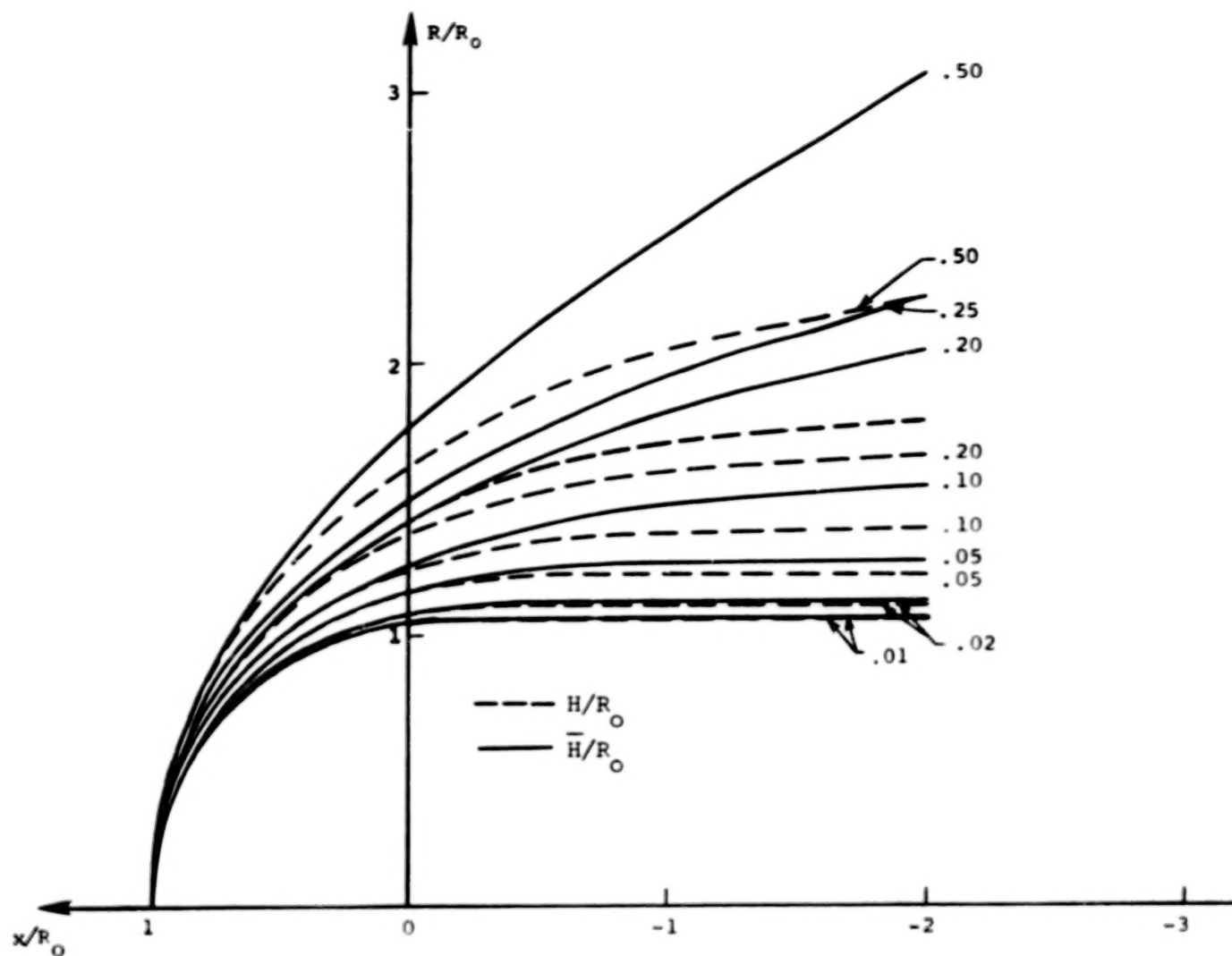
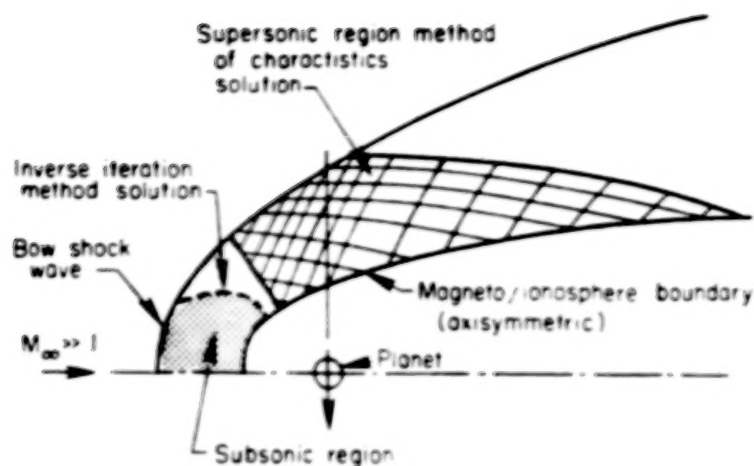
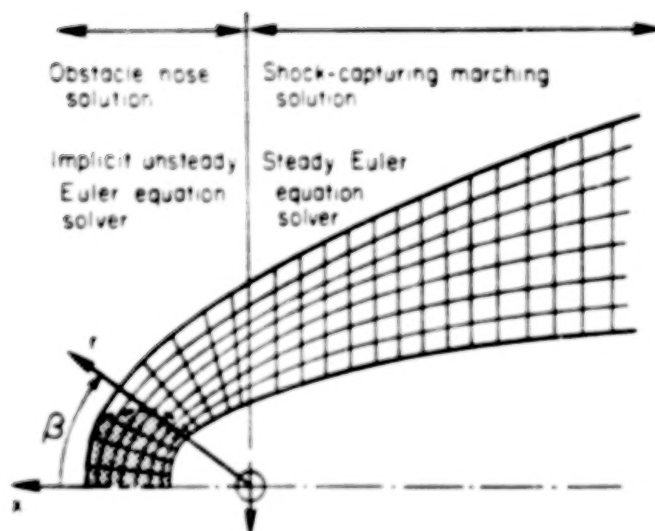


Figure 1.- Illustration of ionopause shapes for atmospheres with various  
 (i) constant scale heights  $H/R_0$  and (ii) gravitational variation  
 included in the scale height  $\bar{H}/R_0$ .



(a) Former method.



(b) Present method.

Figure 2.- Comparison of former and present computational procedures for determining the gasdynamic flow properties of solar wind-magnetosphere/ionopause interactions.

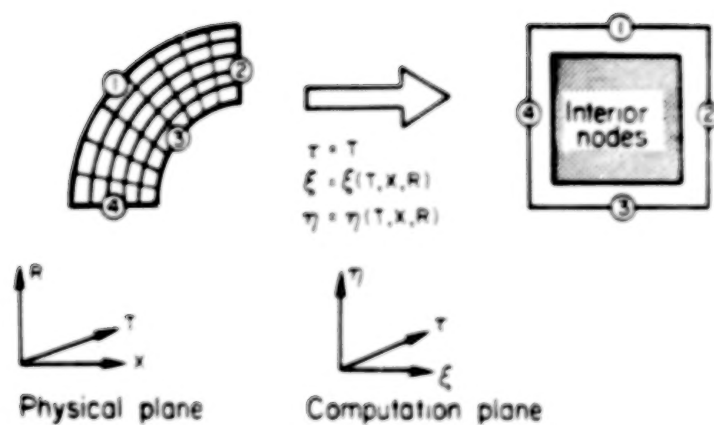


Figure 3.- Transformation from physical domain to rectangular computational domain.

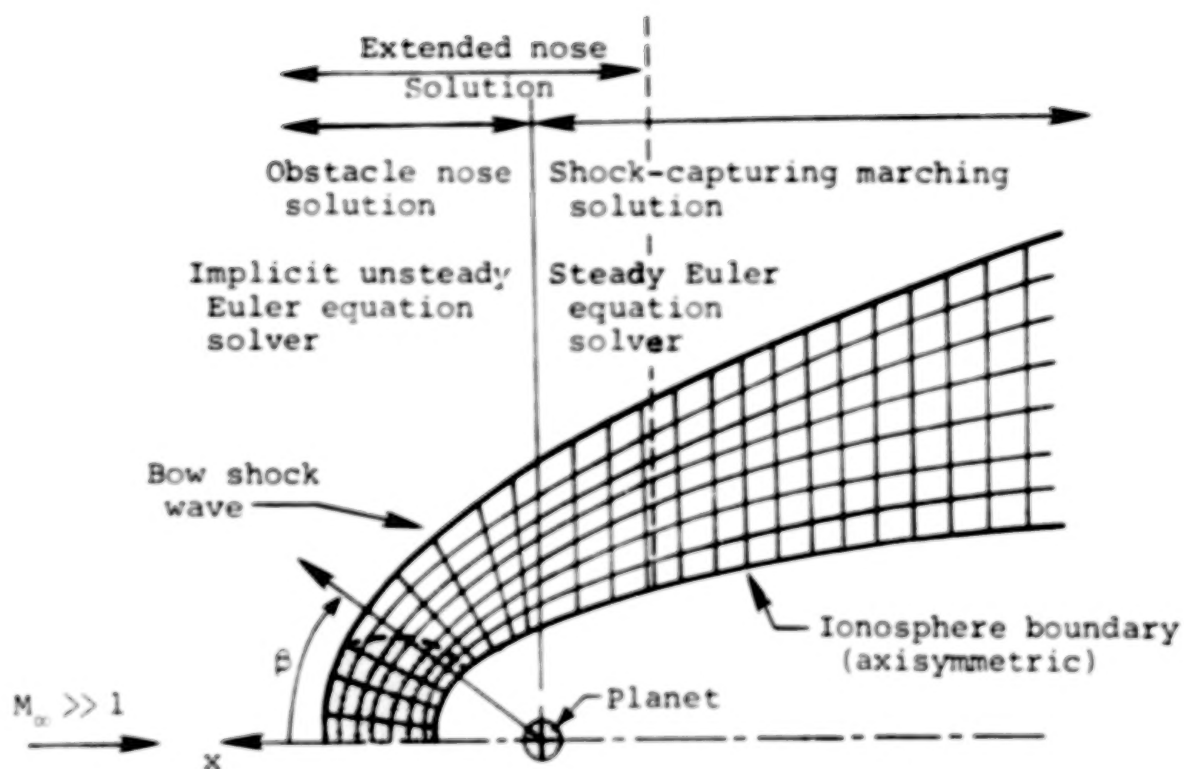


Figure 4.- Illustration of capability for providing an additional flow-field segment to the obstacle nose solution in the computational procedure for determining the gasdynamic flow properties of solar wind-ionopause interactions.



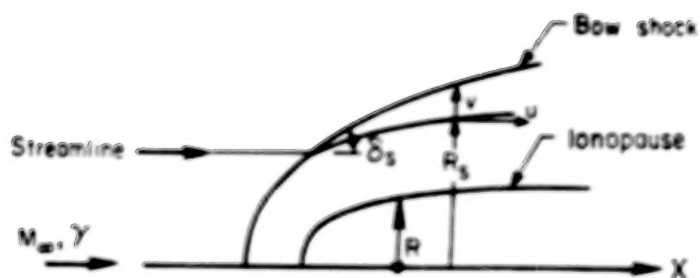


Figure 5.- Illustration of quantities used for streamline calculation.

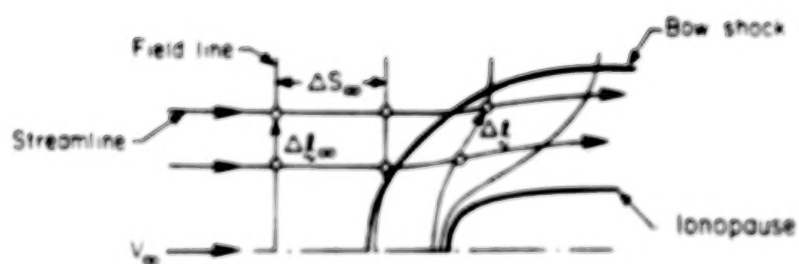


Figure 6.- Illustration of quantities used for magnetic field-line calculation in the plane of magnetic symmetry.

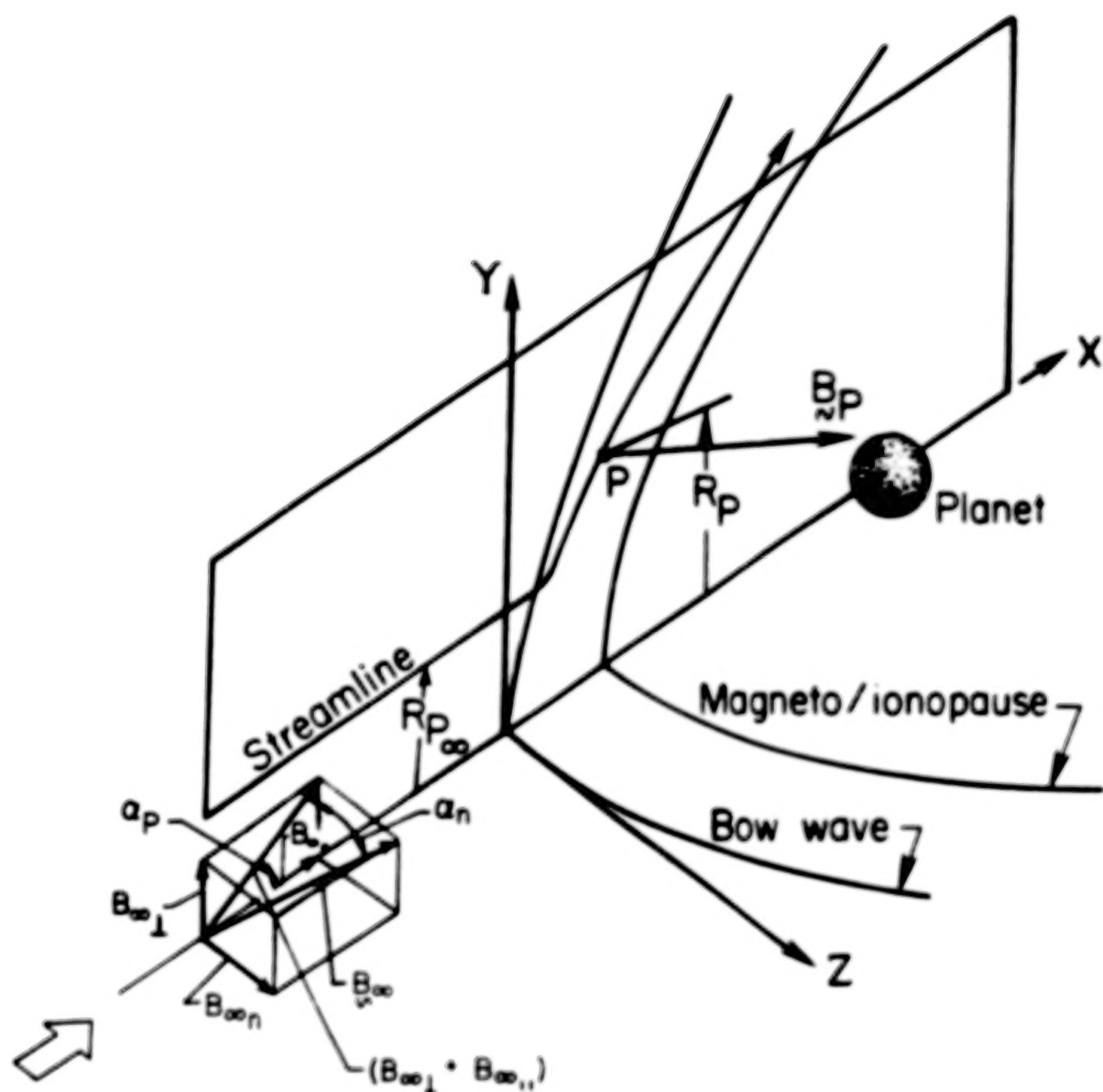


Figure 7.- Illustration of the components of the three-dimensional magnetic field.

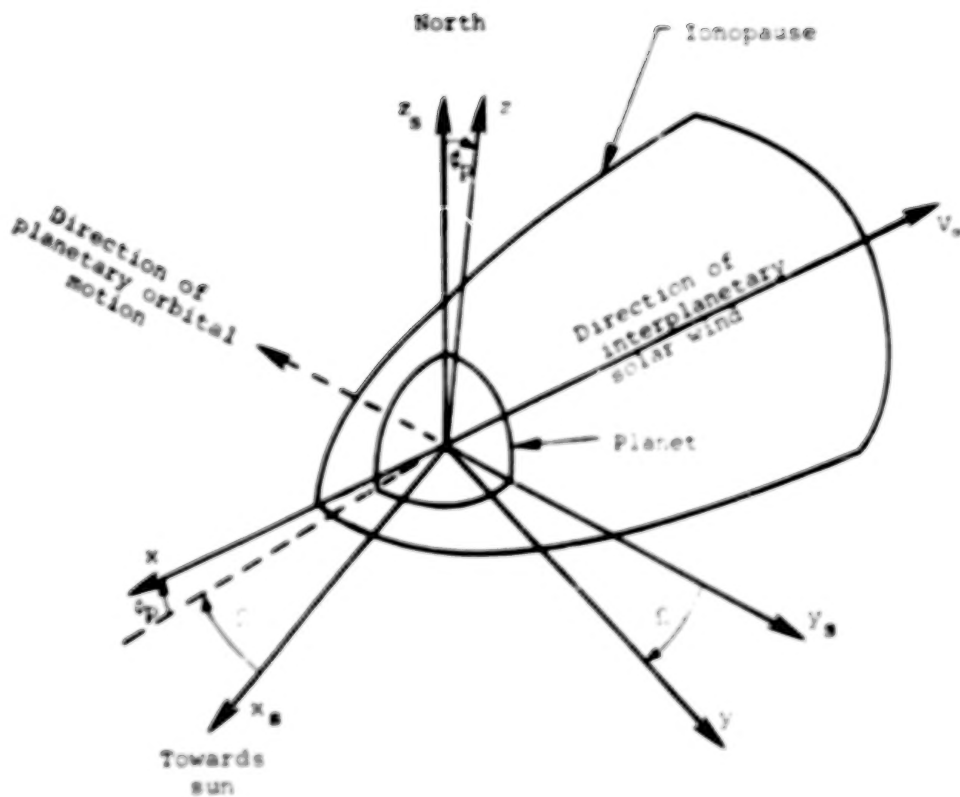


Figure 8.- Illustration of sun-planet  $(x_s, y_s, z_s)$  and solar wind  $(x, y, z)$  coordinate systems and the azimuthal  $(\phi)$  and polar  $(\theta_p)$  solar-wind angles, both shown in a positive sense.

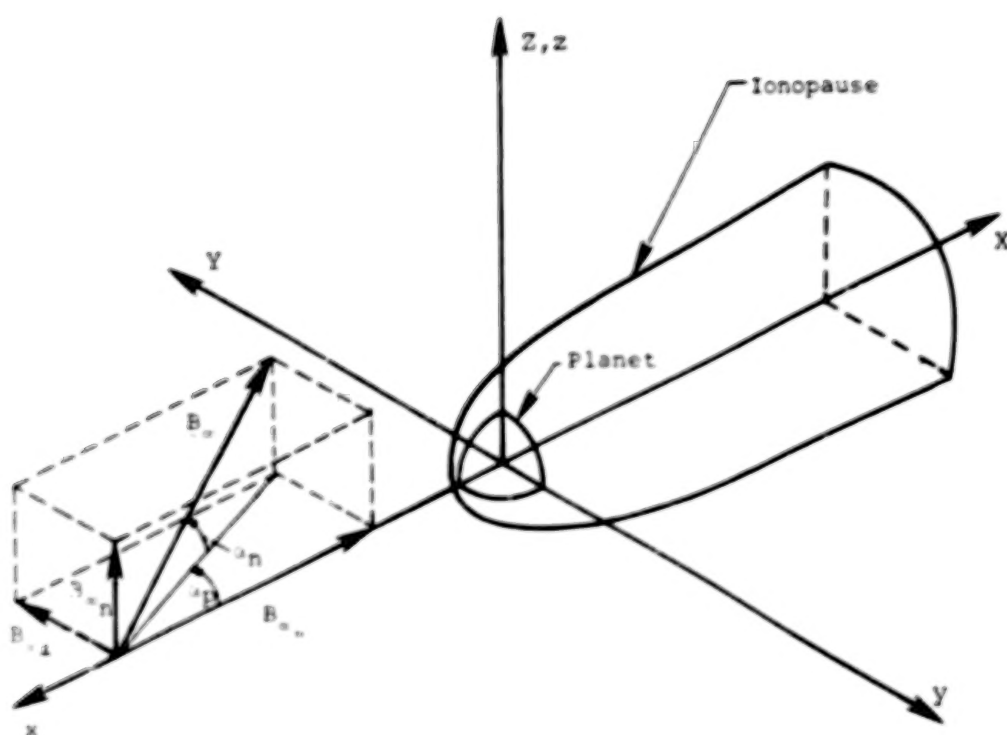


Figure 9.- Illustration of solar-wind  $(x,y,z)$  and  $(X,Y,Z)$  coordinate systems and the interplanetary magnetic field and magnetic-field angles  $(\alpha_p, \alpha_n)$ .

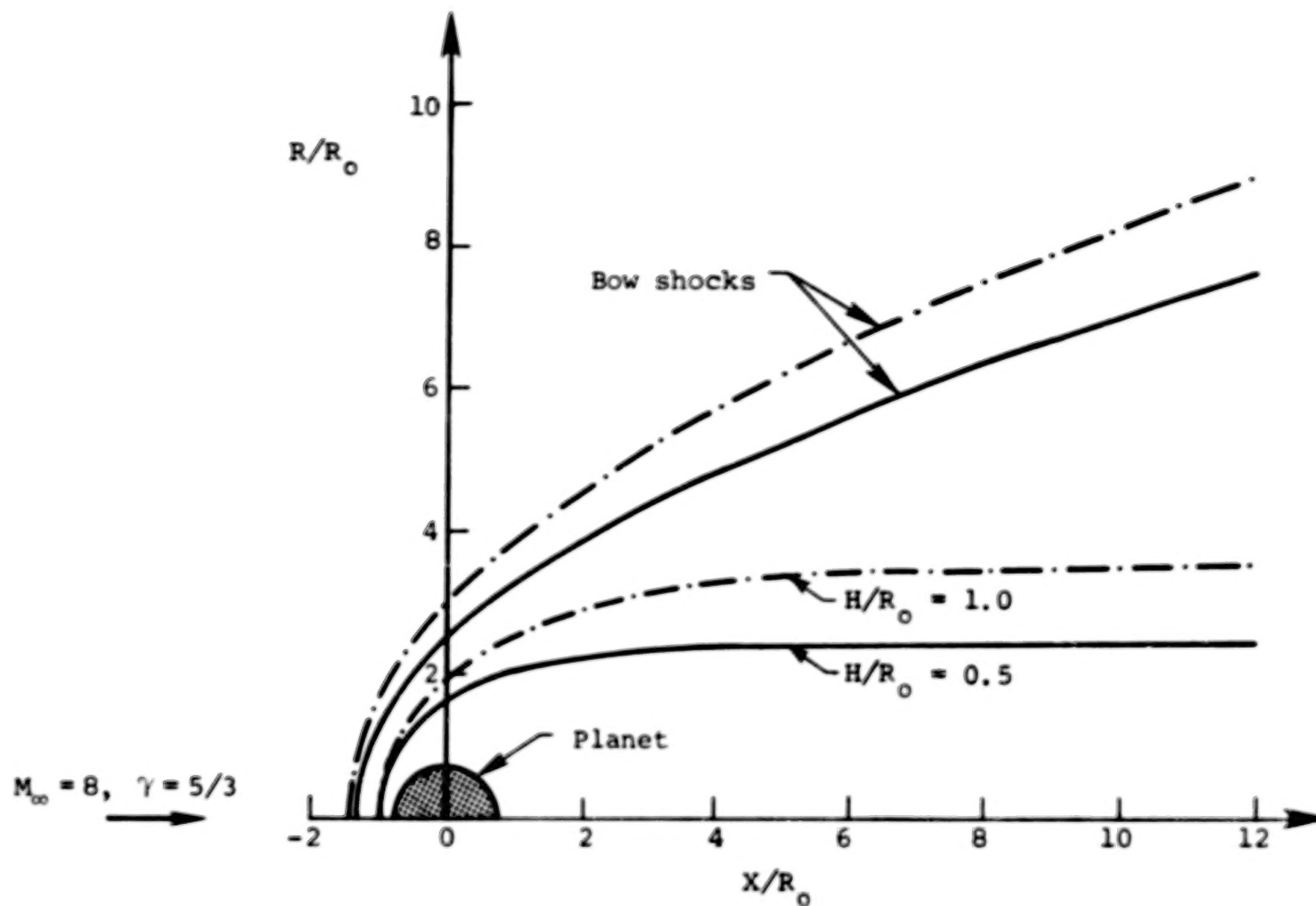


Figure 10.- Bow shock locations for  $M_\infty = 8.0$ ,  $\gamma = 5/3$  flow past constant scale-height ionopause shapes with  $H/R_0 = 0.5$  and  $1.0$ .

**BLANK PAGE**

**BLANK PAGE**

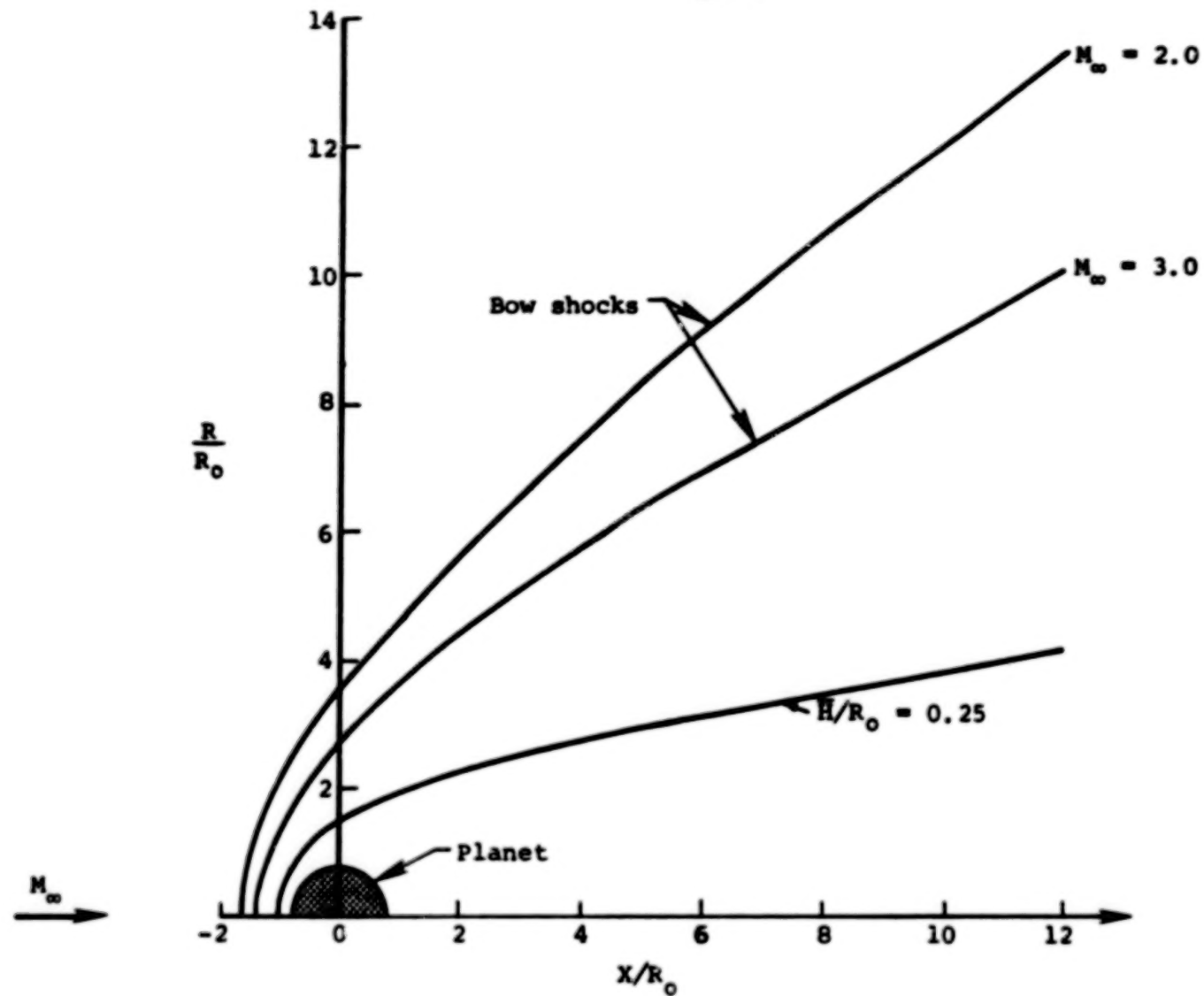


Figure 11.- Bow shock shapes for flow past an ionopause shape with gravitational variation included in scale height with  $H/R_0 = 0.25$ ,  $\gamma = 5/3$  and  $M_\infty = 2.0$  and  $3.0$ .

Ionosphere Properties

$T = \text{Const.}$

Solar Wind Properties

$T_{\infty}, \rho_{\infty}, \gamma,$

$v_{\infty}, B_{\infty}$

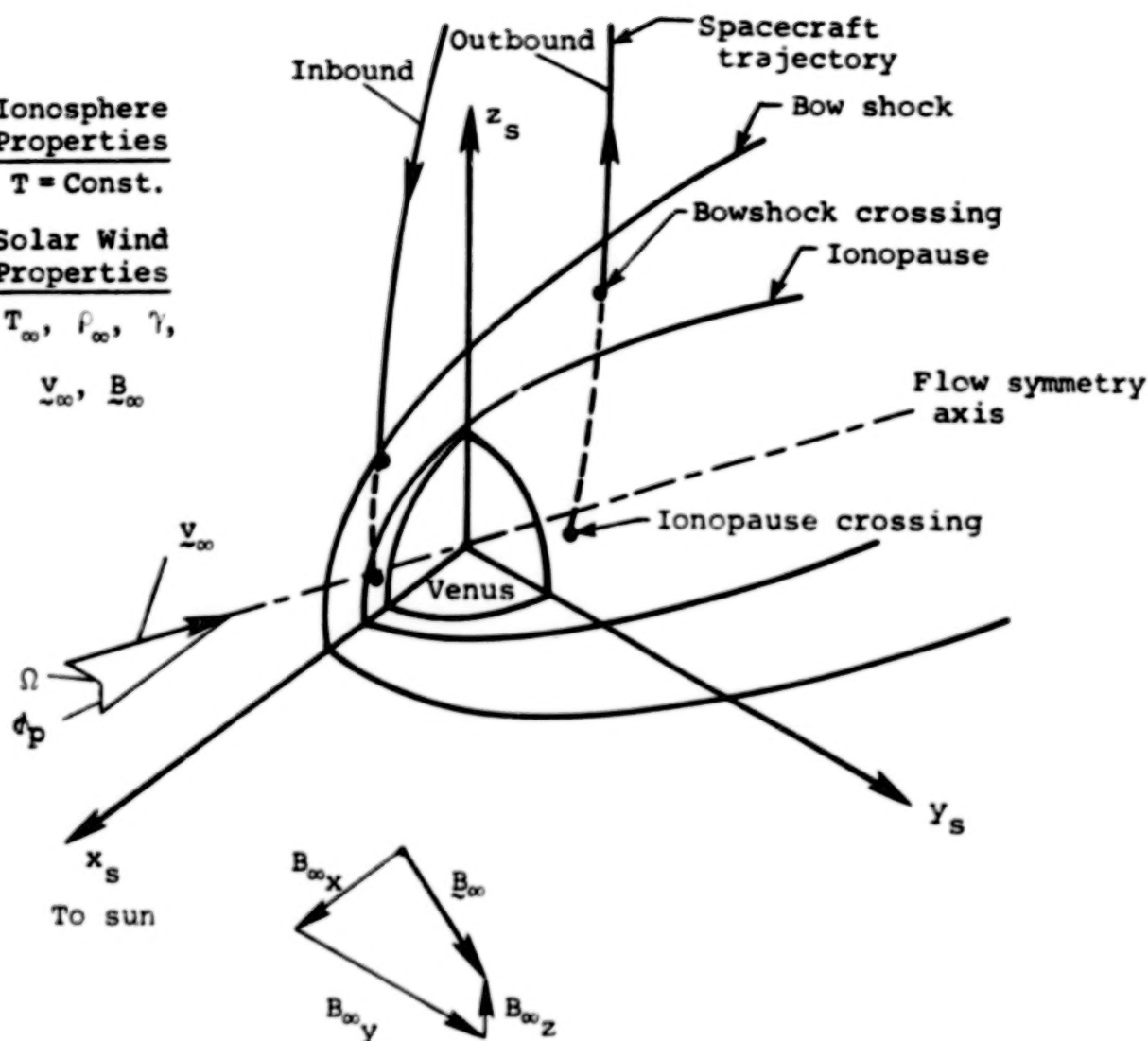


Figure 12.- Overall features of Pioneer-Venus orbiter trajectory crossings of solar-wind/Venus-ionosphere interaction region.



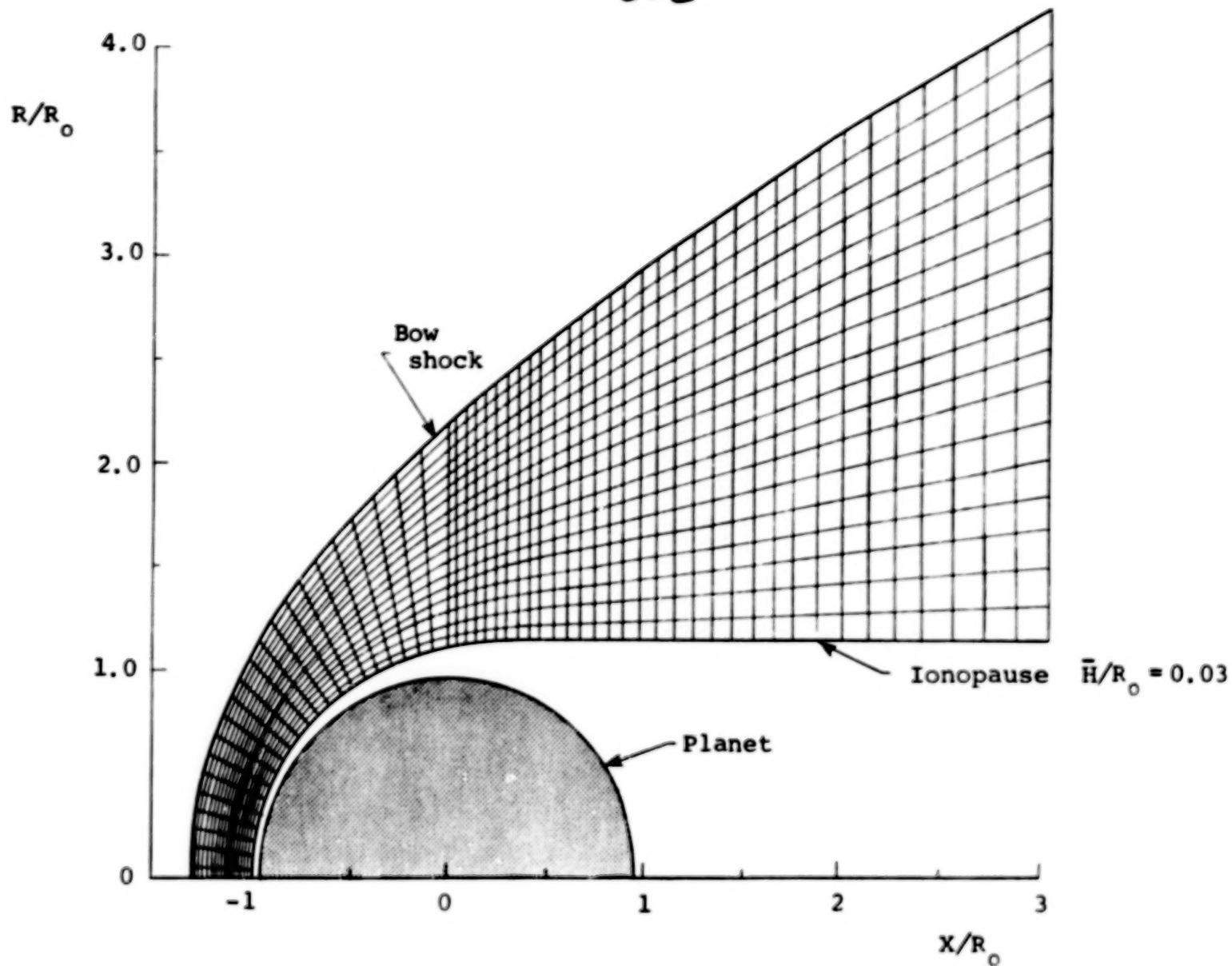


Figure 13.- Illustration of typical flow-field grid density for gasdynamic solution;  $M_\infty = 3.0$ ,  $\gamma = 5/3$ .

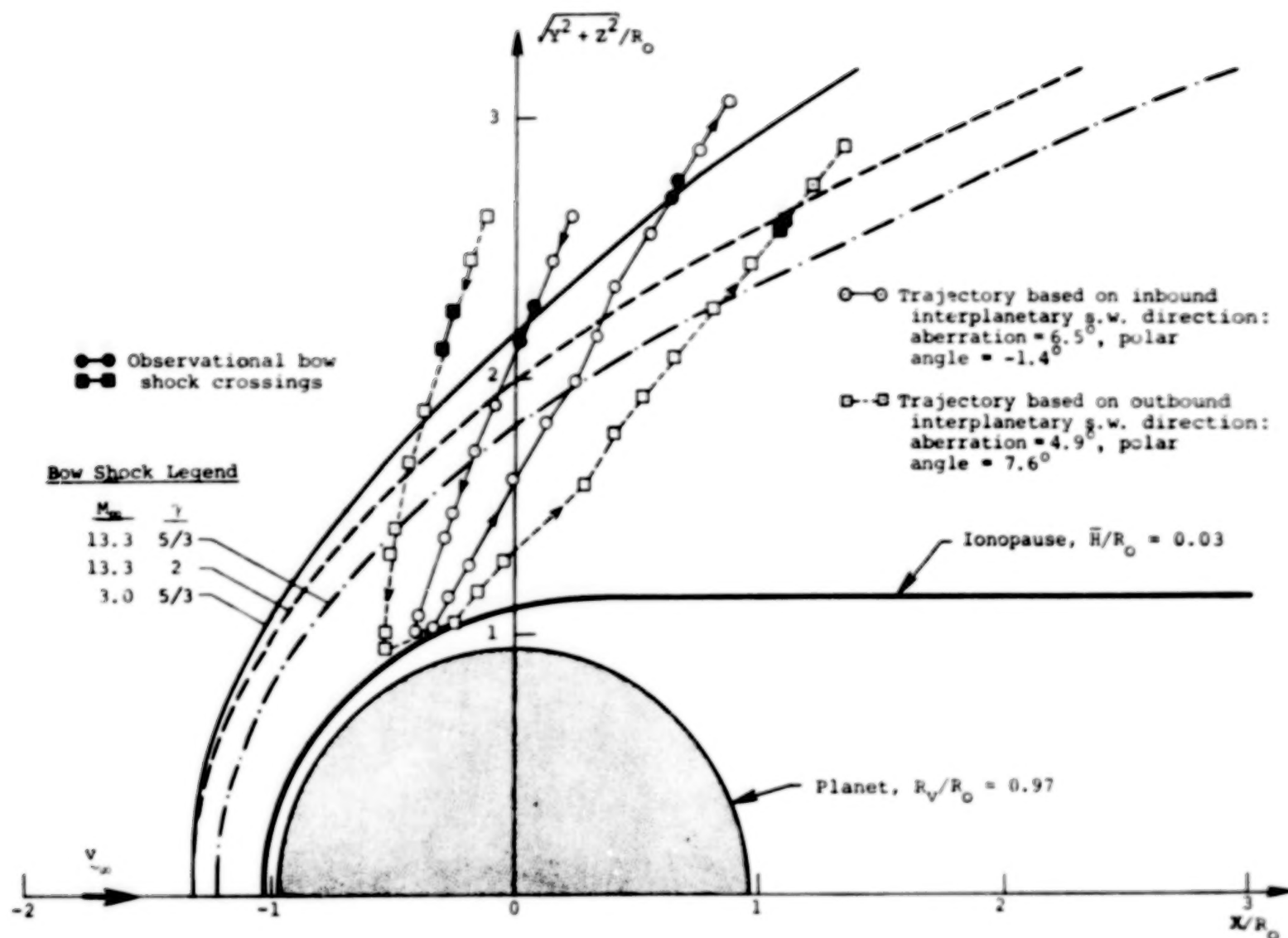


Figure 14.- P-V Orbit 6 trajectories and observational bow shock crossings as viewed in solar-wind coordinates based on inbound and outbound interplanetary solar-wind directions; also, various bow shock shapes for different interplanetary solar-wind conditions.

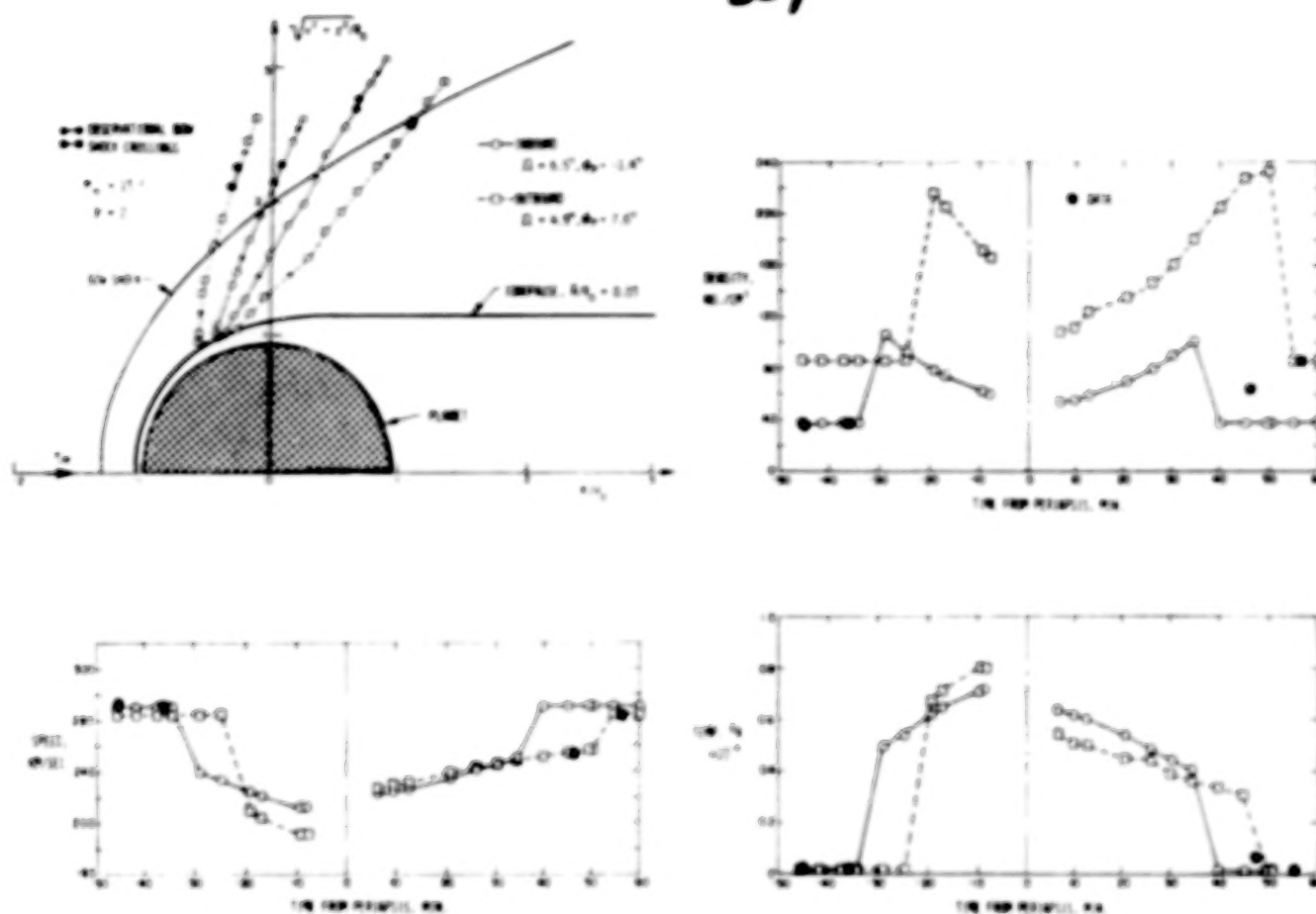
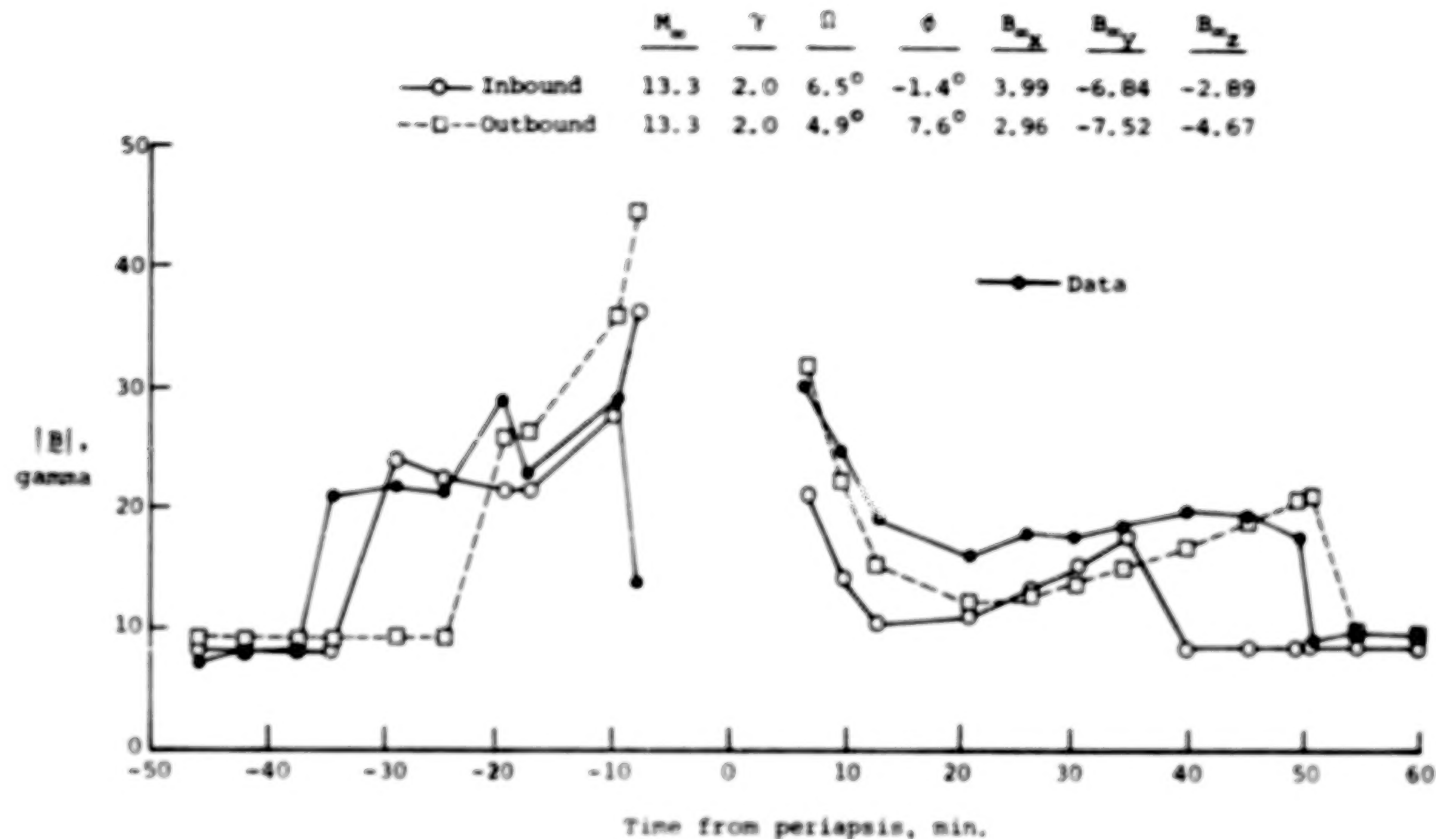
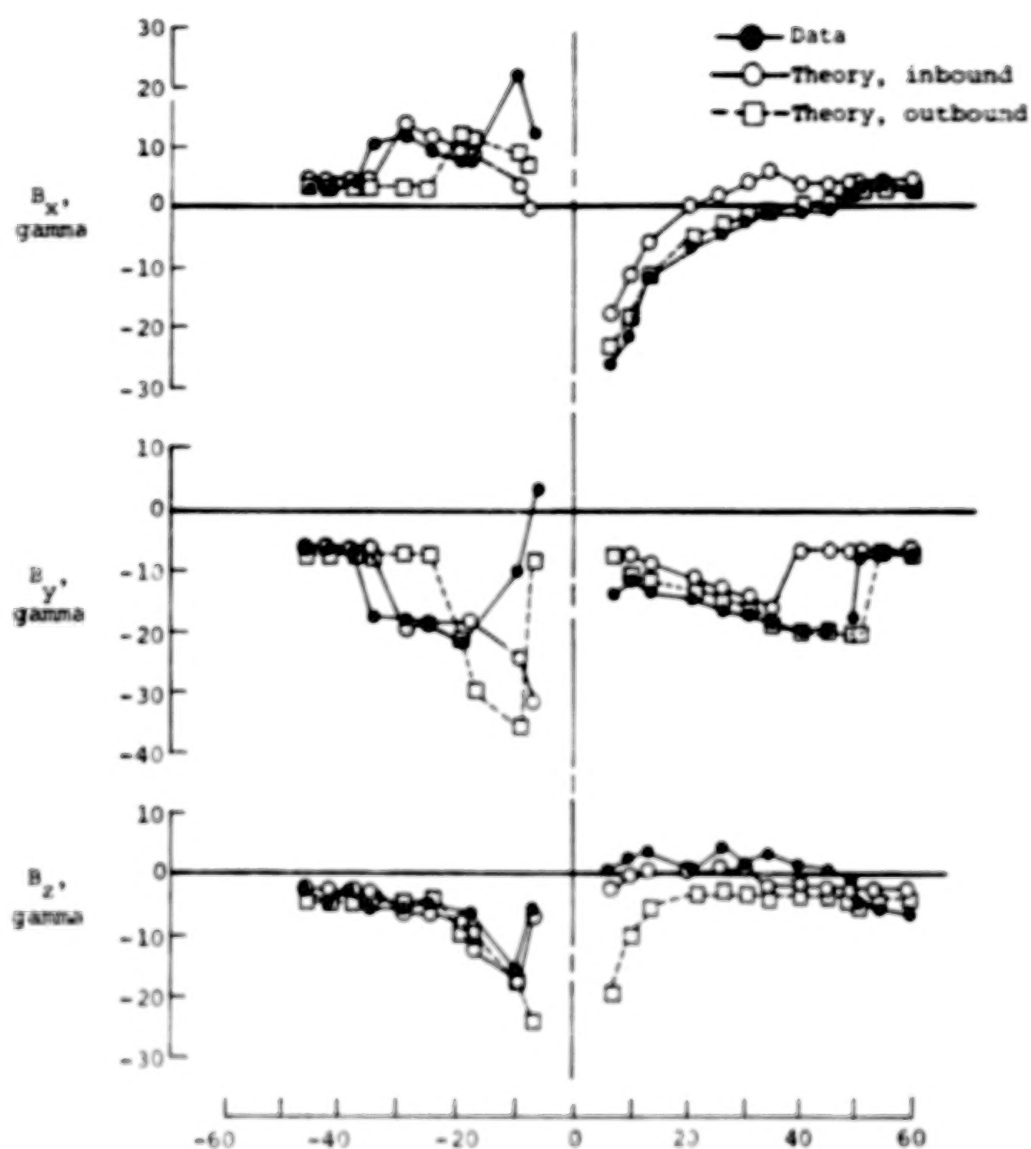


Figure 15.- Comparison of observed (OPA) and theoretical time histories of ionosheath plasma properties for P-V Orbit 6 based on inbound and outbound interplanetary solar-wind conditions using a gasdynamic solution for  $M_{\infty} = 13.3$ ,  $\gamma = 2.0$ .



(a) Magnetic-field magnitude.

Figure 16.- Comparison of observed (OMAG) and theoretical time histories for the magnitude of the magnetic field for P-V Orbit 6 based on inbound and outbound interplanetary conditions using gasdynamic solution for  $M_{\infty} = 13.3$ ,  $\gamma = 2$ .



Time from periapsis, min.  
 (b) Magnetic-field components.

Figure 16.- Concluded.

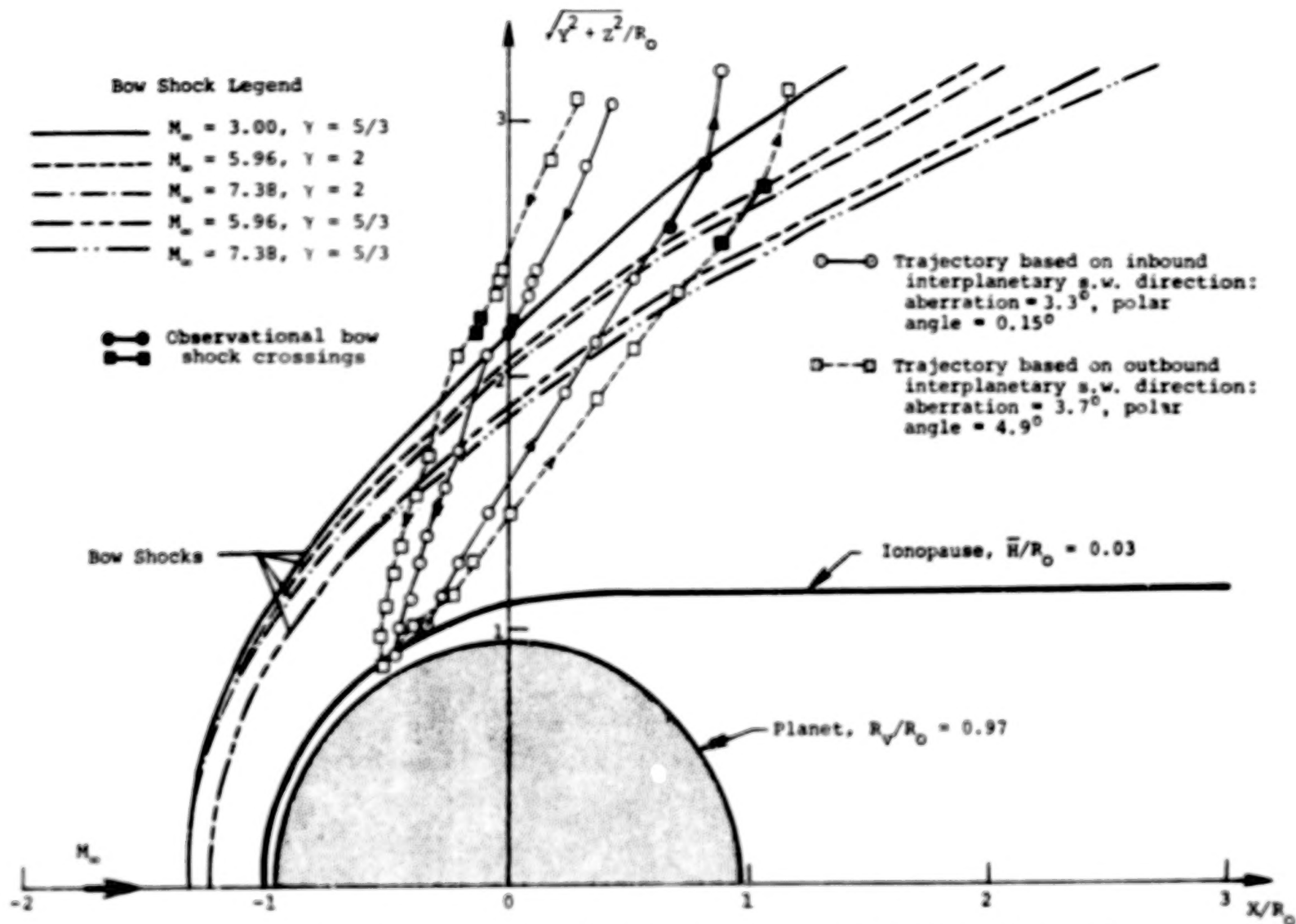


Figure 17.- P-V Orbit 3 trajectories and observational bow shock crossings as viewed in solar-wind coordinates based on inbound and outbound interplanetary solar-wind directions; also, various bow shock shapes for different interplanetary solar wind conditions.

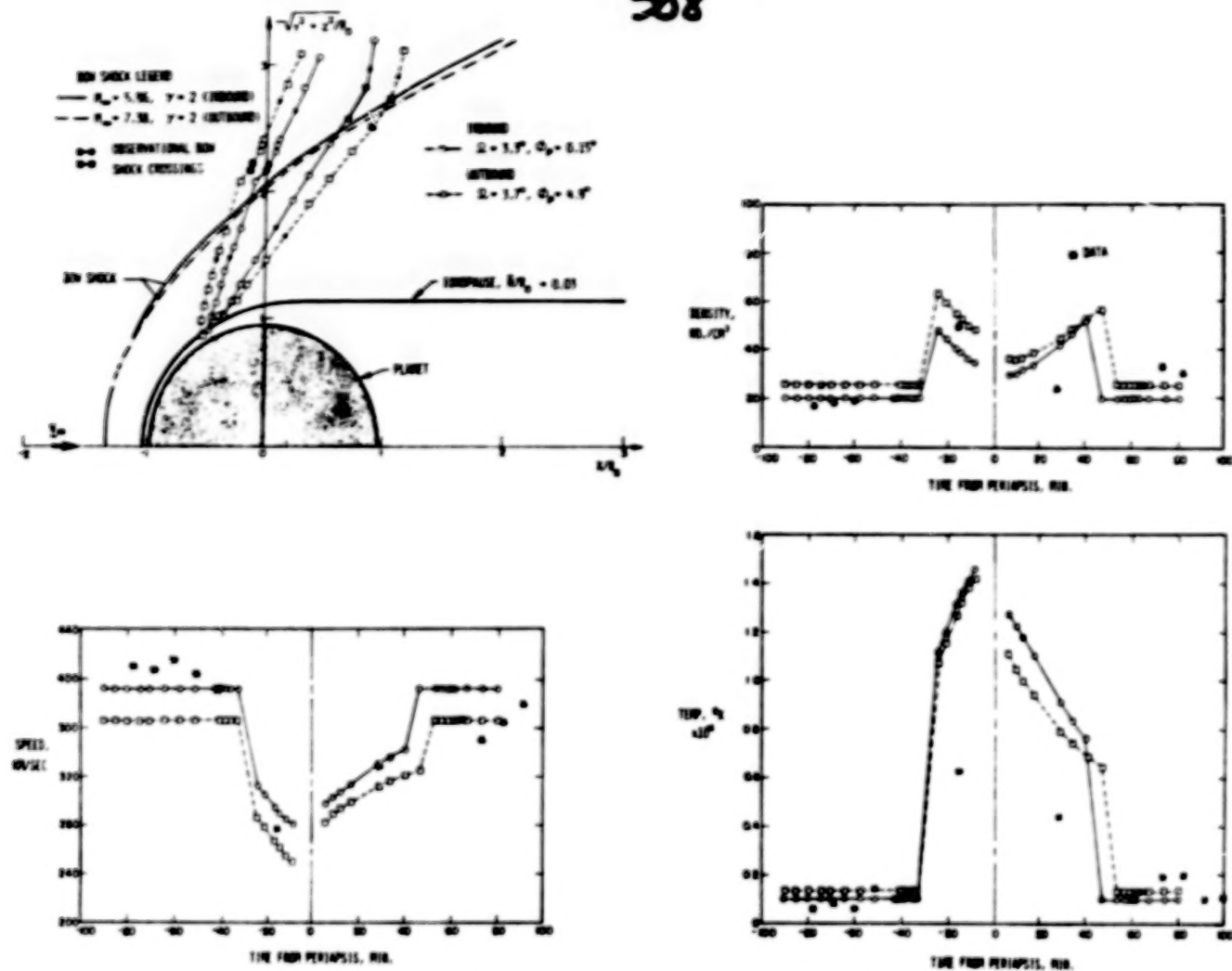
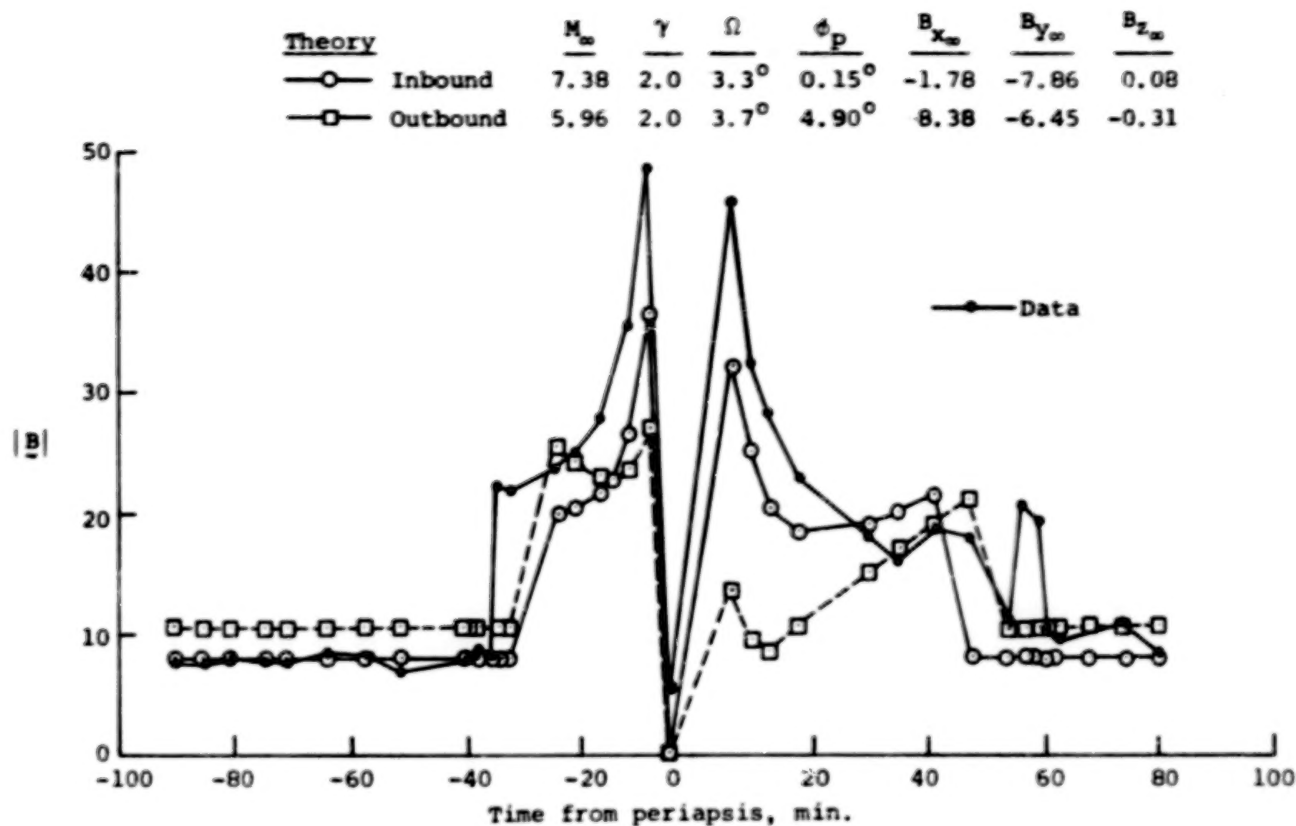


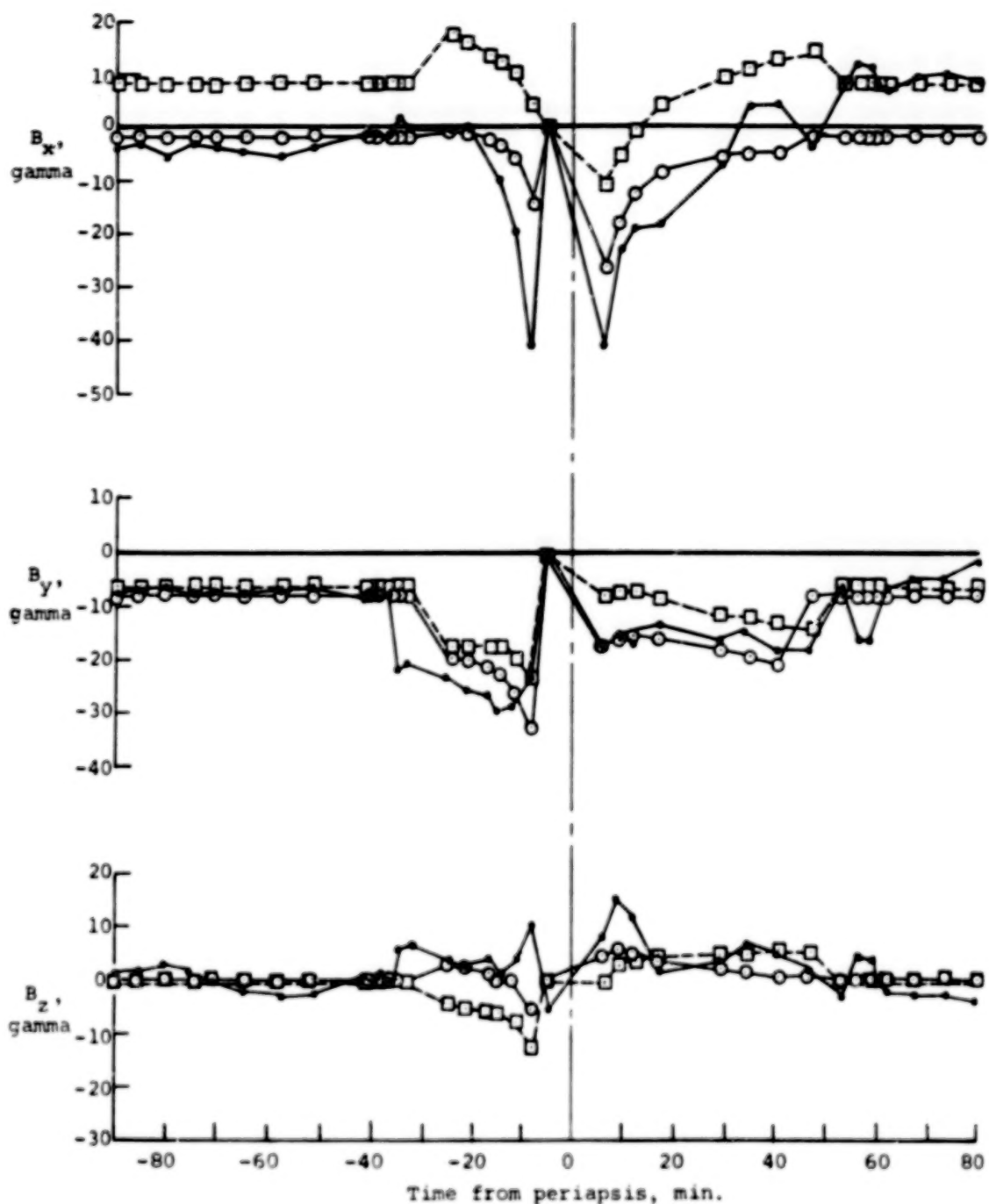
Figure 18.- Comparison of observed and theoretical time histories of ionosheath plasma properties for P-V Orbit 3 based on inbound and outbound interplanetary solar-wind conditions.



(a) Magnetic-field magnitudes.

Figure 19.- Comparison of observed (OMAG) and theoretical time histories for the magnetic field for P-V Orbit 3 based on inbound and outbound interplanetary solar-wind conditions using gasdynamic solutions  $M_{\infty} = 7.38$ ,  $\gamma = 2.0$  for inbound and  $M_{\infty} = 5.96$ ,  $\gamma = 2.0$  for outbound calculations.



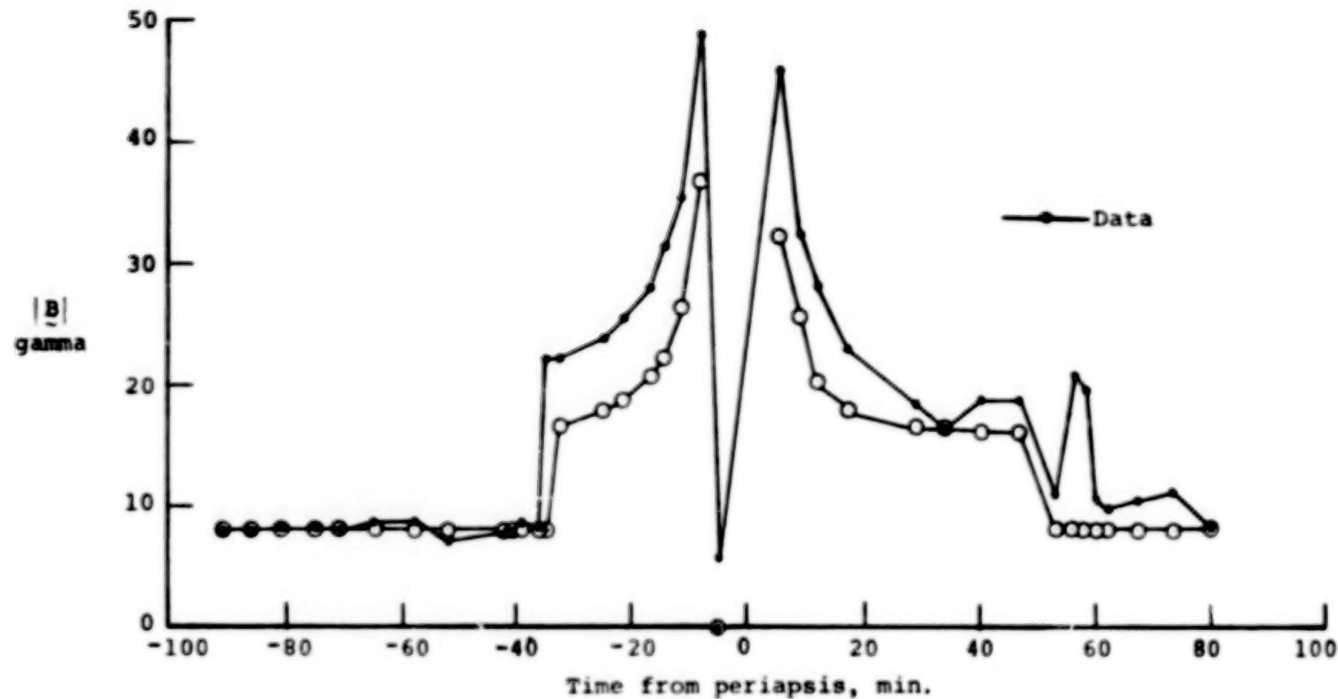


(b) Magnetic-field components.

Figure 19.- Concluded.

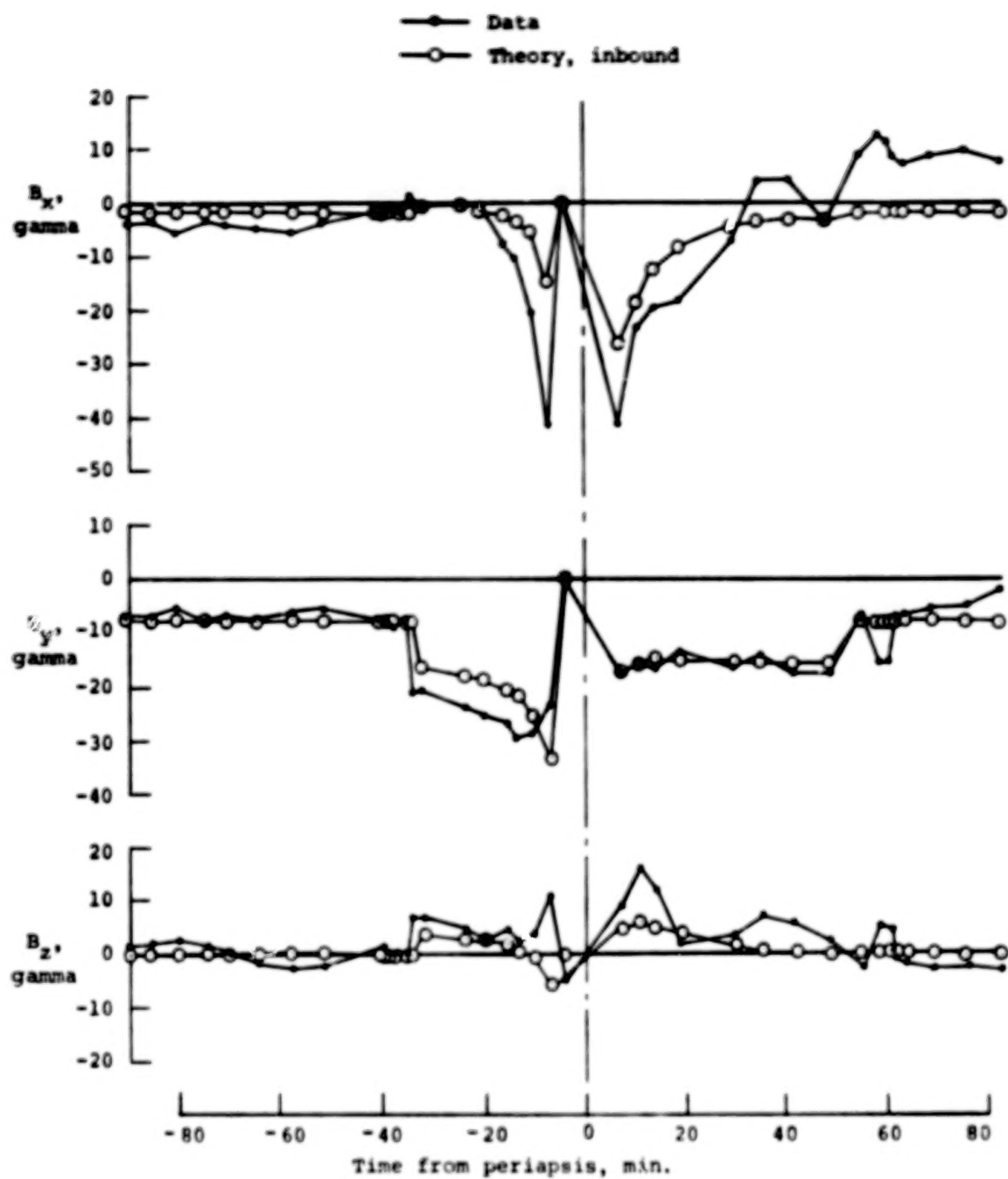
# Interplanetary Conditions

<u>Theory</u>	<u><math>M_\infty</math></u>	<u><math>\gamma</math></u>	<u><math>\Omega</math></u>	<u><math>\phi_P</math></u>	<u><math>B_{x_\infty}</math></u>	<u><math>B_{y_\infty}</math></u>	<u><math>B_{z_\infty}</math></u>
—○— Inbound	3.0	5/3	$3.3^\circ$	$0.15^\circ$	-1.78	-7.86	0.08



(a) Magnetic-field magnitude.

Figure 20.- Comparison of observed (OMAG) and theoretical time histories of the magnetic field for P-V Orbit 3 based on inbound solar wind interplanetary conditions using a gasdynamic solution for  $M_\infty = 3.0$ ,  $\gamma = 5/3$ .



(b) Magnetic-field components.

Figure 20.- Concluded.

1. Report No. NASA CR-3267		2. Government Accession No.		3. Recipient's Catalog No.	
4. Title and Subtitle APPLICATION OF ADVANCED COMPUTATIONAL PROCEDURES FOR MODELING SOLAR-WIND INTERACTIONS WITH VENUS - THEORY AND COMPUTER CODE				5. Report Date May 1980	
				6. Performing Organization Code 498/C	
7. Author(s) Stephen S. Stahara, Daniel Klenke, Barbara C. Trudinger, and John R. Spreiter				8. Performing Organization Report No. NEAR TR 202	
9. Performing Organization Name and Address Nielsen Engineering & Research, Inc. 510 Clyde Avenue Mountain View, CA 94043				10. Work Unit No.	
				11. Contract or Grant No. NASW-3182	
12. Sponsoring Agency Name and Address National Aeronautics and Space Administration Washington, DC 20546				13. Type of Report and Period Covered Contractor Report 7/78 - 9/79	
				14. Sponsoring Agency Code	
15. Supplementary Notes  NASA Headquarters Technical Monitor: Robert E. Murphy					
16. Abstract <p>Advanced computational procedures are developed and applied to the prediction of solar-wind interaction with nonmagnetic terrestrial-planet atmospheres, with particular emphasis to Venus. The theoretical method is based on a single-fluid, steady, dissipationless, magnetohydrodynamic continuum model, and is appropriate for the calculation of axisymmetric, supersonic, super-Alfvénic solar-wind flow past terrestrial planets. The procedures, which consist of finite-difference codes to determine the gasdynamic properties and a variety of special-purpose codes to determine the frozen magnetic field, streamlines, contours, plots, etc. of the flow, are organized into one computational program which has been extensively documented and is presented in a general user's manual included as part of this report.</p> <p>Theoretical results based upon these procedures are reported for a wide variety of solar-wind conditions and ionopause obstacle shapes. Plasma and magnetic-field comparisons in the ionosheath are also provided with actual spacecraft data obtained by the Pioneer-Venus Orbiter. These results have verified the appropriateness of the basic theoretical model, and have indicated the importance of accounting for the variable oncoming direction of the interplanetary solar wind.</p>					
17. Key Words (Suggested by Author(s)) Solar-Wind/Ionosphere Interaction Finite-Difference Methods Steady Flow Frozen Magnetic Field			18. Distribution Statement Unclassified - Unlimited  Subject Category 92		
19. Security Classif. (of this report) Unclassified		20. Security Classif. (of this page) Unclassified		21. No. of Pages 316	
				22. Price* \$11.75	



**END**

*July 2, 1981*